UNIVERSITAT DE BARCELONA

New ORR electrocatalysts and Cu-based MOFs for advanced treatment of pharmaceuticals by electro-Fenton process at near-neutral pH

Lele Zhao

Aquesta tesi doctoral està subjecta a la llicència ***Reconeixement- NoComercial – SenseObraDerivada 4.0. Espanya de Creative Commons***.

Esta tesis doctoral está sujeta a la licencia ***Reconocimiento - NoComercial – SinObraDerivada 4.0. España de Creative Commons***.

This doctoral thesis is licensed under the ***Creative Commons Attribution-NonCommercial-NoDerivs 4.0. Spain License***.

New ORR Electrocatalysts and Cu-Based MOFs for Advanced Treatment of Pharmaceuticals by Electro-Fenton Process at Near-Neutral pH

Lele Zhao

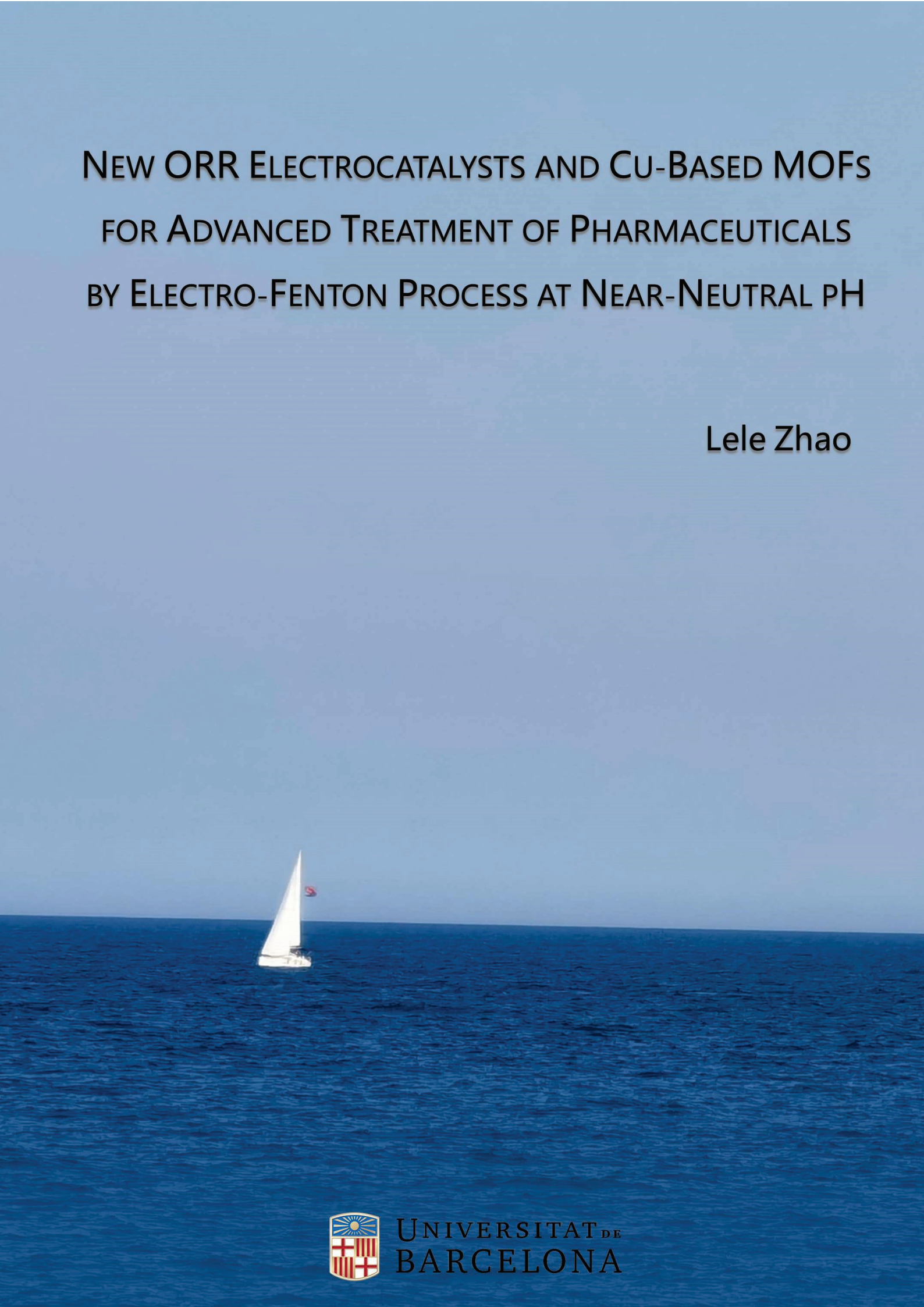

Universitat de Barcelona

UNIVERSITAT DE BARCELONA

Programa de Doctorat en

Electroquímica. Ciència i Tecnologia

NEW ORR ELECTROCATALYSTS AND CU-BASED MOFS FOR ADVANCED TREATMENT OF PHARMACEUTICALS BY ELECTRO-FENTON PROCESS AT NEAR-NEUTRAL pH

Memòria presentada per optar al

Grau de Doctor per la Universitat de Barcelona

Lele Zhao

Director and Tutor

Dr. Ignacio Sirés Sadornil

Professor Agregat

Barcelona, Desembre de 2024

Programa de Doctorat en

Electroquímica. Ciència i Tecnologia

Nous Electrocatalitzadors per ORR i MOFs de Cu per al Tractament Avançat de Fàrmacs Mitjançant el Procés Electro-Fenton a pH Neutre

Memòria presentada per optar al

Grau de Doctor per la Universitat de Barcelona

Lele Zhao

Director and Tutor

Dr. Ignacio Sirés Sadornil

Professor Agregat

Barcelona, Desembre de 2024

If your efforts keep at high level, your future will be close to your ideal.

—— Ignacio Sirés Sadornil

致我亲爱的家人

Acknowledgements

I would like to express my sincere gratitude to my supervisor, Prof. Ignacio Sirés Sadornil for his guidance and trust in me throughout the development of this Thesis. His professionalism and thoroughness for scientific research have been the main driving force that has inspired me towards the fulfilment of this Thesis. I would like to thank Prof. Pere Lluís Cabot Julià as well for his interest in sharing with me his deep knowledge and experience, and Prof. Elvira Gómez for her helpful advice and carefulness over all these years. In addition, I would like to express my gratitude to other professors from our Physical Chemistry section at the Faculty of Chemistry. Moreover, I would also like to thank in advance the jury members for their acceptance and the valuable suggestions that they will for sure make during my defense.

A warm acknowledgment is also to Prof. Christian Durante, for hosting my stay at the University of Padova. His expertise greatly expanded my knowledge of electrochemical characterization. I am also thankful to Prof. Zhihong Ye for providing me the opportunity to visit Chongqing University. His insights and encouragement significantly enhanced my understanding of materials science and cell design. I deeply appreciate the kindness and assistance of the colleagues I met during my stays.

My very sincere thanks also go to all the colleagues at LEMMA group. They have contributed very significantly to my personal and professional growth along these years: Roger, Júlia, Paola, Murilo, Benjamin, Fernanda, Oscar, Karen, Fengxia, Louidi, Matheus, Ferran, Diego, Yuhang, Wang, Pan, Huizhong, Patricia…Without their help and support, this Thesis would have been a much harder path.

A special thanks to my family and Jingjing, who have supported me unconditionally all this time, including those periods that were not always easy. Their support has driven me through all the difficulties that appeared from time to time, becoming a cornerstone to successfully finish my PhD Thesis.

Last, I would like to thank the China Scholarship Council for awarding the scholarship to support my PhD study for four years.

Abstract

Global water crisis has compelled the search for unconventional water resources to meet growing demands. Wastewater, being abundant and easily accessible, is increasingly recognized as resource with great added value. However, the presence of pharmaceuticals in certain wastewater, such as that from urban stations, poses a significant challenge to its efficient and safe reuse. These pollutants, primarily originating from the extensive use of pharmaceuticals at global scale, are characterized by high persistence, polarity, and non-biodegradability, making them difficult to remove using traditional treatment methods. Their continuous discharge exacerbates the degradation of ecosystems and entails severe risks to human health. Addressing these challenges necessitates the development of more efficient and environmentally friendly quaternary wastewater treatment technologies, with a particular focus on the complete degradation of pharmaceutical residues.

In recent years, the electrochemical advanced oxidation processes (EAOPs) have garnered considerable attention for wastewater treatment due to their unique characteristics. Among them, the electro-Fenton (EF) process has demonstrated remarkable performance in degrading organic pollutants even in complex mixtures. However, traditional EF systems face practical limitations, such as high operation costs associated with pH adjustment and catalyst deactivation. This Thesis addresses these challenges by investigating two key innovations: (1) The development of highly active and selective electrocatalysts for the two-electron oxygen reduction reaction ($2e^-$ ORR), which is needed for in-situ H_2O_2 electrogeneration to enhance the process viability; and (2) the synthesis of advanced heterogeneous catalysts with core-shell structure and synergistic mechanisms to significantly improve the H_2O_2 activation efficiency while minimizing leaching and secondary pollution. Furthermore, the integration of heterogeneous EF (HEF) process with ceramic membrane (CM) filtration enabled the development of a bifunctional electrified membrane for pollutant degradation in a flow-through reactor. All materials were studied in model solutions, with some trials involving target pharmaceuticals spiked into actual urban wastewater.

For in-situ H_2O_2 electrogeneration, two novel ORR electrocatalysts were

explored. Sn-doped carbon materials synthesized via a direct thermal method exhibited an outstanding $2e^-$ ORR selectivity of 98.0% and an electron transfer number of 2.04. The gas-diffusion electrodes (GDEs) fabricated with these materials achieved a cumulative H_2O_2 concentration of 20.4 mM at low input current under optimal conditions. The appropriate micro-mesopore structure enables the rapid generation and release of H_2O_2, preventing its further oxidation. Under natural pH conditions, the HEF process achieved nearly 100% degradation of antihystamine drug diphenhydramine (DPH) within 120 min. Nitrogen-doped carbons, prepared via pyrolysis of carbon black mixed with melamine, exhibited a pyrrolic nitrogen content of 3.5% and a $2e^-$ ORR selectivity of 95.3%. The resulting GDEs demonstrated superior H_2O_2 production rates as compared to commercial GDEs, reaching 18 mg h^{-1} cm^{-2}, and exhibited exceptional performance at pH 5.9. Additionally, carbon-based GDEs modified with trace amounts of polymethylhydrosiloxane (PMHS) outperformed conventional PTFE-based GDEs in H_2O_2 generation (1874.8 mg L^{-1} vs. 1087.4 mg L^{-1}). Density functional theory (DFT) calculations carried out by collaborators revealed that $-CH_3$ groups confer superhydrophobic properties to the catalytic layer, while Si-H and Si-O-C sites modulate the coordination environment of active carbon centers. These electrocatalysts achieved efficient degradation of multiple micropollutants, underscoring their potential for wastewater treatment.

For H_2O_2 activation, Cu/NC and FeCu/NC catalysts derived from metal-organic frameworks (MOFs) were developed. In HEF treatment using the former material, complete degradation of DPH was achieved at pH 6–8, outperforming homogeneous EF with Fe^{2+} catalyst under acidic conditions in terms of mineralization, since the formation of Fe(III)-carboxylate complexes could be avoided. FeCu/NC catalysts, synthesized using MIL(Fe)-88B as a precursor, exhibited remarkable performance with only 0.05 g L^{-1} catalyst, achieving 100% removal of antihypertensive drug lisinopril (LSN) within 6 min at pH 3 and 75 min at natural pH. The Fe-Cu synergy accelerated the Fe(II) regeneration, while the core-shell structure minimized metal leaching. The catalyst maintained 86.5% degradation efficiency after five cycles, demonstrating remarkable stability and reusability. These Cu-MOF derived catalysts provide efficient and stable solutions for wastewater treatment applications.

Finally, the integration of HEF processes with CM filtration was investigated.

CMs, known for their chemical and mechanical stability, were employed as ideal catalyst supports and filters. The membrane electrode fabricated in this study enabled both in-situ H_2O_2 generation and its immediate activation, allowing the synergistic occurrence of filtration and reaction phenomena. In a flow-through reactor operated in recirculation mode, this setup effectively removed amoxicillin from model solutions, reduced membrane fouling risks, and enhanced the HEF process applicability.

In conclusion, this Thesis offers a set of novel and innovative electrochemical strategies that successfully addressed the challenge of pharmaceutical pollutant removal from wastewater at the laboratory scale. This work has resulted in five scientific publications, along with multiple oral and poster presentations at international conferences. Furthermore, collaborative research conducted in Italy and China for a total of four months has conferred solid training and international experience to the PhD candidate.

Structure of the Thesis

The present Thesis is structured as follows:

CHAPTER 1 introduces the current concerns posed by global hydric stress, which arises from freshwater resources scarcity combined with increasing wastewater generation. More specifically, the challenges posed by the presence of pharmaceutical contaminants in aquatic environments and the potential of advanced electrochemical technologies to address them are conveniently described. The role of the pharmaceutical industry in water contamination, the ecological impacts of pharmaceutical residues, and the limitations of conventional wastewater treatment methods are discussed. The chapter also reviews current legislation on pharmaceuticals in wastewater and gives the fundamentals of EAOPs, particularly the EF process and the ORR for H_2O_2 production. The section concludes by summarizing the recent research on MOFs, particularly on Cu-based MOFs as HEF catalysts, and highlights the opportunity for process intensification upon integration of MOF-derived catalysts into membrane filtration technology.

CHAPTER 2 outlines the foundational framework of this Thesis by presenting the overarching objectives and detailing the specific goals established to achieve them. An overview of the structure and organization of the manuscript is also provided.

CHAPTER 3 provides a comprehensive overview of the materials, methods, and equipment utilized to perform the experimental and computational work, which were essential for obtaining the results discussed throughout this dissertation.

CHAPTER 4 presents the core research outcomes of this Thesis (as illustrated in **Figure 1** for an easier identification of the work performed), and the related results can be reviewed more in detail in the five scientific articles related to the Thesis. Sn-doped, N-doped, and polymethylhydrosiloxane (PMHS)-modified carbon electrocatalysts were synthesized, achieving high ORR activity and selectivity, as well as efficient H_2O_2 production in bulk electrolytic trials. Cu-based MOFs were also investigated as heterogeneous catalysts, demonstrating superior performance in the HEF process at natural (i.e., near-neutral) pH, avoiding common limitations of conventional homogeneous EF systems. Moreover, the ORR performance of Cu-based MOF derivatives was briefly explored. Additionally, a FeCu/NC bimetallic catalyst exhibited much stronger leaching resistance and high catalytic efficiency in degrading

pharmaceuticals through HEF process, with high stability over multiple cycles. These findings advance sustainable wastewater treatment technologies through the design and optimization of novel electrocatalysts and electrochemical processes. To conclude, a step forward towards the scale-up of robust and reliable technology has been made by investigating the performance of a continuous-flow electrochemical reactor equipped with an electrified CM modified with a SAC.

Finally, **CHAPTER 5** summarizes the conclusions achieved in the Thesis and offers some prospects for future work.

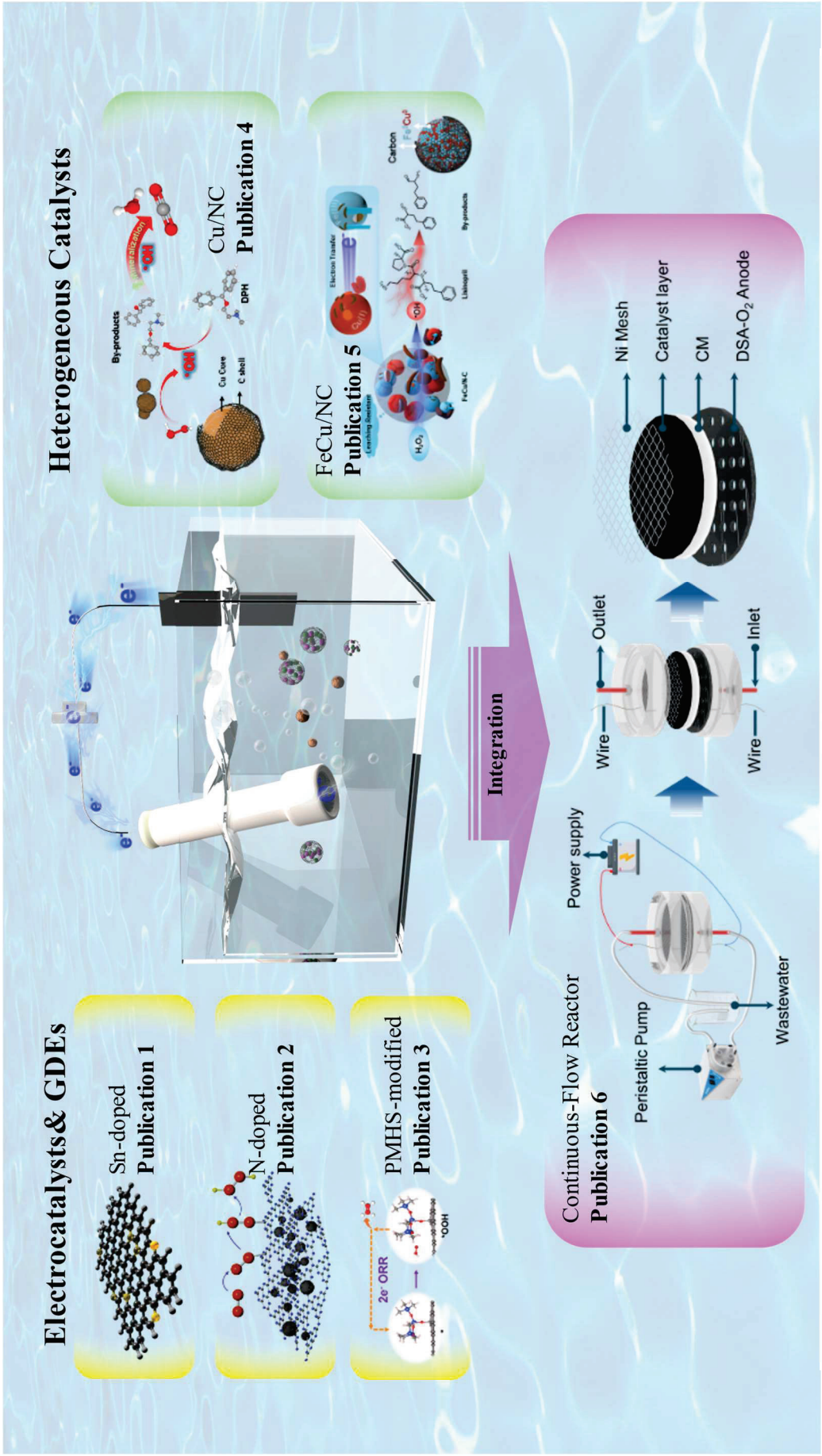

Figure 1. Scheme of the core research outcomes of this Thesis. Note that publication 6 is in preparation at this moment.

TABLE OF CONTENTS

ABSTRACT **iii**

STRUCTURE OF THE THESIS **vii**

List of Equations and Reactions **xv**

List of Acronyms **xix**

List of Symbols **xxiii**

CHAPTER 1. INTRODUCTION **1**

1.1 Pharmaceuticals in the aquatic environment 1

1.1.1 Water and wastewater 1

1.1.2 The pharmaceutical industry 10

1.1.3 Pharmaceutical residues as water contaminants 14

1.1.4 Legislation on pharmaceuticals in wastewater 22

1.1.5 Target organic pollutants of interest in this Thesis: an overview on their occurrence and treatment 25

1.2 Electrochemical advanced oxidation processes (EAOPs) 30

1.2.1 Overview of AOPs 30

1.2.2 Electro-oxidation (EO) process 40

1.2.3 Homogeneous electro-Fenton (EF process) 43

1.2.4 Heterogeneous electro-Fenton (HEF process) 46

1.3 Oxygen reduction reaction (ORR) 51

1.3.1 Fundamentals of the ORR 51

1.3.2 Metal-based electrocatalysts for ORR 56

1.3.3 Metal-free electrocatalysts for ORR 60

1.3.4 Development of cathodes for H_2O_2 electrogeneration 62

1.3.5 Gas-diffusion electrodes 65

1.4 Metal-organic frameworks (MOFs) in HEF process 69

1.4.1 MOFs for cathodic H_2O_2 electrogeneration 72

1.4.2 MOF-based suspended HEF catalysts 74

1.4.3 Cu-based materials as electrocatalysts and HEF catalysts 79

1.5 Electrified membranes 81

CHAPTER 2. OBJECTIVES **89**

CHAPTER 3. MATERIALS, METHODS, AND THEORY **95**

3.1 Chemicals 95
3.2 Water matrices 96
3.3 Cathode materials and heterogeneous catalysts 97
3.3.1 Synthesis of catalysts and preparation of GDEs 98
3.3.2 Characterization 104
3.4 Experimental setup for electrolytic assays 113
3.5 Analytical methods and equipment 116
3.5.1 Quantification of organic pollutants 116
3.5.2 Total organic carbon (TOC) 117
3.5.3 Spectrophotometric quantification of H_2O_2, active chlorine, and iron ions 117
3.5.4 Chromatography combined with mass spectrometry 119
3.5.5 Other analyses 120
3.6 Electrochemical characterization 120
3.6.1 Phenomena affecting the electrochemical reactivity in heterogeneous electrocatalysis 120
3.6.2 Cyclic voltammetry 123
3.6.3 Linear sweep voltammetry 125
3.6.4 Electrochemical impedance spectroscopy 128
3.6.5 Chronoamperometry 129
3.7 Computational 130
3.8 Analysis of performance 131
CHAPTER 4. RESULTS AND DISCUSSION 135
4.1 Development of high-performance electrocatalysts and GDEs for enhanced ORR 137
4.1.1 Boosting the O_2-to-H_2O_2 selectivity using Sn-doped carbon electrocatalysts: Towards highly efficient cathodes for actual water decontamination 137
4.1.2 Complete antihistamine degradation in wastewater matrix using a metal-free N-doped carbon with superior electrocatalytic performance for in-situ H_2O_2 production 167
4.1.3 Polymethylhydrosiloxane-modified gas-diffusion cathode for more efficient and durable H_2O_2 electrosynthesis in the context of water treatment 191

4.2 Cu-based MOFs as efficient and stable catalysts in HEF process 213
4.2.1 Enhanced mineralization of pharmaceutical residues at circumneutral pH by heterogeneous electro-Fenton-like process with Cu/C catalyst 213
4.2.2 Bimetallic FeCu-MOF derivatives as heterogeneous catalysts with enhanced stability for electro-Fenton degradation of lisinopril 237
4.3 Ceramic membrane-confined FeCu/NC catalyst for robust flow-through wastewater treatment by electro-Fenton process 261
CHAPTER 5. CONCLUSIONS AND PERSPECTIVES 271
5.1 Conclusions 271
5.2 Perspectives 275
Resum 279
References 283
Publications and Meetings 339

List of Equations and Reactions

(No.)	*Equation / Reaction*
(1)	Pharmaceutical + hv → Pharmaceutical*
(2)	Pharmaceutical* + hv → DPs
(3)	Photocatalyst + hv → $e_{CB}^- + h_{VB}^+$
(4)	$h_{VB}^+ + H_2O \rightarrow H^+ + {}^\bullet OH$
(5)	$h_{VB}^+ + OH^- \rightarrow {}^\bullet OH$
(6)	$e_{CB}^- + H_2O_2 \rightarrow {}^\bullet OH + OH^-$
(7)	$e_{CB}^- + HSO_5^- \rightarrow SO_4^{\bullet-} + OH^-$
(8)	$e_{CB}^- + HSO_5^- \rightarrow SO_4^{2-} + OH^-$
(9)	$e_{CB}^- + S_2O_8^{2-} \rightarrow SO_4^{2-} + SO_4^{\bullet-}$
(10)	$O_3 + hv \rightarrow O_2 + {}^1O$
(11)	${}^1O + H_2O \rightarrow 2\ {}^\bullet OH$
(12)	$O_3 + H_2O \rightarrow O_2 + H_2O_2$
(13)	$H_2O_2 + hv \rightarrow 2\ {}^\bullet OH$
(14)	$Fe^{2+} + O_3 \rightarrow FeO^{2+} + 2O^\bullet$
(15)	$FeO^{2+} + H_2O \rightarrow Fe^{3+} + {}^\bullet OH + –OH$
(16)	Pharmaceutical +))) → degradation products
(17)	H_2O +))) → ${}^\bullet OH + {}^\bullet H$
(18)	Pharmaceutical + ${}^\bullet OH$ → degradation products
(19)	$Fe^{2+} + H_2O_2 + H^+ \rightarrow Fe^{3+} + {}^\bullet OH + H_2O$
(20)	${}^\bullet OH + H_2O_2 \rightarrow HO_2^\bullet + H_2O$
(21)	$Fe^{3+} + {}^\bullet OH \rightarrow Fe^{2+} + OH^-$
(22)	$Fe^{3+} + H_2O_2 \rightarrow Fe^{2+} + HO_2^\bullet + H^+$
(23)	${}^\bullet OH + {}^\bullet OH \rightarrow H_2O_2$
(24)	$S_2O_8^{2-} + hv \rightarrow 2SO_4^{\bullet-}$
(25)	$SO_4^{\bullet-} + H_2O \rightarrow {}^\bullet OH + SO_4^{2-}$
(26)	$S_2O_8^{2-}$ + heat → 2 $SO_4^{\bullet-}$
(27)	$Fe^{2+} + S_2O_8^{2-} \rightarrow Fe^{3+} + SO_4^{\bullet-} + SO_4^{2-}$
(28)	$Cu^{2+} + S_2O_8^{2-} \rightarrow Cu^{3+} + SO_4^{\bullet-} + SO_4^{2-}$
(29)	$S_2O_8^{2-} + AC \rightarrow SO_4^{\bullet-} + HO^- + AC^+$
(30)	$S_2O_8^{2-} + US \rightarrow 2SO_4^{\bullet-}$

(31) $HSO_5^- + \text{activation condition} \rightarrow SO_4^{\bullet-} + {}^{\bullet}OH$

(32) $M + \text{Pharmaceutical} \rightarrow M({}^{\bullet}\text{Pharmaceutical}) + ne^- \rightarrow \text{Products}$

(33) $M + H_2O \rightarrow M({}^{\bullet}OH) + H^+ + e^-$

(34) $2Cl^- \rightarrow Cl_2 + 2e^-$

(35) $Cl_2 + H_2O \leftrightarrow HClO + H^+ + Cl^-$ (acidic medium)

(36) $Cl_2 + 2OH^- \leftrightarrow ClO^- + Cl^- + H_2O$ (alkaline medium)

(37) $M({}^{\bullet}OH) \rightarrow MO + H^+ + e^-$

(38) $MO + R \rightarrow M + RO$

(39) $MO \rightarrow M + ½\ O_2$

(40) $M({}^{\bullet}OH) + R \rightarrow M + mCO_2 + nH_2O + H^+ + e^-$

(41) $M({}^{\bullet}OH) \rightarrow M + ½\ O_2 + H^+ + e^-$

(42) $Fe^{3+} + e^- \rightarrow Fe^{2+}$

(43) $Fe(II)\text{-}EDTA + H_2O_2 \rightarrow Fe(III)\text{-}EDTA + {}^{\bullet}OH + OH^-$

(44) $Fe(II)\text{-}EDDS + H_2O_2 \rightarrow Fe(III)\text{-}EDDS + {}^{\bullet}OH + OH^-$

(45) $Fe(III)\text{-}EDDS + H_2O_2 \rightarrow Fe(II)\text{-}EDDS + O_2^{\bullet-} + 2H^+$

(46) $Fe(II) + H_2O_2 \rightarrow Fe(III) + {}^{\bullet}OH + OH^-$

(47) $Fe(II)\text{-}OH + H_2O_2 \rightarrow Fe(II)\text{-}OH(H_2O_2)_s$

(48) $Fe(III)\text{-}OH + H_2O_2 \rightarrow Fe(III)\text{-}OH(H_2O_2)_s$

(49) $Fe(II)\text{-}OH(H_2O_2)_s \rightarrow Fe(III)\text{-}OH + {}^{\bullet}OH + OH^-$

(50) $Fe(III)\text{-}OH(H_2O_2)_s \rightarrow Fe(II)\text{-}OH(HO_2^{\bullet})_s + H^+$

(51) $Fe(III)\text{-}OH(HO_2^{\bullet})_s \rightarrow Fe(II)\text{-}OH + HO_2^{\bullet}$

(52) $Fe(III) + H_2O_2 \rightarrow Fe(II) + HO_2^{\bullet} + H^+$

(53) $HO_2^{\bullet} + Fe(III) \rightarrow Fe(II) + H^+ + O_2$

(54) $Fe(III)\text{-}OH + e^- \rightarrow Fe(II)\text{-}OH$

(55) $Fe(III) + e^- \rightarrow Fe(II)$

(56) $O_2 + 2H^+ + 2e^- \rightarrow H_2O_2$

(57) $O_2 + 4H^+ + 4e^- \rightarrow 2\ H_2O$

(58) $O_2 + H_2O + 2e^- \rightarrow HO_2^- + OH^-$

(59) $HO_2^- + H_2O + 2e^- \rightarrow 3OH^-$

(60) $O_2 + 2H_2O + 4e^- \rightarrow 4OH^-$

(61) $O_2 + 2(H^+ + e^-) \rightarrow OOH^* + (H^+ + e^-) \rightarrow H_2O_2$

(62) $O_2 + 4(H^+ + e^-) \rightarrow OOH^* + 3(H^+ + e^-) \rightarrow O^* + 2(H^+ + e^-)$
$\rightarrow OH^* + (H^+ + e^-) \rightarrow H_2O$

(63) $H_2O_2 \rightarrow O_2 + 2H^+ + 2e^-$

(64) $2H_2O_2 \rightarrow 2H_2O + O_2$

(65) $H_2O_2 + e^- \rightarrow OH^- + {}^{\bullet}OH$

(66) $M^{(n-1)+} + H_2O_2 + H^+ \rightarrow M^{n+} + H_2O + {}^{\bullet}OH$

(67) Target pollutant removal (in %) = $(1-\frac{C}{C_0})\times 100$

(68) TOC removal (in %) = $(1-\frac{TOC}{TOC_0})\times 100$

(69) $Ti^{4+} + H_2O_2 + 2SO_4^{2-} \rightarrow (TiO_2(SO_4)_2)^{2-} + 2H^+$

(70) $O_{ads} + ne^- \leftrightarrows R_{ads}$

(71) $J = -D\frac{dc}{dx} - \frac{zF}{RT}Dc\frac{d\Phi}{dx} + cv$

(72) $E(t) = E_i - vt$ for $0 < t < \lambda$

(73) $E(t) = E_i - 2v\lambda + vt$ for $t > \lambda$

(74) $I_{cap} = C_{dl} \times v$

(75) $ECSA = C_{dl} / C_s$

(76) $n = \frac{4I_d}{I_d + I_r/N}$

(77) $\%H_2O_2 = \frac{I_r/N}{I_d + I_r/N} \times 200$

(78) $\eta = a + b \log j$

(79) CE (in %) = $\frac{2F[H_2O_2]V}{1000M(H_2O_2)Q} \times 100$

(80) $C_{17}H_{12}NO{\bullet}HCl + 36H_2O \rightarrow 17CO_2 + Cl^- + NO_3^- + 96H^+ + 94e^-$

(81) $C_{21}H_{31}N_3O_5 + 29H_2O \rightarrow 21CO_2 + 3NO_3^- + 59H^+ + 57e^-$

(82) $C_{16}H_{19}N_3O_5S + 23H_2O \rightarrow 16CO_2 + 3NO_3^- + SO_4^{2-} + 45H^+ + 44e^-$

List of Acronyms

AC	Activated Carbon
ACFs	Activated Carbon Fibers
AOPs	Advanced Oxidation Processes
APIs	Active Pharmaceutical Ingredients
BDD	Boron-doped Diamond
BET	Brunauer-Emmett-Teller
BOD	Biological Oxygen Demand
BPA	Bisphenol A
CAGR	Compound Annual Growth Rate
CB	Carbon Black
CE	Current Efficiency (except Fig. 44, meaning Counter Electrode)
CF	Carbon Felt
CL	Catalytic Layer
CMs	Ceramic Membranes
CNTs	Carbon Nanotubes
COD	Chemical Oxygen Demand
CTAB	Cetyltrimethylammonium Bromide
CV	Cyclic Voltammetry
DDD	Defined Daily Dose
DFT	Density Functional Theory
DLS	Dynamic Light Scattering
DOC	Dissolved Organic Carbon
DRT	Distribution of Relaxation Times
DSA	Dimensionally Stable Anode
EA	Elemental Analysis
EAOPs	Electrochemical Advanced Oxidation Processes
ECs	Emerging Contaminants
ECSA	Electrochemical Active Surface Area
EDDS	Ethylenediamine-N,N'-Disuccinic Acid
EDS	Energy Dispersive X-ray Spectroscopy
EDTA	Ethylenediaminetetraacetic Acid

EEGr	Electrochemically Exfoliated Graphene
EF	Electro-Fenton
EFCCM	Electro-Fenton Catalytic Ceramic Membrane
EIS	Electrochemical Impedance Spectroscopy
EO	Electro-oxidation
FO	Forward Osmosis
FT-IR	Fourier Transform Infrared Spectroscopy
FWHM	Full Width at Half Maximum
GAC	Granular Activated Carbon
GC-MS	Gas Chromatography-Mass Spectrometry
GDEs	Gas-Diffusion Electrodes
GDL	Gas-Diffusion Layer
GF	Graphite Felt
GGA	Generalized Gradient Approximation
GO	Graphene Oxide
GWI	Global Water Intelligence
HEF	Heterogeneous electro-Fenton
HPLC	High-performance Liquid Chromatography
ICP	Inductively Coupled Plasma
LC-MS	Liquid Chromatography-Mass Spectrometry
LOEC	Lowest Observed Effect Concentration
LSV	Linear Sweep Voltammetry
MBR	Membrane Bioreactor
MF	Microfiltration
MOFs	Metal-Organic Frameworks
MOE	Ministry of the Environment
NADEs	Natural Air-Diffusion Electrodes
NC	Nitrogen-Doped Carbon
NF	Nanofiltration
NP	Nonylphenol
NPOC	Non-Purgeable Organic Carbon
NSAIDs	Non-Steroidal Anti-Inflammatory Drugs
OCNTs	Oxidized Carbon Nanotubes
OER	Oxygen Evolution Reaction

OFGs	Oxygen Functional Groups
ORR	Oxygen Reduction Reaction
PAC	Powdered Activated Carbon
PAW	Projector Augmented Wave
PBE	Perdew-Burke-Ernzerhof
PC	Porous Carbon
PDA	Photodiode Array Detector
PEF	Photoelectro-Fenton
PPCPs	Pharmaceuticals and Personal Care Products
PTFE	Polytetrafluoroethylene
RCPs	Representative Concentration Pathways
RCS	Reactive Chlorine Species
RE	Reference Electrode
RHE	Reversible Hydrogen Electrode
rGO	Reduced Graphene Oxide
RO	Reverse Osmosis
ROS	Reactive Oxygen Species
RRDE	Rotating Ring-Disk Electrode
RVC	Reticulated Vitreous Carbon
SACs	Single-Atom Catalysts
SDGs	Sustainable Development Goals
SEM	Scanning Electron Microscopy
SHE	Standard Hydrogen Electrode
SMX	Sulfamethoxazole
SSPs	Socio-Economic Pathways
TC	Total Carbon
TEM	Transmission Electron Microscopy
TN	Total Nitrogen
TOC	Total Organic Carbon
TPB	Three-Phase Interface/Boundary
UASB	Up-flow Anaerobic Sludge Blanket
UCMSs	Unsaturated Coordinated Metal Sites
UF	Ultrafiltration
US	Ultrasound

USGS	U.S. Geological Survey
UV	Ultraviolet
VASP	Vienna Ab initio Simulation Package
WE	Working Electrode
WHO	World Health Organization
WWTPs	Wastewater Treatment Plants
XAS	X-ray Absorption Spectroscopy
XPS	X-ray Photoelectron Spectroscopy
XRD	X-ray Powder Diffraction
ZIFs	Zeolitic Imidazolate Frameworks

List of Symbols

Symbol	*Meaning*	*Units*
C_{dl}	Double-layer capacitance	F
C_s	Specific capacitance	F cm^{-2}
E^0	Standard electrode potential	V
E_f	Final potential	V
E_i	Initial potential	V
E_{onset}	Onset potential	V
E_p	Peak potential	V
F	Faraday constant	C mol^{-1}
h	Planck's constant	(6.626×10^{-34}) J·s
I_d	Disk current	mA
I_r	Ring Current	mA
j_{cap}	Capacitive current density	mA cm^{-2}
j_p	Peak current density	mA cm^{-2}
n	Number of transferred electrons	-
N	Collection efficiency (RRDE)	%
p	System pressure	Pa
p/p^0	Relative pressure	-
p^0	Saturation pressure	Pa
Q	Electric Charge	C
R_{ct}	Charge transfer resistance	Ω
S_{BET}	Surface area from BET model	m^2 g^{-1}
S_{meso}	Total surface area of mesopores	m^2 g^{-1}
S_μ	Total surface area of micropores	m^2 g^{-1}
v	Scan rate	mV s^{-1}
V_{meso}	Total volume of mesopores	cm^3 g^{-1}
V_{tot}	Total pore volume	cm^3 g^{-1}
V_μ	Total volume of micropores	cm^3 g^{-1}
ε_λ	Molar absorptivity	L mol^{-1} cm^{-1}
η	Overpotential	V
λ	Wavelength	nm

Φ	Quantum yield	%
ω	Rotation speed	rpm

Chapter 1

Introduction

CHAPTER 1. Introduction

1.1 Pharmaceuticals in the aquatic environment

1.1.1 Water and wastewater

Water nourishes the Earth and is the support of life. It is the most abundant component of living organisms, essential for their survival, acting as a solvent that dissolves electrolytes and other vital components within the body. It becomes the environment of complex metabolic reactions in the living bodies, facilitating the transport of essential nutrients, metabolic waste products, and endocrine substances such as hormones [1]. Furthermore, its high thermal conductivity and specific heat capacity endow a heat transfer capability that enables heat flow through human skin, which helps regulating the body temperature and maintaining homeostasis [2]. Beyond its indispensable biological functions, water is also essential for plant growth and agricultural productivity, as it is widely used to irrigate farmland.

Additionally, water plays a pivotal role in various industrial processes, where it is utilized to cool machinery, manufacture a broad spectrum of chemicals, and clean a wide range of products. This is a clear evidence of the multifaceted importance of water, encompassing biological, agricultural, and industrial realms. Clean water is crucial for the sustainable development, socio-economic growth, energy and food production, ecosystem balance, factors that determine the survival of humankind [3]. Water is actually the nexus between society and the environment. Competing commercial demands on water resources increase with population, making it imperative to balance these needs to ensure that individual communities are adequately supported. Therefore, it is essential that water resources are valued, managed smartly, and safeguarded, thus ensuring their sustainable use for preserving the ecosystems and human life.

Approximately, 71% of the Earth's surface is covered by water, yet 80% of the ocean floor remains unmapped and unexplored, highlighting the vast unknowns in our global water resources. The total volume of Earth's water resources is around 1,386 million km^3 [4]; nonetheless, despite this abundance of water, the portion available for human use is extremely limited. Up to 97% of the

Earth's total water is saline, primarily found in the oceans, making it unsuitable for direct drinking or agricultural irrigation. The remaining 3% is freshwater, essential for life but not evenly distributed or readily accessible. This freshwater is mostly trapped in glaciers and polar ice caps (69%), often in remote and cold regions that are difficult to reach and exploit. Another 30% of freshwater exists as groundwater, a crucial resource that requires complex extraction methods and is vulnerable to over-exploitation (i.e., over-pumping), leading to environmental issues such as ground subsidence. The fraction of freshwater directly usable by humans, which is only 1% of the total water on Earth, is found in lakes, rivers, and as shallow groundwater, as shown in Fig. 2 [5].

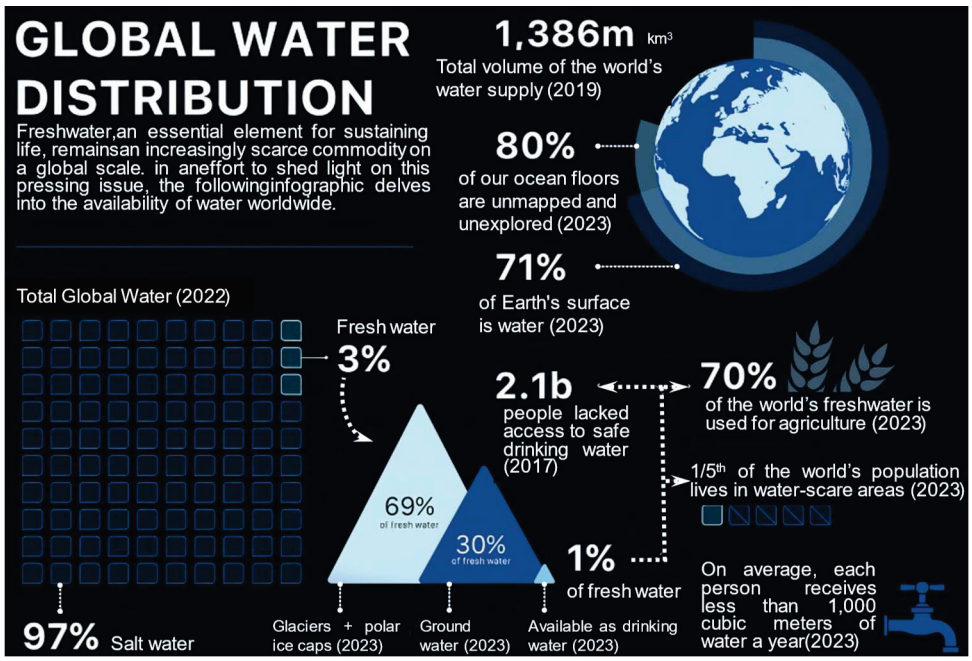

Figure 2. Global water distribution and usage: A 2023 detailed overview [6]. This figure is adapted from an infographic by Chesca Kirkland, with data sourced from Our World in Data, the United Nations, and the U.S. Geological Survey (USGS), as featured by the World Economic Forum.

The accessible freshwater is not only scarce, but it is under tremendous stress due to population growth, industrialization, and increasing agricultural and farm activities. In 2015, the United Nations General Assembly adopted the Sustainable Development Goals (SDGs), which comprise 17 objectives that aimed to promote a more sustainable development by addressing environmental, social, and economic aspects. These goals were announced through the UN 2030 Agenda, which outlines specific actions to ensure their accomplishment by 2030. Notably, the sixth goal, "Clean Water and Sanitation", aims to provide universal access to safe drinking water and sustainable management of freshwater resources and

sanitation facilities [7]. Currently, around 2 billion people worldwide lack access to safe drinking water [8]. At the same time, on average, 70% of the world freshwater is used for agriculture (Fig. 2). More specifically (Fig. 3) [9], in lower-income countries, 90% of water resources are dedicated to agriculture, leaving only 3% for industry and 7% for domestic use. In contrast, in high-income countries, water use is more balanced, with 44% allocated to agriculture, 39% to industry, and 17% to domestic purposes. Upper-middle-income and lower-middle-income countries allocate 66% and 88% of their freshwater to agriculture, respectively, highlighting the global disparity in water use and the critical role of agriculture in water consumption. This intense reliance on agriculture, particularly in lower-income regions, exacerbates water scarcity, especially in areas where the average water availability is lower than 1,000 cubic meters per person per year, affecting about one-fifth of the global population. These challenges underscore the urgency of improving water management practices and advancing wastewater treatment technologies, aiming to eventually mitigate the growing global water scarcity crisis.

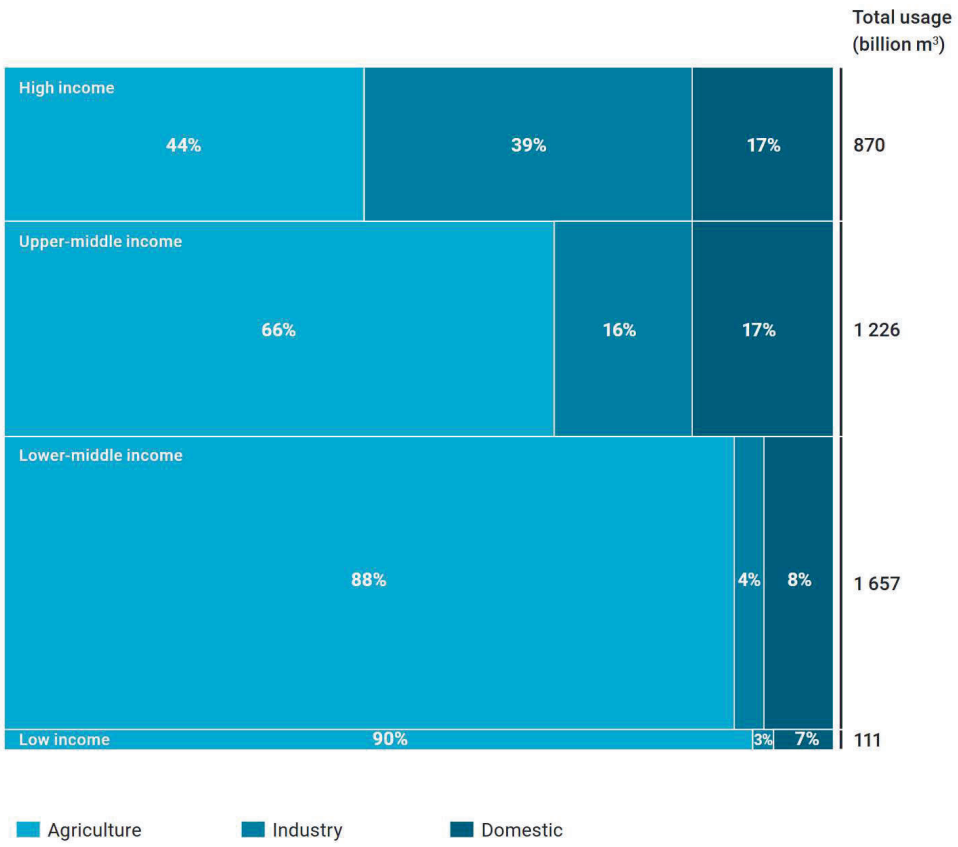

Figure 3. Water withdrawal by sector (percentage of total freshwater withdrawal) by income group (data from year 2020). Source: Kashiwase and Fujs (2023), based on data from the Food and Agriculture Organization of the United Nations (FAO AQUASTAT) [9].

The scarcity of freshwater resources has several negative effects, which have become increasingly noticeable in different regions around the world. For example, drought issues in 2022 led to reduced soil moisture across Europe, with rivers such as the Danube and Rhine facing significant challenges [10]. The water level of the Po River reached a historic minimum, whereas the lack of cooling water causing disruptions in the nuclear power production in France. Water inflows to reservoirs in these areas also decreased. In the United States, the drought caused losses as high as $22 billion due to damages and, moreover, it resulted in 136 deaths. In Africa, 36 million people were affected, with 21 million facing food insecurity. In China, the Yangtze River basin experienced the most severe drought in decades, with a negative impact over nearly 5 million people. Projections of future freshwater distribution are equally worrying; scientific studies have predicted that by the year 2046/2047, the Klang River Basin in Malaysia will face water shortages in most months, and 4 billion people globally will experience severe water shortages for at least one month during the year [11,12]. In addition, about 33% of irrigated farmland and 20% of cropland globally are already affected by soil salinization due to overuse of groundwater and an increase in synthetic wastes, and this percentage is expected to rise significantly by 2050 [13]. A high-resolution analysis conducted by the Pacific Northwest National Laboratory in the USA (Fig. 4) predicts that agricultural, industrial, and domestic water demand will increase dramatically within the period from 2010 to 2100 under various socio-economic and climate change scenarios.

The impacts of freshwater scarcity are not limited to the environment, but they also pose a serious threat to global food safety, human health, and economic stability. By 2050 [14–16], water scarcity is projected to affect 31% of global GDP, estimated at around $70 trillion, a significant increase from 24% in 2010. The number of people affected by extreme water stress is expected to increase by 1 billion, the most affected regions including the Middle East, North Africa, and South Asia, which could lead to widespread economic and political instability. Global water demand is projected to increase by 20-25% from present to the year 2050, with sub-Saharan Africa projected to experience a 163% increase in demand, primarily driven by agricultural activities and household needs. However, 60% of global irrigation intended for agriculture already faces

freshwater scarcity, which puts the sustainability of food production at significant risk. Therefore, the key for addressing these challenges lies in implementing really sustainable water management practices, particularly the use of advanced wastewater treatment technologies that allow conserving, recycling and reusing water in a safe manner for agriculture, industry, and domestic use, thereby alleviating pressure on freshwater supply.

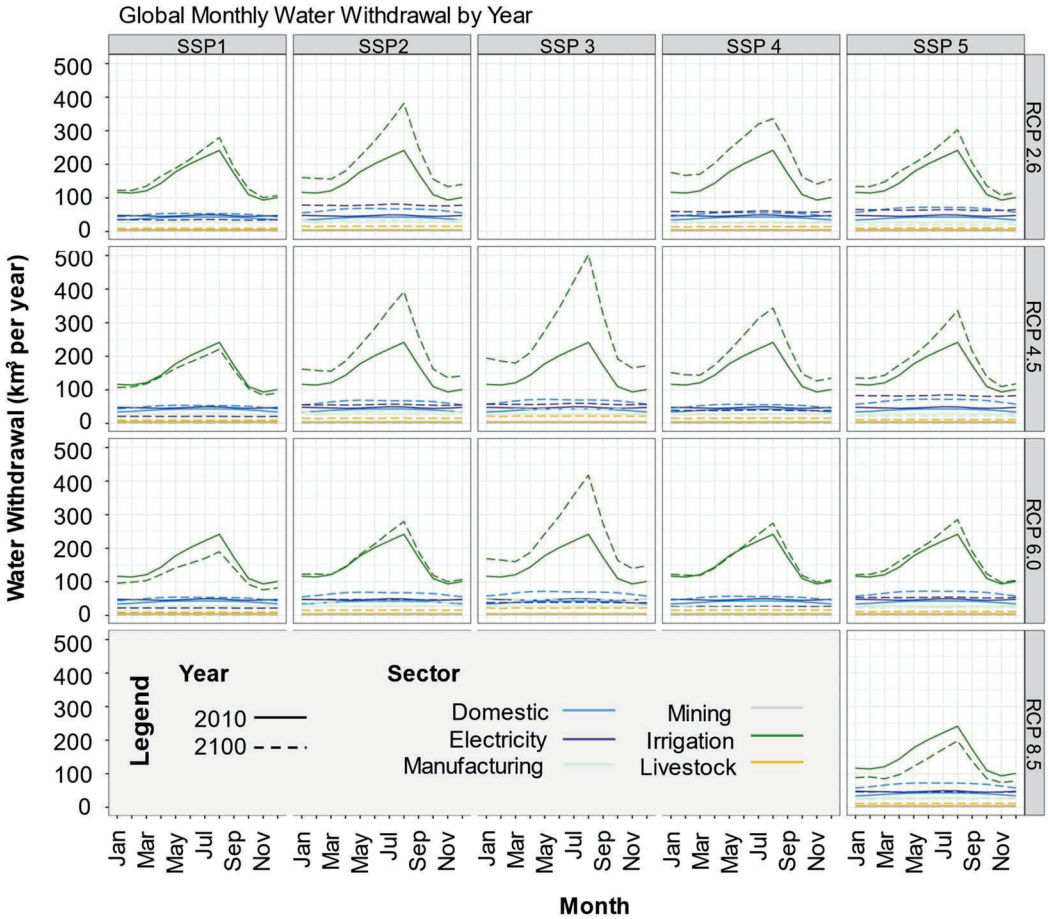

Figure 4. Total annual water withdrawals by sector for different SSP-RCP combinations, projected from year 2010 to 2100. Shared Socio-economic Pathways (SSPs) account for possible socio-economic development scenarios, ranging from low-carbon, highly sustainable development (e.g., SSP1) to high-carbon, fossil fuel-dependent growth paths (e.g., SSP5). Representative Concentration Pathways (RCPs) refer to different greenhouse gas emission concentrations and radiative forcing scenarios. These pathways indicate the level of radiative forcing (i.e., the change in Earth's energy balance caused by factors like greenhouse gases, determining whether the planet warms up or cools down, in W m^{-2}) in the Earth's atmosphere under different greenhouse gas emission scenarios, with higher values of RCP representing higher potential climate change impacts (e.g., RCP 8.5 corresponds to a "high emission" scenario) [17].

The volume of wastewater (i.e., sewage water) generated annually is vast, reaching approximately 380 billion m^3 [18]. However, wastewater treatment and management practices vary considerably across regions (Fig. 5), resulting in diverse environmental and public health challenges. In developed regions such as

North America, Europe, and Australia, where per capita sewage production is high, sewage collection rates are also relatively high, typically treating more than 75% of collected sewage. In contrast, many low- and middle-income countries, such as those in sub-Saharan Africa and South Asia, have lower per capita sewage production and often have sewage collection rates of less than 25%. In these regions, large volumes of sewage are discharged directly into the environment without adequate treatment, which poses serious environmental concerns and public health risks. While some progress has been made in reusing treated sewage, particularly in Europe and Australia, global reuse rates remain low at global scale, and many countries do not fully leverage reclaimed water to alleviate water scarcity. These disparities underscore the critical need for global investment and improvement in wastewater management practices. Effective wastewater treatment and reuse is a smart, relatively recent strategy to significantly reduce the environmental pollution. At present, it plays a key role in addressing the global water crisis by providing a sustainable freshwater source for agriculture, industry, and even drinking water.

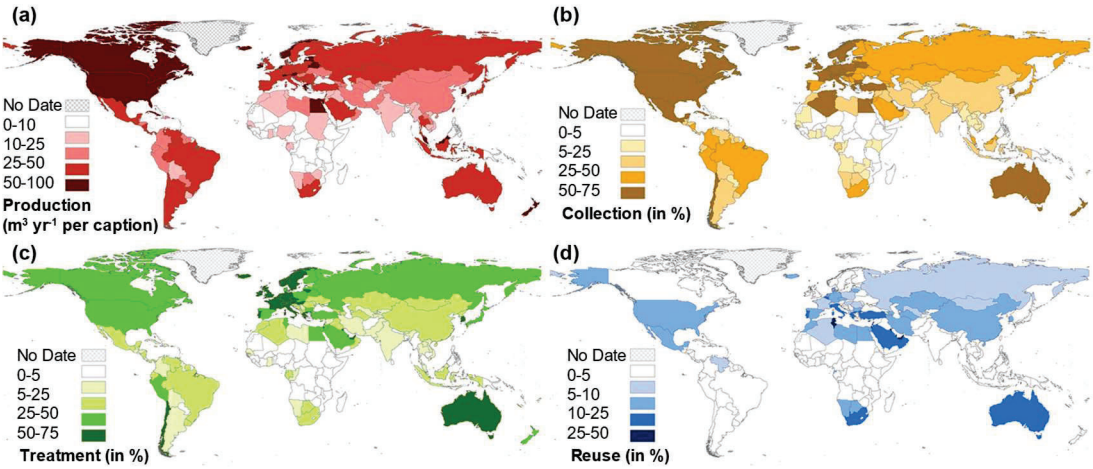

Figure 5. Wastewater in numbers: (a) Production (m^3 yr^{-1} per capita), (b) collection (in %), (c) treatment (in %), and (d) reuse (in %) at the country scale. Sources: Global Water Intelligence (GWI, 2015), the FAO AQUASTAT (2020), Eurostat (Eurostat, 2020), and the United Nations Statistics Division (UNSD, 2020). For consistency, the year 2015 was selected for all wastewater data [19].

Wastewater is liquid waste containing various pollutants from industrial production, domestic sewage, and agricultural drainage. These wastes themselves do not necessarily cause immediate harm to the environment or biological systems. However, when their concentration exceeds the permissible range and negatively affect the ecosystems, water pollution problems are triggered [20]. In

other words, all pollutants are potential sources of pollution, but not all of them bring about pollution problems. Worth noting, since industrialization, water pollution caused by human activities have become increasingly serious, significantly exacerbating global freshwater scarcity [21].

Globally, the main sources of wastewater can be categorized into four main groups: municipal domestic wastewater, industrial wastewater, agricultural runoff, and stormwater runoff [22]. Municipal domestic wastewater comes mainly from daily household activities such as washing, cooking, and sanitary drainage, rich in organic matter, pathogens, and nutrients. This type of wastewater constitutes a major portion of total wastewater in many areas. Industrial wastewater, conversely, comes from large-scale activities such as manufacturing and mining, and usually contains heavy metals, toxic chemicals, and organic solvents. Agricultural runoff, especially during the rainy season, carries nitrogen, phosphorus, and other fertilizers and pesticide residues into water bodies, potentially causing eutrophication. Finally, storm water runoff is a major source of pollution in urban areas, especially during heavy rainfall events, since runoff carries large amounts of pollutants into rivers and lakes [23]. Wastewater contains many inorganic and organic chemicals, toxic metals, aromatic compounds, and dyes, which may contaminate natural resources and interfere with the normal functioning of the ecosystems. In addition, radioactive and acid-base substances are also important components of wastewater; the former mainly come from the operation of nuclear reactors and nuclear power plants, and long-term exposure to these radionuclides may pose serious health risks to living organisms [24,25]; the latter, such as sulfur oxides and nitrogen oxides, may affect the acid-base balance of the water body and damage the ecosystem through acid rain [23].

Aquatic flora and fauna have suffered severe impacts, leading to substantial economic losses. The continued discharge of untreated or improperly treated wastewater into natural water bodies further degrades the aquatic ecosystems, destroys habitats for aquatic organisms, and promotes overgrowths of fungi, bacteria, and algae —especially algal blooms— that block sunlight and nutrient flow, thereby disrupting the ecological balance [26,27]. A more insidious threat is oxygen depletion in these water bodies, creating anoxic environments or 'dead zones' where fish and other aquatic organisms cannot survive [28]. Pollutants like those from oil spills, acids, pesticides, and plastics cause serious physical damage

to aquatic life. Microplastics are particularly harmful, as they can cause mechanical damage to the intestinal lining and may even penetrate the epithelial barrier, entering the lungs, colon, placenta, and bloodstream, thereby posing a health threat to both marine animals and humans [29]. Furthermore, water pollution triggers a chain reaction through the food chain, where animals that rely on fish may become ill or die after consuming contaminated prey.

Similarly, human health may be severely affected by sewage pollution. The large number of pathogenic microorganisms contained in sewage is a major source of waterborne diseases, and these pathogens are transmitted through contaminated water bodies, leading to a wide range of illnesses such as hepatitis, diarrhea, meningitis, poliomyelitis and encephalitis [30,31]. Contaminated water bodies not only directly affect the safety of drinking water but also jeopardize public health by contaminating agricultural irrigation water and fishery resources further into the food chain. For example, contaminated water employed for irrigation may leave harmful microorganism residues on the surface of the crop areas. In contrast, contaminated fishery products may affect higher-order consumers, including humans, through the food chain. In addition, oil spills, as one of the major sources of water pollution, not only damage critical ecosystems such as mangroves and coral reefs but also ultimately threaten human health by contaminating seafood, which may lead to dizziness, nausea, central nervous system damage, and even cancer [32]. Although the frequency of oil spills from tankers has decreased over the past half-century, millions of tons of crude oil still enter the environment through natural seepage each year, posing a long-term threat to ecosystems and human health [33–35]. In addition, the widespread use of pesticides poses an even greater threat to water bodies and human health. Pesticides enter water bodies through runoff, contaminate groundwater and surface water bodies, and not only directly poison aquatic organisms but also lead to long-term exposure of higher-order organisms, including humans, to health risks through bioaccumulation and amplification effects in the food chain. Chronic exposure to pesticides is strongly associated with health problems such as tumor formation and central nervous system disorders [36,37]. Taken together, pathogenic microorganisms in sewage, oil spills, and pesticide contamination together constitute a major threat to global water pollution, which not only has far-reaching impacts on ecosystems but also poses a serious threat to human

health and food security through various pathways. These problems are more serious as contaminants become more concentrated due to water evaporation under higher ambient temperature, and there is an urgent need to strengthen regulation and take effective preventive and control measures to ensure the safety of water bodies and public health.

In addition, the production of synthetic chemicals has increased significantly since the mid-20th century, a phenomenon known as "the second chemical revolution", marking an unprecedented level of development and application of new synthetic chemicals [38]. This growth is reflected in the records of the Chemical Abstracts Service Registry, where the number of registered chemicals increased from 20 million in 2002 to 204 million in 2023, implying that nearly 15,000 new chemicals are registered daily [39]. At the same time, research on genetically engineered microorganisms is increasing significantly. Although these synthetic chemicals and modified microorganisms have made important contributions to human society in drug development, research on advanced materials, and agricultural productivity enhancement, concerns have been raised about the public health and environmental risks they may pose. In particular, newly discovered synthetic or naturally occurring chemical substances and biological agents, which are referred to as emerging contaminants (ECs, the "emergence" of the awareness of emerging contaminants should probably be attributed to Rachel Carson for her 1962 book "Silent Spring"), may pose potential dangers to humans and ecosystems [40,41]. These pollutants include pharmaceuticals and personal care products (PPCPs), perfluoroalkyl substances and poly-fluoroalkyl substances, emerging pathogens, cyanobacterial toxins, other naturally occurring toxins, pesticides, industrial chemicals, micro/nano plastics, nanomaterials, and antibiotic resistance genes, among others [41]. Yet, their impacts on the environment are still poorly understood. These pollutants can enter the environment through industrial emissions, agricultural runoff, and improper waste disposal, thereby contaminating air, water, soil, and food, and may cause secondary contamination in areas far from the source.

Among these ECs, PPCPs are the largest group, covering a large plethora of compounds with different chemical and physical properties. PPCPs are widely used for various daily purposes, including human and animal health care. Currently, more than 50,000 types of PPCPs have been produced globally, with

an annual use of approximately 30 million tons, which is likely to increase yearly [42]. The main families of compounds included among PPCPs include antibiotics, hormones, nonsteroidal anti-inflammatory drugs, anticancer drugs, antiepileptic drugs, antidepressants, and β-blockers, which are widely detected in the environment and their metabolites [43]. This widespread dissemination of pharmaceuticals has become a health concern and is now recognized as a major threat to global public health and to the balance of ecosystems [44].

1.1.2 The pharmaceutical industry

In 1897, the first synthetic drug —aspirin— was introduced [45]. Since then, drug therapy has made significant advancements in addressing a wide range of health issues, including diseases, mental health, and other conditions. Today, more than 200,000 drugs are available on the market that can prevent, treat, and alleviate diseases that were once potentially fatal to earlier generations. Drugs are generally classified based on their mechanism of action (i.e., how they bind to and interact with biological targets), mode of action, chemical structure, and therapeutic use. When categorized by their therapeutic or preventive uses (the pathologies they are intended to treat), common drug categories include antibiotics, sedatives, anti-inflammatory drugs, antivirals, analgesics, antidepressants, cardiovascular drugs, anticoagulants, and beta-blockers, among others (Fig. 6) [46–48].

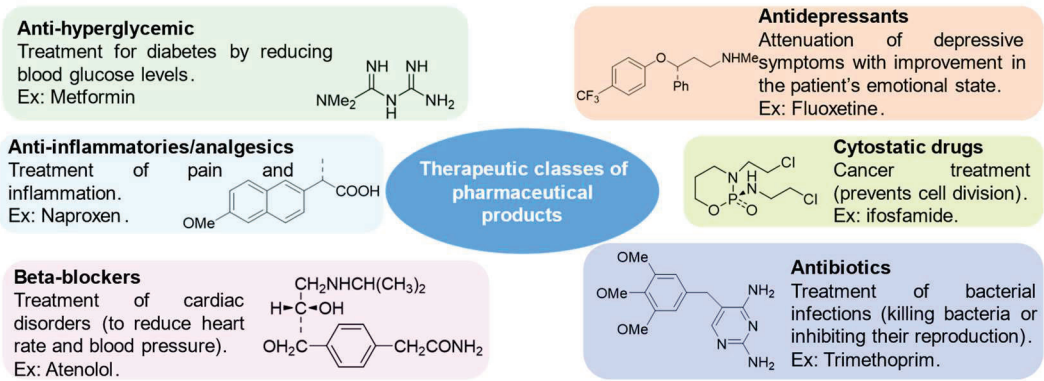

Figure 6. Classification of pharmaceutical products commonly detected in the environment, along with their main intended purpose [48].

The widespread use of pharmaceuticals has significantly improved the quality of human life, particularly in the context of population growth, an aging society, and the increasing prevalence of chronic diseases. This has driven a

continuous rise in global annual drug production and consumption. According to data (Fig. 7) [49], the global annual drug usage increased from 2.96 trillion defined daily doses (DDD) in 2018 to 3.38 trillion DDD in 2023, with an average compound annual growth rate (CAGR) of 2.7%. It is projected that this figure will further rise to 3.78 trillion DDD by 2028. The rapid development of emerging markets, such as China and India, is the primary driver of this growth, with annual growth rates of 3.7% and 3.5%, respectively, in drug usage. Meanwhile, the Latin American market continues to hold a significant share of global drug consumption, with 461 billion DDD in 2023, which is expected to reach 506 billion DDD by 2028. Although the growth rate in Latin America is relatively slower, it still holds a substantial portion of the global pharmaceutical market, especially in the research, development, and application of innovative drugs.

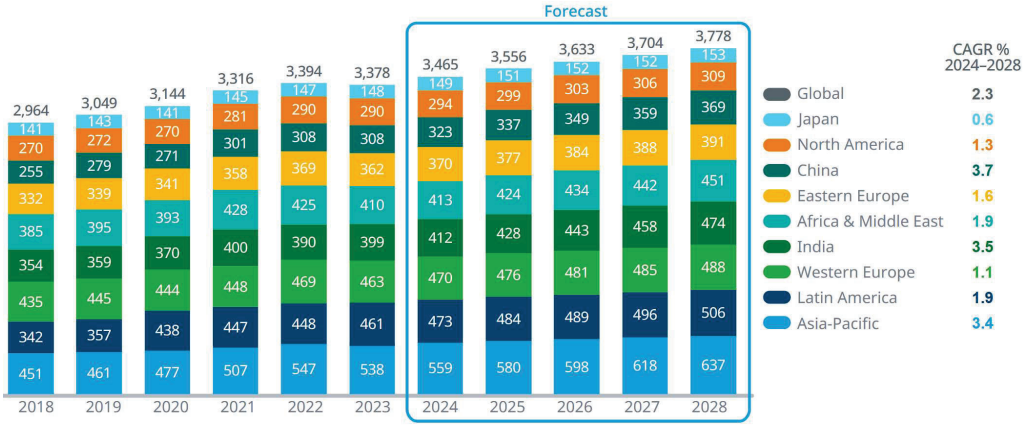

Figure 7. Historical and projected usage of medicines by region, within the period 2018-2028, given as so-called DDD in billions [49].

The global expansion of the pharmaceutical industry is reflected in the growing demand for medications, advancements in production technologies, and the increasing diversity of drug types. With the rapid development of biotechnology, new therapies, such as gene therapy and immunotherapy, have emerged, significantly advancing the treatment of cancer, rare diseases, and chronic conditions. These advances are boosting disease cure rates and impetus to developing emerging drugs. As pharmaceutical production activities gradually shift from developed countries to emerging markets, global drug manufacturing capacity has further increased. For example, countries like China and India have become key hubs for the global pharmaceutical industry, taking on large-scale drug production and becoming frontrunners in the research and development of

innovative medicines.

As global demand for pharmaceuticals continues to rise, both production and consumption within the industry are experiencing sustained growth. This trend is in good agreement with the pursuit of society to achieve a higher quality of life while presenting new challenges for environmental management. Water usage is critical in pharmaceutical production, especially during drug synthesis, material processing, and cooling, where a stable and high-quality water supply is essential. Studies have shown that producing one ton of antibiotics generates between 500 and 6,500 m^3 of wastewater, containing substantially higher organic pollution levels than domestic sewage [50]. Therefore, how to ensure the effective treatment of wastewater while meeting global drug demand has become one of the core challenges faced by the pharmaceutical industry.

Pharmaceutical wastewater primarily originates from process wastewater generated during drug synthesis and formulation processes [51]. Process wastewater refers to water that comes into contact with raw materials, products, intermediates, by-products, or waste during production or processing, and it often contains various pollutants. The main source of these pollutants is the mixture of active pharmaceutical ingredients (APIs), which are produced through organic, inorganic, or biochemical reactions. Due to the multi-product nature of pharmaceutical manufacturing, inefficiencies or overdesign in the reactors and separators often lead to increased wastewater generation. Based on different production processes, the pharmaceutical industry can be divided into four main sub-sectors [52]: fermentation plants, synthetic organic chemical plants, natural/biological product extraction plants (such as antibiotics, vitamins, enzymes), and drug mixing and formulation plants (such as tablets, capsules, and solutions).

Due to the complexity and diversity of substances and reactions involved in pharmaceutical production, the composition and volume of wastewater vary based on geographic location, raw material selection, and seasonal changes, making treatment particularly challenging. As a result, establishing uniform wastewater treatment standards is highly difficult. Currently, pharmaceutical wastewater treatment technologies can be classified into several categories: recycling/recovery of APIs from wash water and solvents, physicochemical treatments (such as precipitation or flotation), biological treatments (such as

membrane bioreactors or aerobic/anaerobic biological processes), advanced oxidation processes (such as UV combined with ozone or hydrogen peroxide), inactivation of infectious and bioactive substances (i.e., disinfection methods), and novel hybrid treatment technologies specifically tailored for the pharmaceutical industry [53].

Recycling is one of the key strategies for treating pharmaceutical wastewater. The pharmaceutical industry uses large quantities of solvents, acids, bases, and other chemical reagents, and many valuable by-products can be reused through wastewater recovery processes. For example, solvents can be recycled and reused in boiler feedwater or cooling tower operations, reducing water consumption. Nanofiltration technology has proven to be an effective method for recovering amoxicillin from pharmaceutical wastewater. Studies have shown that amoxicillin rejection rates ranged from 56.5% to 99.1%, with the highest removal efficiency achieved at pH 9.0, a temperature of 298 K, an operating pressure of 2 MPa, and an initial feed concentration of 20 ppm by nanofiltration membranes, demonstrating significant potential for application [54].

Electrochemical methods have shown great potential for recovering heavy metals, such as chromium and nickel, from pharmaceutical wastewater. Studies have shown that over 100 mg g^{-1} of hexavalent chromium was recovered using electrochemical methods, and more than 2300 mg g^{-1} of heavy metals could also be deposited. Electrochemical techniques efficiently recover these metal resources and reduce environmental pollution [55].

Biological treatment techniques have excelled in dealing with high concentrations of organic matter, especially in treating fermentation and chemical synthesis wastewater. Aerobic biological treatments degrade organic matter through microbial metabolism, with the activated sludge method being one of the most common. This method achieves a biological oxygen demand (BOD) removal rate of over 90% in wastewater. However, for toxic wastewater, anaerobic treatment is more effective, converting organic matter into methane and carbon dioxide in an anaerobic environment [56].

Advanced oxidation processes are suitable for treating recalcitrant organic pollutants, such as antibiotic and hormone residues. Techniques like ozonation and Fenton process generate hydroxyl radicals, which efficiently degrade organic compounds, transforming them into harmless small molecules [57].

Hybrid treatment technologies are becoming the primary approach for handling complex pharmaceutical wastewater [58]. The combination of physicochemical treatments, biological treatments, and advanced oxidation processes can significantly improve the wastewater treatment efficiency. For example, using an up-flow anaerobic sludge blanket (UASB) reactor combined with a membrane bioreactor (MBR) removes organic matter from wastewater and facilitates water recovery and reuse. This hybrid treatment technology has demonstrated high stability and cost-effectiveness in practical applications, representing one of the future directions for pharmaceutical wastewater treatment.

1.1.3 Pharmaceutical residues as water contaminants

The presence of pharmaceuticals in wastewater and natural water was first reported in 1977/1978 [59,60]. Since then, significant progress has been made in understanding the sources, migration pathways, and ecotoxicology of pharmaceuticals in the environment. Today, the presence of pharmaceuticals in groundwater, surface water, wastewater, soil, and biota across the globe is well documented [61–63]. Domestic sewage is typically the primary source of these pollutants, making pharmaceuticals potential markers for contamination of surface and groundwater [64]. However, other sources of pharmaceutical pollution, such as wastewater from aquaculture and livestock industries, should not be overlooked [65]. For example, environmental antibiotics are linked to bacterial resistance, an issue of particular concern. According to institutions like the European Commission and the Helsinki Commission [66], pharmaceuticals have emerged as water stressors. The bibliometric analysis of the presence of pharmaceuticals in the environment reveals the rise in related information appearing in scientific articles, books, conference proceedings, TV programs, social media, and websites [67]. This demonstrates that the issue is of global concern, extending beyond the scientific community. Fig. 8 illustrates the pathways through which pharmaceutical residues from various sources reach water bodies. The various routes include human and animal excretion, hospital wastewater, pharmaceutical manufacturing discharges, sludge treatment, and landfill leakage.

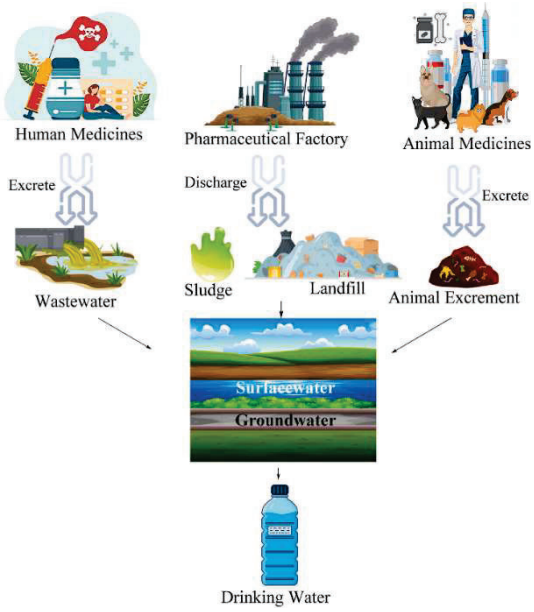

Figure 8. Main routes for the entry of pharmaceutical pollutants into water bodies [68].

These pharmaceuticals, including antibiotics, antivirals, analgesics, and hormones, among others, pose significant challenges to aquatic and terrestrial ecosystems [69,70]. Notably, anti-inflammatory drugs, antibiotics, and analgesics are among the most widely used medications worldwide. Complicating matters further, certain pharmaceutical by-products have toxicity levels equal to or exceeding those of their parent compounds, raising concerns that conventional treatment plants may not effectively remove them [69,71,72]. Fig. 9 highlights significant geographical differences in concentrations of antibiotics, endocrine disruptors, and pharmaceutical pollutants across wastewater treatment plants (WWTPs) globally. Box plots in Fig. 9a and 9d present the concentration distributions of six antibiotics (lincomycin, erythromycin, ciprofloxacin, norfloxacin, tetracycline, and sulfamethoxazole) in both, the influent and the effluent of these plants. For instance, sulfamethoxazole concentrations in Kenya reach 54.8 μg L^{-1}, far exceeding levels in other regions, likely due to the heavy use of antimalarials in response to the high malaria incidence [73]. Similarly, ciprofloxacin concentrations in Southern Africa are as high as 501.6 μg L^{-1}, reflecting significant antibiotic use [74]. The median concentrations of norfloxacin and tetracycline in the influents are notably higher in Africa and Asia, particularly in Asia, where norfloxacin levels in both, the influent and the effluent surpass those in Europe, Oceania, and North America. In South Korea, lincomycin concentrations show a wide range, differing by 2 to 4 orders of

magnitude compared to other countries. These distribution patterns are largely shaped by regional pharmaceutical usage practices [75].

Box plots of Fig. 9b and 9e show the concentration changes of six endocrine disruptors (NP, 4-t-OP, BPA, E3, EE2, and E2) in the influent and the effluent. NP and 4-t-OP concentrations in Asia and North America are notably higher than in other regions, with NP levels in North America reaching nearly 105 ng L^{-1}, indicating the intensive industrial activity and chemical use in these areas. Although effluent concentrations are lower, NP and 4-t-OP residues remain relatively high in North America and Europe, suggesting that these compounds resist complete removal due to their chemical stability or limitations in current treatment technologies.

Plots of Fig. 9c and 9f display the concentration distributions of pharmaceutical pollutants (caffeine, carbamazepine, atenolol, triclosan, acetaminophen, and ibuprofen) in the influents and the effluents. Caffeine concentrations in Africa, Asia, and North America are exceptionally high, particularly in North America, where levels approach 1×10^6 ng L^{-1}, far exceeding those in other regions. This could be due to higher consumption of caffeine-containing beverages. Concentrations of other drugs, such as carbamazepine and ibuprofen, also vary across regions, with higher levels in Asia and North America, reflecting the widespread use of these pharmaceuticals. While concentrations decrease in the effluent, caffeine and ibuprofen residues remain elevated in Africa and Asia, indicating that existing wastewater treatment processes are insufficient to remove these drugs completely.

In summary, higher concentrations of antibiotics and pharmaceutical pollutants in Africa and Asia may indicate inadequate wastewater treatment infrastructure and weaker regulatory controls in these regions. Although Europe and North America perform better in treating some pollutants, endocrine disruptors and pharmaceutical residues remain persistent challenges. Current wastewater treatment technologies are inadequate for removing complex chemical compounds, especially those with resistant chemical structures, highlighting the need for further advancements in treatment technologies.

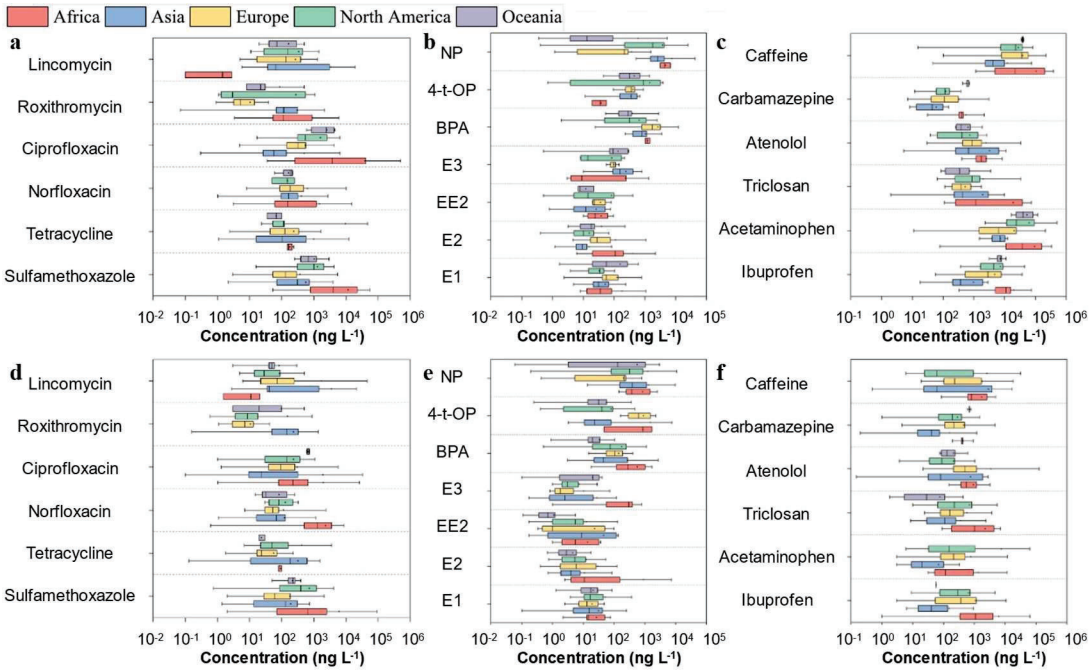

Figure 9. Box plots showing the concentration variations of (a, d) selected antibiotics, (b, e) endocrine-disrupting chemicals, and (c, f) non-steroidal anti-inflammatory drugs in the (a, b, c) influents and (d, e, f) the effluents of WWTPs across different geographical regions. Acronyms: Nonylphenol (NP), 4-tert-octylphenol (4-tOP), bisphenol A (BPA), estriol (E3), 17α-ethinyl estradiol (EE2), estradiol (E2), estrone (E1) [76].

Pharmaceuticals often exhibit biological activity even at low concentrations, meaning that trace amounts in the environment can significantly impact non-target organisms [77]. Fig. 10 summarizes the broad effects of pharmaceutical pollution on various organisms in aquatic ecosystems, encompassing multiple levels from biological mechanisms to population dynamics and ecological functions [78].

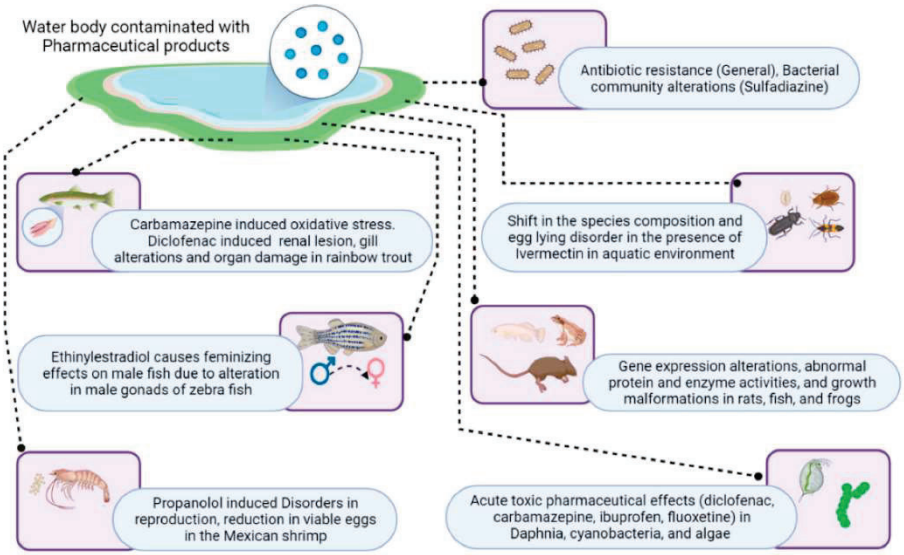

Figure 10. Toxic effects of pharmaceuticals on the nontarget organisms in the environment [78].

Carbamazepine, for instance, induces oxidative stress responses in aquatic organisms like rainbow trout. Diclofenac, known for its high persistence in aquatic environments, causes damage to the kidneys, gills, and other organs in fish. Ethinylestradiol has a pronounced feminizing effect on zebrafish, leading to reduced reproductive capabilities in males. This sex reversal not only affects individual organisms but may also have long-term detrimental effects on the survival and reproduction of entire populations, threatening their stability. Propranolol exhibits toxicity in Mexican shrimp, manifesting in reproductive issues, demonstrating that pharmaceuticals can adversely affect the reproductive systems of invertebrates as well. Invertebrates play crucial roles in aquatic ecosystems, and their population decline may trigger cascading effects throughout the food chain.

Antibiotic accumulation has profound impacts on aquatic microbial communities. Sulfonamides, for example, can alter the structure of these communities and increase bacterial resistance while inhibiting key microbial activities involved in nitrogen and phosphorus cycling. This can negatively affect aquatic plant growth and the self-purification capacity of water bodies. Long-term exposure to pharmaceutical pollution can also lead to changes in gene expression in aquatic organisms, resulting in abnormal protein and enzyme activities, which in turn disrupt normal growth and development, ultimately lowering the overall health of entire populations. Furthermore, drugs like ivermectin can affect species composition in aquatic ecosystems, reducing the number of sensitive species and destabilizing ecological balance and biodiversity.

In summary, the cumulative effects of pharmaceutical residues in aquatic ecosystems may lead to the loss of ecological functions. When key species are at risk, entire food chains and nutrient cycles can be disrupted, jeopardizing ecosystem stability.

Given the widespread negative impacts of pharmaceuticals on aquatic ecosystems, it is critical to explore the effectiveness of wastewater treatment technologies in removing these pollutants. Existing WWTPs are primarily designed to target conventional pollutants, such as organic matter, nitrogen, and phosphorus. However, when facing with structurally complex and persistent pharmaceuticals, traditional treatment methods often prove inadequate. Although some pharmaceuticals are partially removed during wastewater treatment, many

residues still pass through the system and are discharged into natural water bodies.

To mitigate the environmental and biological risks posed by pharmaceutical residues, a variety of advanced wastewater treatment technologies have been proposed and implemented in recent years. Table 1 summarizes the removal rates of different pharmaceutical pollutants under various treatment methods [46]. By evaluating the effectiveness of these technologies, improvements can be made to address better the unique challenges posed by pharmaceutical pollutants, ultimately reducing their environmental footprint and protecting aquatic ecosystems.

Table 1. Various technologies for the treatment of pharmaceutical contaminants [46].

No.	Class/Group of pharmaceutical	Pharmaceutical contaminant	Treatment technology	Removal / in %
1	Psychoanaleptic metabolite	Hydroxybupropion	Ultrafiltration membrane biorreactor (UMBR)	82
	Antirheumatic	Ibuprofen		98
		Metformin		95
	Opiate analgesic	Valsartan		92
2	Macrolide	Azithromycin	Anaerobic treatment in WWTP	88
	Tetracyclin Antibiotic	Tetracyclin		73
		Oxytetracycline		80
		Chlortetracycline		90
3	Analgesic and antipyretic	Acetaminophen	Hydrogen peroxide-induced UFBR reactor	99
	Tetracycline	Chlortetracycline		100
		Metacycline		46
	Sulfonamide	Sulfamerazine		92
	Macrolide	Clarithromycin		59
4	Analgesic and antipyretic	Acetaminophen	Cyclic biological reactor	98
5	Analgesic and antipyretic	Acetaminophen and some other drugs	MBR at real scale	100
			MBR at laboratory scale	95
6	Analgesic and antipyretic	Acetaminophen and some other drugs	Conventional activated sludge process	67
7	Analgesic and antipyretic	Acetaminophen and some other drugs	Submerged membrane bioreactor	92.2
8	Nonsteroidal anti-inflammatory drug (NSAID)	Diclofenac	Advanced biological treatment (WWTP)	61.3
	Anticonvulsant	Carbamazepine		15.6
	NSAID	Diclofenac	Wastewater stabilization pond	93.6
	Anticonvulsant	Carbamazepine		24.4

No.	Class/Group of pharmaceutical	Pharmaceutical contaminant	Treatment technology	Removal / in %
9	Macrolide	Erythromycin	Gamma irradiation	70
			Gamma irradiation with peroxymonosulfate (10 mM)	80
			Gamma irradiation with peroxymonosulfate (50 mM)	100
10	Analgesic / antiinflammatory	Acetaminophen	Stirred tank bioreactor with Trametes versicolor	90.5
		Ibuprofen		17.5
	Antibiotic	Cephalexin		54.8
	Fibrate	Gemfibrozil		93
	Methylxanthine	Caffeine		87.9
11	Antibiotic	Chloramphenicol	Solar photo-Fenton	63
			Adsorption process using avocado seed activated carbon	97
	Triazole	Fluconazole	Solar photo-Fenton	40
			Adsorption process using avocado seed activated carbon	97
	Anti-Testosterone / Anti-Androgen	Flutamide	Solar photo-Fenton	54
			Adsorption process using avocado seed activated carbon	99
	Fibrate	Gemfibrozil	Solar Photo-Fenton	79
			Adsorption process using avocado seed activated carbon	100
12	Anticonvulsant	Carbamazepine	Adsorption process using 25 mg L^{-1} biochar	84
			Idem, using 125 mg L^{-1} biochar	99
			Idem, using 250 mg L^{-1} biochar	99
13	Opiate analgesic	Codeine (+)	Clay mineral along with nonionic organoclay & Cationic organoclay	62.7
	Antibiotic	Trimethoprim (0)		2.6
	NSAID	Ibuprofen (-)		88.6
14	NSAID	Ibuprofen	Biological nutrient removal with an anaerobic configuration	81
		Naproxen		71
15	Beta Blocker	Atenolol	Two sequencing batch reactors with powdered composite adsorbent	52
	Fluoroquinolone	Ciprofloxacin		54
	Benzodiazepine	Diazepam		59
16	NSAID	Naproxen	Conventional activated sludge treatment after aerobic and anaerobic	90

No.	Class/Group of pharmaceutical	Pharmaceutical contaminant	Treatment technology	Removal / in %
			digestion. Finally, a tertiary treatment based on UV oxidation	
17	Diuretic (water pills)	Furosemide	Photolysis	100
			Photocatalysis	97
	Sulfonamide	Sulfadiazine	Photolysis	68
			Photocatalysis	87
18	Fluoroquinolone	Enrofloxacin	Synergic catalytic ozonation and electroflocculation process	99
		Amoxicillin		89
19	Analgesic	Acetaminophen	Primary treatment based on the partial removal of suspended solids and organic matter through coagulation, flocculation, and sedimentation	23
20	Tetracycline antibiotic	Oxytetracycline hydrochloride	Electrocoagulation	88
21	NSAID	Diclofenac	Electrocoagulation	34
	Anticonvulsant	Carbamazepine		35
	Penicillin	Amoxicillin		36
22	Analgesic	Ibuprofen	High rate algal ponds	90–99
			UASB	92
		Acetaminophen	High rate algal ponds	90–99
			UASB	92
23	Antiepileptic	Lamotrigine	High rate algal ponds	47-48
	Hypolipidemic drug	Fenofifibric acid		69-84
	Analgesic and anti-inflammatory drug	Paracetamol		76-100
	Tranquilizer	Pentoxifylline		30-55
24	Antibacterial and Antifungal	Triclosan	Activated sludge	99.8

As can be seen in Table 1, the efficiency of different wastewater treatment technologies in removing pharmaceutical residues varies significantly depending on the type of drug and treatment method. Some advanced treatment technologies, such as advanced oxidation processes (AOPs, as for example photo-Fenton process, photocatalysis and ozonation) and bioreactors (such as UMBR), have demonstrated removal rates exceeding 90% for certain pharmaceuticals, including acetaminophen, ibuprofen, and chloramphenicol.

In contrast, conventional wastewater treatment methods, such as activated sludge processes and anaerobic digestion, show lower removal efficiencies for certain antibiotics and NSAID like carbamazepine and diclofenac, with removal rates ranging from only 15% to 50%. Additionally, specific pharmaceuticals, such as chlortetracycline, exhibit nearly 100% removal efficiency through reactive oxygen species and electrocoagulation methods. However, other drugs, such as amiloride (not shown in Table 1), show very low removal efficiency with similar technologies, highlighting the complex relationship between the drug chemical structure and the effectiveness of the treatment method.

Overall, while certain advanced technologies display high removal efficiency, most conventional treatment processes struggle to completely eliminate pharmaceuticals with complex structures, particularly antibiotics and NSAIDs. This emphasizes the need for further development and optimization of treatment methods to address pharmaceutical pollution in wastewater more effectively.

1.1.4 Legislation on pharmaceuticals in wastewater

To address the increasingly severe environmental problems caused by the presence of pharmaceuticals in wastewater, countries worldwide have implemented regulations aimed at managing and reducing pharmaceutical pollution.

In 2024, the World Health Organization (WHO) released the *Guidelines for Wastewater and Solid Waste Management from Antibiotic Manufacturing* [79], which provides a comprehensive framework for governments, pharmaceutical companies, and wastewater management agencies to control antibiotic pollution. This is the first guidance from WHO specifically addressing wastewater and solid waste pollution generated during antibiotic manufacturing, aiming to reduce the environmental and public health impacts of antibiotic pollution. The guidelines propose a range of risk management and monitoring measures, including establishing emission standards and recommending effective wastewater treatment technologies such as ozonation, UV disinfection, and thermal treatment. A particular emphasis is placed on antibiotic resistance, highlighting that antibiotic pollution affects local ecosystems and facilitates the spread of resistant pathogens through water systems, posing a global public health threat.

In North America, the United States established archives detailing methods to manage endocrine-disrupting chemicals and limit their intrusion into human and wildlife systems. Additionally, the U.S. Food and Drug Administration has published guidelines for evaluating human pharmaceuticals. The *Clean Water Act* (CWA) has long provided strict guidelines for wastewater discharge, with Code of Federal Regulations (CFR, title 40, part 439) setting pollutant emission standards specifically for the pharmaceutical industry. These regulations aim to control the release of harmful substances from the pharmaceutical sector into water bodies to protect water quality and public health [80].

The European Union leads the world in managing pharmaceutical wastewater. The *Water Framework Directive* (WFD 2000/60/EC) [81] and the *Environmental Quality Standards Directive* (2013/39/EU) [82] impose strict limits on pharmaceutical pollutants, including diclofenac, 17-α-ethinylestradiol (EE2), and estradiol (E2), which are listed as priority substances. EU member states are required to ensure that the concentrations of these substances do not exceed environmental safety thresholds. The EU has also introduced the *Strategic Approach to Pharmaceuticals in the Environment* (PiE) [83], which aims to reduce pharmaceutical residues in water systems by improving wastewater treatment technologies and promoting sustainable pharmaceutical consumption. As part of the *European Green Deal*, the *Extended Producer Responsibility* (EPR) mechanism holds pharmaceutical companies accountable for the environmental impacts of their products, a move expected to drive stricter legislation, particularly as the EU plans to set higher environmental standards by 2030 [84,85].

On October 22, 2024, Spain enacted Royal Decree No. 1085/2024, approving the *Water Reuse Regulation* to standardize wastewater reuse, improve water quality, and ensure safety [86]. On November 27, the EU adopted Directive No. 2024/3019 (revised), tightening urban wastewater treatment standards, expanding scope, imposing stricter pollutant limits, promoting reuse, advancing energy neutrality, and establishing producer responsibility [87]. These laws mark significant progress by Spain and the EU in water resource management and wastewater treatment, fostering sustainability and environmental protection.

In South America, progress is being made in managing pharmaceutical pollution in wastewater. Brazil, for example, has enacted the *National Solid Waste Policy (2010)* [88], which mandates the classification and treatment of medical

waste, including pharmaceuticals. With the pharmaceutical industry rapidly growing in Brazil, the issue of pharmaceutical wastewater has become more pressing. In response, some WWTPs in Brazil have introduced advanced technologies to reduce pharmaceutical residues in the environment.

In Oceania, Australia has issued national guidelines on pharmaceutical pollution in wastewater, though they are not yet mandatory. The *Water Services Association of Australia* (WSAA) has called for further research into the long-term environmental effects of pharmaceuticals and for stronger regulations to limit pharmaceutical discharge into the environment. The *Australian Guidelines for Water Recycling* (2006) [89] outline best practices for reusing wastewater, particularly concerning pharmaceutical pollutants. Recent studies have detected antibiotics, NSAIDs, and hormones in Australia's surface water and treated wastewater. To mitigate pharmaceutical pollution, Australia is raising public awareness about the proper disposal of medications and preventing their improper release into sewage systems.

In Asia, China, one of the largest pharmaceutical producers and consumers in the world, faces significant challenges in managing pharmaceutical pollution in water systems. Although China has implemented the *Water Pollution Prevention and Control Action Plan* (2015) and introduced measures through the *Ministry of Ecology and Environment* (MEE) to improve water quality, pharmaceutical wastewater regulation remains in its early stages. In recent years, China has conducted extensive research to monitor pharmaceutical residues, particularly antibiotics, in surface and groundwater. Efforts are underway to upgrade wastewater treatment facilities and develop new technologies to reduce the concentration of pharmaceuticals entering the environment. The *13th Five-Year Plan for Ecological and Environmental Protection* (2016-2020) emphasizes the need for innovation in wastewater treatment technologies, particularly for emerging pollutants like PPCPs. Japan has established a comprehensive pharmaceutical monitoring program; the Ministry of the Environment (MOE) regulates pharmaceutical residues in wastewater through the *Water Pollution Control Act* [90], and pharmaceuticals such as carbamazepine, oseltamivir, and diclofenac have been detected in rivers and WWTPs. Although existing treatment technologies are somewhat effective in reducing the concentrations of certain drugs, others persist. Japan is investing in advanced water treatment technologies,

such as ozonation and MBR systems, to enhance the removal of pharmaceuticals. These technologies are expected to be more widely adopted as Japan strengthens environmental protections to meet international standards.

In Africa, legislation on pharmaceutical wastewater management is relatively underdeveloped, with a primary focus on improving wastewater treatment capacity and infrastructure. South Africa is a leader in managing pharmaceutical wastewater in Africa, researching the pollution caused by antibiotics and hormone-based pharmaceuticals. However, most African countries lack specific regulations for managing pharmaceutical wastewater. The *Sanitation and Wastewater Atlas of Africa* [91] identifies the main challenges in pharmaceutical wastewater management as a lack of technology and resources, making it difficult for many African nations to address emerging pollutants in wastewater effectively.

Managing pharmaceuticals in wastewater has become a critical issue for governments worldwide. While the U.S., EU, China, and Japan have established frameworks for monitoring and controlling pharmaceutical pollutants, developing regions such as Africa and South America are still in the early stages of addressing this issue. Global investment in advanced wastewater treatment technologies and stronger regulatory measures are necessary to protect human health and aquatic ecosystems. Future legislation should prioritize integrating pharmaceutical waste management into existing water quality frameworks and encourage international cooperation to tackle this global challenge.

1.1.5 Target organic pollutants of interest in this Thesis: an overview on their occurrence and treatment

The water matrices in this Thesis have been prepared in two different ways: (i) commercial pharmaceuticals dissolved in model solutions, or (ii) target pharmaceuticals spiked into urban wastewater.

Diphenhydramine (DPH)

DPH is an antihistamine commonly used to treat allergic reactions by blocking the binding of histamine to H1 receptors, thereby alleviating symptoms such as runny nose, itching, and rashes [92]. In addition to its antihistamine effects, DPH can inhibit the secretion of gonadotropin-releasing hormone,

estradiol, and luteinizing hormone in the brain [93]. Moreover, as a serotonin reuptake inhibitor, DPH has been shown to affect feeding behavior by increasing serotonin levels in the brain, a phenomenon observed in mammals and fish [94].

The widespread use of DPH has led to its frequent detection in environmental samples, particularly in rivers, sediments, and aquatic organisms. For example, the highest concentration of DPH measured in samples from two wastewater treatment plants in Mexico during the dry and rainy seasons was 99.1 ng L^{-1} [95], while in two plants in Oregon, USA, it was 554.0 ng L^{-1} [96]. Studies have demonstrated that DPH is acutely toxic to aquatic organisms. For instance, the 48-h LC50 for fathead minnows (*Pimephales promelas*) is 2.09 mg L^{-1}; the 7-day lowest observed effect concentration (LOEC) for growth inhibition is 49.1 μg L^{-1}, whereas the 8-day LOEC for feeding behavior inhibition is as low as 5.6 μg L^{-1} [97].

Various treatment technologies have been explored to remove DPH from water. Denitrification biofilters have shown up to 80% DPH removal [98], while constructed wetlands can achieve over 88% removal efficiency [99]. Photodegradation under alkaline conditions (pH 10) can remove 70% of DPH within 180 min [100], whereas the photo-Fenton process under acidic conditions has achieved a 100% removal rate [101, 102]. Despite these high removal efficiencies, many of these methods require specific pH conditions, and the complete mineralization of DPH remains a challenge, suggesting the need for further optimization of these treatment processes.

Lisinopril (LSN)

LSN is an angiotensin-converting enzyme inhibitor commonly used to treat hypertension, heart failure, and diabetic nephropathy. It works by inhibiting the conversion of angiotensin I to angiotensin II, lowering blood pressure and reducing cardiac load [103]. Additionally, LSN provides renal protection by reducing the activity of the renin-angiotensin-aldosterone system, making it particularly beneficial for diabetic patients [104]. Compared to other ACE inhibitors, LSN has a longer half-life, providing 24-h blood pressure control [105].

Since LSN is not metabolized in the body and is excreted unchanged through urine, it has been detected at concentrations of 15 ng L^{-1} in WWTP influents [106]. Studies have also reported LSN bioaccumulation in fish, with concentrations

ranging from 1.0 to 10.2 ng g^{-1} in samples collected from Croatian rivers [107]. In South Africa, LSN has been detected in rivers and estuaries, eventually flowing into the Indian Ocean [108]. Although present at low concentrations, prolonged exposure to LSN could negatively impact aquatic organisms, particularly by disrupting endocrine systems or inhibiting angiotensin-regulating mechanisms.

There is limited research on effective degradation methods for LSN. Photodegradation and advanced oxidation processes have shown some potential. One study using In_2S_3 nanoflowers as a photocatalyst achieved 80% degradation of LSN under light exposure for 6 h [109]. However, more research is needed to explore LSN degradation mechanisms and develop effective removal technologies.

Amoxicillin (AMX)

AMX is a widely used antibiotic that was first synthesized in the early 1970s by scientists at the Beecham Research Laboratories, who named it "Amoxil", and was first marketed under the trade name "amoxicillin" in 1998 after the merger of Beecham and GlaxoSmithKline. As a member of the β-lactam group of antibiotics, amoxicillin is commonly used to treat various bacterial infections, such as skin infections, pneumonia, and urinary tract infections [110,111].

Within 2 h of AMX ingestion in humans, more than 80% of the drug is excreted through the urine. This rapid excretion, combined with its widespread use, makes AMX one of the most common antibiotics in wastewater [112]. AMX residues in the environment can have direct biological effects on microorganisms, which in turn contribute to the development of drug-resistant bacteria. These resistant bacteria can survive in the environment and may also be transmitted to humans through the food chain or direct contact [113]. Given this, AMX, ciprofloxacin, and representative macrolide antibiotics (e.g., azithromycin, erythromycin, and clarithromycin) are included in the *European Union Emerging Contaminants Watch List* (Decision EU, 2015/495) [114].

AMX concentrations in water bodies vary significantly depending on the source. In wastewater treatment plant influents, levels range from 200 to 6.5×10^3 ng L^{-1}, while effluents contain 0 to 1.6×10^3 ng L^{-1}. Hospital wastewater shows concentrations between 43 and 2.5×10^3 ng L^{-1}, and pharmaceutical industry wastewater exhibits extremely high levels, reaching up to 120×10^6 ng L^{-1}.

Livestock wastewater contains 580 to 12.9×10^3 ng L^{-1} of AMX. In natural water bodies, surface waters like rivers and estuaries contain 0 to 300 ng L^{-1}. These findings highlight the diverse contamination sources and the potential environmental risks associated to the presence of AMX in water [115].

Several wastewater treatment technologies have been explored for removing AMX. Adsorption techniques, particularly those using activated carbon (AC) adsorbents such as powdered activated carbon (PAC) and granular activated carbon (GAC), have shown removal efficiencies of 70% and 80%, respectively [116,117]. Advanced oxidation processes are also highly effective; for example, the Fenton process under acidic conditions can achieve 100% removal [118], while persulfate-mediated oxidation results in 88% removal [119]. Indirect ozonation has demonstrated a removal efficiency of 93.4% [120], whereas photodegradation alone achieves 58.7%, but complete degradation can be attained by adding hydrogen peroxide [121]. Nanofiltration membranes have also been shown to remove over 70% of AMX [122,123]. However, due to the high chemical stability of the β-lactam ring of AMX [124], constructed wetlands exhibit lower removal efficiencies.

Most of these removal technologies have been tested at laboratory or pilot scales. Further research is required to overcome technical challenges and enhance the feasibility of these technologies for industrial-scale wastewater treatment.

2,4-Dicholophenol (2,4-DCP)

Although 2,4-DCP is not used as a pharmaceutical, it is a typical chlorophenol compound widely employed in industries such as herbicides, pharmaceuticals, preservatives, papermaking, and textile dyeing [125]. 2,4-DCP is known for its genotoxic and carcinogenic properties, which can lead to protein denaturation, fainting, anemia, liver and kidney damage, pancreatic injury, respiratory distress, and central nervous system paralysis [126]. Prolonged exposure may result in neuropsychological issues, chronic fatigue, respiratory problems, and skin infections [127].

Due to its high water solubility and stable conjugated structure, 2,4-DCP is poorly biodegradable and strongly resistant to natural and microbial photodegradation [128]. It has been detected in both surface and groundwater at concentrations ranging from ng L^{-1} to μg L^{-1}, mainly from industrial, agricultural,

and domestic wastewater discharges [129]. In 2012, the U.S. EPA listed 2,4-DCP as a priority pollutant, setting a maximum allowable concentration of 0.1 mg L^{-1} in drinking water [130], and many other countries have also designated it as a priority control pollutant [131].

Traditional removal methods include adsorption, chemical oxidation, and photocatalysis, but their actual effectiveness is limited. For example, fly ash-supported zero-valent iron-nickel composites achieve about 70% removal efficiency for 2,4-DCP under laboratory conditions, but practical applications are restricted by cost and efficiency constraints [132]. Silver halide (Ag/AgBr) photocatalysts achieved degradation rates of 83.4% and 89.4% for 2,4-DCP under UV and visible light, respectively, yet the requirement for specific light sources limits their use in actual wastewater treatment [133]. Sequential electrocatalytic oxidation-reduction using Pd-MWCNTs/Ni foam electrodes achieves over 80% removal in lab conditions but involves complex operations and high costs [134]. Thus, developing efficient and economical methods suitable for large-scale water treatment remains a focus of ongoing research. The widespread use of 2,4-DCP has led to its presence across various environmental media, especially in aquatic environments [135], posing significant risks to ecosystems and human health, underscoring the urgent need for effective removal solutions.

The main information about the target organic contaminants studied in this Thesis is collected in Table 2.

Table 2. Organic contaminants studied in this Thesis.

Pollutant	CAS	Formula	MW (g mol^{-1})	Structure
DPH	147-24-0	$C_{17}H_{21}NO$	255.4	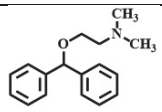
LSN	76547-98-3	$C_{21}H_{31}N_3O_5$	405.5	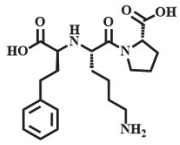
AMX	26787-78-0	$C_{16}H_{19}N_3O_5S$	365.4	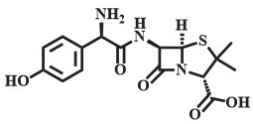
2,4-DCP	120-83-2	$C_6H_4Cl_2O$	163.0	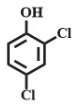

1.2 Electrochemical advanced oxidation processes (EAOPs)

WWTPs typically evaluate the organic matter removal in the mg L^{-1} range, but APIs can have significant environmental impacts even at low concentrations, frequently in the range from μg L^{-1} to pg L^{-1} [136]. To effectively treat residual APIs in wastewater, the AOPs have garnered widespread attention due to their environmental compatibility, operational simplicity, and high efficiency in degrading organic pollutants [137]. These technologies achieve efficient degradation while being ecologically compatible, and are also regarded as key tools for the sustainable treatment of complex contaminants.

1.2.1 Overview of AOPs

AOPs have emerged as cutting-edge methods in modern wastewater treatment, significantly surpassing traditional approaches such as adsorption, coagulation, ion exchange, and bioremediation in efficiency and application scope [138]. AOPs demonstrate remarkable capabilities in breaking down toxic and hazardous pollutants into harmless or less harmful by-products, overcoming common limitations of conventional methods, which often struggle with insufficient removal rates, high operation costs, and the potential accumulation of secondary pollutants such as heavy metals, nitro compounds, and halogenated derivatives [139].

The key AOP technologies include heterogeneous photocatalysis, ozone-based techniques, ultrasonic methods, Fenton-based processes, persulfate-based techniques, and electrochemical AOPs (i.e., EAOPs) that combine chemical oxidation with electrochemical processes. All these technologies rely on the in-situ generation of highly reactive species, particularly hydroxyl radicals ($^{\bullet}OH$), which exhibit an extremely high oxidation potential ($E^{0}_{\bullet OH/H_2O}$ = 2.8 V vs. SHE) and very high reaction rates (10^{8} – 10^{11} M^{-1} s^{-1}), allowing them to react non-selectively with a wide variety of organic pollutants, leading to their cleavage and, eventually, their mineralization [140,141]. In addition to $^{\bullet}OH$, other reactive oxygen species such as sulfate radical anion ($SO_4^{\bullet-}$), superoxide anion ($O_2^{\bullet-}$), singlet oxygen ($^1O_2$), and hydroperoxyl radical ($HO_2^{\bullet}$) also play a role to reach the efficient degradation of organic contaminants [142]. These characteristics enable AOPs to offer more efficient and sustainable pollutant removal solutions,

addressing challenges that traditional wastewater treatment methods are often unable to solve.

Heterogeneous photocatalysis

The photodegradation of pharmaceuticals can be categorized into three types: direct, indirect, and photodegradation in conjunction with heterogeneous photocatalytic materials [143]. In direct photolysis, pharmaceutical-containing wastewater is exposed to high-energy radiation, such as ultraviolet (UV), which interacts with the target pollutants. This radiation excites the pollutant molecules to a higher energy state, initiating a series of reactions that result in the formation of degradation products (DPs), as illustrated by reactions (1) and (2) [144].

$$\text{Pharmaceutical} + h\nu \rightarrow \text{Pharmaceutical}^* \quad (1)$$

$$\text{Pharmaceutical}^* + h\nu \rightarrow \text{DPs} \quad (2)$$

Key parameters that influence the potential for direct photodegradation of pharmaceuticals include the molar absorptivity (ε_λ), quantum yield (Φ), radiation intensity, and the functional groups of the target pollutants [145,146]. The extent of light absorption and quantum yield determine the degradation rate, with pharmaceuticals that absorb more incident radiation degrading more quickly. In contrast, compounds with lower absorptivity degrade at a slower rate [147]. Consequently, direct photolysis results in the cleavage of molecular bonds in the pharmaceutical compounds, leading to the formation of different degradation products.

In indirect photolysis, the incident light is absorbed by a sensitizer, which then reacts directly with the target pollutant or generates reactive radicals that facilitate pollutant degradation [144]. Common sensitizers include nitrate ions (NO_3^-) and dissolved organic matter [148]. These sensitizers become photoexcited under irradiation, producing reactive intermediates such as reactive oxygen species (ROS), as for example $^{\bullet}OH$, $^1O_2$, peroxyl radicals ($ROO^{\bullet}$), and O_2^-. The reaction rate between these intermediates and the target pollutant depends on their concentrations and second-order rate constants. Many pharmaceuticals undergo indirect photodegradation, demonstrating that both direct and indirect photolysis can work synergistically, leading to the effective breakdown of pharmaceuticals into degradation products [63].

Heterogeneous photocatalytic materials such as titanium dioxide (TiO_2), zinc oxide (ZnO), and cerium oxide (CeO_2) have shown exceptional capabilities for degrading organic pollutants under UV, solar, and visible light [149,150]. When exposed to light, these photocatalysts are activated, producing conduction band electrons (e_{CB}^-) and valence band holes (h_{VB}^+), as described in reaction (3).

$$\text{Photocatalyst} + h\nu \rightarrow e_{CB}^- + h_{VB}^+ \quad (3)$$

The h_{VB}^+ species react with water to produce $^{\bullet}OH$, which significantly enhances the degradation efficiency. The reactions are described in reactions (4) and (5) as follows [151]:

$$h_{VB}^+ + H_2O \rightarrow H^+ + {}^{\bullet}OH \quad (4)$$

$$h_{VB}^+ + OH^- \rightarrow {}^{\bullet}OH \quad (5)$$

In the presence of peroxides such as H_2O_2, peroxodisulfate (PDS, $S_2O_8^{2-}$), and peroxymonosulfate (PMS, HSO_5^-), the conduction band electrons attack the O-O bond of the peroxide molecules, breaking them down into $^{\bullet}OH$ and $SO_4^{\bullet-}$, as shown in reactions (6-9) [152]:

$$e_{CB}^- + H_2O_2 \rightarrow {}^{\bullet}OH + OH^- \quad (6)$$

$$e_{CB}^- + HSO_5^- \rightarrow SO_4^{\bullet-} + OH^- \quad (7)$$

$$e_{CB}^- + HSO_5^- \rightarrow SO_4^{2-} + OH^- \quad (8)$$

$$e_{CB}^- + S_2O_8^{2-} \rightarrow SO_4^{2-} + SO_4^{\bullet-} \quad (9)$$

The use of peroxides in photocatalytic systems prevents the recombination of e_{CB}^- and h_{VB}^+, thus allowing h_{VB}^+ to freely react and facilitate the production of $^{\bullet}OH$ and $SO_4^{\bullet-}$ through reactions (4) to (7). One limitation of metal oxide photocatalysts is their typically high bandgap energy, which restricts their activity to the UV region [153]. Doping with metal and non-metal elements reduces the bandgap, enhancing photocatalytic activity under visible light [153,154]. For instance, Khan et al. synthesized N-doped TiO_2 (N-TiO_2) with a bandgap energy of 2.89 eV, lower than the undoped TiO_2 (3.23 eV), demonstrating the effectiveness of doping in reducing the bandgap [155]. Moreover, the photocatalytic performance of both doped and undoped catalysts was further enhanced when coupled with peroxides [153]. Bibi et al. [156] prepared zero-

valent iron (Fe^0)-doped TiO_2, which outperformed undoped TiO_2, and found that coupling with PMS further improved the photocatalytic activity of both doped and undoped catalysts.

Fig. 11 illustrates the activation of modified and unmodified TiO_2 photocatalysts under light irradiation, as well as the production of reactive radicals in the presence and absence of persulfate.

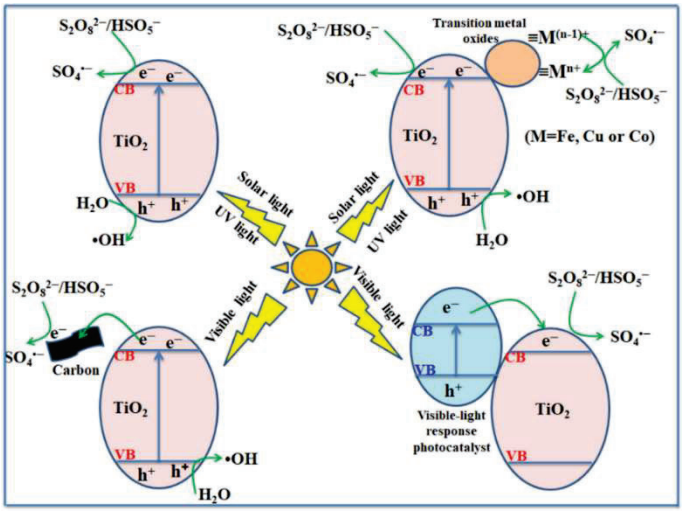

Figure 11. Mechanism of enhanced photocatalytic performance of titanium dioxide-based catalysts in the presence of persulfate [157].

Ozonation (O_3)

O_3 is a powerful oxidizing agent with a high redox potential, capable of degrading a wide range of organic pollutants [158]. However, when used alone, the concentration of $^{\bullet}OH$ generated is relatively low, which limits the degradation rate of persistent pollutants. To enhance the generation of $^{\bullet}OH$ and improve the mineralization efficiency of organic matter, O_3 is often combined with UV (i.e., UV/O_3) or a catalyst. O_3 can effectively absorb UV-C radiation, with a molar absorptivity as high as 3300 M^{-1} cm^{-1} [159]. The UV/O_3 process is considered a highly efficient AOP due to its ability to degrade organic pollutants without producing secondary pollution [160]. Under UV-C radiation, O_3 generates $^{\bullet}OH$ through reactions (10) and (11), as follows:

$$O_3 + hv \rightarrow O_2 + {}^1O \quad (10)$$

$${}^1O + H_2O \rightarrow 2\ {}^{\bullet}OH \quad (11)$$

Ozone (O_3) can undergo indirect reactions to generate $^{\bullet}OH$, as shown in reactions (12) and (13):

$$O_3 + H_2O \rightarrow O_2 + H_2O_2 \quad (12)$$

$$H_2O_2 + h\nu \rightarrow 2\ {}^{\bullet}OH \quad (13)$$

The high generation rate of $^{\bullet}OH$ leads to the rapid degradation of target organic pollutants, particularly when UV-C is combined with O_3, significantly enhancing the effect. This combination not only degrades the pollutants through direct photolysis but also excites the pollutants, making them more susceptible to attack by $^{\bullet}OH$ [161]. Fig. 12 shows the degradation efficiency of sulfamethoxazole (SMX) under different O_3-based AOPs. Studies have demonstrated that all O_3-based processes effectively degrade SMX, with the combined method of UV-C and H_2O_2 showing the best performance, likely due to the higher $^{\bullet}OH$ production rate under these conditions [162].

Ho et al. [163] studied the mineralization of sulfonamide drugs using the UV/O_3 combined with persulfate (UV/O_3/PS) process and found that the degradation rate constant was significantly higher compared to the UV/O_3 process alone. At pH 5 and 7, the UV/O_3/PS rate constants were 0.0802 min^{-1} and 0.0873 min^{-1}, respectively, whereas the degradation rate constants for UV/O_3 were 0.0101 min^{-1} and 0.0116 min^{-1}.

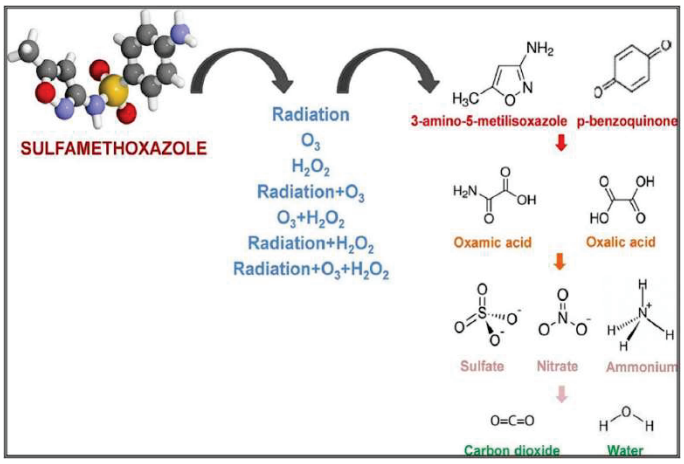

Figure 12. Degradation of sulfamethoxazole by different O_3-based AOPs [162].

In catalytic ozonation, the catalyst facilitates the decomposition of O_3 and promotes the generation of $^{\bullet}OH$, as illustrated in reactions (14) and (15) [164]:

$$Fe^{2+} + O_3 \rightarrow FeO^{2+} + 2O^{\bullet} \quad (14)$$

$$FeO^{2+} + H_2O \rightarrow Fe^{3+} + {}^{\bullet}OH + {-}OH \quad (15)$$

Ultrasound (US)-based technology

The application of US gives rise to another promising AOP, with the advantage of avoiding the need of chemical reagents. In this system, the organic pollutants can be degraded through two primary mechanisms: direct pyrolysis (suitable for volatile compounds, as shown in reaction (16)) and $^{\bullet}OH$ attack (as shown in reactions (17) and (18)). During ultrasonic treatment, cavitation bubbles form in the liquid due to cycles of compression and rarefaction. When these bubbles collapse violently, they generate localized shock waves, causing temperatures to briefly reach around 5000 °C and pressures as high as 500 atmospheres. This cavitation phenomenon leads to the pyrolytic breakdown of molecules (including water molecules) inside the bubbles, triggering chemical reactions with the generated radicals.

$$\text{Pharmaceutical} +))) \rightarrow \text{degradation products} \quad (16)$$

$$H_2O +))) \rightarrow {}^{\bullet}OH + {}^{\bullet}H \quad (17)$$

$$\text{Pharmaceutical} + {}^{\bullet}OH \rightarrow \text{degradation products} \quad (18)$$

where))) represents the applied US energy.

By combining ROS promoters (such as peroxides and O_3) and photocatalysts, ultrasonic radiation can significantly increase the generation of free radicals, effectively enhancing the degradation of target pollutants. Fig. 13 illustrates the sonolytic degradation of antibiotics in polluted water in the presence of peroxides, O_3, and photocatalysts, showing the enhanced generation of reactive radicals [165].

The rate of free radical generation is primarily influenced by the frequency and power of ultrasonic radiation. Studies have found that during sonolytic degradation of levodopa and paracetamol at different frequencies (574, 860, and 1134 kHz), the degradation efficiency decreases as the frequency increases [166]. This is because higher frequencies suppress cavitation effects, reducing the rate of free radical generation, which in turn affects the degradation efficiency of pollutants. Conversely, increasing the ultrasonic radiation power enhances degradation efficiency. Experiments conducted at different ultrasonic power (9, 17, 22, and 32 W) showed a linear positive correlation between increased power and the degradation efficiency of target pollutants [167].

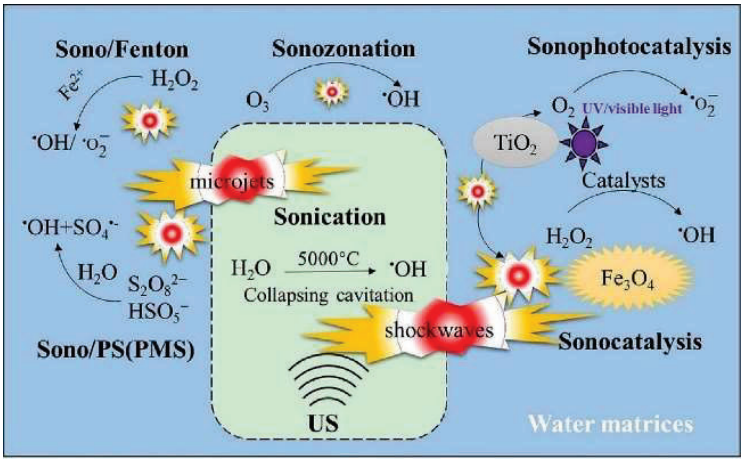

Figure 13. Sonolytic treatment of contaminated water in the presence of peroxides, ozone, and photocatalysts [165]. US: ultrasounds; PMS: peroxomonosulfate; PS: peroxodisulfate or persulfate.

Fenton process

The Fenton process [140] is an AOP that relies on the so-called Fenton's reaction (19). This is the reaction between ferrous iron (Fe^{2+}) and H_2O_2 to generate the strong oxidizing agent $^{\bullet}OH$, which effectively degrades pharmaceutical pollutants in wastewater. Under acidic conditions (with optimum pH of 2.8), Fe^{2+} acts as a catalyst, reacting with H_2O_2 to produce Fe^{3+} and $^{\bullet}OH$.

$$Fe^{2+} + H_2O_2 + H^+ \rightarrow Fe^{3+} + {}^{\bullet}OH + H_2O \quad (19)$$

As mentioned above, $^{\bullet}OH$ is a highly reactive oxidant that can break chemical bonds, such as C-H, N-H, or O-H, or add to unsaturated C=C bonds. This leads to the oxidation of complex organic pollutants into simpler molecules, and in some cases, th the complete mineralization of the organic molecules into CO_2, H_2O and inorganic anions. However, $^{\bullet}OH$ may also react with H_2O_2, according to reaction (20), forming weaker $HO_2^{\bullet}$.

$${}^{\bullet}OH + H_2O_2 \rightarrow HO_2^{\bullet} + H_2O \quad (20)$$

Although $HO_2^{\bullet}$ is a much less powerful oxidant, it can still contribute to the further degradation of pollutants. Additionally, Fe^{3+} is not the final product in the system; it can be reduced back to Fe^{2+} by reacting with $^{\bullet}OH$, as shown in reaction (21), thus sustaining the Fenton's reaction:

$$Fe^{3+} + {}^{\bullet}OH \rightarrow Fe^{2+} + OH^- \quad (21)$$

Fe^{3+} can also react with H_2O_2 to regenerate Fe^{2+} (i.e., Fenton-like reaction (22)), simultaneously catalyzing a greater production of $^{\bullet}OH$.

$$Fe^{3+} + H_2O_2 \rightarrow Fe^{2+} + HO_2^{\bullet} + H^+ \quad (22)$$

This cyclical interconversion between Fe^{2+} and Fe^{3+} ideally enables the continuous reuse of the catalyst, significantly reducing its consumption. As a result, the Fenton process demonstrates a high oxidative capacity for treating refractory organic pollutants, especially under acidic conditions. The generated $^{\bullet}OH$ reacts with organic pollutants to degrade them into various by-products (reaction (18)).

Fig. 14 illustrates the optimal oxidation performance of the Fenton process under acidic conditions, showing an efficient degradation of organic pollutants during wastewater treatment.

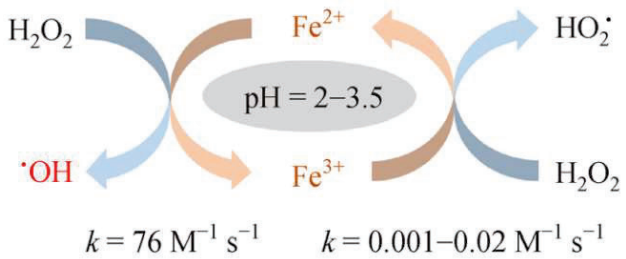

Figure 14. Reaction mechanism involved in the classical homogeneous Fenton process [168].

In the Fenton process, side reactions are also a concern. For example, two $^{\bullet}OH$ may combine to form H_2O_2 (reaction (23)), which reduces the effective concentration of $^{\bullet}OH$ and subsequently lowers the oxidation efficiency.

$$^{\bullet}OH + {}^{\bullet}OH \rightarrow H_2O_2 \quad (23)$$

The classical homogeneous Fenton process faces certain challenges. First, it requires highly acidic conditions to prevent the iron precipitation and maximize the $^{\bullet}OH$ production. This fact may adversely impact aquatic ecosystems and increase treatment costs, particularly the cost of adjusting the pH of the aqueous solution before and after treatment [169]. Another issue is the formation of iron sludge, which requires a post-treatment management.

Process optimization, such as adjusting the ratio of Fe^{2+} to H_2O_2 or employing modifications like the photo-Fenton and electro-Fenton (EF) processes, can improve the efficiency and reduce costs. The photo-Fenton process uses ultraviolet light or sunlight to promote the Fe^{3+} photoreduction thereby increasing the rate of $^{\bullet}OH$ generation. In the EF process, on the other hand, H_2O_2 is generated in situ via cathodic reduction of O_2, and it may also allow the

cathodic Fe^{3+} reduction, thus minimizing the use of chemical reagents and improving catalyst efficiency. These technological advancements enhance the performance of Fenton process and highlight its broad application potential in wastewater treatment.

Persulfate-mediated oxidation

Persulfate is a strong oxidizing agent widely used in AOPs, particularly for degrading pharmaceutical pollutants. Its core mechanism involves activating persulfate through various methods to generate sulfate radical anions ($SO_4^{\bullet-}$), which have a high redox potential ranging from 2.5 to 3.1 V, making them effective in breaking chemical bonds in pharmaceutical molecules [170,171].

There are multiple ways to activate $S_2O_8^{2-}$ to produce $SO_4^{\bullet-}$, including UV irradiation, thermal activation, and transition metal ion activation. UV activation is a facile method, where UV light breaks the O-O bond in persulfate, generating $SO_4^{\bullet-}$ (reaction (24)). Under neutral and alkaline conditions, $SO_4^{\bullet-}$ reacts with water to produce $^{\bullet}OH$, further enhancing the oxidation capacity (reaction (25)) [172]. For example, 94.5% removal of metronidazole was achieved in deionized water within 60 min using UV-activated persulfate [173].

$$S_2O_8^{2-} + hv \rightarrow 2SO_4^{\bullet-} \quad (24)$$

$$SO_4^{\bullet-} + H_2O \rightarrow {}^{\bullet}OH + SO_4^{2-} \quad (25)$$

In addition to UV activation, thermal activation is frequently used in persulfate-mediated degradation. During thermal activation, the O-O bond in persulfate breaks at elevated temperatures, producing $SO_4^{\bullet-}$. Typically, temperatures above 50 °C are required, and as the temperature increases, the generation rate of $SO_4^{\bullet-}$ is accelerated, speeding up the degradation of organic pollutants (reaction (26)) [174]. For instance, 70% of tetracycline removal was achieved at 40 °C after 240 min, whereas 100% degradation was achieved within 30 min at 70 °C [175].

$$S_2O_8^{2-} + \text{heat} \rightarrow 2\ SO_4^{\bullet-}\ (30\ ^{o}C < T < 90\ ^{o}C) \quad (26)$$

Transition metal catalysis is another common method to activate persulfate. This typically occurs in acidic conditions with metal cations like Fe^{2+} or Cu^{2+} (reactions (27) and (28)) [176]. In deionized water, sulfamonomethoxine was

fully degraded in 15 min using iron oxide magnetic nanoparticles as a catalyst [177].

$$Fe^{2+} + S_2O_8^{2-} \rightarrow Fe^{3+} + SO_4^{\bullet-} + SO_4^{2-} \quad (27)$$

$$Cu^{2+} + S_2O_8^{2-} \rightarrow Cu^{3+} + SO_4^{\bullet-} + SO_4^{2-} \quad (28)$$

In recent years, carbon-based materials such as activated carbon and graphene have also been widely used to activate persulfate. Due to their large surface area and excellent catalytic properties, carbon-based materials promote the generation of $SO_4^{\bullet-}$ and enhance free radical production through surface functional group reactions (reaction (29)) [178]. Under conditions of pH 7.2, 0.5 mM persulfate, and 0.1 g L^{-1} activated carbon dosage, sulfamethoxazole degradation reached 91.2% [179].

$$S_2O_8^{2-} + AC \rightarrow SO_4^{\bullet-} + HO^- + AC^+ \quad (29)$$

Ultrasound can also activate persulfate through cavitation effects. When cavitation bubbles collapse, they generate pressures of up to 1000 atm and temperatures as high as 4700 °C, activating persulfate and producing sulfate radicals, according to reaction (30) [179,180]. Under 500 W ultrasonic power and a frequency of 35 kHz, tetracycline degradation reached 96.5% within 120 min [181].

$$S_2O_8^{2-} + US \rightarrow 2SO_4^{\bullet-} \quad (30)$$

In addition to PDS, PMS is also widely used in AOPs. While PMS has a lower redox potential (1.82 V) than persulfate, its advantage lies in its ability to generate two strong oxidants: $SO_4^{\bullet-}$ and $^{\bullet}OH$ [170]. PMS can be activated through various methods, including UV, heat, transition metals, or carbon-based materials, to produce these radicals. By activating PMS, $SO_4^{\bullet-}$ can be generated under acidic conditions, while $^{\bullet}OH$ can be produced in alkaline conditions, allowing PMS to exhibit high efficiency across different pH values. For example, during UV activation of PMS, $SO_4^{\bullet-}$ is efficiently generated in acidic and neutral conditions, while $^{\bullet}OH$ is produced in alkaline conditions (reaction (31)) [171].

$$HSO_5^- + \text{activation condition} \rightarrow SO_4^{\bullet-} + {}^{\bullet}OH \quad (31)$$

Both PS and PMS activation methods exhibit a strong oxidation capacity for

degrading pharmaceuticals, including antibiotics (as shown in Fig. 15). However, the efficiency of PS and PMS is strongly influenced by pH. PS and PMS may react with dissolved inorganic anions (e.g., Cl^-, Br^-) in complex water environments, generating harmful halogenated organic compounds. Also, $SO_4^{\bullet-}$ may react with residual PS or PMS, reducing efficiency. This self-consumption effect limits the optimal dosing range for oxidants, requiring a precise dosage control to avoid resource waste [176].

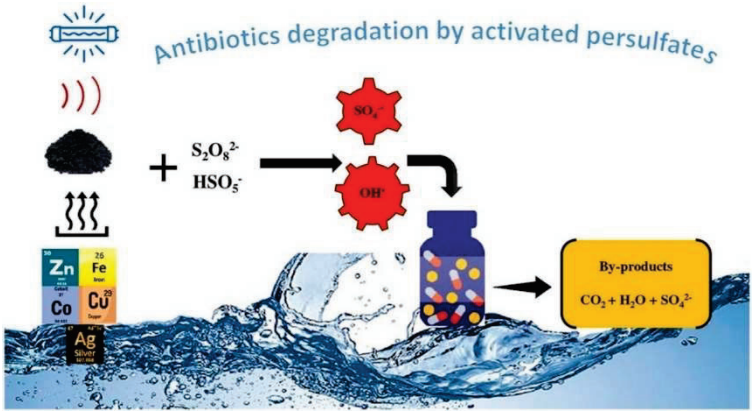

Figure 15. AOPs based on activated PMS and PDS for antibiotic degradation [141].

1.2.2 Electro-oxidation (EO) process

EO process is a straightforward AOP that can be categorized into two types, depending on the oxidation mechanism (Fig. 16): direct oxidation, where pollutants are oxidized directly at the anode surface via electron transfer (reaction (32)); and indirect oxidation, where the anode promotes the generation of oxidants that mediate the oxidation of contaminants. In the latter type, water molecules may lose electrons at the anode to generate $^{\bullet}OH$ (reaction (33)). Or chloride ions (Cl^-) can be oxidized at the anode to produce chlorine (Cl_2) (reaction (34)); then, Cl_2 diffuses away and undergoes disproportionation in the bulk solution, giving rise to hypochlorous acid (HClO) or hypochlorite ion (ClO^-), depending on the pH value (reactions (35) and (36)) [182]. Active chlorine species (i.e., Cl_2, HClO, and ClO^-) are particularly common and effective oxidizing mediators due to their high concentration and significant reactivity, surpassing other oxidants [183].

$$M + \text{Pharmaceutical} \rightarrow M(^{\bullet}\text{Pharmaceutical}) + ne^- \rightarrow \text{Products} \quad (32)$$

$$M + H_2O \rightarrow M(^{\bullet}OH) + H^+ + e^- \quad (33)$$

$$2Cl^- \rightarrow Cl_2 + 2e^- \quad (34)$$

$$Cl_2 + H_2O \leftrightarrow HClO + H^+ + Cl^- \text{ (acidic medium)} \quad (35)$$

$$Cl_2 + 2OH^- \leftrightarrow ClO^- + Cl^- + H_2O \text{ (alkaline medium)} \quad (36)$$

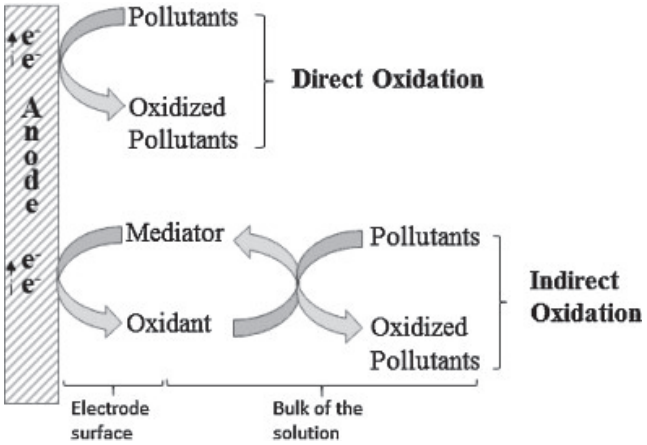

Figure 16. Schematic depiction of the direct and indirect mediated oxidation mechanisms in the EO process [183].

The anode material plays a critical role in the EO process, directly influencing the involved mechanism and the degradation efficiency. Two types of anodes can be distinguished in EO: active and non-active.

Active anodes (such as platinum (Pt) and dimensionally stable anodes (DSA), often coated with IrO_2 or RuO_2) are characterized by a low oxygen evolution overpotential. The surface of these anodes interacts strongly with $^{\bullet}OH$, converting $M(^{\bullet}OH)$ into higher-valent oxides or superoxides (MO, chemically adsorbed $^{\bullet}OH$) (reaction (37)). Their potential typically exceeds the thermodynamic oxygen evolution potential (1.23 V|SHE), resulting in chemically adsorbed $^{\bullet}OH$ that serves as mediator for selective electron transfer (and hence, oxidation) of organic pollutants (reaction (38)). However, the oxidation capacity of active anodes is limited, and complete removal of organic compounds (R) may not be achieved due to side oxygen evolution reaction (OER, reaction ((39)), which reduces the efficiency.

$$M(^{\bullet}OH) \rightarrow MO + H^+ + e^- \quad (37)$$

$$MO + R \rightarrow M + RO \quad (38)$$

$$MO \rightarrow M + \tfrac{1}{2} O_2 \quad (39)$$

Non-active anodes (such as PbO_2, SnO_2, boron-doped diamond (BDD), and

non-stoichiometric TiO_2) exhibit larger oxygen evolution overpotentials [184,185]. These anodes do not participate directly in oxidation reactions; instead, they generate large quantities of physically adsorbed $^{\bullet}OH$, which subsequently reacts with organic molecules (reaction (40)). During this transformation of pollutants, $^{\bullet}OH$ may also undergo side reactions, being partially converted into oxygen (reaction (41)).

$$M(^{\bullet}OH) + R \rightarrow M + mCO_2 + nH_2O + H^+ + e^- \quad (40)$$

$$M(^{\bullet}OH) \rightarrow M + \frac{1}{2} O_2 + H^+ + e^- \quad (41)$$

Generally, the larger the oxygen evolution overpotential of the non-active anode, the weaker the interaction between surface-generated hydroxyl radicals and the anode surface, which favors a more efficient organic pollutant oxidation. Table 3 lists common oxygen evolution potentials and the corresponding oxidation ability of the anodes. Active electrodes such as Ti|RuO_2, Ti|IrO_2, and Pt typically show oxygen evolution potentials lower than 1.8 V|SHE. In contrast, non-active electrodes such as Ti|PbO_2, Ti|SnO_2, Ti|Ti_4O_7, and BDD have potentials ranging from 1.7 to 2.6 V|SHE.

Table 3. Classification of anode materials based on their oxidation power and potential for O_2 evolution in acidic medium [186].

Anode material	Electrocatalytic activity (OER)	Oxygen evolution potential (V vs. SHE)	$^{\bullet}OH$ adsorption type	Oxidation ability
RuO_2	High	1.4 - 1.7	Chemical adsorption	Low
IrO_2		1.5 - 1.8		
Pt		1.6 - 1.9		
Graphite		1.7		
Ti_4O_7		1.7 - 1.8		
PbO_2		1.8 - 2.0		
SnO_2		1.9 - 2.2		
BDD	Low	2.2 - 2.6	Physical adsorption	High

Ti|PbO_2 is widely used among non-active anodes due to its low cost, large oxygen evolution potential, and high stability. However, the leaching of lead ions may cause secondary water pollution. Ti|SnO_2 is a semiconductor material with limited conductivity, often requiring antimony (Sb) doping to improve this parameter. In comparison, BDD electrodes possess unique sp^3 bonding structures, offering high electrochemical stability, corrosion resistance, and mechanical strength. They are less prone to contamination or passivation but are costly to

produce and challenging to scale up for large applications.

The performance of anodes in degrading pharmaceuticals via EO varies significantly, with BDD anodes showing the best results. For example, at a current density of 8 mA cm^{-2}, BDD anodes yielded 100% tetracycline degradation [175], whereas at 5 mA cm^{-2}, a 90% ampicillin destruction was achieved under analogous conditions [187]. In contrast, the degradation efficiency attained using metal oxides depends heavily on the applied current density. For instance, using PbO_2 as the anode, 90% levofloxacin was removed at 30 mA cm^{-2} [188], whereas using Sb-doped SnO_2 anodes, 98% norfloxacin degradation was reached at a current density of 50 mA cm^{-2} [189]. It is thus clear that achieving 100% degradation or complete mineralization solely via EO is challenging.

In summary, high cost and limited oxidation efficiency are key drawbacks for the large-scale application of EO technology for water treatment [190]. Current and future research should focus on optimizing the anode materials and operation conditions to improve both the economic viability and effectiveness of this technology in practical applications.

1.2.3 Homogeneous electro-Fenton (EF process)

The EF process has emerged as a prominent technique within the EAOPs, valued for its simplicity, low toxicity and environmental compatibility combined with fast reaction kinetics. It is especially suitable for removing pharmaceutical pollutants from wastewater. The core mechanism relies on the in-situ generation of strong oxidants, particularly $^{\bullet}OH$, with their aforementioned extremely high reactivity. The current development of EF process is based on the extensive research over the past 30 years, with significant contributions from the research groups of Prof. Brillas and Oturan, which have propelled the evolution of this process to overcome the limitations of the classical Fenton process [140].

In the EF process, H_2O_2 is continuously generated at the cathode via the two-electron oxygen reduction reaction ($2e^-$ ORR, as described with more detail in section 1.3). This eliminates the need for long-distance transportation of H_2O_2, avoiding logistical challenges related to the supply chain and relevant safety risks. The electrogenerated H_2O_2 reacts with Fe^{2+} (either present or added to the solution) to produce $^{\bullet}OH$ according to Fenton's reaction (19), rapidly degrading complex organic pollutants, such as pharmaceuticals, ultimately mineralizing

them into CO_2, H_2O and inorganic anions. Additionally, the EF process allows the regeneration of Fe^{2+} upon cathodic reduction, thereby reducing the consumption of H_2O_2 and Fe^{2+} and enhancing the overall process efficiency [191]. Based on the nature of the Fenton catalyst, the EF process can be considered either homogeneous or heterogeneous.

In the homogeneous EF process, the Fenton catalyst primarily consists of soluble Fe(II), which reacts with the electrogenerated H_2O_2 to produce $^{\bullet}OH$ (reaction (19)) [192]. The effectiveness of the process depends on the regeneration of Fe(II) (reactions (22) and (42)). However, rapid accumulation of Fe^{3+} ions due to a slow Fe(II) regeneration can hinder the process efficiency, leading to insufficient H_2O_2 decomposition and excessive iron hydroxide precipitation, which lowers the removal efficiency of pharmaceuticals and other organic pollutants [193].

$$Fe^{3+} + e^{-} \rightarrow Fe^{2+} \tag{42}$$

To maximize the catalyst efficiency and prevent the precipitation of inactive iron hydroxides (Fig. 17), strong acidic conditions (pH 2.8–3.5) must be maintained. From pH of approximately 1, the free Fe(III) concentration decreases, leading to the formation of $FeOH^{2+}$ and $Fe(OH)_2^{+}$ aqueous complexes. At pH 2.0–3.0, $FeOH^{2+}$ dominates, ensuring the maximum system reactivity. However, as the pH rises above 3.0, reactivity declines due to a decrease in $FeOH^{2+}$ and dissolved iron concentrations. When pH exceeds 4.0, dissolved iron precipitates as $Fe(OH)_3$ [194]. This poses a challenge for treating wastewater with near-neutral pH, as pH adjustment to around 3 before and after treatment increases process complexity and cost, limiting the large-scale application of the technology.

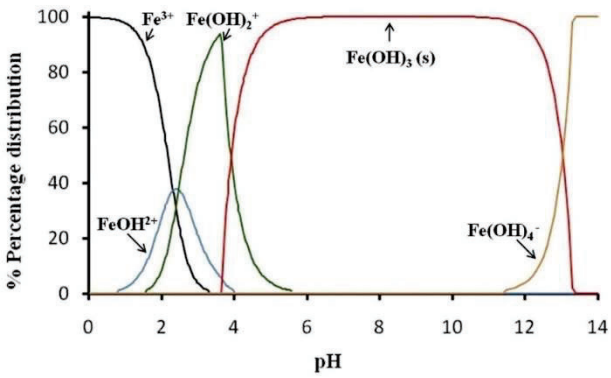

Figure 17. Speciation diagram of ferric-hydroxyl species as a function of pH for a solution containing 1.0×10^{-5} M of Fe(III) at 25 °C [194].

Researchers have introduced various iron complexes as catalysts to address the issue of Fe(III) precipitation. These catalysts consist in stable chelates of organic molecules with iron ions, preventing iron precipitation and accelerating the Fe(III)-to-Fe(II) reduction cycle.

Ethylenediaminetetraacetic acid (EDTA) was one of the earliest iron complexing agents applied in the EF process, forming stable complexes with Fe^{2+} and Fe^{3+} to prevent iron precipitation (reaction (43)) [195]. EDTA effectively chelates iron ions across a wide pH range and has demonstrated good catalytic performance in various wastewater systems. However, a major issue with EDTA is its poor biodegradability, which can cause secondary pollution in water bodies and the environment. Thus, despite the excellent performance of EDTA in stabilizing iron ions, its environmental impact limits its use in sustainable wastewater treatment [196].

$$\text{Fe(II)-EDTA} + H_2O_2 \rightarrow \text{Fe(III)-EDTA} + {}^{\bullet}OH + OH^- \quad (43)$$

To overcome the environmental concerns associated with EDTA, researchers have developed biodegradable alternatives, with ethylenediamine-N,N'-disuccinic acid (EDDS) being one of the most notable [197]. EDDS forms stable complexes with Fe^{2+} and Fe^{3+}, which remain soluble over a wide pH range, facilitating reactions at near-neutral pH (reactions (44) and (45)) [196]. When combined with the EF process, EDDS significantly enhances the pollutant removal rates. Unlike EDTA, EDDS is easily biodegradable, making it more environmentally friendly and reducing the potential environmental risks.

$$\text{Fe(II)-EDDS} + H_2O_2 \rightarrow \text{Fe(III)-EDDS} + {}^{\bullet}OH + OH^- \quad (44)$$

$$\text{Fe(III)-EDDS} + H_2O_2 \rightarrow \text{Fe(II)-EDDS} + O_2^{\bullet-} + 2H^+ \quad (45)$$

Additionally, tartrate and oxalate can also form complexes with iron, but their ability to extend the pH window is limited. Fe(III)-tartrate complexes do not exist at pH above 5 [194], and the proportions of the various forms of oxalate-iron complexes ($[FeHC_2O_4]^{2+}$, $[Fe(C_2O_4)]^+$, $[Fe(C_2O_4)_2]^-$, and $[Fe(C_2O_4)_3]^{3-}$) in solution depend largely on the molar ratio of iron to oxalate and the pH [198].

Despite the feasibility of homogeneous EF to treat pharmaceutical wastewater and the introduction of iron complex catalysts improving its

practicality, the process still depends on acidic conditions for optimal efficiency. Additionally, the complex recovery of catalysts and the eventual generation of iron sludge limit its advantages when aiming at continuous-flow operation mode [199]. Therefore, more advanced EAOP technologies are needed to overcome these drawbacks and achieve a more efficient and sustainable wastewater treatment.

1.2.4 Heterogeneous electro-Fenton (HEF process)

Compared to traditional homogeneous EF, the HEF process effectively addresses the iron ion loss caused by precipitation. To this aim, solid-state catalysts are employed, which also reduces the risk of secondary pollution. The core mechanism of HEF still relies on the in-situ generation of highly reactive $^{\bullet}OH$. If high stability and reusability of the heterogeneous catalysts is ensured, HEF maintains high treatment efficiency even under near-neutral pH conditions, making it a promising alternative technology [200,201].

In the HEF process, the iron species on the surface of the solid serve as the main catalysts for the decomposition of H_2O_2, promoting the formation of $^{\bullet}OH$ (see Fig. 18).

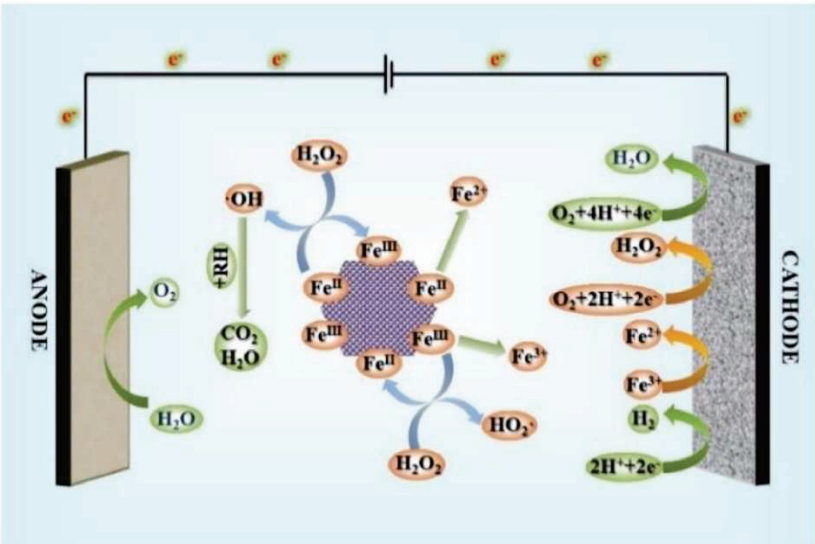

Figure 18. Scheme of the mechanism for organic matter degradation by HEF process [202].

Under acidic conditions, H_2O_2 reacts with Fe(II) on the catalyst surface (i.e., $\equiv Fe^{2+}$, where ≡ accounts for the catalyst surface), generating $^{\bullet}OH$ and oxidizing Fe(II) to Fe(III) (reaction (46)). Additionally, in the HEF process, conventional Fenton's reaction (19) may also occur due to partial release or leaching of Fe^{2+}

from the solid catalyst. The generated $^{\bullet}OH$ subsequently attacks the organic pollutants and, in some cases, a large mineralization can be achieved. However, an excess of H_2O_2 can scavenge some of the produced $^{\bullet}OH$ (reaction (20)), which reduces the process efficiency [203].

$$Fe(II) + H_2O_2 \rightarrow Fe(III) + {}^{\bullet}OH + OH^- \quad (46)$$

Under neutral or alkaline conditions, a different surface catalytic mechanism can be proposed for HEF process. First, the electrogenerated H_2O_2 preferentially interacts with the Fe(II)-OH/Fe(III)-OH active sites of the iron-based catalyst (reactions (47) and (48)), forming surface complexes Fe(II)-OH$(H_2O_2)_s$ and Fe(III)-OH$(H_2O_2)_s$. Subsequently, the H_2O_2 adsorbed on the Fe(II) catalyst decomposes to produce $^{\bullet}OH$, converting the Fe(II)-OH to Fe(III)-OH (reaction (49)). Next, the surface Fe(III)-OH$(H_2O_2)_s$ complex undergoes ligand-to-metal electron transfer, being transformed into Fe(III)-OH$(HO_2^{\bullet})_s$ (reaction (50)), which further regenerates Fe(II)-OH (reaction (51)). Increasing the pH to alkaline conditions accelerates this reaction, as the consumption of H^+ shifts the equilibrium, promoting the formation of more Fe(II)-OH species, thereby enhancing the generation of $^{\bullet}OH$ radicals [204].

$$Fe(II)\text{-}OH + H_2O_2 \rightarrow Fe(II)\text{-}OH(H_2O_2)_s \quad (47)$$

$$Fe(III)\text{-}OH + H_2O_2 \rightarrow Fe(III)\text{-}OH(H_2O_2)_s \quad (48)$$

$$Fe(II)\text{-}OH(H_2O_2)_s \rightarrow Fe(III)\text{-}OH + {}^{\bullet}OH + OH^- \quad (49)$$

$$Fe(III)\text{-}OH(H_2O_2)_s \rightarrow Fe(II)\text{-}OH(HO_2^{\bullet})_s + H^+ \quad (50)$$

$$Fe(III)\text{-}OH(HO_2^{\bullet})_s \rightarrow Fe(II)\text{-}OH + HO_2^{\bullet} \quad (51)$$

The reduction of Fe(III) to Fe(II) is crucial to increase the efficiency of the HEF process, as its rate directly affects the production of $^{\bullet}OH$. In this system, surface Fe(III) can be reduced back to Fe(II) through the action of H_2O_2 and $HO_2^{\bullet}$ (reactions (52) and (53)). However, the regeneration rate of Fe(II) is relatively slow, with rate constants ranging from 0.001 to 0.01 M^{-1} s^{-1}, which is significantly lower than the rate of Fe(III) formation (40-80 M^{-1} s^{-1}) [205,206]. To enhance the regeneration rate of Fe(II), catalyst structures can be modified to promote interfacial electron transfer. Specific strategies include the use of metal-

metal oxide compounds, different types of metal oxides, and highly conductive non-metal materials such as graphene as supports [207]. Additionally, functional electrodes can act as reducing agents, directly accelerating the Fe(II) regeneration through electrochemical reduction (reactions (54) and (55)). Carbon-based electrodes doped with heteroatoms further enhance the electrocatalytic activity, enabling a more efficient Fe(II) regeneration [206].

$$Fe(III) + H_2O_2 \rightarrow Fe(II) + HO_2^{\bullet} + H^+ \quad (52)$$

$$HO_2^{\bullet} + Fe(III) \rightarrow Fe(II) + H^+ + O_2 \quad (53)$$

$$Fe(III)\text{-}OH + e^- \rightarrow Fe(II)\text{-}OH \quad (54)$$

$$Fe(III) + e^- \rightarrow Fe(II) \quad (55)$$

Various catalysts have been developed and explored for HEF and similar processes, which can be classified according to different criteria. Based on their origin, catalysts can be categorized as natural or synthetic; according to their application site, they can be divided into suspended and functional cathode catalysts; chemically, they are classified into iron-based, non-iron-based, bimetallic, and iron-free catalysts; in terms of physical form, they are classified into nano, cluster, and single-atom catalysts (SACs); and based on the assembly method, there are composite materials and metal-organic frameworks (MOFs) as catalysts. Each type of catalyst has distinct characteristics, and the activity of HEF process is influenced by factors such as the catalyst specific surface area, surface charge distribution, and surface functional groups [208].

Natural minerals such as hematite (α-Fe_2O_3), pyrite (FeS_2), goethite (α-FeOOH), and magnetite (Fe_3O_4) have demonstrated good catalytic performance as iron sources in the HEF process. For example, using pyrite, complete degradation of textile dyes (175 mg L^{-1}) was achieved within 30 min, attaining 90% mineralization within 300 min, with energy consumption 20% lower than that of the traditional EF process [209]. Similarly, chalcopyrite ($CuFeS_2$) showed an efficient pollutant removal thanks to the synergistic action of Fe(II) and Cu(I), achieving complete mineralization of tetracycline (0.2 mM) at pH 7.0 [210]. Hematite modified through non-thermal plasma treatment exhibited a significant increase in surface area, enhancing its degradation efficiency of paraquat (20 mg

L^{-1}) by 52.2% and reducing the energy consumption [211].

Zero-valent iron (Fe^0, ZVI), due to its low cost and high reducing power, is an effective alternative catalyst source in the HEF process. Fe^0 can enhance Fenton's reaction efficiency by generating Fe^{2+} at neutral pH, avoiding the Fe^{3+} precipitation as iron hydroxides. Pre-magnetized Fe^0, compared to untreated Fe^0, achieved complete removal of *p*-nitrophenol (10 mg L^{-1}) at pH 7.0 within 90 min, and it allowed the removal of 60% of total organic carbon (TOC) in 480 min, while the use of untreated Fe^0 only yielded 54% degradation and 48% of TOC removal [212]. Additionally, sulfur-modified Fe^0 (S/Fe^0) exhibited superior performance in carbamazepine treatment, achieving complete removal in the pH range of 3.0 to 10.0, while untreated Fe^0 was only effective at pH 3.0 and 4.0 [213].

Metal nanoparticles, with their small particle size, provide a larger active surface area, significantly improving the efficiency of the EF process. Magnetic nanoparticles have garnered attention due to their easy separation via external magnetic fields and their ability to generate minimal iron sludge at near-neutral pH. Introducing ions such as Co(II), Fe(II), and Cu(I) enhances the cyclic electron transfer, improving the efficiency of $^{\bullet}OH$ generation from H_2O_2. For instance, the use of bimetallic Fe/Cu nanoparticles enhanced the nafcillin removal by 30% and 60% as compared to that attained employing single metals (Fe and Cu nanoparticles, respectively), at neutral pH [214]. Additionally, metal nanoparticles encapsulated in carbon shells, such as FeS_2@BrGO, completely degraded bisphenol A (50 mg L^{-1}) within 20 min at neutral pH [215]. Nitrogen-doped carbon-based materials improved the interfacial electron transfer and promoted the H_2O_2 generation, as found with Fe_2Co/NPC catalysts that successfully degraded and mineralized tetracycline at pH 7.0 [216].

In recent years, MOFs have been applied as suspended catalysts for the HEF treatment of recalcitrant organic pollutants. Series like MIL(Fe)-53, MIL(Fe)-88, and their metal core and porous carbon (PC) shell derivatives, with their core-shell or hollow structures, have shown an excellent pollutant removal efficiency. For example, the use of 0.05 g L^{-1} Fe/Fe_3C@PC led to the removal of 90% of sulfamethazine within 20 min at pH 4, with iron leaching below 2 mg L^{-1} [217]. Doping with non-metal elements such as nitrogen and sulfur further enhances

catalytic activity. S-doped MIL-53(Fe)/S exhibited a reaction rate 8 times higher than undoped materials within the pH range from 3 to 9, efficiently activating H_2O_2 at neutral pH [218]. Additionally, nano-ZVI@C–N powder degraded 84% of gemfibrozil within 1 h at neutral pH, demonstrating its strong potential in HEF process [219]. The application of MOF catalysts will be discussed with greater detail in Section 1.4.

SACs have attracted considerable attention in HEF process due to their atomically dispersed metal sites and their high atomic efficiency. MOFs, with their tunable pore structures and coordination environments, are ideal precursors for SACs. Researchers have prepared single-iron atom catalysts embedded in nitrogen-doped carbon (Fe/NC) through carbonization of Fe-doped zeolitic imidazolate frameworks (Fe-ZIFs). The optimum Fe/NC catalyst exhibited excellent carbamazepine degradation performance across the pH range from 3 to 11, maintaining a high efficiency even after 10 cycles [220], suggesting that MOF-derived SACs have broad applications in HEF process.

Besides iron, other transition metals such as copper, cobalt, manganese, cerium, and chromium can also activate H_2O_2 to generate $^{\bullet}OH$ [221]. These metals, with their multiple oxidation states, regenerate active species through simple redox cycles and remain stable across a wide pH range. For example, Cu(I) reacts with H_2O_2 much faster than Fe(II), and copper-based catalysts show higher pH adaptability and catalytic activity under neutral conditions [222]. However, since Cu(I) is easily oxidized by oxygen, more H_2O_2 is required to compensate for its consumption, increasing process costs and limiting large-scale applications [223]. Additionally, multi-metal composite catalysts are widely used to enhance the degradation efficiency [224]. The combination of different metals introduces multiple active sites and abundant defects, enhancing reactivity and conductivity. The electron transfer between different metal redox pairs (e.g., Fe(III)/Fe(II), Co(III)/Co(II), Cu(II)/Cu(I), Mn(III)/Mn(II), and Ce(IV)/Ce(III)) facilitates the regeneration of active sites [225]. In the N-doped PC rod-supported Fe_2Co HEF process, the removal degrees of tetracycline in river water and municipal wastewater were 80.1% and 71.9%, respectively [226]. In industrial and secondary wastewater containing 20 mg L^{-1} sulfamethazine, the FeMo@PC-2/HEF process degraded 93.2% and 98.0% of sulfamethazine within 60 min,

indicating great application potential for this system [227].

On the other hand, functional cathode catalysts, which have a dual function that involves the generation and activation of H_2O_2, are still in the early stages of research in HEF process. Drawing inspiration from the activity of iron carbides and nitrides in ORR and heterogeneous Fenton reactions, researchers have developed solid heterogeneous catalysts like Fe_3C and FeN_x nanoparticles wrapped in porous graphite layers (Fe/NC@C) for the synergistic generation and decomposition of H_2O_2 [228]. In this Fe/NC@C-catalyzed HEF system, the degradation efficiency of 2-chlorophenol exceeded 90% within 30 min, and the TOC removal rate reached 65.3% within 120 min. Experimental results and density functional theory (DFT) calculations showed that Fe_3C and FeN_x active sites play key roles in H_2O_2 generation and decomposition, respectively. Under acidic conditions, the degradation mechanism primarily relies on the role of $^{\bullet}OH$, whereas under neutral conditions, both $^{\bullet}OH$ and Fe(IV) contribute to pollutant degradation.

1.3 Oxygen reduction reaction (ORR)

The ORR is one of the most extensively studied reactions in the field of electrocatalysis, gaining significant attention due to its importance both in energy conversion (e.g., electrolyzers employing oxygen depolarized cathodes) and environmental protection. In aqueous solutions, the ORR mechanism can vary depending on the pH and the number of electrons transferred. One of the main challenges in current ORR research is the development of highly efficient (i.e., selective) and stable catalysts capable of lowering the reaction overpotential while increasing the reaction rate (i.e., reaching a high activity). As a result, recent studies have focused on designing catalytic materials with high activity, low cost, and excellent durability, such as carbon- and nitrogen-doped carbon-based materials, and non-precious metal oxides.

1.3.1 Fundamentals of the ORR

The ORR is a complex, multi-step process involving the coupling or decoupling of electron and proton transfers rather than a simple one-step reaction. Typically, two major pathways can be clearly distinguished: in acidic media, O_2 undergoes a 2-proton/2-electron reduction reaction ($2e^-$ ORR, reaction (56)) to

produce H_2O_2. This reaction is often considered an undesirable competing reaction to the four-electron ORR ($4e^-$ ORR, reaction (57)) that produces water, which is preferred in fuel cells [229]. However, in alkaline media, the reaction mechanism differs due to the involvement of OH^- (reactions (58)-(60)). Understanding the specific ORR mechanisms is crucial for developing more efficient electrochemical technologies.

In acidic electrolytes:

$$O_2 + 2H^+ + 2e^- \rightarrow H_2O_2,\ E^0 = 0.68\ \text{V}\ vs.\ \text{RHE} \tag{56}$$

$$O_2 + 4H^+ + 4e^- \rightarrow 2\ H_2O,\ E^0 = 1.23\ \text{V}\ vs.\ \text{RHE} \tag{57}$$

In alkaline electrolytes:

$$O_2 + H_2O + 2e^- \rightarrow HO_2^- + OH^-,\ E^0 = 0.08\ \text{V}\ vs.\ \text{RHE} \tag{58}$$

$$HO_2^- + H_2O + 2e^- \rightarrow 3OH^-,\ E^0 = 0.880\ \text{V}\ vs.\ \text{RHE} \tag{59}$$

$$O_2 + 2H_2O + 4e^- \rightarrow 4OH^-,\ E^0 = 0.401\ \text{V}\ vs.\ \text{RHE} \tag{60}$$

For many years, the actual mechanism of ORR has been the subject of debate due to the interaction of electrochemical and purely chemical steps in such a complex reaction. Wroblowa et al. [230] proposed a scheme in 1976 that summarized the possible steps involved, as illustrated in Fig. 19. Even if not completely accurate, this scheme summarizes the possible paths. First, the occurrence of oxygen adsorption, which depends on the adsorption sites; then, one possible route is the direct four-electron reaction from O_2 to H_2O (k_1), another one is the redox equilibrium between O_2 and intermediate H_2O_2 ($k_{\pm 2}$), and thirdly, the electrochemical reduction of H_2O_2 to H_2O (k_3). Eventually, desorption (k_5) and adsorption of H_2O_2 (k_6) from/onto the electrode is also considered. The chemical H_2O_2 decomposition to H_2O and O_2 (k_4) could also occur in parallel with the electrochemical reduction of H_2O_2 to H_2O.

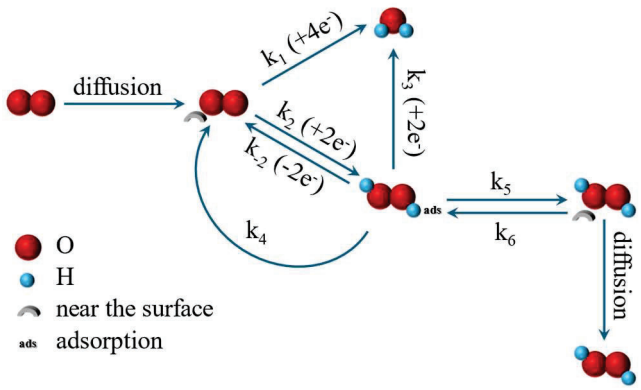

Figure 19. Scheme of possible chemical and electrochemical reactions that can occur during the ORR. Modified from elsewhere [228].

With the growing demand of H_2O_2 production in recent years, research interest in $2e^-$ ORR catalysts has increased significantly. To optimize the catalytic performance, it is crucial to accurately identify the active catalytic sites and gain a deep understanding of the reaction steps and mechanisms involved. In the $2e^-$ ORR, catalytic active sites are involved by adsorbing O_2 molecules and converting them into the OOH* intermediate, where the asterisk (*) denotes unoccupied active sites on the catalyst surface.

There are three primary modes of O_2 molecule adsorption on catalyst surfaces [231]: Pauling model (end-on adsorption), Griffiths model (side-on adsorption), and Bridge model (bridging adsorption on two active sites), as illustrated in Fig. 20.

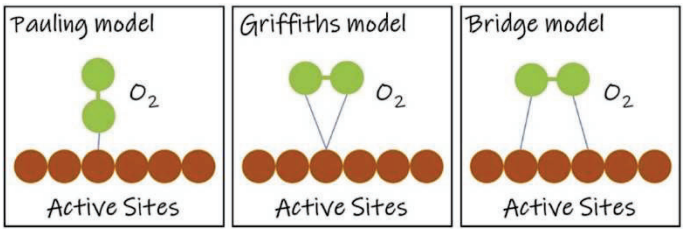

Figure 20. Schematic diagram of three O_2 adsorption models [231].

Different adsorption modes lead to different electron transfer pathways, so the adsorption strength of the catalyst with OOH* needs to be properly balanced. Fig. 21 illustrates the volcano relationship between the catalytic performance and the binding energy of the OOH* intermediate. Catalysts on the left side of the curve exhibit overly strong adsorption of OOH*, hindering its further reduction to H_2O_2; on the right side, catalysts with weak OOH* adsorption fail to effectively stabilize the intermediate, thus reducing the reaction efficiency. The peak of the

curve represents the optimal balance of adsorption strength, where the catalyst achieves the highest limiting potential for H_2O_2 production. Therefore, selecting a catalyst with the appropriate adsorption capability is crucial (reactions (61) and (62)). In the context of $2e^-$ ORR, the Pauling model is considered more suitable because it effectively avoids excessive O-O bond cleavage [232,233].

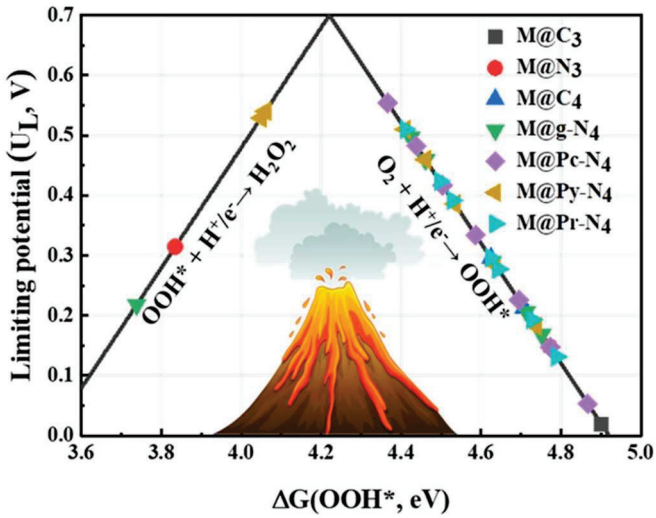

Figure 21. Volcano plot of several single-atom centers as a function of OOH* adsorption free energy [234].

$$O_2 + 2(H^+ + e^-) \rightarrow OOH^* + (H^+ + e^-) \rightarrow H_2O_2,\ E^0 = 0.7\ \text{V}\ vs.\ \text{RHE} \quad (61)$$

$$O_2 + 4(H^+ + e^-) \rightarrow OOH^* + 3(H^+ + e^-) \rightarrow O^* + 2(H^+ + e^-) \rightarrow OH^* + (H^+ + e^-) \rightarrow H_2O,\ E^0 = 1.23\ \text{V}\ vs.\ \text{RHE} \quad (62)$$

Side reactions also frequently occur during the $2e^-$ ORR process. For instance, under certain electrochemical potentials, H_2O_2 may be oxidized back to O_2 (reaction (63)). Moreover, in alkaline media, H_2O_2 can spontaneously decompose into O_2 and water (reaction (64)) and may also generate hydroxyl radicals and hydroxide ions through electron reactions (reaction (65)).

$$H_2O_2 \rightarrow O_2 + 2H^+ + 2e^-,\ E^0 = 1.78\ \text{V}\ vs.\ \text{RHE} \quad (63)$$

$$2H_2O_2 \rightarrow 2H_2O + O_2 \quad (64)$$

$$H_2O_2 + e^- \rightarrow OH^- + {}^{\bullet}OH \quad (65)$$

To enhance the efficiency of H_2O_2 electrosynthesis, researchers have developed various strategies such as facet engineering, defect engineering, chemical doping, and surface functionalization (Fig. 22a). These strategies

significantly improve the reaction kinetics by tuning the electronic structure of the catalyst.

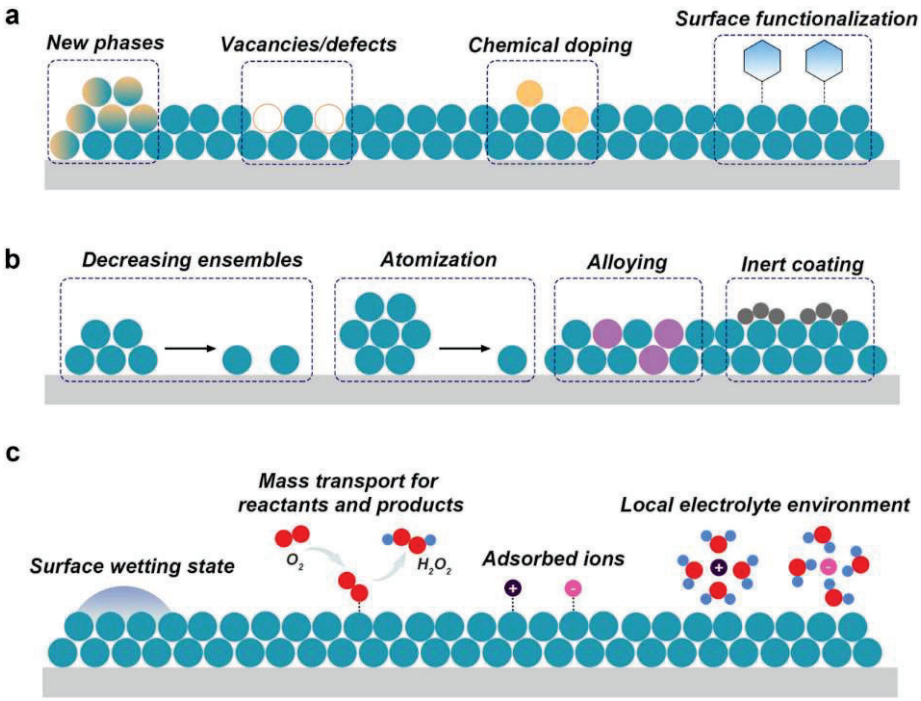

Figure 22. Schematic illustration of strategies for the design of electrocatalysts for $2e^-$ ORR: (a) Facet engineering, defect engineering, chemical doping, and surface functionalization. (b) Site isolation via decreasing ensembles, atomization, alloying with a secondary metal, and coating with inert materials. (c) Tuning of the surface wetting state, promoting mass transport, altering adsorbed ions, and modifying the local electrolyte environment [235].

In addition, the mode of O_2 adsorption plays a crucial role in enhancing the efficiency. Studies have shown that optimizing the end-on adsorption configuration of O_2 by eliminating metal aggregation sites, atomizing the metal, alloying with a second metal, and coating the surface with inert materials (Fig. 22b) can not only improve reaction selectivity but also reduce the decomposition and further electrochemical reduction of H_2O_2.

Another effective strategy is to optimize the design of the solid-liquid-gas three-phase interface between oxygen, the solid catalyst, and the electrolyte solution. Proper design of the catalyst and electrode must ensure rapid transport of both reactants and products to enhance the overall reaction efficiency. Adjusting the porosity of the electrode surface, particularly pore connectivity, length, size distribution, and surface wettability, can greatly improve the overall performance. At the same time, the electrolyte provides a proton source and plays a critical role in ion transport. The local electrolyte environment (e.g., pH and ion composition) can greatly affect the catalyst performance through various

mechanisms (Fig. 22c). Therefore, optimizing the composition and conditions of the electrolyte provides new opportunities to improve the overall efficiency of H_2O_2 production.

The combined application of these strategies offers a strong theoretical foundation and practical guidance for efficient H_2O_2 electrosynthesis and holds promise for advancing this technology for large-scale applications [235].

1.3.2 Metal-based electrocatalysts for ORR

Noble metal catalysts

Gold (Au), palladium (Pd), and platinum (Pt) have long been recognized for their catalytic properties in ORR. Historically, these metals have primarily been used for promoting the $4e^-$ ORR pathway leading to water production. However, recent research has shown that specific surface modifications, alloying, and atomic dispersion of these metals can enhance their selectivity for the $2e^-$ ORR pathway to produce H_2O_2.

Au has garnered significant attention due to its high selectivity for promoting the $2e^-$ ORR. Studies have shown that the crystal orientation of Au significantly affects the reaction pathway. Au(100) favors the $4e^-$ reduction to water, whereas Au(111) is more inclined to reduce O_2 to H_2O_2 [236,237]. Additionally, Au binds weakly to OOH*, making it an ideal catalyst for selective H_2O_2 production. Au nanoparticles smaller than 6 nm exhibit higher selectivity for the $2e^-$ ORR [238], as the smaller particle size increases the number of edge and corner sites, which are favorable for H_2O_2 formation. However, the relatively low activity of Au has led researchers to explore alloying it with other metals, such as Pd.

Au-Pd alloys have been pioneering systems for the electrochemical synthesis of H_2O_2. In 2011, Jirkovský et al. [239] developed a Pd-doped Au-on-C catalyst, where isolated Pd atoms served as catalytic centers. This Pd-doped Au catalyst improved the $2e^-$ ORR selectivity while maintaining reasonable activity. DFT calculations showed that isolated Pd atoms in the Au matrix stabilize the OOH* intermediate without promoting O-O bond cleavage, thus enhancing the H_2O_2 selectivity. This concept was further extended in subsequent studies, with similar effects observed in Au-based alloys doped with mercury (Hg) and silver

(Ag) [240,241].

Another important noble metal system involves atomically precise Au nanoclusters. In 2014, Lu et al. [242] demonstrated that $Au_{25}(SR)_{18}$ nanoclusters exhibit 89% selectivity for H_2O_2 production in alkaline media (0.1 M KOH), attributed to the efficient electron transfer to oxygen. This atomically precise structure provides a unique electronic environment stabilizing the key intermediates in the $2e^-$ ORR, making it a model system for studying how nanostructures influence the H_2O_2 production.

Pt, traditionally used for $4e^-$ ORR, can be engineered for enhancing the $2e^-$ ORR by manipulating its surface geometry and atomic dispersion. For example, amorphous Pt nanoparticles synthesized via in-situ electrochemical deposition have shown selectivity for the $2e^-$ pathway [243]. Introducing Pt-Pt pair reductions and defects alters the oxygen adsorption configuration, favoring the end-on adsorption necessary for H_2O_2 production [244]. In particular, Pt-Hg alloys have been extensively studied, owing to their high selectivity towards H_2O_2. Siahrostami et al. [241,244], using DFT, screened over 30 alloy catalysts and identified $PtHg_4$ as one of the most promising systems, with experimental validation showing 96% selectivity for H_2O_2. The geometric structure of the Pt-Hg alloy disrupts Pt-Pt bonding, preventing O-O bond dissociation, eventually achieving high H_2O_2 yields.

Non-noble metal catalysts

Although noble metals offer high selectivity for the $2e^-$ ORR, their high cost and limited availability have prompted the exploration of non-precious metal catalysts. Transition metals, particularly Fe, Co, and Ni, have been shown promising as cost-effective alternatives for H_2O_2 production. These metals are often incorporated into nitrogen-doped carbon (M-N-C) materials, where metal atoms are active sites for ORR.

Iron-based catalysts, especially in the form of Fe-N-C moieties, have been extensively studied due to their good activity and selectivity in both, the $4e^-$ and $2e^-$ ORR pathways. The coordination environment of iron plays a key role in modulating the selectivity. Fe-N-C catalysts, particularly as $Fe\text{-}N_4$, can promote the $2e^-$ ORR by optimizing the adsorption energy of the OOH* intermediate [245].

Hu et al. [228] developed an Fe_3C catalyst that facilitates H_2O_2 generation under both acidic and neutral conditions, mainly due to its electronic structure and active sites, which determine its high selectivity for the $2e^-$ pathway.

Cobalt-based catalysts have also gained attention for their tunable ORR selectivity. Co-N-C materials, where cobalt atoms are coordinated with nitrogen atoms in a carbon matrix, have been shown to selectively produce H_2O_2 under various conditions [246]. Several M-N-C catalysts (M = Fe, Co, Ni) synthesized based on metallophthalocyanines have demonstrated that Co-N-C exhibits superior selectivity for the $2e^-$ ORR due to its optimal adsorption energy for the OOH* intermediate [245]. Nitrogen atoms in the Co-N-C structure can stabilize the cobalt active sites, improving both the activity and selectivity. Introducing oxygen-containing groups can further alter the electronic properties of the Co center, allowing better adsorption and stabilization of the OOH* intermediate while preventing the O-O bond cleavage, achieving up to 90% selectivity for H_2O_2 in alkaline media [247]. Assembling permanent porous supramolecular cages based on cobalt tetraphenylporphyrin (Co-TPP) yielded Co-PB-1(6) and Co-rPB-1(6), which achieved 90%-100% selectivity at neutral pH due to site isolation within discrete molecular units in each supramolecular assembly [248].

Nickel-based catalysts, though less studied, also show potential for H_2O_2 production. Ni-N-C catalysts, especially those with Ni-N_4 or Ni-N_2O_2 coordination environments, have been found to selectively reduce O_2 to H_2O_2 in alkaline media. The coordination between nickel and oxygen weakens the binding of OOH*, leading to higher selectivity for H_2O_2. Ni-N_2O_2 catalysts have demonstrated high current density and H_2O_2 production in a three-phase flow cell [249].

Other interesting non-noble metals remain quite unexplored in the field, thus being the subject of research of one of the parts of this Thesis.

Nanoparticle-based catalysts

The composition, morphology, and existence of oxygen vacancies in synthesized nanoparticles influence their selectivity and activity regarding the $2e^-$ ORR.

The choice of **composition** plays a significant role in the catalytic performance, with special emphasis put in bimetallic nanoparticles. For example,

bimetallic Pd-Au and Pt-Ni nanoparticles exhibit high H_2O_2 yields due to the synergistic interaction between the two metals. The synergy between Pd and Au optimizes the electronic structure of the catalyst, making oxygen adsorption more favorable for H_2O_2 formation [241,250]. Similarly, Pt-Ni nanoparticles show enhanced H_2O_2 activity and selectivity by optimizing the adsorption energy of the OOH* intermediate [251,252]. The interaction between different metal atoms during alloying can regulate the electronic distribution, changing the oxygen adsorption configuration and inhibiting the O-O bond cleavage, further improving the catalytic performance.

The surface **morphology** is also crucial for nanoparticles. For instance, ultrathin nanosheet structures expose more active sites, increasing the H_2O_2 production. Ji et al. [253] synthesized ultrathin $CoSe_2$ nanosheets, demonstrating a 92% selectivity for the $2e^-$ ORR. The 2D structure increased the number of under-coordinated active sites and improved the oxygen adsorption capability. Designing nanoparticles with specific surface morphologies that expose a larger number of active sites enhances the reaction selectivity.

Oxygen vacancies are introduced into metal oxide nanoparticles as an effective strategy to tune the $2e^-$ ORR performance. Oxygen vacancies alter the electronic structure and stabilize the OOH* intermediate, improving the H_2O_2 production efficiency. For example, oxygen vacancies in TiO_2-x and Co_3O_4-x nanoparticles change the oxygen adsorption behavior and inhibit the O-O bond cleavage [254,255]. These studies demonstrate the critical role of defect engineering in adjusting the $2e^-$ ORR catalytic performance of nanoparticles.

Single-atom catalysts (SACs)

SACs represent cutting-edge innovation in the field of electrocatalysis, where each isolated metal atom is dispersed on a support material, acting as an independent active site. This design maximizes the utilization of metal atoms and allows a precise control of the catalytic performance, particularly demonstrating high selectivity for $2e^-$ ORR.

Zeolitic imidazolate frameworks (ZIFs) are common precursors for SAC preparation [256]. After high-temperature pyrolysis, metal atoms within the ZIF structure, along with carbon and nitrogen from the ligands, form abundant active sites and defects. For instance, the pyrolysis of ZIF-67 produces a nitrogen-doped

carbon catalyst containing both Co nanoparticles and single-atom Co sites. This catalyst exhibits significant improvements in the selective production of H_2O_2 (73.3%) and faradaic efficiency (87%) [257]. Similarly, a Zn-N_3O SAC, synthesized using a "pre-adsorption-anchoring and pyrolysis" method, reached a high loading of 11.3 wt.% and demonstrated nearly 100% H_2O_2 selectivity for the $2e^-$ ORR [258]. Additionally, manganese-doped SACs have shown high H_2O_2 selectivity by regulating their active sites, further confirming the potential of ZIF-derived SACs for the $2e^-$ ORR [259].

Noble metal-based SACs have also attracted much attention, owing to their high selectivity for H_2O_2 production. In Pt-SACs, isolated Pt atoms dispersed on nitrogen-doped carbon supports can effectively interact with oxygen intermediates in a manner favorable to the $2e^-$ ORR, significantly increasing the H_2O_2 selectivity [260]. Similarly, Au atoms dispersed on nitrogen-doped carbon show over 90% H_2O_2 selectivity in alkaline media [261]. The support material plays a crucial role in stabilizing the metal atoms in SACs and tuning their catalytic performance. Carbon-based materials, such as graphene and carbon nanotubes, are commonly used as supports due to their high conductivity and surface area [261,262]. Introducing heteroatoms like nitrogen or sulfur can further enhance the stability and activity of SACs [263].

Research has also shown that hollow CuS_x-supported Pt-SACs, leveraging the strong Pt-S interaction and hollow structure, enhance the catalytic activity and improve the mass transport of H_2O_2 [264]. To prevent metal atom agglomeration in SACs, strong metal-support interactions are often employed to anchor the atoms securely to the support, ensuring the metal atoms remain isolated and fully participate in the catalytic reaction [265]. Recent advancements in synthesis techniques, such as atomic layer deposition and wet chemical methods, have further improved the stability and catalytic activity of SACs by precisely controlling the placement of metal atoms on the support surface, resulting in an enhanced catalytic performance [266].

1.3.3 Metal-free electrocatalysts for ORR

In addition to metal-based catalysts, non-metallic ones are among the most promising classes of materials. Carbon-based materials doped with heteroatoms such as nitrogen (N), oxygen (O), fluorine (F), boron (B), sulfur (S), and

phosphorus (P) have demonstrated a remarkable catalytic performance due to their tunable electronic properties, abundant precursor sources (including renewable waste), and low cost.

N-doped carbon materials have shown outstanding performance for the $2e^-$ ORR. The introduction of N atoms, with an electronegativity (χ) of 3.04, disrupts the π-coupling system of C (χ = 2.55), leading to charge redistribution and causing the alteration of the adsorption properties of the carbonaceous materials regarding the OOH*, thereby improving the H_2O_2 production efficiency. N-doped graphitized porous carbon achieved an H_2O_2 production rate of 2.09 mg h^{-1} cm^{-2} under near-neutral conditions [267]. In alkaline media, metal-free N-doped ordered mesoporous carbon, prepared via a solvent-free method, also exhibited high selectivity and stability (~12 h) [268]. N-doped carbon catalysts synthesized by microwave-assisted methods demonstrated an efficiency of up to 90% [269], further highlighting the correlation between nitrogen content and H_2O_2 selectivity. Different nitrogen functionalities, including pyridinic, pyrrolic, and graphitic groups, play distinct roles in catalysis, with pyrrolic nitrogen leading to H_2O_2 selectivity above 80% and stability in alkaline media for about 8 h [270]. An optimized N_x-doped graphene achieved a selectivity of 78.0% at neutral pH, indicating that graphitic nitrogen promotes the H_2O_2 formation, whereas pyridinic nitrogen is thought to further catalyzes the conversion of H_2O_2 into $^{\bullet}OH$ [271].

Oxygen functional groups have also been observed to effectively enhance the catalytic activity of carbon-based materials regarding the $2e^-$ ORR. Mesoporous carbon hollow spheres showed over 90% H_2O_2 selectivity in neutral electrolytes, attributed to their mesoporous structure and oxygen-containing functional groups [272]. Carbon xerogel-80, prepared by hydrothermal carbonization, exhibited the highest catalytic activity and 94% H_2O_2 selectivity due to its high content of C=O groups [273].

Fluorine-doped carbon materials leverage the high electronegativity of F (χ = 3.98) to regulate electron transfer and optimize the adsorption and desorption of the OOH* on carbon materials. F-doped porous carbon achieved an H_2O_2 selectivity between 83.0% and 97.5% under acidic conditions, with CF_2 and CF_3 groups promoting the O_2 activation while maintaining the O-O bond strength

[274]. F-doped carbon nanotubes further validated the role of CF_2 and CF_3, as the weaker binding energies of the OOH* with these fluorinated groups enhanced the H_2O_2 selectivity [275].

Boron-doped carbon materials offer the advantage of nearly zero overpotential, with a faradaic efficiency of up to 85% and excellent stability after continuous electrolysis for 30 h [276]. By adjusting the boron source and annealing temperature, the H_2O_2 selectivity of B-doped carbon materials can reach 98%, with a high boron doping level (5.3 at%) and a rich porous structure [277].

Sulfur-doped carbon materials improve electron conductivity by introducing sulfur nanocrystals, resulting in H_2O_2 selectivity exceeding 70%. The high lattice energy and bond strength of sulfur nanocrystals also enhance the stability of these materials [278].

Phosphorus-doped carbon materials, on the other hand, incorporate phosphorus atoms ($\chi = 2.19$), creating lattice defects in the carbon matrix, further improving the H_2O_2 generation efficiency [279].

In conclusion, metal-free electrocatalysts have significantly enhanced the $2e^-$ ORR performance of carbon-based materials through the incorporation of various non-metal elements. The difference in electronegativity between the doping elements and carbon plays a crucial role in O_2 adsorption and OOH* intermediate desorption, which ultimately determines the catalytic activity and selectivity.

1.3.4 Development of cathodes for H_2O_2 electrogeneration

In addition to developing efficient electrocatalysts for the $2e^-$ ORR, the cathode is a critical component in the electrochemical system for H_2O_2 electrogeneration. It directly interacts with the electrolyte and provides the necessary reaction sites for the $2e^-$ ORR. An ideal cathode should have a large surface area, suitable pore structure, good conductivity, and mechanical robustness to achieve a high electrochemical activity. Commonly used cathodes include immersed cathodes, gas diffusion electrodes (GDEs), and air-breathing electrodes.

Immersed cathodes

Immersed cathodes are fully soaked in the electrolyte, where O_2 is dissolved through aeration and then diffuses into the electrode pores to react at the active sites [280]. The preparation methods and materials used for submerged cathodes significantly impact their performance. Common immersed cathode materials include graphite, graphite felt (GF), carbon felt (CF), reticulated vitreous carbon (RVC), and activated carbon fibers (ACFs) [281].

Graphite-based cathodes: Graphite, with its hexagonal crystal structure and layered arrangement, exhibits excellent chemical stability and conductivity, making it widely used in early research on H_2O_2 electrosynthesis. However, the H_2O_2 production rate is limited due to its small surface area. Researchers have improved graphite electrodes through physical and chemical modifications. For example, acid treatments (employing HNO_3 or H_2SO_4) introduce oxygen-containing functional groups on the graphite surface, thus enhancing its hydrophilicity and increasing the number of active sites, which improves the ORR activity [282,283]. Additionally, loading conductive polymers (such as polypyrrole or polyaniline) and carbon nanomaterials (such as carbon nanotubes or graphene) onto the graphite surface can significantly increase the electrode conductivity and active area. For instance, when carbon nanotubes (CNTs) are loaded onto a graphite electrode, the H_2O_2 production rate significantly increases, attributed to the high surface area and good conductivity of CNTs [284].

Graphite felt and carbon felt cathodes: GF and CF, with their three-dimensional porous structures, large surface area, and good conductivity, are commonly used submerged cathode materials. Methods for preparing GF/CF cathodes include heat treatment, electrochemical oxidation, and chemical modification. Chemical treatments (such as acid or alkali treatments) and electrochemical oxidation introduce more oxygen functional groups (OFGs) and defects on the GF/CF surface, increasing the hydrophilicity and ORR activity [285,286]. Le et al. [287] prepared a porous CF electrode with a high surface area and large pore volume through heat treatment and oxidation, significantly improving the H_2O_2 production and current efficiency. Additionally, loading high-activity materials onto GF/CF electrodes enhances their performance. For example, loading nitrogen-doped porous carbon, carbon black (CB), or carbon nanotubes increases the number of active sites, improving the ORR selectivity

and activity [288,289]. By loading electrochemically exfoliated graphene (EEGr) onto carbon cloth electrodes, the H_2O_2 production rate and current efficiency was improved due to EEGr providing a larger surface area and abundant active sites [290].

Reticulated vitreous carbon cathodes: RVC is a porous carbon material with a glass-like crystal structure, high surface area, and excellent mass transport properties [291,292]. The preparation of RVC electrodes typically involves the polymerization and carbonization of resins and the performance can be adjusted by controlling pore size and density. RVC electrodes have demonstrated excellent performance for H_2O_2 electrosynthesis, especially under high current densities and low oxygen concentrations [293]. Anodic oxidation-modified RVC electrodes show an increased number of surface oxygen functional groups, enhancing the hydrophilicity and the number of active sites, which eventually boosts the H_2O_2 production [294].

Activated carbon fiber cathodes: ACFs possess extremely high surface areas and good porosity, but their application in H_2O_2 electrosynthesis is limited by the low selectivity and current efficiency. Surface modification and the development of composite materials are key strategies for improving ACF cathode performance. By compositing nitrogen-doped porous carbon and carbon nanotubes onto ACF, the H_2O_2 production rate and current efficiency can be significantly enhanced [295].

Gas-diffusion electrodes (GDEs)

The fabrication of GDEs typically involves mixing carbon materials with binders, spraying or rolling them onto substrate materials, and forming a stable electrode structure through heat treatment [296,297]. Due to the importance and widespread use of GDEs in H_2O_2 electrosynthesis, this topic will be discussed in detail in the following Section 1.3.5.

Air-breathing electrodes

Researchers have developed air-breathing electrodes to avoid the need for external air supply and the associated complexity and cost of GDE-based systems. These electrodes do not require external aeration or pressurized oxygen, but instead use oxygen from the ambient air, which diffuses through the hydrophobic

layer of the electrode into the catalyst layer to perform the ORR. The fabrication of air-breathing electrodes (so-called natural air-diffusion electrodes, NADEs) typically involves rolling carbon materials (such as carbon black or graphite) mixed with polytetrafluoroethylene (PTFE) onto a stainless steel mesh current collector, forming both a catalyst layer and a gas diffusion layer [298,299].

The key to designing air-breathing electrodes lies in balancing hydrophilicity and hydrophobicity and optimizing the pore structure to maintain an effective three-phase interface. Air-breathing cathodes with high activity and stability can be obtained by adjusting the ratio of carbon materials, PTFE content, and rolling process parameters. These electrodes exhibit excellent H_2O_2 production rates and current efficiency without external aeration [300,301].

Moreover, other researchers have developed similar air-breathing electrodes, such as floating cathodes and superhydrophobic electrodes, further expanding the potential of these electrodes for H_2O_2 electrosynthesis [301–304]. The simple fabrication process and cost advantages of air-breathing electrodes make them highly promising for practical applications.

1.3.5 Gas-diffusion electrodes

GDEs consist of three main components: a substrate, a gas-diffusion layer (GDL), and a catalytic layer (CL) (as shown in Fig. 23). These electrodes are fabricated by integrating a catalyst into the gas-diffusion layer [305]. The primary function of the electrode substrate is to conduct the electrons and provide structural support, requiring it to maintain good mechanical strength and electrical conductivity under various temperature and pH conditions. Common substrates include carbonaceous materials (carbon cloth, carbon paper) [306] and high-surface-area metal foams [307].

The GDL facilitates the gas transport and diffusion during the electrochemical reactions, necessitating an optimized porous structure to ensure a rapid gas delivery to the catalyst. In addition, the GDL acts as a barrier between the catalyst layer and the substrate, protecting the substrate from corrosion or damage. Good hydrophobicity is essential to prevent electrolyte penetration into the GDL (i.e., flooding), which could lead to performance degradation.

The CL is where gaseous reactants, electrolytes, and catalysts interact, forming the electrochemical reaction three-phase interface/boundary (TPB).

Maintaining a high and stable gas concentration at this interface can significantly enhance the current efficiency, thereby increasing the H_2O_2 production [308]. Therefore, constructing an effective "solid-liquid-gas" TPB is crucial for ensuring the efficient reaction of materials in this region. This efficiency depends on the structure of the catalytic electrode, the choice of catalytic materials, and the optimization of gas mass transport.

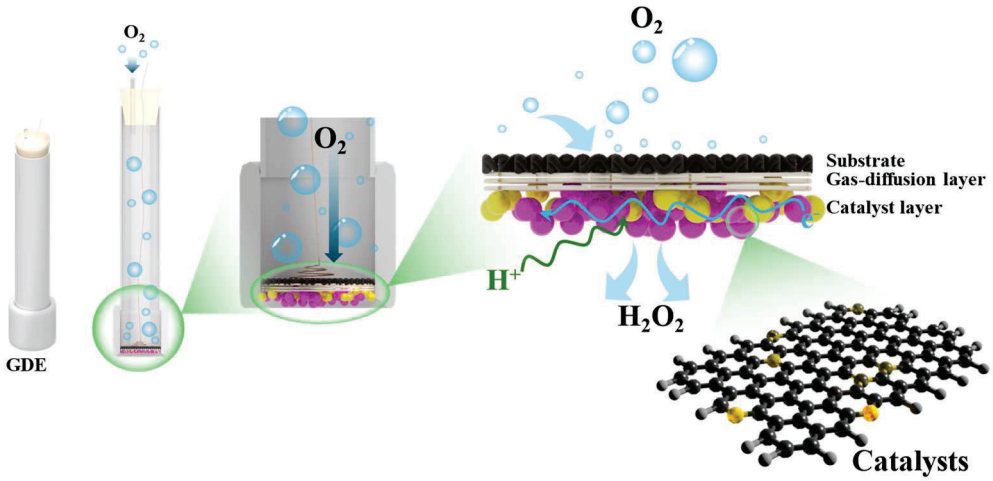

Figure 23. Architecture of GDEs.

The performance of the GDL depends on several key characteristics, needing: (i) High conductivity to facilitate efficient electron transfer; (ii) high porosity to promote effective gas diffusion; (iii) a smooth surface to allow easy deposition of the catalyst layer; and (iv) a well-balanced hydrophobicity to prevent flooding.

Flooding typically occurs due to the excessive hydrophilicity of the GDL, where the electrolyte leaks into the GDE, blocking the pores and reducing the number of active catalytic sites. This disruption of the TPB ultimately degrades the electrode performance and drastically decreases the H_2O_2 production, as shown in Fig. 24.

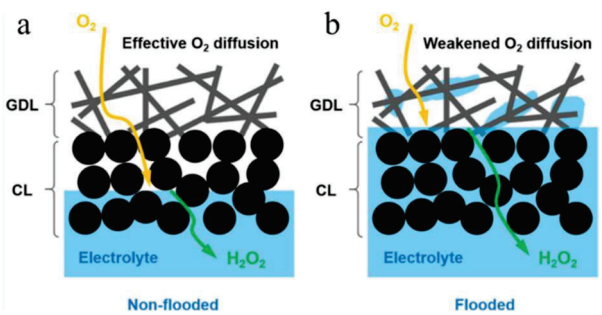

Figure 24. (a) Non-flooded GDE, and (b) flooded GDE [309].

The catalyst layer, composed of electrocatalytic materials, is typically positioned on the wet side of the GDL (i.e., in contact with the electrolyte). This layer forms a microchannel network that provides an effective TPB, ensuring adequate gas delivery and efficient contact between the electrolyte and the catalyst [310]. To optimize the performance of the catalyst layer, the catalyst must be in intimate contact with the electrolyte while maintaining the equilibrium with the gaseous reactant. Thus, the wettability or hydrophilicity of the catalyst plays a crucial role in stabilizing the gas concentration and enhancing the interface between the electrolyte and the catalyst [311].

The catalyst layer is usually prepared using a catalyst ink, which consists of catalyst powder, a solvent (such as water, ethanol, or isopropanol), and a binder (such as PTFE or Nafion) [312]. CB or CNTs are often used as supports for the catalyst or mixed directly into the ink to improve the conductivity of the catalyst layer [313]. When the catalyst ink is deposited onto the GDL, as the solvent evaporates, the catalyst layer forms a unique microstructure. Key parameters affecting the overall performance of the GDE include the composition ratio of the catalyst ink (catalyst-to-binder ratio), choice of solvent, solvent evaporation rate, and conditions, and the method of catalyst ink deposition. These factors influence mass transport within the catalyst layer, the concentration of H_2O_2 produced, the formation of the TPB, and the structure, robustness, and conductivity of the catalyst layer [314].

Common catalyst deposition methods based on an ink include spraying, drop-casting, and hand-painting [315–317], as shown in Fig. 25. Spraying is advantageous because the rapid evaporation of the solvent and the quick fixation of the sprayed droplets onto the drying layer allow for the formation of a well-defined catalyst layer with appropriate thickness [318]. Drop-casting can also create uniform layers, as the moderate solvent evaporation rate prevents excessive penetration of the catalyst ink into the GDL. In contrast, with hand-painting, the slower evaporation rate increases the risk of ink penetrating the GDL, leading to an excessively thin catalyst layer. While increasing the CL thickness, reactivity and mass transport resistance can be enhanced. Also, hand-painting can lead to catalyst aggregation, resulting in fewer electrochemical active sites as compared to spraying and drop-casting methods. An uneven catalyst layer might expose the carbon-based GDL to the aqueous electrolyte, which can cause GDE flooding.

Therefore, the catalyst layer must have an appropriate thickness and uniform distribution to minimize contact between the electrolyte and the carbon-based GDL, thus maintaining a dry inner surface of the GDL.

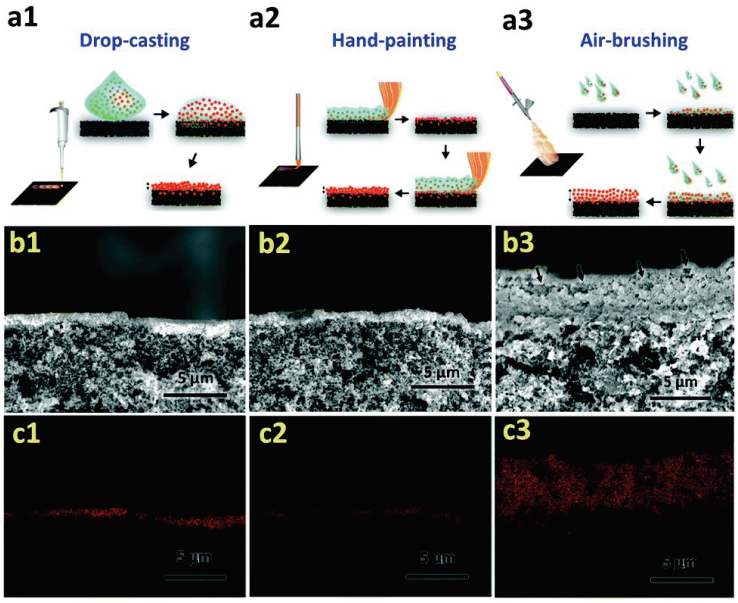

Figure 25. Scheme of the fabrication procedure of the CL in a GDE, following various ink-based methods: (a1) Drop-casting: the catalyst ink is cast by a pipette on the GDL; (a2) hand-painting: the catalyst ink is painted on the GDL using a brush; and (a3) air-brushing: the catalyst ink is sprayed on the GDL employing a manual or automatic spray gun. (b1–b3) Cross-sectional SEM images of Cu-based CLs prepared with respective ink-based methods. (c1–c3) Energy-dispersive X-ray spectroscopy (EDS) elemental mapping of Cu for CLs prepared by respective ink-based methods (0.6 mg cm^{-2} catalyst loading for all methods) [308].

Research indicates that loading catalyst ink at higher temperatures accelerates solvent evaporation, resulting in a thicker CL. For example, spraying at 75 °C can produce a CL nearly three times thicker than at 25 °C [318]. With a constant catalyst loading, increasing the CL thickness enhances its porosity, leading to higher diffusion rates and improved gas mass transport. Additionally, increasing the catalyst loading in the CL raises the current density by providing more active catalytic sites. However, higher catalyst loading does not necessarily result in greater faradaic efficiency regarding the target product. Therefore, the catalyst loading must be optimized based on the specific reaction and desired product [319].

The ionic binder content in the CL significantly impacts the GDE performance by affecting its microstructure, gas diffusion, and catalytic pathways [320]. In some cases, the binder may even serve as a co-catalyst in the reaction [321]. The binder forms a continuous network within the CL, connecting catalyst

particles and facilitating the proton and ion transport, which is crucial for proton conductivity and ion transport. A suitable binder content improves the mechanical stability and conductivity (although this depends on the type of binder) of the CL. Conversely, insufficient binder content can restrict ion transport, cause catalyst particle aggregation, and increase the ohmic resistance. Excessive binder content, however, may obstruct the contact between the CL and the electrolyte, reducing the pore volume and gas permeability while increasing the mass transport polarization, resulting in a poorer GDE performance [320].

The size and morphology of the electrocatalysts also play a critical role in the electrochemical reaction performance. Nanoscale catalysts typically provide more active sites, enhancing the reaction efficiency, especially at high current densities [322]. Additionally, unique nanostructures (e.g., nanosheets, nanoflowers, or nanodendrites) with high surface roughness and sharp edges help regulate catalytic pathways and improve reaction selectivity [323,324]. Nanostructured catalysts with specific crystal facets can facilitate the formation of desired products, thus increasing the selectivity and yield of H_2O_2.

Therefore, optimizing the electrocatalyst loading, nanostructure, and size, along with the preparation method and composition of the catalyst ink, is crucial for achieving optimal electrochemical performance tailored to specific reactions and target products.

1.4 Metal-organic frameworks (MOFs) in HEF process

MOFs are composed of metal clusters connected by organic ligands (Fig. 26). These materials, which include one-dimensional (1D) rod structures, two-dimensional (2D) sheets, and even three-dimensional (3D) networks, exhibit unique physical and chemical properties and have attracted widespread attention over the past two decades [325–327]. Compared to traditional porous materials, MOFs possess fascinating characteristics such as ultra-high surface area, high porosity, tunable chemical composition, and exceptional customizability, making them promising for various applications [328]. However, in practice, the use of MOFs in aqueous media is limited by their poor stability, particularly their sensitivity to moisture and weak conductivity [329].

Fortunately, through effective post-treatment, especially controlled pyrolysis, MOFs can serve as sacrificial templates or versatile precursors, transforming into

more stable and conductive derivatives such as carbon materials, metal oxides, and metal/carbon composites. These derivatives inherit many properties of the original MOFs [330]. Among these derivatives, MOF-derived metal/carbon composites, due to their hierarchical structures and metal content, combine the properties of both metals and carbon, exhibiting synergistic effects [331]. More importantly, these materials effectively address issues like metal ion leaching in metal oxides and the difficulty of recovering carbon materials, offering unprecedented opportunities in advanced materials for environmental remediation, electrochemical energy storage, and conversion [219,332–334].

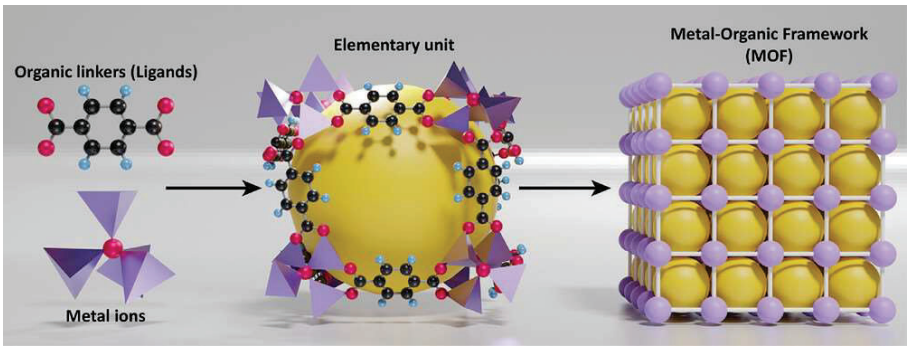

Figure 26. Schematic image of MOF fabrication [335].

The solvothermal/hydrothermal method is the most popular synthesis technique (Fig. 27). This method involves dissolving ligands containing metal ions or clusters in a solvent, placing them in a PTFE-lined autoclave, and heating them to a specific temperature [336]. Coordination reactions require high temperature and pressure, and this technique offers several advantages, including precise crystal production, ease of use, and minimal energy consumption. Most well-known MOFs are produced using this method, including the MOFs developed by the University of Oslo (UiO-66), the zeolitic imidazolate framework (ZIF) series, isoreticular metal-organic frameworks (IRMOF) series, the Materials of the Lavoisier Institute (MIL) series, and MOFs developed by the Hong Kong University of Science and Technology (HKUST-1) [337,338]. Other synthesis methods, such as electrochemical techniques and microwave/ultrasound-assisted methods, are alternative approaches for synthesizing MOFs used in solid-phase extraction [339,340].

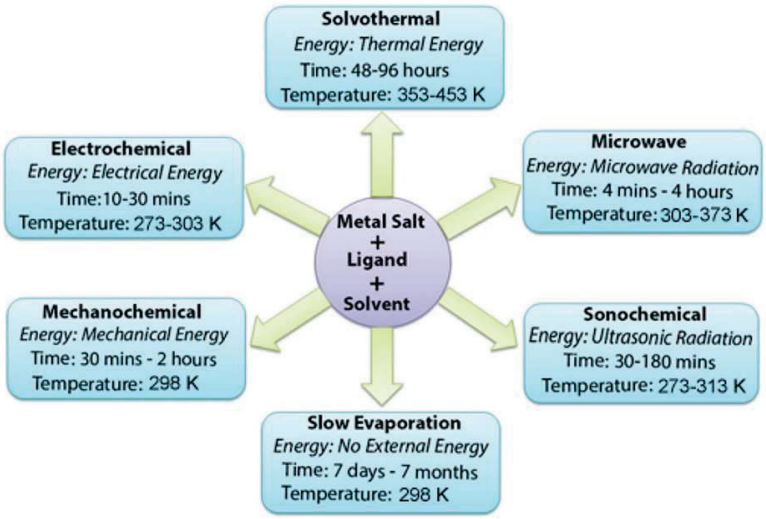

(*a*)

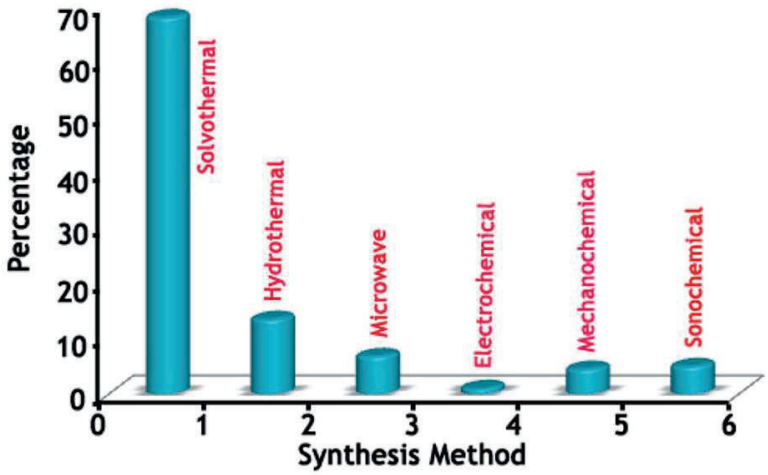

(*b*)

Figure 27. (a) Synthesis conditions commonly used for MOFs preparation; (b) indicative summary of the percentage of MOFs synthesized using the various preparation routes [341].

By pyrolyzing or acidifying pristine MOFs, derived metal/carbon composites can be obtained, offering several unique advantages. These benefits are primarily reflected in the following aspects: (i) The synthesis process is straightforward and does not require additional templates. Since MOFs can serve as excellent carriers for combining with other species, pre-designing the MOF precursor can establish the structure-performance relationship; (ii) the large surface area and high porosity of the original MOFs is retained, exposing a large number of accessible reactive sites; (iii) the organic ligands in MOFs can be transformed into a carbon matrix during high-temperature pyrolysis without introducing an external carbon source. This carbon matrix forms a conductive network facilitating electron transfer [342]. At the same time, the metal nodes can form corresponding metal nanoparticles (NPs) or single atoms (SAs), which are

uniformly distributed within the carbon matrix [343]. The synergistic effect between these two components often results in enhanced performance; and finally, (iv) some organic ligands containing heteroatoms (such as N, P, S, etc.) can be directly incorporated into the carbon matrix after pyrolysis [344]. As mentioned above, heteroatom doping not only generates more defects that provide additional active sites and modulates electrons to enhance electrochemical activity, but it also aids in the preparation of functional NPs such as metal nitrides, phosphates, and sulfides. Therefore, due to these unique advantages, MOF-derived metal/carbon composites have garnered widespread attention as highly attractive advanced materials.

1.4.1 MOFs for cathodic H_2O_2 electrogeneration

The interaction between the central metal and ligands in MOFs significantly influences the activity of the ORR, particularly the binding energy of the key intermediate OOH*. The mechanism and application of pristine MOFs in the $2e^-$ ORR have attracted substantial attention. For instance, researchers have explored the ORR performance of various Prussian Blue analogs (PBAs) with different metal centers, such as Co, Ni, Zn, and Cu, finding that Zn-PBA exhibited the best $2e^-$ ORR performance. Zn-PBA achieved an average electron transfer number of 2.3–2.5 and 88% H_2O_2 selectivity at 0 V vs. RHE. DFT calculations indicated that the formation of *O on Zn sites was energetically unfavorable, which inhibited the $4e^-$ pathway while promoting the $2e^-$ pathway. Additionally, enhancing the unsaturated coordinated metal sites (UCMSs) in MOFs has further improved $2e^-$ ORR performance [345].

Using a novel liquid-liquid interfacial reaction method, 2D Ni-MOF nanosheets were synthesized, allowing precise control over UCMSs by adjusting the ratio of metal precursors to organic linkers. The optimized Ni MOF NS-6 exhibited near-zero overpotential, 98% H_2O_2 selectivity, and an 80 mmol g cat^{-1} h^{-1} production rate. X-ray absorption fine structure (XAFS) spectroscopy showed that Ni MOF NS-6 had the highest Ni^{2+}/Ni^{3+} atomic ratio, which facilitated OOH* formation. Moreover, conductive metal-organic frameworks (*c*MOFs) have emerged as promising $2e^-$ ORR electrocatalysts. Among several *c*MOFs with different metal centers and redox-active organic linkers, Cu-

hexahydroxytriphenylene demonstrated excellent $2e^-$ ORR performance, with 95% H_2O_2 selectivity and a production rate of 792.7 mmol g cat^{-1} h^{-1} [346]. In-situ XAFS measurements revealed that dynamic hydroxyl coupling at Cu sites induced self-polarization of π-conjugated Cu–O–C metal-ligand sites, promoting the formation of OOH*. Furthermore, confining halide anions within the nanopores of *c*MOFs further enhanced the H_2O_2 selectivity [347].

Given the instability of H_2O_2 in alkaline conditions, producing H_2O_2 in neutral or acidic solutions is more desirable. For example, using a 2D MOF, Ni_3(hexaaminobenzene)$_2$, 90% selectivity and 662 mg L^{-1} H_2O_2 yield was achieved in 0.1 M PBS [348]. In-situ X-ray absorption spectroscopy (XAS) suggested a $2e^-$ ORR mechanism involving the ligand and Ni sites. The 2D layered conductive Mg_3(2,3,6,7,10,11-hexaiminotriphenylene)$_2$ also demonstrated over 90% selectivity and impressive H_2O_2 yield of 3400 mg L^{-1} [349].

MOF composites, formed by combining MOFs with other functional materials, further enhance the $2e^-$ ORR performance. For instance, 5,10,15,20-tetrakis(4-carboxyphenyl) porphyrin cobalt(III) chloride (CoTCPP) combined with graphene oxide (GO) was used for H_2O_2 production. Graphene, as an effective support, facilitated the electron transfer and oxygen species adsorption at CoTCPP active sites, achieving 93.4% faradaic efficiency and excellent $2e^-$ performance in 0.5 M H_2SO_4 [350]. Recently, MZIF8/GF composites (i.e., MGF) were synthesized using a microwave-assisted method for $2e^-$ ORR. The ultra-small MZIF8 particles were uniformly dispersed on GF, forming N–Zn–O active sites that promoted oxygen and water adsorption. A high selectivity of 95% and 90% was achieved in 0.1 M KOH and 0.5 M Na_2SO_4, respectively, with 191% increase in H_2O_2 production as compared to conventional methods [351]. MOF composites offer enhanced conductivity and stability, with synergistic effects between components, providing new avenues for improving the $2e^-$ ORR performance. Given the diversity of MOFs and functional materials, MOF composites hold great potential in the field.

MOF derivatives, obtained through thermal or chemical treatment, involve the conversion of MOFs into carbon, metal compounds, or composites, exhibiting excellent $2e^-$ ORR performance. Unlike pristine MOFs, MOF derivatives

generally have higher chemical stability and conductivity. For instance, hierarchically porous carbon with high defect density and sp^3-C content was prepared as the platform with OOH* active sites, achieving 95% selectivity and a high H_2O_2 yield of 395.7 mmol g_{cat}^{-1} h^{-1} [352]. The introduction of heteroatoms, such as fluorine, further optimized the active sites and enhanced the electrochemical activity [353]. Metal-doped carbon materials have also gained attention, such as Zn-based carbon materials produced by pyrolyzing MOFs with different ligands, where ZnO_3C active sites favored the $2e^-$ ORR pathway, yielding approximately 350 mmol g_{cat}^{-1} h^{-1} of H_2O_2 [354]. Moreover, MOF-derived SACs have shown excellent $2e^-$ ORR performance. Pyrolyzing Pd-doped ZIF-8 produced SACs with Pd–N_4 active sites, achieving about 95% selectivity and approximately 30 mmol g_{cat}^{-1} h^{-1} H_2O_2 [355].

MOF-derived transition metal chalcogenides also show promise as $2e^-$ ORR electrocatalysts. For example, titanium-doped Zn–Co sulfide hollow superstructures (Ti–ZnCoS HSS) exhibited 98% selectivity and an H_2O_2 production rate of 675 mmol g_{cat}^{-1} h^{-1} in 0.1 M KOH. The multi-metal doping optimized the d-band center, enhancing the OOH* adsorption [356]. However, complete decomposition of MOFs can lead to structural degradation and reduced surface area. To address this, controlled pyrolysis strategies have been proposed, allowing partial retention of the MOF crystalline structure while generating functional oxides. For example, MOF nanosheets-300 demonstrated excellent H_2O_2 selectivity and yield [357].

Table 4 summarizes and compares the results reported in the literature for in-situ H_2O_2 electrogeneration with MOF-based cathodes.

1.4.2 MOF-based suspended HEF catalysts

Pristine MOFs have received attention as potential heterogeneous catalysts in the EF process due to their unique structural characteristics. As mentioned previously, MOFs exhibit highly ordered porous structures, large specific surface areas, and abundant active sites, thus becoming very promising in catalysis. However, the direct application of pristine MOFs in EF systems faces challenges, such as poor conductivity and limited stability in aqueous solutions [358]. To enhance the performance of these materials, researchers have combined MOFs

with functional materials, improving their catalytic efficiency. For example, when Fe-Co-85 PBA (a Prussian blue analog based on [$K_3Co(CN)_6$]) is mixed with oxidized carbon nanotubes (OCNTs), the conductivity and stability of the catalyst are effectively improved. Fe-Co-85 PBA exposes six well-defined (100) facets during the composite formation, which contain abundant Fe(II) sites. These sites efficiently adsorb H_2O_2 and promote the generation and separation of $^{\bullet}OH$, enhancing the degradation efficiency of organic pollutants [359]. Additionally, with their higher surface area and larger number of active sites, two-dimensional MOFs have demonstrated excellent performance in EF process. The synthesis of 2D Fe-MOFs based on 2,2'-bipyridine-5,5'-dicarboxylate (bpydc) revealed an outstanding degradation of fenofibrate in the photoelectro-Fenton (PEF) process. The 2D structure significantly improved the catalyst conductivity and stability, further enhancing its catalytic activity [360].

After pyrolysis or acidification, MOFs can be converted into porous carbon materials or composites, which exhibit notable advantages in the EF process, such as high catalytic activity, stability across a wide pH range, and easy recyclability. High-temperature carbonization of MOFs under inert (e.g., Ar, N_2) or reducing (e.g., Ar/H_2) atmospheres produces porous structures, while subsequent acid washing removes residual metal components, increasing the surface area and catalytic efficiency [361]. For instance, magnetic N-doped nano zero-valent iron@C (nano-ZVI@NC) derived from MIL-type Fe-MOFs has been applied in the EF process, demonstrating a high catalytic efficiency. Through carbonization, Fe(III) is gradually reduced to Fe_3O_4 and Fe^0, with NH_2-BDC serving as a reductant to facilitate the Fe^0 formation. This catalyst exhibits excellent stability in the EF process, with its core-shell structure effectively preventing iron oxidation and iron ion deposition on the catalyst surface, achieving over 95% gemfibrozil removal within 60 min [219]. Additionally, Fe-based NPs (Fe@MesoC) embedded in mesoporous carbon, synthesized using MIL-100(Fe) as the precursor, led to 100% degradation of sulfamethoxazole within 120 min, significantly outperforming H_2O_2 (4.5%) and Fe@MesoC alone (47.1%). This excellent performance is attributed to the synergistic interaction between the Fe-based material and the carbon matrix. Sulfamethoxazole is adsorbed onto the catalyst via π-π interactions, rapidly diffusing through mesoporous channels to the Fe-based NP surface, inducing a Fe^{3+}/Fe^{2+}-like Fenton system. Notably, the

electron transfer from Fe^0 to Fe^{3+} accelerates the Fe^{3+}/Fe^{2+} redox cycle, ensuring continuous $^{\bullet}OH$ generation. Furthermore, the mesoporous carbon matrix acts as a barrier, enhancing the catalyst stability and reusability [362]. Researchers also developed Cu@C nanoparticles embedded in a 3D reduced graphene oxide (rGO) network (derived from HKUST-1), effectively preventing Cu nanoparticle aggregation and improving the catalytic performance in the HEF process [363]. Using Fe-MOFs and sulfur, FeS_2/C nanocomposites with core-shell structures were synthesized via sulfuration and carbonization, demonstrating higher degradation efficiency and reduced iron leaching for fluoxetine under mild pH conditions, thereby enhancing the stability and catalytic performance [333]. Other studies have shown that CMIL-88-NH_2, a porous core-shell catalyst prepared by pyrolyzing MIL-88(Fe)-NH_2, also exhibited outstanding catalytic performance in EF process [364]. Fdez-Sanromán et al. demonstrated the effectiveness of the commercial Fe-MOF Basolite® F-300 as a heterogeneous catalyst for degradation of antipyrine by EF process. Additionally, two immobilization techniques for Fe-MOF were developed to prepare electrocatalytic cathodes, achieving antipyrine removal rates of up to 82.5% under acidic conditions [365]. Introducing bimetallic porous carbon materials, such as Fe/Cu, Fe/Co, Fe/Mn, and Fe/Ce, further improved the pollutant removal efficiency. The electron transfer between multivalent metals accelerates the regeneration of active sites needed for Fenton's reaction (19), while the embedding of bimetallic nanoparticles prevents aggregation and increases the number of active sites [366–368]. Tang et al. [369] developed a novel 3D flower-like FeCu@C Fenton-like catalyst and investigated its application in degrading sulfamethazine. The FeCu@C led to 100% removal rate of sulfamethazine within 90 min, as compared to only 51.6% using Fe/C in 180 min, which demonstrates that the presence of Cu enhances the catalytic activity. Specifically, the second metal, Cu, provided additional active sites for SMT degradation and induced a synergistic effect that promoted more $^{\bullet}OH$ generation.

MOF-based SACs also exhibit great potential in EF process due to their high atomic utilization and unique electronic structures. MOFs can serve as templates to prepare SACs with uniformly distributed metal atoms and unsaturated coordination environments [370]. These SACs combine the advantages of homogeneous and heterogeneous catalysts, enhancing the catalytic activity. For

example, by pyrolyzing Cu/MIL-88B(Fe) followed by acid washing, a single-atom iron catalyst embedded in 3D porous carbon (AD-Fe/3DPC) was synthesized, which showed excellent degradation of sulfamethoxazole [371]. The introduction of Cu helped to create unsaturated Fe sites in the MOF and prevented metal aggregation during pyrolysis. Transmission electron microscopy and high-angle annular dark-field scanning transmission electron microscopy revealed that single atoms of Fe were uniformly distributed within the 3D porous carbon material.

Further studies showed that using ZIF-8 as a precursor combined with the surfactant cetyltrimethylammonium bromide (CTAB) resulted in abundant and stable FeN_4 sites. In the HEF process, these sites led to complete degradation of 2,4-dichlorophenol. The single-atom Fe active sites accelerated the electron transfer by modulating the electronic structure while neighboring pyrrolic N atoms enhanced the adsorption of organic pollutants [343]. Therefore, MOF-based SACs hold tremendous potential for EF applications. Future research should further explore synthesis methods, metal atom selection, and catalyst structure optimization to improve the catalytic performance.

Table 4 summarizes and compares the performance of MOF-based suspended HEF catalysts reported in the literature.

Table 4. Summary of MOF-based materials as electrocatalysts and suspended HEF catalysts described in Subsections 1.4.1 and 1.4.2.

➢ **Summary of MOFs for cathodic H_2O_2 electrogeneration**

Material	H_2O_2 selectivity	Experimental conditions for H_2O_2 yield	Yield	Reference
Cu-hexahydroxytriphenylene	95% at 0.2 ~ 0.6 V *vs.* RHE	0.6 V *vs.* RHE, O_2-saturated 0.1 M KOH solution, 60 min. The diameter of *WE* is 4 mm, the catalyst loading was about 0.2 mg·cm^{-2}.	792.7 mmol·g_{cat}^{-1}·h^{-1}	[347]
Ni_3(hexaaminobenzene)$_2$	90% at ~ 0.55 V *vs.* RHE	0.4 V *vs.* RHE, O_2-saturated 0.05 M NaPi buffer solution (pH 6.64), 90 min. The mass of catalyst was about 30 µg.	662 mg L^{-1}	[348]
Mg_3(hexaiminotriphenylene)$_2$	~90% at −0.2 to 0.7 V *vs.* RHE	2.5 V *vs.* E_{cell}, O_2 flow rate 30 sccm, in 0.1 M phosphate buffered solution (pH 7.2), after 8 h. The mass of catalyst was about 0.1 mg.	3400 mg L^{-1}	[349]
Hierarchically Porous Carbon	>90.0 % at pH 1–4, >80.0 % at pH 7	−0.5 V *vs.* RHE after 2.5 h in 0.1 M Na_2SO_4 (pH 1–7). The mass of catalyst was about 4.5 mg.	395.7 mmol·g_{cat}^{-1}·h^{-1}	[352]
ZnO_3C	80-86% at 0.5 to 0.7 V *vs.* RHE	0.3 V *vs.* RHE in 0.1 M KOH solution. The catalyst loading was 0.255 mg cm^{-2}.	~350 mmol g_{cat}^{-1} h^{-1}	[354]
$Pd_{0.157}$-NC	~95% at 0.5 to 0.7 V *vs.* RHE	0.5 V *vs.* RHE in 0.1 M KOH solution after 4 h. The mass of catalyst was 40 µg.	~30 mmol g_{cat}^{-1} h^{-1}	[355]
Ti–ZnCoS HSS	98% at 0.774 V *vs.* RHE	0.6 V *vs.* RHE in 0.1 M KOH solution after 90 min. The mass of catalyst was 5.2 mg.	675 mmol·g_{cat}^{-1}·h^{-1}	[356]

➢ **Summary of MOF-based suspended HEF catalysts**

Catalyst	Target pharmaceutical	Experimental conditions	Removal	Reference
Nano-ZVI@C-N	Gemfibrozil	pH 5.5; initial drug at 10 mg L^{-1}; catalyst at 0.2 g L^{-1}; 16.67 mA cm $^{-2}$; 35 °C; 60 min..	95%	[219]
Fe@MesoC	Sulfamethoxazole	pH, 4.0; initial drug at 20 mg L^{-1}; catalyst at 0.2 g L^{-1}; [H_2O_2], 3 mM; 25 °C; 120 min.	100%	[362]
FeS_2/C	Fluoxetine	pH 6.0; initial drug at 10 mg C L^{-1}; catalyst at 0.5 g L^{-1}; 16.67 mA cm $^{-2}$; 35 °C; 60 min..	91%	[333]
FeCu@C	Sulfamethazine	pH 3.0; initial drug at 20 mg C L^{-1}; catalyst at 0.25 g L^{-1}; [H_2O_2], 1.5 mM; 25 °C; 90 min.	100%	[369]

1.4.3 Cu-based materials as electrocatalysts and HEF catalysts

As explained in Section 1.2.1, the Fenton's reaction was initially developed for the catalytic reaction between Fe(II) and H_2O_2 and, in fact, traditional HEF technology primarily uses iron-based catalysts. However, these catalysts present several challenges in practical applications, such as the slow reduction rate of Fe(III), the potential for secondary pollution by iron species, and a weakened catalytic performance under neutral and alkaline conditions. In recent years, with the advancement of research, other transition metals different from iron have emerged as important alternatives for catalyzing the H_2O_2 activation, especially at pH higher than 4, where they comparatively exhibit an advantageous performance. For example, transition metals such as Cu, Co, Mn, and Ni, which possess redox activity, have also demonstrated Fenton-like properties in their reactions with H_2O_2, producing $^{\bullet}OH$. This reaction mechanism (see reaction (66)) is similar to that of the Fenton's reaction (reaction (19)) and is thus classified as an HEF-like process [372].

$$M^{(n-1)+} + H_2O_2 + H^+ \rightarrow M^{n+} + H_2O + {}^{\bullet}OH \quad (66)$$

Table 5 outlines the basic applications of these multivalent metals in Fenton and Fenton-like processes [373]. Copper, in particular, is considered one of the key catalysts in both homogeneous and heterogeneous Fenton systems, besides iron, due to its abundance as a natural resource [363]. Copper-based functional materials have gained attention for their low cost, strong reducing ability, and suitability across a broader pH range [374]. Theoretically [375], copper-based composites are considered more efficient Fenton-like catalysts because Cu(I) activates H_2O_2 much faster than Fe(II) ($k_{Cu(I),\ H_2O_2} = 4.7\times10^3\ M^{-1}\ s^{-1}$, $k_{Fe(II),\ H_2O_2} = 76\ M^{-1}\ s^{-1}$). Moreover, copper-based materials are more suitable than iron-based ones in neutral or alkaline HEF systems. Catalysts containing iron or loaded with iron components exhibit minimal activity at neutral pH, while copper demonstrates optimal Fenton activity in the pH range of 5.5–9.5. This is due to the significantly lower solubility of $Fe(OH)_3$ ($K_{sp} = 4.0\times10^{-38}$) as compared to $Cu(OH)_2$ ($K_{sp} = 6.0\times10^{-20}$). Cu^{2+} exists in media at neutral pH as a soluble copper aqua-complex ($[Cu(H_2O)_6]^{2+}$) [363]. Additionally, the rate constant for the reduction of Fe(III) to Fe(II) by H_2O_2 is relatively low ($k_{Fe3+/H_2O_2} = 9.1\times10^{-7}\ M^{-1}$

s^{-1}), which significantly limits the Fe(III)/Fe(II) redox cycle. In contrast, Cu(II) is more readily reduced to Cu(I) by H_2O_2 ($k_{Cu2+/H2O2}$ = 4.6×10^2 M^{-1} s^{-1}) [373]. Furthermore, compared to Fe(III), Cu(II) complexes with organic degradation intermediates (organic acids) are more easily decomposed by $^{\bullet}OH$, which facilitates the Cu(II)/Cu(I) redox cycle [376]. These properties make copper highly promising for application in HEF-like process.

Table 5. Comparison of several typical metals used in Fenton/Fenton-like process [373].

Metal	Catalyst	pH range	Application cases*	Standard redox potential (V *vs.* SHE)
Cu	Cu, Cu^+, Cu^{2+}	2-10	11.6%	$E^0(Cu^{2+}/Cu^+)$ = 0.159 $E^0(Cu^+/Cu^0)$ = 0.520
Fe	Fe^0, Fe^{2+}, Fe^{3+}	3-7	54.3%	E^0 (Fe^{3+}/Fe^{2+}) = 0.770 $E^0(Fe^{2+}/Fe^0)$ = -0.447
Co	Co^0, Co^{2+}, Co^{3+}	4-7	12.9%	$E^0(Co^{3+}/Co^{2+})$ = 1.920 $E^0(Co^{2+}/Co^0)$ = -0.277
Mn	Mn^{2+}, Mn^{4+}	Natural pH	4.4%	$E^0(Mn^{3+}/Mn^{2+})$ = 1.500 $E^0(MnO_2/Mn^{2+})$ = 1.230

* Statistics of the proportion of typical metals used for H_2O_2 activation in Fenton's reaction in published literature from 2000 to 2023.

Moreover, copper-based MOF derivatives also exhibited outstanding performance in the EF process. A nitrogen-doped carbon-encapsulated Cu/NC catalyst derived from a Cu-MOF showed excellent bisphenol A removal efficiency in the HEF process at an initial pH of 4. After ten degradation cycles, the catalyst maintained its high reusability, demonstrating good stability and practical application potential. The nitrogen-doped carbon layer improved the material conductivity by providing enhanced electron transfer pathways and introducing additional active sites, contributing to the improved pollutant degradation efficiency [363].

Introducing a second metal into Cu-MOFs can significantly enhance the efficiency of the HEF process. For instance, a simple sulfidation of the Cu-MIL-88B(Fe) precursor produced a $Cu_{0.5}Fe_{2.5}S_4$ nanocatalyst. This catalyst retained the features of the MOF precursor, such as its well-defined morphology and uniform distribution of metal active centers, effectively addressing the rate-limiting step of Fe(II) regeneration in HEF systems, thus improving H_2O_2 activation. During the reaction, the reduction rate of Fe(III) was even higher than the consumption rate of Fe(II), due to S^{2-} in the sulfide and Cu species acting as electron donors and shuttles, respectively. Copper significantly accelerated the internal electron

transfer between sulfur and iron, increasing the corrosion potential of iron, which reduced the dissolution of adjacent iron sites. This ensured the sustained reduction capacity of the catalyst, thereby enhancing the overall catalytic efficiency [377].

In summary, these findings indicate that copper-based MOFs and their derivatives hold great potential for application in HEF-like processes. By adjusting metal centers, introducing bimetallic systems, and modifying structures, the performance of catalysts can be significantly improved, providing new pathways for the efficient degradation of organic pollutants.

Furthermore, the application of copper-based MOF derivatives in the $2e^-$ ORR offers new opportunities for the EF process. A carbon-layer-encapsulated copper oxide composite catalyst was prepared using a carbon-additive pyrolysis strategy with Cu-MOF as the base. The carbon capsule blocked the channels for Cu sites to enter the electrolyte while converting metal-centered active sites into carbon sites, thereby suppressing the $4e^-$ ORR side reaction caused by exposed metal sites. Meanwhile, the internal copper oxide with trace oxygen vacancies selectively induced terminal adsorption of $*O_2$ and rapid formation of the key intermediate OOH* at the carbon sites. As a result, the composite catalyst exhibited high H_2O_2 selectivity (98%) and maintained long-term durability for 60 h in an alkaline environment [378].

Additionally, an interface synthesis strategy was employed to fabricate a series of bimetallic Ni-M (M = Co, Fe, Cu) MOFs. The strong synergistic effects between the metal ions effectively regulated the electronic structure, enhancing the catalytic activity of Ni active sites. Among them, the Ni-Cu system yielded a H_2O_2 selectivity of 67%, higher than the 54% achieved by Ni-Fe [379].

In conclusion, copper-based MOFs and their derivatives show great promise in EF process. By adjusting metal centers, introducing bimetallic systems, modifying structures, and exploring two-electron ORR, the performance of catalysts can be significantly enhanced, offering new strategies for efficient pollutant degradation.

1.5 Electrified membranes

Separation processes are ubiquitous in municipal and industrial wastewater treatment plants, owing to their versatility to remove different types of

contaminants, with different sizes, and present within a wide range of concentrations. In particular, membrane technology is very flexible, offering robust solutions that can be adapted to polluted solutions with different complexity. Therefore, it plays a central role in conventional (and, sometimes, in modern) water treatment facilities, accounting for over 50% of the global water purification processes. Water purification requires the removal of various dissolved contaminants, including organic, inorganic, and biological substances, as well as suspended solids and microorganisms, to produce clean water that meets the quality standards established for each purpose [380].

Membrane filtration

Based on pore size, pressure-driven membrane technologies are classified into four distinct processes (Fig. 28): microfiltration (MF), ultrafiltration (UF), nanofiltration (NF), and osmosis (i.e., reverse osmosis (RO), and forward osmosis (FO)). These processes aim to enhance the wastewater treatment efficiency, contributing to more environmentally sustainable production. Both polymeric and ceramic membranes are utilized across various filtration technologies, offering a range of pore sizes, from dense to porous membranes. Due to their diverse pore structures, these membranes cater to different filtration needs, enabling both fine and coarse filtration processes. The pore size range influences the membrane ability to separate substances based on molecular size, making membranes an effective tool for applications requiring precise filtration control [381].

Pressure-driven membrane processes rely on the pressure difference between the feed and permeate compartments as the primary force driving the solvent, typically water, through the membrane [382]. These pressure-driven processes can be categorized based on various factors, including the size, form, and charge of the retained substances, as well as the pressure applied to the membrane [383].

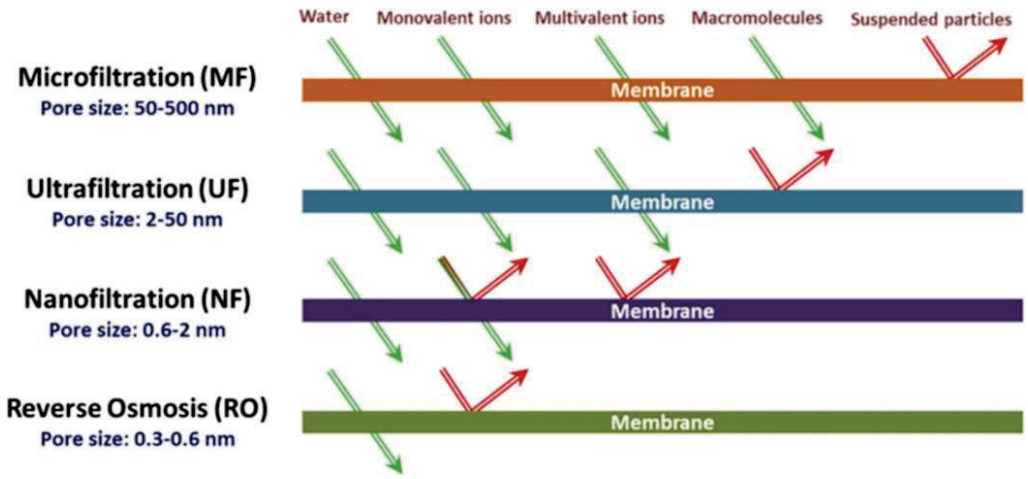

Figure 28. Schematic diagram of MF, UF, NF, and RO membrane filtration processes [384].

MF is unable to remove contaminants smaller than 1 μm; therefore, it is ineffective against emerging organic pollutants. UF, NF, FO, and RO, with smaller pore sizes than MF, have been used to remove emerging pollutants from water. As the pore size decreases, the removal efficiency of these pollutants significantly increases [385]. However, membrane fouling due to pore blockage and restriction is a major obstacle in filtration processes, often leading to higher operational and maintenance costs. For instance, when treating wastewater with high organic loads, organic contamination can cause a short-term flux decline of nearly 50% [386]. Additionally, biofouling, caused by the growth and proliferation of microorganisms, particularly affects the long-term use of membranes. Additionally, hybrid systems like PAC-UF show promise in overcoming limitations of conventional UF and RO systems by achieving higher removal efficiencies for organic micropollutants. However, challenges such as increased operational costs and membrane fouling remain key considerations [387].

Reactive membranes

The development of reactive membranes represents a significant advancement in addressing membrane fouling, with composite ceramic membranes being a major innovation. These membranes not only enhance the physical filtration of wastewater but also introduce chemical treatments [384]. For example, titanium oxide-based composite membranes combined with alumina or silica can simultaneously filter and degrade organic compounds, and they have been designed with anti-fouling and antibacterial properties [388].

Ceramic membranes embedded with iron oxide nanoparticles can catalyze ozonation to degrade organic matter, reducing disinfection by-products. Silver nanoparticle-infused ceramic membranes exhibit excellent resistance to biofouling, making them suitable for drinking water purification. Ceramic-zirconium MOF membranes excel in removing fluoride and multivalent ions from drinking water, while ceramic-zinc MOF membranes enhance NF efficiency for dyes, heavy metal ions, and organic solvents by strengthening the bond between the membrane layer and the ceramic substrate. Ceramic-chitosan UF membranes effectively remove heavy metals such as mercury and arsenic from water, and ceramic-cellulose acetate membranes exhibit oil retention rates as high as 99% in the treatment of oil-water emulsions. Additionally, innovative NF membranes, such as those integrating NH_2-MIL-101(Al) MOF and ZnO nanoparticles, exhibit enhanced hydrophilicity and antifouling properties, with high selectivity for magnesium (90.1%) and calcium (86.5%) ions, offering a promising approach for applications in zero liquid discharge and minimal liquid discharge systems [389].

Ceramic membrane electrode

Recently, the emergence of electrified membranes has provided new solutions for membrane fouling prevention and efficient separation[390]. These membranes integrate electrochemical processes into membrane systems, allowing the membrane to function as an electrode, further degrading pollutants via direct or indirect electrochemical reactions occurring during separation. In particular, the electrified membranes seem to be highly effective in HEF process, where charged membranes generate $^{\bullet}OH$ to remove organic pollutants efficiently. Carbon-based materials, such as graphite and carbon nanotubes, are commonly used to manufacture these electrified membranes due to their low cost and tunable structure. At cathodic potentials ranging from 0.5 to 2 V, electrified membranes can produce 10-40 μM of H_2O_2 in a stable manner, being sufficient to initiate the Fenton's reaction [391]. Additionally, an oxygen-enriched feed stream can promote the H_2O_2 production, which can be controlled by adjusting the transmembrane pressure and flow rate [392].

Fig. 29 illustrates the key developmental milestones and applications of conductive ceramic membranes (CMs) in water treatment. The earliest research, conducted by Hibino et al. in 1995, investigated $BaCe_{0.8}G_{0.2}O_3$ ceramic

membranes for methane catalytic oxidation, though not in wastewater treatment. After 2001, conductive CMs were gradually applied to water treatment, including seawater desalination and organic pollutant removal. A notable advancement was the development of ceramic-based electrosorption membranes for seawater desalination. Although these membranes demonstrated excellent wastewater purification capabilities, they exacerbated membrane fouling. In 2003, SnO_2-Sb-carbon black CMs were introduced as anodes, significantly enhancing the degradation of organic pollutants (with phenol degradation rates of 40-60%) and mitigating membrane fouling issues. By 2008, carbon fiber/alumina composite membranes showed improved performance in industrial wastewater treatment. In 2014, research on Ti_4O_7 reactive membranes revealed the interfacial reaction mechanisms under anodic polarization, particularly the role of direct electron transfer. In 2019, studies further explored the role of reactive oxygen species (ROS) and reactive chlorine species (RCS) in reducing membrane fouling. Additionally, electrocatalytic CMs were combined with other treatment technologies, such as photocatalysis, EF, and electro-activated PMS to prevent membrane fouling. By 2020, the latest Janus conductive CMs, featuring dual electrochemical reaction zones, greatly enhanced pollutant degradation efficiency and energy efficiency [393]. In 2022, the LEMMA research group in situ grew a nucleated MOF on the surface of a CM to obtain an NH_2-MIL-88B(Fe)-functionalized catalytic ceramic membrane (NH_2-MIL-88B(Fe)@CM). They systematically investigated its ability to remove naproxen from aqueous matrices through the so-called EF catalytic ceramic membrane (EFCCM) process, paving the way for the coupling of CMs with EAOPs [394].

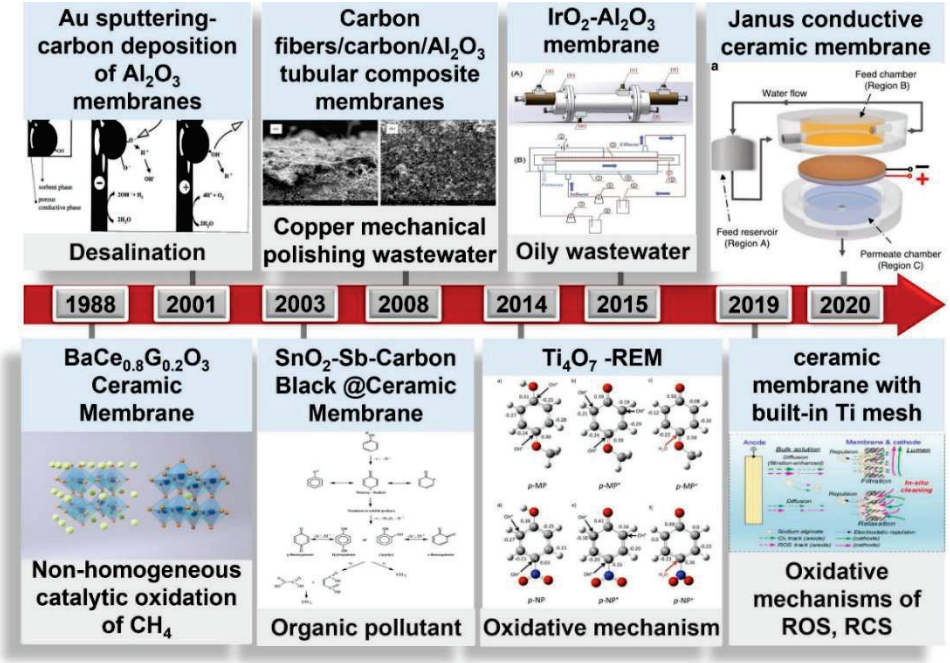

Figure 29. Development of conductive ceramic membranes and related applications [393].

Despite the numerous advancements, the integration of CMs-based membrane filtration with EAOPs for efficiently treating emerging pollutants remains in its infancy. Exploration of key factors, such as catalyst stability, conductivity, electrocatalytic performance, and homogeneity, is still limited, with few studies reported even at the laboratory scale. As a result, the efficiency and adaptability of this novel hybrid technology for treating different pollutants require further investigation, particularly in balancing the conductivity, durability, and cost-effectiveness of membrane materials. In complex wastewater environments, the kinetics of electrochemical reactions on membrane surfaces and the pathways of pollutant degradation need additional experimental and theoretical support. Furthermore, issues such as the long-term stability of membrane fouling, material costs, removal efficiency of persistent pollutants in complex water matrices, and operational energy consumption still demand further exploration. In this regard, the final chapter of this Thesis explores a proof of concept for an advanced membrane filtration system that aims at integrating new HEF catalysts into CM-based filtration.

Chapter 2

Objectives

CHAPTER 2. Objectives

The work conducted in this Thesis aims to achieve four general objectives (GO), by studying and optimizing new ORR electrocatalysts for the efficient electrogeneration of H_2O_2, and by developing Cu-MOF-based heterogeneous catalysts for fast H_2O_2 activation to yield $^{\bullet}OH$. All these catalysts are applied in the HEF treatment of organic pollutants, mainly pharmaceuticals, in model and actual wastewater matrices at circumneutral pH. Finally, in order to fulfill GO4, the work is moved from the stirred-tank electrochemical cell to a continuous-flow reactor to assess the performance of electrified CMs as cathodes for simultaneous ORR and H_2O_2 activation by HEF process. To achieve these main goals, some specific goals (SG) have been defined as well. Please note that a graphical scheme of the present Thesis can been observed in Fig. 1.

GO1: Develop, characterize, and optimize electrocatalysts to enhance the $2e^-$ ORR performance of metal-based and metal-free electrocatalysts, as well as the in-situ electrogeneration of H_2O_2 using GDEs across a wide pH range, further applying them in the HEF treatment of pharmaceuticals operating in batch mode.

- **SG1:** Carry out the synthesis of a series of electrocatalysts and perform their physicochemical characterization using surface and bulk analytical techniques. Additionally, determine their catalytic activity, electron transfer number, and H_2O_2 selectivity through a rotating ring-disk electrode (RRDE) technique.
- **SG2:** Explore the factors influencing the activity and selectivity ($2e^-$ or $4e^-$ ORR), such as the metal doping, the hydrophobic/hydrophilic properties, the textural properties, and the presence of surface functionalities.
- **SG3:** Prepare 3-cm^2 GDEs via hot-press method, and examine the effect of catalyst loading and catalyst/binder ratio on the H_2O_2 accumulation and production rate.
- **SG4:** Evaluate the performance of the GDEs in the HEF

treatment of DPH and 2,4-DCP solutions at natural pH.

GO2: Synthesize and characterize Cu-MOF derivatives, and employ them in the HEF treatment of pharmaceuticals operating in batch mode, aiming to overcome the drawbacks found in homogeneous EF process. In addition, assess the ORR performance of these catalysts.

- **SG5:** Examine the effect of the conditions of hydrothermal synthesis and pyrolysis on the catalyst yield and physicochemical characteristics.
- **SG6:** Optimize the operation parameters (applied current density, catalyst dosage, anode type) to achieve the maximum degradation rate and mineralization efficiency for the HEF treatment of DPH solutions at their natural pH.
- **SG7:** Evaluate the treatment efficiency in an actual urban wastewater matrix under optimal conditions.
- **SG8:** Identify the degradation by-products and propose a degradation pathway for each organic pollutant.
- **SG9:** Assess the potential of Cu-based MOF derivatives for the $2e^-$ ORR.

GO3: Prepare FeCu-MOF bimetallic catalysts by introducing iron in the previous material (GO2), expecting a superior catalytic performance as compared to monometallic counterparts, investigate their synergistic effects, and address the limitations of monometallic catalysts in HEF process.

- **SG10:** Synthesize FeCu-MOF bimetallic catalysts to enhance the Fe(II) regeneration and accelerate the degradation rate of LSN, and carry out their physicochemical characterization.
- **SG11:** Minimize the metal leaching and improve the stability of the catalysts.
- **SG12:** Elucidate the advantages of bimetallic catalysts using electrochemical methods to characterize their behavior.

GO4: Leverage the advantages of bimetallic Fenton catalysts to synthesize bimetallic SACs, with a bifunctional role as electrocatalysts and heterogeneous catalysts, supporting them on CMs for their application as cathodes in the HEF process in a continuous-flow reactor, thereby validating their performance in the in-situ degradation of wastewater containing pharmaceuticals, serving as a proof of concept for future scale-up of the EF technology.

SG13: Synthesize bimetallic SACs and assess their physicochemical and electrochemical properties.

SG14: Design and fabricate a continuous-flow electrochemical reactor.

SG15: Fabricate SAC-modified CMs and investigate how the relevant parameters affect the degradation efficiency for the HEF treatment of AMX solutions.

SG16: Achieve an efficient degradation of pharmaceuticals spiked into actual wastewater without requiring external aeration, combining the filtration/degradation properties of the catalyzed CM with its role as micropore diffuser to promote size reduction of oxygen bubbles.

Chapter 3

Materials, Methods, and Theory

CHAPTER 3. Materials, Methods, and Theory

3.1 Chemicals

The properties, environmental concerns, and degradation results reported in the literature for the model micropollutants investigated in this Thesis have been discussed in detail in subsection 1.1.5 (see also Table 2). All of them were of analytical grade provided by Sigma-Aldrich. The rest of chemicals and reagents were as follows:

Electrolytes. Anhydrous Na_2SO_4 was supplied by Merck.

pH adjustment. Concentrated H_2SO_4 solution and NaOH pellets were supplied by Merck.

H_2O_2 quantification. Ti(IV) oxysulfate was provided by Panreac.

Active chlorine analysis. *N,N*-Diethyl-*p*-phenylenediamine sulfate salt (DPD) was acquired from Fluka Analytical, EDTA dehydrate (99%–101% assay, ACS reagent grade) from Sigma-Aldrich, as well as pure potassium dihydrogen phosphate (KH_2PO_4, USP, Ph. Eur.) and disodium hydrogen phosphate anhydrous (Na_2HPO_4, reag. USP, Ph. Eur., analytical grade) were from PanReac AppliChem.

Dissolved iron analysis. 1,10-Phenanthroline monohydrate, (≥99%) was purchased from Alfa Aesar, whereas glacial acetic acid (reag. USP, Ph. Eur., analytical grade) and ammonium acetate (reag. USP, Ph. Eur., analytical grade) were from PanReac AppliChem, and anhydrous L-ascorbic acid (ACS reagent, ≥99%) was from Merck.

Mobile phase preparation. Formic acid (Optima LC/MS) was purchased from Fisher Chemical and acetonitrile (reag. Ph. Eur. for UHPLC Supergradient, ACS) was from PanReac AppliChem.

Homogeneous catalysts (commercial source). $FeSO_4 \cdot 7H_2O$ was from J.T. Baker.

Commercial carbon black. Vulcan XC72 (reagent grade) was acquired from Fuel Cell Store.

Metal source reagents for catalyst synthesis. Ferric nitrate nonahydrate ($Fe(NO_3)_3 \cdot 9H_2O$, 100%) was from PROBUS S.A., whereas copper(II) nitrate trihydrate ($Cu(NO_3)_2 \cdot 3H_2O$, 99%–104%), zinc nitrate hexahydrate

($Zn(NO_3)_2 \cdot 6H_2O$, reagent grade, 98%) and $SnCl_2 \cdot 2H_2O$ (98%) were purchased from Sigma-Aldrich.

Organic reagents for catalyst synthesis. 2-Aminoterephthalic acid (NH_2-BDC), trimesic acid ($C_6H_3(COOH)_3$, 95%), melamine (99%), and 2-methylimidazole (99%) were purchased from Sigma-Aldrich. For 1,10-phenanthroline, see above. *N,N*-dimethylformamide (DMF, 99.9%) was from Sigma-Aldrich, and methanol (CH_3OH, ≥99.9%) from Scharlau.

Ink preparation. Inks were prepared using PTFE (Aldrich, 60 wt.% dispersion in water) or Nafion (Sigma-Aldrich, 5 wt.% in a mixture of lower aliphatic alcohols and water, 45% water content) as binder, and 2-propanol dry (PanReac AppliChem, max. 0.01% water) as vehicle.

Cleaning of glassy carbon electrode. Diamond paste (¼ µm) and self-adhesive polishing cloths (satin woven natural silk) were purchased from Struers.

CM. The circular CM was purchased from Morui Xincailiao Shop (Online, China) with a diameter of 46 mm, a thickness of 3 mm, and a pore size of 220 nm.

Other reagents. CTAB, ≥99.0% (for ion pair chromatography) from Merck, and polymethylhydrosiloxane (PDMS-H or PMHS) were acquired from Macklin Technology Co., Ltd.

All synthetic aqueous solutions were prepared with Milli-Q water obtained from a Merck Life Science Synergy UV device (resistivity > 18.2 MΩ cm).

3.2 Water matrices

The electrolytic trials were carried out using two types of aqueous matrices: urban wastewater and synthetic water. Pharmaceuticals (10 mg C L^{-1} in most cases) were spiked into water matrices as model organic compounds.

Actual wastewater

Actual wastewater effluents were periodically collected from the secondary decanter of an urban wastewater treatment plant located near Barcelona. Immediately after collection, the water was filtered and then preserved in a refrigerator at 4 °C to maintain its characteristics. Each target pollutant of interest was spiked into this wastewater at a given concentration to evaluate the performance of the degradation process. The specific parameters of the raw wastewater are summarized in Table 6 and Table 7.

Table 6. Characterization of the urban wastewater (collected in June 2024).

Parameter	Unit	Value
Total carbon (TC) [a]	mg C L^{-1}	75.4
Non-purgeable organic carbon (NPOC) [a]	mg C L^{-1}	11.2
Total nitrogen (TN) [a]	mg N L^{-1}	17.1
Specific conductivity [b]	mS	1.7
pH		7.7
Concentration of cations [c]	mg L^{-1}	207.8 (Na^+)
		30.7 (K^+)
		95.1 (Ca^{2+})
		26.6 (Mg^{2+})
		0.2 (Fe (total))
		16.3 (NH_4^+)
Concentration of anions	mg L^{-1}	128.7 (SO_4^{2-})
		401.8 (Cl^-)
		7.2 (NO_3^-)
		5.9 (NO_2^-)

[a] Measured using a Shimadzu TOC-VCNS analyzer; [b] measured with a Crison Basic 30 conductometer; [c] measured by ICP-OES using a Perkin Elmer Optima 8300 analyzer, except NH_4^+, which was measured by UV/Vis spectrophotometry following the indophenol blue method; [d] measured by ion chromatography using a Shimadzu 10Avp liquid chromatograph.

Table 7. Characterization of the urban wastewater (collected in June 2021).

Parameter	Unit	Value
Total carbon (TC)	mg C L^{-1}	48.3
Total organic carbon (TOC) as non-purgeable organic carbon (NPOC)	mg C L^{-1}	9.494 (20.6) [a]
Total nitrogen (TN)	mg N L^{-1}	30.09
Conductance, *G*	mS	1.25
pH		8.04
Concentration of cations	mg L^{-1}	245.3 (Na^+)
		41.8 (K^+)
		114.3 (Ca^{2+})
		31.6 (Mg^{2+})
		0.2 (Fe)
Concentration of anions	mg L^{-1}	146.3 (SO_4^{2-})
		361.1 (Cl^-)
		< 1 (NO_3^-)

[a] After DPH addition, the TOC_0 value of the wastewater is 20.6 mg C L^{-1}.

Synthetic solutions

The electrolyte solutions were prepared in Milli-Q water with the addition of Na_2SO_4 to provide enough conductivity.

3.3 Cathode materials and heterogeneous catalysts

The catalysts used in HEF process include three kinds of cathode electrocatalysts (Sn-doped carbon, N-doped carbon and PMHS-modified carbon) and two kinds of heterogeneous catalysts (Cu/NC, and FeCu/NC). Note that Cu/NC was also evaluated as electrocatalyst for $2e^-$ ORR in paper 4.

3.3.1 Synthesis of catalysts and preparation of GDEs

Synthesis of Sn-doped carbon and manufacture of GDEs

The synthetic route followed to obtain the Sn-doped electrocatalysts is illustrated in Fig. 30. Briefly, 2.0 g of $SnCl_2 \cdot 2H_2O$ and 2.24 g of 1,10-phenanthroline monohydrate was weighed and dissolved in ethanol. The latter solution was added dropwise over the former, while keeping it under stirring. A yellow precipitate was quickly formed, being recovered by filtration and placed in an oven at 80 ºC overnight; it is denoted as $Sn(phen)Cl_2$. Then, 1.0 g of $Sn(phen)Cl_2$ was mixed well with 1.39 g of XC72, followed by pyrolysis at 900 ºC under N_2 atmosphere for 2 h. The resulting black powder, SnC1(raw), is named as SnC1. This powder was dispersed in 1 M H_2SO_4, followed by stirring in an oil bath at 100 ºC for 3 h. The powder was recovered by filtration and dried at 80 ºC, giving rise to SnC2(pickled), so-called SnC2. The resulting powder was pyrolyzed at 900 ºC under N_2 atmosphere for 2 h to finally obtain SnC3(repyrolyzed), named as SnC3.

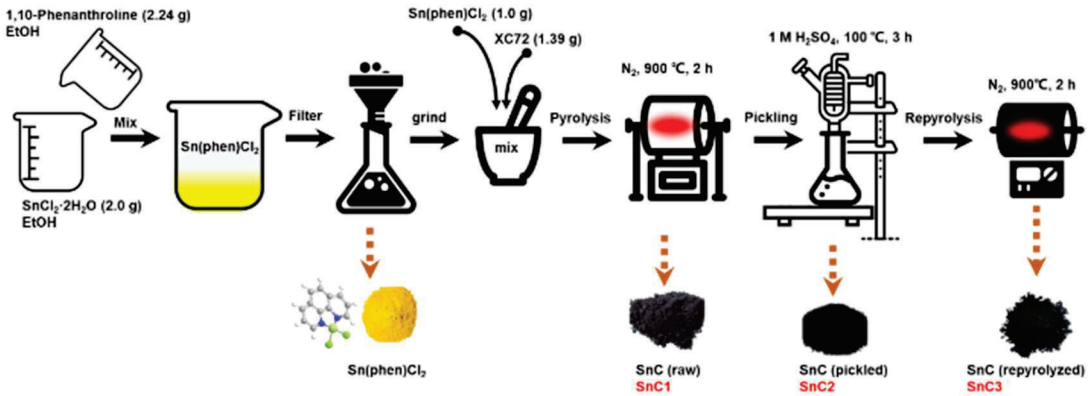

Figure 30. Scheme of the synthesis procedure to obtain three different Sn-doped carbons: SnC1, resulting from a first pyrolysis step; SnC2, obtained upon pickling of SnC1; and SnC3, produced through a second pyrolysis step applied to SnC2 [395].

As shown in Fig. 31, GDEs made with Sn-doped carbon materials were prepared from each type of synthesized powder using the hot-press method. A suitable quantity of binder (PTFE or Nafion) was mixed with 1 mL of Milli-Q water and sonicated. Subsequently, a specific amount of catalyst was added and sonicated for 30 min. To this mixture, 4 mL of 2-propanol was added, keeping the mixture under sonication for 10 min to produce the final ink. On the other hand, a squared carbon cloth (BIASWP, carbon cloth designation A, standard wet proofing) with an approximate area of 9 cm^2 was prepared as the gas-diffusion

layer. It was ultrasonicated using ethanol for 30 min and thoroughly dried at 80 ºC. The previous ink was drop-cast onto one side of the carbon cloth using a micropipette, with approximately 0.4 mL of ink transferred each time. After preparing each layer, the carbon cloth was placed on a heated platform at 80 ºC to ensure complete drying. Once all the ink was cast, the catalyzed carbon cloth was dried, wrapped in multiple layers of aluminum foil, and placed in a press set to a pressure of 6 ton at 210 ºC for 2 h. The final GDE was obtained after cooling down to ambient temperature, and then cut into circles (area of 3 cm^2) for electrolytic trials.

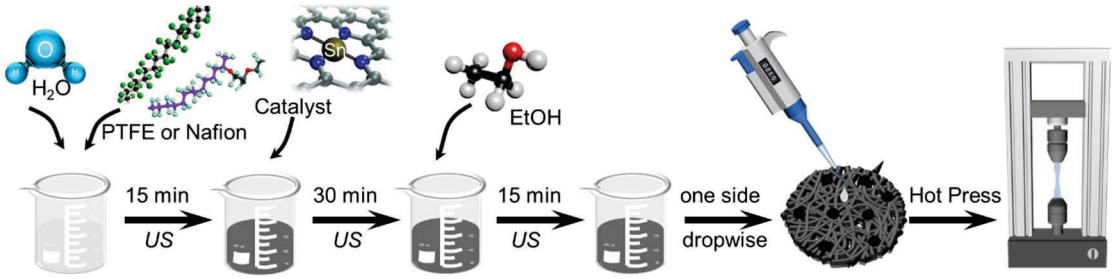

Figure 31. Scheme of the procedure for GDE fabrication using the Sn-doped electrocatalysts, with the final hot-press step (US means ultrasound) [395].

Synthesis of N-doped carbon and manufacture of GDEs

N-doped carbons derived from melamine were synthesized using a direct pyrolysis method (as shown in Fig. 32). Briefly, a certain amount of melamine and 0.5 g of Vulcan XC72 carbon were weighed and then mixed uniformly by grinding on an agate mortar. Each resulting mixture was treated thermally at 600 °C for 2 h under N_2 atmosphere, finally obtaining the electrocatalyst to be studied. The masses of melamine employed were 0.5 (50 wt.%), 1.25 (71.4 wt.%), and 2.5 g (83.3 wt.%), giving rise to samples labeled as M1, M2.5, and M5, respectively. Pure g-C_3N_4 was derived upon pyrolysis of melamine alone (100 wt.%).

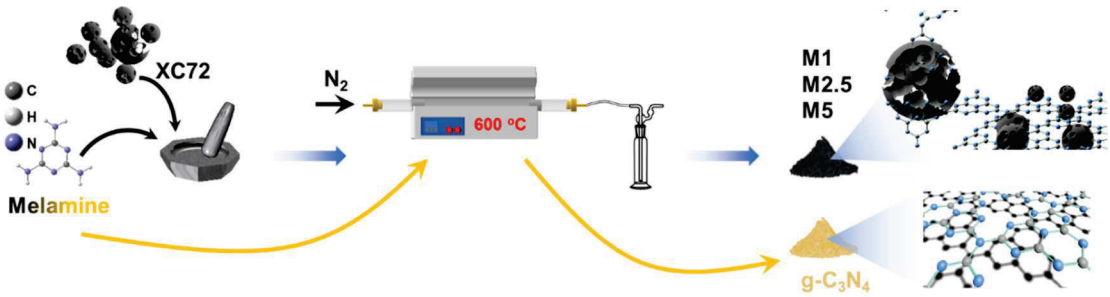

Figure 32. Scheme of the synthesis procedure to obtain four electrocatalysts with different melamine/XC72 mass ratios: 1:1 (M1), 2.5:1 (M2.5), 5:1 (M5), and 100% melamine (g-C_3N_4) [396].

Several GDEs based on melamine-derived N-doped carbons were manufactured via hot-press method, employing different loadings of the optimal electrocatalyst (as shown in Fig. 33). PTFE, which served as the binder, was mixed with 1 mL of Milli-Q water and sonicated. Subsequently, a specific amount of electrocatalyst was added and dispersed ultrasonically for 30 min. Next, 4 mL of 2-propanol was added to this dispersion, keeping it under sonication for 10 min to produce the final ink. On the other hand, a squared waterproof carbon cloth coupon from Fuel Cell Store (area of ~9 cm^2) was prepared as the gas-diffusion layer. The piece was ultrasonicated using ethanol for 30 min, and thoroughly dried at 80 °C. The abovementioned ink was loaded dropwise onto the side of the carbon cloth using a micropipette, approximately transferring 0.4 mL of ink each time. The carbon cloth was placed on a heated platform at 80 ºC to ensure complete drying after preparing each layer, until finishing the total ink volume. Subsequently, the catalyzed carbon cloth was dried, then wrapped in multiple layers of aluminum foil, and finally placed for 2 h inside a press set to a pressure of 6 ton and 210 ºC. The final GDEs were obtained after cooling down to ambient temperature, followed by cutting them into circles (area of 3 cm^2) to carry out the electrolytic trials.

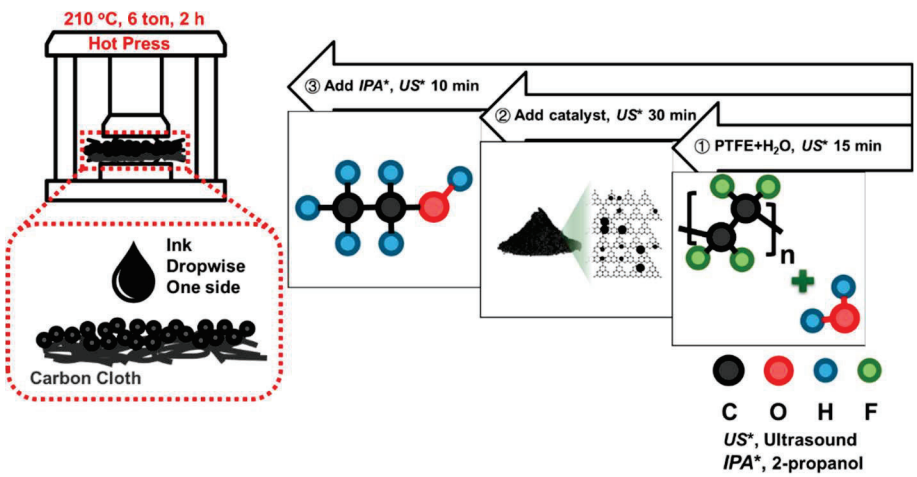

Figure 33. Scheme of the procedure for GDE fabrication using the melamine-derived N-doped carbons, with the final hot-press step (US means ultrasound) [396].

Manufacture of GDEs based on PMHS-modified carbon

These gas-diffusion electrodes consisted of a mixture of CB and PTFE, with or without PMHS addition, acting as both CL and GDL that served to coat a carbon cloth substrate (Fig. 34). To prepare the GDE, commercial cloth with a

geometric area of 9 cm^2 was ultrasonically cleaned in deionized water and ethanol, each for 30 min, and then dried at 80 °C for 12 h. Then, 200 mg carbon black, 0.685 mL PTFE (60 wt.% emulsion) and a certain amount of PMHS were uniformly dispersed in 10 mL ethanol using an ultrasonic bath for 30 min, followed by heating at 80 °C until the mixture turned into a paste. The ointment was coated onto the pretreated carbon cloth substrate, followed by pressing at 5 MPa. The resulting electrode was dried and calcined at 350 °C for 120 min to obtain the PTFE/PMHS-GDE. For comparison, the same manufacturing procedure was carried out in the absence of PMHS, giving rise to the conventional PTFE-GDE.

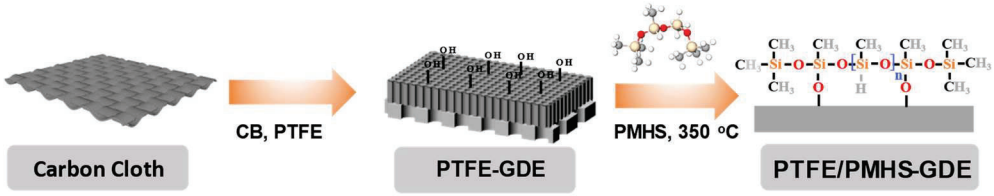

Figure 34. Scheme of the procedure for GDE fabrication of PTFE/PMHS-GDEs [397].

Cu/NC catalyst

The synthesis sequence for obtaining the Cu/C catalysts is schematized in Fig. 35. Briefly, to prepare the Cu-MOF, 0.09 M (1.81 g) $Cu(NO_3)_2 \cdot 3H_2O$ and 0.04 M (0.88 g) $C_6H_3(COOH)_3$ solutions were separately prepared in 50 mL methanol, then sonicated for 10 min to ensure homogeneity, and further stirred using a magnet at very slow rate for uniform mixing. The aging was then carried out under three different conditions: in a beaker at room temperature for 2 h, in an autoclave at 120 °C for 2 h, and in an autoclave at 120 °C for 12 h. After cooling down to room temperature, the product was separated by centrifugation and washed with ethanol three times. Finally, the Cu-MOFs were dried in a vacuum oven (Vaciotem-T from Selecta) at 50 °C for 5 h. These samples were labeled as Cu-MOF-x, where x accounts for the above synthesis conditions. For example, Cu-MOF-A2 refers to the synthesis in an autoclave for 2 h.

Each MOF was pyrolyzed at 600 °C for 2 h under Ar or Ar/H_2 atmosphere at heating rate of 10 °C min^{-1}. It is worth noting that the powder obtained by pyrolysis in Ar atmosphere was dark brown/red, whereas that prepared in Ar/H_2 was almost black. The powder sample was washed several times with ethanol and milli-Q water, then dried and stored in the vacuum oven at 50 °C. They are

denoted as Cu/C-a&b where a and b represent the MOF synthesis conditions and the pyrolysis atmosphere, respectively. For example, Cu/C-A2&Ar/H_2 represents synthesis in an autoclave for 2 h and pyrolysis in Ar/H_2 atmosphere.

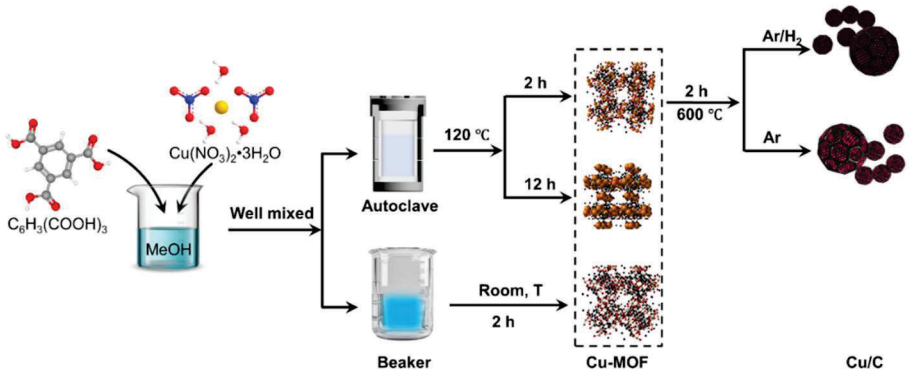

Figure 35. Scheme of the Cu/C catalysts synthesis [398].

FeCu/NC catalyst

The synthesis was based on a previous procedure followed by LEMMA group, and it is schematized in Fig. 36. To synthesize the FeCu-MOF, 5 mmol (2.020 g) $Fe(NO_3)_3$•$9H_2O$ and 5 mmol (1.208 g) $Cu(NO_3)_2$•$3H_2O$ was dissolved in 35 mL DMF, respectively. Also, 10 mmol (1.791 g) NH_2-BDC was dissolved in 25 mL DMF. Both solutions were sonicated for 10 min to ensure homogeneity, whereupon they were mixed evenly and transferred to an autoclave, kept at 110 °C for half a day. The resulting dark red powder, corresponding to FeCu-MOF, was collected by centrifugation and repeatedly washed with ethanol. Then, the FeCu-MOF was vacuum-dried at 50 ºC overnight. The powder was then pyrolyzed at 800 ºC for three hours under N_2 atmosphere (heating rate of 5 ºC min^{-1}). The carbonization product was treated by reflux using a 0.2 M HCl solution for 2 h at 50 ºC. This was followed by rinsing with deionized water and overnight drying, yielding FeCu/NC catalyst. Fe/NC and Cu/NC were obtained similarly, using only one nitrate salt in the first step.

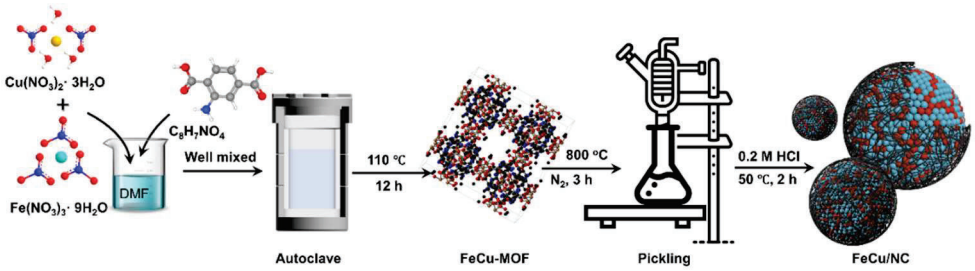

Figure 36. Scheme of the FeCu/NC catalyst synthesis. In the case of Fe/NC and Cu/NC catalysts, only one of the two initial nitrates was employed [399].

FeCu-SAC catalyst and manufacture electrified membranes

The synthesis procedure to obtain FeCu-SAC is illustrated in Fig. 37. Briefly, 1.00 g of CTAB, 4.76 g of $Zn(NO_3)_3 \cdot 6H_2O$, 0.40 g of $Fe(NO_3)_3 \cdot 9H_2O$, and 0.23 g of $Cu(NO_3)_2 \cdot 3H_2O$ was dissolved in 100 mL of methanol to form a clear solution. Subsequently, 100 mL of methanol containing 7.26 g of 2-methylimidazole was slowly added to the above mixture. The mixed solution was stirred at room temperature for 24 h. The resulting precipitate was then collected by centrifugation at 10,000 rpm for 10 min, washed several times with ethanol, and dried under vacuum at 50 °C for 12 h. The dried powder was then transferred to a tube furnace and heated at 900 °C for 3 h under N_2 atmosphere. The final catalyst is denoted as FeCu-SAC.

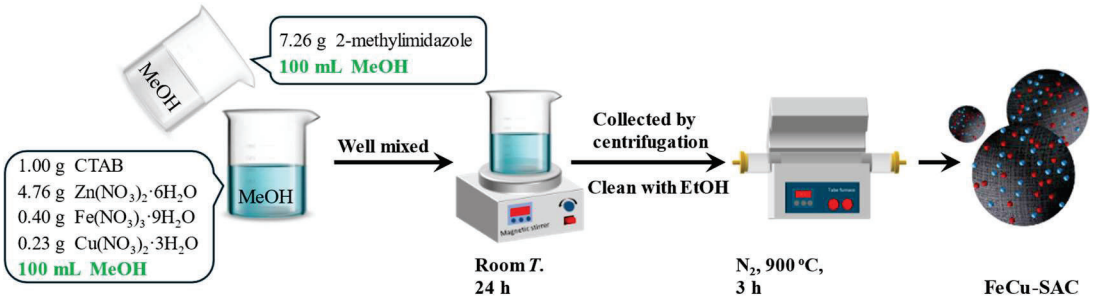

Figure 37. Scheme of the FeCu-SAC catalyst synthesis.

To prepare the electrified CM, the process begins with a cleaning step, placing the CM in ethanol for 10 min of ultrasonic cleaning, followed by 20 min of ultrasonic cleaning in Milli-Q water. Once cleaned, the CM is dried on a heating platform at 80 °C for 30 min. Meanwhile, the FeCu-SAC ink is prepared by weighing a specific amount of the catalyst into a 50 mL centrifuge tube, adding Milli-Q water, 2-propanol, and Nafion, and then sonicating the mixture for 30 min to ensure proper dispersion. Once the ink is ready, the heating platform is set to 80 °C, and the CM is placed on a piece of 5×5 cm aluminum foil on the platform. Using a 1-mL pipette, 800 μL of ink is drop cast onto the CM at a time, ensuring even coverage over the surface, and the ink is dried on the hot plate. This step is repeated until all the ink has been used up, with only one side of the CM coated with the catalyst. Finally, the catalyst-loaded CM is fully dried at 80 °C, completing the preparation of the electrified membrane. The raw and catalyst-loaded CMs are shown in Fig. 38.

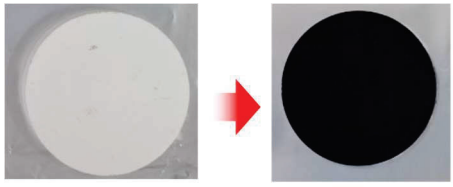

Figure 38. A raw CM and catalyst-loaded CM.

3.3.2 Characterization

The main catalyst characterization techniques involved in this Thesis are listed in Table 8. Most of these analyses have been carried out at the *Centres Científics i Tecnològics de la UB* (CCiT-UB). The measurements were done by specialized technicians in charge of each apparatus, whereas data processing was totally done by the PhD candidate (except in the case of synchrotron measurements). The interpretation of all results was elaborated by the candidate, the supervisor and different co-authors listed in the publications.

Table 8. Characterization techniques used in this Thesis.

Technique	Sn-doped catalyst	N-doped catalyst	PMHS-modified catalyst	Cu/NC catalyst	FeCu/NC catalyst
Elemental analysis (EA)		√			
X-ray powder diffraction (XRD)	√	√		√	√
X-ray photoelectron spectroscopy (XPS)	√	√	√	√	√
Raman spectroscopy	√	√			
N_2 physisorption	√	√			√
Dynamic light scattering (DLS)				√	
Fourier transform infrared spectroscopy (FT-IR)	√	√			
Scanning electron microscopy (SEM)			√		
Transmission electron microscopy (TEM)	√	√		√	√
X-ray absorption spectroscopy (XAS)	√				
Inductively coupled plasma with optical emission spectroscopy (ICP-OES)				√	

Elemental Analysis

EA was performed using a Flash 2000 analyzer (Thermo Scientific) to determine the bulk content of hydrogen, carbon, nitrogen, and sulfur in some

samples. The instrument was calibrated with 2,5-bis(5-*tert*-butyl-benzoxazol-2yl)thiophene as the standard. The sample, weighed into a tin cell with V_2O_5 as the combustion catalyst, was fully combusted. The analyzer, equipped with a CuO/Cu column heated to promote the reaction, converts H, C, N, and S into H_2O, CO_2, NO_x, and SO_x. Helium, used as the carrier gas, transports these products through the copper section, where they are exit as H_2O, CO_2, N_2, and SO_2. The gases then pass through a molecular exclusion chromatographic column linked to a thermal conductivity detector (TCD). The peak responses are compared to the standard, and the quantities of H, C, N, and S are determined based on the peak area ratios.

XRD analysis

X-ray diffraction (XRD) is a widely used technique to study the crystallinity of structures. When radiation hits a crystal, it causes electrons to vibrate, producing scattered radiation. Constructive interference occurs in specific directions, depending on the atomic arrangement of the crystal. The kinematic theory, applied to powders, focuses on elastically scattered radiation, where waves are in phase if their optical path difference is a multiple of the wavelength. By adjusting the angle and rotating the sample, the diffraction pattern provides information on the symmetry and physical properties of the crystal, such as its crystallite size.

XRD analysis for Sn-doped and N-doped electrocatalysts was performed using a Bruker AXS D8 ADVANCE Plus diffractometer, utilizing a Cu source ($\lambda_{K\alpha 1}$ = 1.5406 Å) on a Si zero-background sample holder. For heterogeneous catalysts Cu/NC and FeCu/NC, XRD analysis was carried out using a PANalytical X'Pert PRO MPD Alpha-1 powder diffractometer in Bragg-Brentano $\theta/2\theta$ geometry with the same Cu source. All data obtained were analyzed using HighScore Plus software (v. 3.0.5), and the reference codes of the identified structures were also derived from it.

XPS analysis

X-ray photoelectron spectroscopy (XPS) is a powerful surface characterization technique based on the photoelectric effect, allowing analysis of the outermost atomic layers of a material. Upon irradiation of a material with X-

rays, the photons interact with the atoms, causing the ejection of core electrons. The kinetic energy of these emitted electrons is then measured, and from this, the binding energy of the electrons can be determined, which is specific to the elements present and their chemical states. XPS operates in ultra-high vacuum (UHV) conditions and typically probes depths of just a few nanometers. The X-ray source, usually aluminum (Al Kα) or magnesium (Mg Kα), emits photons that bombard the sample, and the emitted electrons are then analyzed using an electron spectrometer. The resulting XPS spectrum consists of sharp peaks corresponding to photoelectrons that have not lost energy (elastic scattering), along with a background related to inelastic scattering. The position and intensity of the peaks inform about the elemental composition, chemical bonding, and oxidation states of the surface atoms. This technique is particularly useful for interpreting the evolution of surfaces, functional groups, and elemental distributions.

In this study, XPS analysis of Sn-doped and N-doped electrocatalysts was carried out using a SPECS system equipped with a high-intensity twin anode X-ray source (XR50) and a Phoibos 150 MCD-9 XP detector (2400 V). The Large Area analyzer lens operated at 1.5 kV in Fixed Analyzer Transmission mode with an excitation energy of 1486.61 eV. For the heterogeneous catalysts, Cu/NC and FeCu/NC, a PHI 5500 Multitechnique System from Physical Electronics was used, featuring an Al Kα monochromatized X-ray source at 486.6 eV and 350 W, positioned perpendicular to the analyzer axis. The system was calibrated using the Ag $3d_{5/2}$ line (full width at half maximum, FWHM 0.8 eV), and the analyzed area was a 0.8 mm diameter circle. General spectra were recorded with a pass energy of 187.85 eV and a step size of 0.8 eV, while high-resolution spectra used 23.5 eV pass energy and 0.1 eV step size. All measurements were performed under ultra-high vacuum (5×10^{-9} to 2×10^{-8} Torr), and data were analyzed with Avantage software, using the C 1s peak at 284.8 eV as the internal reference.

Raman spectroscopy

Raman spectroscopy is a vibrational spectroscopy technique that exploits the inelastic scattering of photons, known as Raman scattering. When monochromatic light, typically from a laser, interacts with a material, most scattered light retains the same frequency (Rayleigh scattering), but a small fraction undergoes inelastic scattering, resulting in two components: Stokes

(lower frequency) and anti-Stokes (higher frequency) shifts. These shifts provide insights into the vibrational modes of the material. In Raman spectroscopy, the resulting spectrum is typically plotted as a function of Raman shift, which allows comparison across different laser excitations. For carbonaceous materials, Raman spectra provide information about graphitization and crystallinity, with key peaks including the G band (~1580-1600 cm^{-1}) from the in-plane stretching of sp^2 carbons, and the D band (~1350 cm^{-1}) associated with defects in the structure. The ratio of the D and G band intensities (I_D/I_G), along with the FWHM of the G band, allows the evaluation of the degree of graphitization. Additionally, the 2D band (~2700 cm^{-1}) and other higher-order peaks offer further insights into the structure and defects.

This technique is widely used to assess the structural characteristics of carbon-based materials and the degree of disorder in their graphitic domains. In this Thesis, Raman characterization of samples (Table 8) was carried out employing a LabRAM HR Horiba Jobin Yvon 330-1993 cm^{-1}, equipped with a 532 nm laser for photoexcitation. Curve fitting of Raman spectra was made using pseudo-Voigt function.

N_2 physisorption analysis

N_2 physisorption technique is based on the measurement of the surface area and pore size distribution of a material through adsorption and desorption of nitrogen gas at 77 K. This evaluation is essential for analyzing porous materials, which require high surface areas for effective catalytic activity and diffusion of reactants. Adsorption occurs when gas molecules adhere to the surface, while desorption is the reverse process. Two adsorption types exist: physisorption, involving weak intermolecular forces, and chemisorption, where chemical bonds form.

In N_2 physisorption, the analysis focuses on understanding the external and internal surfaces of materials, particularly for porous adsorbents. The external surface refers to the area outside the pores, while the internal surface includes the inner surface of the pore walls. Pores are categorized into three types based on size: micropores (less than 2 nm), mesopores (2-50 nm), and macropores (greater than 50 nm). The process involves measuring the quantity of gas adsorbed at different relative pressures and plotting isotherms, which can provide insights into

the pore structure and adsorption properties.

The Brunauer-Emmett-Teller (BET) method is commonly used to calculate the specific surface area of materials by applying a linear form of the BET equation. This method assumes multilayer adsorption and allows determining parameters such as the monolayer capacity. For materials with micropores, more advanced methods like DFT are often coupled with BET to improve the accuracy.

Hysteresis in the adsorption-desorption isotherms indicates the presence of pores with complex structures or metastable adsorption states. This behavior is particularly significant in mesoporous materials and provides valuable insights into pore connectivity and adsorption dynamics.

Adsorption/desorption isotherms:

As expected, the adsorption and desorption curves often do not overlap, which demonstrates distinct patterns based on the properties of the material and are classified by IUPAC into various types (as shown in Fig. 39).

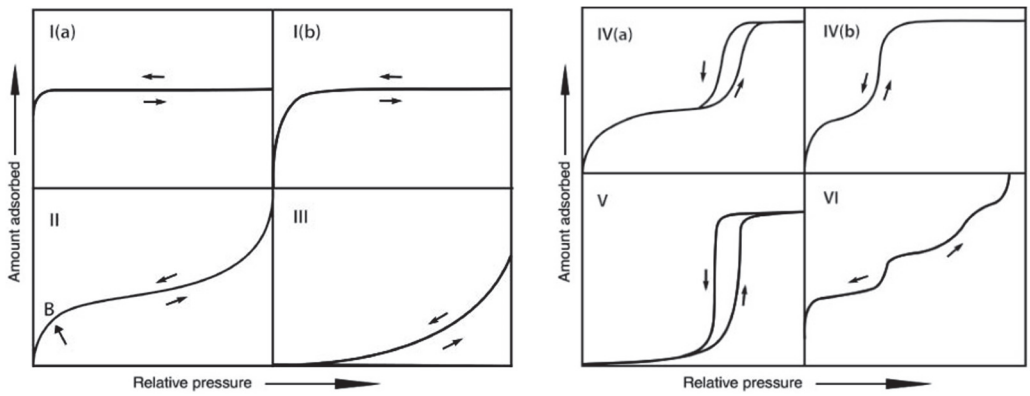

Figure 39. Physisorption isotherm as classified by IUPAC [400].

Type I isotherms are characteristic of microporous solids with limited external surface areas, such as activated carbons, zeolites, and certain porous oxides. These isotherms exhibit a concave shape relative to the p/p_0 axis and approach a saturation limit. Subtypes include Type I(a), associated with materials dominated by narrow micropores (<1 nm), and Type I(b), related to materials with a broader pore size distribution, including wider micropores and small mesopores (<2.5 nm).

Type II isotherms are related to physisorption of gases on non-porous or macroporous adsorbents; they exhibit a distinct shoulder at Point B, accounting for the transition from monolayer to multilayer adsorption.

Type III isotherms lack a distinct Point B, which can be related to weak

adsorbent-adsorbate interactions, where molecules cluster around favorable surface sites of non-porous or macroporous materials.

Type IV isotherms describe mesoporous adsorbents, combining monolayer-multilayer adsorption and capillary condensation. Subtype IV(a) features hysteresis due to larger mesopores (>4 nm), whereas Type IV(b) shows reversibility in smaller mesopores.

Type V isotherms are similar to Type III at low p/p_0 but involve pore filling at higher pressures, as has been observed in hydrophobic micro- and mesoporous materials with water adsorption.

Type VI isotherms account for stepwise adsorption on uniform non-porous surfaces, with each step reflecting the capacity of a single adsorbed layer, such as highly graphitized CB.

Hysteresis Loops:

Hysteresis in adsorption/desorption isotherms is often due to pore structure or metastable adsorption effects. The main types are (see Fig. 40):

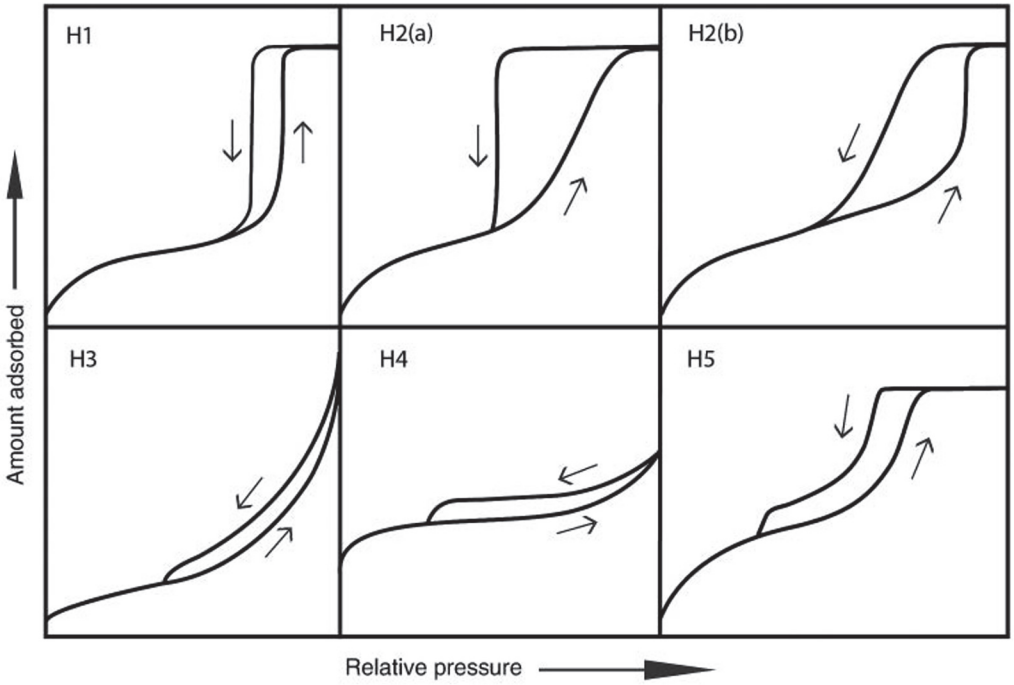

Figure 40. Possible hysteresis cycle in the physisorption isotherm as classified by IUPAC [400].

H1 loops: Typical of materials with uniform mesopores (e.g., MCM-41, SBA-15, mesoporous carbons).

H2 loops: Associated to complex pore structures, with H2(a) seen in silica gels and some porous glasses, and H2(b) in mesocellular silica foams, both linked

to pore blocking or percolation.

H3 loops: Typically found in non-rigid aggregates of lamellar particles (e.g., clays) or incomplete macropore filling.

H4 loops: A hybrid of Type I and II, often seen in zeolite aggregates or mesoporous carbons.

H5 loops: Rare, they are linked to structures with open and partially blocked mesopores (e.g., capped hexagonal silica).

In this study, N_2 adsorption and desorption isotherms were measured using a Micromeritics TriStar 3000 analyzer. The specific surface areas of the samples (Table 8) were calculated using the BET method. Prior to the measurements, the samples were degassed under vacuum for 4 h at 40 ºC. The total pore volume was determined based on the amount of N_2 adsorbed at a relative pressure (p/p_0) of 0.97.

DLS analysis

Dynamic light scattering (DLS) is a technique used to measure the size distribution of particles in suspension by analyzing their Brownian motion. When a laser is directed at the sample, the particles scatter light, and the fluctuations in scattered light intensity, caused by particle motion, are measured over time. The diffusion coefficient obtained from these fluctuations is used to calculate the hydrodynamic diameter of the particles via the Stokes-Einstein equation. DLS is commonly used to analyze nanoparticles, proteins, and other macromolecules in solution, with typical particle sizes ranging from nanometers to micrometers.

The DLS analysis of some samples (Table 8) was done using an LS 13 320 laser diffraction particle size analyzer from Beckman Coulter. The dispersion medium was acetone and the samples were sonicated at 30 kHz and 200 W for 5 min before analysis.

FT-IR spectroscopy

Fourier transform infrared spectroscopy (FT-IR) is a technique used to obtain the infrared spectrum of absorption or emission of a solid, liquid, or gas. It works by passing infrared radiation through a sample, where different molecular bonds absorb specific frequencies of the infrared light, causing them to vibrate. These vibrations can be related to different functional groups in the

molecule, providing a molecular fingerprint. FT-IR uses an interferometer to collect all wavelengths of light simultaneously, and a mathematical process called Fourier transform converts the raw data into a spectrum. This technique is widely used to identify chemical bonds and functional groups, making it essential for material analysis, chemical identification, and studying molecular structures.

The FT-IR analysis was performed using a Thermo Scientific Nicolet 6700 equipped with a Smart Orbit Diamond. OMNIC software was run in the wavenumber range from 4000 to 500 cm^{-1}.

SEM

Scanning electron microscopy (SEM) utilizes a focused high-energy electron beam to analyze the morphology of the sample, as well as its chemical composition via X-rays needed to carry out the simultaneous EDS analysis. SEM operates by directing an electron beam onto the sample, causing the emission of secondary electrons, which are captured by a detector and used to create an image. These secondary electrons provide detailed information about the sample surface morphology and topography, while backscattered electrons are useful for highlighting compositional contrasts in multiphase materials. The electron beam typically has an energy in the range of 100 eV to 30 keV, being generated by a heated tungsten filament.

The analysis was conducted on a ZEISS Gemini 300 SEM microscope coupled to a Smartedx detector operated in backscattering electron mode at an acceleration voltage of 15 kV.

TEM-EDS

Transmission electron microscopy - energy dispersive spectroscopy (TEM-EDS) is used to obtain high-resolution, high-magnification images, providing detailed information about the micro/nanostructure of samples. It works by irradiating the sample with an electron beam in a high vacuum environment. The electron beam is generated through the thermionic emission of a heated tungsten filament and is then manipulated using electromagnetic lenses to focus on the sample. The resulting image, displayed on a fluorescent screen, is formed based on electron scattering by the sample, producing areas of varying contrast. Typically, metal nanoparticles appear as dark spots on a lighter background of

carbon particles. In addition to imaging, TEM can be coupled with EDS to analyze the elemental composition of the sample, providing information about the distribution and quantity of elements present.

In the context of this Thesis, TEM-EDS was employed to evaluate the sample morphology and composition (Table 8). For this purpose, a JEM-2100 (LaB6) microscope from JEOL was operated at 200 kV in STEM mode with a dark-field detector, being coupled to an Oxford INCA EDS detector. The TEM images were analyzed by means of the Digital Micrograph software, while elemental mapping was feasible thanks to the INCA Microanalysis Suite software (v. 4.09).

XAS analysis

X-ray absorption spectroscopy (XAS) is a powerful technique for studying the local atomic and electronic structure of materials. It uses synchrotron-generated X-rays to probe core-level transitions, with XANES providing information on the geometry and oxidation state, and EXAFS offering insights into coordination numbers, bond lengths, and disorder through single scattering events. By analyzing the absorption spectra, researchers can determine the structure around specific atoms in a material. XAS is commonly used in fluorescence mode to achieve high sensitivity, and advanced software like GNXAS is used to interpret the complex data by modeling coordination environments.

In this Thesis, Sn K-edge XAS spectra were measured at the SAMBA beamline of the SOLEIL synchrotron (Saint-Aubin, France) at room temperature in the fluorescence mode using a Ge 33-pixel detector. The beamline was equipped with a sagittal focusing Si 220 monochromator and two Pd-coated mirrors that were used to remove X-ray harmonics.

ICP-OES analysis

Inductively coupled plasma optical emission spectroscopy (ICP-OES) is an analytical technique used to detect and quantify the elemental composition of a sample, including the metal content. The method operates by generating a high-temperature plasma, typically around 10,000 K, using an inductively coupled radio frequency (RF) field. A sample, usually in liquid form, is introduced into

the plasma where the high energy environment causes the atoms and ions to become excited. As these excited species return to their ground state, they emit light at characteristic wavelengths for each element. The emitted light is passed through a spectrometer, where the intensity of the light at specific wavelengths is measured and correlated to the concentration of elements in the sample. ICP-OES is highly sensitive and capable of detecting multiple elements simultaneously.

The ICP-OES analysis was carried out using an Optima 3200 L spectrometer from PerkinElmer.

3.4 Experimental setup for electrolytic assays

Most of the experiments were conducted in an undivided, open, jacketed cylindrical glass cell, with a capacity of 200 mL (as shown in Fig. 41a) and connected to a water bath (Fig. 41b) to maintain water circulation at a constant temperature of 25 °C. A magnetic stirrer was used to fix the stirring rate. The aqueous medium to be electrolyzed usually consisted of 150 mL of 0.050 M Na_2SO_4 solution, whose pH was regulated as needed. In some experiments, actual wastewater was employed instead. A double-sided dimensionally stable anode (DSA-Cl_2 consisting of a Ti|RuO_2 plate, or DSA-O_2 made of Ti|IrO_2) provided by NMT Electrodes, or a single-side boron doped diamond (BDD) anode supplied by NeoCoat, in all cases with dimensions of 50 mm×20 mm×1 mm, was exposed to the solution by delimiting the active area to 3 cm^2 (only 1 side exposed) by using PTFE tape (Fig. 41c). The cathode was a 3 cm^2 carbon PTFE gas-diffusion electrode, either a commercial one supplied by E-TEK or a purpose-made one based on the electrocatalytic materials developed in the Thesis. The circular GDE was placed inside a purpose-made polypropylene holder that served as the air chamber (Fig. 41d). A circular Ni-Cr mesh was put in contact with the GDE, and then a silicone gasket was added to ensure that the ensemble was watertight. The electric contact was made through a Ni-Cr wire, and compressed air was supplied through a glass tube using a KNF LAB air pump (Fig. 41e) that fed compressed air at 0.4 L min^{-1}. The air flow rate was measured using an air flowmeter from Iberfluid Instruments, S.A. The interelectrode gap was about 1 cm. The anode and cathode were directly connected to an Amel 2053 power supply, and a Demestres DM610 BR digital voltmeter served to monitor the cell voltage (as shown in Fig. 41f).

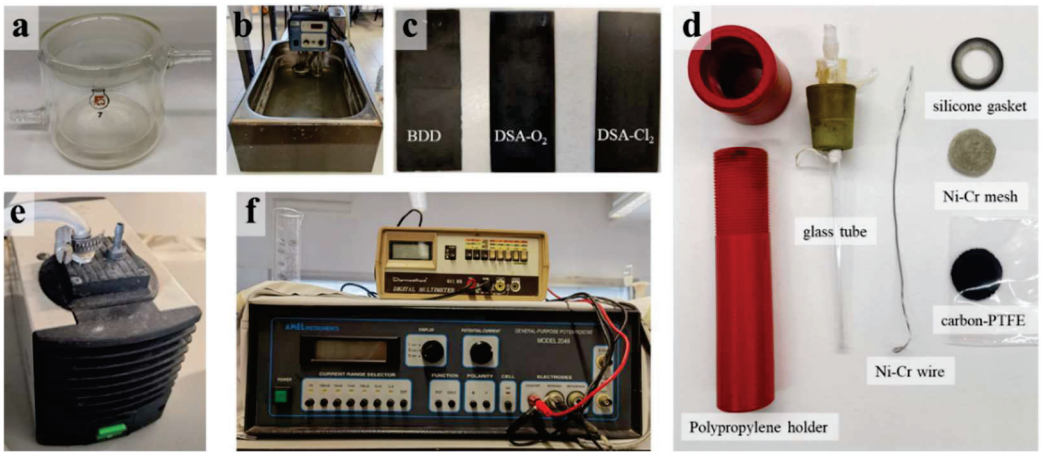

Figure 41. Materials and equipment used to carry out the bulk electrolytic trials.

As explained in Section 1.3.5, GDEs exhibit an advanced TPB structure that allows overcoming the limitations associated with oxygen solubility and transport, making it possible to continuously reduce O_2 to H_2O_2 via $2e^-$ ORR at high production efficiency.

Before first use, the GDE and the anode employed for the trials are polarized in 150 mL of 0.050 M Na_2SO_4 solution, at constant current of 300 mA for 180 min for surface cleaning and activation. After each experiment, the reactor, cathode, and anode are thoroughly cleaned using a 4 M HCl solution to remove any catalyst or organic residues, followed by rinsing with Milli-Q water to ensure no interference in subsequent experiments.

In this Thesis, dead-end filtration (in recirculation mode) is employed to evaluate the performance of membrane filtration, as shown in Fig. 42. The reactor consists of two circular acrylic plates, each with a thickness of 1.8 cm and a diameter of 10 cm. On one side of each plate, a hemispherical cavity has been machined to accommodate the anode, and the CM/cathode ensemble (i.e., catalyzed CM). When the two plates are assembled with the concave sides facing each other, the reactor has an effective internal volume of approximately 30 mL. At the top and bottom ends of the reactor, 5 mm diameter holes are provided to serve as the inlet and outlet for the solution. The peristaltic pump is equipped with Tygon® A-60-G tubing from Saint-Gobain.

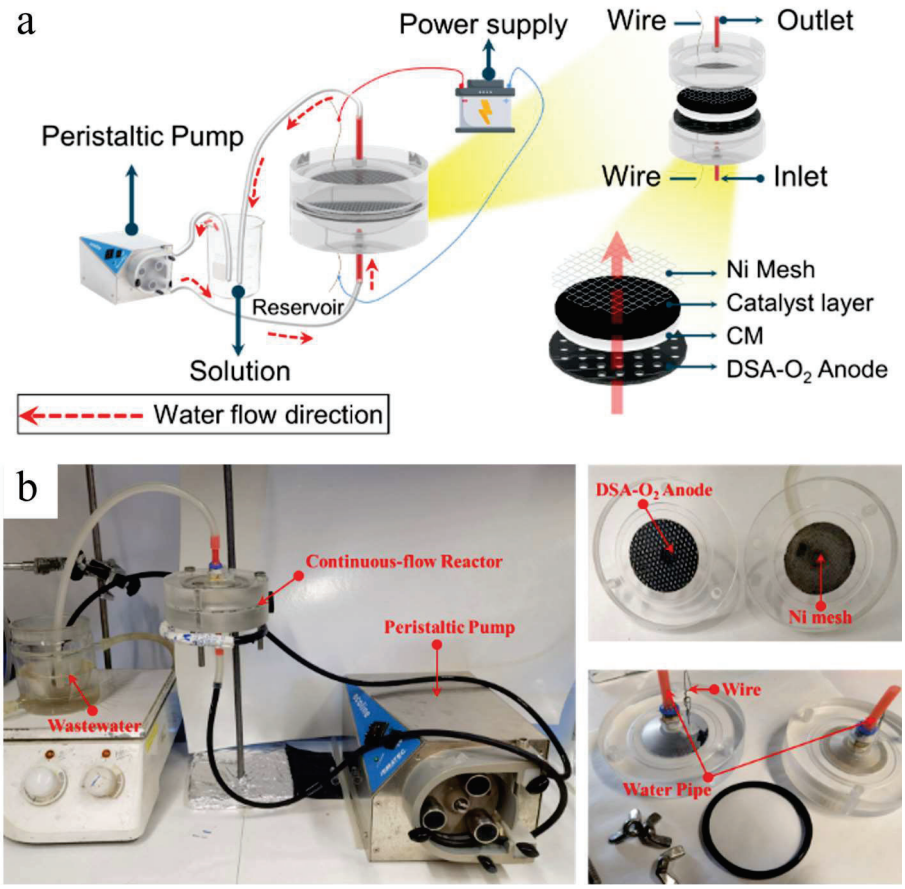

Figure 42. Scheme of the dead-end filtration mode employed in the membrane filtration system, and detailed structure of the continuous-flow electrochemical reactor. (a) schematic diagram, and (b) physical diagram.

The reactor is equipped with a 46 mm diameter DSA-O_2 disk as the anode. The cathode consists of a catalyst layer coated on one side of a 46 mm CM, which is in full contact with a 46 mm nickel mesh to ensure electrical conductivity. To control the flow rate of the circulating solution, the system is equipped with an ISM1079 peristaltic pump manufactured by ISMATEC. The current control and voltage measurements are carried out using an Amel 2053 power supply and a Demestres DM610 BR digital voltmeter, as shown in Fig. 41f.

The aqueous solution used in the experiments consists of 200 mL of 10 mg C L^{-1} pharmaceutical pollutant in 0.050 M Na_2SO_4 medium, which is stored in a 250 mL reservoir. The peristaltic pump draws the solution from the reservoir at a preset flow rate, circulates it through the reactor, and then returns it to the reservoir. At regular time intervals, 0.5 mL samples are collected from both the reactor outlet and the reservoir. The samples are immediately mixed with an equal volume of mobile phase solution to quench (i.e., stop the degradation process).

Before starting each degradation experiment, the peristaltic pump is turned on to ensure that the solution fully fills the system. Once the hydraulic system and reactor are completely charged with the solution, the power supply is activated to initiate the filtration or filtration/degradation experiment. During the trial, a magnetic stirrer is used to ensure thorough mixing of the solution stored in the reservoir.

3.5 Analytical methods and equipment

3.5.1 Quantification of organic pollutants

DPH and **LSN** investigated in this Thesis were determined by reversed-phase high-performance liquid chromatography (HPLC) using a Waters 600 chromatograph coupled to a Waters 996 photodiode array detector (PDA). A Kinetex 5 µm Biphenyl 100 Å (250 mm×4.6 mm) LC column, kept at 35 °C, was employed for accurate separation. **2,4-DCP** were measured by reversed-phase HPLC (SCION6000, China), employing a chromatograph equipped with a Chromcore C18 (5 µm, 4.6 mm × 250 mm) column at 35 °C and coupled to a SC6000 detector. **AMX** concentration was determined on a Waters HPLC (1525 Binary HPLC pump, 2707 Autosampler, Millipore Temperature Control Module (TCM), 2998 Photodiode Array Detector), the separation was made with a Biphenyl column (10 µm, 150 mm×4.6 mm) at 35 °C, whose outlet was connected to a PDA detector. Optimized experimental conditions were used to analyze each pollutant.

Before any analysis, all the samples were microfiltered (0.45 µm, Whatman syringe filters). The samples were diluted by adding half of the volume of the specific mobile phase, in order to ensure the process quenching.

The performance of the electrochemical and filtration/degradation systems was mainly assessed from the concentration decays of the pharmaceutical contaminants, which were determined by calculating the so-called pollutant removal efficiency (i.e., percentage removal of target molecules), according to equation (67).

$$\text{Target pollutant removal (in \%)} = (1-\frac{C}{C_0})\times 100 \qquad (67)$$

where C is the pollutant concentration measured at each treatment time, and C_0 is

the initial concentration, both in mg L^{-1}.

The mobile phases were always prepared by mixing an aqueous layer (A: 0.1% formic acid in Milli-Q water) and an organic layer (B: CH_3CN). Table 9 summarizes the information related to the HPLC analysis, which was always performed with an injection volume of 20 μL, and flow rate of 1.0 mL min^{-1}.

Table 9. HPC analysis conditions.

Pollutant	Mobile phase (A:B)	Detection λ (nm)	Retention time (min)
DPH	60:40	276	3.7
LSN	85:15	227	4.0
AMX	90:10	230	3.5
2,4-DCP [a]	20:80	284	5.2

[a] A: 10 mM KH_2PO_4 solution in Milli-Q water, at pH 4.0; B: CH_3OH. Injection volume of 10 μL.

3.5.2 Total organic carbon (TOC)

The TOC of the solution was measured using a Shimadzu TOC VCSN analyzer. Samples of 5 mL were collected during the treatments, filtered, and mixed with 3 drops of concentrated sulfuric acid before immediately measuring the non-purgeable organic carbon (NPOC) to assess the mineralization. Reproducible values with an accuracy of ±1% were consistently obtained. Total carbon (TC), representing the sum of inorganic and organic carbon, was determined by direct combustion of the sample in a catalytic furnace at 680 °C. The NPOC values correspond to the dissolved organic carbon (DOC) in the solution. The mineralization efficiency of each pollutant is defined as follows:

$$\text{TOC removal (in \%)} = (1-\frac{TOC}{TOC_0})\times 100 \quad (68)$$

where TOC is the concentration measured at each treatment time, and TOC_0 is the initial value, both in mg L^{-1}.

3.5.3 Spectrophotometric quantification of H_2O_2, active chlorine, and iron ions

H_2O_2

The concentration of H_2O_2 was determined by adding a Ti(IV) oxysulfate solution to the samples, which reacts under acidic conditions to form a yellow complex. This complex exhibits maximum light absorption at 408 nm, as

described in reaction (69).

$$Ti^{4+} + H_2O_2 + 2SO_4^{2-} \rightarrow (TiO_2(SO_4)_2)^{2-} + 2H^+ \quad (69)$$

The formation of this complex, proportional to the concentration of H_2O_2, was measured at 408 nm using a Shimadzu 1800 UV/Vis spectrophotometer. To prepare the Ti(IV) solution, 3.2 g of $TiO(SO_4)$ was dissolved in 1 L of Milli-Q water, with 180 mL of concentrated sulfuric acid added to assist the dissolution, yielding a 20 mM Ti(IV) solution.

For the analysis, a small volume of the sample was combined with required volumes of Ti(IV) solution and Milli-Q water, and the obtained mixture served to measure the absorbance.

Active chlorine

The concentration of active chlorine was determined using the *N,N*-diethyl-*p*-phenylenediamine (DPD) colorimetric method (4500-Cl. G). When DPD reacts with small amounts of active chlorine at near-neutral pH, the resulting pink color is directly proportional to the concentration of active chlorine. At higher concentrations of active chlorine, however, a colorless imine forms, reducing the intensity of the color. To minimize interference from other oxidants like manganese or copper, EDTA was added to the solution.

The measurement procedure involved adding small volumes of phosphate buffer solution and DPD solution to 10 mL of the sample, sequentially. The samples need to be diluted as required. The absorbance of the resulting solution was measured at 515 nm using the same spectrophotometer mentioned above.

Iron ions

The concentration of soluble iron was determined using the 1,10-phenanthroline method. To measure Fe^{2+}, 1 mL of sample was mixed with 1 mL of 0.2% (v/v) 1,10-phenanthroline and a small volume of acetate/acetic acid buffer (pH ~4), thereafter being diluted with Milli-Q water. The same procedure was followed to measure total dissolved iron ions, but ascorbic acid was added beforehand to reduce Fe^{3+} to Fe^{2+} before dilution. In both cases, the Fe^{2+} concentration was determined by measuring the absorbance of its complex with 1,10-phenanthroline at $\lambda = 510$ nm using the abovementioned spectrophotometer.

3.5.4 Chromatography combined with mass spectrometry

GC-MS

The pharmaceutical contaminants and their by-products were identified using gas chromatography-mass spectrometry (GC-MS). To detect as many reaction intermediates as possible, 150 mL of synthetic solutions containing the organic molecules under study was electrolyzed under different conditions. The final solutions were extracted with CH_2Cl_2 (3×15 mL). The resulting organic extracts were dried over anhydrous Na_2SO_4, filtered, dried under a gentle N_2 stream, and concentrated for analysis (stored at 4 °C away from light.).

GC-MS analysis was performed using an Agilent Technologies system, consisting of a 6890 N gas chromatograph equipped with a 7683B series injector and a 5975 mass spectrometer in electron impact mode at 70 eV. Either a nonpolar Agilent J&W DB-5 or a polar HP INNOWax column (0.25 μm film thickness, 30 m×0.25 mm) was used. The temperature program started at 36 °C for 1 min, followed by an increase of 5 °C per minute up to 300 °C, with a hold time of 10 min. The inlet, source, and transfer line operated at 250 °C, 230 °C, and 280 °C, respectively. The NIST05 MS library made it possible the compound identification.

LC-MS/MS

If effective identification of by-products was not feasible by GC-MS, liquid chromatography-mass spectrometry (LC-MS) was subsequently employed for analysis. In those cases, the analytes were dentified and quantified through multiple rounds of mass spectrometry analysis (LC-MS/MS). Samples were collected under different experimental conditions the day before testing, filtered, and stored in a light-protected environment at 4 °C.

The analysis was performed using a Thermo Fisher Scientific system, consisting of an Ultimate 3000 HPLC equipped with an Acquity BEH C18 column (1.7 μm, 100 mm×2.1 mm) maintained at 40 °C, coupled with an LTQ-Orbitrap Velos and an Accela PDA. Gradient elution was used to obtain signals for the initial pollutants and by-products, which were identified by searching references in the bibliography.

3.5.5 Other analyses

The electrical conductance and pH were measured with a Metrohm 644 conductometer and a Crison GLP 22 pH-meter, respectively.

3.6 Electrochemical characterization

The electrochemical characterization of the catalysts and electrocatalysts was conducted in a conventional three-electrode glass cell containing a 0.1 M Na_2SO_4 solution at natural pH, maintained at room temperature. Depending on the testing requirements, three different models of electrochemical workstations were used: Autolab PGSTAT100 and 101N potentiostats, both equipped with a motor controller for the electrode rotator from Metrohm, and the Solartron SI-1287 potentiostat combined with an SI 1255 frequency response analyzer from Artisan Technology Group.

3.6.1 Phenomena affecting the electrochemical reactivity in heterogeneous electrocatalysis

In heterogeneous electrocatalysis, reactions occur due to the electronic properties of the catalyst active sites, which are located on the surface of the catalyst. The electron transfer process can be described using the following general reduction reaction (70):

$$O_{ads} + ne^- \leftrightarrows R_{ads} \quad (70)$$

In this reaction, O_{ads} represents the oxidized species adsorbed on the surface, which undergoes electron transfer to become the reduced species R_{ads}. In reversible electrochemical reactions, the cathodic component represents the reduction of O_{ads} to R_{ads}, while the anodic component describes the reverse oxidation process. However, beyond electron transfer, additional surface and chemical processes must be considered (as shown in Fig. 43):

1. Pre- or post-electron transfer chemical reactions, including both homogeneous and heterogeneous reactions, which may influence the overall reaction kinetics.

2. Adsorption and desorption processes, where species attach or detach from the electrode surface.

3. Mass transport processes: These include diffusion, migration, and

convection of species between the electrode surface and the bulk solution.

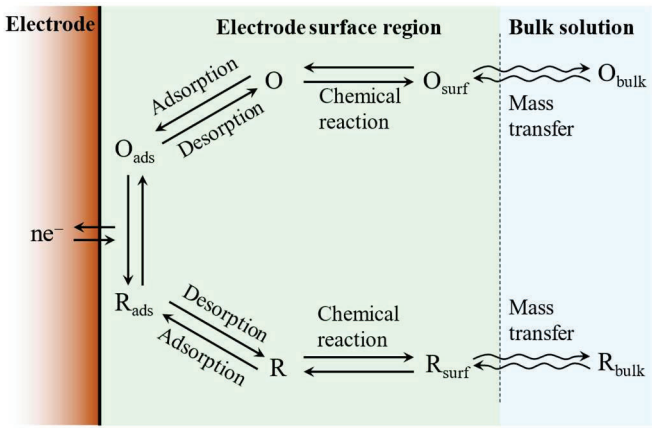

Figure 43. Steps involved for the occurrence of a general electrode reaction [401].

When an electrode is polarized, moving it away from equilibrium, either a reduction or oxidation process is favored depending on the direction of the applied potential. The difference between the applied and equilibrium potential is termed overpotential (η), and this drives the overall reaction. In electrochemical processes, assuming the no resistance control affects the measurements, the required η value depends on two main factors: electron transfer rate and mass transport rate.

To determine the η value, electrochemical characterization is typically carried out using a three-electrode cell. As depicted in Fig. 44, this system consists of:

Working electrode (WE), where the reaction of interest takes place.

Counter electrode (CE), which serves to close the current circuit.

Reference electrode (RE), which provides a stable potential reference for accurate control (i.e., scan or measure) of the WE potential.

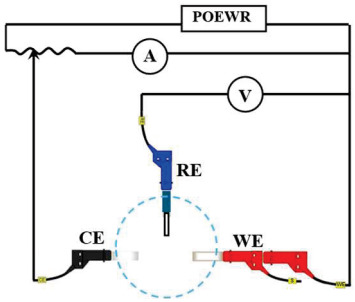

Figure 44. Electrical scheme in a 3-electrode configuration: WE, CE, and RE. The amperometric circuit is used to measure the current (*I*), while the potentiometric is used to measure the WE potential (*E*) [402].

Some advanced techniques, such as linear voltammetry on a rotating ring-

disk electrode (RRDE), may require an additional working electrode (WE2) and a bi-potentiostat, in order to control both the ring and disk potentials simultaneously.

The reaction rate in electrochemical systems is not solely governed by electron transfer, but also by the transport of species to and from the electrode surface. Mass transport can be achieved by three distinct mechanisms:

Convection is the transport of mass due to density gradients and/or mechanical vibrations (i.e., natural convection) or due to forced stirring when using rotating electrodes, flow electrodes or flow cells (i.e., forced convection). Generally, convection is controlled by thermosetting the cell and/or by rotating the electrode.

Migration of charged species, which occurs due to the movement of ions under an electric field. To minimize this effect, a supporting electrolyte is added, ensuring that ion transport is primarily governed by diffusion. The supporting electrolyte should be a strong electrolyte that fully dissociates, be electrochemically and chemically inert, and have an approximately unitary transport number, meaning the electric current is carried uniformly by the ions. The transport number reflects the fraction of current carried by an individual ion relative to the total current. Additionally, the supporting electrolyte maintains the ionic conductivity, ensuring the efficient charge transfer without interfering with the electrochemical reactions.

Finally, **diffusion** is the phenomenon due to movement of dissolved species induced by a concentration gradient. In electrochemical systems, gradients are generated as a result of reactions on the electrode surface. In the absence of convection and migration phenomena, it is possible to work only under diffusion control. From a mathematical point of view, the flow of matter in the presence of the three contributions can be expressed through the overall Nernst-Planck equation (71); the first term is sufficient to describe the case of rotating electrodes (assuming that a supporting electrolyte is employed), whereas time dependency of flux is needed in the case of stationary electrodes.

$$J = -D\frac{dc}{dx} - \frac{zF}{RT}Dc\frac{d\Phi}{dx} + cv \qquad (71)$$

• diffusion, • migration, • convection.

where, J is the flux of the species, D is the diffusion coefficient, dc/dx is the concentration gradient, $d\Phi/dx$ is the potential gradient (related to migration), and cv represents the convection term.

3.6.2 Cyclic voltammetry

Cyclic voltammetry (CV) is an electrochemical technique in which the potential of the WE is swept linearly between an initial value (E_i) and a final value (E_f), and then reversed back to the initial value. As shown in Fig. 45, the scan starts at E_i, proceeds to a turning point at E_λ, and then reverses the direction until it reaches E_i again (in cases where $E_f = E_i$, which are the most typical). This process is expressed by the following equations (72) and (73).

$$E(t) = E_i - vt \text{ for } 0 < t < \lambda \quad (72)$$

$$E(t) = E_i - 2v\lambda + vt \text{ for } t > \lambda \quad (73)$$

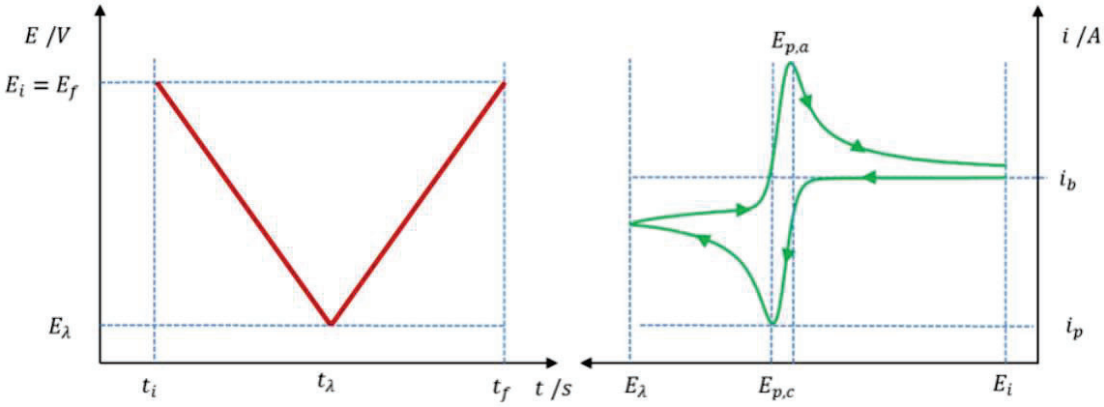

Figure 45. Variation of the potential over time, in red. Voltammetric profile, in green [403,404].

Considering a reversible redox pair (O↔R), during the scanning of the potential, the system responds immediately by changing the concentrations. By applying the described potential program to a WE immersed in a solution containing only O, the voltametric response shown in Fig. 45 (green curve) is obtained. The curve can be understood as follows: initially, no redox reaction occurs, and only a capacitive current is observed. As the potential progresses, the reduction of O starts, leading to the appearance of a faradaic current. As the potential continues to change, the reaction accelerates until it reaches the diffusion-controlled region, at which point the current adheres to the Cottrell equation, becoming independent of the applied potential. The transition from the initial phase to the diffusion-controlled regime is marked by a peak, characterized

by the peak potential (E_p) and peak current density (j_p).

As the potential reaches its limit and begins to reverse, the subsequent profile depends on the reaction reversibility. In the case of a reversible reaction, the system adjusts quickly when the potential sweeps back, allowing the reverse reaction (oxidation of R back to O) to take place. This produces a second peak corresponding to oxidation, which is typically symmetric to the reduction peak seen during the forward scan. The positions of these peaks (anodic, $E_{p,a}$ and cathodic, $E_{p,c}$) remain largely unaffected by the scan rate, while their magnitude (anodic, $i_{p,a}$ and cathodic, $i_{p,c}$) increases in a predictable manner with the square root of the scan rate (i.e., Randles-Sevcik equation). This behavior indicates a diffusion-controlled process, where the reaction rate depends on how quickly the reactants can diffuse to the electrode surface from the bulk solution.

On the other hand, if the reaction is irreversible, as occurs with the ORR, the reverse reaction does not take place, or at least not easily, when the potential is reversed. As a result, only one peak (i.e., cathodic) is observed during the scan. In these cases, $E_{p,c}$ shifts with the scan rate, and the $i_{p,c}$ no longer follows the same pattern as it would in a reversible system. Instead, the reaction is governed by slower processes, such as chemical transformations or bond-breaking, and is no longer diffusion-controlled.

On the other hand, the electrochemical active surface area (ECSA) is a critical parameter for assessing the performance of electrocatalysts, as it represents the actual surface area available for electrochemical reactions. A higher ECSA indicates a greater number of active sites on the electrode surface, which typically leads to enhanced catalytic activity. This is particularly important in reactions such as the $2e^-$ ORR for H_2O_2 generation, where increasing the accessible surface area can significantly improve performance. Furthermore, ECSA also provides insight into the active sites responsible for H_2O_2 activation, which are distinct from those involved in its generation. To calculate the ECSA, one must first measure the double-layer capacitance (C_{dl}), which is directly proportional to the active surface area.

The measurement of C_{dl} is typically performed using the CV technique in the non-faradaic region, where no significant redox reactions occur. In this region, the current is dominated by the charging and discharging of the electrical double

layer at the electrode-electrolyte interface. By conducting CV scans at various scan rates (e.g., 10, 20, 50, 100, 200 mV s^{-1}), the capacitive current density (j_{cap}) is measured, which is proportional to the scan rate v. The relationship between the capacitive current and the scan rate can be described by the equation (74). By plotting the capacitive current against the scan rate, the slope corresponds to the C_{dl}.

$$I_{cap} = C_{dl} \times v \tag{74}$$

Once the C_{dl} value is determined, the ECSA can be calculated using equation (75), where C_s is the specific capacitance of a smooth electrode surface, typically obtained from literature values for the relevant material in a given electrolyte. This calculation provides a more accurate value of the true active surface area, which is often much larger than the geometric area, particularly for porous or nanostructured catalysts.

$$\text{ECSA} = C_{dl} / C_s \tag{75}$$

3.6.3 Linear sweep voltammetry

Linear sweep voltammetry (LSV) is a crucial technique for investigating electrochemical processes, particularly the kinetics and mechanisms of redox reactions. In LSV, the potential of the WE is varied linearly over time, and the resulting current is recorded. This current response provides essential information on how the redox reactions at the electrode surface proceed, how fast they occur, and the limitations of the system. By analyzing the shape of the current-potential curve, one can distinguish between kinetic and mass transport limitations.

Initially, as the potential is scanned, electron transfer begins to occur, and the current increases. The rate at which the electroactive species are reduced or oxidized is controlled both by the electron transfer kinetics and the mass transport of species to the electrode surface. However, as the potential increases further, the system typically transitions to a diffusion-limited regime, where the rate of reaction is no longer controlled by the potential but by the rate at which reactants are transported from the bulk solution to the electrode surface.

A rotating electrode setup is commonly employed to control and enhance the mass transport, as shown in Fig. 46a. By rotating the electrode at a specific angular velocity, a well-defined Nernst diffusion layer is formed near the

electrode surface. This thin stationary layer is where the concentration of the reacting species (O, for a reduction reaction) changes significantly, as depicted in Fig. 46b. The rest of the solution is kept well mixed, ensuring a constant concentration of reactants in the bulk solution. The thickness of the diffusion layer, denoted by δ, is inversely proportional to the rotation speed of the electrode, which directly impacts the rate of mass transport to the surface.

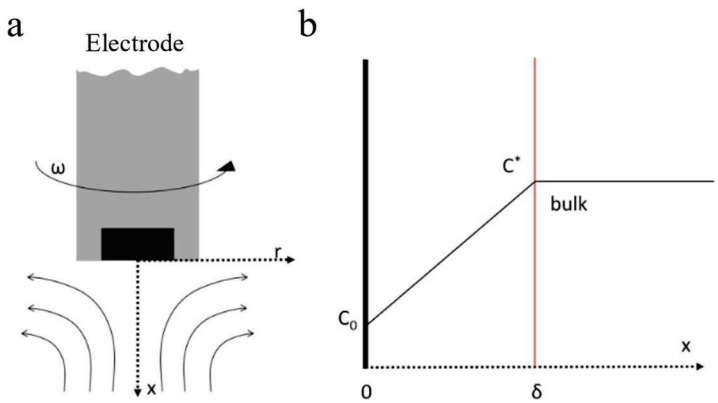

Figure 46. (a) Electrode under rotation; the solution flux is highlighted. (b) Profile of concentration of O species as a function of the distance from the electrode surface; the linear section is the Nernst layer (δ) [405].

At higher potentials, the system reaches a point where the current becomes diffusion-limited, resulting in a characteristic limiting current. In this regime, the current no longer increases with the applied potential, as shown by the *plateau* in the current response. This behavior is a signature of systems where mass transport governs the overall reaction rate, as the supply of reactants to the electrode surface becomes the limiting factor.

For more complex reactions, such as the ORR, intermediate species may form, and the mechanism becomes more challenging to analyze. This is where more sophisticated techniques like the RRDE become valuable. In this setup, as illustrated in Fig. 47, the disk electrode allows investigating the target reduction or oxidation reaction, while the ring electrode detects partially reduced or oxidized species, respectively, such as H_2O_2 in ORR. The simultaneous measurement of current at both the disk and the ring allows researchers to quantify the production of intermediate species and assess the overall reaction efficiency.

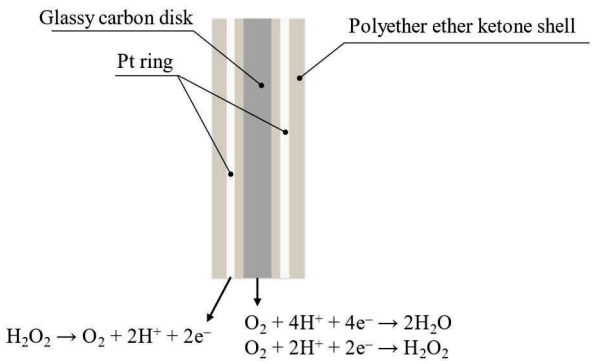

Figure 47. RRDE electrode used for ORR evaluation [406].

The RRDE setup enables the determination of the number of electrons transferred during the reaction, which is a crucial parameter in evaluating catalytic performance. Using equations (76) and (77), the electron transfer number (n) and H_2O_2 selectivity (as $\%H_2O_2$) can be calculated from the current responses of the disk (I_d) and ring (I_r):

$$n = \frac{4I_d}{I_d + I_r/N} \tag{76}$$

$$\%H_2O_2 = \frac{I_r/N}{I_d + I_r/N} \times 200 \tag{77}$$

where N is the collection factor, close to 25% for our RRDE. Operationally, an RRDE measurement is analogous to those done with an RDE, with the foresight of having to use a bipotentiostat for the independent control of the two potentials (disk and ring). Two different current-potential curves are thus obtained: one related to the disk, in which the current read is a function of a potential made to vary over time, and the other to the ring whose applied potential is fixed and is expressed as a function of the disk potential.

The Tafel slope is also an important parameter in electrocatalysis. In LSV analysis, the Tafel slope is obtained by plotting η against the logarithm of the current density ($\log j$) in the kinetic region of the current-potential curve, where the reaction is controlled by electron transfer rather than mass transport. The resulting linear section of the plot, referred to as the Tafel region, can be expressed by the equation (78).

$$\eta = a + b \log j \tag{78}$$

where a is the intercept (related to the exchange current density, j_0), and b is the Tafel slope.

The Tafel slope represents the change in overpotential required to increase the current density by one order of magnitude. It is a critical indicator of how efficiently the catalyst facilitates electron transfer. For example, a lower Tafel slope denotes the need of a smaller overpotential to drive the reaction at a higher rate, accounting for a more efficient electron transfer. The Tafel slope is thus a key indicator of catalytic efficiency. Conversely, a higher Tafel slope implies that a greater overpotential is required, pointing to slower reaction kinetics or a less active catalyst surface. The Tafel slope is not only used to evaluate catalyst performance but also to compare different catalysts under identical conditions.

3.6.4 Electrochemical impedance spectroscopy

Electrochemical impedance spectroscopy (EIS) is a powerful technique used to investigate the interactions between electron transfer, mass transport, and surface phenomena in electrochemical systems. Unlike the aforementioned electrochemical techniques, it operates by applying a small alternating current (AC) signal across a range of frequencies, which allows the separation and analysis of various electrochemical processes occurring at different time scales.

In a typical EIS experiment, an AC potential is applied to the electrode-electrolyte interface, and the impedance of the system is measured over a broad frequency range. The resulting data can be analyzed in terms of resistive and capacitive elements that correspond to specific processes, such as charge transfer, adsorption, diffusion, and mass transport:

(i) Charge transfer resistance (R_{ct}): This parameter reflects the efficiency of electron transfer between the electrode and the heterogeneous catalyst. A lower R_{ct} denotes a more efficient electron transfer, which is critical for reactions such as the ORR or the subsequent activation of H_2O_2 in the EF process.

(ii) C_{dl}: This is a measurement of the charge storage capacity at the electrode-electrolyte interface, often linked to the active surface area of the catalyst and its interaction with the electrolyte.

(iii) Mass transport and diffusion effects: At lower frequencies, EIS can reveal limitations in the transport of reactive species (such as O_2 or H_2O_2) to and from the catalyst surface. Understanding these limitations is crucial in determining whether mass transport is governing the reaction kinetics in the EF system.

However, the impedance data collected in EIS are typically presented as a function of frequency, and the contributions from different electrochemical processes can overlap, complicating the interpretation of individual processes. To address this, the distribution of relaxation times (DRT) technique can be employed. DRT transforms frequency-domain impedance data into the time domain, isolating the overall response into discrete relaxation times, each representing a distinct process such as charge transfer, diffusion, or adsorption.

(i) Charge transfer process: One of the characteristic relaxation times may correspond to the ORR at the heterogeneous catalyst surface, a key step in the generation of H_2O_2. DRT allows this process to be distinguished from other overlapping phenomena.

(ii) Mass transport and diffusion: In EF process, diffusion limitations can significantly affect the performance. DRT allows identifying the specific time scale associated with the diffusion of O_2 or H_2O_2 to the catalyst surface, providing a clearer picture of how mass transport influences the overall process.

(iii) Catalyst fouling and stability: Over time, catalysts may experience fouling or deactivation. By tracking changes in relaxation times, DRT can help detect when processes like mass transport or charge transfer become hindered due to surface fouling or catalyst degradation.

The combination of EIS and DRT provides a more refined and detailed analysis of heterogeneous EF systems. While EIS gives a broad overview of how the system behaves across a range of frequencies, DRT enhances this by breaking the data into specific time scales. This makes it easier to pinpoint bottlenecks—whether related to slow electron transfer, diffusion limitations, or catalyst degradation—thereby helping to optimize the system performance for practical applications.

3.6.5 Chronoamperometry

This technique involves applying a WE potential far from its equilibrium, which results in very fast electron transfer, and studying the evolution of current over time. The resulting current profile can be described using the Cottrell equation. In this Thesis, it is used for the long-term analysis of the $2e^-$ ORR to electrogenerate H_2O_2, focusing on the stability and performance of the electrocatalyst over extended periods.

3.7 Computational calculations

DFT is a theoretical framework in quantum mechanics that serves to simplify the complex problem of multi-electron processes by focusing on electron density rather than the many-body wavefunction. Grounded in the Hohenberg-Kohn theorems and the Kohn-Sham formalism, DFT approximates electron exchange and correlation effects using functionals, making it computationally efficient while maintaining reasonable accuracy. Owing to its great versatility and scalability, DFT has become an essential tool for evaluating the structural, electronic, and energetic properties of chemical systems and materials.

In the particular case of the study of the $2e^-$ ORR, DFT is expected to unravel the catalytic mechanism at the atomic scale. This methodology facilitates the assessment of adsorption energies for oxygen and intermediates (i.e., OOH* and OH*), enabling the identification of the most favorable reaction pathways to produce H_2O_2. Furthermore, DFT allows gaining insights into the role of catalyst composition, electronic structure, and active site configuration, which are crucial factors to tune the selectivity and activity. Such theoretical understanding is critical for rational design of catalysts with enhanced performance for $2e^-$ ORR in energy and environmental applications.

In paper 3 (Chapter 4.1.3), structural modeling and DFT calculations were carried out using the Vienna ab initio simulation package (VASP), considering the generalized gradient approximation (GGA) and the Perdew-Burke-Ernzerhof (PBE) functional. The description of ionic cores was done by means of the projector augmented wave (PAW) pseudo-potentials. A plane-wave basis set, with a kinetic-energy cut-off of 400 eV, was employed to expand the wave function of valence electrons. Van der Waals interactions were described by means of the DFT-D3 empirical correction method. The geometry was optimized until the force convergence was smaller than 0.05 eV $Å^{-1}$. Monkhorst-Pack k-points of 1×1×1 were applied for all calculations.

It should be noted that the computational DFT studies included in this Thesis were carried out by EAOPs group at Chongqing University (China). I was not directly involved in the design, execution, or interpretation of this part of the research, although I am able to discern the practical interest of the obtained results.

3.8 Analysis of performance

The removal efficiency of target pollutants and the corresponding mineralization efficiency are shown in equations (67) and (68), respectively.

Current efficiency (CE) values during H_2O_2 electrogeneration were calculated from the applied charge, according to equation (79).

$$\text{CE (in \%)} = \frac{2F[H_2O_2]V}{1000M(H_2O_2)Q} \times 100 \quad (79)$$

where 2 is the stoichiometric number of electrons transferred for ORR to form H_2O_2, F is the Faraday's constant (96,487 C mol^{-1}), $[H_2O_2]$ is the concentration attained for the accumulated H_2O_2 (mg L^{-1}), V is the volume of the electrolyzed solution (L), 1000 is a conversion factor, $M(H_2O_2)$ is the molecular weight of H_2O_2 (34 g mol^{-1}), and Q is the charge that has been consumed during the electrolysis in C.

The calculations for C_{dl} and ECSA are shown in equations (74) and (75), respectively.

The calculations for the electron transfer number n and the H_2O_2 selectivity are shown in equations (76) and (77), respectively.

The calculation of the Tafel slope is shown in equation (78).

The theoretical total mineralization reactions for the three target pharmaceuticals studied in this Thesis can be written as follows:

$$C_{17}H_{12}NO{\bullet}HCl + 36H_2O \rightarrow 17CO_2 + Cl^- + NO_3^- + 96H^+ + 94e^- \quad (80)$$

$$C_{21}H_{31}N_3O_5 + 29H_2O \rightarrow 21CO_2 + 3NO_3^- + 59H^+ + 57e^- \quad (81)$$

$$C_{16}H_{19}N_3O_5S + 23H_2O \rightarrow 16CO_2 + 3NO_3^- + SO_4^{2-} + 45H^+ + 44e^- \quad (82)$$

CHAPTER 4

RESULTS AND DISCUSSION

CHAPTER 4. Results and Discussion

This chapter summarizes the most relevant results obtained from the research carried out in this Thesis, in good accordance with the following scientific articles that have been either published in indexed Q1 journals, submitted or under preparation:

1. **L. Zhao**, M. Mazzucato, S. Lanzalaco, M. Parnigotto, A. Khan, A. Zitolo, P. L. Cabot, C. Durante*, I. Sirés*. Boosting the O_2-to-H_2O_2 Selectivity using Sn-doped Carbon Electrocatalysts: Towards Highly Efficient Cathodes for Actual Water Decontamination.
   ChemSusChem 18 (2025) e202401758.
   https://doi.org/10.1002/cssc.202401758

2. **L. Zhao**, M. Mazzucato, S. Lanzalaco, M. Parnigotto, P. L. Cabot, C. Durante*, I. Sirés*. Complete antihistamine degradation in wastewater matrix using a metal-free N-doped carbon with superior electrocatalytic performance for in-situ H_2O_2 production.
   Separation and Purification Technology 361 (2025) 131590.
   https://doi.org/10.1016/j.seppur.2025.131590

3. P. Xia, **L. Zhao**, X. Chen, Z. Ye*, Z. Zheng, Q. He, I. Sirés*. Polymethylhydrosiloxane-modified gas-diffusion cathode for more efficient and durable H_2O_2 electrosynthesis in the context of water treatment.
   Applied Catalysis B: Environmental 343 (2024) 123467.
   https://doi.org/10.1016/j.apcatb.2023.123467

4. **L. Zhao**, J. A. Padilla, E. Xuriguera, P. L. Cabot, E. Brillas*, I. Sirés*. Enhanced mineralization of pharmaceutical residues at circumneutral pH by heterogeneous electro-Fenton-like process with Cu/C catalyst.
   Chemosphere 364 (2024) 143249.
   https://doi.org/10.1016/j.chemosphere.2024.143249

5. **L. Zhao**, M. F. Murrieta, J. A. Padilla, S. Lanzalaco*, P. L. Cabot, I. Sirés*. Bimetallic FeCu-MOF derivatives as heterogeneous catalysts with enhanced stability for electro-Fenton degradation of lisinopril.

Science of the Total Environment 953 (2024) 176110.
https://doi.org/10.1016/j.scitotenv.2024.176110

6. **L. Zhao**, Z. Ye*, S. Lanzalaco, I. Sirés*. Ceramic membrane-confined FeCu/NC catalyst for robust flow-through wastewater treatment by electro-Fenton process.
In preparation.

The main goals, findings, and conclusions from each article are summarized below, accompanied with an electronic copy of the manuscripts and supplementary files.

4.1 Development of high-performance electrocatalysts and GDEs for enhanced ORR

Section 4.1 presents three articles related to **GO1** and **SG1-4**: (i) synthesis and characterization of Sn-containing and metal-free electrocatalysts plus PMHS-modified CB; (ii) studies to unveil their activity/selectivity; (iii) GDE preparation for efficient H_2O_2 electrogeneration; and (iv) HEF treatment at natural pH.

4.1.1 Boosting the O_2-to-H_2O_2 selectivity using Sn-doped carbon electrocatalysts: Towards highly efficient cathodes for actual water decontamination

The market of H_2O_2 has experienced an awesome increase in recent years. H_2O_2 is widely valued as a green oxidizing agent, transversally across various industries but notably in environmental treatments, where it allows degrading organic pollutants through EAOPs like the EF process by generating $^{\bullet}OH$ in the bulk solution. Although currently the market is still dominated by the energy-intensive anthraquinone process, which accounts for 95% of world H_2O_2 production, the attention has shifted toward decentralized, more sustainable and responsible methods, with the $2e^-$ ORR emerging as a highly promising alternative due to its efficiency and flexibility, which allows envisaging the design of compact systems. A key innovation in the field involves anchoring active catalytic materials onto porous carbon substrates, further integrating them within an air chamber to give rise to GDEs. In these systems, air or pure oxygen flows through the porous GDL to reach a TPB, where the electrocatalyst converts the gaseous O_2 to H_2O_2, while the immediate activation of the latter provides a steady supply of reactive oxygen species for an efficient EF treatment of pollutants. Various electrocatalysts —including metal-doped carbons, noble metal alloys, and SACs— have been developed to enhance ORR activity and selectivity. Among these, Sn has very recently emerged as an abundant, low cost and safe element that can form highly stable Sn–C bonds: it exhibits strong adsorption affinity for O_2, and shows promise as a potentially stable ORR catalyst for accelerating the O_2 electroreduction, even under alkaline conditions. Notably, it has never been tested for the $2e^-$ ORR.

In this study, three SnC electrocatalysts, namely SnC1 (after the first

pyrolysis), SnC2 (after further acid washing), and SnC3 (after subsequent pyrolysis, i.e., repyrolysis), were synthesized and characterized to expand the pH range for in-situ H_2O_2 production using GDEs, assessing their activity and selectivity for O_2-to-H_2O_2 conversion at circumneutral pH. The most effective catalyst was then used to create a GDE, which was tested for H_2O_2 production. DPH was chosen as a target pollutant to evaluate the EF process performance for the first time.

The ORR performance of the as-synthesized catalyst and commercial carbon black (Vulcan XC72) was first investigated by LSV analysis employing the RRDE technique. Vulcan carbon displayed the lowest ORR activity, as deduced by a low onset potential (E_{onset} = 331.9 mV *vs*. RHE). The incorporation of Sn as dopant significantly improved this onset potential, enhancing the ORR activity at near-neutral pH. SnC1 and SnC2 presented similar onset potentials (0.536 and 0.525 mV, respectively) and nearly optimum electron transfer numbers (n ~2), achieving O_2-to-H_2O_2 selectivities near 100%. SnC1 and SnC2 also surpassed the SnC3 in activity and selectivity. Overall, this work revealed that the SnC electrocatalysts effectively electrogenerate H_2O_2, outperforming the commercial XC72 carbon.

A comprehensive physicochemical characterization of the three synthesized Sn catalysts and XC72 was performed to give a rational explanation of the different electrocatalytic properties. XPS analysis shows that the Sn content in SnC3 is significantly higher than in SnC1 and SnC2, attributed to enhanced exposure of Sn sites due to the second thermal treatment. Compared to Vulcan XC72, the Sn-doped materials have increased N content, with SnC2 having the highest N content (close to 2 at.%), indicating the role of phenanthroline as an N source. SnC1 and SnC3 contain higher amounts of graphitic and pyridinic N, which supports H_2O_2 generation, while SnC2 has a higher pyrrolic N content (over 1.5 at.%), favoring the ORR. Sn 3d spectra show the presence of Sn^{4+} across all samples, with a small amount of Sn^0 detected in SnC3. Raman characterization assessed the graphitization degree of the four carbon materials. XC72 typically consists of nanocrystalline graphite with surface and edge defects, along with some amorphous carbon from polycyclic aromatic compounds. The deconvolution of Raman spectra helps evaluate the impact of the metal on

graphitization. The analysis revealed that Sn doping caused no significant structural change, with only a slight increase in graphitization, and the amorphous carbon content remained around 8%. Additionally, no SnO_2 signal was detected in SnC2, despite the longer acquisition times. XRD analysis showed a transition from metallic Sn in SnC1 to SnO_2 in SnC2, and back to metallic Sn in SnC3. SnC2 had smaller crystalline domains (~4 nm) compared to SnC1 and SnC3 (~25 nm), likely due to acid washing, which oxidized Sn and reduced particle size. The final reduction to metallic Sn in SnC3 was facilitated by carbon, removing oxygen as CO_2/CO. A peak near 26° indicated the carbon support, more distinct in SnC2 due to lower crystallinity in SnC1 and SnC3. FT-IR analysis showed an adsorption band at 2362 cm^{-1} in SnC1, SnC2, and SnC3, attributed to C≡N stretching vibrations. This group can enhance H^+ adsorption, potentially accelerating H_2O_2 electrogeneration, as H^+ is essential for its formation. BET analysis determined the specific surface area of the catalysts, while QSDFT provided detailed pore size distribution, better suited for disordered carbons. Isotherms indicated that SnC1 and SnC2 had lower adsorption than XC72, while SnC3 showed a slight increase, with SnC2 displaying the highest mesopore-to-micropore volume ratio. This ratio is beneficial as mesopores facilitate H_2O_2 release, preventing its further reduction, and micropores provide active sites for ORR. Structural changes in SnC1 (Sn nanoparticles), SnC2 (SnO_2), and SnC3 (reduced Sn) affected pore size, with SnC3 showing some pore growth due to CO_2 formation during reduction. HRTEM and EDS showed that the SnC catalysts consist of agglomerated carbon particles. Sn particles were mostly undetectable in SnC1 and SnC3 but were visible in SnC2, where SnO_2 nanoparticles (~9 nm) formed a C-wrapped core structure. HRTEM images of SnC2 revealed crystal planes of SnO_2, with numerous grain boundaries that enhance interfacial contact with the electrolyte, lower the diffusion barrier, and improve electron transfer for ORR. Elemental mapping confirmed aligned Sn and O with SnO_2 particles, while C and N were uniformly distributed, verifying N-doping. In-situ XAS spectra of SnC3 in 0.5 M H_2SO_4 showed no changes in the Sn K-edge XANES spectra between 200 and 900 mV *vs.* RHE, corresponding to regions with and without oxygen reduction. This stability across potentials suggests acceptable stability for the Sn-based electrocatalysts, consistent with previous findings for materials with

Sn-N_x sites.

Initial electrolytic trials assessed H_2O_2 generation performance of SnC catalysts in a 3-electrode cell with O_2-saturated 0.1 M Na_2SO_4 at natural pH 5.9, using an RDE at a potential value of -0.25 V vs. RHE. The cumulative H_2O_2 concentration after 10 h showed SnC2 as the best catalyst (0.19 mM), followed by XC72 (0.15 mM), SnC1 (0.13 mM), and SnC3 (0.12 mM). The superior ORR activity and structural properties of SnC2 enhanced its performance, while the relatively high mesopore-to-micropore ratio of Vulcan carbon allowed it to retain H_2O_2 effectively, highlighting the importance of both electrochemical and physical attributes over prolonged electrolysis.

Based on all these results, SnC2 was chosen as the optimal electrocatalyst for scale-up tests, thereby being integrated into a GDE for bulk electrolysis in a two-electrode cell. Different GDEs (3 cm^2) were tested for H_2O_2 generation under various conditions. Using PTFE as the binder at 0.5 mg cm^{-2} catalyst loading, with a current density of 33.3 mA cm^{-2} at natural pH (5.9), yielded the highest H_2O_2 concentration (20.4 mM) after 300 min. The hydrophobicity conferred by PTFE contributed to maintain the contact between O_2 and the electrocatalyst, while higher catalyst loading or lower current density reduced the H_2O_2 output due to increased electroreduction and pore blockage. Overall, current efficiency was highest under optimized conditions, though it declined over time due to H_2O_2 oxidation in the undivided cell.

H_2O_2 activation was tested under conventional EF conditions (pH 3 with Fe^{2+} as Fenton catalyst) and EF-like conditions (pH 5.9 with Cu/C as heterogeneous catalyst; note that this material is explored in detail in Section 4.2.1) using a SnC2-based GDE with PTFE binder. After 300 min at 10 mA cm^{-2}, H_2O_2 concentrations reached ~2 mM, indicating effective decomposition in the presence of Fenton catalysts. The EF-like process with Cu/C required more time to activate H_2O_2 due to its heterogeneous, stabilizing after 60 min. For degrading DPH (14.3 mg L^{-1}), the EO process at 10 mA cm^{-2} achieved limited removal (<20% at 120 min), whereas in the EF-like treatment at pH 5.9, 75% degradation was achieved, with complete removal at higher currents (33.3 mA cm^{-2}). Under EF conditions (pH 3), the SnC2-GDE enabled rapid DPH degradation in just 15 min.

Check for updates

ChemSusChem

Research Article
doi.org/10.1002/cssc.202401758

Chemistry Europe
European Chemical Societies Publishing

www.chemsuschem.org

Boosting the O_2-to-H_2O_2 Selectivity Using Sn-Doped Carbon Electrocatalysts: Towards Highly Efficient Cathodes for Actual Water Decontamination

Lele Zhao,[a] Marco Mazzucato,[b] Sonia Lanzalaco,[c] Mattia Parnigotto,[b] Anastassiya Khan,[d] Andrea Zitolo,[d] Pere L. Cabot,[a] Christian Durante,*[b] and Ignasi Sirés*[a]

The high cost and often complex synthesis procedure of new highly selective electrocatalysts (particularly those based on noble metals) for H_2O_2 production are daunting obstacles to penetration of this technology into the wastewater treatment market. In this work, a simple direct thermal method has been employed to synthesize Sn-doped carbon electrocatalysts, which showed an electron transfer number of 2.04 and outstanding two-electron oxygen reduction reaction (ORR) selectivity of up to 98.0%. Physicochemical characterization revealed that this material contains 1.53% pyrrolic nitrogen, which is beneficial for the production of H_2O_2, and -C≡N functional group, which is advantageous for H^+ transport. Moreover, the high volume ratio of mesopores to micropores is known to favor the quick escape of H_2O_2 from the electrode surface, thus minimizing its further oxidation. A purpose-made gas-diffusion electrode (GDE) was prepared, yielding 20.4 mM H_2O_2 under optimal electrolysis conditions. The drug diphenhydramine was selected for the first time as model organic pollutant to evaluate the performance of an electrochemical advanced oxidation process. In conventional electro-Fenton process (pH 3), complete degradation was achieved in only 15 min at 10 mA cm^{-2}, whereas at natural pH 5.9 and 33.3 mA cm^{-2}, almost overall drug removal was reached in 120 min.

Introduction

Hydrogen peroxide (H_2O_2) is an efficient green oxidizing agent, widely utilized in medicine, textile industry, industrial synthesis, and water treatment.[1,2] Within environmental protection, H_2O_2 is primarily employed in the electrochemical advanced oxidation processes (EAOPs), facilitating the in-situ generation of $^{\bullet}OH$ to degrade and mineralize organic pollutants in sewage.[3,4] Against the backdrop of rapid industrial expansion and in response to global public health safety concerns, the demand for H_2O_2 has experienced a sharp escalation. By the end of 2024, global H_2O_2 consumption is projected to reach 6 million tons,[5] with an annual growth rate of approximately 5.5%.[6] At present, 95% of industrial H_2O_2 is predominantly synthesized using the anthraquinone auto-oxidation process developed in 1939.[7] However, this approach is energy-demanding and is restricted to centralized factories. Moreover, its intricate procedure incurs costs related to dangerous H_2O_2 manipulation, storage, and transportation.[8] Considering that, for water treatment through EAOPs, H_2O_2 concentrations ranging from 3.0–15.0 mM are adequate for ensuring rapid decontamination,[9] researchers are motivated to develop simpler and more compact on-site H_2O_2 production systems.

In recent years, scholars have conducted research on direct H_2O_2 synthesis as well as on photocatalytic methods. However, drawbacks such as high risks, low light utilization, and limited transparency put constraints on their widespread implementation.[10,11] In this context, the electrochemical 2-e$^-$ oxygen reduction reaction (ORR) is explored as an appealing alternative for H_2O_2 synthesis. This approach is not only particularly well-suited for decentralized H_2O_2 production, but it has a big potential for reducing energy consumption and secondary pollution.[12] Especially in the field of the electro-Fenton (EF) process (i.e., the metal-catalyzed decomposition of H_2O_2 to yield $^{\bullet}OH$),[2] anchoring active catalytic materials onto the surface of a porous carbon cloth substrate and combining the ensemble with an air chamber to create a gas-diffusion electrode (GDE) has gained attention. In such systems, air (or pure O_2) flows from the gas chamber through the porous cloth to reach the triple-phase boundary, where the active electrocatalyst transforms it into H_2O_2, thus providing a continuous

[a] Laboratori d'Electroquímica dels Materials i del Medi Ambient, Departament de Ciència de Materials i Química Física, Secció de Química Física, Facultat de Química, Universitat de Barcelona, Barcelona, Spain
[b] Department of Chemical Sciences, University of Padua, Padova, Italy
[c] Departament d'Enginyeria Química, EEBE Universitat Politècnica de Catalunya, Barcelona, Spain
[d] Synchrotron SOLEIL L'Orme des Merisiers, Saint-Aubin, France

Correspondence: Ignasi Sirés, Laboratori d'Electroquímica dels Materials i del Medi Ambient, Departament de Ciència de Materials i Química Física, Secció de Química Física, Facultat de Química, Universitat de Barcelona, Martí i Franquès 1–11, 08028 Barcelona, Spain.
Email: i.sires@ub.edu

Christian Durante, Department of Chemical Sciences, University of Padua, Via Marzolo 1, 35131 Padova, Italy.
Email: christian.durante@unipd.it

Supporting information for this article is available on the WWW under https://doi.org/10.1002/cssc.202401758

© 2024 The Authors. ChemSusChem published by Wiley-VCH GmbH. This is an open access article under the terms of the Creative Commons Attribution Non-Commercial License, which permits use, distribution and reproduction in any medium, provided the original work is properly cited and is not used for commercial purposes.

© 2024 The Authors. ChemSusChem published by Wiley-VCH GmbH

ChemSusChem
Research Article
doi.org/10.1002/cssc.202401758
Chemistry Europe
European Chemical Societies Publishing

1864564x, 2025, 3, Downloaded from https://chemistry-europe.onlinelibrary.wiley.com/doi/10.1002/cssc.202401758 by 3eadcube (Labtiva Inc.), Wiley Online Library on [07/02/2025]. See the Terms and Conditions (https://onlinelibrary.wiley.com/terms-and-conditions) on Wiley Online Library for rules of use; OA articles are governed by the applicable Creative Commons License

source of reactive oxygen species for efficiently applying the EF process.[13,14]

To enhance the efficiency of H_2O_2 production, researchers have focused on optimizing the 2-e$^-$ ORR, trying to disentangle the activity-selectivity trade-off.[12] Some authors have investigated various carbon-supported electrocatalytic materials, following doping strategies that allow decorating the carbon substrate with a range of metal-based structures that span from nanoparticles (NPs) to atomically-dispersed catalysts. These include metal alloys and bimetallic NPs,[15–19] metal oxides and sulphides,[20,21] metal complexes,[22] and single-atom catalysts,[23–26] which exhibit improved performance, especially among the d-block metals (fourth period),[27] as well as metal-free materials.[28,29] In all these cases, the aim is to decrease the overpotential required for ORR, as the oxygen supply is enhanced, thereby increasing the generation of H_2O_2.[26]

Stephens, Rossmeisl, and co-workers carried out a rational design of new electrocatalysts for H_2O_2 production by alloying a strong O_2-adsorbing element like Pt or Pd, with a weaker oxygen adsorbing element (Hg), thus providing optimized electronic and geometric effects.[16,17] More recently, the 2-e$^-$ ORR mechanism on Au–Pd nanoalloy surfaces has been unveiled via computational methods.[19] On the other hand, Félix-Navarro et al. deposited bimetallic Pt–Pd nanoparticles on MWCNTs; the resulting material was sprayed onto a reticulated vitreous carbon (RVC) GDE, producing 71 mM H_2O_2 in 0.5 M H_2SO_4 solution after 20 min at $E_{cath} = -0.50$ V vs Ag/AgCl.[15] Lanza's group has specialized in preparing GDEs for in-situ electrogeneration of H_2O_2 using a range of organic and inorganic carbon black modifiers. For example, they have recently reported that anchoring gold nanoparticles onto Printex L6 carbon black (PCL6), giving rise to an Au-ZrO_2/PL6 C hybrid support, led to a simultaneous increase in catalytic activity and selectivity (ORR onset potential of 0.34 V vs Ag/AgCl, and H_2O_2 selectivity around 97%).[30] The resulting GDE, prepared by hot-pressing of the active modified carbon between two steel sheets generated 17.6 mM H_2O_2 for 120 min in 0.1 M K_2SO_4 solution (pH 2.5) at 50 mA cm^{-2}. The Pd1%/PCL6 catalyst obtained by dispersing palladium nanoparticles on PCL6 also showed high activity, and the starting potential was 320 mV lower than that of the unmodified PCL6. Employing carbon cloth as the substrate, a certain amount of Pd1%/PCL6 was coated, followed by drying under N_2 gas flow; the accumulated H_2O_2 concentration with such GDE was 1.69-fold higher than that reached with pristine PLC6.[31] The same group, in collaboration with Santos' group, employed ruthenium and niobium oxides as carbon black modifiers to obtain 5.0% $Ru_{05}Nb_{95}O$/C, and the corresponding GDE yielded 8.2 mM H_2O_2 after 2 h at a current density (j) of 100 mA cm^{-2}.[32] In other works, they showed that tungsten is also an interesting surface modifier; after adding $WO_{2.72}$, the production yield increased from 67%–87%, and the energy consumption decreased.[33] Zhou's group has also made significant contributions to the manufacture of GDEs. Using carbon felt as substrate and commercial carbon black as active material, a superhydrophobic natural air-diffusion electrode (NADE) was fabricated, resulting in rapid H_2O_2 production (101.67 mg h^{-1} cm^{-2}) with high oxygen utilization (44.5%–64.9%) and oxygen diffusion coefficients (5.7 times that of air-pumped GDEs).[34] Fe-loaded carbons have also been studied to a large extent, not only for H_2O_2 production but for simultaneous heterogeneous Fenton's reaction, as shown for carbonaceous cathodes with confined iron.[35] Apart from doping with metallic entities, heteroatoms like S and N are also known to favor the 2-e$^-$ ORR.[28,29] S and N self-doped biomass carbon (SN-BC) was obtained from discarded ginkgo biloba leaves; when applied to both sides of a carbon felt, the cumulative concentration of H_2O_2 was about 3 mM at 50 mA for 2 h.[36] In all these commented studies on GDEs, note that carbon and stainless steel are ubiquitous as substrates. However, using Ni mesh, and carbon black as the catalyst, the electroproduction of H_2O_2 after 48 h of testing showed good stability (60 mM for 25 h), whereas a gradual decline was observed with the other two supports, which must be carefully considered for GDE scale-up.[37]

Many of the metals referred above, especially the noble ones like the platinum-group metals (PGMs), are categorized as endangered elements.[38] In contrast, tin is a good example of a relatively abundant material, but no attempts to manufacture Sn-based GDEs have been reported so far.[39] An advantage of Sn, as compared to other metals with similar abundance (like Co and Ni), is its safety and environmental compatibility, since there is no evidence that tin or its compounds can cause cancer or other severe reactions in humans.[40] The price of Sn is somewhat higher than that of base metals, but in line with other widespread elements in the field of electrocatalysis like Co and Mo, making it a feasible choice. Gao et al. have recently summarized the potentialities of this metal in electrocatalytic oxidation and reduction reactions.[40] Certainly, there is a growing interest in *p*-block elements, mainly Sn, Sb, and Bi, in the field of heterogeneous electrocatalysis.[41] Regarding the ORR, the ability of Sn to form single-atom catalysts (M–N–C materials), aiming at replacing precious metals in PEMFCs, promising results have been evidenced as compared to classical Fe–N–C catalysts.[42] The effectiveness of single-atom catalysts based on Sn has been shown computationally,[43] and also as a possible co-catalyst with Fe for ORR.[44] Tin can form highly stable Sn–C bonds and exhibits strong adsorption affinity for O_2, which might bring about bright perspectives for accelerating the O_2 electroreduction, as demonstrated even under alkaline conditions.[45,46] More specifically, N-doped tin catalysts supported on commercial carbon black (XC72) have demonstrated improved half-wave potentials and higher j values under alkaline conditions,[27] which seems clearly advantageous for utilizing this type of material for H_2O_2 production for water treatment under near-neutral conditions.

Aiming to expand the operational pH window for in-situ H_2O_2 electrosynthesis using GDEs, a set of SnC catalysts has been prepared in this work. First, a comprehensive physicochemical characterization of the synthesized catalysts was carried out, whereas their O_2-to-H_2O_2 activity and selectivity at neutral pH were assessed via rotating ring-disk electrode (RRDE) tests. The best electrocatalyst was selected to manufacture a GDE, in order to evaluate its ability to produce H_2O_2 in electrolytic assays at constant j. Moreover, diphenhydramine

© 2024 The Authors. ChemSusChem published by Wiley-VCH GmbH

ChemSusChem
Research Article
doi.org/10.1002/cssc.202401758
Chemistry Europe
European Chemical Societies Publishing

(DPH), a first-generation antihistamine with good inhibitory effects on allergies and vomiting, was selected as a target contaminant to investigate the performance of the electro-Fenton (EF) process for the first time. DPH cleavage is incomplete during wastewater treatment, being detected in 25% of downstream surface water samples, with a maximum concentration of about 45 ng L^{-1}.[47,48] Municipal wastewater treatment removes only about 69% of DPH present in the influent.[49,50]

Results and Discussion

Three Sn-doped carbon electrocatalysts were synthesized following the procedure depicted in Figure S1: sample named SnC1 was obtained upon direct pyrolysis of the mixture between a prepared Sn salt and commercial Vulcan XC72 conductive carbon black, at 900 °C for 2 h; SnC2 resulted from acid pickling of the previous sample; and SnC3 was obtained after repyrolysis of the latter sample at 900 °C for 2 h. Vulcan XC72 was also investigated for comparison. Details of the synthesis protocol are given in the Supporting Information file.

Electrochemical Performance of the Catalysts

The ORR performance of the three SnC electrocatalysts and the commercial carbon black was investigated by linear sweep voltammetry (LSV) measurements. The H_2O_2 oxidation current was collected at the ring of an ink-modified RRDE and, consequently, the dependence of the H_2O_2 selectivity and the electron transfer number were calculated as described in Text S5 of the SI file. The ring collection efficiency (N) was determined as 24.6% from LSV curves obtained with the RRDE (Figure S2). Regarding the O_2 reduction assays, as can be deduced from the low onset potential (E_{onset} = 331.9 mV, Table S1 and Figure 1a), Vulcan XC72 exhibited the poorest ORR activity. The onset potential was significantly improved upon Sn doping, suggesting that the introduction of Sn is certainly beneficial to improve the ORR activity at near-neutral pH. In particular, SnC1 and SnC2 exhibited a similar E_{onset} of 0.536 and 0.525 mV, respectively. It can also be seen from Figure 1b and Table S1 that those two catalysts had similar electron transfer numbers, very close to optimum $n = 2$, thus yielding very high O_2-to-H_2O_2 selectivities close to 100%. It is also evident that SnC1 and SnC2 outperformed SnC3, in terms of both activity and selectivity. Nonetheless, it can be concluded that the three SnC electrocatalysts behaved positively, presumably showing an outstanding ability to electrogenerate H_2O_2 in an efficient manner as compared to XC72.

Physicochemical Characterization

The general XPS spectra of Vulcan XC72 and the three SnC catalysts can be observed in Figure S3. Trace Sn contents below 0.1 at.% were found in SnC1 and SnC2, in contrast to the much

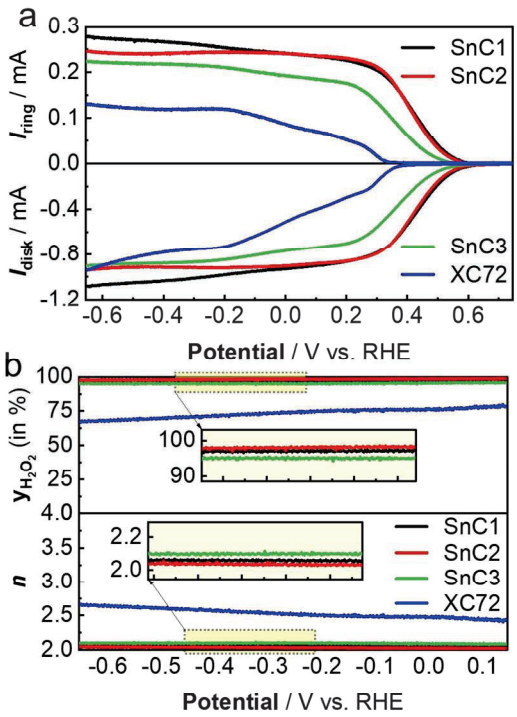

Figure 1. a) Linear sweep voltammograms obtained at an RRDE modified with either Vulcan XC72 carbon black, SnC1, SnC2, or SnC3. The electrocatalysts were drop-cast on the GC disk (catalyst loading: 0.6 mg cm^{-2}), and voltammograms were recorded in an O_2-saturated 0.1 M Na_2SO_4 electrolyte at natural pH 5.9, at v_{scan} = 10 mV s^{-1}. b) Top plot: H_2O_2 selectivity; bottom plot: number of transferred electrons. These two parameters were determined from the data of plot (a) at 1600 rpm, at E_{ring} = 1.54 V *vs.* RHE. A graphite rod and Ag | AgCl (3 M KCl) were used as CE and RE, respectively.

stronger peak appearing in the spectrum of SnC3 (Sn content close to 1%). The latter is partly due to better exposure of the Sn-containing sites/particles upon the second thermal treatment. A clear increase in the N content can also be observed from the spectra of the Sn-doped materials, as compared to the spectrum of Vulcan XC72, which supports the positive role of phenanthroline as an N-doping source during the synthesis. The N content was superior in SnC2, reaching almost 2 at.%. The high-resolution XPS spectra and the deconvolution results for N 1s are shown in Figure 2a–d. Pyridinic and graphitic N seemed to be present in XC72, although they could not be reliably quantified due to the uncertainty in the measurement; greater amounts of both types of N were attained in SnC1 and SnC3, which is relevant because graphitic N is one of the key factors to promote the synthesis of H_2O_2. However, a more crucial role in ORR is played by pyrrolic N.[51,52] The SnC2 catalyst presented this type of N in a relatively high amount (above 1.5 at.%), along with a small amount of oxidized N that resulted from the acid pickling applied for its synthesis. Figure S4 summarizes the distribution of the different N types. On the other hand, the deconvolution of Sn 3d peaks (i.e., Sn $3d_{3/2}$ and

© 2024 The Authors. ChemSusChem published by Wiley-VCH GmbH

1864564x, 2025, 3, Downloaded from https://chemistry-europe.onlinelibrary.wiley.com/doi/10.1002/cssc.202401758 by Readcube (Labtiva Inc.), Wiley Online Library on [07/02/2025]. See the Terms and Conditions (https://onlinelibrary.wiley.com/terms-and-conditions) on Wiley Online Library for rules of use; OA articles are governed by the applicable Creative Commons License

ChemSusChem
Research Article
doi.org/10.1002/cssc.202401758
Chemistry Europe
European Chemical Societies Publishing

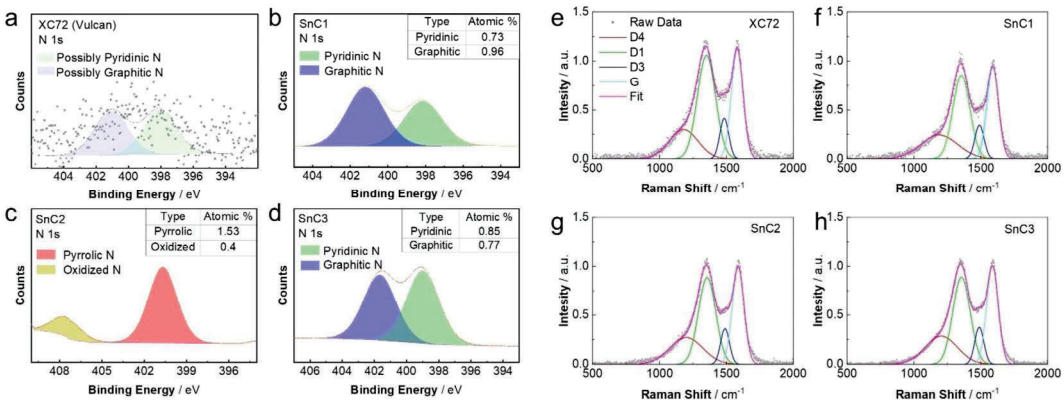

Figure 2. High-resolution XPS spectra of N 1s for (a) XC72, (b) SnC1, (c) SnC2, and (d) SnC3. Deconvoluted Raman spectra of (e) XC72, (f) SnC1, (g) SnC2, and (h) SnC3.

Sn $3d_{5/2}$ at higher and lower binding energy, respectively) is shown in Figure S5, showing the presence of Sn^{4+} in all the Sn-doped carbons, alongside a very weak Sn^0 signal that could only be detected in SnC3. From this figure, it is clear that the surface of all the prepared electrocatalysts becomes easily oxidized upon contact with air; however, such an oxidation is only superficial, as demonstrated by the bulk particle analysis confirming the presence of metal in SnC1 and SnC3 (Figure 3a).

Raman characterization was then employed to gain information on the graphitization degree of the four carbonaceous materials in terms of the degree of crystallinity (i.e., predominance of sp^2 or sp^3 configuration). Carbon black is usually describable as nanocrystalline graphite, namely, particles composed of an ordered graphitic domain of tens of nanometers in dimension interrupted by surface and edge defects. In addition, a certain amount of amorphous carbon is frequently present, which can be related to polycyclic aromatic compounds regarded as graphene layer precursors. Therefore, the deconvolution of Raman spectra of metal-doped carbon-supported catalysts is useful to evaluate the effects of the metal on the graphitization degree. Note that the use of high temperatures during synthesis and possible metal-catalyzed reactions could bring about the modification of the carbon, as has been reported in the case of Fe.[53] For the materials prepared in the present work, the most common five bands were sufficient to describe the main features of the carbon surface. These bands include so-called D1, D2, and D4, which are linked with disordered graphitic lattice, D3 that accounts for amorphous carbon, and G, which is linked to ideal graphite lattice. Figure 2e–h and Table S2 summarize, respectively, the deconvoluted bands and the calculated parameters for the sole Vulcan XC72 and the three SnC catalysts. The position of the G band and the D1-to-G intensity ratio are linked with the properties of the material, as described by Ferrari,[54] indeed recognizing material spanning from graphite to defective diamond. For reference, note that carbon black materials typically show a G band around 1590 cm^{-1} and an I_{D1}/I_G ratio close to 1, which may become lower when transitioning toward

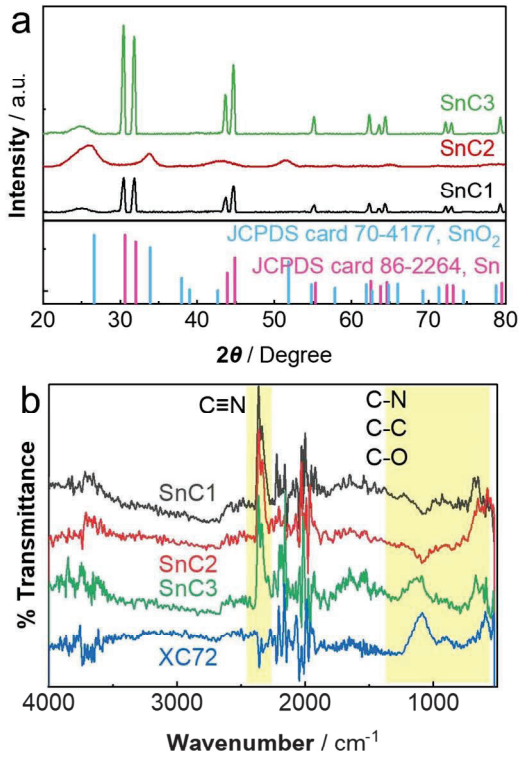

Figure 3. (a) Powder X-ray diffractograms of SnC1, SnC2, and SnC3, as compared to reference patterns of Sn and SnO_2. (b) FT-IR spectra of XC72, SnC1, SnC2, and SnC3.

pure graphite. The latter parameter can also be presented as the ratio between D1 intensity or area and that of other bands (D1, G, and D2) and is called R2;[55,56] it assumes a value higher than 0.5 for a poorly organized structure and lower than 0.5 for a well-organized one. In Table S2, considering the position of

© 2024 The Authors. ChemSusChem published by Wiley-VCH GmbH

18645641, 2025, 3, Downloaded from https://chemistry-europe.onlinelibrary.wiley.com/doi/10.1002/cssc.202401758 by Readcube (Labtiva Inc.), Wiley Online Library on [07/02/2025]. See the Terms and Conditions (https://onlinelibrary.wiley.com/terms-and-conditions) on Wiley Online Library for rules of use; OA articles are governed by the applicable Creative Commons License

ChemSusChem
Research Article
doi.org/10.1002/cssc.202401758
Chemistry Europe
European Chemical Societies Publishing

the D1 and G bands, their intensity ratio, and the R2 parameter, it can be concluded that no significant variations occurred upon Sn doping, apart from a slight increment of the graphitization degree. The amorphous content, evaluated as the percentage of the total spectra area, remained around 8% (Table S2), thus concluding that the amorphous carbon did not change. This permits to exclude the effect of the presence of Sn on the graphitization of the carbon, unlike that observed for other metals like iron.[53] It is also worth remarking that for SnC2, a longer acquisition time was recorded to evaluate the possible presence of SnO_2 (plausible from the acid pickling step), but a signal at around 630 cm^{-1} was not observed.

The XRD analysis evidenced a clear transition from metallic Sn to SnO_2 and then, metallic Sn again, when moving forward from SnC1–SnC2 and, finally, SnC3 (Figure 3a). In other words, SnC2 was characterized by the presence of SnO_2, with no mixed phases observed in each diffractogram. Another important difference was the particle dimensions or, better said, the crystalline domain dimensions, being around 25 nm for SnC1 and SnC3 and around 4 nm for SnC2. The formation of the metallic phase in SnC1 was induced by the presence of C as strong reductant at high temperature (pyrolysis at 900 °C in N_2), which occurred in concomitance with partial C oxidation to CO and/or CO_2 gases. The acid washing employed to synthesize SnC2 favored the oxidation of Sn to SnO_2, probably through a mechanism that involved the destruction of the bigger nanoparticles since it caused a significant reduction in nanoparticle size (i.e., one order of magnitude lower). The last step to produce SnC3 caused a further reduction of SnO_2 to metallic Sn, catalyzed by the presence of carbon that allowed the removal of the oxygen as a CO_2/CO mixture. Note that the peak at around 26° is associated with the C support, being less marked in SnC1 and SnC3 simply because of the sharper Sn peaks, for byrather than the result of a less crystalline in carbon.

The functional groups present in the synthesized catalysts were ascertained by FT-IR (Figure 3b). Worth highlighting, an adsorption band at 2362 cm^{-1} was observed in SnC1, SnC2, and SnC3, which is attributed to the stretching vibrations of C≡N, a group that is known to promote the adsorption of H^+,[57] which is expected to synergistically accelerate the H_2O_2 electrogeneration because H^+ is needed for its formation.

The specific surface area of the electrocatalysts was determined by BET analysis, and detailed information on the pore size distribution was obtained by means of the Quenched Solid Density Functional Theory (QSDFT) model, which is more accurate than the Non-Local Density Functional Theory (NLDFT).[58–60] This is because it takes into account the roughness of the surface and chemical heterogeneity, being more suitable for disordered carbons. The total pore volume was determined by applying the Gurvitsch law at $P/P_0 \approx 0.98$. The pore size distribution was determined using a slit/cylindrical pore model because it allows a better fit to the experimental data in terms of fitting error.

The shape of the isotherms (Figure 4a) offers the first indication of the properties of the four materials. For all samples, the profile can be considered as that typical of a hybrid II/III type, with H3/H4 hysteresis that is traceable to a

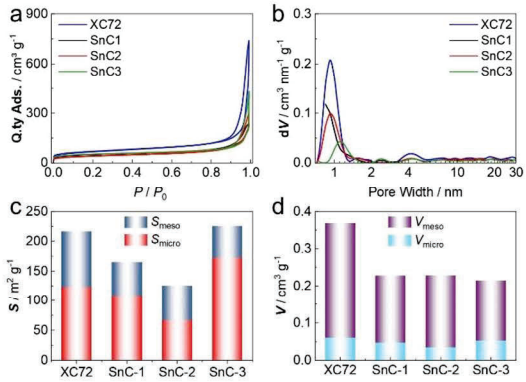

Figure 4. (a) N_2 adsorption/desorption isotherms, (b) pore size distribution, (c) specific surface area analysis along with the contribution of micropores and mesopores, and (d) pore volume analysis of micropores and mesopores for XC72, SnC1, SnC2, and SnC3.

medium-low porous material with a modest content of micro and mesopore. Moving from Vulcan XC72 to SnC3, an inverse volcano trend can be identified (note that this is clearer from the values of surface areas shown in Figure 4c); indeed, the isotherm of SnC1 is lower in adsorption with respect to XC72 within all the relative pressure range, and SnC2 is even lower, whereas for SnC3 an ascent is observed. In all samples, the presence of a small hysteresis is due to the presence of some micro and mesopores. The inclination of the isotherms in the central region of Figure 4a is instead linked to the presence of mesopores with different dimensions. With the QSDFT method, a more precise pore size distribution (PSD) has been obtained. Figure 4b shows some differences in the dimensions of the pores. To gain better information, the subdivisions in micro and mesopore surface area (Figure 4c) and volume (Figure 4d) have been extrapolated using the QSDFT method (see also Table 1). The formation of Sn nanoparticles (SnC1), their conversion into SnO_2 (SnC2), and their final reduction to Sn again (SnC3) seem to have some effect on the pore dimensions, smaller in SnC1 and bigger in SnC3. More in general, as observed from the sole isotherm, in SnC1 there is the occlusion of micro and mesopores, with the latter being more affected, probably due to the growth of the nanoparticles or other phenomena that cause the collapse of the pore network. In SnC2, mainly the micropores are affected; in this case, the SnO_2 particles may grow in proximity to micropores or smaller pores, as suggested by TEM (Figure 5, see below) and XRD (Figure 3a) analysis. In SnC3, there is a growth of micropores by widening the existing ones or by opening new ones, which can be attributed to an activation effect of SnO_2 on the carbon. The reduction of stannic oxide to metallic tin indeed entails the loss of oxygen, which is mostly released as escaping CO_2 gas with the contribution of carbon that is gradually consumed. CO_2 can further react, depending on the temperature, giving CO as the final product.[61] This is in good agreement with the fact that mesopores are very similar in amount to SnC2, since CO_2 should favor the evolution of micropores and, in addition, the regrowth

© 2024 The Authors. ChemSusChem published by Wiley-VCH GmbH

1864564x, 2025, 3, Downloaded from https://chemistry-europe.onlinelibrary.wiley.com/doi/10.1002/cssc.202401758 by Readcube (Labtiva Inc.), Wiley Online Library on [07/02/2025]. See the Terms and Conditions (https://onlinelibrary.wiley.com/terms-and-conditions) on Wiley Online Library for rules of use; OA articles are governed by the applicable Creative Commons License

ChemSusChem

Research Article
doi.org/10.1002/cssc.202401758

Chemistry Europe
European Chemical Societies Publishing

1864564x, 2025, 3, Downloaded from https://chemistry-europe.onlinelibrary.wiley.com/doi/10.1002/cssc.202401758 by Readcube (Labtiva Inc.), Wiley Online Library on [07/02/2025]. See the Terms and Conditions (https://onlinelibrary.wiley.com/terms-and-conditions) on Wiley Online Library for rules of use; OA articles are governed by the applicable Creative Commons License

Table 1. Data obtained from the N_2 physisorption analysis of XC72, SnC1, SnC2, and SnC3.

	S_{BET} $m^2\ g^{-1}$	$S_{\mu+m}$ [a] $m^2\ g^{-1}$	S_{μ} [b] $m^2\ g^{-1}$	S_m [c] $m^2\ g^{-1}$	$V_{\mu+m}$ [a] $cm^3\ g^{-1}$	V_{μ} [b] $cm^3\ g^{-1}$	V_m [c] $cm^3\ g^{-1}$	V_{tot} $cm^3\ g^{-1}$
XC72	225	216	123	93	0.369	0.061	0.309	1.055
SnC1	158	166	108	58	0.228	0.047	0.180	0.356
SnC2	132	125	67	58	0.229	0.034	0.194	0.420
SnC3	170	226	172	53	0.214	0.053	0.162	0.511

[a] $d < 40$ nm, [b] $d < 2$ nm, [c] $2\ nm < d < 40$ nm

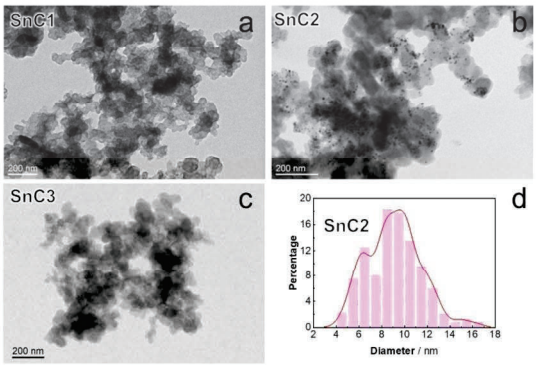

Figure 5. TEM images of (a) SnC1, (b) SnC2, (c) SnC3, and (d) particle size distribution of SnC2.

of big Sn nanoparticles (see comment on XRD above) could again bring to a mesopore occlusion. A note on SnC3 is that there is an evident discrepancy between BET and QSDFT analysis of the surface area (Table 1), which could be caused by the BET method that is not able to well describe this material. BET is a very diffuse method but, in most cases, it is not correctly applied, since it is extremely useful as a qualitative guide, but actually, it is not always quantitatively correct. For example, it should be used only for type II isotherm and having care that the C parameter is not negative,[62] which is exactly what append for SnC3, of which we report the data for completeness. This highlights the need for different methods, such as DFT ones, which can be more reliable to evaluate the surface area of some materials.

Among the four catalysts, SnC2 had the highest mesopore-to-micropore volume ratio (Figure S6). This is a very relevant feature since mesopores contribute to quickly evacuating the generated H_2O_2 as it is produced, thereby avoiding its further reduction to H_2O. Furthermore, SnC2 is the material with the most balanced mesopore-to-micropore surface ratio (Figure 4c and Table 1), which is advantageous because micropores enhance the ORR activity by offering a large number of active sites for O_2 reduction.

HRTEM and EDS were then employed to analyze the morphology and element distribution on the catalyst surface. Figure 5 depicts the representative TEM images of the SnC catalysts, which were composed of agglomerated carbon particles. Sn particles were hardly found in SnC1 (Figure 5a) and SnC3 (Figure 5c) catalysts, whereas they could be easily detected in SnC2 (Figure 5b). Here, the Sn-based nanoparticles are irregularly distributed on the surface of the carbon particles or surrounded by carbon, forming a C-wrapped Sn-containing core structure. The size of the SnO_2 particles in the SnC2 catalyst was measured to be about 9 nm (Figure 5d).

Figure S7 shows the HRTEM images of the SnC2 catalyst, with crystal plane spacings of 0.338 nm, 0.263 nm, and 0.235 nm, corresponding to the (110), (101), and (200) crystal planes of SnO_2 (JCPDS card 70–4177), respectively. The presence of a large number of grain boundaries between these SnO_2 particles, formed by the accumulation of individual SnO_2 nanocrystals, is expected to: (i) Increase the interfacial contact between the supported electrocatalyst and the electrolyte during the electrolyzes; (ii) decrease the diffusion energy barrier toward the active sites; and (iii) facilitate the electron transfer for ORR.

The elemental distribution was confirmed by selecting a more uniform location of Sn (Figure S8): Sn and O were perfectly aligned with the particle location, being consistent with the XRD pattern. C and N were uniformly distributed throughout the region, confirming the N doping ascertained by XPS analysis.

To identify the local structure of Sn sites, ex-situ XAS measurements have been performed at the Sn K-edge for SnC1 and SnC3. Figure 6 shows the comparison of Sn K-edge XANES spectra of the investigated materials with the reference Sn foil and SnO_2 spectra. The threshold position of the spectra of SnC1 and SnC3 lies between those of Sn foil and SnO_2 (Figure 6a), indicating an intermediate oxidation state between that of the zero-valent metal and Sn^{4+}. Note that, since the curves for SnC1 and SnC3 are quite superimposable, it is expected that the tin sites are essentially formed during the first thermal treatment. Hence, the XANES spectrum of SnC2 would show no remarkable differences. Fourier Transform (FT) of the corresponding EXAFS spectra (Figure 6b) reveals a first-shell peak at 1.5–1.6 Å (uncorrected for phase shift) associated with the coordination to light atoms (O/N), whereas the presence of peaks at 2.25, 2.75 and 3.4 Å is assigned to the Sn–Sn backscattering in metallic Sn, and the peak at 3.4 Å to Sn–Sn backscattering in SnO_2, thus suggesting the coexistence of crystalline Sn and SnO_2 nanoparticles in these samples. Possibly this is due to the surface oxidation of metallic tin, as seen from XPS analysis since

© 2024 The Authors. ChemSusChem published by Wiley-VCH GmbH

ChemSusChem
Research Article
doi.org/10.1002/cssc.202401758
Chemistry Europe
European Chemical Societies Publishing

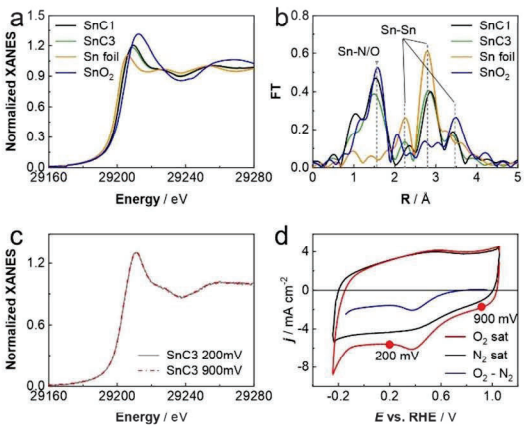

Figure 6. (a) Comparison between the Sn K-edge XANES experimental spectra of SnC1, and SnC3, with the reference SnO_2 and Sn foil spectra; (b) Fourier transform of the experimental EXAFS spectra of SnC1, and SnC3, with the reference SnO_2 and Sn foil spectra. (c) In situ Sn K-edge XANES spectra of SnC3 at 200 (grey curve) and 900 mV (dotted red curve) vs. RHE (O_2 saturated 0.5 M H_2SO_4 solution). (d) CVs recorded at 20 mV s^{-1} in N_2- and O_2-saturated 0.5 M H_2SO_4 solution and the difference between the two (blue line).

the metallic component was only slightly visible (Figure S5c), while XRD suggests that it is the main crystalline component.

In-situ XAS spectra of SnC3, taken as an example due to its higher tin content, have been collected at the different applied potentials in 0.5 M H_2SO_4 solution. Figure 6c demonstrates that no changes were detected in-between Sn K-edge XANES spectra at 200 and 900 mV vs. RHE. The two potentials were chosen according to CVs recorded in the in-situ cell (Figure 6d): in a zone with no oxygen reduction (900 mV vs. RHE), and a zone after the O_2 reduction peak (200 mV). This is in line with what has been previously reported for similar types of materials containing Sn-N_x sites, showing independence from the applied potential.[63] Somehow, this behavior offers a first clue about the acceptable stability of the synthesized Sn-based electrocatalysts.

Preliminary H_2O_2 Production Tests

After demonstrating the appealing characteristics of the SnC materials to be employed as electrocatalysts for two-electron ORR, a first set of electrolytic trials was carried out. Aiming to evaluate the actual H_2O_2 electrogeneration performance, a closed 3-electrode cell with O_2-saturated (and continuously fed) 0.1 M Na_2SO_4 electrolyte at natural pH 5.9 was utilized (Text S6). A rotating-disk electrode (RDE) modified with each of the inks was the working electrode, thereby conducting a 10 h H_2O_2 accumulation assay at a constant potential of $E_{disk} = -0.25$ V vs. RHE ($n \sim 2$, Figure 1). To minimize immediate reduction of the generated H_2O_2 on the electrode surface, the working electrode was kept rotating at 1600 rpm throughout the process. As can be seen from Figure S9, the cumulative H_2O_2 concentration at 10 h increased in the order: SnC3 (0.12 mM) < SnC1 (0.13 mM) < Vulcan (0.15 mM) < SnC2 (0.19 mM). This result emphasizes the great relevance of combining different types of properties, as occurred with SnC2; its great ORR activity and selectivity, as well as the surface and compositional features, made it the best among all tested materials. This idea is even better exemplified by the behavior of Vulcan carbon: it was the worst in terms of electrocatalytic properties (Figure 1 and Table S1), but Figure S9 reveals that it was the second best in terms of performance under practical electrolytic operation. This can thus be explained by its non-electrochemical characteristics, especially its high V_{meso}/V_{micro} ratio (Figure S6). In the very short time framework typical of the electrochemical analysis of Figure 1, the purely electrolytic parameters determine the ranking. In contrast, once performing a long (10 h) electrolysis like that of Figure S9, the H_2O_2 accumulation is determined not only by its production (i.e., activity and selectivity of each material to electrogenerate it), but also by its ability to escape from the cathode surface and minimize its further reduction. The abundant mesopores of Vulcan contribute to preserve the H_2O_2 once produced.

GDE Manufacture and Performance

To gain deeper insight into the previous results and consider the further scale-up of the water treatment process, SnC2 was selected as the optimum electrocatalyst and then integrated into an actual GDE for bulk electrolysis testing in an undivided two-electrode cell (see experimental details in Text S7 and S8). A variety of SnC2-based 3 cm^2 GDEs was prepared using the hot pressing method (the fabrication process is schematized in Figure S10) for evaluating the effect of binder, catalyst loading, applied j, and pH on the H_2O_2 electrogeneration. The assays were made for 300 min under galvanostatic conditions.

Figure 7 shows the time course of accumulated H_2O_2 concentration using the prepared GDE in 150 mL of 0.050 M Na_2SO_4 electrolyte, in the absence of contaminants, under different conditions.

At natural pH 5.9 and $j = 33.3$ mA cm^{-2}, using a GDE with a catalyst loading of 0.5 mg cm^{-2}, the final concentration when either PTFE or Nafion was used as binder attained 20.4 and 12.2 mM H_2O_2, respectively. PTFE has obvious advantages to perform long-term electrolyzes at relatively high currents since its hydrophobicity can minimize the flooding and increase the effective contact between O_2 and electrocatalyst; in contrast, Nafion has hydrophilic channels filled with sulfonate, which is more conducive to the transport of hydrated protons. Consequently, PTFE was the binder chosen for the subsequent trials. When increasing the electrocatalyst loading (2.5 mg cm^{-2}) in the GDE, the H_2O_2 accumulation was very negatively affected, only reaching 9.3 mM at 300 min. This can be explained by the promotion of H_2O_2 electroreduction in the presence of an excess of electrocatalyst, as well as the partial blockage of the pores of the gas-diffusion layer, ending in an adverse effect. When, however, the loading was kept at 0.5 mg cm^{-2} but the applied current was reduced significantly ($j = 10$ mA cm^{-2}), the

© 2024 The Authors. ChemSusChem published by Wiley-VCH GmbH

1864564x, 2025, 3, Downloaded from https://chemistry-europe.onlinelibrary.wiley.com/doi/10.1002/cssc.202401758 by Readcube (Labtiva Inc.), Wiley Online Library on [07/02/2025]. See the Terms and Conditions (https://onlinelibrary.wiley.com/terms-and-conditions) on Wiley Online Library for rules of use; OA articles are governed by the applicable Creative Commons License

ChemSusChem
Research Article
doi.org/10.1002/cssc.202401758
Chemistry Europe
European Chemical Societies Publishing

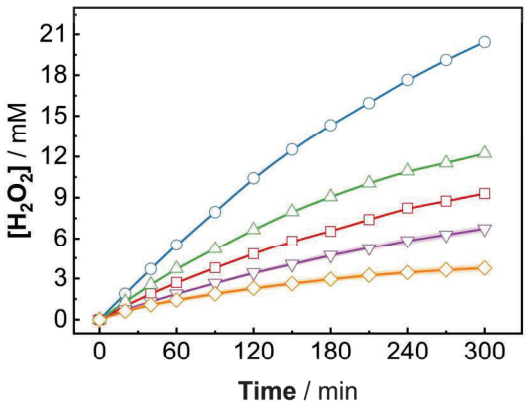

Figure 7. H_2O_2 concentration accumulated in an undivided 2-electrode cell over the electrolysis time. The cathode was a 3 cm^2 GDE fabricated with SnC2 electrocatalyst, fed with compressed air at 0.4 L min^{-1}, and coupled to a 3 cm^2 DSA-Cl_2 plate as the anode. Conditions: 150 mL of a 0.050 M Na_2SO_4 solution at 25 °C. (○) Catalyst loading of 0.5 mg cm^{-2}, PTFE as the binder, j = 33.3 mA cm^{-2}, natural pH 5.9; (△) catalyst loading of 0.5 mg cm^{-2}, Nafion as the binder, j = 33.3 mA cm^{-2}, natural pH 5.9; (□) catalyst loading of 2.5 mg cm^{-2}, PTFE as the binder, j = 33.3 mA cm^{-2}, natural pH 5.9; (▽) catalyst loading of 0.5 mg cm^{-2}, PTFE as the binder, j = 10 mA cm^{-2}, natural pH 5.9; (◇) catalyst loading of 0.5 mg cm^{-2}, PTFE as the binder, j = 10 mA cm^{-2}, pH 3.

cumulative H_2O_2 concentration was reduced to 6.7 and 3.8 mM at natural pH 5.9 and pH 3, respectively. Nonetheless, it must be noted that those values are still sufficient to degrade the organic pollutants in Fenton-based processes,[9] which can be of interest for industrial application because the use of a lower j entails a lower energy consumption and hence, a lower operation cost.

The corresponding time course of current efficiency, calculated from the applied charge as described in previous work,[28] is shown in Figure S11. Notably, during almost the whole electrolysis period, the efficiency was higher when the GDE was manufactured under the optimum conditions (catalyst loading of 0.5 mg cm^{-2}, PTFE as the binder), especially at the lowest j. At higher j values, undesired reactions such as the 4-e^- ORR and hydrogen evolution may dominate, particularly under acidic conditions, which diminishes catalytic activity. Note also that, in all trials, the current efficiency decayed over time, which is simply due to the partial H_2O_2 oxidation at the anode because of the use of an undivided electrolytic cell.

As explained above, another objective of this work was to demonstrate the effective degradation of organic pollutants by the EF process using a GDE based on these low-cost SnC electrocatalysts. Therefore, the activation of H_2O_2 was investigated under conventional EF conditions (pH 3, in the presence of 0.5 mM Fe^{2+}) and EF-like conditions (pH 5.9, in the presence of 0.1 g L^{-1} of heterogeneous Cu/C catalyst). The GDE was prepared with a catalyst loading of 0.5 mg cm^{-2} and PTFE as the binder. As shown in Figure S12, the concentrations of H_2O_2 after 300 min at j = 10 mA cm^{-2} were around 2 mM. This value is clearly lower than those attained in the absence of a Fenton catalyst (Figure 7), confirming the effective decomposition of H_2O_2. In Figure S12, it can be noted that, since Cu/C is a heterogeneous catalyst, it takes a longer time to activate the H_2O_2; the concentration of H_2O_2 in the bulk rose rapidly, and from 60 min it remained almost constant.

The viability of electro-oxidation (EO), EF, and EF-like processes to degrade 14.3 mg L^{-1} (i.e., 10 mg C L^{-1}) DPH in solutions containing 0.050 M Na_2SO_4 under different electrolysis conditions is compared in Figure 8. SnC2-based GDE and DSA-Cl_2 served as cathode and anode, respectively. The EO process at j = 10 mA cm^{-2} was too weak to remove DPH, regardless of the solution pH, only yielding less than 20% concentration decay at 120 min. Operating at pH 5.9 and j = 10 mA cm^{-2}, the EF-like process with Cu/C as a heterogeneous catalyst was still insufficient to provide total removal of DPH, although the 75% degradation corroborates that the low H_2O_2 accumulation of Figure S11 was due to H_2O_2 activation into reactive oxygen species like •OH. Worth remarking, an increase of j up to 33.3 mA cm^{-2} allowed the greater accumulation of H_2O_2, leading to an enhanced activation as demonstrated by the almost complete DPH disappearance at 120 min. The SnC2-based GDE could also serve to treat DPH solutions under acidic conditions, as demonstrated by the fast degradation achieved by the conventional EF process at initial pH 3 and 10 mA cm^{-2}, only requiring 15 min.

Conclusions

This work demonstrates the successful preparation of low-cost and highly selective Sn-based carbons as electrocatalysts for O_2-to-H_2O_2 conversion. Among the synthesized materials, the one obtained from pyrolysis in the presence of an N dopant, followed by acid pickling, outperformed the others as well as

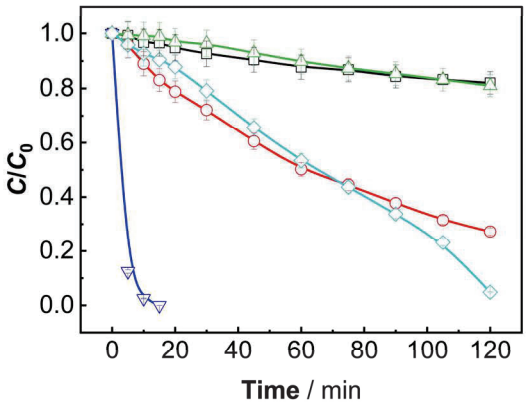

Figure 8. Time course of normalized DPH concentration during the treatment of 150 mL of solutions with 10 mg C L^{-1} drug + 0.050 M Na_2SO_4, at 25 °C, using an undivided cell with the SnC2-GDE fed with air at 0.4 mL min^{-1} and a DSA-Cl_2 plate as the anode. (□), Electro-oxidation process, at natural pH 5.9, j = 10 mA cm^{-2}. (○), EF-like process, at natural pH 5.9, with 0.1 g L^{-1} of Cu/C, j = 10 mA cm^{-2}. (△), Electro-oxidation, at pH 3, j = 10 mA cm^{-2}. (▽), EF process, at pH 3 with 0.5 mM of Fe^{2+}, j = 10 mA cm^{-2}. (◇), EF-like process, at natural pH 5.9, with 0.1 g L^{-1} of Cu/C, j = 33.3 mA cm^{-2}.

© 2024 The Authors. ChemSusChem published by Wiley-VCH GmbH

18645648, 2025, 3, Downloaded from https://chemistry-europe.onlinelibrary.wiley.com/doi/10.1002/cssc.202401758 by Readcube (Labtiva Inc.), Wiley Online Library on [07/02/2025]. See the Terms and Conditions (https://onlinelibrary.wiley.com/terms-and-conditions) on Wiley Online Library for rules of use; OA articles are governed by the applicable Creative Commons License

ChemSusChem
Research Article
doi.org/10.1002/cssc.202401758
Chemistry Europe
European Chemical Societies Publishing

1864564x, 2025, 3, Downloaded from https://chemistry-europe.onlinelibrary.wiley.com/doi/10.1002/cssc.202401758 by Readcube (Labtiva Inc.), Wiley Online Library on [07/02/2025]. See the Terms and Conditions (https://onlinelibrary.wiley.com/terms-and-conditions) on Wiley Online Library for rules of use; OA articles are governed by the applicable Creative Commons License

commercial carbon black, exhibiting superior two-electron ORR performance. This SnC showed a better balance of N-functionalities and mesopore-to-micropore surface and volume ratio. A GDE loaded with a low amount of this electrocatalyst and PTFE as binder resulted in higher H_2O_2 accumulation, which was sufficient for the treatment of organic contaminants by the EF process, even under the most unfavorable conditions. At circumneutral pH, the EF-like process ensured the complete degradation of the drug DPH in 120 min. The excellent performance of the Sn-based GDE is promising for future scale-up of advanced electrochemical treatment of wastewater at relatively low input current.

Acknowledgements

The authors are grateful to project PID2022-140378OB-I00, funded by MICIU/AEI/10.13039/501100011033 (Spain) and by ERDF/EU, as well as to P-DISC Grant (project No. P-DISC#03NExuS_BIRD2021-UNIPD, University of Padova, Italy). MIUR is also acknowledged for the support to the project Finanziato dall'Unione europea – Next Generation EU – Bando PRIN 2022 PNRR – M4.C2.1.1,: Progetto: P2022WANKS – ECHO-EF. M.P. acknowledges PON "Ricerca e Innovazione" 2014–2020 for the Ph.D. fellowship support. The Ph.D. scholarship awarded to L.Z. (State Scholarship Fund, CSC, China) is also acknowledged. BET, XRD, TEM and XPS analyses from the *Centres Científics i Tecnològics de la UB* (CCiT-UB) are also acknowledged. We acknowledge support from the French ANR project ANR-19-CE05-0006 (SPECTROSCOPE), and Synchrotron SOLEIL (Gif-sur Yvette, France) for provision of synchrotron radiation facilities at beamline SAMBA under the Proposal 20220248.

Conflict of Interests

The authors declare no conflict of interest.

Data Availability Statement

The data that support the findings of this study are available from the corresponding author upon reasonable request.

Keywords: Electro-Fenton process · Gas-diffusion electrode · Hydrogen peroxide · SnC nanoparticles · Water treatment

[1] M. Mazzucato, C. Durante, *Curr. Opin. Electrochem.* **2022**, *35*, 101051.
[2] M. Mazzucato, A. Facchin, M. Parnigotto, C. Durante, *ACS Catal.* **2024**, *14*, 6369–6403.
[3] I. Sirés, E. Brillas, *Curr. Opin. Electrochem.* **2021**, *27*, 100686.
[4] Y. Xu, P. Xia, C. Wang, J. Cai, H. Li, Z. Ye, H. Zhang, *Chem. Eng. J.* **2023**, *462*, 142021.
[5] G.-F. Han, F. Li, W. Zou, M. Karamad, J.-P. Jeon, S.-W. Kim, S.-J. Kim, Y. Bu, Z. Fu, Y. Lu, S. Siahrostami, J.-B. Baek, *Nat. Commun.* **2020**, *11*, 2209.
[6] L. Li, L. Xu, A. W. M. Chan, Z. Hu, Y. Wang, J. C. Yu, *Chem. Mater.* **2022**, *34*, 63–71.
[7] C. Xia, J. Y. (T.) Kim, H. Wang, *Nat. Catal.* **2020**, *3*, 605–607.
[8] Y. Wen, T. Zhang, J. Wang, Z. Pan, T. Wang, H. Yamashita, X. Qian, Y. Zhao, *Ang. Chem. Int. Ed.* **2022**, *61*, e202205972.
[9] O. M. Cornejo, I. Sirés, J. L. Nava, *Electrochim. Acta* **2022**, *404*, 139621.
[10] A. P. Reyes-Cruzaley, R. M. Félix-Navarro, B. Trujillo-Navarrete, C. Silva-Carrillo, J. R. Zapata-Fernández, J. M. Romo-Herrera, O. E. Contreras, E. A. Reynoso-Soto, *Electrochim. Acta* **2019**, *296*, 575–581.
[11] X. Ren, X. Dong, L. Liu, J. Hao, H. Zhu, A. Liu, G. Wu, *SusMat* **2023**, *3*, 442–470.
[12] C. A. Martínez-Huitle, M. A. Rodrigo, I. Sirés, O. Scialdone, *Appl. Catal. B: Environ.* **2023**, *328*, 122430.
[13] O. M. Cornejo, I. Sirés, J. L. Nava, *J. Electroanal. Chem.* **2020**, *873*, 114419.
[14] Ş. Camcıoğlu, B. Özyurt, N. Oturan, D. Portehault, C. Trellu, M. A. Oturan, *Chemosphere* **2023**, *341*, 140129.
[15] R. M. Félix-Navarro, M. Beltrán-Gastélum, M. I. Salazar-Gastélum, C. Silva-Carrillo, E. A. Reynoso-Soto, S. Pérez-Sicairos, S. W. Lin, F. Paraguay-Delgado, G. Alonso-Núñez, *J. Nanopart. Res.* **2013**, *15*, 1802.
[16] S. Siahrostami, A. Verdaguer-Casadevall, M. Karamad, D. Deiana, P. Malacrida, B. Wickman, M. Escudero-Escribano, E. A. Paoli, R. Frydendal, T. W. Hansen, I. Chorkendorff, I. E. L. Stephens, J. Rossmeisl, *Nat. Mater.* **2013**, *12*, 1137–1143.
[17] A. Verdaguer-Casadevall, D. Deiana, M. Karamad, S. Siahrostami, P. Malacrida, T. W. Hansen, J. Rossmeisl, I. Chorkendorff, I. E. L. Stephens, *Nano Lett.* **2014**, *14*, 1603–1608.
[18] E. Pizzutilo, O. Kasian, C. H. Choi, S. Cherevko, G. J. Hutchings, K. J. J. Mayrhofer, S. J. Freakley, *Chem. Phys. Lett.* **2017**, *683*, 436–442.
[19] W. Liu, L. Tian, L. Shi, *J. Phys. Chem. C* **2024**, *128*, 6682–6688.
[20] S. G. F. Eggermont, R. Prato, X. Dominguez-Benetton, J. Fransaer, *React. Chem. Eng.* **2021**, *6*, 1031–1041.
[21] P. J. M. Cordeiro Junior, A. S. Martins, G. B. S. Pereira, F. V. Rocha, M. A. R. Rodrigo, M. R. V. Lanza, *Electrochim. Acta* **2022**, *430*, 141067.
[22] F. L. Silva, R. M. Reis, W. R. P. Barros, R. S. Rocha, M. R. V. Lanza, *J. Electroanal. Chem.* **2014**, *722–723*, 32–37.
[23] J. Liu, Z. Wei, Z. Gong, M. Yan, Y. Hu, S. Zhao, G. Ye, H. Fei, *Appl. Catal. B: Environ.* **2023**, *324*, 122267.
[24] Y. Wu, Y. Ding, X. Han, B. Li, Y. Wang, S. Dong, Q. Li, S. Dou, J. Sun, J. Sun, *Appl. Catal. B: Environ.* **2022**, *315*, 121578.
[25] Y.-X. Du, Q. Yang, W.-T. Lu, Q.-Y. Guan, F.-F. Cao, G. Zhang, *Adv. Funct. Mater.* **2023**, *33*, 2300895.
[26] J. Xi, S. Yang, L. Silvioli, S. Cao, P. Liu, Q. Chen, Y. Zhao, H. Sun, J. N. Hansen, J.-P. B. Haraldsted, J. Kibsgaard, J. Rossmeisl, S. Bals, S. Wang, I. Chorkendorff, *J. Catal.* **2021**, *393*, 313–323.
[27] M. Mazzucato, L. Gavioli, V. Balzano, E. Berretti, G. A. Rizzi, D. Badocco, P. Pastore, A. Zitolo, C. Durante, *ACS Appl. Mater. Interfaces* **2022**, *14*, 54635–54648.
[28] G. Daniel, Y. Zhang, S. Lanzalaco, F. Brombin, T. Kosmala, G. Granozzi, A. Wang, E. Brillas, I. Sirés, C. Durante, *ACS Sustain. Chem. Eng.* **2020**, *8*, 14425–14440.
[29] Y. Zhang, G. Daniel, S. Lanzalaco, A. A. Isse, A. Facchin, A. Wang, E. Brillas, C. Durante, I. Sirés, *J. Hazard. Mater.* **2022**, *423*, 127005.
[30] M. S. Kronka, G. V. Fortunato, L. Mira, A. J. dos Santos, M. R. V. Lanza, *Chem. Eng. J.* **2023**, *452*, 139598.
[31] G. V. Fortunato, M. S. Kronka, A. J. dos Santos, M. Ledendecker, M. R. V. Lanza, *Chemosphere* **2020**, *259*, 127523.
[32] R. B. Valim, L. C. Trevelin, D. C. Sperandio, J. F. Carneiro, M. C. Santos, L. A. Rodrigues, R. S. Rocha, M. R. V. Lanza, *J. Environ. Chem. Eng.* **2021**, *9*, 106787.
[33] E. C. Paz, L. R. Aveiro, V. S. Pinheiro, F. M. Souza, V. B. Lima, F. L. Silva, P. Hammer, M. R. V. Lanza, M. C. Santos, *Appl. Catal. B: Environ.* **2018**, *232*, 436–445.
[34] Q. Zhang, M. Zhou, G. Ren, Y. Li, Y. Li, X. Du, *Nat. Commun.* **2020**, *11*, 1731.
[35] P. Su, M. Zhou, G. Ren, X. Lu, X. Du, G. Song, *J. Mater. Chem. A* **2019**, *7*, 24408–24419.
[36] X. Wang, Q. Zhang, J. Jing, G. Song, M. Zhou, *Chem. Eng. J.* **2023**, *466*, 143283.
[37] G. Ren, S. Lanzalaco, M. Zhou, P. L. Cabot, E. Brillas, I. Sirés, *Chem. Eng. J.* **2023**, *454*, 140515.
[38] ACS, "The Periodic Table of Endangered Elements", https://www.acs.org/greenchemistry/research-innovation/endangered-elements.html. Last access: 9 October 2024.
[39] A. A. Yaroshevsky, *Geochem. Int.* **2006**, *44*, 48–55.
[40] M. Gao, X. Zhang, S. Dai, K.-W. Wang, *Inorg. Chem. Front.* **2024**, *11*, 1019–1047.
[41] C. Lv, J. Liu, C. Lee, Q. Zhu, J. Xu, H. Pan, C. Xue, Q. Yan, *ACS Nano* **2022**, *16*, 15512–15527.

© 2024 The Authors. ChemSusChem published by Wiley-VCH GmbH

ChemSusChem

Research Article
doi.org/10.1002/cssc.202401758

Chemistry Europe
European Chemical Societies Publishing

[42] F. Luo, A. Roy, L. Silvioli, D. A. Cullen, A. Zitolo, M. T. Sougrati, I. C. Oguz, T. Mineva, D. Teschner, S. Wagner, J. Wen, F. Dionigi, U. I. Kramm, J. Rossmeisl, F. Jaouen, P. Strasser, *Nat. Mater.* **2020**, *19*, 1215–1223.
[43] Y. Zhang, B. Li, Y. Su, *Molecules* **2023**, *28*, 5571.
[44] F. Luo, A. Roy, M. T. Sougrati, A. Khan, D. A. Cullen, X. Wang, M. Primbs, A. Zitolo, F. Jaouen, P. Strasser, *J. Am. Chem. Soc.* **2023**, *145*, 14737–14747.
[45] X. Zhang, J. Liu, Y. Qiao, A. Kong, R. Li, Y. Shan, *Electrochim. Acta* **2019**, *320*, 134593.
[46] E. Negro, A. Bach Delpeuch, K. Vezzù, G. Nawn, F. Bertasi, A. Ansaldo, V. Pellegrini, B. Dembinska, S. Zoladek, K. Miecznikowski, I. A. Rutkowska, M. Skunik-Nuckowska, P. J. Kulesza, F. Bonaccorso, V. Di Noto, *Chem. Mater.* **2018**, *30*, 2651–2659.
[47] E. Topp, M. W. Sumarah, L. Sabourin, *Sci. Total Environ.* **2012**, *439*, 136–140.
[48] P. E. Stackelberg, E. T. Furlong, M. T. Meyer, S. D. Zaugg, A. K. Henderson, D. B. Reissman, *Sci. Total Environ.* **2004**, *329*, 99–113.
[49] S. Wolfson, A. W. Porter, T. S. Villani, J. E. Simon, L. Y. Young, *Chemosphere* **2018**, *202*, 460–466.
[50] B. Du, A. E. Price, W. C. Scott, L. A. Kristofco, A. J. Ramirez, C. K. Chambliss, J. C. Yelderman, B. W. Brooks, *Sci. Total Environ.* **2014**, *466–467*, 976–984.
[51] L. Li, C. Tang, Y. Zheng, B. Xia, X. Zhou, H. Xu, S.-Z. Qiao, *Adv. Energy Mater.* **2020**, *10*, 2000789.
[52] Z. Zhang, H. Zhao, Z. Wang, Z. Hu, Q. Wang, E. Meng, S. Lai, J. Ying, H. Li, C. Wu, *Environ. Res.* **2023**, *236*, 116794.
[53] D. Liu, X. Zhao, R. Su, Z. Hao, B. Jia, S. Li, L. Dong, *Processes* **2019**, *7*, 300.
[54] A. C. Ferrari, *Diamond Relat. Mater.* **2002**, *11*, 1053–1061.
[55] O. Beyssac, B. Goffé, J.-P. Petitet, E. Froigneux, M. Moreau, J.-N. Rouzaud, *Spectrochim. Acta Part A: Molecul. Biomolecul. Spectrosc.* **2003**, *59*, 2267–2276.
[56] G. Daniel, T. Kosmala, F. Brombin, M. Mazzucato, A. Facchin, M. C. Dalconi, D. Badocco, P. Pastore, G. Granozzi, C. Durante, *Catalysts* **2021**, *11*, 390.
[57] X. Zhang, P. Ma, C. Wang, L. Gan, X. Chen, P. Zhang, Y. Wang, H. Li, L. Wang, X. Zhou, K. Zheng, *Energy Environ. Sci.* **2022**, *15*, 830–842.
[58] A. M. Puziy, O. I. Poddubnaya, B. Gawdzik, M. Sobiesiak, *Adsorption* **2016**, *22*, 459–464.
[59] G. Y. Gor, M. Thommes, K. A. Cychosz, A. V. Neimark, *Carbon* **2012**, *50*, 1583–1590.
[60] J. Landers, G. Y. Gor, A. V. Neimark, *Colloid. Surf. A: Physicochem. Eng. Aspects* **2013**, *437*, 3–32.
[61] R. Padilla, H. Y. Sohn, *Metall. Trans. B* **1979**, *10*, 109–115.
[62] J. Rouquerol, P. Llewellyn, F. Rouquerol, in *Studies in Surface Science and Catalysis* (Eds.: P. L. Llewellyn, F. Rodriquez-Reinoso, J. Rouqerol, N. Seaton), Elsevier B.V., Amsterdam, 2007, pp. 49–56.
[63] W. Qiu, Y. Liu, M. Xie, Z. Jin, P. Li, G. Yu, *EES Catal.* **2024**, *2*, 202–219.

Manuscript received: August 7, 2024
Revised manuscript received: September 2, 2024
Accepted manuscript online: September 9, 2024
Version of record online: October 25, 2024

© 2024 The Authors. ChemSusChem published by Wiley-VCH GmbH

1864564x, 2025, 3, Downloaded from https://chemistry-europe.onlinelibrary.wiley.com/doi/10.1002/cssc.202401758 by 3readcube (Labtiva Inc.), Wiley Online Library on [07/02/2025]. See the Terms and Conditions (https://onlinelibrary.wiley.com/terms-and-conditions) on Wiley Online Library for rules of use; OA articles are governed by the applicable Creative Commons License

ChemSusChem

Supporting Information

Boosting the O_2-to-H_2O_2 Selectivity Using Sn-Doped Carbon Electrocatalysts: Towards Highly Efficient Cathodes for Actual Water Decontamination

Lele Zhao, Marco Mazzucato, Sonia Lanzalaco, Mattia Parnigotto, Anastassiya Khan, Andrea Zitolo, Pere L. Cabot, Christian Durante,* and Ignasi Sirés*

ChemSusChem

SUPPORTING INFORMATION

Boosting the O_2-to-H_2O_2 Selectivity using Sn-doped Carbon Electrocatalysts: Towards Highly Efficient Cathodes for Actual Water Decontamination

Lele Zhao,[a] Marco Mazzucato,[b] Sonia Lanzalaco,[c] Mattia Parnigotto,[b] Anastassiya Khan,[d] Andrea Zitolo,[d] Pere L. Cabot,[a] Christian Durante*[b], Ignasi Sirés*[a]

[a] L. Zhao, Prof. Dr. P. L. Cabot, Prof. Dr. I. Sirés
Laboratori d'Electroquímica dels Materials i del Medi Ambient, Departament de Ciència de Materials i Química Física, Secció de Química Física, Facultat de Química
Universitat de Barcelona
Martí i Franquès 1-11, 08028 Barcelona, Spain
E-mail: i.sires@ub.edu

[b] Dr. M. Mazzucato, M. Parnigotto, Prof. Dr. C. Durante
Department of Chemical Sciences
University of Padua
Via Marzolo 1, 35131 Padova, Italy
E-mail: christian.durante@unipd.it

[c] Prof. Dr. S. Lanzalaco
Departament d'Enginyeria Química, EEBE
Universitat Politècnica de Catalunya
C/ Eduard Maristany, 10–14, Ed. I2, 08019 Barcelona, Spain

[d] Dr. A. Khan, Dr. A. Zitolo
Synchrotron SOLEIL
L'Orme des Merisiers, Départementale 128, 91190 Saint-Aubin, France

TABLE OF CONTENTS

1. Experimental Section 2
2. Additional Tables 8
3. Additional Figures 9
4. References 15

1. Experimental Section

***Text S1*. Chemicals and materials.** For the synthesis of the carbons, the following reagent grade chemicals were used: $SnCl_2$•$2H_2O$ (Sigma-Aldrich, 98%), 1,10-phenanthroline monohydrate (Thermo Scientific, ≥99%), Vulcan XC 72 carbon black (Fuel Cell Store). The following reagents were used for the preparation of the inks: Nafion (Sigma-Aldrich, 5 wt.% in mixture of lower aliphatic alcohols and water, 45% water content), polytetrafluoroethylene (Aldrich, 60 wt.% dispersion in water), 2-propanol dry (PanReac AppliChem, max. 0.01% water). The reagents used for H_2O_2 concentration measurement and degradation experiments were: Ti(IV) oxysulfate (Sigma-Aldrich, ≥29%), sodium sulfate (Sigma-Aldrich, 99%), diphenhydramine hydrochloride (DPH, Merck, ≥98%), sulfuric acid (PanReac AppliChem, 96%), and sodium hydroxide pellets (Scharlau, extrapure, Ph Eur, BP, NF). The catalysts employed for Fenton-based degradation of DPH were a Cu/C powder, synthesized by us through pyrolysis of a Cu-based MOF, and soluble Fe^{2+} from $FeSO_4$•$7H_2O$ (J.T. Baker, > 98%). Diamond pastes (Struers, ¼ μm) and self-adhesive polishing cloths (Struers, satin woven natural silk) were used for grinding and cleaning the glassy carbon electrodes. Alpha Gaz N_2, O_2 and Ar were supplied by Air Liquid at the highest available purity (>99.99%). Formic acid (Fisher Chemical, Optima LC/MS) and acetonitrile (PanReac Applichem, Reag. Ph. Eur. for UHPLC Supergradient, ACS) were used to prepare the mobile phase. All the reagents were used as received without further purification. All aqueous solutions were prepared with Milli-Q water from a Merck Life Science Synergy UV device (resistivity > 18.2 MΩ cm).

***Text S2*. Synthesis of the Sn-doped carbon electrocatalysts.** The catalysts were prepared by pyrolysis, acid washing and re-pyrolysis (Fig. S1). Briefly, 2.0 g of $SnCl_2 \cdot 2H_2O$ and 2.24 g of 1,10-phenanthroline monohydrate was weighed and dissolved in ethanol. The latter solution was added dropwise over the former, while keeping it under stirring. A yellow precipitate was quickly formed, being recovered by filtration and placed in an oven at 80 ºC overnight; it is denoted as $Sn(phen)Cl_2$. Then, 1.0 g of $Sn(phen)Cl_2$ was mixed well with 1.39 g of XC72, followed by pyrolysis at 900 ºC under N_2 atmosphere for 2 h. The resulting black powder, SnC1(raw), is named as SnC1. This powder was dispersed in 1 M H_2SO_4, followed by stirring in an oil bath at 100 ºC for 3 h. The

powder was recovered by filtration and dried at 80 ºC, giving rise to SnC2(picked), so-called SnC2. The resulting powder was pyrolyzed at 900 ºC under N_2 atmosphere for 2 h to finally obtain SnC3(repyrolyzed), named as SnC3.

***Text S3*. Protocol to manufacture the GDEs.** GDEs were prepared from each type of synthesized powder using the hot press method. A suitable quantity of binder (PTFE or Nafion) was mixed with 1 mL of Milli-Q water and sonicated. Subsequently, a specific amount of catalyst was added and sonicated for 30 min. To this mixture, 4 mL of 2-propanol was added, keeping the mixture under sonication for 10 min to produce the final ink. On the other hand, a squared carbon cloth (BIASWP, carbon cloth designation A, standard wet proofing) with an approximate area of 9 cm² was prepared as the gas-diffusion layer. It was ultrasonicated using ethanol for 30 min and thoroughly dried at 80 ºC. The previous ink was drop-cast onto one side of the carbon cloth using a micropipette, with approximately 0.4 mL of ink transferred each time. After preparing each layer, the carbon cloth was placed on a heated platform at 80 ºC to ensure complete drying. Once all the ink was cast, the catalyzed carbon cloth was dried, wrapped in multiple layers of aluminium foil, and placed in a press set to a pressure of 6 ton at 210 ºC for 2 h. The final GDE was obtained after cooling down to ambient temperature, and then cut it into circles with an area of 3 cm^2 for electrolytic trials.

***Text S4*. Structural characterization.** The X-ray diffraction (XRD) analysis was performed on a Bruker AXS D8 ADVANCE Plus diffractometer with a Cu source ($\lambda_{K\alpha 1}$ = 1.5406 Å) from 20 to 80° (2θ) and a 0.05° step on a Si zero-background sample holder. The X-ray photoelectron microscopy (XPS) analysis was performed with a SPECS system equipped with a high-intensity twin anode X-ray source XR50 and using a Phoibos 150 MCD-9 XP detector (2400 V). A Large Area analyzer lens (1.5 kV) was used, whereas the scan mode was Fixed Analyzer Transmission and the excitation energy was 1486.61 eV. As the internal reference, C 1s peak with a binding energy of 284.8 eV was used. The spectra were analyzed using the Avantage Software. The specific surface area was determined using the Brunauer–Emmett–Teller (BET) method, where N_2 was used as the adsorbate gas. The data where obtained using a TriStar 3000 surface area analyzer from Micromeritics within the range $0.05 \leq P/P_0 \leq 0.25$. Sample

outgassing was performed under vacuum at 40 °C for 4 h. The morphology was assessed by high-resolution transmission electron microscopy (HRTEM), using a JEOL JEM-2100 (LaB6) microscope operating at 200 kV in STEM mode with a dark-field detector, and coupled to an Oxford Inca energy-dispersive X-ray spectrometer (EDS). HRTEM analysis was made with Digital Micrograph software, whereas mapping acquisition was accomplished with the Inca Microanalysis Suite version 4.09 software. Fourier Transform Infrared Spectroscopy (FT-IR) was done on a Nicolet 6700 with Smart Diamond Orbit ATR (Thermo Scientific), software OMNIC from 4000 to 500 cm^{-1} wavenumber. Raman spectroscopy was carried out in a LabRAM HR Horiba Jobin Yvon 330-1993 cm^{-1}, equipped with a 532 nm laser as the photoexcitation source. Curve fitting of the Raman spectra was made using pseudo-Voigt function. Sn K-edge X-ray absorption spectroscopy (XAS) spectra were measured at the SAMBA beamline (SOLEIL synchrotron) at room temperature in the fluorescence mode using a Ge 33-pixel detector. The beamline was equipped with a sagittally focusing Si 220 monochromator and two Pd-coated mirrors that were used to remove X-ray harmonics. The catalysts were pelletized as disks of 10 mm diameter using graphite as a binder for the ex-situ analysis, while for the in-situ analysis, the catalyst was drop casted onto a graphite sheet and mounted on a three-electrode liquid electrochemical cell available at SAMBA through collaboration with the beamline scientist Dr. Andrea Zitolo.[1]

***Text S5*. *Electrochemical characterization*.** The linear sweep voltammetry (LSV) analysis was carried out on a rotating ring-disk electrode (RRDE, Metrohm; *d* = 5 mm GC disk and a Pt ring), in both Ar-purged and O_2-saturated 0.1 M Na_2SO_4 solution using an Autolab model 101N potentiostat. All measurements were done in a three-electrode cell thermostated at 25 °C. The RRDE tip was used as the working electrode, a graphite rod was used as the counter electrode, and Ag|AgCl (3 M KCl) as the reference electrode.

For the RRDE conditioning, a small amount of diamond plaster was applied to the tip of the electrode, which was placed perpendicularly to the polishing cloth. Then the axis of the electrode was rotated clockwise for 100 cycles, whereupon the tip of the electrode was immersed into acetone for ultrasonication for 5 min. This was repeated using 2-propanol, and the tip was finally left for natural drying.

For catalyst loading onto the RRDE, 5 mg of a given powder was weighed, then adding 100 μL of 2-propanol, 500 μL of Milli-Q water, and 30 μL of Nafion sequentially. A water bath sonicator was employed, at controlled temperature, to ensure full dispersion of the powder. The ink loading onto the RRDE was determined to be 0.6 mg cm^{-2}.

Prior to electrochemical characterization, each given material loaded on the RRDE was initially activated in Ar-purged electrolyte by recording several cycling voltammetries (CV), cycling at 100, 50 and 10 mV s^{-1} until a stable signal was observed. In ORR tests, O_2 was bubbled into the electrolyte for at least 30 min. The number of transferred electrons (n) was determined by LSV, according to the following equation.

$$n = \frac{4\,|I_D|}{|I_D|+|I_R|/N}$$

where I_D is the current recorded at disk, I_R is the current recorded at ring, and N is the collection factor, which was close to 25% (i.e., 0.246, Fig. S2). From the same LSV analysis with the RRDE, it is also possible to evaluate the O_2-to-H_2O_2 selectivity or H_2O_2 yield (i.e., the percentage of hydrogen peroxide produced at the working electrode):

$$y_{H_2O_2} = \frac{2|I_R|}{N\times|I_D|+|I_R|}\times 100$$

For in-situ XAS, 50 μL of an ink made with 10 mg of catalyst, 50 μL H_2O and 100 μL Nafion was drop casted on graphite sheet. CVs were performed at 20 mV s^{-1} and actual in-situ measurements were recorded under constant potential (0.2 and 0.9 V vs. RHE). The available cell at beamline is equipped with Ag|AgCl (3M KCl) as the reference electrode and Pt as counter electrode, whereas a graphite sheet serve as working electrode.

***Text S6*. Small reaction cell for preliminary study of H_2O_2 electrogeneration (RDE setup).** The first H_2O_2 accumulation tests were carried out in a small closed cell under potentiostatic conditions, aiming to mimic the conditions determined in the LSV study. The potential of the working electrode (rotating disk electrode –RDE-, *d* = 5 mm) was set at -0.8 V (i.e., -0.25 V *vs.* RHE). O_2 was continuously supplied to ensure saturation of the 30 mL of 0.1 M Na_2SO_4 solution at natural pH. The loading of catalyst on the RDE tip was 0.5 mg cm^{-2}.

Pt and Ag|AgCl (3 M KCl) were used as counter electrode and reference electrode, respectively.

The reaction was performed continuously for 10 h. For analysis, 0.5 mL of the electrolyzed solution was withdrawn after 4, 8, and 10 h and immediately added to a mixture of 1 mL H_2O and 1 mL Ti(IV). Colorimetric analysis of the yellowish complex formed between Ti(IV) and H_2O_2 was performed using a Unicam UV/Vis spectrophotometer set at λ_{max} = 408 nm. The corresponding calibration curve equation was: y = 0.0341x, where *x* denotes the H_2O_2 concentration in mM, and *y* accounts for the absorbance.

***Text S7*. Larger undivided open cell to study the H_2O_2 electrogeneration performance (Bulk electrolytic trials).** All trials were performed in an undivided open cylindrical glass cell of 200 mL capacity with a double jacket for recirculating water at 25 ºC. A magnetic stirrer was used to keep a constant stirring rate. 150 mL of 0.050 M Na_2SO_4 solution at different pH was used as the electrolyte. The anode was a DSA-Cl_2 (RuO_2-based) metal plate (50 mm × 20 mm × 1 mm, double-sided) supplied by NMT Electrodes. The exposed are of 3 cm^2 was delimited by using Teflon tape. The cathode was an air diffusion electrode (GDE, 3 cm^2) composed of a polypropylene air chamber machined in the factory of the University of Barcelona, which contained a silicone gasket, Ni-Cr mesh as current collector, the carbon cloth modified as explained above, a Ni-Cr wire as contact, and a glass tube for air supply. A KNF LAB air pump provided compressed air, and the flowrate was measured with a flow meter from Iberfluid Instruments, S.A. Constant current was supplied by an Amel 2053 power supply, and a Demestres DM610 BR digital voltmeter served to monitor the cell voltage.

***Text S8*. Diphenhydramine (DPH) degradation assays.** Solutions of 150 mL of 14.3 mg DPH/L (i.e., 10 mg C/L) + 0.050 M Na_2SO_4 were stored at 4 ºC, away from light. For electro-oxidation experiments, the tests were performed both at natural pH and pH 3, without catalyst addition to the solution. For electro-Fenton experiments, 0.1 g/L Cu/C catalyst was added in trials performed at natural pH, whereas 0.5 mM $FeSO_4$•$7H_2O$ catalyst was added in trials at pH 3.

The drug concentration decay over time was measured by reversed-phase HPLC. A Waters 600 chromatograph, equipped with a Biphenyl (100 Å, 150 × 4.6 mm) column, thermostated at 35 ºC, and connected to a photodiode array

detector was employed. A thin peak with λ_{max} = 220 nm related to DPH appeared at retention time of 3.6 min. A 40:60 (v/v) mixture containing the organic (acetonitrile) and aqueous (0.1% of formic acid) layer was recirculated at 1.0 mL min^{-1} as the mobile phase. For the HPLC analysis, aliquots of 0.5 mL of a given sample were mixed with the same volume of the mobile phase. After mixing, the volume was filtered (0.22 μm syringe filter).

ChemSusChem

2. Additional Tables

Table S1.

Onset potential, electron transfer number (n) and H_2O_2 selectivity of the three synthesized electrocatalysts, as compared to commercial carbon black, determined by LSV tests with an RRDE.

Sample	E_{onset} / mV *vs.* RHE (at I_D = -0.1 mA)	*n*	y_{H2O2} / %
SnC1	535.9	2.06	97.0
SnC2	525.2	2.04	98.0
SnC3	478.3	2.10	95.1
Vulcan XC72	331.91	2.18	91.1

Table S2.

Data obtained from the deconvolution of Raman spectra of the three synthesized electrocatalysts, as compared to commercial carbon black.

Sample	D1	I_{D1}	G	I_G	I_{D1}/I_G	R2	A_{D3}/A_{tot}
	/ cm^{-1}	-	/ cm^{-1}	-	-		/ %
SnC1	1355	0.86	1590	0.94	0.91	0.57	8.4
SnC2	1356	0.89	1588	0.99	0.89	0.57	8.2
SnC3	1356	0.89	1588	1.00	0.89	0.57	8.6
XC72	1351	1.06	1581	1.12	0.95	0.59	8.2

3. Additional Figures

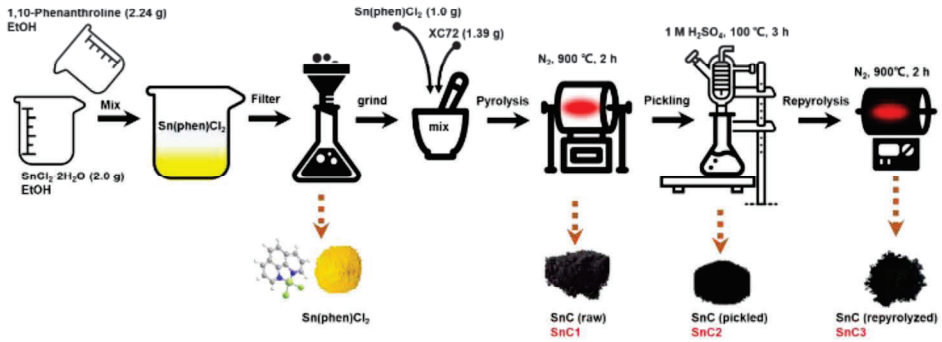

Figure S1. Scheme of the synthesis procedure followed to obtain three different Sn-doped carbons: SnC1, resulting from a first pyrolysis step; SnC2, obtained upon pickling of SnC1; and SnC3, produced through a second pyrolysis step applied to SnC2.

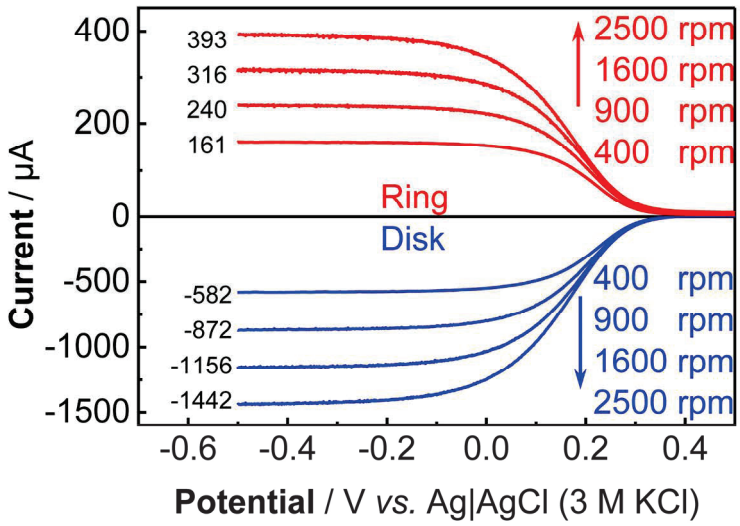

Figure S2. The collection factor of RRDE was calibrated using the LSV curves obtained at different rotation rates. 100 mL of 1 M KCl + 10 mM $K_3[Fe(CN)_6]$ solution under N_2-saturated was used. Parameters: scan rate of 10 mV s^{-1}, E_{ring} = 1.1 V. Pt and Ag|AgCl (3 M KCl) were used as counter and reference electrodes, respectively.

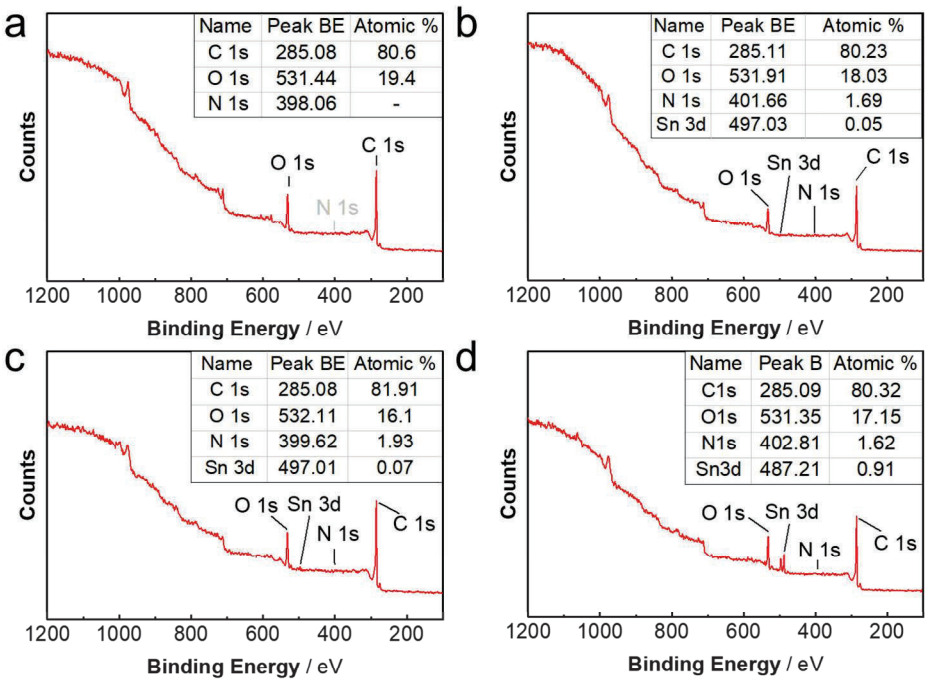

Figure S3. Full XPS spectra of (a) XC72, (b) SnC1, (c) SnC2, and (d) SnC3.

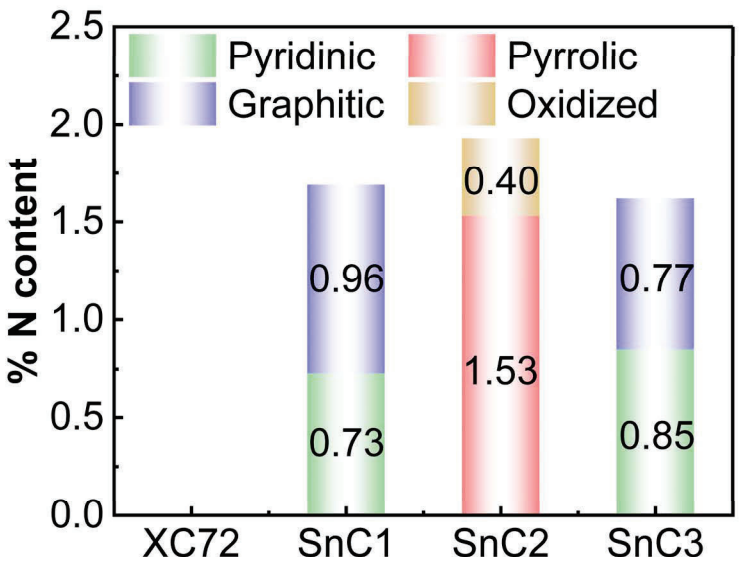

Figure S4. N content in the surface of XC72, SnC1, SnC2, and SnC3, determined by XPS.

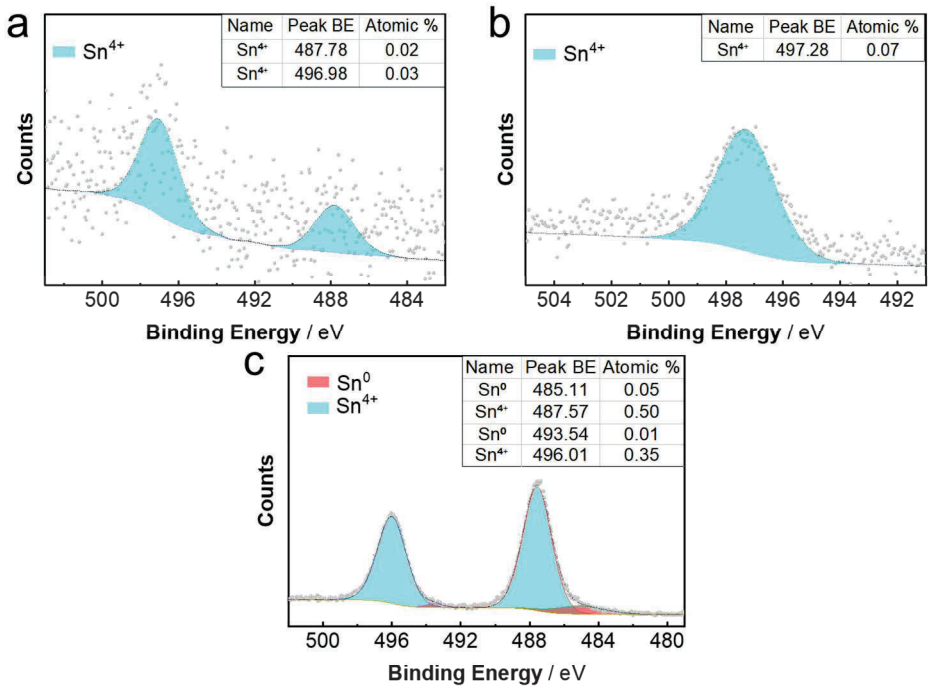

Figure S5. High-resolution XPS spectra of Sn 3d for (a) SnC1, (b) SnC2, and (c) SnC3.

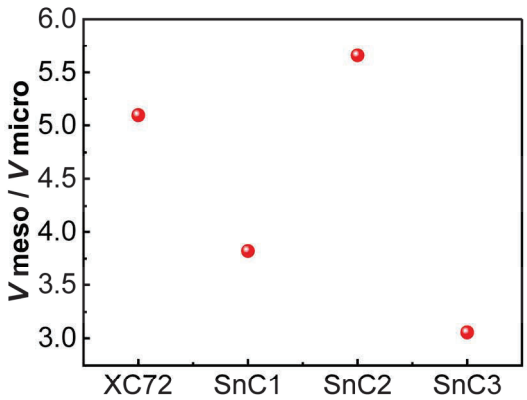

Figure S6. Mesopores-to-micropores volume ratio for XC72, SnC1, SnC2, and SnC3.

ChemSusChem

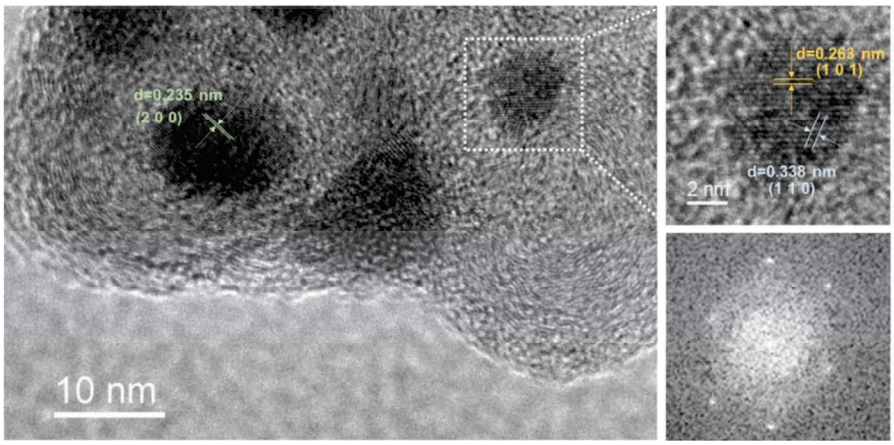

Figure S7. HRTEM analysis of SnC2 sample.

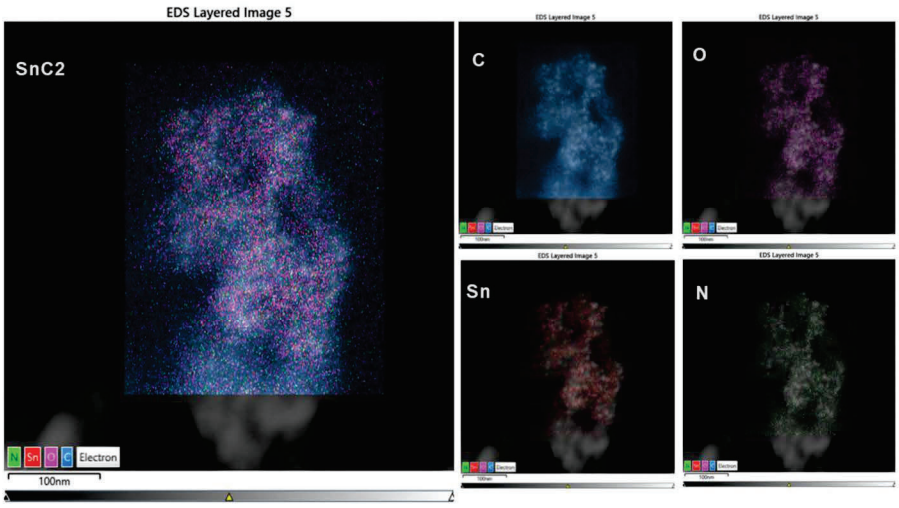

Figure S8. Site of interest along with EDS elemental mapping showing the distribution of C, O, N and Sn for the SnC2 sample.

ChemSusChem

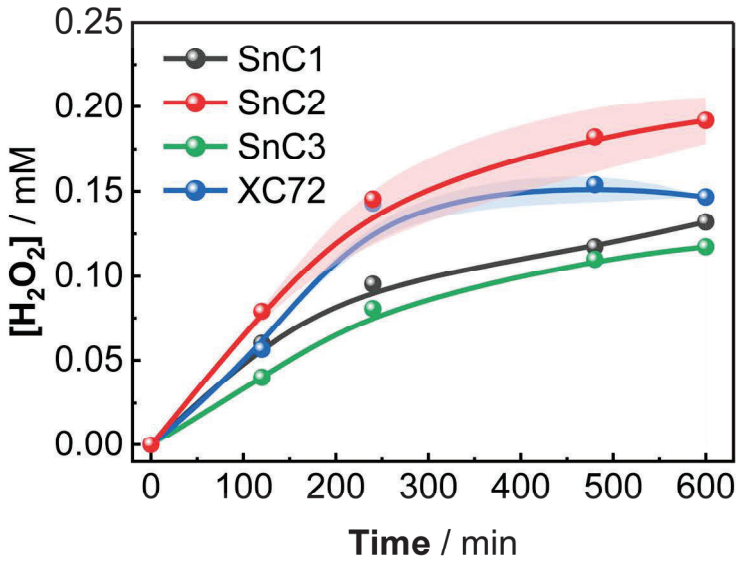

Figure S9. H_2O_2 concentration accumulated in an undivided 3-electrode cell over the electrolysis time. The working electrode was a glassy carbon RDE modified with each electrocatalyst (loading of 0.5 mg cm^{-2}): S_{disk} = 0.196 cm^2 (*d* = 5 mm), E_{disk} = -0.25 V *vs.* RHE. O_2 was continuously supplied to ensure saturation of the 30 mL of 0.1 M Na_2SO_4 electrolyte at natural pH 5.9. Pt and Ag|AgCl (3 M KCl) were used as CE and RE, respectively.

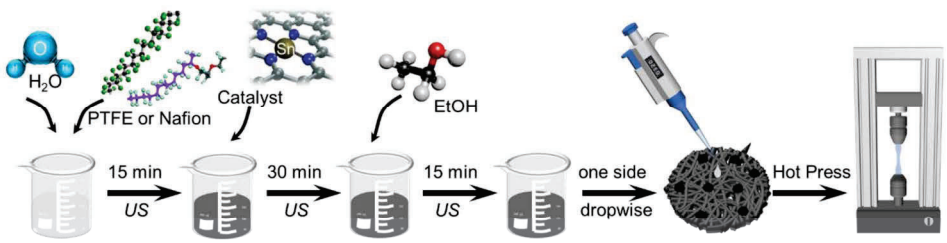

Figure S10. Scheme of the GDE fabrication using the electrocatalysts, with the final hot pressing step (US means ultrasound).

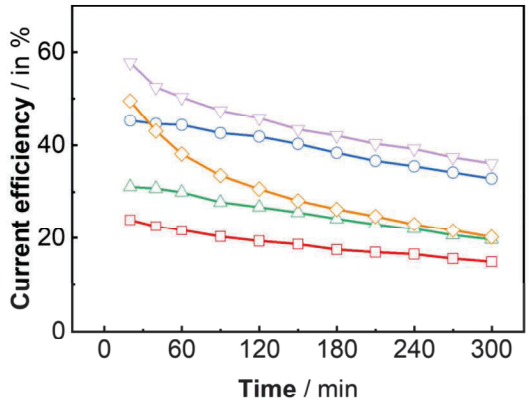

Figure S11. Time course of current efficiency for the H_2O_2 electrogeneration profiles shown in Fig. 7.

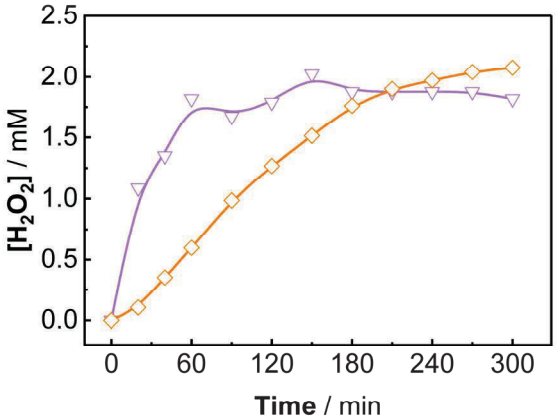

Figure S12. H_2O_2 concentration accumulated in an undivided 2-electrode cell over the electrolysis time. The cathode was a 3-cm^2 GDE fabricated with SnC2 electrocatalyst (loading of 0.5 mg cm^{-2}), fed with compressed air at 0.4 L min^{-1}, and coupled to a 3-cm^2 DSA-Cl_2 plate as the anode, whereas the current density was 10 mA cm^{-2}. Catalyst: (▽) 0.1 g L^{-1} Cu/C was added at natural pH 5.9; (◇) 0.5 mM Fe^{2+} was added at pH 3.

References

[1] A. Zitolo, N. Ranjbar-Sahraie, T. Mineva, J. Li, Q. Jia, S. Stamatin, G. F. Harrington, S. M. Lyth, P. Krtil, S. Mukerjee, E. Fonda, F. Jaouen, *Nat Commun* **2017**, *8*, 957.

4.1.2 Complete antihistamine degradation in wastewater matrix using a metal-free N-doped carbon with superior electrocatalytic performance for in-situ H_2O_2 production

The previous study demonstrated the excellent H_2O_2 electrogeneration performance of metal (Sn)-based electrocatalysts under near-neutral pH conditions; however, metal leaching remains an unavoidable issue after prolonged use. The goal of this second study is to propose an alternative approach, using metal-free, porous carbons, particularly N-doped carbons with heteroatoms like S or O incorporated into the carbon framework, which has been shown promising for the efficient H_2O_2 production with high selectivity, especially under alkaline conditions. Here, melamine —a nitrogen-rich precursor— was thermally treated to synthesize N-doped carbons, enhancing their electrocatalytic performance. GDEs were fabricated from melamine-derived carbon to assess the H_2O_2 generation efficiency and pollutant degradation under EF conditions at different pH values. Additionally, as a unique and remarkable contribution from this work, a radar chart was created to correlate the physicochemical properties of the carbons with the electrocatalytic performance (H_2O_2 selectivity and activity), providing insights into optimizing these materials for EF applications.

Electrochemical tests were performed on four synthesized catalysts with different melamine/Vulcan carbon ratios; the mass of melamine employed was 50 wt.% (sample denoted as M1), 71.4 wt.% (M2.5), and 83.3 wt.% (M5), whereas pure g-C_3N_4 was derived upon pyrolysis of melamine alone. Additionally, the commercial Vulcan carbon was denoted as XC72. The CV analysis of the five electrocatalysts in O_2-saturated electrolyte (pH 5.9) allowed distinguishing between two different groups of materials. XC72, M1, and M2.5 showed more positive ORR peak potentials and higher peak currents, accounting for an enhanced ORR kinetics, with M2.5 displaying the highest ORR catalytic activity. In contrast, an excess of melamine in M5 and g-C_3N_4 led to negative reduction potential and lower currents, reducing the ORR efficiency. Further LSV analysis with RRDE showed that XC72, M1, and M2.5 had similar E_{onset} values, but M1 and M2.5 demonstrated superior H_2O_2 selectivity and electron transfer numbers close to 2. Among them, M2.5 achieved a remarkable H_2O_2 yield of 95.3%. Tafel plot analysis supported these findings, with M2.5 maintaining an excellent ORR

kinetics, evidenced by a low Tafel slope (8.9 mV dec^{-1}) similar to XC72 while achieving superior $2e^-$ ORR selectivity due to effective N-doping. This doping enhanced the electron transfer and stabilized the active sites, boosting the catalytic efficiency.

The physicochemical properties of the five catalysts were analyzed to understand their electrocatalytic performance in H_2O_2 production. Elemental analysis showed a steady increase in nitrogen content at higher melamine ratios, reaching up to 54.8 wt.%. M1 and M2.5 showed lower N incorporation (34% and 48%), while M5 and g-C_3N_4 exceeded 50%, accompanied by a marked decrease in carbon content. Sulfur content decreased with increased melamine, likely due to carbon oxidation and SO_x formation. The N/C ratio increased from M1 to g-C_3N_4, with M2.5 having the most effective N doping for catalytic activity, while in M5 and g-C_3N_4, nitrogen mainly served as a structural element, reducing electrocatalytic efficiency. Elemental analysis confirmed that N-doping is essential for enhancing ORR performance, with XPS spectra revealing C, O, and N peaks. The N 1s spectra identified five nitrogen types: pyridinic, C=N, pyrrolic, graphitic, and oxidized N. Pyridinic N, associated with H_2O_2 decomposition, was lower in M2.5, while pyrrolic N, beneficial for H_2O_2 retention, was higher. This favorable N composition in M2.5 enhanced its $2e^-$ ORR selectivity. Excessive pyrrolic N in M5, however, impacted catalyst stability, while g-C_3N_4 showed C=N predominance, which correlated with lower ORR activity. Thus, the well balanced N functionalities of M2.5 promoted the efficient and selective H_2O_2 electrogeneration. FT-IR analysis revealed rich surface functional groups in g-C_3N_4, with characteristic peaks indicating high N and O content, such as N-H and O-H stretching (3100-3500 cm^{-1}), C≡N (2362 cm^{-1}), and C=N (1600-1650 cm^{-1}) bonds. M1, M2.5, and M5 shared structural features with g-C_3N_4, showing increasing peak intensities at higher melamine content, consistent with elemental analysis. XC72, as a pure carbon black, displayed few surface groups. Peaks near 808 cm^{-1} in g-C_3N_4 and M5 indicated heptazine ring formation, confirming graphitic carbon nitride. As found for Sn-doped carbons in Section 4.1.1, the C≡N peak, present in all samples except XC72, aids H^+ adsorption, which accelerates the H_2O_2 production. XRD patterns of the samples showed that XC72 exhibited characteristic graphite peaks at 24.7° and 43.4° (002 and 101 planes). For g-C_3N_4,

additional peaks at 13.1° and 27.4° corresponded to aromatic stacking in the 100 and 002 planes, indicative of C_3N_4 structure. As the melamine content increased from XC72 to g-C_3N_4, the 24.7° peak shifted to a higher angle, the 13.1° peak intensity rose, and the 43.4° peak decreased, reflecting the transformation from graphitic carbon to carbonitride. This combination of amorphous carbon black and layered g-C_3N_4 likely creates a conductive, active composite, enhancing the ORR rate and selectivity. In the Raman spectra for XC72, M1, and M2.5 (M5 and g-C_3N_4 were excluded due to fluorescence issues), minor variations in the D1/G intensity ratio suggested a slight increase in graphitization. Amorphous carbon content (D3) averaged 8-9%, with minimal variation. The R2 parameter remained above 0.5, indicating low structural organization. Overall, Raman results showed similar graphitization degrees among XC72, M1, and M2.5, although Raman was limited in detecting carbon nitride components. Isotherm profiles showed that increasing the melamine content reduced the overall porosity, with carbon nitride displaying minimal micropore adsorption and XC72 showing some due to its micro- and mesoporous structure. g-C_3N_4, largely non-porous, lacked a hysteresis loop, unlike XC72. Micropores at ~1 nm were consistent across samples, with the rise in melamine causing pore occlusion rather than dimensional changes. This trend supports the formation of a Vulcan/carbon nitride composite in highly N-doped samples (above 71.4 wt.% melamine) rather than pure N-doped carbon. A high specific surface area enhances reagent contact with active sites, promoting the ORR, while pore distribution determines the reaction pathway ($2e^-$ or $4e^-$). Literature suggests that micropores support the H_2O_2 production, and mesopores facilitate its release. Upon increase in the melamine content, the mesopore volume ratio rises despite the overall mesopore content decline, enhancing the role of mesoporosity in carbon nitride-rich samples. Sample M2.5, with a BET surface area of 81 $m^2\ g^{-1}$ and a 92.6% mesopore volume ratio, showed an optimal balance for H_2O_2 generation without prolonged residence that could lead to decomposition. HRTEM images illustrated the morphology: g-C_3N_4 shows smooth, layered nanosheets, largely amorphous. Upon addition of XC72, M2.5 developed ordered 002 lattice fringes, suggesting XC72 induces crystallinity in the g-C_3N_4 matrix, enhancing layer alignment. The EDX mapping results of M2.5 confirmed a uniform C, N, and O distribution with minor S, consistent with

elemental analysis.

Based on all these results, M2.5 emerged as the most effective $2e^-$ ORR electrocatalyst, achieving an efficient H_2O_2 electrosynthesis through a synergistic balance of key factors. As main finding of this work, a radar chart analysis correlated its physicochemical and electrocatalytic properties, positioning M2.5 as the top performer in nearly all parameters. M2.5 was thus selected for further electrolytic trials with GDEs.

To support sustainable advanced wastewater treatment via continuous H_2O_2 production, GDEs with different M2.5 catalyst loadings were evaluated. At 0.1 mg cm^{-2}, the GDE achieved an impressive H_2O_2 concentration of 34.8 mM over 5 h at pH 5.9 and 33.3 mA cm^{-2}, outperforming commercial and other purpose-made GDEs. Higher loadings (0.5–2.5 mg cm^{-2}) resulted in decreased H_2O_2 production due to gas-diffusion channel blockage, although 2.5 mg cm^{-2} unexpectedly recovered optimal H_2O_2 output by increasing the number of active sites. Excessive loading, however, caused production decline due to thicker layers hindering diffusion.

The study further validated the GDE suitability for pollutant degradation. With Fe^{2+} (EF) or Cu/C (HEF, see section 4.2.1 below) catalysts, in-situ H_2O_2 activation confirmed the $^{\bullet}OH$ formation. EF at pH 3 enabled a rapid 100% degradation of DPH within 30 min, whereas HEF at pH 5.9 also achieved complete degradation at 120 min, demonstrating the effective pollutant removal at near-neutral pH. These results underscore the great adaptability and efficiency of the melamine-based GDEs across varying conditions in advanced water treatment.

Separation and Purification Technology 361 (2025) 131590

Contents lists available at ScienceDirect

Separation and Purification Technology

journal homepage: www.elsevier.com/locate/seppur

Complete antihistamine degradation in wastewater matrix using a metal-free N-doped carbon with superior electrocatalytic performance for in-situ H_2O_2 production☆

Lele Zhao [a], Marco Mazzucato [b], Sonia Lanzalaco [c], Mattia Parnigotto [b], Pere L. Cabot [a], Christian Durante [b,*], Ignasi Sirés [a,*]

[a] Laboratori d'Electroquímica dels Materials i del Medi Ambient, Departament de Ciència de Materials i Química Física, Secció de Química Física, Facultat de Química, Universitat de Barcelona, Martí i Franquès 1-11, 08028 Barcelona, Spain
[b] Department of Chemical Sciences, University of Padua, Via Marzolo 1, 35131 Padova, Italy
[c] Departament d'Enginyeria Química, EEBE, Universitat Politècnica de Catalunya, C/ Eduard Maristany, 10–14, Ed. I2, 08019 Barcelona, Spain

ARTICLE INFO

Editor: B. Van der Bruggen

Keywords:
Electro-Fenton process
Hydrogen peroxide electrosynthesis
Oxygen reduction reaction
Pharmaceutical pollutant
Radar chart

ABSTRACT

A new gas-diffusion electrode (GDE) has been developed and optimized to apply the heterogeneous electro-Fenton (EF) process to the degradation of the antihistamine diphenhydramine. The complete removal of this hazardous drug pollutant was achieved within only 120 min in actual urban wastewater at pH 5.9. Nitrogen-doped carbon electrocatalysts were first synthesized by direct pyrolysis of blends of commercial Vulcan carbon and melamine as nitrogen dopant. A radar chart was proposed to correlate the tested physicochemical and electrochemical properties. A well-balanced surface area, mesopores volume and defective carbon content were critical to ensure the highest activity (E_{onset} = 0.38 V *vs.* RHE) and selectivity ($n \sim 2$, $y_{H2O2} \sim 95.3$ %) for two-electron oxygen reduction reaction (ORR), which allowed the efficient in-situ production of H_2O_2 as $^{\bullet}OH$ precursor. N-doping (10.5 wt%), along with the presence of pyrrolic N (3.5 %), are also key factors to explain the enhancement. GDEs fabricated with the optimal electrocatalyst (71.4 wt% melamine content) were capable of accumulating up to ~35 mM H_2O_2 within 5 h, outperforming the commercial GDEs. This work evidences the interplay of physicochemical and electrocatalytic parameters in H_2O_2-based advanced water treatment, demonstrating that it is possible to envisage a more efficient and greener tertiary wastewater treatment.

1. Introduction

The electro-Fenton (EF) process is prominent among the electrochemical advanced oxidation processes (EAOPs) to achieve rapid wastewater decontamination, primarily because of its ability for in-situ cathodic production of H_2O_2 and its immediate activation to hydroxyl radicals ($^{\bullet}OH$) [1,2]. It has been proven that these radicals are extremely effective in degrading persistent pharmaceutical residues in model aqueous solutions [2], and even in actual wastewater [3,4]. Diphenhydramine (DPH) is one of the most widespread, longest-used antihistamine drugs [5], thus occurring in drinking water within the μg L^{-1} range [6]. Although the removal of DPH from water has been attempted by photodegradation [7,8], adsorption [9], photo-Fenton [10], and electro-oxidation (EO) [11], results are unsatisfactory and hence, EF emerges as an unexplored and promising route.

H_2O_2 has become an industrial commodity due to its increased usage in various applications [12]. The electrochemical oxygen reduction reaction (ORR) provides a simple and cost-effective green approach to the cathodic synthesis of this chemical under mild conditions [12,13]. This method offers remarkable advantages, such as decentralized production and lower environmental impact than the conventional anthraquinone auto-oxidation process [3,4,14,15]. Nonetheless, the ORR in acidic media may follow a two- or four-electron pathway (reaction (1) and (2)), with the latter being thermodynamically favored [16]. Consequently, the simultaneous achievement of high activity and selectivity for the $2e^-$ ORR, which is crucial for viable H_2O_2 electrogeneration, remains a challenge.

☆ This article is part of a special issue entitled: 'Sustain energy & environ' published in Separation and Purification Technology.

* Corresponding authors.
E-mail addresses: christian.durante@unipd.it (C. Durante), i.sires@ub.edu (I. Sirés).

https://doi.org/10.1016/j.seppur.2025.131590
Received 19 November 2024; Received in revised form 28 December 2024; Accepted 10 January 2025
Available online 11 January 2025
1383-5866/© 2025 Elsevier B.V. All rights are reserved, including those for text and data mining, AI training, and similar technologies.

$$O_2 + 2H^+ + 2e^- \leftrightarrows H_2O_2 \ (E^0 = 0.695 \text{ V } vs. \text{ SHE}) \quad (1)$$

$$O_2 + 4H^+ + 4e^- \leftrightarrows 2H_2O \ (E^0 = 1.229 \text{ V } vs. \text{ SHE}) \quad (2)$$

In recent years, efforts to develop efficient cathodic systems for 2e⁻ ORR have brought about various types of high-performance electrocatalysts. Carbon-supported metal catalysts, particularly those based on iron [17] and cobalt [18–20], have significantly boosted the H_2O_2 concentration. However, transition metal-based catalysts tend to suffer from metal leaching and degradation in acidic environments, as well as passivation in alkaline conditions, which limits their long-term stability and effectiveness [21]. Noble metal (Pd, Au) nanoparticles also behave satisfactorily, showing excellent H_2O_2 selectivity and resistance to corrosion and fouling [22], but such expensive materials pose serious limitations to scalability [23].

In contrast, metal-free carbons have garnered significant attention due to their lower cost, abundance, and tunable surface properties. Carbon-based electrocatalysts with micro/mesoporous structures have demonstrated excellent performance under alkaline conditions, achieving onset potentials (E_{onset}) close to the thermodynamic value (0.7 V *vs.* RHE) and H_2O_2 selectivity exceeding 70 % [24]. A higher porosity tends to be preferred because it enhances the accessibility of O_2 gas to active sites; moreover, the presence of mesopores restricts the accumulation of the generated H_2O_2 near the cathode surface, thus minimizing its destruction [25–27]. Additionally, the incorporation of heteroatoms such as N, O, and S in the carbonaceous backbone has been shown favorable to modulate the electronic properties, eventually reducing the energy requirements for the 2e⁻ ORR [28]. S-doped carbons have an increased charge density at active sites, whereas O-doping provides additional reactive sites, thereby boosting the ORR performance [29,30]. Among the various doping strategies, N-doping has been most extensively studied due to its positive effects, such as the reduced 2e⁻ ORR overpotential [31]. More specifically, the presence of different N functionalities can selectively shift the ORR toward the 2e⁻ route. Pyrrolic and graphitic N have been identified as the most crucial active sites for the selective O_2-to-H_2O_2 conversion [32], existing a linear relationship between the content of pyrrolic N and the H_2O_2 yield in some carbons [33]. Conversely, pyridinic N, while typically facilitating the H_2O_2 reduction to water, may also play a positive role depending on its protonation state [34]. The non-hybrid lone-pair electrons of pyridinic N can induce electron transfer from π orbitals to antibonding orbitals, weakening the O-O bond of the key OOH* intermediate to finally cause dissociation to water, in contrast to the enhanced electron distribution in pyrrolic N [35].

Melamine is a commonly used raw material with high nitrogen content, which easily undergoes polycondensation upon heating, thus giving rise to graphitic carbon nitrides [36]. It has been employed as a source of N-containing catalysts in distinct fields such as fuel cells, mainly to favor the 4e- ORR in the presence of supported metals [37]. Some catalysts synthesized using melamine and $FeCl_3$ (i.e., hole activator) exhibited considerable CO_2RR activity [38]. In contrast, there are few reports on the use of melamine for EF application. Zhu et al. [39] prepared a cathode by heating commercial melamine foam at 900 °C, and the accumulated H_2O_2 concentration was about 87 μM for 1 h at a current density (j) of 1 mA cm^{-2}. Su et al. [40] doped graphene with melamine, and then prepared a modified carbon mat as cathode, attaining a production rate of 8.6 mg h^{-1} cm^{-2}. Despite the publication of these examples on the feasibility of in-situ H_2O_2 electrogeneration, further enhancement is yet to be achieved with cathodes fabricated with melamine-derived N-doped carbons. In particular, the gas-diffusion electrodes (GDEs) enable the electrocatalytic materials to come into close contact with both electrolyte and O_2 gas simultaneously, thus allowing for the most efficient H_2O_2 production [3,14,41] and long-term stability [14,15]. As far as we are concerned, there are no reports about the fabrication of GDEs with melamine-derived carbon and their application in EF treatment.

In this study, commercial melamine and Vulcan XC72 have been employed as raw materials to improve the electrocatalytic properties of both of them by synthesizing N-doped carbons through thermal treatment. Their features were investigated prior to optimizing the fabrication of GDEs by drop-cast on carbon cloth. The GDEs were utilized to degrade DPH as a model pollutant by the EF process in acidic and near-neutral pH. Worth highlighting, one of the goals of this study was to draw a radar chart showing the correlation between the physicochemical properties of the tested carbons and their inherent electrocatalytic performance (i.e., activity and H_2O_2 selectivity).

2. Materials and methods

2.1. Chemicals

Reagent grade Vulcan XC72 carbon black (Fuel Cell Store) and melamine (Sigma-Aldrich, 99 %) were used in the synthesis of carbons. Nafion (Sigma-Aldrich, 5 wt% in a mixture of lower aliphatic alcohols and water, 45 % water content) and 2-propanol dry (PanReac AppliChem, max. 0.01 % water) were employed for ink preparation. For the measurement of the H_2O_2 concentration, Ti(IV) oxysulfate (Sigma-Aldrich, ≥29 %) was used. DPH hydrochloride (Merck, ≥98 %), sodium sulfate (Sigma-Aldrich, 99 %), sulfuric acid (PanReac AppliChem, 96 %), and sodium hydroxide pellets (Scharlau, extrapure, Ph Eur) were employed in degradation experiments. The catalysts employed for Fenton-based degradation of DPH were a Cu/C powder, synthesized by us through pyrolysis of a Cu-based MOF, and soluble Fe^{2+} from $FeSO_4 \cdot 7H_2O$ (J.T. Baker, > 98 %). Diamond paste (¼ μm) and self-adhesive polishing cloths (satin woven natural silk), both from Struers, were needed to clean and polish the glassy carbon electrodes. Alpha Gaz N_2, O_2, and Ar gases were acquired from Air Liquid (highest available purity > 99.99 %). The mobile phase was prepared by mixing formic acid (Fisher Chemical, Optima LC/MS) and acetonitrile (PanReac Applichem, Reag. Ph. Eur. for UHPLC Supergradient, ACS). No purification was required before using all the reagents. The aqueous solutions were prepared with Milli-Q water with a resistivity greater than 18.2 MΩ cm (Synergy UV device from Merck Life Science).

2.2. Synthesis of electrocatalysts

Melamine-derived N-doped carbons were synthesized using a direct pyrolysis method (Fig. 1). Briefly, a certain amount of melamine and 0.5 g of Vulcan XC72 carbon were weighed and then mixed uniformly by grinding on an agate mortar. Each resulting mixture was treated thermally at 600 °C for 2 h under N_2 atmosphere, finally obtaining the electrocatalyst to be studied. The masses of melamine employed were 0.5 (50 wt%), 1.25 (71.4 wt%), and 2.5 g (83.3 wt%), giving rise to samples labeled as M1, M2.5, and M5, respectively. Pure g-C_3N_4 was derived upon pyrolysis of melamine alone (100 wt%).

2.3. Protocol to manufacture the GDEs

Several GDEs were manufactured via hotpress method, employing different loadings of the optimal electrocatalyst (Fig. S1). PTFE, which served as the binder, was mixed with 1 mL of Milli-Q water and sonicated. Subsequently, a specific amount of electrocatalyst was added and dispersed ultrasonically for 30 min. Next, 4 mL of 2-propanol was added to this dispersion, keeping it under sonication for 10 min to produce the final ink. On the other hand, a squared waterproof carbon cloth coupon from FuelCell Store (area of ~9 cm^2) was prepared as the gas-diffusion layer. The piece was ultrasonicated using ethanol for 30 min, and thoroughly dried at 80 °C. The abovementioned ink was loaded dropwise onto the side of the carbon cloth using a micropipette, approximately transferring 0.4 mL of ink each time. The carbon cloth was placed on a heated platform at 80 °C to ensure complete drying after preparing each layer, until finishing the total ink volume. Subsequently, the catalyzed carbon cloth was dried, then wrapped in multiple layers of

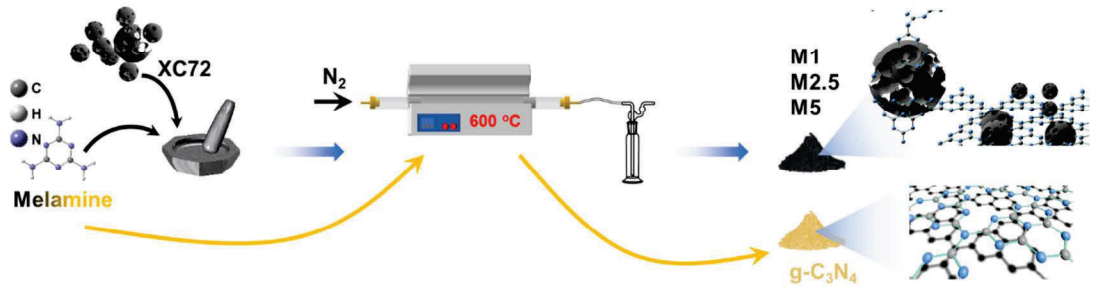

Fig. 1. Scheme of the synthesis procedure followed to obtain four electrocatalysts with different melamine/XC72 mass ratios: 1:1 (M1), 2.5:1 (M2.5), 5:1 (M5), and 100 % melamine (g-C_3N_4).

aluminum foil, and finally placed for 2 h inside a press set to a pressure of 6 ton and 210 °C. The final GDEs were obtained after cooling down to ambient temperature, followed by cutting them into circles with an area of 3 cm^2 to carry out the electrolytic trials.

2.4. Physicochemical characterization

Various methods were employed to examine the morphological, structural, textural, and chemical characteristics of the synthesized materials. Elemental analysis (EA) was carried out using a Thermo Scientific Flash 2000 analyzer. The X-ray diffraction (XRD) patterns were obtained using a Bruker AXS D8 ADVANCE Plus diffractometer, utilizing a Cu source ($\lambda_{K\alpha 1} = 1.5406$ Å) from 10 to 85° (2θ) with a 0.026° step on a Si zero-background sample holder. The X-ray photoelectron microscopy (XPS) analysis was carried out on a SPECS device equipped with a high-intensity twin anode X-ray source XR50 and using a Phoibos 150 MCD-9 XP detector (2400 V) and a Large Area analyzer lens (1.5 kV). The scan mode was Fixed Analyzer Transmission, whereas the excitation energy was 1486.61 eV. C 1 s peak, with a binding energy of 284.8 eV, was used as the internal reference. The spectral analysis was done with the Avantage Software. The Brunauer-Emmett-Teller (BET) method served to determine the specific surface area, with N_2 as the adsorbate gas. The equipment for this was a Micromeritics TriStar 3000 surface area analyzer operated within the range of $0 < P/P_0 < 1$. The samples were outgassed under vacuum at 40 °C for 4 h. High-resolution transmission electron microscopy (HRTEM) was employed to evaluate the sample morphology. For this purpose, a JEM-2100 (LaB6) microscope from JEOL was operated at 200 kV in STEM mode with a dark-field detector, being coupled to an Oxford Inca energy-dispersive X-ray spectrometer (EDS). The HRTEM images were analyzed by means of the Digital Micrograph software, while elemental mapping was feasible thanks to the Inca Microanalysis Suite version 4.09 software. Fourier transform infrared spectroscopy (FT-IR) was performed using a Thermo Scientific Nicolet 6700 equipped with a Smart Orbit Diamond. OMNIC software was run in the wavenumber range from 4000 to 500 cm^{-1}. A LabRAM HR Horiba Jobin Yvon (operated in the range 330–1993 cm^{-1} and equipped with a 532 nm laser as the photoexcitation source) was needed for Raman analysis. Curve fitting of the resulting spectra was done using the pseudo-Voigt function.

2.5. Electrochemical characterization

The voltammetric analysis of each sample was carried out by conducting linear sweep voltammetries (LSV) with an Autolab 101 N potentiostat, employing a Metrohm rotating ring-disk electrode (RRDE, composed of a glassy carbon –GC- disk of $\varnothing = 5$ mm and a Pt ring). All measurements were performed in a jacketed three-electrode cell filled with Ar-purged or O_2-saturated 0.1 M Na_2SO_4 solutions kept at 25 °C. The RRDE GC disk, a graphite rod, and Ag|AgCl (3 M KCl) served as the working, counter, and reference electrodes (WE, CE, and RE, respectively).

The RRDE GC disk must be cleaned prior to each use. For this, diamond plaster was applied to the GC disk, which was then placed perpendicularly to the polishing cloth; subsequently, the axis of the RRDE was rotated clockwise for 100 cycles, followed by the tip immersion into acetone to undergo ultrasonication for 5 min. The same was repeated using 2-propanol, and the disk was finally left to dry naturally.

In order to load a given electrocatalyst onto the GC disk, 5 mg of the powder was weighed, followed by the sequential addition of 100 μL of 2-propanol, 500 μL of Milli-Q water, and 30 μL of Nafion. A water bath sonicator at a controlled temperature was employed to ensure the powder dispersion. The ink loading onto the GC disk was determined to be 0.6 mg cm^{-2}.

Once loaded onto the RRDE and before starting with its electrochemical characterization, the electrocatalyst was initially activated by repeatedly recording cyclic voltammograms (CV) in the above-mentioned Ar-purged electrolyte. This was done at 10, 50, and 100 mV s^{-1} until a stable signal was observed. In the ORR tests, O_2 was sparged into the electrolyte for at least 30 min. The electron transfer number (n) was determined by LSV, according to Eq. (3).

$$n = \frac{4\,|I_D|}{|I_D| + |I_R|/N} \tag{3}$$

where I_D is the current recorded at the disk, I_R is the current recorded at the ring, and N is the collection efficiency or factor. The latter was calibrated using the LSV curves obtained at different rotation rates (400–2500 rpm) in 1 M KCl + 10 mM $K_3[Fe(CN)_6]$ solution, resulting in a value of N close to 25 % (N = 0.246). Using this value, it is also possible to evaluate the H_2O_2 selectivity (i.e., the percentage of H_2O_2 produced via $2e^-$ ORR) at the working electrode, according to Eq. (4).

$$y_{H_2O_2} = \frac{2|I_R|}{N \times |I_D| + |I_R|} \times 100 \tag{4}$$

2.6. H_2O_2 electrogeneration assays

All the experiments were conducted in an undivided, open cylindrical glass cell with a capacity of 200 mL, featuring a glass jacket for recirculating water at 25 °C. A magnetic stirrer was used to fix the stirring rate. The electrolyte consisted of 150 mL of 0.050 M Na_2SO_4 solution, whose pH was regulated as needed. A double-sided dimensionally stable anode (DSA-Cl_2, consisting of a RuO_2-coated Ti plate) with dimensions of 50 mm × 20 mm × 1 mm, provided by NMT Electrodes, was exposed to the solution by delimiting the active area to 3 cm^2 by using PTFE tape. The cathode was a GDE prepared as explained in section 2.3. The manufactured circular GDE (3 cm^2) was placed inside a purpose-made polypropylene holder that served as the air chamber. A circular Ni-Cr mesh was put in contact with the GDE, and then a silicone gasket was added to ensure that the ensemble was watertight. The

electric contact was made through a Ni-Cr wire, and compressed air was supplied through a glass tube using a KNF LAB air pump. The air flow rate was measured using an air flowmeter from Iberfluid Instruments, S. A. The anode and cathode were directly connected to an Amel 2053 power supply, and a Demestres DM610 BR digital voltmeter served to monitor the cell voltage.

The H_2O_2 electrogeneration assays were performed for 5 h, at different current densities. The tests were made in duplicate for each tested condition. To monitor the H_2O_2 accumulation, an aliquot of 0.25 mL was taken at regular time intervals during the electrolysis, and then immediately added to a mixture of 2.75 mL H_2O + 2 mL Ti(IV). The colorimetric analysis of the yellowish complex formed between Ti(IV) and H_2O_2 was performed on a Unicam UV/Vis spectrophotometer set at λ_{max} = 408 nm.

2.7. DPH degradation assays

The experimental setup was analogous to that described in the previous section, but before starting each assay, DPH was spiked into the electrolyte at a concentration of 14.3 mg L^{-1} (i.e., 10 mg C L^{-1}). The performance of electro-oxidation process was assessed without catalyst addition to the solution, at pH 3 and natural pH 5.9. For the conventional (i.e., homogeneous) EF process, carried out at pH 3, 0.5 mM $FeSO_4{\cdot}7H_2O$ was added as a catalyst. For the heterogeneous EF (i.e., HEF) process, done at natural pH 5.9, 0.1 g L^{-1} Cu/C catalyst was added (Heterogeneous catalyst with good performance in our previous work) [42]. The tests were made in duplicate for each tested condition.

To analyze the electrolyzed samples by high-performance liquid chromatography (HPLC), aliquots of 0.5 mL were withdrawn and thoroughly mixed with the same volume of mobile phase, whereupon the mixtures were filtered using a 0.22 μm syringe filter. The HPLC analysis was performed on a Waters 600 chromatograph, equipped with a Biphenyl (100 Å, 150 × 4.6 mm) column maintained at 35 °C and connected to a photodiode array detector. A distinct peak corresponding to DPH, with a maximum wavelength (λ_{max}) of 220 nm, was observed at a retention time of 3.6 min. The mobile phase, consisting of a 40:60 (*v*/*v*) mixture of organic (acetonitrile) and aqueous (0.1 % formic acid) layers, was recirculated at a flow rate of 1.0 mL min^{-1}.

3. Results and discussion

3.1. ORR performance of N-doped carbon electrocatalysts

The cyclic voltammograms of the five electrocatalysts under study (XC72, M1, M2.5, M5, and g-C_3N_4), recorded in O_2-saturated electrolyte at natural pH 5.9, are compared in Fig. S2. The O_2 reduction peak potential and corresponding peak current of these five samples were 0.33 (−0.12 mA), 0.34 (−0.14 mA), 0.31 (−0.17 mA), 0.23 (−0.07 mA), and 0.04 (−0.04 mA) V *vs.* RHE, respectively. Two distinct groups can then be observed, with XC72, M1, and M2.5 exhibiting a close and markedly more positive peak potential (along with clearly greater peak current values), suggesting a more favored ORR kinetics [43]. Among them, M2.5 had the highest peak current, thus accounting for the highest ORR catalytic activity, implying a higher electron transfer rate [44]. On the other hand, the use of an excess of melamine in the electrocatalyst precursor (>83 % in M5 and g-C_3N_4) was detrimental, giving rise to more negative reduction potentials and much lower peak currents.

Aiming to make a more detailed assessment of the ORR performance of the five catalysts, they were systematically evaluated by LSV with an RRDE, thus collecting the disk and ring currents to determine the electron transfer number and H_2O_2 selectivity. According to the profiles shown in Fig. 2a and b, the characteristic electrochemical parameters are those summarized in Table S1. In good agreement with the peak layout discussed in Fig. S2, the E_{onset} values of XC72, M1, and M2.5 are closely aligned, with values ranging from 0.37 to 0.40 V. In contrast, g-C_3N_4 exhibits the lowest value (0.04 V), whereas M5 has an intermediate E_{onset}, which corroborates the negative influence of an excess of melamine, at least from the point of view of the overpotential needed for the occurrence of the ORR. Worth highlighting, despite the similar E_{onset} of the three best catalysts, their *n* and y_{H2O2} show remarkable differences. Commercial XC72 carbon was clearly outperformed by the two materials prepared in the presence of a suitable amount of melamine, since M1 and M2.5 have *n* values closer to 2 (i.e., 2.33 and 2.09, respectively), and ORR selectivities higher than 80 %, attaining an impressive y_{H2O2} = 95.3 % in the case of M2.5. These substantial variations suggest that factors beyond the inherent electroactivity of the active sites of the carbons must play a crucial role in determining the $2e^-$ ORR pathway. Note also that, although the higher melamine contents (M5 and g-C_3N_4) yielded a lower electroactivity as compared to the other group, the selectivity was improved, especially as compared to XC72 carbon. This confirms the interest in trying to enhance the electrochemical performance of commercial Vulcan carbon black by inducing its N-doping. Based on this analysis, it seems evident that M2.5 is the most promising electrocatalyst for the $2e^-$ ORR, making it particularly effective for H_2O_2 production.

Considering Fig. 2a, the corresponding Tafel plot for the different electrocatalysts is illustrated in Fig. S3. From the perspective of the Tafel slope, which informs about the relationship between the overpotential required for a specific electrode reaction and the reaction rate in terms of flowing current, the ORR activities of the five samples showed obvious differences. Under fixed operation conditions, a lower slope can be usually correlated with an enhanced kinetics (i.e., a better

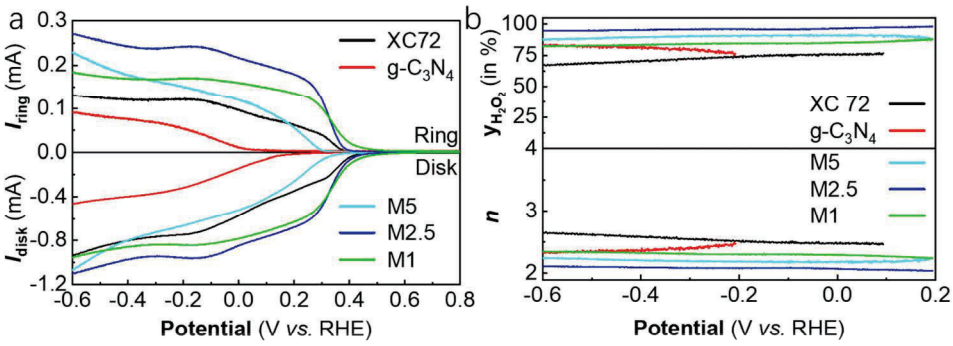

Fig. 2. (a) Linear sweep voltammograms obtained at an RRDE modified with either Vulcan XC72 carbon black, M1, M2.5, M5, or g-C_3N_4. The electrocatalysts were drop-cast on the GC disk (catalyst loading of 0.6 mg cm^{-2}), and voltammograms were recorded in an O_2-saturated 0.1 M Na_2SO_4 electrolyte at natural pH 5.9, at v_{scan} = 10 mV s^{-1}. (b) Top plot: H_2O_2 selectivity; bottom plot: electron transfer number. These two parameters were determined from the data of plot (a) at 1600 rpm, at E_{ring} = 1.54 V *vs.* RHE. A graphite rod and Ag|AgCl (3 M KCl) were used as CE and RE, respectively.

electrocatalytic performance). XC72 had the lowest slope (8.5 mV dec^{-1}), being consistent with the highly positive E_{onset} (which is related to the overpotential to start the ORR), although the value was closely followed by that of M2.5 (8.9 mV dec^{-1}). This means that this specific N-doping allowed preserving the excellent reaction kinetics typical of XC72, while acquiring superior 2e$^-$ ORR performance, evidenced by the low n and high y_{H2O2} of M2.5. This N-doping enhanced the electron transfer and stabilized the active sites, leading to an improved catalytic efficiency. M5 and M1, with greater Tafel slopes of 10.8 and 14.3 mV dec^{-1} respectively, also possessed a good ORR kinetics, although less optimal than M2.5. Conversely, g-C_3N_4, with the highest Tafel slope, was confirmed to be less favorable for H_2O_2 production.

In summary, M2.5 exhibited not only high activity and excellent reaction kinetics but also the greatest H_2O_2 selectivity, which further features its suitability as a very promising electrocatalyst for the 2e$^-$ ORR in the context of in-situ H_2O_2 generation.

3.2. Physicochemical characterization of N-doped carbon electrocatalysts

The four melamine-derived N-doped carbons and the commercial XC72 carbon black were thoroughly analyzed by different techniques, aiming to justify the electrocatalytic performance discussed in section 3.1. The elemental analysis illustrated in Fig. 3a shows an increase of the N content as the proportion of melamine in the precursor rose, growing from 0.8 wt% in M1 to the highest content of 54.8 wt% in g-C_3N_4. However, taking into account that melamine contains 66.7 wt% of N, the efficiency of the N-doping was dissimilar. For M1 and M2.5, the incorporation of N was much below the maximum attainable (around 34 % and 48 %, respectively); in contrast, for M5 and g-C_3N_4, the doping efficiency surpassed 50 %. This tendency can be directly correlated with the evolution of the C content. Close and very high values of 95.9 % and 85.8 % were determined in M1 and M2.5, which drastically decayed for M5 and g-C_3N_4, thus explaining the greater relative impact of N-doping on the product mass. In good agreement with the behavior of the N element, the H content also followed an increasing trend, although distinct for the two groups of samples: 0.1 % and 0.3 % for M1 and M2.5, further growing drastically to 1.1 % and 1.8 % for the other two catalysts. Finally, the S content was always in the low range, but clearly decaying as the melamine proportion was increased. This fact can be related to the concomitant decay in C content, since the reactions that cause the evolution of CO and CO_2 gases are also responsible for the elimination of structural S (present in XC72 carbon, which is manufactured from fossil fuels) in the form of SO_x gases.

Overall, the N/C ratio grew in the order: M1 (0.01) < M2.5 (0.12) < M5 (0.64) < g-C_3N_4 (1.6). Aiming to obtain a well-balanced composition, it is important to consider that carbon is important to ensure good electrical conductivity. C content was the highest in M1 and M2.5, but in M1 the N sites that are expected to modulate the ORR seem too dilute. In contrast, N is present in M2.5 really as a dopant (ca. 10 % as compared to C). The active site density in M5 and g-C_3N_4 is presumably excessive, with N acting as a structural element rather than a dopant, which partly explains their worse electrocatalytic properties discussed above.

Based on the elemental analysis, N-doping is presumed to be one of the key factors to enhance the ORR performance of the synthesized electrocatalysts. Nonetheless, the effect of this dopant on the ORR depends on the type of functionality, as mentioned in the introduction. The fine structure of the prepared materials was unveiled by XPS analysis. In the XPS full spectra of Fig. S4, it can be observed that all the samples have obvious energy peaks near 285 and 532 eV, which are attributed to C and O elements, respectively, according to the Thermo Scientific Avantage data system. The peak appearing near 400 eV can be linked to N element, which can be observed in the curves of samples M2.5, M5, and g-C_3N_4, but it is less obvious in the spectrum of M1 due to its comparatively lower N content, and almost absent in XC72 (Fig. 3a and

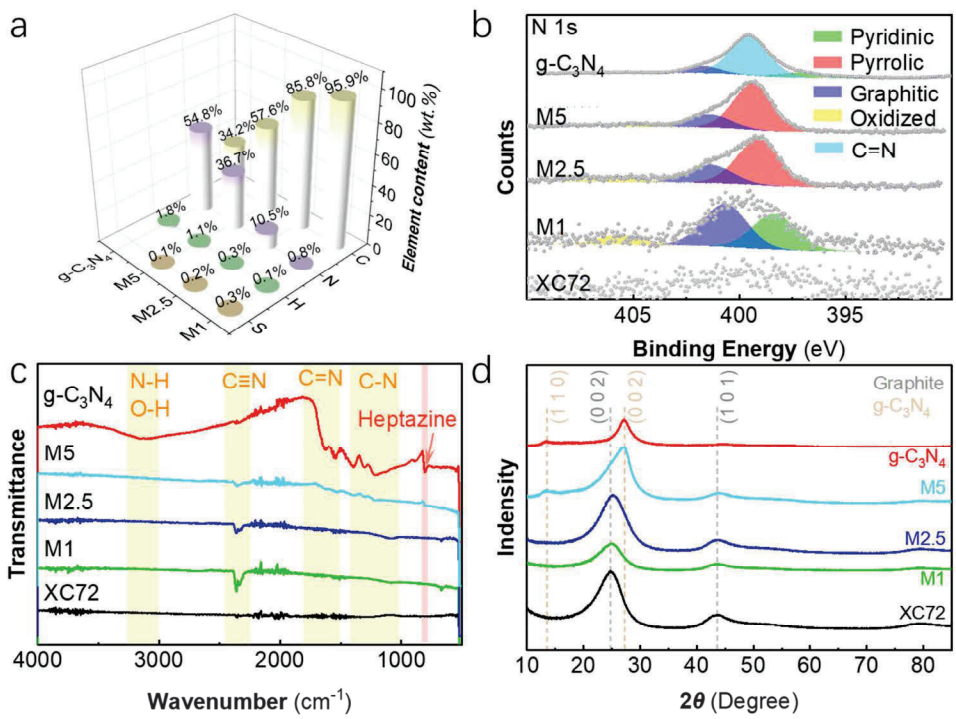

Fig. 3. (a) Composition of the M1, M2.5, M5, and g-C_3N_4 electrocatalysts, found from elemental analysis (C, N, H, S). (b) High-resolution XPS spectra of N 1s for XC72, M1, M2.5, M5, and g-C_3N_4. (c) FT-IR spectra of the same electrocatalysts. (d) Powder X-ray diffractograms of the same electrocatalysts, as compared to reference patterns of graphite and C_3N_4.

Fig. S5). More specifically, the atomic percentages of these three main elements on the surface of the five samples are summarized in Table S2. The trends of C and N elements are in good agreement with those discussed in Fig. 3a (in weight percent), in particular the gradual increase of N content as the melamine proportion in the precursor rose, as well as the moderate content of N in M2.5. Note also that the surface of this sample is the least oxidized among all.

The high-resolution N 1 s XPS spectra of Fig. 3b show the presence of up to five types of N: pyridinic N (397.8–398.3 eV), C=N functionality (398.4–398.7 eV), pyrrolic N (398.9–400.0 eV), graphitic N (400.9–401.7 eV), and oxidized N (402.7–405.4 eV) [33,39,45]. Pyridinic N is usually located on the edge or defective sites of carbon materials, and it is known to be detrimental for $2e^-$ ORR because it promotes the destruction of the key OOH* intermediate [46], and also activates the H_2O_2 decomposition [47]. Conversely, pyrrolic N is located at the edges of the five-member rings, being beneficial to improve the adsorption/retention of OOH* intermediate [35]. A decrease in the ratio of pyrrolic-to-pyridinic N has been shown to deteriorate the $2e^-$ ORR performance [48]. On the other hand, graphitic N is good for promoting electron conduction [49], whereas oxidized N usually has a low impact on ORR catalysis [50], as is also expected for C=N. The specific content of each type of nitrogen in each sample can be found in Fig. S5. In XC72, it was impossible to quantify the N content, owing to its expected low content (Table S2); despite this, it can be speculated that the small XPS signals at 397.8–401.7 eV, although difficult to be reliably deconvoluted, could agree with the presence of some pyridinic and graphitic N. In any case, with such content only in trace amounts and the absence of favorable functionalities, the low H_2O_2 selectivity of XC72 (70.6 %, Table S1) can be readily justified. The same two types of N (pyridinic and graphitic) were well balanced in M1, approaching 1 %, which was accompanied by some oxidized N. Again, the absence of pyrrolic N may have limited the production of H_2O_2, despite the greater y_{H2O2} as compared to XC72 carbon. In contrast, in M2.5, the pyridinic N was replaced by pyrrolic N (3.5 at.%), also showing a moderate amount of graphitic and oxidized N. This composition radically enhanced the $2e^-$ ORR pathway, as discussed above. The moderate amount of graphitic N ensures the stability of the material without over-promoting the $4e^-$ ORR. M5 presents a quite higher pyrrolic N content, without significant variation in the graphitic and oxidized N contents. Therefore, it can be concluded that too much pyrrolic N may cause the instability of the carbon structure, thus disrupting the overall equilibrium of the catalyst. Moreover, it cannot be excluded that part of this signal assigned to pyrrolic N may correspond to C=N functionalities, given the relatively high amount of melamine in the precursor. The replacement of pyrrolic N by C=N groups clearly occurred in g-C_3N_4, as supported by the XPS peak shift to 398.7 eV, along with the presence of characteristic FT-IR bands (see below). Such strong peak has been interpreted as sp^2-polarized nitrogen (i.e., C=N-C) in studies focused on g-C_3N_4 nanosheets [45]. The practical disappearance of pyrrolic N can then be correlated with the worse electrocatalytic results obtained with this material. Based on these findings, the balanced proportion of the different types of N in M2.5 gave rise to an optimum electrocatalytic effect for enhancing the $2e^-$ ORR.

The surface functional groups of the five samples were explored in more detail by FT-IR (Fig. 3c). The spectrum of g-C_3N_4 was the richest among all materials, showing multiple characteristic absorption peaks. For example, the broad absorption peak in the range of 3100–3500 cm^{-1} is attributed to the stretching vibrations of the N-H and O-H bonds (note the high N and O surface content of this sample in Table S2). These can be explained by the residual unpolymerized amino groups (on carbon nitride sheet edges), alongside physisorbed water molecules [51]. The peak located at 2362 cm^{-1} may account for the presence of the C≡N bond, whereas the peak at 1600–1650 cm^{-1} corresponds to the stretching vibration of the C=N bond. Finally, the peaks in the range of 1200–1400 cm^{-1} are mainly attributed to the vibrations of the C-N bond. These features agree with the presence of abundant N-containing groups in g-C_3N_4. The spectra of the M1, M2.5, and M5 samples show some similarity as compared to g-C_3N_4, suggesting that during the blending of the carbon black with the aminated chemical, some structural features of g-C_3N_4 were introduced. In general, the intensity of these characteristic peaks gradually increased as the melamine content was risen, from M1 to M5, being consistent with the results of elemental analysis. The FT-IR spectrum of XC72, as a pure carbon black, is relatively simple and lacks obvious characteristic absorption peaks, which reflects the existence of fewer surface functional groups. Further analysis shows that the characteristic peaks appearing near 808 cm^{-1} for samples g-C_3N_4 and M5 correspond to the out-of-plane bending vibrational modes of the heptazine ring, which proves the formation of graphitic carbonitride [52], thereby confirming the observations done in Fig. 3b about the C=N peak. Worth highlighting, the peak attributed to C≡N vibration in all samples except XC72, is a feature that is related to the promotion of H^+ adsorption, a phenomenon that synergistically accelerates the production of H_2O_2 [53].

Fig. 3d shows the XRD patterns of the five samples. XC72 only shows two characteristic peaks, at 24.7° and 43.4°, which can be readily attributed to the 002 and 101 diffraction peaks of graphite, respectively [54]. On the other hand, the characteristic peaks at 13.1° and 27.4° are interlayer stacking peaks specific to aromatic systems, corresponding to 100 and 002 planes of C_3N_4, respectively; these two diffraction peaks match well with those appearing in sample g-C_3N_4 [55]. The diffraction peak at 24.7° was progressively shifted to a greater angle as the melamine content has risen from pure XC72 to g-C_3N_4 and, simultaneously, the intensity of the peak at 13.1° grew and that of the peak at 43.4° decayed. This is in good agreement with the transformation of the pure graphitic network into a planar carbonitride as the N content was increased. The combination of the amorphous structure of carbon black with the layered structure of g-C_3N_4 may form a composite material with both, high conductivity and rich active sites, ideal to simultaneously improve the ORR rate and selectivity.

Raman analysis was then employed to gain information on the graphitization degree (sp^2 *vs.* sp^3 configuration) and crystallite dimensions. Carbon black is generally categorized as nanocrystalline graphite with a certain amount of amorphous carbon. To fully interpret the spectra of disordered carbons, in the region between 900 and 1800 cm^{-1}, 4 or 5 bands are needed [56]. For the materials studied in this work, the most common 4 bands were sufficient: D1 and D4, linked with disordered graphitic lattice; D3 related to amorphous carbon; and G, linked to an ideal graphite lattice. The position of the G band and the D1-to-G intensity ratio are linked with the properties of the material, as described by Ferrari [57]. Fig. 4a compares the Raman profiles of XC72, M1, and M2.5, whereas M5 and g-C_3N_4 are not shown due to fluorescence problems at 532 nm and even at 785 nm. For comparison, the spectra were normalized considering the G band around 1590 cm^{-1}, a very characteristic feature of carbon blacks. Only small variations can be observed; in particular, a slight but noticeable diminution of the D1/G intensity ratio (with a value around 1 for carbon blacks), which could be associated with a slight increase in graphitization. This is more evident from the deconvoluted spectra (Fig. 4b–d) and, more specifically, the related quantitative information (Table 1). Indeed high temperatures applied in synthesis by pyrolysis are known to promote graphitization and, at the same time, the precursor decomposition may cause the etching of defective carbon, thereby increasing the amount of crystalline carbon [58,59]. The band of amorphous carbon (D3) averaged around 8–9 % of the total signal, showing neither appreciable variation nor a clear trend. In addition, there was a slight decrease in the R2 parameter, but it always was above 0.5, meaning that these are poorly organized structures [60]. Additionally, one can argue that since carbon nitride is not detectable at 532 nm, the observed signal is only linked to doped or undoped carbon black (XC72), used as support, which does not appear to be substantially affected by the conditions of synthesis. This means that, in this particular case, Raman spectroscopy is not fully able to describe the carbonaceous structure properties of the prepared catalysts;

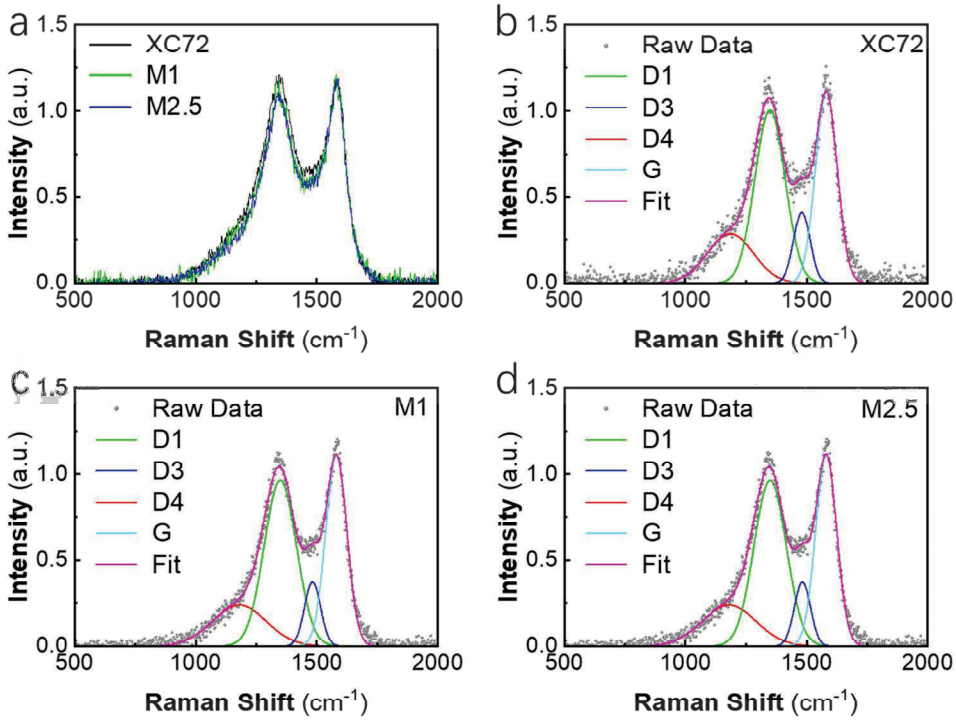

Fig. 4. (a) Comparison between Raman spectra of XC72, M1, and M2.5 samples, and (b-d) their respective deconvolution.

Table 1
Data obtained from the deconvolution of Raman spectra of XC72, M1, and M2.5 samples (see Fig. 4a–b).

	D1 (cm^{-1})	I_{D1} –	G (cm^{-1})	I_G –	I_{D1}/I_G –	R2 –	A_{D3}/A_{tot} (in %)
XC72	1351	1.06	1581	1.12	0.95	0.59	8.2
M1	1349	1.01	1581	1.11	0.91	0.56	9.2
M2.5	1349	0.96	1581	1.11	0.87	0.57	8.2

$R2 = A_{D1} / (A_{D1} + A_G)$.

however, for a relatively low level of N-doping, it is still possible to conclude that XC72, M1, and M2.5 had a very similar graphitization degree.

The specific surface area of the same samples was determined by BET analysis, and the data were fitted using the quenched solid density functional theory (QSDFT) model, which was proven to be more accurate than NLDFT, even if limited to a pore dimension of 40 nm [61–63]. The model takes into account the surface roughness and chemical heterogeneity, thus leading to a better fit of experimental data, in particular for disordered carbons as is the case (see Raman analysis). The total pore volume was obtained using the Gurvitsch law at $P/P_0 \sim 0.98$. The pore size distribution (PSD) was determined using a slit/cylindrical pore model because it is more accurate in terms of fitting error.

The first indication of the material sorbing properties, namely of the pore network structure, can be directly obtained from the sole isotherm profile (Fig. 5a). As the melamine content was incremented, starting from no melamine in XC72, a gradual decay of the amount of adsorbed N_2 was attained in the whole relative pressure range, meaning that the micro, meso, and macroporosity is decreasing. More in detail, in the region of P/P_0 close to 0, which is related to micropore filling, carbon nitride shows almost no adsorption while Vulcan XC72 has some. This is more evidenced as P/P_0 approaches 1, which means that the total volume of pores is increasing. In general, the shape is a hybrid II/III type with H3/H4 hysteresis that is caused by a low-porosity material with a relatively low content of micro and mesopores (see also Table 2). In fact, g-C_3N_4 is substantially non-porous; indeed, no hysteresis loop, which is one of the characteristic features expected when the material contains micro/mesopores, is observed. On the other hand, XC72 carbon shows a hysteresis due to the presence of some micro and mesopores, having a medium–low surface area. The inclination of the isotherms in the central region of Fig. 5a is instead linked to the presence of mesopores with different dimensions. These considerations were confirmed by applying the QSDFT method to obtain a more precise PSD. Fig. 5b shows a peak centered at 1 nm related to the micropores. It can be deduced that there is no significant change in the intrinsic pore dimensions (i.e., pore width) when comparing the different samples; however, the relative proportion of pores with such size changes as a result of the use of a greater amount of melamine in the precursor mixture, which causes the partial pore blockage and a reduction in number of available pores. This tendency is particularly evident for mesopores, where an increase in melamine content reduces the proportion of this type of pores. This is also evident by looking at the actual values of the surface area and pore volume (Fig. 5c and 5d and Table 2). This tendency supports the aforementioned idea of the formation of a Vulcan/carbon nitride composite as the melamine proportion surpasses 71.4 wt% (i.e., samples with N-doping greater than M2.5), instead of a real N-doped carbon maintaining the original pore distribution. Moreover, the trends of Fig. 5c and 5d allow for excluding some activation of XC72 by decomposition products of melamine that could potentially increase the surface area.

To sum up, a high specific surface area can increase the chances of contact between reagents and active sites, which can promote the ORR. However, the distribution of pores is also the key to determining the different pathways ($2e^-$ or $4e^-$). According to published literature [64,65], micropores favor the H_2O_2 production and mesopores facilitate the escape of produced H_2O_2 into the bulk solution. From Fig. S6, it is interesting to note that the mesopore volume ratio increased as the

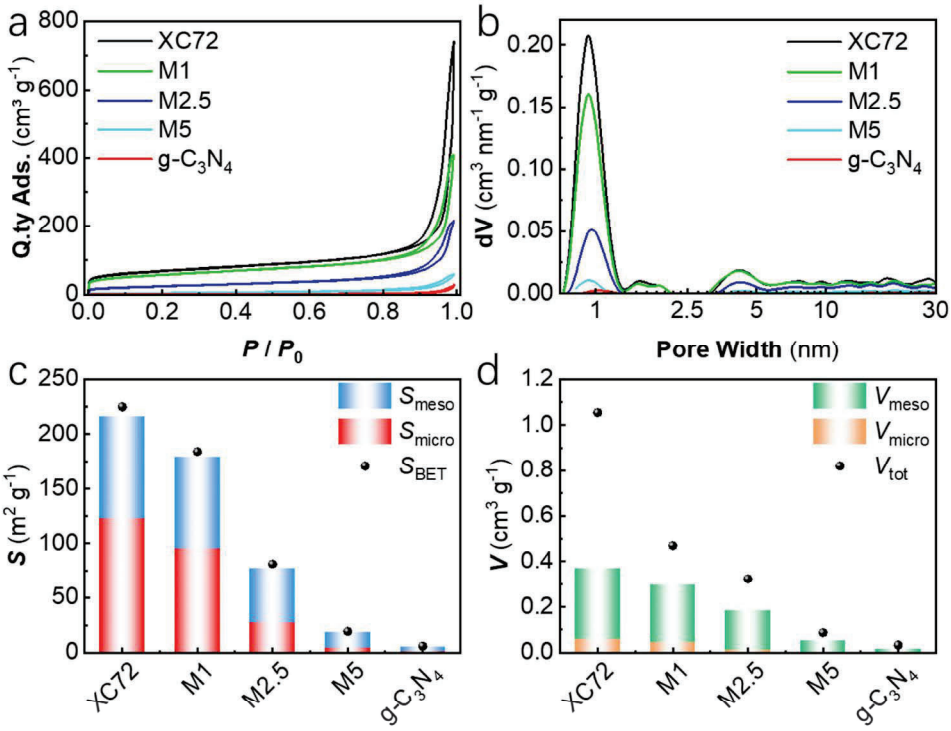

Fig. 5. (a) N_2 adsorption/desorption isotherms, (b) pore size distribution, (c) specific surface area analysis of micropores and mesopores (along with the total surface area), and (d) pore volume analysis of micropores and mesopores (along with the total pore volume) for the five electrocatalysts under study.

Table 2
Data obtained from the N_2 physisorption analysis of the five electrocatalysts under study.

	S_{BET} ($m^2\ g^{-1}$)	$S_{\mu+m}$ [a] ($m^2\ g^{-1}$)	S_{μ} [b] ($m^2\ g^{-1}$)	S_m [c] ($m^2\ g^{-1}$)	$V_{\mu+m}$ [a] ($cm^3\ g^{-1}$)	V_{μ} [b] ($cm^3\ g^{-1}$)	V_m [c] ($cm^3\ g^{-1}$)	V_{tot} ($cm^3\ g^{-1}$)
XC72	225	216	123	93	0.369	0.061	0.309	1.055
M1	184	179	96	83	0.296	0.047	0.249	0.471
M2.5	81	77.0	28	49	0.184	0.014	0.170	0.323
M5	19	18	4.9	13	0.053	0.002	0.051	0.087
g-C_3N_4	5.8	5.3	1.2	4.1	0.016	<0.001	0.016	0.034

[a] d < 40 nm,
[b] d < 2 nm,
[c] 2 nm < d < 40 nm.

melamine content was risen, in contrast to the progressive decay of the overall mesopore content for the same samples (Fig. 5c and d). This means that the relative importance of mesoporosity is enhanced when moving toward pure carbon nitride. It can also be noticed that sample M2.5 had a BET surface area of 81 $m^2\ g^{-1}$ and a mesopore volume ratio of 92.6 %, values that are close to the midpoint of both curves, which seems a very relevant feature to favor the H_2O_2 electrogeneration while preventing an excessively long residence time that would promote its decomposition.

To illustrate the morphology of the synthesized samples, the HRTEM images of g-C_3N_4 and M2.5 as examples are presented in Fig. S7. Sample g-C_3N_4 consisted of stacked thin nanosheets with relatively smooth surfaces, characteristic of the layered structure of carbon nitride [45,66]. In the pristine g-C_3N_4, the absence of distinct lattice fringes suggests that the material primarily exhibited an amorphous or highly disordered structure. Upon incorporating the XC72 in the precursor blend, the morphology and structure of g-C_3N_4 underwent noticeable changes. The HRTEM images of sample M2.5 reveal the emergence of ordered structures, specifically indicated by the appearance of 002 lattice fringes corresponding to g-C_3N_4, with a spacing of approximately 0.33 nm [67]. The crystalline domains of carbon blacks are composed of turbostratically stacked graphene layers [68]. Therefore, it is suggested that blending of melamine with XC72 not only confers a physical support but XC72 also plays a crucial role in inducing a degree of crystallinity within the g-C_3N_4 matrix. The interaction between the XC72 and g-C_3N_4 during the synthesis process likely promotes the alignment of g-C_3N_4 layers, leading to the formation of localized ordered domains. The EDS mapping analysis of the M2.5 sample (Fig. S7) provides insights into the elemental distribution within the composite. The results demonstrate a uniform distribution of C, N, and O elements, along with a small amount of S, in agreement with elemental analysis (Fig. 3a).

In summary, M2.5 is identified as the most effective electrocatalyst for the $2e^-$ ORR pathway, leading to an efficient H_2O_2 electrosynthesis due to a synergistic combination of several critical factors rather than the prevailing role of any single parameter alone. As shown in the radar chart of Fig. 6, it is possible to correlate the physicochemical and electrocatalytic properties; the outer the position of material in each specific electrocatalytic property, the better (i.e., higher activity and/or

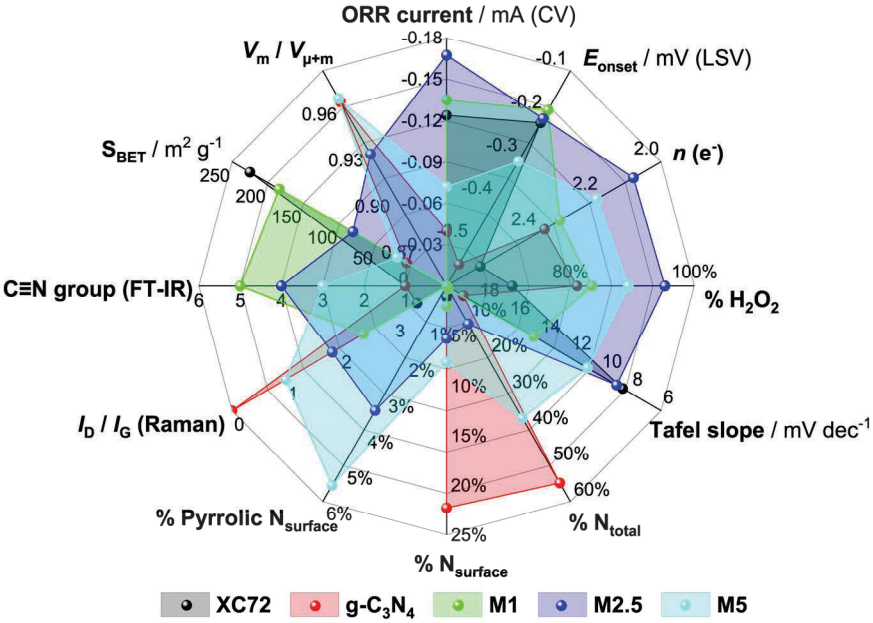

Fig. 6. Radar chart summarizing the analysis of XC72, M1, M2.5, M5, and g-C_3N_4 samples.

selectivity). M2.5 occupies that position in almost all cases, except for E_{onset} (although it is very close to M1) and Tafel slope (although close to XC72). Meanwhile, M2.5 has well-balanced physicochemical properties, never located in the outermost position of any physicochemical parameter. Therefore, the M2.5 electrocatalyst was selected as the research object to carry out all subsequent electrolytic trials with manufactured GDEs.

3.3. GDE fabrication and electrolytic performance

To develop sustainable advanced wastewater treatment systems relying on Fenton's reaction, it is crucial to maintain a continuous H_2O_2 production employing a very effective cathode. Therefore, the performance of GDEs with varying loadings of the M2.5 electrocatalyst was evaluated (the fabrication process of the GDEs is detailed in section 2.3). The H_2O_2 accumulation was analyzed over 5 h, in a conductive electrolyte at natural pH 5.9 and $j = 33.3$ mA cm^{-2}, as shown in Fig. 7a. At a catalyst loading of 0.1 mg cm^{-2}, the accumulated H_2O_2 concentration reached its peak at 34.8 mM after a progressive rise during the whole electrolysis. The productivity of this GDE, whose calculated H_2O_2 yield at 30 min was 18 mg h^{-1} cm^{-2}, is certainly outstanding as compared to those reported in the literature. For example, under quite analogous electrolysis conditions and employing a commercial GDE based on Vulcan carbon, Brillas et al. [69] achieved a slightly lower H_2O_2 yield and the H_2O_2 concentration at 5 h was below 20 mM. On the other hand, our GDE outperforms all the commercial and purpose-made GDEs summarized in the literature by Daniel et al. [26], behaving similarly to a natural air-diffusion electrode developed by the group of Zhou [70]. Furthermore, the obtained H_2O_2 yield was much superior to that achieved using melamine as precursor to modify a carbon mat cathode [40].

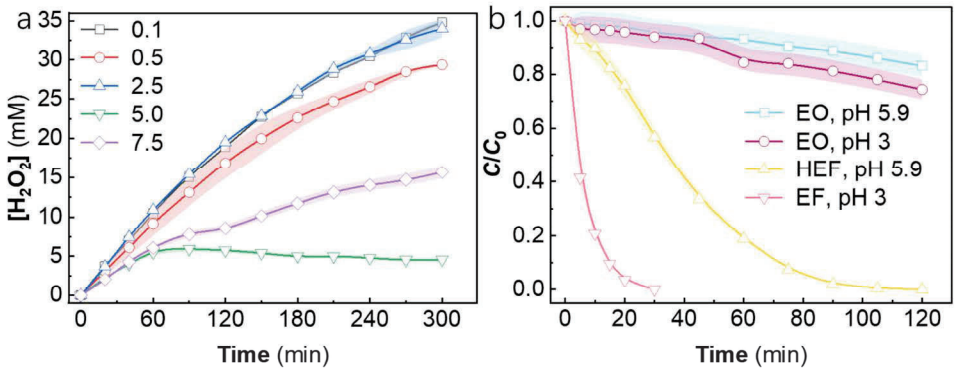

Fig. 7. (a) Effect of catalyst loading (from 0.1 to 7.5 mg cm^{-2}) on the H_2O_2 concentration accumulated in an undivided 2-electrode cell over the electrolysis time. The cathode was a 3-cm^2 GDE fabricated with the M2.5 electrocatalyst, fed with compressed air at 0.4 L min^{-1}, and coupled with a 3-cm^2 DSA-Cl_2 plate as the anode. Conditions: 150 mL of a 0.050 M Na_2SO_4 solution at natural pH 5.9, $j = 33.3$ mA cm^{-2} and 25 °C. (b) Time course of normalized DPH concentration during the treatment of 150 mL of solutions with 10 mg C L^{-1} drug (14.3 mg L^{-1} DPH) + 0.050 M Na_2SO_4, at 33 mA cm^{-2} and 25 °C, using an undivided cell with the M2.5-GDE (loading of 0.1 mg cm^{-2}) fed with air at 0.4 mL min^{-1} and a DSA-Cl_2 plate as the anode. EF treatment was carried out at pH 3, with 0.5 mM Fe^{2+} as the catalyst; HEF treatment was performed at natural pH 5.9, using 0.1 g L^{-1} Cu/C as the heterogeneous catalyst.

However, when the loading was increased to 0.5 mg cm^{-2}, the final concentration dropped to 29.4 mM. This reduction is attributed to a decrease in the available gas-diffusion channels in the carbon cloth substrate, caused by the excessive catalyst loading that likely impedes the diffusion of oxygen to the active sites. Surprisingly, a further increase of the loading to 2.5 mg cm^{-2} resulted in the total recovery of the best H_2O_2 production, which means that the number of active sites in the catalytic layer was risen sufficiently to counter-balance the detrimental blockage of gas channels. However, all subsequent increments of loading negatively affected the H_2O_2 production, reaching 15 mM as a maximum at 5 h. This sharp decline can be attributed to the excess of electrocatalyst, which not only blocked the gas channels but also fostered the cathodic reduction of the produced H_2O_2 since the product must go through a thicker catalytic layer to escape from the pores. In conclusion, the optimal loading was the lowest (0.1 mg cm^{-2}, because lower values led to non-uniform coatings that accelerated the flooding), highlighting that an optimal balance between electrocatalytic reaction and gas diffusion is essential for maximizing the H_2O_2 production.

Another key objective of this study was to validate the viability of the manufactured GDEs for water treatment by evaluating the EF degradation of organic pollutants. Before this, the activation of the in-situ generated H_2O_2 with the M2.5-GDE (0.1 mg cm^{-2}) in the presence of a metal catalyst was investigated. The decomposition of H_2O_2 was assessed in both EF (pH 3, with 0.5 mM Fe^{2+}) and heterogeneous EF (i.e., HEF) process (pH 5.9, with 0.1 g L^{-1} Cu/C catalyst) at a current density of 33.3 mA cm^{-2}. As depicted in Fig. S8, following the addition of Fe^{2+} and Cu/C catalysts, the H_2O_2 concentration was gradually accumulated, but attained much lower values as compared to Fig. 7a. This is a confirmation of the H_2O_2 conversion to $^{\bullet}OH$ upon reaction with the metal catalyst [1,2]. The Fe^{2+} catalyst was very effective, being superior during the first 120 min because it kept a lower H_2O_2 concentration in that period. This is due to the greater mass transport in homogeneous systems, which facilitates the reactive events between H_2O_2 and the dissolved catalyst. The activation of H_2O_2 with Cu/C was slower, as indicated by the greater initial H_2O_2 accumulation, but the final value was much lower (0.2 mM *vs* 0.7 mM). Being a heterogeneous process, the activation was slower, whereupon the catalytic effect was kept for a longer time.

The effectiveness of the EO, EF, and HEF processes to degrade 14.3 mg L^{-1} DPH (10 mg C L^{-1}) from 0.050 M Na_2SO_4 solutions was compared at different pH, using the M2.5-based GDE (0.1 mg cm^{-2}) as the cathode and a DSA-Cl_2 plate as the anode. As shown in Fig. 7b, the drug removal in the EO process was not effective, with removal percentages of 25.7 % and 16.9 % at pH 3 and natural pH 5.9, respectively, after 120 min. In contrast, the HEF process at pH 5.9, employing Cu/C as the catalyst, required full activation to decompose H_2O_2 effectively but, once activated, it enabled 100 % degradation of DPH within 120 min, demonstrating the great potential of the prepared GDE to run water decontamination under near-neutral conditions. The EF process at pH 3, using Fe^{2+} as the catalyst, was the most efficient treatment, achieving complete degradation within just 30 min, owing to the optimal generation of hydroxyl radicals in an acidic medium [1,2]. These findings underscore the excellent performance of the developed GDE in both EF and HEF processes, particularly highlighting its adaptability and effectiveness for treating wastewater under varying pH conditions.

4. Conclusions

This study successfully reports the synthesis and characterization of a metal-free, melamine-based electrocatalyst with high activity and selective for the $2e^-$ ORR As an original contribution, the work provides a radar chart that allows visualizing the correlation between the physicochemical and electrocatalytic properties of the synthesized materials. As an N-rich compound, melamine proved to be an excellent precursor for the preparation of N-doped carbons. The electrochemical tests revealed the superiority of the M2.5 electrocatalyst (71.4 wt% melamine in the precursor) in terms of E_{onset}, Tafel slope, n, and y_{H2O2}. A GDE prepared with a trace amount of M2.5 (0.1 mg cm^{-2}) exhibited an H_2O_2 yield of 18 mg h^{-1} cm^{-2}, greater than the values reported so far under analogous electrolysis conditions. When coupling a DSA-Cl_2 anode and the M2.5-GDE in a HEF system at near-neutral pH, the complete degradation of 14.3 mg L^{-1} DPH was feasible within 120 min; at pH 3, only 30 min was needed. This optimized GDE has demonstrated its ability to operate across a wide pH range, showcasing its good perspectives for wastewater treatment.

Declaration of competing interest

The authors declare that they have no known competing financial interests or personal relationships that could have appeared to influence the work reported in this paper.

Acknowledgments

The authors are thankful to project PID2022-140378OB-I00 and E3TECH-PLUS Network RED2022-134552-T, funded by MICIU/AEI/10.13039/501100011033 (Spain) and by ERDF/EU, as well as to P-DISC Grant (project No. P-DISC#03NExuS_BIRD2021-UNIPD, University of Padova, Italy). MIUR is also acknowledged for the support to the project financed by the European Union - Next Generation EU - Bando PRIN 2022 PNRR – M4.C2.1.1: Progetto: P2022WANKS - ECHO-EF. The Ph.D. scholarship awarded to L.Z. (State Scholarship Fund, CSC, China) is also acknowledged. M.P. acknowledges PON "Ricerca e Innovazione" 2014-2020 for the PhD fellowship support. Help from the *Centres Científics i Tecnològics de la UB* (CCiT-UB) to carry out the physicochemical analysis (BET, elemental analysis, TEM, XPS, and XRD) is also acknowledged.

Appendix A. Supplementary material

Supplementary data to this article can be found online at https://doi.org/10.1016/j.seppur.2025.131590.

References

[1] N. Oturan, J. Bo, C. Trellu, M.A. Oturan, Comparative performance of ten electrodes in electro-Fenton process for removal of organic pollutants from water, ChemElectroChem 8 (2021) 3294–3303, https://doi.org/10.1002/celc.202100588.

[2] P. Xia, Z. Ye, L. Zhao, Q. Xue, S. Lanzalaco, Q. He, X. Qi, I. Sirés, Tailoring single-atom FeN_4 moieties as a robust heterogeneous catalyst for high-performance electro-Fenton treatment of organic pollutants, Appl. Catal. B: Environ. 322 (2023) 122116, https://doi.org/10.1016/j.apcatb.2022.122116.

[3] G. Ren, S. Lanzalaco, M. Zhou, P.L. Cabot, E. Brillas, I. Sirés, Replacing carbon cloth by nickel mesh as substrate for air-diffusion cathodes: H_2O_2 production and carbenicillin degradation by photoelectro-Fenton, Chem. Eng. J. 454 (2023) 140515, https://doi.org/10.1016/j.cej.2022.140515.

[4] L.E. Quispe Cardenas, P.J. Deptula, C.S. Huerta, C. Zhu, Y. Ye, S. Wang, Y. Yang, Electro-Fenton and induced electro-Fenton as versatile wastewater treatment processes for decontamination and nutrient removal without byproduct formation, ACS EST Engg. 3 (10) (2023) 1547–1556, https://doi.org/10.1021/acsestengg.3c00128.

[5] A.R. Wolfson, D. Wong, E.M. Abrams, S. Waserman, G.L. Sussman, Diphenhydramine: time to move on? J. Allergy Clin. Immunol.: Pract. 10 (2022) 3124–3130, https://doi.org/10.1016/j.jaip.2022.07.018.

[6] P.E. Stackelberg, E.T. Furlong, M.T. Meyer, S.D. Zaugg, A.K. Henderson, D. B. Reissman, Persistence of pharmaceutical compounds and other organic wastewater contaminants in a conventional drinking-water-treatment plant, Sci. Total Environ. 329 (2004) 99–113, https://doi.org/10.1016/j.scitotenv.2004.03.015.

[7] L.M. Pastrana-Martínez, S. Morales-Torres, V. Likodimos, J.L. Figueiredo, J. L. Faria, P. Falaras, A.M.T. Silva, Advanced nanostructured photocatalysts based on reduced graphene oxide–TiO_2 composites for degradation of diphenhydramine pharmaceutical and methyl orange dye, Appl. Catal. B: Environ. 123–124 (2012) 241–256, https://doi.org/10.1016/j.apcatb.2012.04.045.

[8] L. Song, C. Yi, Q. Wu, Z. Li, W. Zhang, H. Hong, Photocatalytic degradation of diphenhydramine in aqueous solution by natural dolomite, RSC Adv. 10 (2020) 38663–38671, https://doi.org/10.1039/D0RA07533G.

[9] F. Ghiasi, A.R. Solaimany Nazar, M. Farhadian, S. Tangestaninejad, N. Emami, Synthesis of aqueous media stable MIL101-OH/chitosan for diphenhydramine and

metronidazole adsorption, Environ. Sci. Pollut. Res. 29 (2022) 24286–24297, https://doi.org/10.1007/s11356-021-17739-1.
[10] N. López, S. Plaza, A. Afkhami, P. Marco, J. Giménez, S. Esplugas, Treatment of Diphenhydramine with different AOPs including photo-Fenton at circumneutral pH, Chem. Eng. J. 318 (2017) 112–120, https://doi.org/10.1016/j.cej.2016.05.127.
[11] C. Espinoza, N. Contreras, C. Berríos, R. Salazar, Degradation of a veterinary pharmaceutical product in water by electro-oxidation using a BDD anode, J. Chil. Chem. Soc. 59 (2014) 2507–2511, https://doi.org/10.4067/S0717-97072014000200024.
[12] M. Mazzucato, A. Facchin, M. Parnigotto, C. Durante, New and revised aspects of the electrochemical synthesis of hydrogen peroxide: from model electrocatalytic systems to scalable materials, ACS Catal. 14 (2024) 6369–6403, https://doi.org/10.1021/acscatal.4c01011.
[13] Y. Ding, W. Zhou, J. Gao, F. Sun, G. Zhao, H_2O_2 electrogeneration from O_2 electroreduction by N-doped carbon materials: a mini-review on preparation methods, selectivity of N sites, and prospects, Adv. Mater. Interfaces 8 (2021) 2002091, https://doi.org/10.1002/admi.202002091.
[14] P. Xia, L. Zhao, X. Chen, Z. Ye, Z. Zheng, Q. He, I. Sirés, Polymethylhydrosiloxane-modified gas-diffusion cathode for more efficient and durable H_2O_2 electrosynthesis in the context of water treatment, Appl. Catal. B: Environ. 343 (2024) 123467, https://doi.org/10.1016/j.apcatb.2023.123467.
[15] A. Xu, Z. Yang, Z. Zhou, P. Yang, Y. Yu, J. Liu, Y. Zhang, Trans-electrode pressure of gas-diffusion electrodes significantly influencing the electrochemical hydrogen peroxide production, Chemosphere 361 (2024) 142464, https://doi.org/10.1016/j.chemosphere.2024.142464.
[16] A. Kulkarni, S. Siahrostami, A. Patel, J.K. Nørskov, Understanding catalytic activity trends in the oxygen reduction reaction, Chem. Rev. 118 (2018) 2302–2312, https://doi.org/10.1021/acs.chemrev.7b00488.
[17] J. Hu, S. Wang, J. Yu, W. Nie, J. Sun, S. Wang, Duet Fe_3C and FeN_x sites for H_2O_2 generation and activation toward enhanced electro-Fenton performance in wastewater treatment, Environ. Sci. Technol. 55 (2021) 1260–1269, https://doi.org/10.1021/acs.est.0c06825.
[18] Y. Sun, L. Silvioli, N.R. Sahraie, W. Ju, J. Li, A. Zitolo, S. Li, A. Bagger, L. Arnarson, X. Wang, T. Moeller, D. Bernsmeier, J. Rossmeisl, F. Jaouen, P. Strasser, Activity–selectivity trends in the electrochemical production of hydrogen peroxide over single-ste metal–nitrogen–carbon catalysts, J. Am. Chem. Soc. 141 (2019) 12372–12381, https://doi.org/10.1021/jacs.9b05576.
[19] F. Alcaide, G. Álvarez, D.R.V. Guelfi, E. Brillas, I. Sirés, A stable CoSP/MWCNTs air-diffusion cathode for the photoelectro-Fenton degradation of organic pollutants at pre-pilot scale, Chem. Eng. J. 379 (2020) 122417, https://doi.org/10.1016/j.cej.2019.122417.
[20] X. Qin, P. Cao, X. Quan, K. Zhao, S. Chen, H. Yu, Y. Su, Highly efficient hydroxyl radicals production boosted by the atomically dispersed Fe and Co sites for heterogeneous electro-Fenton oxidation, Environ. Sci. Technol. 57 (2023) 2907–2917, https://doi.org/10.1021/acs.est.2c06981.
[21] L. Ge, Z. Peng, W. Wang, F. Tan, X. Wang, B. Su, X. Qiao, P.K. Wong, g-C_3N_4/MgO nanosheets: light-independent, metal-poisoning-free catalysts for the activation of hydrogen peroxide to degrade organics, J. Mater. Chem. A 6 (2018) 16421–16429, https://doi.org/10.1039/C8TA05488F.
[22] Q. Chang, P. Zhang, A.H.B. Mostaghimi, X. Zhao, S.R. Denny, J.H. Lee, H. Gao, Y. Zhang, H.L. Xin, S. Siahrostami, J.G. Chen, Z. Chen, Promoting H_2O_2 production via 2-electron oxygen reduction by coordinating partially oxidized Pd with defect carbon, Nat. Commun. 11 (2020) 2178, https://doi.org/10.1038/s41467-020-15843-3.
[23] K. Jiang, J. Zhao, H. Wang, Catalyst design for electrochemical oxygen reduction toward hydrogen peroxide, Adv. Funct. Mater. 30 (2020) 2003321, https://doi.org/10.1002/adfm.202003321.
[24] S. Chen, Z. Chen, S. Siahrostami, T.R. Kim, D. Nordlund, D. Sokaras, S. Nowak, J. W.F. To, D. Higgins, R. Sinclair, J.K. Nørskov, T.F. Jaramillo, Z. Bao, Defective carbon-based materials for the electrochemical synthesis of hydrogen peroxide, ACS Sustain. Chem. Eng. 6 (2018) 311–317, https://doi.org/10.1021/acssuschemeng.7b02517.
[25] Y. Zhang, G. Daniel, S. Lanzalaco, A.A. Isse, A. Facchin, A. Wang, E. Brillas, C. Durante, I. Sirés, H_2O_2 production at gas-diffusion cathodes made from agarose-derived carbons with different textural properties for acebutolol degradation in chloride media, J. Hazard. Mater. 423 (2022) 127005, https://doi.org/10.1016/j.jhazmat.2021.127005.
[26] G. Daniel, Y. Zhang, S. Lanzalaco, F. Brombin, T. Kosmala, G. Granozzi, A. Wang, E. Brillas, I. Sirés, C. Durante, Chitosan-derived nitrogen-doped carbon electrocatalyst for a sustainable upgrade of oxygen reduction to hydrogen peroxide in UV-assisted electro-Fenton water treatment, ACS Sustain. Chem. Eng. 8 (2020) 14425–14440, https://doi.org/10.1021/acssuschemeng.0c04294.
[27] M. Mazzucato, C. Durante, Insights on oxygen reduction reaction to H_2O_2: the role of functional groups and textural properties on the activity and selectivity of doped carbon electrocatalysts, Curr. Opinion Electrochem. 35 (2022) 101051, https://doi.org/10.1016/j.coelec.2022.101051.
[28] V. Perazzolo, C. Durante, A. Gennaro, Nitrogen and sulfur doped mesoporous carbon cathodes for water treatment, J. Electroanal. Chem. 782 (2016) 264–269, https://doi.org/10.1016/j.jelechem.2016.10.037.
[29] Z. Yang, Z. Yao, G. Li, G. Fang, H. Nie, Z. Liu, X. Zhou, X. Chen, S. Huang, Sulfur-doped graphene as an efficient metal-free cathode catalyst for oxygen reduction, ACS Nano 6 (2012) 205–211, https://doi.org/10.1021/nn203393d.
[30] K.H. Koh, Y.J. Kim, A.H.B. Mostaghim, S. Siahrostami, T.H. Han, Z. Chen, Elaborating nitrogen and oxygen dopants configurations within graphene electrocatalysts for two-electron oxygen reduction, ACS Mater. Lett. 4 (2022) 320–328, https://doi.org/10.1021/acsmaterialslett.1c00660.
[31] C. Tang, Q. Zhang, Nanocarbon for oxygen reduction electrocatalysis: dopants, edges, and defects, Adv. Mater. 29 (2017) 1604103, https://doi.org/10.1002/adma.201604103.
[32] V. Perazzolo, G. Daniel, R. Brandiele, L. Picelli, G.A. Rizzi, A.A. Isse, C. Durante, PEO-b-PS block copolymer templated mesoporous carbons: a comparative study of nitrogen and sulfur doping in the oxygen reduction reaction to hydrogen peroxide, Chem. Eur. J. 27 (2021) 1002–1014, https://doi.org/10.1002/chem.202003355.
[33] M. Mazzucato, G. Daniel, V. Perazzolo, R. Brandiele, G.A. Rizzi, A.A. Isse, A. Gennaro, C. Durante, Mesoporosity and nitrogen doping: the leading effect in oxygen reduction reaction activity and selectivity at nitrogen-doped carbons prepared by using polyethylene oxide-block-polystyrene as a sacrificial template, Electrochem. Sci. Adv. 3 (2023) e2100203, https://doi.org/10.1002/elsa.202100203.
[34] V. Perazzolo, C. Durante, R. Pilot, A. Paduano, J. Zheng, G.A. Rizzi, A. Martucci, G. Granozzi, A. Gennaro, Nitrogen and sulfur doped mesoporous carbon as metal-free electrocatalysts for the *in situ* production of hydrogen peroxide, Carbon 95 (2015) 949–963, https://doi.org/10.1016/j.carbon.2015.09.002.
[35] Y. Zhang, L. Zhan, L. Hu, G. Fan, Oxygen-assisted one-step fabrication and concomitant regulation of hierarchical carbon nanosheet assemblies with conjugated binding configurations for promoted H_2O_2 electrosynthesis, Fuel 354 (2023) 129300, https://doi.org/10.1016/j.fuel.2023.129300.
[36] N. Lu, T. Zhang, X. Yan, Y. Gu, H. Liu, Z. Xu, H. Xu, X. Li, Z. Zhang, M. Yang, Facile synthesis of 3D N-doped porous carbon nanosheets as highly active electrocatalysts toward the reduction of hydrogen peroxide, Nanoscale 10 (2018) 14923–14930, https://doi.org/10.1039/C8NR02573H.
[37] Y. Ni, T. Wang, Y. Zhou, C. Wang, Y. Tang, T. Li, B. Geng, Synergistic melamine intercalation and $Zn(NO_3)_2$ activation of N-doped porous carbon supported Fe/Fe_3O_4 for efficient electrocatalytic oxygen reduction, RSC Adv. 12 (2022) 15705–15712, https://doi.org/10.1039/D2RA02170F.
[38] X. Hao, X. An, A.M. Patil, P. Wang, X. Ma, X. Du, X. Hao, A. Abudula, G. Guan, Biomass-derived N-doped carbon for efficient electrocatalytic CO_2 reduction to CO and Zn–CO_2 batteries, ACS Appl. Mater. Interfaces 13 (2021) 3738–3747, https://doi.org/10.1021/acsami.0c13440.
[39] Y. Zhu, S. Qiu, F. Ma, G. Li, F. Deng, Y. Zheng, Melamine-derived carbon electrode for efficient H_2O_2 electro-generation. Electrochim. Acta 261 (2018) 375–383, https://doi.org/10.1016/j.electacta.2017.12.122.
[40] P. Su, M. Zhou, X. Lu, W. Yang, G. Ren, J. Cai, Electrochemical catalytic mechanism of N-doped graphene for enhanced H_2O_2 yield and in-situ degradation of organic pollutant, Appl. Catal. B: Environ. 245 (2019) 583–595, https://doi.org/10.1016/j.apcatb.2018.12.075.
[41] A.A. Márquez, I. Sirés, E. Brillas, J.L. Nava, Mineralization of Methyl Orange azo dye by processes based on H_2O_2 electrogeneration at a 3D-like air-diffusion cathode, Chemosphere 259 (2020) 127466, https://doi.org/10.1016/j.chemosphere.2020.127466.
[42] L. Zhao, J.A. Padilla, E. Xuriguera, P.L. Cabot, E. Brillas, I. Sirés, Enhanced mineralization of pharmaceutical residues at circumneutral pH by heterogeneous electro-Fenton-like process with Cu/C catalyst, Chemosphere 364 (2024) 143249, https://doi.org/10.1016/j.chemosphere.2024.143249.
[43] G. Ma, R. Jia, J. Zhao, Z. Wang, C. Song, S. Jia, Z. Zhu, Nitrogen-doped hollow carbon nanoparticles with excellent oxygen reduction performances and their electrocatalytic kinetics, J. Phys. Chem. C 115 (2011) 25148–25154, https://doi.org/10.1021/jp208257r.
[44] F. Cao, Z. Zang, S. Sun, X. Sun, X. Li, T. Liu, J. Wu, The influence of deposited potential on the ORR activity of Pt catalysts on glassy carbon electrode, RSC Adv. 7 (2017) 25429–25436, https://doi.org/10.1039/C7RA02444D.
[45] J.-R. Zhang, Y. Ma, S.-Y. Wang, J. Ding, B. Gao, E. Kan, W. Hua, Accurate K-edge X-ray photoelectron and absorption spectra of g-C_3N_4 nanosheets by first-principles simulations and reinterpretations, Phys. Chem. Chem. Phys. 21 (2019) 22819, https://doi.org/10.1039/C9CP04573B.
[46] D. Iglesias, A. Giuliani, M. Melchionna, S. Marchesan, A. Criado, L. Nasi, M. Bevilacqua, C. Tavagnacco, F. Vizza, M. Prato, P. Fornasiero, N-doped graphitized carbon nanohorns as a forefront electrocatalyst in highly selective O_2 reduction to H_2O_2, Chem 4 (2018) 106–123, https://doi.org/10.1016/j.chempr.2017.10.013.
[47] Y. Guo, C. Tang, C. Cao, X. Hu, N-doped carbon-based catalysts in situ generation hydrogen peroxide via 2-electron oxygen reduction reaction for degradation of organic contaminants in heterogeneous electro-Fenton process: a mini review, Surf. Interfaces 38 (2023) 102879, https://doi.org/10.1016/j.surfin.2023.102879.
[48] Q. He, J. Li, Y. Qiao, S. Zhan, F. Zhou, Investigation of two-electron ORR pathway of non-metallic carbon-based catalysts with P-C bond structure in Cl– bearing electrolytes, Appl. Catal. B: Environ. 339 (2023) 123087, https://doi.org/10.1016/j.apcatb.2023.123087.
[49] Z. Zhang, H. Zhao, Z. Wang, Z. Hu, Q. Wang, E. Meng, S. Lai, J. Ying, H. Li, C. Wu, Strategies for promoting the degradation of phenol by electro-Fenton: simultaneously promoting the generation and utilization of H_2O_2, Environ. Res. 236 (2023) 116794, https://doi.org/10.1016/j.envres.2023.116794.
[50] T. Shen, X. Huang, S. Xi, W. Li, S. Sun, Y. Hou, The ORR electron transfer kinetics control via Co-N_x and graphitic N sites in cobalt single atom catalysts in alkaline and acidic media, J. Energy Chem. 68 (2022) 184–194, https://doi.org/10.1016/j.jechem.2021.10.027.
[51] J. Feng, M. Cao, L. Wang, X. Ran, B. Xiao, J. Zhu, Z. Liu, X. Xi, G. Feng, R. Li, Ultra-thin $DyFeO_3$/g-C_3N_4 p-n heterojunctions for highly efficient photo-Fenton removal of oxytetracycline and antibacterial activity, J. Alloys Compd. 939 (2023) 168789, https://doi.org/10.1016/j.jallcom.2023.168789.

[52] J. Yuan, H. Zhou, D. Li, F. Xu, Construction of Fe_3S_4/g-C_3N_4 composites as photo-Fenton-like catalysts to realize high-efficiency degradation of pollutants, Ceram. Int. 49 (2023) 16070–16079, https://doi.org/10.1016/j.ceramint.2023.01.205.
[53] X. Zhang, P. Ma, C. Wang, L. Gan, X. Chen, P. Zhang, Y. Wang, H. Li, L. Wang, X. Zhou, K. Zheng, Unraveling the dual defect sites in graphite carbon nitride for ultra-high photocatalytic H_2O_2 evolution, Energy Environ. Sci. 15 (2022) 830–842, https://doi.org/10.1039/D1EE02369A.
[54] L. Gu, Y. Dong, Y. Zhang, B. Wang, Q. Yuan, H. Du, J. Zhao, Insights into the role of an Fe–N active site in the oxygen reduction reaction on carbon-supported supramolecular catalysts, RSC Adv. 10 (2020) 8709–8716, https://doi.org/10.1039/C9RA09301J.
[55] S.C. Yan, Z.S. Li, Z.G. Zou, Photodegradation performance of g-C_3N_4 fabricated by directly heating melamine, Langmuir 25 (2009) 10397–10401, https://doi.org/10.1021/la900923z.
[56] A.C. Ferrari, J. Robertson, Interpretation of Raman spectra of disordered and amorphous carbon, Phys. Rev. B 61 (2000) 14095–14107, https://doi.org/10.1103/PhysRevB.61.14095.
[57] A.C. Ferrari, Determination of bonding in diamond-like carbon by Raman spectroscopy, Diamond Relat. Mater. 11 (2002) 1053–1061, https://doi.org/10.1016/S0925-9635(01)00730-0.
[58] M. Pawlyta, J.-N. Rouzaud, S. Duber, Raman microspectroscopy characterization of carbon blacks: Spectral analysis and structural information, Carbon 84 (2015) 479–490, https://doi.org/10.1016/j.carbon.2014.12.030.
[59] D. Liu, X. Zhao, R. Su, Z. Hao, B. Jia, S. Li, L. Dong, Highly porous graphitic activated carbons from lignite via microwave pretreatment and iron-catalyzed graphitization at low-temperature for supercapacitor electrode materials, Processes 7 (2019) 300, https://doi.org/10.3390/pr7050300.
[60] G. Daniel, T. Kosmala, F. Brombin, M. Mazzucato, A. Facchin, M.C. Dalconi, D. Badocco, P. Pastore, G. Granozzi, C. Durante, Highly graphitized Fe-N-C electrocatalysts prepared from chitosan hydrogel frameworks, Catalysts 11 (2021) 390, https://doi.org/10.3390/catal11030390.
[61] G.Y. Gor, M. Thommes, K.A. Cychosz, A.V. Neimark, Quenched solid density functional theory method for characterization of mesoporous carbons by nitrogen adsorption, Carbon 50 (2012) 1583–1590, https://doi.org/10.1016/j.carbon.2011.11.037.
[62] J. Landers, G.Y. Gor, A.V. Neimark, Density functional theory methods for characterization of porous materials, Colloid. Surf. A: Physicochem. Eng. Aspects 437 (2013) 3–32, https://doi.org/10.1016/j.colsurfa.2013.01.007.
[63] A.M. Puziy, O.I. Poddubnaya, B. Gawdzik, M. Sobiesiak, Comparison of heterogeneous pore models QSDFT and 2D-NLDFT and computer programs ASiQwin and SAIEUS for calculation of pore size distribution, Adsorption 22 (2016) 459–464, https://doi.org/10.1007/s10450-015-9704-6.
[64] Y. Liu, X. Quan, X. Fan, H. Wang, S. Chen, High-yield electrosynthesis of hydrogen peroxide from oxygen reduction by hierarchically porous carbon, Angew. Chem Int. Ed. 54 (2015) 6837–6841, https://doi.org/10.1002/anie.201502396.
[65] X. Huang, J. Zhang, G. Luo, D. Wang, Cobalt atoms anchored on nitrogen-doped hollow carbon spheres for efficient electrocatalysis of oxygen reduction to H_2O_2, J. Phys. Energy 5 (2023) 025001, https://doi.org/10.1088/2515-7655/acbabc.
[66] X. Liu, N. Chen, Y. Li, D. Deng, X. Xing, Y. Wang, A general nonaqueous sol-gel route to g-C_3N_4-coupling photocatalysts: the case of Z-scheme g-C_3N_4/TiO_2 with enhanced photodegradation toward RhB under visible-light, Sci. Rep. 6 (2016) 39531, https://doi.org/10.1038/srep39531.
[67] L. Shen, Z. Xing, J. Zou, Z. Li, X. Wu, Y. Zhang, Q. Zhu, S. Yang, W. Zhou, Black TiO_2 nanobelts/g-C_3N_4 nanosheets laminated heterojunctions with efficient visible-light-driven photocatalytic performance, Sci. Rep. 7 (2017) 41978, https://doi.org/10.1038/srep41978.
[68] A. Sadezky, H. Muckenhuber, H. Grothe, R. Niessner, U. Pöschl, Raman microspectroscopy of soot and related carbonaceous materials: spectral analysis and structural information, Carbon 43 (2005) 1731–1742, https://doi.org/10.1016/j.carbon.2005.02.018.
[69] E. Brillas, J.C. Calpe, J. Casado, Mineralization of 2,4-D by advanced electrochemical oxidation processes, Water Res. 34 (2000) 2253–2262, https://doi.org/10.1016/S0043-1354(99)00396-6.
[70] Q. Zhang, M. Zhou, G. Ren, Y. Li, Y. Li, X. Du, Highly efficient electrosynthesis of hydrogen peroxide on a superhydrophobic three-phase interface by natural air diffusion, Nat. Commun. 11 (2020) 1731, https://doi.org/10.1038/s41467-020-15597-y.

SUPPLEMENTARY MATERIAL

Complete antihistamine degradation in wastewater matrix using a metal-free N-doped carbon with superior electrocatalytic performance for in-situ H_2O_2 production

Lele Zhao [a], Marco Mazzucato [b], Sonia Lanzalaco [c], Mattia Parnigotto [b], Pere L. Cabot [a], Christian Durante [b,*], Ignasi Sirés [a,*]

[a] *Laboratori d'Electroquímica dels Materials i del Medi Ambient, Departament de Ciència de Materials i Química Física, Secció de Química Física, Facultat de Química, Universitat de Barcelona, Martí i Franquès 1-11, 08028 Barcelona, Spain*

[b] *Department of Chemical Sciences, University of Padua, Via Marzolo 1, 35131 Padova, Italy*

[c] *Departament d'Enginyeria Química, EEBE, Universitat Politècnica de Catalunya, C/ Eduard Maristany, 10–14, Ed. I2, 08019 Barcelona, Spain*

* Corresponding author: christian.durante@unipd.it (C. Durante); i.sires@ub.edu (I. Sirés).

Content **Page**

Table S1 and S2	2
Figure S1 and S2	3
Figure S3 and S4	4
Figure S5 and S6	5
Figure S7	6
Figure S8	7

SUPPLEMENTARY MATERIAL

Table S1. Values of the onset potential, electron transfer number and H_2O_2 selectivity determined from the electrochemical characterization assays with RRDE for all the electrocatalysts under study.

Electrocatalyst	E_{onset} / V *vs.* RHE (at -0.1 mA)	*n*	$y_{H_2O_2}$ (in %)
XC72	0.37	2.59	70.6
M1	0.40	2.33	83.5
M2.5	0.38	2.09	95.3
M5	0.28	2.21	89.3
g-C_3N_4	0.04	2.38	81.1

Table S2. Element content on the surface of all the electrocatalysts under study, as obtained from the XPS full spectrum analysis.

Sample	C (in at.%)	O (in at.%)	N (in at.%)
XC72	80.6	19.4	-
M1	63.1	34.9	2.0
M2.5	77.2	17.5	5.3
M5	70.0	22.3	7.7
g-C_3N_4	45.6	32.1	22.3

SUPPLEMENTARY MATERIAL

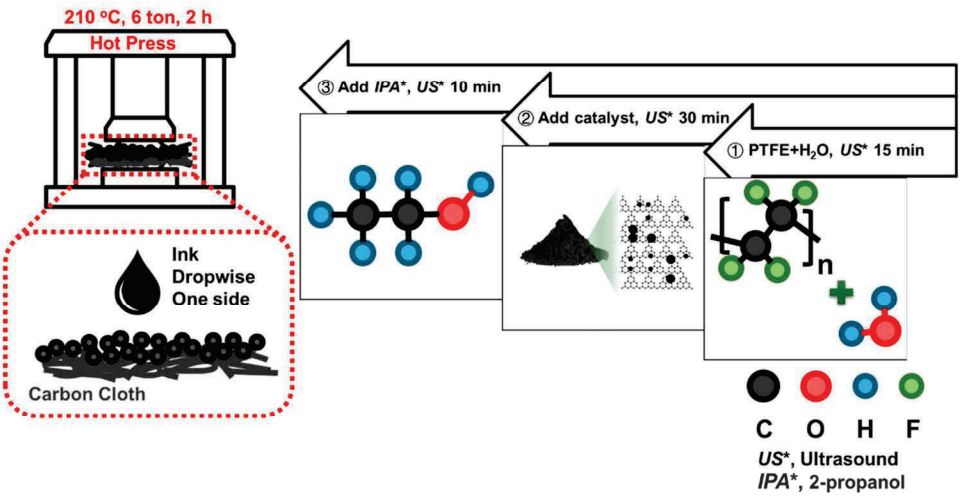

Figure S1. Scheme of the GDE fabrication using the electrocatalysts, with the final hot pressing step.

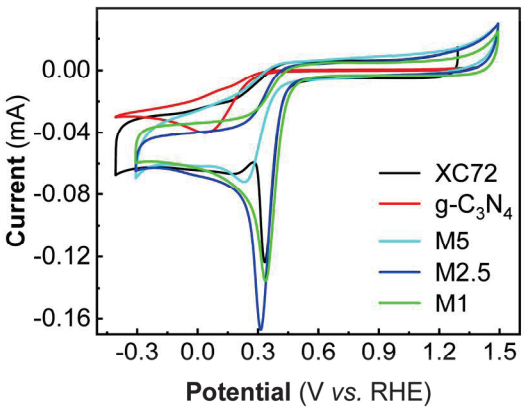

Figure S2. Cyclic voltammograms obtained using each of the electrocatalysts under study, which were drop-casted onto glassy carbon (catalyst loading of 0.6 mg cm^{-2}), at v_{scan} = 10 mV s^{-1}. The assays were performed in an O_2-saturated 0.1 M Na_2SO_4 electrolyte at natural pH 5.9. Carbon rod and Ag|AgCl (3 M KCl) were used as CE and RE, respectively.

SUPPLEMENTARY MATERIAL

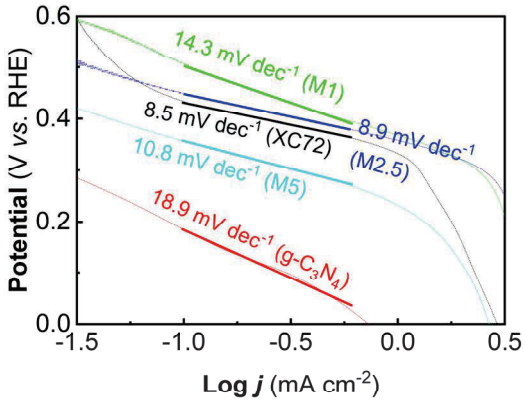

Figure S3. Tafel slopes for all the electrocatalysts, obtained from the LSV curves shown in Fig. 2a.

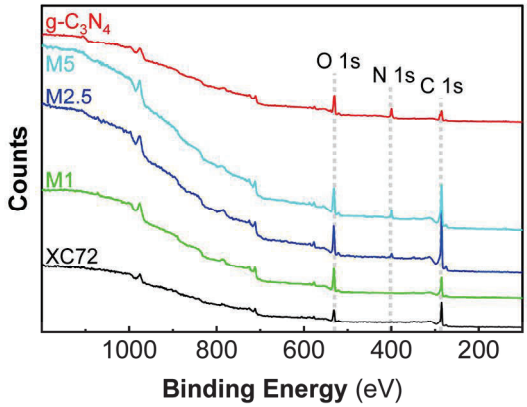

Figure S4. XPS full spectra of all the electrocatalysts under study.

SUPPLEMENTARY MATERIAL

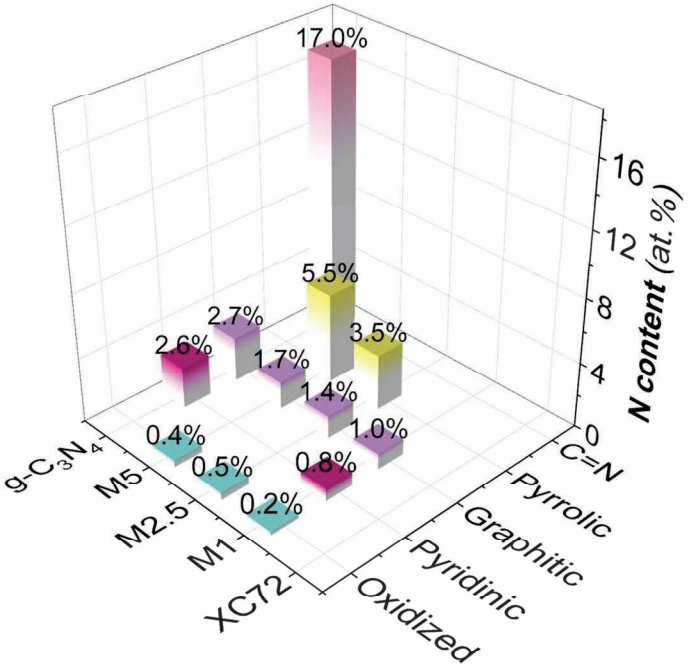

Figure S5. N content on the surface of each electrocatalyst under study, as determined by XPS.

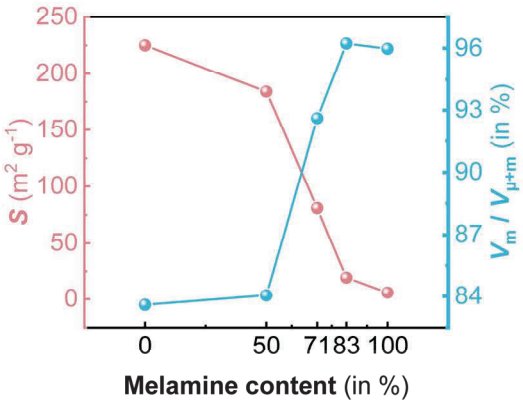

Figure S6. Relationship between BET specific surface area and mesopore volume percentage for each electrocatalyst under study.

SUPPLEMENTARY MATERIAL

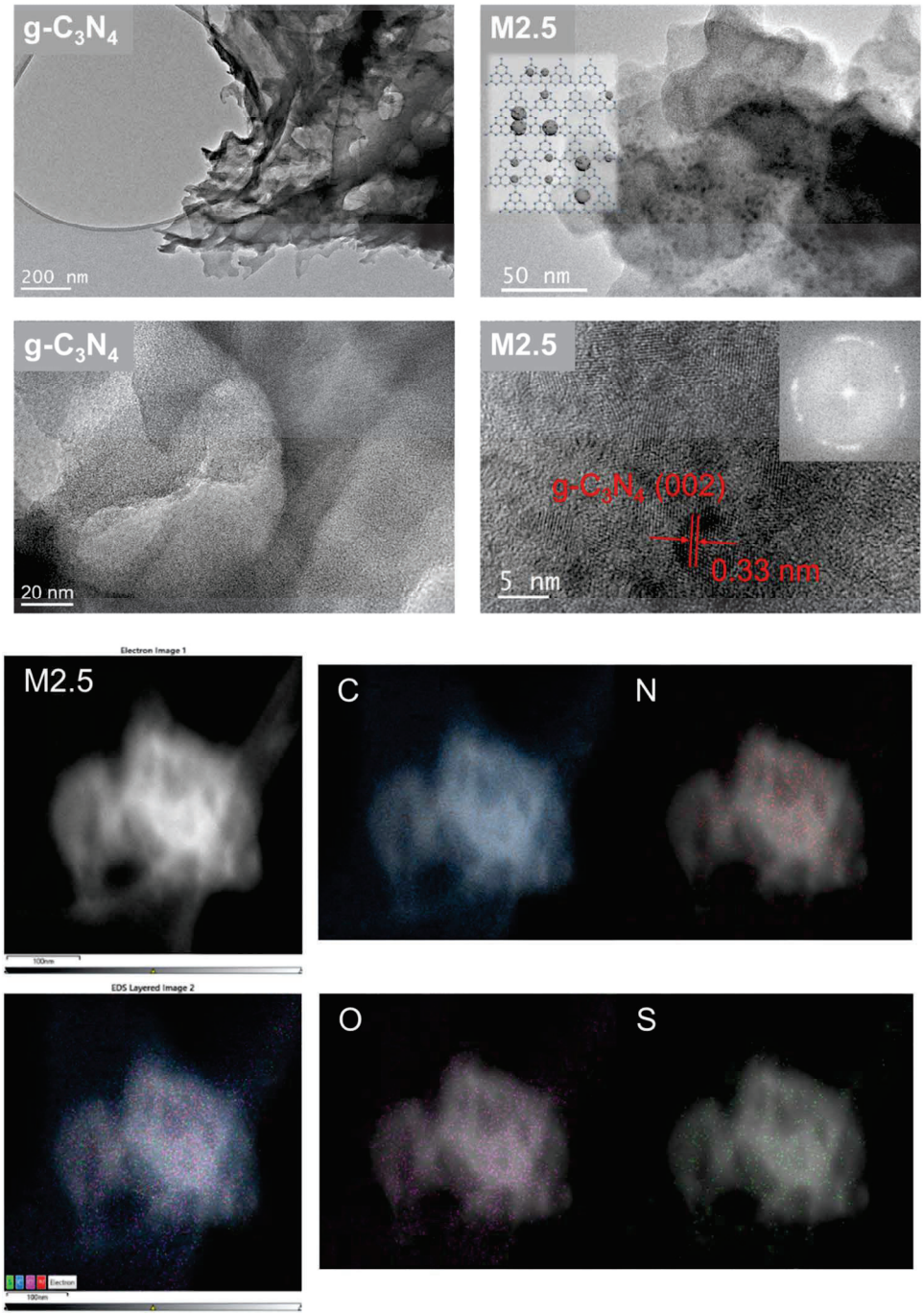

Figure S7. TEM and HRTEM images of M2.5 (with FFT in the inset) and g-C_3N_4 samples, and site of interest along with EDS elemental mapping showing the distribution of C, N, O, and S for the M2.5 sample.

SUPPLEMENTARY MATERIAL

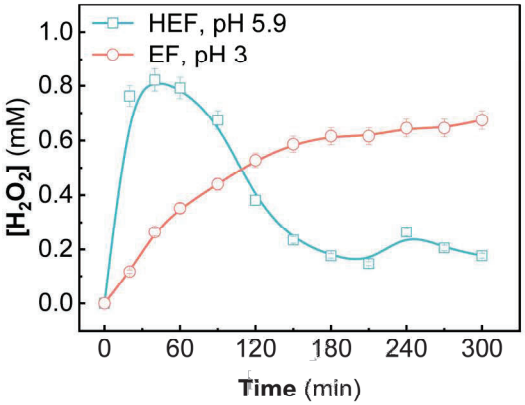

Figure S8. H_2O_2 concentration accumulated in an undivided 2-electrode cell over the electrolysis time. Conditions: same as in Fig. 7a (i.e., GDE made by drop-casting the M2.5 electrocatalyst with loading of 0.1 mg cm^{-2}), but in the presence of a catalyst to carry out Fenton's reaction: 0.1 g L^{-1} of Cu/C as the heterogeneous catalyst at natural pH 5.9, or 0.5 mM Fe^{2+} as the catalyst at pH 3.

4.1.3 Polymethylhydrosiloxane-modified gas-diffusion cathode for more efficient and durable H_2O_2 electrosynthesis in the context of water treatment

In the two previous studies, we have explored several metal and metal-free electrocatalysts for electrochemical H_2O_2 synthesis under near-neutral conditions. Building on this, the present study focuses on the modification of PTFE-GDEs with trace amounts of PMHS to enhance both the O_2 permeability and H_2O_2 selectivity. Following a rational design, it was presumed that the -CH_3 groups in PHMS could provide stable superhydrophobicity, while the -Si-H bonds and Si-O-C groups were intended to introduce new active sites, eventually optimizing the H_2O_2 production efficiency and improving the catalyst layer durability. Therefore, this work not only addresses the improvement of the electrocatalytic properties, but also the enhancement of the integration of such electrocatalysts into the GDEs.

Trace PMHS addition enabled the Si-O-C bonding on the carbon black surface, forming a superhydrophobic interface with Si-H and Si-O-C sites. The -CH_3 groups in PMHS increased the electrode water contact angle from 104.5° to 148.3°, thereby enhancing the O_2 permeation required for a better $2e^-$ ORR. SEM and EDX mapping showed a uniform PTFE/PMHS catalytic layer (~547.1 μm) with well-dispersed C, F, O, and Si elements. XPS analysis confirmed the incorporation of PMHS onto the GDE surface. In PMHS-free GDEs, peaks for C 1s, O 1s, and F 1s appeared, with O 1s linked to oxygen groups like C-OH and C=O from carbon black. Upon PMHS addition, Si 2p and Si 2s peaks at 103.4 eV and 154.4 eV, respectively, appeared, and the O 1s intensity increased, indicating Si oxidation. High-resolution spectra showed C-Si bonds (from $-Si-CH_3$ of PMHS) and Si-H, Si-C, and Si-O bonds, confirming the formation of Si-O-C moieties and PMHS stable integration into the catalytic layer.

The electrochemical characterization revealed a slight reduction in the ECSA for CB-PTFE/PMHS (8.3 vs 7.5 cm^2) due to decreased catalyst-electrolyte contact from the enhanced hydrophobicity. EIS analysis showed significantly reduced mass transport and charge transfer resistances for CB-PTFE/PMHS (23.6 and 3.8 kΩ, respectively, as compared to 47.5 and 7.6 kΩ for CB-PTFE). This improvement is attributed to the -Si-H and Si-O-C groups of PMHS that enhanced the O_2 transport and electron transfer. LSV results indicated an optimal ORR

performance for the catalyst with a PMHS/PTFE ratio of 0.038, achieving the most positive onset potential (0.56 V vs RHE) and highest cathodic current density (-0.42 mA cm^{-2}). RRDE measurements showed an electron transfer number near 2 (approximately 2.4) and H_2O_2 selectivity of 80% for CB-PTFE/PMHS, clearly superior to CB-PTFE (45%). In a continuous 3-h test, the current density for CB-PTFE/PMHS remained above 80%, outperforming CB-PTFE (45.8%).

To optimize the H_2O_2 production in an undivided cell with a Ti|IrO_2 anode, GDEs with various PTFE/CB ratios were tested, with the optimal ratio of 3 yielding 1087.4 mg L^{-1} of H_2O_2 after 360 min. This setup balanced the stability and O_2 transport, overcoming the active site blockage. The PTFE/PMHS-GDE with a 0.038 PMHS/PTFE ratio achieved even higher H_2O_2 production (1874.8 mg L^{-1}), underscoring the role of PMHS in enhancing the performance. Alternative modifiers such as PDMS-NH_2 and PDMS-Cl showed lower H_2O_2 yields, highlighting the key importance of Si-H bonds for H_2O_2 generation.

An optimal H_2O_2 production occurred within a pH range of 3-9, declining at pH 11 due to rapid H_2O_2 decomposition. Higher current densities also increased H_2O_2 output without the faradaic efficiency drop seen in other GDEs, making the PTFE/PMHS-GDE promising for industrial applications. Long-term testing over 10 cycles showed a sustained H_2O_2 production with only a 22.7% decrease, compared to a 36.5% reduction in PTFE-GDE, confirming the PTFE/PMHS-GDE stability and high hydrophobicity retention.

After confirming the high H_2O_2 production and durability of the PTFE/PMHS-GDE, its effectiveness for EF treatment of eight common organic micropollutants was assessed. Initially, the influence of Fe^{2+} dosage and current density on 2,4-DCP degradation was examined. Higher Fe^{2+} levels (0.2-0.3 mM) accelerated the degradation, achieving complete removal in 50 min, with the rate constant rising from 0.028 to 0.095 min^{-1}. Similarly, increased current density boosted the degradation rate, peaking at 37.5 mA cm^{-2} with a rate constant of 0.117 min^{-1}, though an excessive H_2O_2 concentration at 50 mA cm^{-2} slightly inhibited the $^{\bullet}OH$ efficiency.

Further tests with seven additional micropollutants showed around 90% removal within 20 min for most, except for 2,4-DCP and diclofenac sodium,

likely due to structural resistance to $^{\bullet}OH$. The PTFE/PMHS-GDE outperformed the conventional PTFE-GDE in all cases, underscoring its potential as a cathode for efficient EF-based wastewater treatment.

To better elucidate the role of PMHS in enhancing the $2e^-$ ORR, DFT calculations were conducted by our colleagues in Dr. Ye's group in China, aiming to assess the Gibbs free energies of each ORR step and charge distributions on graphene and PMHS@Graphene structures. In the $2e^-$ ORR pathway producing H_2O_2, the OOH* generation and retention are crucial, since the O-O bond cleavage in this intermediate species favors the competing $4e^-$ route. The Gibbs free energy required to form OOH* (ΔG_{OOH*}) on PMHS@Graphene was significantly lower than on sole graphene (0.02 vs. 0.23 eV), indicating that PMHS promotes the OOH* formation. Conversely, the ΔG for *OOH conversion to *O (ΔG_{*O}) was more positive on PMHS@Graphene, inhibiting the $4e^-$ ORR pathway. Further, the OOH* adsorption-free energy analyses showed that the Si-H site closely aligned with the ideal $2e^-$ ORR energy, suggesting a weak OOH* adsorption that supports the selective H_2O_2 production. Additionally, charge density analysis revealed the electron accumulation around Si sites in PMHS, modulating the local electric field and enhancing the electron transfer. These results confirm that Si-H and Si-O-C sites in PMHS not only act as active sites but also optimize the electron transfer for an efficient $2e^-$ ORR.

Applied Catalysis B: Environmental 343 (2024) 123467

Contents lists available at ScienceDirect

Applied Catalysis B: Environmental

journal homepage: www.elsevier.com/locate/apcatb

Polymethylhydrosiloxane-modified gas-diffusion cathode for more efficient and durable H_2O_2 electrosynthesis in the context of water treatment

Pan Xia [a], Lele Zhao [b], Xi Chen [a], Zhihong Ye [a,*], Zhihong Zheng [a], Qiang He [a], Ignasi Sirés [b,*]

[a] Key Laboratory of Eco-environments in Three Gorges Reservoir Region, Ministry of Education, College of Environment and Ecology, Chongqing University, Chongqing 400045, China

[b] Laboratori d'Electroquímica dels Materials i del Medi Ambient, Departament de Ciència de Materials i Química Física, Secció de Química Física, Facultat de Química, Universitat de Barcelona, Martí i Franquès 1–11, 08028 Barcelona, Spain

ARTICLE INFO

Keywords:
Electro-Fenton process
Gas-diffusion electrode
Electrocatalytic hydrogen peroxide synthesis
Oxygen reduction reaction
Siloxane

ABSTRACT

On-site H_2O_2 electrosynthesis via two-electron oxygen reduction reaction (ORR) is attracting great interest for water treatment. The use of carbon black-based gas-diffusion electrodes (GDEs) is especially appealing, but their activity, selectivity and long-term stability must be improved. Here, a facile GDEs modification strategy using trace polymethylhydrosiloxane (PMHS) allowed reaching a outstanding H_2O_2 production, outperforming the conventional polytetrafluoroethylene (PTFE)-GDE (1874.8 vs 1087.4 mg L^{-1} at 360 min). The superhydrophobicity conferred by PMHS endowed the catalytic layer with high faradaic efficiencies (76.2%–89.7%) during long-term operation for 60 h. The electrochemical tests confirmed the high activity and selectivity of the PMHS-modified GDE. Moreover, the efficient degradation of several micropollutants by the electro-Fenton process demonstrated the great potential of the new GDE. An in-depth understanding of the roles of PMHS functional groups is provided from DFT calculations: the $-CH_3$ groups contribute to form a superhydrophobic interface, whereas Si-H and as-formed Si-O-C sites modulate the coordination environment of active carbon centers.

1. Introduction

Hydrogen peroxide (H_2O_2), an eco-friendly and versatile oxidant with only H_2O and O_2 as by-products, has been intensively employed for environmental remediation, as well as in medical disinfection or industrial bleaching and synthesis [1–3]. Nonetheless, critical risks associated with transportation, storage and manipulation of H_2O_2 pose extraordinary technological and economic challenges that limit its application [4,5]. In addition, the anthraquinone process for industrialized production of H_2O_2 has serious limitations, such as high-energy consumption and substantial waste generation [6]. In this context, the in-situ electrosynthesis of H_2O_2 via the two-electron oxygen reduction ($2e^-$ ORR) opens up a new avenue to the H_2O_2 market [7,8].

The electro-Fenton process (EF), one of the most popular advanced technologies for wastewater treatment, combines the merits of both Fenton's reaction and $2e^-$ ORR [9,10]. Its successful implementation at large scale highly relies on the cathodic H_2O_2 yield. For this, molecular oxygen must be efficiently reduced to H_2O_2 via the so-called $2e^-$ pathway (Reaction (1)), which occurs upon co-existence of a triple phase (i.e., O_2 gas and hydrated proton at the catalytic surface site) during the electron supply. Therefore, the gas-liquid-solid balance at the three-phase boundary is of paramount importance for efficient H_2O_2 production [8,11]. Carbonaceous materials are usually preferred as the electrocatalyst in EF due to their favorable activity and H_2O_2 selectivity, low cost, and moderate durability at low-medium current [12–14].

In recent years, most efforts to improve the cathodic H_2O_2 yield have focused on the enhancement of O_2 mass transport, electron transfer, and H_2O_2 selectivity [15,16]. For this purpose, the gas-diffusion electrode (GDE) architecture is widely employed [12,17,18]. The utilization of a GDE as the cathode minimizes the barrier to O_2 permeation through the cavities to the catalytic sites, overcoming the low solubility (8 mg L^{-1}) and poor diffusion rate of O_2 that are inherent to immersed cathodes [3]. However, even with GDEs, the production of H_2O_2 cannot reach its maximum during long-term operation [19], which is partly caused by flooding due to insufficient hydrophobicity, leading to the inactivation of the catalytic layer [19–21]. On the other hand, due to the competing scaling relationship between the $2e^-$ ORR (Reaction (1)) to form H_2O_2 and the $4e^-$ ORR (Reaction (2)) to generate H_2O, the strategies aimed at

* Corresponding authors.
E-mail addresses: yezhihong@cqu.edu.cn (Z. Ye), i.sires@ub.edu (I. Sirés).

https://doi.org/10.1016/j.apcatb.2023.123467
Received 22 August 2023; Received in revised form 9 October 2023; Accepted 2 November 2023
Available online 4 November 2023
0926-3373/© 2023 The Author(s). Published by Elsevier B.V. This is an open access article under the CC BY-NC-ND license (http://creativecommons.org/licenses/by-nc-nd/4.0/).

improving the former frequently enhance the $4e^-$ pathway as well [22,23].

$$O_{2(g)} + 2\,H^+ + 2\,e^- \rightarrow H_2O_2 \quad (1)$$

$$O_{2(g)} + 4\,H^+ + 4\,e^- \rightarrow 2\,H_2O \quad (2)$$

The construction of stable superhydrophobic three-phase boundaries in GDEs has been proven a successful approach to increase the O_2 utilization efficiency and decrease the cathode flooding. In 2015, Yu and co-workers employed polytetrafluoroethylene (PTFE) as hydrophobizing material to fabricate a water-proof GDE, obtaining a 10.7-fold increase in H_2O_2 concentration at 60 min under an optimal PTFE/carbon black (CB) mass ratio of 5 [24]. In such cathode, the hydrophobic sites confine the O_2 bubbles, thereby feeding the hydrophilic sites where the $2e^-$ ORR occurs in the presence of hydrated protons. Significant efforts have been further made to regulate the hydrophilicity/hydrophobicity ratio. Zhang et al. claimed that a CB-to-PTFE ratio of 5:3 yielded the highest H_2O_2 production efficiency [25], whereas He et al. reported that the yield of H_2O_2 varied insignificantly when the mass ratio of graphite to PTFE was decreased [26]. However, although the introduction of PTFE seems to be a facile and effective way to enhance the O_2 supply and avoid excessive water transport into the pores, it may block the catalytic sites.

The development of selective electrocatalysts to ensure both, the systematic control of the $2e^-$ ORR route and the improvement of their catalytic activity, is another effective strategy to synthesize H_2O_2. The $2e^-$ ORR associative pathway proceeds through two main steps, namely O_2 activation (Reaction (3)) and further reduction of the *OOH intermediate (Reaction (4)). In contrast, the competitive $4e^-$ ORR pathway involves three reaction intermediates (*OOH, *O, and *OH) [27]. Therefore, H_2O_2 can be selectively formed if one can ensure that *OOH is the only intermediate [28], and it is neither too strongly nor too weakly bound to the catalyst surface, aiming at preventing the O–O bond dissociation, as has been determined via density functional theory (DFT) calculations [29]. So far, a wide range of electrocatalysts has been designed to fabricate GDEs with enhanced $2e^-$ ORR activity/selectivity, including modified carbon materials, non-noble metal-nitrogen moieties, molecular complexes, and single-atom catalysts [3,8,18]. These electrocatalysts may play one or several roles [30–33]. Nonetheless, these catalyst layers usually own weak bonds and low tolerance to acidic conditions. As a result, they can be gradually dissolved, especially during long electrolytic trials, causing severe electrode deactivation.

$$* + O_{2(g)} + H^+ + e^- \rightarrow *OOH \quad (3)$$

$$*OOH + H^+ + e^- \rightarrow * + H_2O_2 \quad (4)$$

Recently, silicon derivatives have been proposed as surface modifiers to improve water proof and O_2 transport for H_2O_2 production [20]. Among these compounds, polysiloxanes have demonstrated their utility in fabricating O_2-selective membranes for Li-air batteries with low water transport [34]. In particular, polymethylthydrosiloxane (PHMS, $-(CH_3(H)Si-O)-$), a non-toxic and easy-to-handle hydride source, has been widely employed as hydrophobic modifier as well as catalytic center in chemical synthesis and membrane separation, since it can be chemically attached to the surface of substrates while retaining the functional groups for further catalytic reactions [35,36]. PMHS contains a large number of $-CH_3$ and $-Si-H$ groups. The former own low surface energy, becoming optimum to construct highly hydrophobic interfaces [37–39]. For instance, Liu et al. prepared a filter paper/PMHS hybrid with a surface water contact angle ranging from 9.0° to 131.8° by regulating the PMHS dosage [40]. On the other hand, the $-Si-H$ groups may serve as chemical links to react with the unsaturated C=C or HO-C bonds of substrates, resulting in the formation of Si-O-C moieties. Wójcik-Bania et al. reported the in-situ reduction of Pt^{4+} from $PtCl_4$ solution to Pt^0 by the Si-H moieties of the siloxane backbone of PHMS under an inert atmosphere [41]. Moreover, it has been proven that Si-doped graphene material is a promising $4e^-$ ORR catalyst due to the presence of abundant Si-O sites, which favors the adsorption and dissociation of O_2 [42,43].

Only very recently, the potential combination of polysiloxanes and hydrophobic perfluorinated polymers has been suggested as a promising strategy for the fabrication of gas-diffusion layers, although it has been not explored in the context of the $2e^-$ ORR [44]. Inspiringly, the present study focuses on the utilization of trace PMHS to modify PTFE-GDEs, for the first time, aiming at synchronously enhancing the O_2 permeability and H_2O_2 selectivity for ORR. The $-CH_3$ groups of PHMS are expected to confer stable superhydrophobicity to the catalytic interface, whereas the Si-H bonds, as well as the as-formed Si-O-C moieties, might serve as new active sites to enhance the $2e^-$ ORR.

2. Materials and methods

2.1. Chemicals

2,4 Dichlorophenol (2,4-DCP) and naproxen (NPX) were purchased from Aladdin Biological Technology Co., Ltd. (Shanghai, China). Analytical grade Na_2SO_4, H_2SO_4 (95% solution), NaOH pellets, and $FeSO_4 \cdot 7\,H_2O$ were supplied by Chengdu Kelong Chemical Co., Ltd. (Chengdu, China). Bisphenol A (BPA), ciprofloxacin (CIP), amoxicillin (AMX), diclofenac sodium (DCF), Rhodamine B (RhB), Methyl Orange (MO), poly(dimethylsiloxane)etherimide (PDMS-NH_2), 1,3-bis-(dichloromethyl)– 1,1,3,3-tetramethyldisiloxane (PDMS-Cl) and polymethylhydrosiloxane (PDMS-H or PMHS) were acquired from Macklin Technology Co., Ltd. (Shanghai, China). Nafion (5 wt% suspension in lower aliphatic alcohol) was purchased from Sigma-Aldrich (Shanghai, China). PTFE emulsion (60 wt%) was purchased from Hesen Co., Ltd. (Henan, China). 1,10-Phenanthroline monohydrate, L(+)-ascorbic acid and $TiOSO_4$ were used for colorimetric analyses. Solvents and other reagents were supplied by Merck and Chengdu Kelong Chemical Co., Ltd. (Chengdu, China). Unless otherwise specified, all chemicals were of analytical grade and used as received, and all solutions were prepared with deionized water (resistivity higher than 18.2 MΩ·cm, Millipore Milli-Q system).

2.2. Cathode preparation

The gas-diffusion electrode consisted of a mixture of carbon black and PTFE, with or without PMHS modification, acting as catalytic and gas-diffusion layers that served to coat a carbon cloth substrate (Fig. 1a). To prepare the GDE, commercial cloth with a geometric area of 9 cm^2 was ultrasonically cleaned in deionized water and ethanol, each for 30 min, and then dried at 80 °C for 12 h. Then, 200 mg carbon black, 0.685 mL PTFE (60 wt% emulsion) and a certain amount of PMHS were uniformly dispersed in 10 mL ethanol using an ultrasonic bath for 30 min, followed by heating at 80 °C until the mixture turned into a paste. The ointment was coated onto the pretreated carbon cloth substrate, followed by pressing at 5 MPa. The resulting electrode was dried and calcined at 350 °C for 120 min to obtain the PTFE/PMHS-GDE. For comparison, the same manufacturing procedure was carried out in the absence of PMHS, giving rise to the conventional PTFE-GDE.

2.3. Performance evaluation and analytical methods

The electrolytic trials were carried out under continuous stirring in a single-compartment glass cell containing 160 mL of solution equipped with an IrO_2-based dimensionally stable anode (DSA) plate (3 cm^2) from NMT Electrodes and one of the as-prepared GDEs as the cathode. The interelectrode gap was 1.0 cm, and the GDE was fed with air at 1 L min^{-1} for permanent H_2O_2 electrogeneration. The trials were carried out galvanostatically by supplying a constant current from a high-stability DC voltage controller (IT6302 from ITECH, China). In EF trials, a salt was employed as Fe^{2+} source that served as Fenton's catalyst.

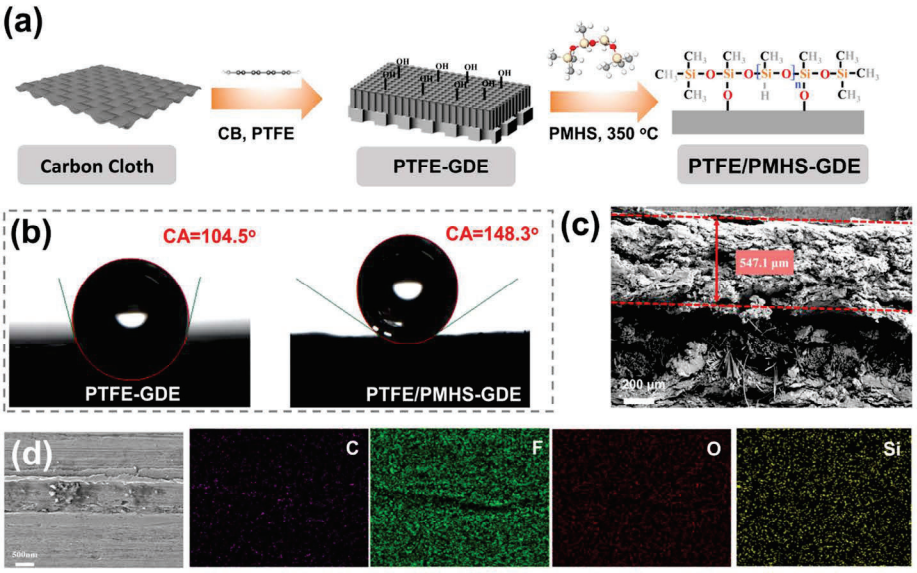

Fig. 1. (a) Schematic illustration of PTFE/PMHS-GDE fabrication. (b) Contact angle of conventional PTFE-GDE and novel PTFE/PMHS-GDE. SEM images of (c) cross-section and (d) surface of PTFE/PMHS-GDE, with the corresponding surface EDS elemental mapping.

Samples were collected at different time intervals, being immediately mixed with NaOH to quench the reaction and then filtered with 0.2 μm PTFE syringe filters. The solution pH was determined using a PHS-3 C pH-meter. The accumulated H_2O_2 concentration was measured colorimetrically, by mixing the collected sample with an acidic Ti(IV) solution and then setting the UV/Vis spectrophotometer (UNIC, UV2365, China) at $\lambda = 408$ nm. The Faradaic efficiency (FE) for H_2O_2 generation was calculated from Eq. (5) [30].

$$\mathrm{FE(in\%)} = \frac{2C_{H_2O_2}FV}{\int_0^t I\mathrm{d}t} \times 100 \tag{5}$$

where F is the Faraday constant (C mol^{-1}), C is the concentration of H_2O_2 (mol L^{-1}), V is the solution volume (L), I is the applied current (A), and t is the reaction time (s).

The concentration of micropollutants was determined on a reversed-phase high-performance liquid chromatograph (HPLC, SCION6000, China) equipped with a Chromcore C18 (5 μm, 4.6 mm × 250 mm) column and a photodiode array SC6000 detector. The mobile phase was a mixture of CH_3OH and 10 mM KH_2PO_4 solution at pH 4.0 (80:20 (v/v)) that was eluted at 1.0 mL min^{-1}.

2.4. Characterization and electrochemical tests

The morphology and elemental composition of the GDEs were analyzed by SEM-EDX, which was conducted on a ZEISS Gemini 300 SEM microscope coupled to a Smartedx detector operated in backscattering electron mode at an acceleration voltage of 15 kV. The chemical composition and state were determined by XPS on a Thermo Scientific K-alpha system with Al Kα radiation at a high voltage of 12 kV, calibrated internally using the C 1 s ($E_b = 284.80$ eV). The hydrophobicity of the GDEs was investigated by measuring the water contact angle on an interface tension meter (SDC-100S).

Cyclic voltammetry (CV), linear sweep voltammetry (LSV) and electrochemical impedance spectroscopy (EIS) were conducted on an electrochemical workstation (CHI 760E, Chenhua, Shanghai), equipped with a three-electrode cell that comprised a working electrode (glassy carbon, 3-mm disk), Ag/AgCl (saturated KCl) as reference electrode, and a Pt sheet as counter electrode. The catalyst ink (CB-PTFE/PMHS) was prepared by dispersing carbon black (10 mg) in a solvent mixture consisting of 800 μL of H_2O + 200 μL of isopropanol + 50 μL of Nafion (5 wt% suspension) + 50 μL of PTFE (60 wt% suspension), and a certain amount of PMHS, followed by 30 min sonication. Subsequently, 10 μL of catalyst ink were drop-casted onto a glassy carbon electrode, resulting in a catalyst loading of ~1.4 mg cm^{-2}. For comparison, the CB-PTFE ink was prepared using the same procedure but in the absence of PMHS. LSV measurements were performed in O_2-saturated 0.05 M Na_2SO_4 aqueous solution at room temperature at a scan rate of 10 mV s^{-1} within the potential range from 0.6 to − 0.4 V vs RHE. EIS analysis was made in the frequency domain from 0.01 Hz to 100 kHz at an alternating current signal amplitude of 5 mV. Cyclic voltammograms were obtained in $Fe(CN)_6^4$ + $Fe(CN)_6^3$ (each at 0.01 M) aqueous solution with a scan rate of 10 mV s^{-1}, within a range from − 0.2–1.4 V vs RHE, and the electrochemical surface area (ECSA) was calculated from the Randles-Sevcik Eq. (6) [11].

$$I_p = 2.69 \times 10^5\, ACD^{1/2}n^{3/2}\nu^{1/2} \tag{6}$$

where I_p is the oxidation peak current (A), A is the area of the electrode (cm^2), C is the concentration of the electroactive species (= 0.01 M of $[Fe(CN)_6]^{4-}$ + $[Fe(CN)_6]^{3-}$), n is the number of electrons transferred contributing to the redox reaction (= 1 in this case), D is the diffusion coefficient, and ν is the scan rate (V s^{-1}).

The 2e$^-$ ORR activity and selectivity were evaluated by RRDE (5-mm glassy carbon disk, Pt ring) tests in 0.10 M O_2-saturated Na_2SO_4 electrolyte. In RRDE experiments, the ring potential (E_{ring}) was set to 1.54 V vs RHE. The H_2O_2 selectivity (in %) and electron transfer number (n) of the catalysts were determined based on the current of both disk (I_D) and ring (I_R) electrodes (Eqs. (7) and (8), respectively) [30].

$$H_2O_2(\%) = 200\frac{I_R}{NI_D + I_R} \tag{7}$$

$$n = 4\frac{I_D}{I_D + I_R/N} \tag{8}$$

where N, representing the empirical collection efficiency, was calculated by measuring the ratio between the ring limiting current and the disk

limiting current obtained from LSV tests in an N_2-saturated 10 mM $K_3Fe(CN)_6$ + 1 M KCl solution, resulting in a value of $N = 0.276$.

2.5. Computational details

Structural modeling and DFT calculation were carried out using the Vienna ab initio simulation package (VASP), considering the generalized gradient approximation (GGA) and the Perdew-Burke-Ernzerhof (PBE) functional. To describe ionic cores, the projector augmented wave (PAW) pseudo-potentials were employed. A plane-wave basis set, with a kinetic-energy cut-off of 400 eV, was used to expand the wave function of valence electrons. Van der Waals interactions were described by means of the DFT-D3 empirical correction method. The geometry optimization was terminated once the force convergence was smaller than 0.05 eV $Å^{-1}$. Monkhorst-Pack k-points of 1 × 1 × 1 were applied for all calculations.

3. Results and discussion

3.1. Characterization of PTFE/PMHS-GDE

Upon addition of a trace amount of PMHS, the hydroxyl groups on the CB surface react with the Si-H bonds to form Si-O-C moieties, thus ensuring a strong chemical bonding of PMHS chains to the electrode surface. This gives rise to a superhydrophobic interface that retains abundant Si-H and Si-O-C sites [35,40]. As a result of the introduction of low surface energy $-CH_3$ groups of PMHS, the water contact angle of the electrode significantly increased from 104.5° to 148.3°, which could greatly favor the O_2 permeation during the $2e^-$ ORR (Fig. 1b). The cross-section SEM image of the PTFE/PMHS-GDE in Fig. 1c allows distinguishing a dense skin (top layer) with a thickness of about 547.1 μm, which can be attributed to the PTFE- and PMHS-rich catalytic layer immobilized on the carbon cloth. In addition, the SEM image of the surface in Fig. 1d shows a relatively smooth catalytic interface with several wrinkles, and the corresponding EDS-mapping reveals the uniform distribution of C, F, O and Si in the as-prepared GDE, suggesting the homogeneous dispersion of both polymers throughout the CB layer.

XPS analysis was performed to determine the chemical composition at the surface of GDEs with and without PMHS. Fig. 2a shows three peaks assigned to C 1*s*, O 1*s* and F 1*s* in the spectrum of PMHS-free GDE. The presence of O 1*s* is attributed to diverse oxygen functional groups, such as C-OH and C=O, formed on the surface of CB during the air thermal treatment, in addition to the intrinsic oxygen functionalities [45,46]. After the introduction of PMHS, new signals attributed to Si 2*p* and Si 2*s* emerged at 103.4 eV and 154.4 eV, respectively, whereas the peak intensity of O 1*s* dramatically increased. These results confirm the successful incorporation of PMHS onto the catalytic interface of the GDE. Note also that the peak intensity of O 1*s* is much higher than that of Si, which can be explained by the increased oxidation states of Si in the immobilized PMHS chains [40]. More specifically, the high-resolution C 1*s* spectrum of the PTFE/PMHS-GDE (Fig. 2b) has been deconvoluted into five peaks centered at 283.9, 284.8, 285.7, 286.7 and 292.4 eV, assigned to C-Si, C-C, C-O, C=O and C-F bonds, respectively. The former bond can be related to the $-Si-CH_3$ of PMHS [47]. The deconvolution of the O 1*s* spectrum yields three peaks: C=O, C-O, and Si-O at 535.07, 534.03 and 533.29 eV, respectively (Fig. 2c) [48]. As mentioned above, the oxidation of CB gave rise to some oxygen functional groups, such as C=O and C-O, which can favor the adsorption of O_2 molecules during ORR. Moreover, the characteristic Si 2*p* signal was deconvoluted into three peaks at 102.7, 103.5 and 104.4 eV, attributed to Si-H (18.34%), Si-C (54.05%) and Si-O (27.57%) bonds, respectively (Fig. 2d) [49]. The formation of Si-O bonds demonstrates the conversion of partial Si-H bonds to Si-O-C moieties during the synthesis, corroborating the tight chemical attachment of PMHS in the catalytic layer.

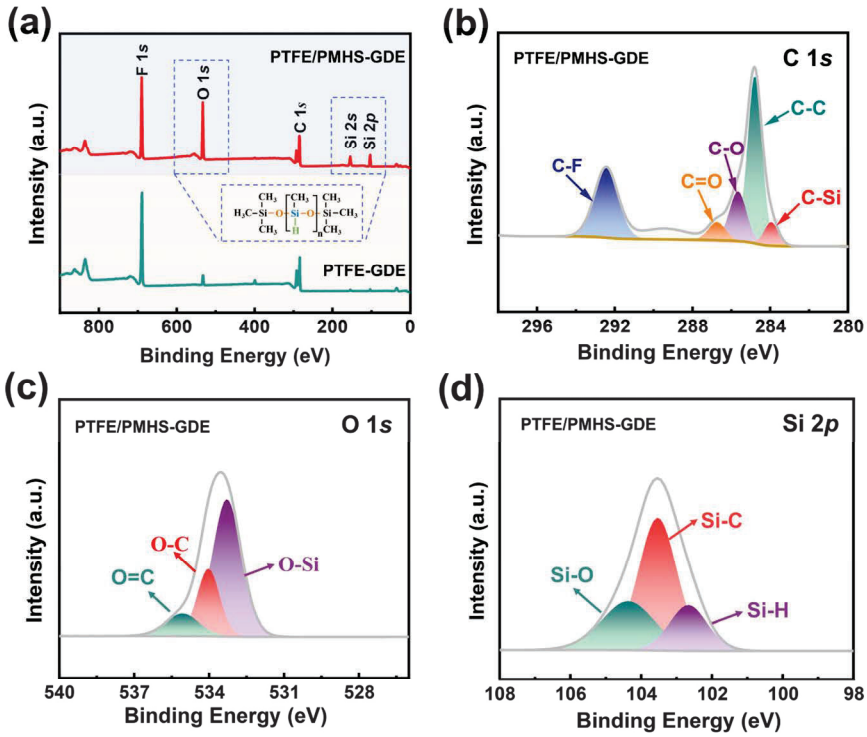

Fig. 2. (a) XPS full spectra of conventional PTFE/GDE and novel PTFE/PMHS-GDE. High-resolution XPS spectra of (b) C 1*s*, (c) Si 2*p*, and (d) O 1*s* of PTFE/PMHS-GDE.

3.2. Electrocatalytic ORR activity of PTFE/PMHS-GDE

First, the cyclic voltammograms for the $[Fe(CN)_6]^{3-}/[Fe(CN)_6]^{4-}$ redox system were recorded to evaluate the electrochemically active surface area (ECSA) of the synthesized materials. As illustrated in Fig. 3a, the CB-PTFE electrocatalyst had slightly greater oxidation and reduction peak current densities (see also Table S1), which led to a slightly higher area than the CB-PTFE/PMHS (8.3 vs 7.5 cm^2). The ECSA represents the area that is accessible to the electrolyte and hence, it can be concluded that the great increase of hydrophobicity (Fig. 1b) caused by PHMS leads to a smaller contact between the catalytic layer and electrolyte [16]. Nonetheless, the formation of the superhydrophobic three-phase boundary turned out to be beneficial for the ORR thanks to the enhanced O_2 permeability, as will be demonstrated below.

Further analysis of the electron/ion transport behavior of the GDEs was conducted by electrochemical impedance spectroscopy (EIS). The Nyquist plots shown in Fig. 3b were fitted to an equivalent circuit model, yielding the values of mass transport resistance (R_{mt}) and charge transfer resistance (R_{ct}). Surprisingly, the introduction of a trace amount of PMHS into the CB-PTFE gave rise to extremely low R_{mt} and R_{ct} values. The abundant $-CH_3$ groups in PHMS created a hydrophobic interface without significant destruction of the porous structures, which is excellent for promoting the O_2 transport. Moreover, the Si-H and Si-O-C bonds arising from PHMS incorporation may accelerate the electron transfer on the catalytic interface, leading to the reduction of R_{ct}. Consequently, the CB-PTFE/PMHS particles displayed much lower R_{mt} and R_{ct} values (23.6 and 3.8 kΩ) than the CB-PTFE (47.5 and 7.6 kΩ), demonstrating the enhancement of both mass and electron transports (Table S1). Fig. 3c displays the linear sweep voltammograms of five catalysts with different PMHS content for ORR in 0.05 M Na_2SO_4 aqueous solution. The catalyst with a PHMS/PTFE mass ratio of 0.038 exhibited excellent ORR performance, reaching the most positive onset potential (0.56 V vs RHE) and the highest cathodic current density (-0.42 mA cm^{-2} at -0.4 V vs RHE). Meanwhile, the catalysts with PMHS/PTFE ratios of 0, 0.019, 0.075 and 0.125 achieved more negative onset potentials of 0.36, 0.48, 0.47, 0.45 V vs RHE and lower current densities of -0.20, -0.30, -0.36, -0.28 mA cm^{-2}, respectively. As reported, the current response would be suppressed as the amount of hydrophobic binder is increased, since it can partially block active sites of CB for ORR [24]. In contrast, the introduction of an appropriate

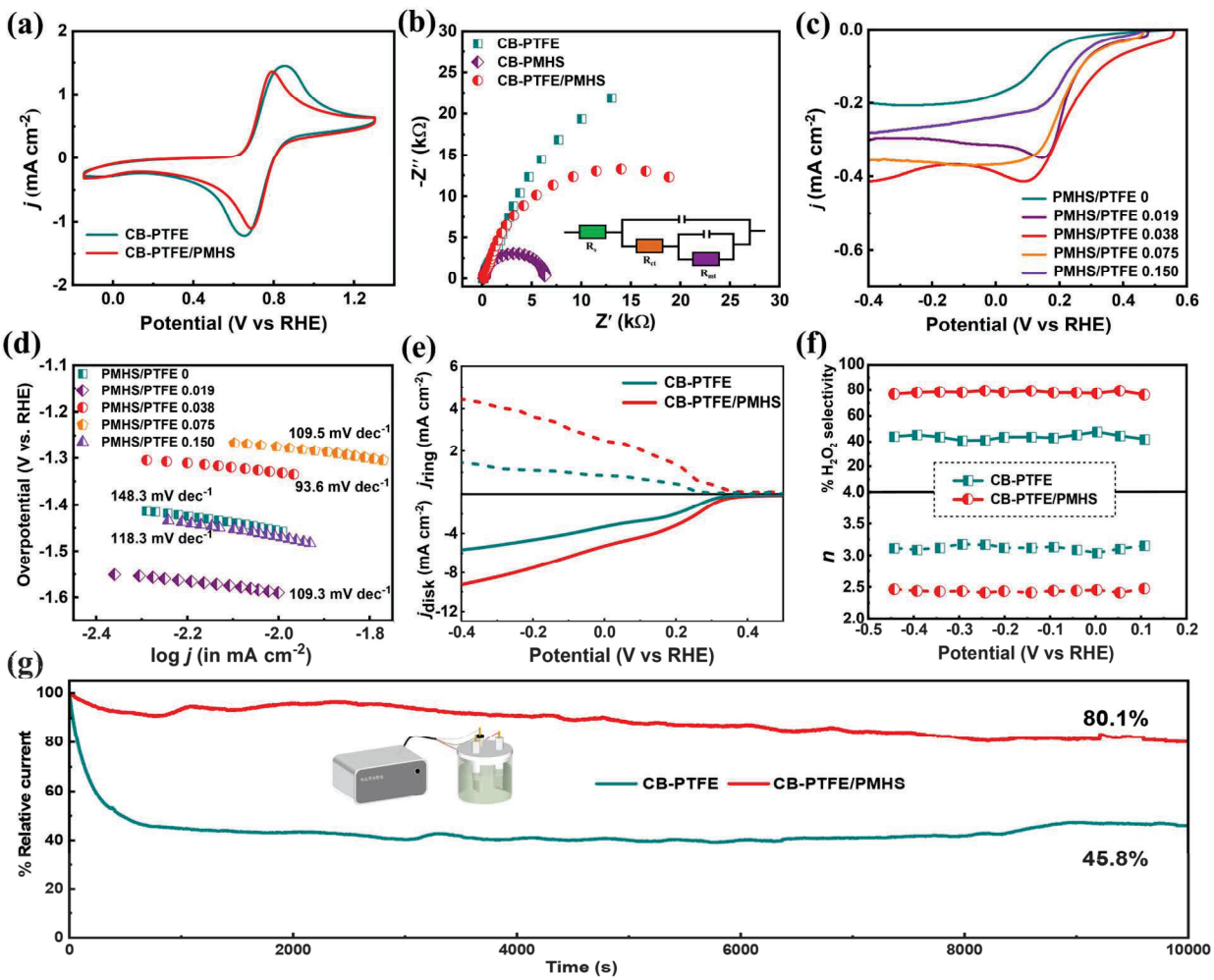

Fig. 3. Electrochemical tests of different catalysts. (a) Cyclic voltammograms obtained in 0.01 M $[Fe(CN)_6]^{3-}$ + 0.01 M $[Fe(CN)_6]^{4-}$ solution at pH 5.2; (b) Nyquist plots; (c) linear sweep voltammograms in 0.05 M Na_2SO_4 solution, and (d) corresponding Tafel plot; (e) RRDE tests in O_2-saturated 0.1 M Na_2SO_4 at pH 6.1 at a scan rate of 10 mV s^{-1} (E_{ring} = 1.54 V vs RHE), and (f) the corresponding H_2O_2 selectivity and electron transfer number (n). and (g) chronoamperometric responses for CB-PTFE and CB-PTFE/PMHS.

amount of PMHS is proven positive. This behaviour agrees with the enhanced mass and charge transfer determined from EIS analysis, attributable to the new Si-H and Si-O-C functional groups that favor the $2e^-$ ORR. At an excessively high PMHS content, the ORR is gradually inhibited due to the reduction of exposed active sites. From these voltammograms, the corresponding Tafel plots for the different catalysts are illustrated in Fig. 3d. A lower Tafel slope suggests a faster electrode reaction at constant operation conditions. As can be observed, the results are consistent with the previous LSV tests, since the smallest Tafel slope of 93.6 mV dec^{-1} was achieved with the PMHS/PTFE ratio of 0.038, implying the best electrochemical performance. Therefore, it can be concluded that the ORR activity of conventional CB/PTFE cathodes can be substantially improved upon simple modification with an appropriate amount of PMHS.

The ORR performance of CB-PTFE and CB-PTFE/PMHS electrocatalysts was further evaluated in O_2-saturated 0.1 M Na_2SO_4 electrolyte using an RRDE at a rotation rate of 1600 rpm. Fig. 3e displays the polarization curves of the two materials, including the O_2 reduction currents detected on the disk (solid lines) and the H_2O_2 oxidation currents measured on the ring (dashed lines). At the disk, much higher current and more positive reduction potential were obtained using the CB-PTFE/PMHS, confirming the enhanced ORR kinetics, in good agreement with the results of Tafel plots. In addition to the higher ORR activity, the electron transfer number calculated from the RRDE results for CB-PTFE/PMHS was around 2.4 (Fig. 3f), which was close to the theoretical value ($n = 2$) required for H_2O_2 formation. The electron transfer number increased to around 3.1 for CB-PTFE. The corresponding H_2O_2 selectivity for the CB-PTFE/PMHS was around 80%, being superior to that of CB/PTFE (less than 45% on average). In addition, even after subjecting the electrode to about 3 h of continuous chronoamperometric measurement at − 0.1 V, the current density at CB-PTFE/PMHS remained above 80.0%, being much higher than that at CB-PTFE (45.8%) (Fig. 3g). This significant difference underscores the robust catalytic ability of CB-PTFE/PMHS. Therefore, the activity, selectivity, and stability towards the $2e^-$ ORR were significantly improved by the introduction of a low amount of PMHS, as a result of the better O_2 mass transport and electron transfer.

3.3. Electrochemical H_2O_2 accumulation and durability tests

A demonstration of the presumed superiority of as-prepared PTFE/PMHS-GDE for H_2O_2 production was carried out in an undivided cell with an IrO_2-based anode. Prior to this, the accumulation of H_2O_2 concentration using conventional PTFE-GDEs with different PTFE/CB mass ratios was determined to optimize the PTFE loading (Fig. S1a). The optimal PTFE/CB ratio was found to be 1, since it yielded a remarkable H_2O_2 production of 1483.7 mg L^{-1}, whereas further rise the PTFE content proved to be detrimental. The water contact angle of the cathode surface gradually increased from 94.3° to 128.5° when the PTFE/CB ratio was risen from 1 to 5 (Fig. S2a), in agreement with the greater hydrophobicity of the GDE interface that is expected to enhance the O_2 permeability. However, the number of active sites decreased concomitantly due to the agglomeration of PTFE during the sintering process [24,50]. On the other hand, despite the outstanding H_2O_2 synthesis performance of the GDEs with PTFE/CB ratios of 1 and 2, such low PTFE loadings resulted in the easy collapse of the catalytic layer, which was structurally unstable in the absence of a greater amount of binder that could sustain the CB particles. Therefore, a moderate PTFE/CB ratio of 3 was selected to provide a sufficient number of stable pore channels for rapid O_2 transport, without compromising the electron transfer, as proven by the good H_2O_2 accumulation of up to 1087.4 mg L^{-1} at 360 min. Based on this and the result discussed in Fig. 3c, the performance of a PTFE/PMHS-GDE fabricated with the optimized PTFE loading and a PMHS/PTFE ratio of 0.038 was evaluated. As depicted in

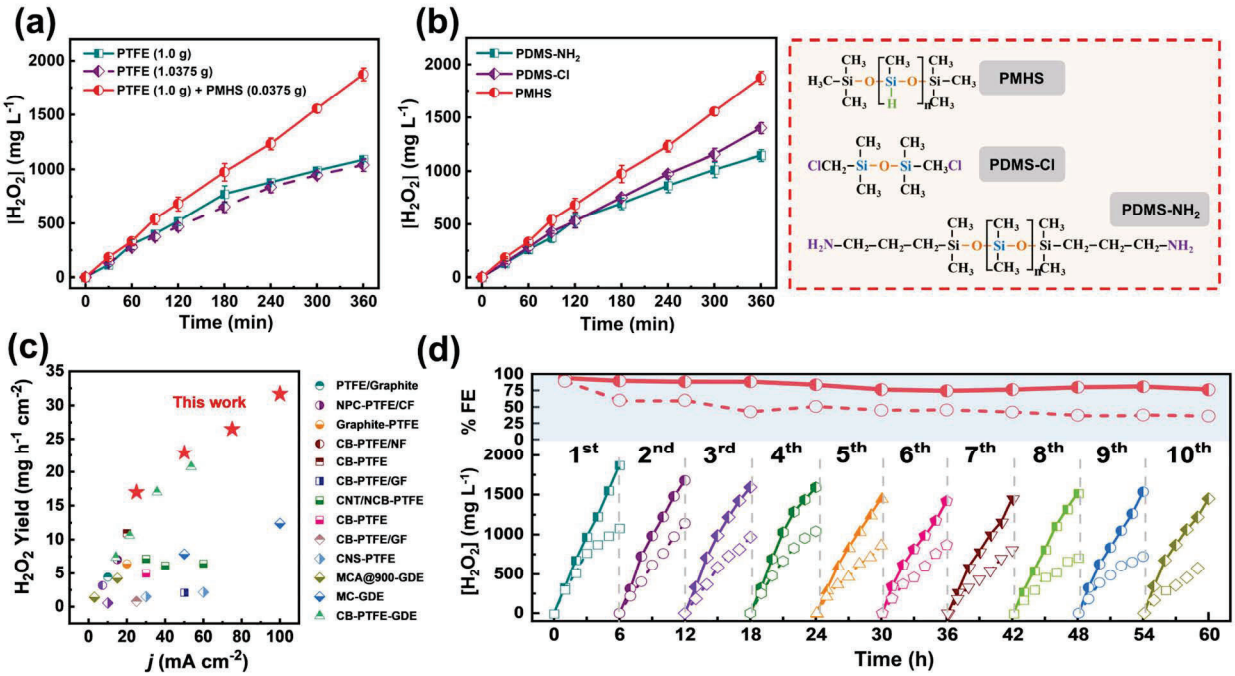

Fig. 4. (a) Comparison of H_2O_2 concentration profiles using conventional two GDEs with different PTFE loadings and a novel PTFE/PMHS-GDE, in 0.05 M Na_2SO_4 at pH 6.1 and 25.0 mA cm^{-2}. (b) H_2O_2 concentration profiles using siloxane-modified GDEs (see structures of the modifiers), under the same conditions described in plot (a). (c) Comparison of the H_2O_2 yield at different current densities with values reported in the literature for carbonaceous cathodes [4,12,25,26,51–57]. (d) Stability test performed with the PTFE-GDE (dashed curves) and the PTFE/PMHS-GDE (solid curves) in ten consecutive runs, each of 6 h duration in 0.05 M Na_2SO_4 at pH 6.1 and 25 mA cm^{-2}.

Fig. 4a, the accumulated H_2O_2 concentration was excellent, attaining up to 1874.8 mg L^{-1} after 360 min, being much higher than that attained with a conventional PTFE-GDE (1087.4 mg L^{-1}). In addition, another GDE was fabricated employing an equivalent amount of PTFE to substitute PMHS, but the result was similar to the latter GDE (Fig. 4a), which corroborates the indispensable role of PMHS in boosting H_2O_2 production.

Aiming to further highlight the relevance of the Si-H bonds, poly (dimethylsiloxane)etherimide (PDMS-NH_2) and 1,3-bis-(dichloromethyl)- 1,1,3,3-tetramethyldisiloxane (PDMS-Cl) with similar molecular structures but different functional groups (see Fig. 4b) were used to prepare modified GDEs, following the same fabrication procedure. As shown in Fig. 4b, the H_2O_2 concentrations accumulated with the PDMS-NH_2-GDE and PDMS-Cl-GDE were 1145.9 and 1401.1 mg L^{-1} at 360 min, respectively, being slightly higher than that attained with the conventional PTFE-GDE but much lower than using the PTFE/PMHS-GDE. These results demonstrate the crucial role of the electron-withdrawing Si-H bonds in the enhancement of H_2O_2 generation.

The effect of several experimental parameters, including relative PMHS content, solution pH, and current density on the H_2O_2 concentration profiles was investigated. The final accumulation of H_2O_2 was substantially improved from 1345.0 to 1874.8 mg L^{-1} with an appropriate increase in the PMHS/PTFE ratio from 0.019 to 0.038, whereas higher loadings of PMHS significantly hampered the H_2O_2 generation (Fig. S1b). This observation is consistent with the maximum water contact angle (148.3°) measured at the PMHS/PTFE ratio of 0.038 (Fig. S2b). A low-to-moderate PMHS loading allows the creation of a superhydrophobic interface that ensures an efficient O_2 supply and the presence of new active sites, but an excess of PMHS significantly decreases the surface hydrophobicity, consequently hindering the O_2 transport. As reported, redundant PMHS can fill the surface concave regions, resulting in a decrease in surface roughness. Note that this kind of correlation between the contact angle and surface roughness has been described for a hydrophobic surface [40]. These findings fully agree with the results presented in Figs. 3c and 3d. The effect of solution pH, between 3.0 and 11.0, on the accumulated H_2O_2 concentration using the PTFE/PMHS-GDE was studied as well. As depicted in Fig. S1c, the H_2O_2 accumulation was very high (1487.6–1874.8 mg L^{-1}) within a wide pH range from 3.0 to 9.0, whereas its values dramatically dropped off to 794.4 mg L^{-1} after 360 min at pH 11.0. This decrease can be attributed to the rapid decomposition of H_2O_2 via the disproportionation Reactions (9) and (10), and the lack of protons required for H_2O_2 electrosynthesis in such a strong alkaline environment [12].

$$H_2O_2 + OH^- \rightarrow H_2O + HO_2^- \quad (9)$$

$$H_2O_2 + HO_2^- \rightarrow H_2O + O_2 + OH^- \quad (10)$$

Current density also has a significant influence on H_2O_2 production. Fig. 4c shows the H_2O_2 yields using the PTFE/PMHS-GDE at different current densities up to 100 mA cm^{-2}, as compared to results reported in the literature for H_2O_2 accumulation with GDEs. It can be observed that the new PTFE/PMHS-GDE exhibits the best $2e^-$ ORR performance among all the GDEs, and the H_2O_2 productivities were progressively enhanced as the applied current was increased. Worth noticing, the H_2O_2 accumulation was only slightly improved or even inhibited with other GDEs at high current density, which has been usually explained from competitive parasitic reactions, such as the $4e^-$ ORR, hydrogen evolution reaction and cathodic H_2O_2 decomposition [12]. Consequently, most of the reported $2e^-$ ORR systems based on GDEs exhibited a dramatic decay of Faradaic efficiency at elevated current density, making them unsuitable for industrial application [58]. In contrast, the PTFE/PMHS-GDE displayed only a slight decrease in efficiency, from 100% to 82.2%, as the current density increased from 25 to 100 mA cm^{-2}, demonstrating the high activity and selectivity of the PTFE/PMHS-GDE towards the H_2O_2 electrosynthesis even at demanding conditions (Fig. S3). This finding is very inspiring and favorable for the industrial scale-up of electrochemical devices, since they frequently require cathodes that can work at high current density.

To inspect the long-term durability of the PTFE/PMHS-GDE, ten consecutive H_2O_2 production trials (each cycle prolonged for 6 h) were conducted at 25 mA cm^{-2}. As depicted in Fig. 4d, the accumulated H_2O_2 concentration was kept at high levels ranging between 1874.8 and 1449.3 mg L^{-1}, accounting for a 22.7% decrease as maximum after the 10 runs. Accordingly, this was accompanied by very high faradaic efficiencies ranging from 89.7% to 76.2%. The decay in performance is attributed to the imbalance between gas and liquid supply to the active sites of the GDE as the electrolysis is prolonged. This causes the gradual flooding of the pores by electrolyte penetration, inactivating some of the catalytic sites upon lack of sufficient O_2 permeation [20]. Despite the observed decline in performance over prolonged exposure, the long-term running performance was superior to that of the PTFE-GDE, which suffered from more severe reductions in both H_2O_2 accumulation (36.5% decrease) and faradaic efficiency (from 89.1% to 36.1%). Additionally, the contact angle of the PMHS-modified cathode underwent only a slight decrease from 148.3° to 125.5° after the consecutive runs, still surpassing that of PTFE-GDE. The preserved superhydrophobic surface ensured efficient O_2 diffusion (Fig. S4). Overall, these results confirm the promising long-term stability of the PTFE/PMHS-GDE, exhibiting great potential for larger-scale H_2O_2 electrosynthesis.

3.4. EF treatment of micropollutants with the PTFE/PMHS-GDE

Once demonstrated that the PTFE/PMHS-GDE is able to boost the H_2O_2 production and perform very well for a long period, its feasibility to conduct the EF treatment of eight target organic micropollutants widely detected in water streams was evaluated. Prior to this, the effect of Fe^{2+} dosage and current density on the EF performance was evaluated for 60 min using a solution containing 20.0 mg L^{-1} 2,4-dichlorophenol (2,4-DCP). As can be seen in Fig. 5a, the decay of 2,4-DCP was enhanced at gradually higher Fe^{2+} dosage, and its total disappearance could be achieved in only 50 min employing 0.2 and 0.3 mM Fe^{2+}. As shown in the inset, the pseudo-first-order rate constant increased (from 0.028 to 0.095 min^{-1}) as the Fe^{2+} dosage rose from 0.1 to 0.3 mM. Since abundant H_2O_2 can be produced in this EF system, the increase in Fe^{2+} dosage favors the Fenton's reaction, eventually yielding a higher amount of hydroxyl radical ($^{\bullet}OH$) that accelerate the 2,4-DCP degradation. Similarly, the increase in current density also showed a positive influence, as deduced from Fig. 5b. A significant enhancement in the degradation rate constant, from 0.037 to 0.117 min^{-1} was achieved when increasing the current density from 12.5 to 37.5 mA cm^{-2}. Conversely, at 50.0 mA cm^{-2}, the improvement was minor, due to the fact that an excessively high H_2O_2 concentration partly scavenges the $^{\bullet}OH$ [59]. The degradation of other micropollutants was then carried out with 0.20 mM Fe^{2+} at 25 mA cm^{-2}. Fig. 5c shows that around 90% removal of each micropollutant (except 2,4-DCP and DCF) can be obtained in only 20 min using the PTFE/PMHS-GDE. Its performance was superior to that of EF with a conventional PTFE-GDE in all the cases, in good agreement with the previous characterization of the GDEs. The low degradation efficiencies for 2,4-DCP and diclofenac sodium (DCF) solutions are explained by their specific molecular structures, which may be more resistant to $^{\bullet}OH$ attack [60]. Moreover, the residual H_2O_2 concentrations after the treatment with PTFE/PMHS-GDE were much higher. Overall, these results demonstrate the great potential of the PTFE/PMHS-GDE as the cathode in EF system for wastewater treatment.

3.5. Mechanistic insights

To gain an in-depth understanding of the role of PMHS in the enhancement of the $2e^-$ ORR, DFT calculations were performed. This allowed determining the Gibbs free energies of each elementary step of the ORR, as well as the charge distributions on the coordination

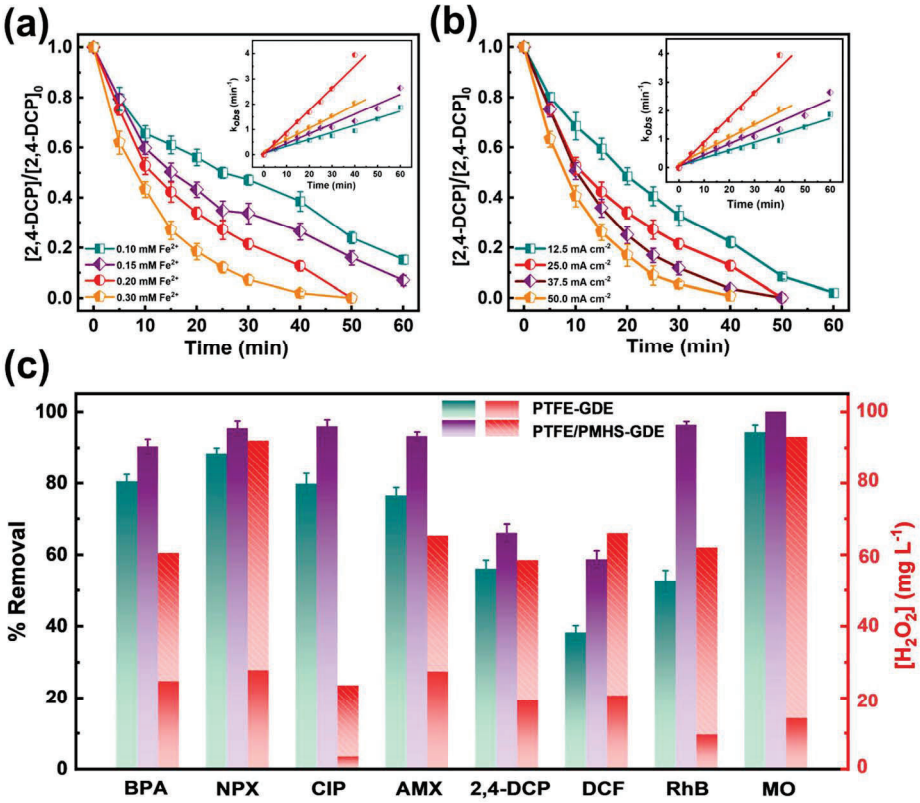

Fig. 5. Effect of (a) Fe^{2+} dosage and (b) applied current density on the decay of 2,4-dichlorophenol (2,4-DCP) during EF process using a PTFE/PMHS-GDE. In the insets, the corresponding pseudo-first-order kinetic analysis is illustrated. (c) Micropollutant removals and residual H_2O_2 concentrations achieved after 20 min of EF treatment using the conventional PTFE-GDE and the novel PTFE/PMHS-GDE. Conditions for trials in plot (c): [Micropollutant] = 20 mg L^{-1}; [Fe^{2+}] = 0.20 mM; initial pH 3.0; current density = 25 mA cm^{-2}. Micropollutants: bisphenol A (BPA), naproxen (NPX), ciprofloxacin (CIP), amoxicillin (AMX), diclofenac sodium (DCF), Rhodamine B (RhB), Methyl Orange (MO) and 2,4-DCP.

structures of sole graphene and PMHS@Graphene. As shown in Fig. 6a, the $2e^-$ ORR pathway producing H_2O_2 competes with the $4e^-$ reaction pathway. Specifically, the former consists of two steps, namely the generation and removal of the *OOH intermediate, while the cleavage of the O-O bond in *OOH to produce *O and *OH as intermediates gives rise to the $4e^-$ route [28]. Therefore, the key to minimize the latter is to prevent the dissociation of the O-O bond in *OOH. As depicted in the free energy diagram calculated at 0 V vs RHE (Fig. 6b), the formation of *OOH via an endothermic O_2 hydrogenation step is uphill, whereas other steps remain downhill for the materials under consideration, implying that it is the potential limiting step [61]. The Gibbs free energy difference of this step (ΔG_{*OOH}) on PMHS@Graphene is much lower than that on sole graphene (0.02 vs 0.23 eV), demonstrating that the presence of PMHS favors the *OOH generation. On the other hand, the free energy change for the conversion of *OOH to *O (ΔG_{*O}) on sole graphene is − 2.93 eV, much more negative than − 1.80 eV for the H_2O_2 formation (ΔG_{H2O2}), suggesting that the $2e^-$ ORR on this material is suppressed. Regarding the PMHS@Graphene electrocatalyst, the ΔG_{*O} becomes much more positive (−1.86 eV) than that of graphene, while the ΔG_{H2O2} remains very similar (1.60 vs 1.80 eV), thereby corroborating that the presence of PMHS significantly inhibits the $4e^-$ ORR pathway by preserving the *OOH intermediate from dissociation without sacrificing the $2e^-$ ORR activity. Moreover, more insights into the role of the Si-H and Si-O-C groups in the enhancement of the $2e^-$ ORR were provided by investigating the *OOH adsorption free energy on three different sites. The *OOH adsorption largely determines the ORR and hence, the free energy for ideal $2e^-$ ORR is 3.52 eV at the equilibrium potential of 0.70 V vs RHE [22]. As shown in Fig. 6c, the Si-H site has a free energy of 4.41 eV, being the closest to the ideal value, which means that the weakest adsorption of *OOH occurred on this site. The free energy on the Si-O-C site is also slightly more negative than that on the C site in PMHS@Graphene, suggesting its positive contribution to the $2e^-$ ORR. On the other hand, the charge density analysis depicted in Fig. 6d reveals that the electrons tend to accumulate around the Si sites in PMHS, which modulated the local electric field of C sites in graphene, resulting in moderate charge transfer. These DFT results demonstrate that the Si-H and Si-O-C sites cannot only act as the active sites for the $2e^-$ ORR, but they also promote electron transfer during the reaction.

4. Conclusions

In summary, a highly hydrophobic PTFE/PMHS-GDE that can simultaneously enhance the O_2 transport, H_2O_2 selectivity, and catalytic activity, has been rationally developed, thereby significantly improving the H_2O_2 yield as compared to other reported GDEs. The $-CH_3$ groups in PMHS, with low surface energy, create a superhydrophobic three-phase interface that eliminates the O_2 mass transport barrier for ORR, whereas the Si-H bonds and the as-formed Si-O-C sites modulate the coordination environment of carbon centers, achieving faster electron transfer and higher H_2O_2 selectivity. Consequently, the PTFE/PMHS-GDE yields the maximum H_2O_2 concentration of 1874.8 mg L^{-1} after 360 min at 25 mA cm^{-2}, being much higher than that of a conventional GDE. Moreover, the enhancement of EF system for wastewater treatment using the PTFE/PMHS-GDE was confirmed by the efficient degradation

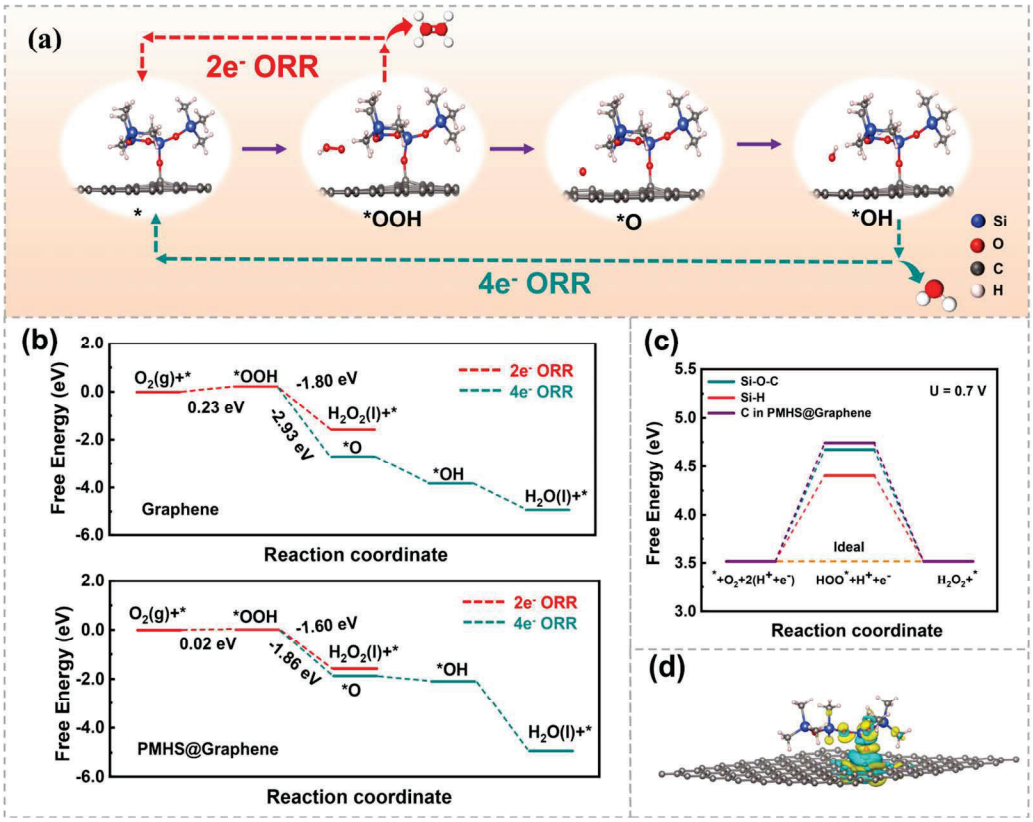

Fig. 6. (a) Possible reaction pathways during the ORR. (b) Gibbs free energy diagram for $2e^-$ and $4e^-$ ORR on sole graphene and PMHS@Graphene centers at 0 V vs RHE. (c) Free energy diagram for $2e^-$ ORR to H_2O_2 at equilibrium potential of 0.70 V vs RHE. (d) Charge density difference in the PMHS@Graphene model (the azure regions denote charge depletion, whereas yellow regions denote charge accumulation).

of 8 micropollutants. This study is expected to exert a positive impact on EF systems that are designed by many scholars and, beyond this, the positive effects of the active sites in PMHS may serve to fabricate novel GDEs with better performance in other fields, such as electrochemical CO_2 reduction.

CRediT authorship contribution statement

Pan Xia: Conceptualization, Data curation, Investigation, Validation; **Lele Zhao:** Investigation, Formal analysis; **Xi Chen:** Data curation, Investigation; **Zhihong Ye:** Conceptualization, Funding acquisition, Investigation, Methodology, Project administration, Resources, Supervision, Writing – original draft; **Zhihong Zheng:** Data curation, Formal analysis; **Qiang He:** Resources, Supervision; **Ignasi Sirés:** Funding acquisition, Methodology, Project administration, Resources, Supervision, Writing – review & editing.

Declaration of Competing Interest

The authors declare that they have no known competing financial interests or personal relationships that could have appeared to influence the work reported in this paper.

Data availability

Data will be made available on request.

Acknowledgments

The authors acknowledge financial support from the National Natural Science Foundation of China (No.52100073), the PhD Gateway Program of Chongqing, (CSTB2022BSXM-JCX0140), the Graduate Scientific Research and Innovation Foundation of Chongqing (CYB23065), the Natural Science Foundation of Chongqing, (CSTB2022NSCQ-MSX0432) and the Venture and Innovation Support Program for Chongqing Over–seas Returnees (cx2022048, China). I.S. is thankful to projects PID2019–109291RB-I00, PID2022–140378OB-I00 and PDC2022–133624-I00 (MCIN/AEI/10.13039/501100011033, Spain). The Ph.D. scholarship awarded to L.Z. (State Scholarship Fund, CSC, China) is also acknowledged.

Appendix A. Supporting information

Supplementary data associated with this article can be found in the online version at doi:10.1016/j.apcatb.2023.123467.

References

[1] R. Mehrotra, D. Oh, J.W. Jang, Unassisted selective solar hydrogen peroxide production by an oxidised buckypaper-integrated perovskite photocathode, Nat. Commun. 12 (2021) 1–9.

[2] H. Li, P. Wen, D.S. Itanze, Z.D. Hood, S. Adhikari, C. Lu, X. Ma, L. Dun, L. Jiang, D. L. Carroll, Y. Qiu, S.M. Geyer, Scalable neutral H_2O_2 electrosynthesis by platinum diphosphide nanocrystals by regulating oxygen reduction reaction pathways, Nat. Commun. 11 (2020) 1–12.

[3] C.A. Martínez-Huitle, M.A. Rodrigo, I. Sirés, O. Scialdone, A critical review on latest innovations and future challenges of electrochemical technology for the abatement of organics in water, Appl. Catal. B: Environ. 328 (2023), 122430.

[4] Y. Zhang, G. Daniel, S. Lanzalaco, A.A. Isse, A. Facchin, A. Wang, E. Brillas, C. Durante, I. Sirés, H_2O_2 production at gas-diffusion cathodes made from agarose derived carbons with different textural properties for acebutolol degradation in chloride media, J. Hazard. Mater. 423 (2022), 127005.

[5] G. Ren, S. Lanzalaco, M. Zhou, P.L. Cabot, E. Brillas, I. Sirés, Replacing carbon cloth by nickel mesh as substrate for air-diffusion cathodes: H_2O_2 production and carbenicillin degradation by photoelectro-Fenton, Chem. Eng. J. 454 (2023), 140515.

[6] Q. Wu, J. Cao, X. Wang, Y. Liu, Y. Zhao, H. Wang, Y. Liu, H. Huang, F. Liao, M. Shao, Z. Kang, A metal-free photocatalyst for highly efficient hydrogen peroxide photoproduction in real seawater, Nat. Commun. 12 (2021) 1–10.

[7] X. Zhao, Q. Yin, X. Mao, C. Cheng, L. Zhang, L. Wang, T. Liu, Y. Li, Y. Li, Theory-guided design of hydrogen-bonded cobaltoporphyrin frameworks for highly selective electrochemical H_2O_2 production in acid, Nat. Commun. 13 (2022) 1–8.

[8] I. Sirés, E. Brillas, Upgrading and expanding the electro-Fenton and related processes, Curr. Opin. Electrochem. 27 (2021), 100686.

[9] N. Oturan, J. Bo, C. Trellu, M.A. Oturan, Comparative performance of ten electrodes in electro-Fenton process for removal of organic pollutants from water, ChemElectroChem 8 (2021) 3294–3303.

[10] P. Xia, Z. Ye, L. Zhao, Q. Xue, S. Lanzalaco, Q. He, X. Q, I. Sirés, Tailoring single-atom FeN_4 moieties as a robust heterogeneous catalyst for high-performance electro-Fenton treatment of organic pollutants, Appl. Catal. B: Environ. 322 (2023), 122116.

[11] J. Lu, X. Liu, Q. Chen, J. Zhou, Coupling effect of nitrogen-doped carbon black and carbon nanotube in assembly gas diffusion electrode for H_2O_2 electro-generation and recalcitrant pollutant degradation, Sep. Purif. Technol. 265 (2021), 118493.

[12] G.O.S. Santos, P.J.M. Cordeiro-Junior, I. Sánchez-Montes, R.S. Souto, M.S. Kronka, M.R.V. Lanza, Recent advances in H_2O_2 electrosynthesis based on the application of gas diffusion electrodes: challenges and opportunities, Curr. Opin. Electrochem. 36 (2022), 101124.

[13] W. Zhou, L. Rajic, X. Meng, R. Nazari, Y. Zhao, Y. Wang, J. Gao, Y. Qin, A. N. Alshawabkeh, Efficient H_2O_2 electrogeneration at graphite felt modified via electrode polarity reversal: Utilization for organic pollutants degradation, Chem. Eng. J. 364 (2019) 428–439.

[14] Y. Song, A. Wang, S. Ren, Y. Zhang, Z. Zhang, Flow-through heterogeneous electro-Fenton system using a bifunctional FeOCl/carbon cloth/activated carbon fiber cathode for efficient degradation of trimethoprim at neutral pH, Environ. Res. 222 (2023), 115303.

[15] H. Zhang, Y. Zhao, Y. Li, G. Li, J. Li, F. Zhang, Janus electrode of asymmetric wettability for H_2O_2 production with highly efficient O_2 utilization, ACS Appl. Mater. Inter. 3 (2019) 705–714.

[16] P. Cao, X. Quan, K. Zhao, X. Zhao, S. Chen, H. Yu, Durable and selective electrochemical H_2O_2 synthesis under a large current enabled by the cathode with highly hydrophobic three-phase architecture, ACS Catal. 11 (2021) 13797–13808.

[17] Y. Li, C.J. Miller, L. Wu, T.D. Waite, Hydroxyl radical production via a reaction of electrochemically generated hydrogen peroxide and atomic hydrogen: An effective process for contaminant oxidation? Environ. Sci. Technol. 56 (2022) 5820–5829.

[18] F. Deng, J. Jiang, I. Sirés, State-of-the-art review and bibliometric analysis on electro-Fenton process, Carbon Lett. 33 (2023) 17–34.

[19] J. Au, N. Li, Y. Wu, S. Wang, C. Liao, Q. Zhao, L. Zhou, T. Li, X. Wang, Y. Feng, Revealing decay mechanisms of H_2O_2-based electrochemical advanced oxidation processes after long-term operation for phenol degradation, Environ. Sci. Technol. 54 (2020) 10916–10925.

[20] A. Xu, B. He, H. Yu, W. Han, J. Li, J. Shen, X. Sun, L. Wang, A facile solution to mature cathode modified by hydrophobic dimethyl silicon oil (DMS) layer for electro-Fenton processes: Water proof and enhanced oxygen transport, Electrochim. Acta 308 (2019) 158–166.

[21] M.E. Leonard, L.E. Clarke, A. Forner-Cuenca, S.M. Brown, F.R. Brushett, Investigating electrode flooding in a flowing electrolyte, gas-fed carbon dioxide electrolyzer, ChemSusChem 13 (2020) 400–411.

[22] Y. Zheng, X. Xu, J. Chen, Q. Wang, Surface O_2-regulation on POM electrocatalyst to achieve accurate $2e^-/4e^-$ ORR control for H_2O_2 production and Zn-air battery assemble, Appl. Catal. B: Environ. 285 (2021), 119788.

[23] P. Xia, C. Wang, Q. He, Z. Ye, I. Sirés, MOF-derived single-atom catalysts: the next frontier in advanced oxidation for water treatment, Chem. Eng. J. 452 (2023), 139446.

[24] F. Yu, M. Zhou, X. Yu, Cost-effective electro-Fenton using modified graphite felt that dramatically enhanced on H_2O_2 electro-generation without external aeration, Electrochim. Acta 163 (2015) 182–189.

[25] Q. Zhang, M. Zhou, G. Ren, Y. Li, Y. Li, X. Du, Highly efficient electrosynthesis of hydrogen peroxide on a superhydrophobic three-phase interface by natural air diffusion, Nat. Commun. 11 (2020) 1–11.

[26] H. He, B. Jiang, J. Yuan, Y. Liu, X. Bi, S. Xin, Cost-effective electrogeneration of H_2O_2 utilizing HNO_3 modified graphite/polytetrafluoroethylene cathode with exterior hydrophobic film, J. Colloid Interf. Sci. 533 (2019) 471–480.

[27] Y. Tian, D. Deng, L. Xu, M. Li, H. Chen, Z. Wu, S. Zhang, Strategies for sustainable production of hydrogen peroxide via oxygen reduction reaction: from catalyst design to device setup, Nano Micro Lett. 15 (2023) 1–45.

[28] Q. Yang, W. Xu, S. Gong, G. Zheng, Z. Tian, Y. Wen, L. Peng, L. Zhang, Z. Lu, L. Chen, Atomically dispersed Lewis acid sites boost 2-electron oxygen reduction activity of carbon-based catalysts, Nat. Commun. 11 (2020) 5478.

[29] Y. Tian, M. Li, Z. Wu, Q. Sun, D. Yuan, B. Johannessen, L. Xu, Y. Wang, Y. Dou, H. Zhao, S. Zhang, Edge-hosted atomic Co-N_4 sites on hierarchical porous carbon for highly selective two-electron oxygen reduction reaction, Angew. Chem. Int. Ed. 61 (2022), 02213296.

[30] G. Daniel, Y. Zhang, S. Lanzalaco, F. Brombin, T. Kosmala, G. Granozzi, A. Wang, E. Brillas, I. Sirés, C. Durante, Chitosan-derived nitrogen-doped carbon electrocatalyst for a sustainable upgrade of oxygen reduction to hydrogen peroxide in UV-assisted electro-Fenton water treatment, ACS Sustain, Chem. Eng. 8 (2020) 14425–14440.

[31] Y. Huang, W. Zhou, L. Xie, J. Li, Y. He, S. Chen, X. Meng, J. Gao, Y. Qin, Edge and defect sites in porous activated coke enable highly efficient carbon-assisted water electrolysis for energy-saving hydrogen production, Renew, Energ 195 (2022) 283–292.

[32] C. Dong, K.S. Lee, Y. Cho, S. Wang, X. Fan, F. Bai, J.H. Park, K. Zhang, Precise synthesis of single-atom Mo, W, Nb coordinated with oxygen functional groups of graphene oxide for stable and selective two-electron oxygen reduction in neutral media, J. Mater. Chem. A 10 (2022) 9488–9496.

[33] M. Mazzucato, C. Durante, Insights on oxygen reduction reaction to H_2O_2: the role of functional groups and textural properties on the activity and selectivity of doped carbon electrocatalysts, Curr. Opin. Electrochem. 35 (2022), 101051.

[34] O. Crowther, B. Meyer, M. Morgan, M. Salomon, Primary Li-air cell development, J. Power Sources 196 (2011) 1498–1502.

[35] N. Singh, H. Kakiuchida, T. Sato, R. Hönes, M. Yagihashi, C. Urata, A. Hozumi, Omniphobic metal surfaces with low contact angle hysteresis and tilt angles, Langmuir 34 (2018) 11405–11413.

[36] X. Zhu, X. Yang, C. Lv, S. Guo, J. Li, Z. Zheng, H. Zhu, D. Yang, New approach to create TiO_2(B)/carbon core/shell nanotubes: Ideal structure for enhanced lithium ion storage, ACS Appl. Mater. Inter. 8 (2016) 18815–18821.

[37] X. Zhang, F. Xiao, Q. Feng, J. Zheng, C. Chen, H. Chen, W. Yang, Preparation of SiO_2 nanoparticles with adjustable size for fabrication of SiO_2/PMHS ORMOSIL superhydrophobic surface on cellulose-based substrates, Prog. Org. Coat. 138 (2020), 105384.

[38] H. Lin, Q. Hu, T. Liao, X. Zhang, W. Yang, S. Cai, Highly hydrophobic cotton fabrics modified by poly(methylhydrogen) siloxane and fluorinated olefin: Characterization and applications, Polymers 12 (2020) 833.

[39] Z. Liu, X. Pang, K. Wang, X. Lv, X. Cui, Superhydrophobic coatings prepared by the in situ growth of silicone nanofilaments on alkali-activated geopolymers surface, ACS Appl. Mater. Interf. 11 (2019) 22809–22816.

[40] Z. Liu, J. Yu, W. Lin, W. Yang, R. Li, H. Chen, X. Zhang, Facile method for the hydrophobic modification of filter paper for applications in water-oil separation, Surf. Coati, Tech 352 (2018) 313–319.

[41] M. Wójcik-Bania, A. Łącz, A. Nyczyk-Malinowska, M. Hasik, Poly (methylhydrosiloxane) networks of different structure and content of Si-H groups: Physicochemical properties and transformation into silicon oxycarbide ceramics, Polymer 130 (2017) 170–181.

[42] A.V. Kuzmin, B.A. Shainyan, Single Si-doped graphene as a catalyst in oxygen reduction reactions: an in silico study, ACS Omega 5 (2022) 15268–15279.

[43] V.M. Truong, N.B. Duong, H. Yang, Comparison of carbon supports in anion exchange membrane fuel cells, Materials 13 (2020) 5370.

[44] G. Cihanoğlu, Ö. Ebil, CVD-deposited oxygen-selective fluorinated siloxane copolymers as gas diffusion layers, Ind. Eng. Chem. Res. 61 (2022) 2633–2642.

[45] Z. Qi, H. Dong, H. Yu, M. Zhao, H. Yu, In-situ electrochemical NO_x removal process for the lean-burn engine exhaust based on carbon black gas diffusion electrode, J. Clean. Prod. 151 (2017) 465–474.

[46] O. Garcia-Rodriguez, Y. Lee, H. Olvera-Vargas, F. Den, Z. Wang, O. Lefebvre, Mineralization of electronic wastewater by electro-Fenton with an enhanced graphene-based gas diffusion cathode, Electrochim. Acta 276 (2018) 12–20.

[47] H. Zhang, Y. Li, Y. Zhao, G. Li, F. Zhang, Carbon black oxidized by air calcination for enhanced H_2O_2 generation and effective organics degradation, ACS Appl. Mater. Inter. 11 (2019) 27846–27853.

[48] T. Thami, L. Tauk, V. Flaud, Controlled structure and hydrophilic property of polymethylhydrosiloxane thin films attached on silicon support and modified with phosphorylcholine group, Thin Solid Films 709 (2020), 138196.

[49] Y. Wang, M. Wang, J. Wang, H. Wang, X. Men, Z. Zhang, A rapid, facile and practical fabrication of robust PDMS@ starch coatings for oil-water separation, J. Taiwan Inst. Chem. E 99 (2019) 215–223.

[50] F. Cao, D. Kim, X. Li, C.X. Feng, Y. Song, Synthesis of polyaluminocarbosilane and reaction mechanism study, J. Appl. Polym. Sci. 85 (2002) 2787–2792.

[51] P. Ding, L. Cui, D. Li, W. Jing, Innovative dual-compartment flow reactor coupled with a gas diffusion electrode for in situ generation of H_2O_2, Ind. Eng. Chem. Res. 58 (2019) 6925–6932.

[52] Y. Zhu, F. Deng, S. Qiu, F. Ma, Y. Zheng, R. Lian, Enhanced electro-Fenton degradation of sulfonamides using the N, S co-doped cathode: Mechanism for H_2O_2 formation and pollutants decay, J. Hazard. Mater. 403 (2021), 123950.

[53] X. Yu, M. Zhou, G. Ren, L. Ma, A novel dual gas diffusion electrodes system for efficient hydrogen peroxide generation used in electro-Fenton, Chem. Eng. J. 263 (2015) 92–100.

[54] W. Wang, Y. Li, Y. Li, M. Zhou, O.A. Arotiba, Electro-Fenton and photoelectro-Fenton degradation of sulfamethazine using an active gas diffusion electrode without aeration, Chemosphere 250 (2020), 126177.

[55] B. Garza-Campos, D. Morales-Acosta, A. Hernández-Ramírez, J.L. Guzmán-Mar, L. Hinojosa-Reyes, J. Manríquez, E.J. Ruiz-Ruiz, Air diffusion electrodes based on synthetized mesoporous carbon for application in amoxicillin degradation by electro-Fenton and solar photo electro-Fenton, Electrochim. Acta 269 (2018) 232–240.

[56] X. Sun, J. Lv, Z. Yan, Z. Sun, A three-dimensional gas diffusion electrode without external aeration for producing H_2O_2 and eliminating amoxicillin using electro-Fenton, Process, J. Environ. Chem. Eng. 10 (2022), 107301.

[57] Z. Zhang, H. Meng, Y. Wang, L. Shi, X. Wang, S. Chai, Fabrication of graphene@graphite-based gas diffusion electrode for improving H_2O_2 generation in Electro-Fenton process, Electrochim. Acta 260 (2018) 112–120.
[58] G.O. Santos, P.J.M. Cordeiro-Junior, I. Sánchez-Montes, R.S. Souto, M.S. Kronka, M.R. Lanza, Recent advances in H_2O_2 electrosynthesis based on the application of gas diffusion electrodes: challenges and opportunities, Curr. Opin. Electrochem. 36 (2022), 101124.
[59] Z. Ye, J.A. Padilla, E. Xuriguera, E. Brillas, I. Sirés, Magnetic MIL(Fe)-type MOF-derived N-doped nano-ZVI@C rods as heterogeneous catalyst for the electro-Fenton degradation of gemfibrozil in a complex aqueous matrix, Appl. Catal. B: Environ. 266 (2022), 118604.
[60] Z. Xie, C. He, H. Zhou, L. Li, Y. Liu, Y. Du, W. Liu, Y. Mu, B. Lai, Effects of molecular structure on organic contaminants' degradation efficiency and dominant ROS in the advanced oxidation process with multiple ROS, Environ. Sci. Technol. 56 (2022) 8784–8795.
[61] B.W. Zhang, T. Zheng, Y. Wang, Y. Du, S. Chu, Z. Xia, R. Amal, S. Dou, L. Dai, Highly efficient and selective electrocatalytic hydrogen peroxide production on Co-OC active centers on graphene oxide, Commun. Chem. 5 (2022) 1–7.

SUPPLEMENTARY MATERIAL

Polymethylhydrosiloxane-modified gas-diffusion cathode for more efficient and durable H_2O_2 electrosynthesis in the context of water treatment

Pan Xia [a], Lele Zhao [b], Xi Chen [a], Zhihong Ye [a,*], Zhihong Zheng [a], Qiang He [a], Ignasi Sirés [b,**]

[a] *Key Laboratory of Eco-environments in Three Gorges Reservoir Region, Ministry of Education, College of Environment and Ecology, Chongqing University, Chongqing, 400045, China*

[b] *Laboratori d'Electroquímica dels Materials i del Medi Ambient, Departament de Ciència de Materials i Química Física, Secció de Química Física, Facultat de Química, Universitat de Barcelona, Martí i Franquès 1-11, 08028 Barcelona, Spain*

* Corresponding author: yezhihong@cqu.edu.cn (Z. Ye)

** Corresponding author: i.sires@ub.edu (I. Sirés)

This document includes supplementary text, figures and tables, distributed as follows:

Figure S1-S4	**Page S2-S5**
Table S1	**Page S6**

SUPPLEMENTARY MATERIAL

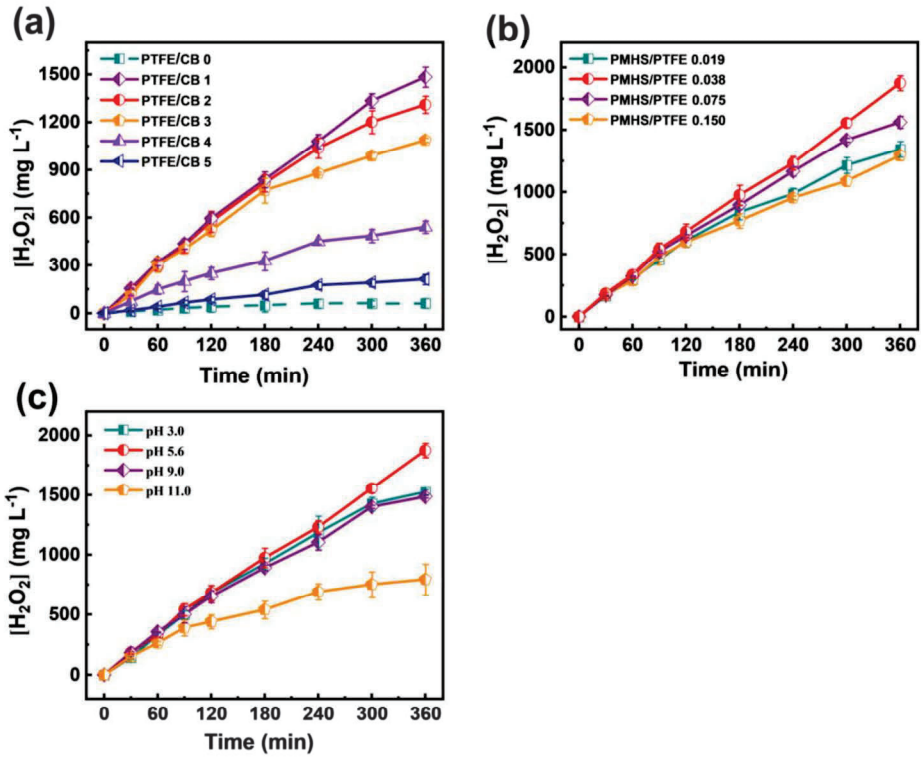

Fig. S1. Effect of (a) PTFE dosage, (b) PMHS/PTFE, and (c) initial pH on the time course of accumulated H_2O_2 concentration in 0.05 M Na_2SO_4 at 25.0 mA cm^{-2}.

SUPPLEMENTARY MATERIAL

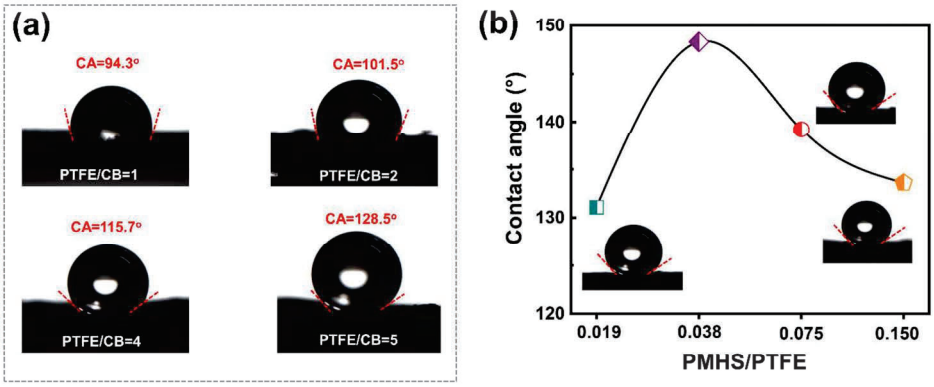

Fig. S2. Contact angle of GDEs prepared with different mass ratios of (a) PTFE/CB and (b) PMHS/PTFE.

SUPPLEMENTARY MATERIAL

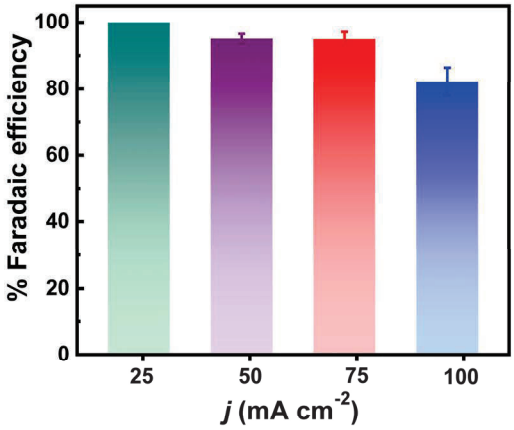

Fig. S3. Faradaic efficiency for H_2O_2 production with the PTFE/PMHS-GDE at different current densities. See conditions in Fig. 4.

SUPPLEMENTARY MATERIAL

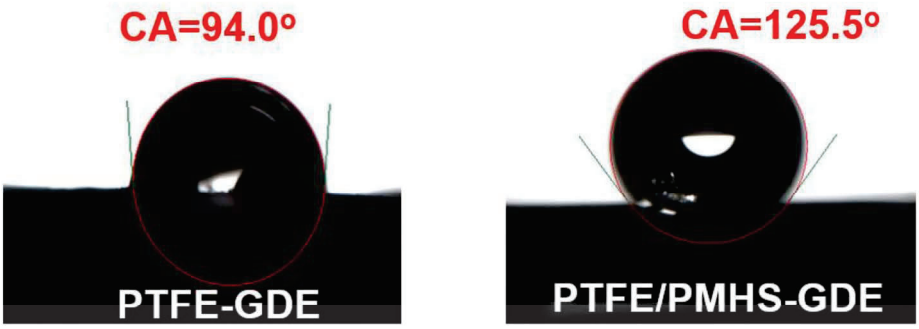

Fig. S4. Contact angles of used PTFE-GDE and PTFE/PMHS-GDE after ten consecutive runs (see conditions in Figure 4d).

SUPPLEMENTARY MATERIAL

Table S1

Summary of electrochemical parameters, determined from the redox properties of the $[Fe(CN)_6]^{3-}/[Fe(CN)_6]^{4-}$ couple (each at 0.01 M, pH 5.2), for three different types of electrocatalysts.

	$j_{o,p}$ (mA cm^{-2})[a]	$j_{r,p}$ (mA cm^{-2})[b]	ΔE_p (mV)[c]	ECSA (cm^2)[d]	R_s (kΩ)[e]	R_{ct} (kΩ)[f]	R_{mt} (kΩ)[g]
CB-PTFE	1.221	1.449	202	8.3	0.15	7.6	47.5
CB-PMHS	-	-	-	-	0.17	0.07	6.1
CB-PTFE/PMHS	1.103	1.362	100	7.5	0.17	3.8	23.6

[a] Oxidation peak current density. [b] Reduction peak current density. [c] Peak-to-peak separation. [d] Electroactive surface area. [e] Solution resistance. [f] Charge transfer resistance. [g] Mass transport resistance.

4.2 Cu-based MOFs as efficient and stable catalysts in HEF process

Section 4.2 covers two articles relative (**GO2**, **GO3** and **SG5-12**), including: (i) synthesis of two Cu-MOF-based heterogeneous catalysts (monometallic Cu and bimetallic FeCu), examination of Cu-based catalysts yield, and complete physicochemical and electrochemical characterization; (ii) evaluation of pharmaceutical degradation and mineralization in synthetic and real wastewater using HEF at natural pH; (iii) investigation of catalyst performance under various experimental conditions; (iv) assessment of reusability and metal leaching; and (v) elucidation of degradation pathways and mechanisms based on pharmaceutical intermediates.

4.2.1 Enhanced mineralization of pharmaceutical residues at circumneutral pH by heterogeneous electro-Fenton-like process with Cu/C catalyst

As summarized in Chapter 1.1.5, organic micropollutants like pharmaceuticals bring about increasing environmental risks due to their persistence and toxicity, with DPH frequently found in water bodies, which is mostly due to incomplete metabolization in humans. To address the limitations of conventional EF treatments, which rely on Fe^{2+} and operate optimally at low pH, researchers are turning to heterogeneous catalysts that can operate at near-neutral pH. Although iron is certainly the gold standard, Cu-based catalysts have been shown promising in EF-like processes due to the favorable Cu(II)/Cu(I) redox cycle, which generates reactive $^{\bullet}OH$ for pollutant degradation, even in a mixed homogeneous/heterogeneous regime. While traditional Cu-supported catalysts often suffer from excessive Cu leaching, MOFs pyrolyzed into Cu/C catalysts were expected to exhibit a durable core-shell structure that allows reducing leaching, thus extending the catalyst lifespan. This study presents a comprehensive synthesis and analysis of pyrolytic Cu-MOF derivatives to be employed as Cu/C catalysts, evaluating their efficacy in degrading DPH in synthetic solutions, and further exploring their performance in actual wastewater.

Some characterization techniques were initially applied to investigate the physicochemical properties of the Cu/C catalysts. Cu-MOF synthesis yields were below 10% at room temperature but exceeded 20% under hydrothermal

conditions (120 °C) due to faster crystallization. XRD results confirmed Cu-MOF formation, with peaks at 6.7º, 9.5º, 11.6º, and 13.4°. For Cu/C catalysts, pyrolysis in Ar/H_2 yielded pure Cu nanocrystals (43.3°, 50.4°, 74.1°; JCPDS 04-0836), while pyrolysis in Ar alone resulted in partial Cu_2O formation (36.4°; JCPDS 05-0667), confirmed by the red-brown coloring of the latter materials. Cu/C-A2-Ar/H_2 (Autoclave – 2 h, pyrolyzed under Ar/H_2), with the highest yield among Ar/H_2 samples, was selected for further study. The TEM analysis of this catalyst revealed the presence of round nanoparticles (20-40 nm) with a core-shell structure, where Cu cores were wrapped in a porous carbon shell (1.5-10 nm thick). This protective layer was expected to limit Cu erosion and dissolution while maintaining the catalytic efficiency. HRTEM confirmed lattice spacings of 0.208 and 0.181 nm for the (111) and (200) planes of Cu, aligning with XRD data. EDX mapping showed Cu concentrated in the nanoparticle core, surrounded by C on the surface, with minimal O. Elemental analysis by EDS indicated a distribution of elements as: 61.5% Cu, 21.5% C, and 17.0% O, verifying the catalyst composition. XPS analysis confirmed that the surface of the catalyst consisted of Cu, C, and O. High-resolution spectra revealed the existence of Cu peaks at 932.4, 944.1, 952.2, and 962.5 eV, indicating a mix of Cu(I) and Cu(II) states, with Cu_2O being dominant as shown by the Cu LMM band at 916.8 eV. Combined with XRD and HRTEM findings, this suggests that the catalyst strictly comprises zero-valent copper cores within a carbon shell, with slight surface oxidation. To maintain the active Cu states, storage in a vacuum oven at 50 °C is recommended. DLS analysis of Cu/C-A2-Ar/H_2 showed an average particle size of 695 nm, larger than the 20-40 nm observed via TEM. This discrepancy, with high standard deviation and covariance, suggests minor clustering in solution, which DLS detects as hydrodynamic diameter. TEM, capturing particles in a dried state, does not fully represent the dispersion seen in liquid.

The efficiency of the catalyst in degrading DPH through HEF-like process in 0.050 M Na_2SO_4 medium was evaluated by selecting different anodes, catalyst doses, pH values, and current densities. Initial tests showed only 5% DPH decay at pH 6 via adsorption. Without the catalyst, EO-H_2O_2 using a DSA-Cl_2/GDE cell achieved 35% removal in 180 min, whereas using raw Cu-MOF yielded 32% degradation, evidencing the necessity of MOF pyrolysis for improved stability and effectiveness. Among the tested anodes, BDD ensured the fastest DPH

degradation, achieving complete removal in 150 min; nonetheless, DSA-Cl_2 was selected for subsequent trials due to its cost-effectiveness and the presence of chloride in wastewater, aiding active chlorine formation for faster degradation. Increasing the catalyst dosage from 0.05 to 0.5 g L^{-1} enhanced the DPH removal, with optimal performance at 0.1 g L^{-1}. A higher initial pH reduced the degradation rates, with complete removal at pH 3 in 20 min, extending to 180 min at pH 6 and 8. A higher pH lowered the $^{\bullet}OH$ activity but reduced the copper leaching, shifting the process to a slower heterogeneous pathway. Increasing current density from 8.3 to 50 mA cm^{-2} at pH 6 enhanced the DPH removal by boosting the H_2O_2 and $^{\bullet}OH$ production, eventually achieving the complete degradation within 90 min at higher current values.

The performance of Cu/C-A2-Ar/H_2 catalyst was evaluated in actual urban wastewater containing 14.3 mg L^{-1} DPH and an initial TOC of 20.6 mg C L^{-1} at pH 8. Using a DSA-Cl_2 anode and commercial GDE cathode with a current density of 16.7 mA cm^{-2}, DPH degradation was faster in wastewater than in a 0.050 M Na_2SO_4 model solution at pH 6, attaining the total removal in 150 min, as compared to 180 min needed in the synthetic medium. This acceleration is attributed to active chlorine (HClO) formed from chloride present in the wastewater, which acted alongside M($^{\bullet}OH$) and $^{\bullet}OH$ to enhance the degradation. However, TOC reduction showed a slower, opposite trend, with 60% removal in the synthetic solution versus 30% in wastewater after 360 min, likely due to recalcitrant chlorinated by-products from HClO oxidation in the wastewater matrix.

The mineralization efficiency reached using the Cu/C-A2-Ar/H_2 catalyst in the HEF-like treatment of DPH solutions at pH 6 was evaluated against a traditional homogeneous EF process with Fe^{2+} at pH 3. At 16.7 mA cm^{-2}, the HEF-like process achieved 58% TOC reduction, surpassing the 42% removal observed in EF. Increasing the current to 50 mA cm^{-2} in the HEF-like system further boosted the mineralization to 68%, which was notably higher than the 52% attained by EF at 100 mA cm^{-2}. These are very relevant results from this work, since they indicate that the $\equiv Cu^{2+}/\equiv Cu^{+}$ pair in the Cu/C catalyst effectively activates H_2O_2, generating abundant $^{\bullet}OH$ radicals that enhance the mineralization beyond that achieved by the homogeneous EF method. The comparable TOC

reduction at pH 3 and 6 in HEF-like treatment implies that recalcitrant by-products are primarily degraded through surface-generated $^{\bullet}OH$ radicals.

In terms of by-products, a lower accumulation of oxalic acid was observed in the HEF-like treatment, suggesting ag more efficient degradation of short-chain products. In contrast, the EF process led to Fe(III)-oxalate complexes, which are more resistant to further oxidation, thereby limiting mineralization. The use of a BDD anode in the HEF-like process further improved TOC reduction by generating highly reactive BDD($^{\bullet}OH$) radicals, aligned with the lower oxalic acid levels detected. Additionally, homogeneous EF-like treatments with Cu^{+} or Cu^{2+} catalysts displayed markedly lower degradation and mineralization efficiency, achieving only 10% TOC removal, becoming a clear proof of the superiority of Cu/C-catalyzed HEF for effective pollutant mineralization.

In HEF-like treatments, the Cu/C-A2-Ar/H_2 catalyst showed higher initial Cu^{2+} leaching at pH 3 than at pH 6, enhancing the $^{\bullet}OH$ generation and DPH degradation under acidic conditions. After the first hour, the leaching was stabilized, with minimal additional release, indicating stability of copper within the carbon shell. Reusability tests showed a degradation efficiency declining from 96% to 34% over five cycles, though cleaning partially restored it to 56%. XPS analysis confirmed predominant Cu(II) formation, which provided an explanation for the diminished H_2O_2 activation and oxidation power.

GC/MS analysis allowed identifying six aromatic and three aliphatic by-products, including oxalic acid, and the possible degradation pathway of this drug resulting from DPH oxidation in HEF-like treatments at pH 6 was consequently elucidated.

Furthermore, the feasibility of using Cu/C-A2-Ar/H_2 as an electrocatalyst for H_2O_2 generation in HEF systems was explored by evaluating its ORR performance in 0.1 M Na_2SO_4 at pH 4 and 6. As an electrocatalyst, this material showed promising ORR activity, especially at circumneutral pH, achieving limiting currents of -0.24 mA at pH 4 and -0.76 mA at pH 6. In the latter medium, the electron transfer number approached 2, with an H_2O_2 selectivity of 80%, whereas at pH 4, the electron transfer number was closer to 3, with 60% selectivity.

Chemosphere 364 (2024) 143249

Contents lists available at ScienceDirect

Chemosphere

journal homepage: www.elsevier.com/locate/chemosphere

Enhanced mineralization of pharmaceutical residues at circumneutral pH by heterogeneous electro-Fenton-like process with Cu/C catalyst

Lele Zhao [a], José A. Padilla [b,c], Elena Xuriguera [b], Pere L. Cabot [a], Enric Brillas [a,*], Ignasi Sirés [a,**]

[a] Laboratori d'Electroquímica dels Materials i del Medi Ambient, Departament de Ciència de Materials i Química Física, Secció de Química Física, Facultat de Química, Universitat de Barcelona, Martí i Franquès 1-11, 08028, Barcelona, Spain

[b] DIOPMA, Departament de Ciència de Materials i Química Física, Secció de Ciència de Materials, Facultat de Química, Universitat de Barcelona, Martí i Franquès 1-11, 08028, Barcelona, Spain

[c] Grup de Recerca en Tecnologies de Fabricació, Departament d'Enginyeria Mecànica, Escola Tècnica Superior d'Enginyeria Industrial de Barcelona, Av. Diagonal 647, 08028, Barcelona, Spain

HIGHLIGHTS

- First investigation of DPH degradation by the electro-Fenton process.
- Only trace amount of core-shell Cu/C catalyst needed for complete degradation of DPH.
- Remarkable mineralization (68%) at pH 6 by Cu/C-catalyzed HEF-like process.
- Degradation rates in urban wastewater are greater than in model solutions.
- Cu/C is also envisaged as a promising electrocatalyst for $2e^-$ ORR at pH 6.

GRAPHICAL ABSTRACT

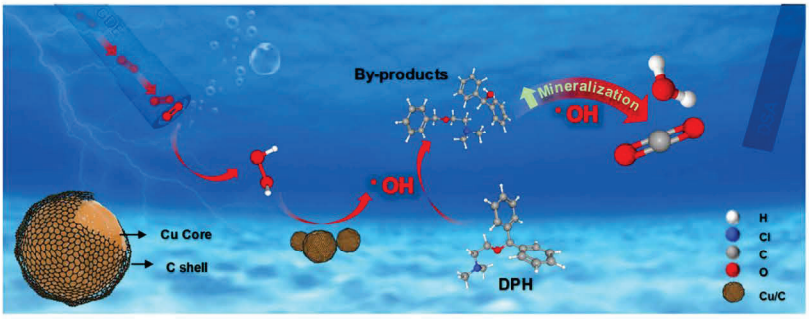

ARTICLE INFO

Handling editor: Sonia Lanzalaco

Keywords:
Electrochemical advanced oxidation process
Electro-Fenton process
Metal-organic framework
Pharmaceutical pollutant
Water treatment

ABSTRACT

Conventional electro-Fenton (EF) process at acidic pH ~3 is recognized as a highly effective strategy to degrade organic pollutants; however, homogeneous metal catalysts cannot be employed in more alkaline media. To overcome this limitation, pyrolytic derivatives from metal-organic frameworks (MOFs) have emerged as promising heterogeneous catalysts. Cu-based MOFs were prepared using trimesic acid as the organic ligand and different pyrolysis conditions, yielding a set of nano-Cu/C catalysts that were analyzed by conventional methods. Among them, XPS revealed the surface of the Cu/C-A2-Ar/H_2 catalyst was slightly oxidized to Cu(I) and, combined with XRD and HRTEM data, it can be concluded that the catalyst presents a core-shell structure where metallic copper is embedded in a carbon layer. The antihistamine diphenhydramine (DPH), spiked into either synthetic Na_2SO_4 solutions or actual urban wastewater, was treated in an undivided electrolytic cell equipped with a DSA-Cl_2 anode and a commercial air-diffusion cathode able to electrogenerate H_2O_2. Using Cu/C as suspended catalyst, DPH was completely degraded in both media at pH 6–8, outperforming the EF process with Fe^{2+} catalyst at pH 3 in terms of degradation rate and mineralization degree thanks to the absence of refractory

* Corresponding author.
** Corresponding author.
E-mail addresses: brillas@ub.edu (E. Brillas), i.sires@ub.edu (I. Sirés).

https://doi.org/10.1016/j.chemosphere.2024.143249
Received 19 July 2024; Received in revised form 21 August 2024; Accepted 31 August 2024
Available online 2 September 2024
0045-6535/© 2024 Elsevier Ltd. All rights are reserved, including those for text and data mining, AI training, and similar technologies.

Fe(III)-carboxylate complexes that typically decelerate the TOC abatement. From the by-products detected by GC/MS, a reaction sequence for DPH mineralization is proposed.

1. Introduction

Pharmaceuticals and microplastics pose an emerging concern after their release into the environment due to their persistence or their role as endocrine disruptors, among other effects (Morin-Crini et al., 2022; Priyadarshini et al., 2022). Diphenhydramine (DPH), a first-generation antihistamine with good inhibitory effect on allergies and vomiting, is one of these substances. Since it is a component of common cough and cold preparations (Aziz et al., 2020), which are massively consumed by humans, DPH is widely present in the influent and effluent streams of sewage plants, also being detected in surface water (Topp et al., 2012; Wolfson et al., 2018). This adversely affects the life of aquatic animals and fish, potentially threatening the Earth's ecosystems. Compared with traditional pollutants such as sulfur and nitrogen oxides, most organic micropollutants have more obvious persistence, accumulation, and migration characteristics, limiting the removal efficiency (Kumar et al., 2022).

In modern concepts for wastewater treatment plants, the advanced oxidation processes (AOPs) have become a hot topic, with growing market penetration forecast in the near future. The electro-Fenton (EF) technology belongs to the family of electrochemical AOPs (i.e., EAOPs), with well-proven effective and rapid degradation of organic pollutants (Ren et al., 2023; Sirés and Brillas, 2021; Villanueva-Rodríguez et al., 2019; Xia et al., 2023; Ye et al., 2022; Zhang et al., 2022). The traditional EF technique can destroy organic pollutants by decomposing in-situ electrogenerated H_2O_2 in the presence of homogeneous Fe^{2+} catalyst at optimum pH ~3, according to Fenton's reaction (1) that produces reactive oxygen species (ROS). In particular, the strong oxidation ability is associated to the formation of homogeneous •OH. The Fe^{3+} originated from reaction (1) can be continuously reduced to Fe^{2+}, as shown in reaction (2) (Chou et al., 1999), which occurs at the cathode surface to a certain degree depending on the electrolysis conditions and the cathode nature (Brillas et al., 2009; Brillas, 2020).

$$Fe^{2+} + H_2O_2 \rightarrow Fe^{3+} + {}^{\bullet}OH + OH^- \quad (1)$$

$$Fe^{3+} + e^- \rightarrow Fe^{2+} \quad (2)$$

However, the efficiency of the conventional EF method is highly dependent on the solution pH. $Fe(OH)_3$ is readily formed at pH > 4, causing the precipitation of iron sludge that needs to be treated after the EF treatment. Note that the aforementioned Fe^{2+} regeneration via reaction (2) is optimal at pH 2 (Chou et al., 1999; He and Zhou, 2017), whereas many industrial wastes and municipal sewage have a pH close to neutral.

Aiming to solve this limitation, several materials have been used as heterogeneous catalysts in EF, with prevalence of synthetic iron-containing structures such as carbon nanotubes (Su et al., 2019), resins (Fernández et al., 2018), zeolites or bio-absorbents, zero-valent iron (Ganiyu et al., 2018), iron-rich soils such as clays (dos Santos et al., 2020), and minerals such as iron oxides or pyrite (Ltaïef et al., 2018). However, these materials undergo severe iron leaching upon long-term usage. In this context, metal-organic frameworks (MOFs) have emerged as potential well-engineered materials that are expected to alleviate some of the current technological limitations for industrial applications (Li et al., 2019). MOFs are crystalline structures with high order and porosity, and are easily synthesized from metal ions/clusters and multivalent organic linkers. Due to their large porosity and structural tunability, these materials have inherent advantages in catalysis, presenting great interest in the absorption, filtration, and degradation of organic matter in water (Dias and Petit, 2015). The catalytic performance of MOFs in AOPs has been recently validated (Sharma and Feng, 2019).

Copper, an Earth-abundant transition metal, is considered one of the most preeminent iron-free catalysts for wastewater processing in EF-like systems (Wang et al., 2021). Reactions (3) and (4) show the formation of •OH from the Cu^{2+}/Cu^+ redox pair in the bulk solution in homogeneous EF-like process, or from $\equiv Cu^{2+}/\equiv Cu^+$ at the surface of a solid catalyst in the Cu-based heterogeneous EF (HEF)-like process (Bokare and Choi, 2014; Droguett et al., 2020; Sheng et al., 2018). Unlike iron species, the leached Cu^{2+} from solids predominantly appears as soluble $[Cu(H_2O)_6]^{2+}$ at neutral pH, which may be beneficial to operate in a mixed homogeneous/heterogeneous regime even when the stability of the catalyst does not reach 100% in long-term operation (Wang et al., 2021). Many efforts have been made to support or anchor Cu on certain substrates such as zeolite (Singh et al., 2016), alumina (Zhang et al., 2011), and SBA-15 (Qiao et al., 2012). Although satisfactory degradation effects can be obtained, the amount of Cu leaching is also unacceptable in those cases. Inspired by the appealing properties of MOFs, it has been found that their pyrolysis-derived products tend to exhibit a core-shell structure in which metal particles are wrapped by a carbon shell (Ye et al., 2020a, 2020b). Such an architecture can enhance the durability of metal catalysts, thereby reducing the metal leaching. Based on this, Cu-MOFs can be explored as a source of heterogeneous catalysts for HEF-like process.

$$Cu^{2+} (\equiv Cu^{2+}) + H_2O_2 \rightarrow Cu^+ (\equiv Cu^+) + HO_2^{\bullet} + H^+ \quad (3)$$

$$Cu^+ (\equiv Cu^+) + H_2O_2 \rightarrow Cu^{2+} (\equiv Cu^{2+}) + {}^{\bullet}OH + OH^- \quad (4)$$

This work reports the synthesis of pyrolytic derivatives of Cu-MOFs and their use as Cu/C catalysts. The properties of the prepared materials were comprehensively understood by means of physicochemical characterization. Their ability as heterogeneous catalyst for the degradation of DPH by HEF-like process in synthetic solutions was assessed at laboratory scale. Once the optimum experimental variables were optimized, the use of Cu/C in longer experiments was explored through mineralization trials. The viability of Cu/C catalysts for DPH degradation and mineralization in actual wastewater at neutral pH was finally evaluated. The advantages of this heterogeneous process as compared to conventional EF with Fe^{2+} is also discussed. Aromatic and aliphatic by-products were identified by gas chromatography coupled to mass spectrometry (GC/MS), allowing the proposal of a mineralization sequence. The last section describes the preliminary results on the potential use of the Cu/C materials as electrocatalysts for $2e^-$ oxygen reduction reaction (ORR), which could serve to devise an integral route for H_2O_2 production and its activation employing the same catalyst.

2. Materials and methods

2.1. Chemicals

High-performance liquid chromatography (HPLC) quality diphenhydramine hydrochloride (≥98% purity) was purchased from Merck. Sodium sulfate, sodium chloride, sodium hydroxide pellets, and sulfuric acid (96%–98%) were of analytical grade from Merck. Copper(II) nitrate trihydrate ($Cu(NO_3)_2 \bullet 3H_2O$, 99–104%) and trimesic acid ($C_6H_3(COOH)_3$, 95%), purchased from Sigma-Aldrich, and methanol (CH_3OH, ≥99.9%) from Scharlau were employed for the synthesis of the Cu-MOF. Analytical grade $FeSO_4 \bullet 7H_2O$ and CuCl used as catalyst sources in homogeneous EF were purchased from J.T. Baker. Nafion® perfluorinated resin solution 5 wt% was from Sigma-Aldrich. Analytical grade ethanol (96% v/v, Reag. USP, Ph. Eur.) and Ti(IV) oxysulfate for H_2O_2 determination were purchased from Panreac. All the reagents were

used as received without further purification. All aqueous solutions were prepared with Milli-Q water from a Merck Life Science Synergy UV device (resistivity >18.2 MΩ cm).

2.2. Preparation of the Cu/C catalysts

The synthetic route followed to obtain the Cu/C catalysts was adapted from Wang et al. (2021). Briefly, to prepare the Cu-MOF, 0.09 M (1.81 g) $Cu(NO_3)_2 \bullet 3H_2O$ and 0.04 M (0.88 g) $C_6H_3(COOH)_3$ solutions were separately prepared in 50 mL methanol, then sonicated for 10 min to ensure homogeneity, and further stirred using a magnet at very slow rate for uniform mixing. The aging was then carried out under three different conditions: in a beaker at room temperature for 2 h, in an autoclave at 120 °C for 2 h, and in an autoclave at 120 °C for 12 h. After cooling down to room temperature, the product was separated by centrifugation and washed with ethanol three times. Finally, the Cu-MOFs were dried in a vacuum oven (Vaciotem-T from Selecta) at 50 °C for 5 h. These samples were labeled as Cu-MOF-x, where x accounts for the above synthesis conditions. For example, Cu-MOF-A2 refers to the synthesis in an autoclave for 2 h.

Each MOF was pyrolyzed at 600 °C for 2 h under Ar or Ar/H_2 atmosphere at heating rate of 10 °C min^{-1}. It is worth noting that the powder obtained by pyrolysis in Ar atmosphere was dark brown/red, whereas that prepared in Ar/H_2 was almost black. The powder sample was washed several times with ethanol and Milli-Q water, then dried and stored in the vacuum oven at 50 °C. They are denoted as Cu/C-a&b where a and b represent the MOF synthesis conditions and the pyrolysis atmosphere, respectively. For example, Cu/C-A2&Ar/H_2 represents synthesis in an autoclave for 2 h and pyrolysis in Ar/H_2 atmosphere. The synthesis sequences for obtaining the Cu/C catalysts are schematized in Fig. 1.

2.3. Electrolytic trials

An undivided glass cell filled with 150 mL solution of DPH +50 mM Na_2SO_4 (as supporting electrolyte), thermostated at 25 °C and vigorously stirred with a magnetic PTFE follower, was employed to carry out all the electrolytic trials at constant current (*I*) supplied by an Amel 2053 potentiostat-galvanostat. The anode (3 cm^2) was an IrO_2- (DSA-O_2) or RuO_2- (DSA-Cl_2) plate from NMT Electrodes, or a boron-doped diamond (BDD) thin film supplied by NeoCoat. The cathode (3 cm^2) was a carbon cloth coated with carbon-PTFE (i.e., gas-diffusion electrode, GDE) from Fuel Cell Store, mounted into a purpose-designed air chamber, and fed with compressed air pumped at 0.4 L min^{-1} for continuous H_2O_2 electrogeneration. The anode-cathode gap was about 1.0 cm. Before first use, a polarization in a 50 mM Na_2SO_4 solution at 100 mA cm^{-2} for 3 h allowed the simultaneous cleaning and activation of both, the anode and cathode. The HEF-like treatments were performed by adding a given amount of one of the synthesized catalysts, or $FeSO_4$ for comparison. Some degradation tests were performed with actual wastewater instead of the 50 mM Na_2SO_4 solution.

2.4. Catalyst characterization

Various techniques were used to analyze the structure, morphology and physicochemical properties of the synthesized materials. The X-ray diffraction (XRD) analysis of the Cu-MOFs and Cu/C powders was made on a PANalytical X'Pert PRO MPD θ/θ powder diffractometer of 240 mm of radius, using Cu Kα radiation (λ = 1.5418 Å), operating at 45 kV and 40 mA. The $2\theta/\theta$ scans ranged from 2° to 88° 2θ with a step size of 0.026° 2θ and a measuring time of 200 s per step. The data obtained were analyzed using HighScore Plus version 3.0.5 software, and the reference codes of the identified structures were also derived from it. The morphology was assessed by high-resolution transmission electron microscopy (HRTEM), using a JEOL JEM-2100 electron transmission microscope operating at 200 kV in STEM mode with a dark-field detector, and coupled to an Oxford Inca energy-dispersive X-ray spectrometer (EDS). HRTEM analysis was made with the Digital Micrograph software, whereas mapping acquisition was accomplished with the Inca Microanalysis Suite version 4.09 software. X-ray photoelectron spectroscopy (XPS) analysis was performed with a PHI 5500 Multitechnique System from Physical Electronics using an Al-Kα monochromatized X-ray source of 486.6 eV and 350 W placed perpendicularly to the analyzer axis and calibrated with the $3d_{5/2}$ line of Ag (full width at half maximum –FWHM-of 0.8 eV). The analyzed area was a circle of 0.8 mm diameter. The selected resolution for the spectra was 187.85 eV of pass energy (PE) and 0.8 eV $step^{-1}$ for the general spectra, and 23.5 eV of PE and 0.1 eV $step^{-1}$ for the high-resolution spectra of the different elements. A low-energy electron gun <10 eV was used. All measurements were made under ultra-high vacuum at pressures between 5×10^{-9} and 2×10^{-8} Torr. The spectra were analyzed using the ULVAC-PHI MultiPakTM version 9.3 software.The particle size distribution was measured by dynamic light scattering (DLS), using an LS 13 320 laser diffraction particle size analyzer from Beckman Coulter. The dispersion medium was acetone and the samples were sonicated at 30 kHz and 200 W for 5 min before analysis.

2.5. Electrochemical measurements

The $2e^-$ ORR activity and selectivity of the Cu/C catalyst was

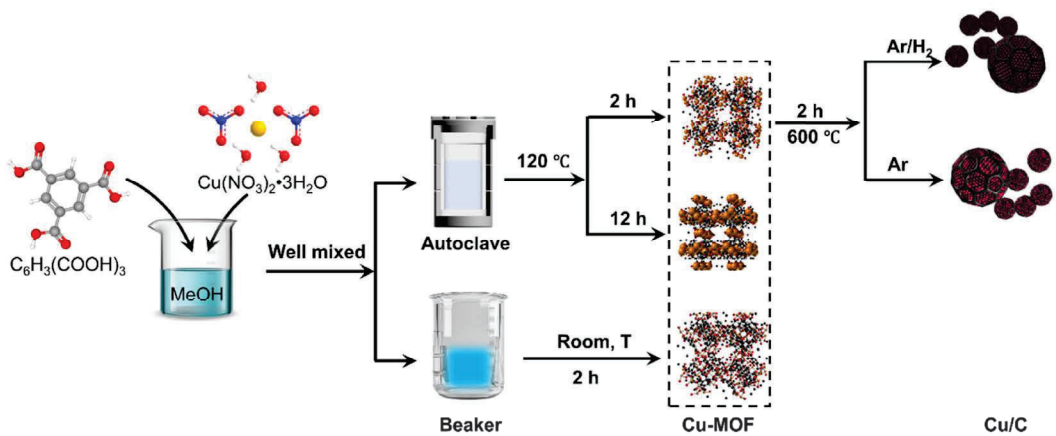

Fig. 1. Scheme of the Cu/C catalysts synthesis.

evaluated in a conventional three-electrode cell from Metrohm (Autolab PGSTAT100) filled with 0.1 M Na_2SO_4 solution at pH 4 or 6 at room temperature. The working electrode was a Metrohm rotating ring-disk electrode (RRDE) composed of a glassy carbon disk (5 mm in diameter, area of 0.196 cm^2) and a Pt ring (collection efficiency N of 24.9%). The counter and reference electrodes were a Pt foil and Ag|AgCl (3 M KCl), respectively. The catalyst ink was optimized by mixing 5 mg of catalyst, 9 μL of Nafion, and different volumes of Milli-Q water in an ultrasonic bath for 1 h before use. Before creating the thin film, the RRDE was polished with Micropolish II deagglomerated alumina of 0.3 and 0.05 μm on Buehler PSA-backed white felt cloth. After each polishing step, the tip was sonicated in Milli-Q water. Suitable amounts of the catalyst were deposited onto the glassy carbon disk to reach an overall catalyst loading of 2.0 mg cm^{-2}. The RRDE loaded with the catalyst ink was dried under an infrared lamp, thereby letting it cool down naturally to room temperature. In RRDE measurements, the ring potential (E_{ring}) was set to 1.0 V vs. Ag|AgCl (3 M KCl). The H_2O_2 selectivity (in %) and the number of electrons transferred (n) were determined from the disk and ring currents, following the corresponding equations (Zhang et al., 2022).

2.6. Analytical methods

The specific conductivity of solutions to be electrolyzed was determined with a Metrohm 644 conductometer, whereas pH was measured on a Crison GLP 22 pH meter. Before analysis, all samples were microfiltered with 0.22 μm syringe filters from Whatman. The time course of H_2O_2 concentration was assessed from the absorption value of its yellow complex with Ti(IV), at $\lambda = 408$ nm, measured on a Shimadzu 1800 UV/Vis spectrophotometer kept at room temperature. Some samples were also analyzed by inductively coupled plasma with optical emission spectroscopy (ICP-OES) using an Optima 3200 L spectrometer from PerkinElmer.

In the collected samples during the trials, the degradation process was terminated after adding a small volume of methanol, and measurements were performed after filtration. The solution total organic carbon (TOC) was determined on a Shimadzu TOC-VCNS analyzer, using the non-purgeable organic carbon (NPOC) method that yielded reproducible TOC values with ±1 % accuracy. DPH concentration was measured by reversed-phase HPLC using a Waters 600 chromatograph coupled to a Waters 996 photodiode array detector set at $\lambda = 276$ nm. A Kinetex® 5 μm Biphenyl 100 Å (250 mm × 4.6 mm) column at 35 °C was fitted to the equipment. The mobile phase was a 40:60 (v/v) CH_3CN/0.1% formic acid solution, eluted at 1.0 mL min^{-1}, and the peak of DPH appeared at 3.7 min. The carboxylic acids were determined at $\lambda = 210$ nm by ion-exclusion HPLC using the same Waters 600 LC, fitted with a Bio-Rad Aminex HPX 87H, 300 mm × 7.8 mm, column at 30 °C. The elution was carried out with 4 mM H_2SO_4 solution as mobile phase at 0.6 mL min^{-1}. All analyses were made at least in duplicate, and all figures show the error bars calculated with a 95% confidence interval.

The aromatic by-products were analyzed by GC/MS using an Agilent Technologies system composed of a 6890 N gas chromatograph equipped with a 7683B series injector and a 5975 mass spectrometer operating in EI mode at 70 eV. Non-polar Teknokroma Sapiens-X5.ms and polar HP INNOWax columns, with dimensions of 0.25 μm, 30 cm × 0.25 mm (i.d.), were used under the same conditions as given in previous work (Ye et al., 2022). The mass spectra were interpreted from comparison with those reported in the NIST05 MS database.

3. Results and discussion

3.1. Characterization of the synthesized catalysts

The yields of Cu-MOFs synthesized under different conditions are shown in Table S1. The less efficient method involved the use of room temperature, yielding less than 10% of material. Substantially higher yields were achieved under hydrothermal conditions (Cu-MOF-A2, and Cu-MOF-A12), attaining more than 20% in the former case. The superiority of this synthesis conditions can be related to the faster crystallization promoted at 120 °C as compared to the method under atmospheric conditions (Min Wang et al., 2002). In the XRD diffraction patterns of the synthesized Cu-MOFs shown in Fig. S1, it can be observed that the intensity of the signals was relatively weak, being the first four located around 6.7°, 9.5°, 11.6°, and 13.4°, consistent with those previously reported by Ediati et al. (2021), which confirms that the Cu-MOF was successfully synthesized in all cases. On the other hand, the XRD characterization of Cu/C catalysts obtained by pyrolysis in different atmospheres is depicted in Fig. 2a. The main diffraction peaks of the three materials obtained in Ar/H_2 appeared at 2θ values of 43.3°, 50.4°, and 74.1°, which can be related to the (111), (200), and (220) planes of face-centered cubic (FCC) Cu nanocrystals, according to the Cu standard (JCPDS card 04–0836). Conversely, the analogous Cu/C samples prepared in Ar atmosphere show a clear peak near 36.4°, which is readily associated to traces of Cu_2O in the material, as confirmed upon comparison with the standard (JCPDS card 05–0667). The presence of other smaller peaks typical from Cu_2O confirms the surface oxidation, which is partial because other peaks related to Cu are still distinguished. Note that these observations are in accordance with the visual color of the obtained powders in each atmosphere. The powder containing Cu_2O appeared as dark brown/red, whereas the one containing only Cu was darker, almost black. From these result, it is evident that the pyrolysis needs to be carried out in Ar/H_2, in order to ensure the complete transformation of the Cu-MOF into Cu/C nanocomposites. As shown in Table S2, the Cu/C-A2-Ar/H_2 catalyst yield was the highest among those obtained in Ar/H_2 and hence, this catalyst was selected for a more comprehensive analysis and for the electrochemical application.

The TEM image of a representative as-synthesized Cu/C-A2-Ar/H_2 catalyst is shown in Fig. 3a. As can be observed, it is composed of round nanoparticles of about 20–40 nm (see particle size distribution in the inset, calculated from 85 particles selected randomly). The nanoparticles present a core-shell structure, with Cu embedded in C (see Fig. 3b), being their outermost layer protected by a C shell of about 1.5–10 nm (see Fig. 3b and c). This protected metal core can minimize the significant erosion and dissolution of Cu nanoparticles. Note that, according the existing literature on MOFs pyrolysis, including works in which 1,3,5-benzenetricarboxylic acid serves as the organic linker, the carbon shell wrapping the core is porous (Payam et al., 2024). This fact ensures that a sufficiently high catalytic performance can be maintained while adding the protective feature. From the HRTEM image of the Cu/C-A2-Ar/H_2 given in Fig. 2b, the lattice spacing was measured; it was found that the distances of (111) and (200) crystalline planes corresponding to Cu were equal to 0.208 and 0.181 nm, respectively. These results correlate perfectly with those obtained by XRD (Fig. 2a), which evidenced the prevalence of (111) and (200) planes. The EDS mapping of the same sample, shown in Fig. 2c, confirms that the carbon shell surrounded a core essentially composed of Cu. Specifically, the Cu element (shown in red color) is concentrated in the center of the nanoparticle, whereas the C element (green color) is dispersed in the surface and around, which can be mutually verified in Fig. 3a. In addition, the O content is so low that it can be hardly observed. The EDS spectrum of Cu/C-A2-Ar/H_2 in Fig. S2 indicates the presence of Cu, C, and O, with a weight percentage of 61.5%, 21.5%, and 17.0%, respectively. This result is in good agreement with Fig. 2a, corroborating that the synthesized catalyst mainly contains zero-valent copper and carbon.

The elements present in the surface of the Cu/C-A2-Ar/H_2 catalyst and their valence state were further investigated by XPS analysis. From the full spectrum of Fig. S3a, it can be concluded that the material surface contains Cu, C, and O. The high-resolution Cu 2p XPS spectrum of the as-synthesized catalyst depicted in Fig. 2d displays the presence of four main peaks at 932.4, 944.1, 952.2, and 962.5 eV, corresponding to the Cu $2p_{3/2}$, Cu(I) or Cu(II) satellite, Cu $2p_{1/2}$, and Cu(I) or Cu(II) satellite, respectively. From this, and according to the Thermo database

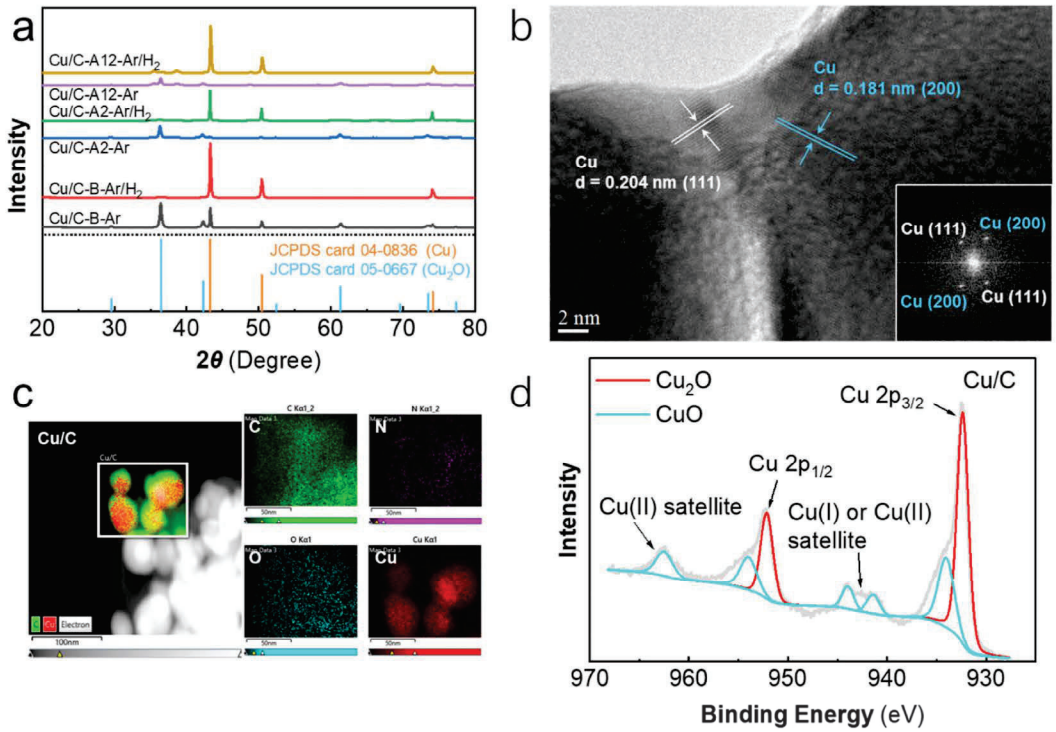

Fig. 2. (a) XRD diffraction patterns of Cu/C catalysts obtained from Cu-MOF pyrolysis. (b) HRTEM image (inset: FFT pattern). (c) Site of interest and EDS elemental mapping showing the Cu, O, C, and N distribution. (d) High resolution Cu 2p of XPS spectrum for the Cu/C-A2-Ar/H_2 catalyst.

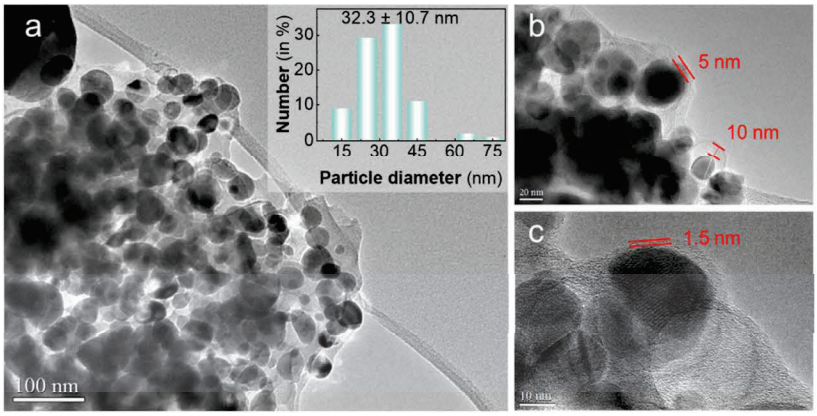

Fig. 3. TEM images of Cu/C-A2-Ar/H_2 catalyst at (a) 3000X (inset panel: particle size distribution), (b) 100000X, and (c) 300000X.

and the manual of Briggs (2005), it can be speculated that the sample can contain a mixture of Cu(I) and Cu(II) species. Nonetheless, the Cu LMM band of this sample shown in Fig. S3b presents its maximum kinetic energy at 916.8 eV, as expected for the Cu_2O species, in good agreement with the prevalence of this oxide over CuO (see Fig. 2d). In conclusion, the as-synthesized Cu/C-A2-Ar/H_2 catalyst is mainly composed of a Cu(I) core embedded in a carbon shell. Note that XPS is mainly used to measure the surface characteristics (few nanometers), which allows inferring that the surface of the catalyst is susceptible to oxidation within a short time. Based on the characteristic peaks of XRD pattern and the lattice spacing from HRTEM, one can conclude that the Cu/C-A2-Ar/H_2 catalyst is certainly zero-valent copper wrapped in a carbon layer, but the prepared materials must be preferentially in a vacuum oven at 50 °C to preserve the active metallic state.

The data included in the DLS analysis report of Fig. S4 inform about an average diameter of 695 nm for the Cu/C-A2-Ar/H_2 nanoparticles, a value much higher than 20–40 nm found through TEM. The standard deviation (0.449 μm) and covariance (64.7%) values suggest the presence of some particles with larger diameters or clustered together in the catalyst. The presence of such large particles can affect the diameter quantification by DLS, even on a relatively small amount. Moreover, the DLS results account for by the hydrodynamic volume of the nanoparticles, whereas the TEM analysis reveals the actual dimension of Cu/C-A2-Ar/H_2 (Feng et al., 2009; Blosi et al., 2014). In other words, the

dispersion state of the catalyst nanoparticles once in liquid is lower than expected. This cannot be deduced from TEM images, as those recorded for nanoparticles in dried state, but even well-dispersed nanoparticles can form clusters on TEM grids.

3.2. Catalytic properties of Cu/C-A2-Ar/H_2

The efficiency of heterogeneous Cu/C-A2-Ar/H_2 catalyst for the DPH degradation by HEF-like process in 50 mM Na_2SO_4 medium was assessed using different anodes, catalyst doses, initial pH, and applied *j*. Fig. S5 shows a 5% of DPH decay when treating a 14.3 mg L^{-1} drug solution at pH 6 after 180 min of vigorous stirring, pointing to a negligible adsorption of the drug onto the Cu/C-A2-Ar/H_2 surface. In the absence of the catalyst, the electrochemical oxidation with electrogenerated H_2O_2 (EO-H_2O_2) served to remove 35% of the drug at 180 min from an analogous solution, using a DSA-Cl_2/GDE cell at $j = 16.7$ mA cm^{-2}. A similar experiment but in the presence of 0.1 g L^{-1} of raw Cu-MOF-A2 (i.e., HEF-like process) led to a similar degradation efficiency of 32%, which means that the MOF needs to be pyrolyzed in order to be effective, since otherwise its stability in such an oxidizing environment is greatly compromised. In these two preliminary electrochemical trials, the drug removal can be mainly associated to the attack of the strong heterogeneous M(•OH) oxidant formed at the surface of the anode (M) from water oxidation by reaction (5). The cathode accounts for the production of a weak oxidant, H_2O_2, from the two-electron reduction of injected O_2 following reaction (6) (Sirés et al., 2014).

$$M + H_2O \rightarrow M(\bullet OH) + H^+ + e^- \quad (5)$$

$$O_2 + 2H^+ + 2e^- \rightarrow H_2O_2 \quad (6)$$

Since it is well known that the oxidation power of M(•OH) depends on the anode tested, BDD, DSA-O_2, and DSA-Cl_2 anodes were coupled to the commercial GDE cathode to comparatively study the DPH degradation. Fig. 4a highlights that the BDD anode yielded the fastest degradation, ensuring complete drug disappearance in 150 min under the above conditions with 0.1g L^{-1} catalyst at pH 6, owing to the larger generation of physisorbed M(•OH) from reaction (5), acting in concomitance with •OH promoted at the catalyst surface by the $\equiv Cu^{2+}/\equiv Cu^+$ pair (reactions (3) and (4)). Only slightly slower degradation can be observed in Fig. 4a with less expensive DSA-Cl_2 and DSA-O_2 anodes, both of them giving overall drug removal in 180 min. Note that DPH contains a small amount of chloride that can be oxidized in all anodes, preferentially by DSA-Cl_2, to form active chlorine through reactions (7) and (8) (Panizza and Cerisola, 2009), which can increase the degradation rate. Since chloride is present in the actual wastewater further tested, and considering the high cost of BDD, DSA-Cl_2 was selected as the anode material for all subsequent trials. Note that the DPH concentration decays could be fitted to a pseudo-first-order kinetic model, as shown by the excellent linear fittings of Fig. S6. The apparent kinetic constant values summarized in Fig. S6 corroborate the superiority of HEF-like treatment with BDD anode.

$$2\,Cl^- \rightarrow Cl_2 + 2e^- \quad (7)$$

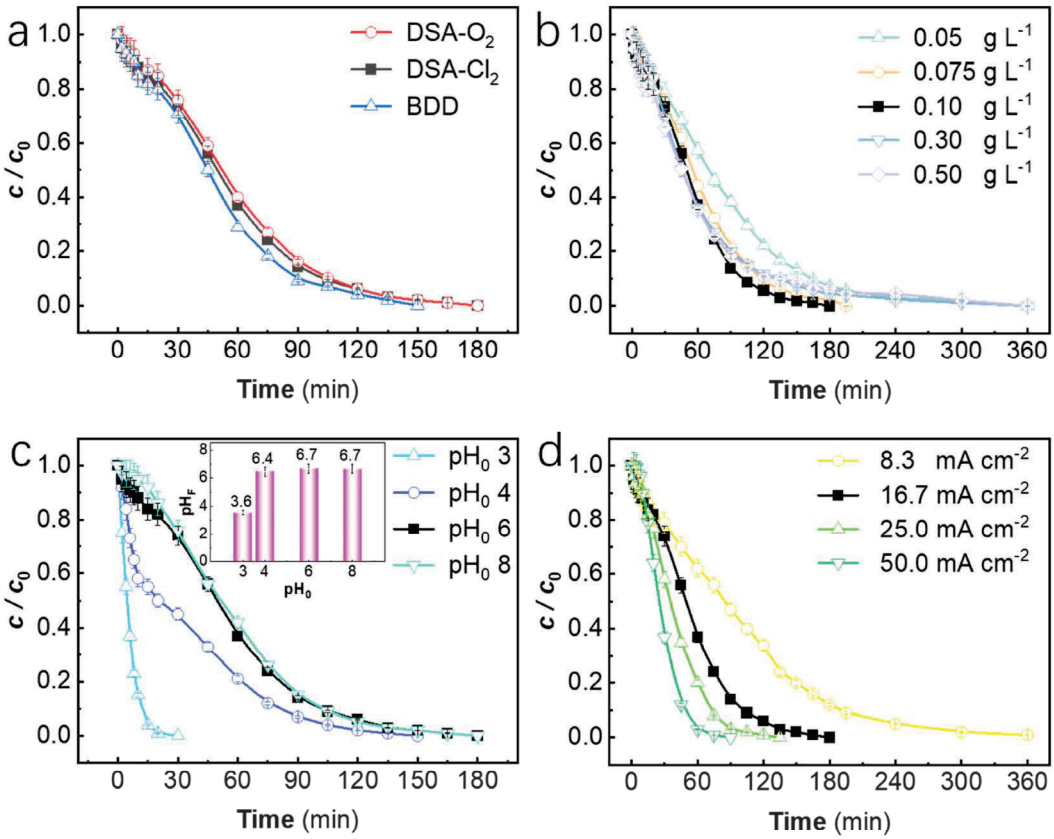

Fig. 4. Normalized DPH concentration vs. electrolysis time during the HEF-like treatment of 150 mL of suspensions with 14.3 mg L^{-1} drug (10 mg C L^{-1} TOC_0) and 50 mM Na_2SO_4 at 25 °C, in an anode/GDE cell using Cu/C-A2-Ar/H_2 as suspended catalyst. (a) Effect of the anode type, using 0.1 g L^{-1} catalyst at 16.7 mA cm^{-2} and initial pH 6. The other tests were done using the DSA-Cl_2 anode to assess the effect of: (b) The catalyst dosage, at 16.7 mA cm^{-2} and initial pH 6; (c) the initial pH, using 0.1 g L^{-1} catalyst at 16.7 mA cm^{-2}; and (d) the applied current density, using 0.1 g L^{-1} catalyst at initial pH 6.

$$Cl_2 + H_2O \rightarrow HOCl + H^+ + Cl^- \quad (8)$$

Fig. 4b depicts that the rise of catalyst dosages from 0.05 to 0.5 g L^{-1} reduced the time for total DPH removal from 360 to 180 min. The greater enhancement of DPH degradation occurred when the catalyst dosage increased from 0.05 to 0.1 g L^{-1}, whereupon no amelioration was achieved. This behavior can be related to a rise in the production of reactive •OH from the larger amount of $\equiv Cu^{2+}/\equiv Cu^{+}$ sites up to 0.1 g L^{-1} catalyst; in contrast, at higher dosage, the excess of this radical is consumed by its faster non-oxidizing parasitic reactions, with the consequent loss of oxidation ability of the system (Sirés et al., 2014). The catalyst dosage of 0.1 g L^{-1} was then chosen for further assays.

As shown in Fig. 4c, the degradation rate of DPH diminished when the initial pH was increased from pH 3 to 8. At pH 3, complete removal was achieved in only 20 min, then requiring 150 min at pH 4 and 180 min at pH 6 and 8. The similar behavior in the two latter conditions foreshadows the viability of the HEF-like process to treat actual wastewater. The loss of oxidation power with raising pH can be justified by two phenomena: (a) H_2O_2 tends to decompose into H_2O and O_2 at more alkaline pH, and the oxidation power of •OH also weakens when pH is increased, from $E^0 = +2.8$ V/SHE at pH 0 to $E^0 = +1.98$ V/SHE at pH 14 (Song et al., 2021); and (b) the decay of leaching (i.e., copper dissolution) at higher pH (see Fig. S8), which greatly reduces the contribution of the homogeneous Fenton-like reaction (4) in which dissolved Cu^+ promotes the •OH formation. Hence, at more alkaline pH, the process is purely heterogeneous, which is slower than the corresponding homogenous EF.

The positive contribution of j to remove DPH when it was increased from 8.3 to 50 mA cm^{-2} at pH 6 is revealed in Fig. 4d, decreasing the time needed for total drug removal from 360 to 90 min. This effect can be related to the larger electrogeneration of H_2O_2 from reaction (6) that originated a larger amount of oxidant •OH from reactions (3) and (4).

3.3. Removal of DPH from urban wastewater matrix

The study of the performance of heterogeneous Cu/C-A2-Ar/H_2 catalyst was extended to a real urban wastewater, whose physicochemical properties are listed in Table S3. To verify the ability of the HEF-like system in a realistic case, the assays were performed by injecting 14.3 mg L^{-1} of DPH in 150 mL of the urban wastewater TOC_0 = 20.6 mg C L^{-1} and pH_0 8) and adding 0.1 g L^{-1} Cu/C-A2-Ar/H_2 catalyst. This suspension was placed in the cell equipped with a DSA-Cl_2 anode and a commercial GDE as cathode, and j = 16.7 mA cm^{-2} was supplied. Fig. 5a and b compare the normalized drug concentration and TOC decays with time in both, the 50 mM Na_2SO_4 model solution at pH 6 and the urban wastewater. As can be seen in Fig. 5a, DPH was removed more rapidly in the latter matrix, with total disappearance in 150 min (as compared to 180 min needed in the synthetic medium). This faster decay can be attributed to the generation of active chlorine (HClO) from chloride present in the urban wastewater by reactions (7) and (8), which oxidizes to the drug in parallel to M(•OH) formed from reaction (5) and •OH produced from reactions (3) and (4). In contrast, Fig. 5b reveals a relatively slow TOC decay in both media, with opposite tendency as compared to Fig. 5a. About 60% and 30% reduction was attained in synthetic medium and urban wastewater, respectively, after 360 min of electrolysis. This represents a similar abatement of 6 mg C L^{-1} in both media. Taking into account that the organic matter of the urban wastewater was also partially mineralized, one can infer that a lower amount of DPH was mineralized in such matrix as compared to the synthetic one, which can be explained by the expected formation of recalcitrant chloroderivatives resulting from the HClO attack (Sirés et al., 2014).

3.4. Comparison of Cu/C-A2-Ar/H_2 and homogeneous catalysts to mineralize DPH solutions

The oxidation ability of the HEF-like process with 0.1 g L^{-1}Cu/C-A2-Ar/H_2 to mineralize DPH in synthetic solution at pH 6 was compared with that of classical homogeneous EF process with soluble catalyst (0.5 mM Fe^{2+}) at optimum pH 3. Fig. 6a and b reveal that at j = 16.7 mA cm^{-2}, the Cu/C-catalyzed HEF-like process was superior, yielding 58% TOC removal instead of 42% achieved in EF. When the current was risen to 50 mA cm^{-2} in the former process, a 68% mineralization was attained, which is even much greater than the 52% reached in EF at 100 mA cm^{-2}. From these trends, it can be deduced that the $\equiv Cu^{2+}/\equiv Cu^{+}$ pair in the heterogeneous catalyst surface allows a great activation of H_2O_2 from reactions (3) and (4). This brings about the production of a significant quantity of •OH, sufficiently high to degrade the organic matter even to a larger extent than homogeneous EF. In Fig. 6a, note also that the similar TOC abatement in HEF-like treatment operating at pH 3 and 6 suggests a large recalcitrance of the resulting by-products, which are mainly destroyed by •OH produced at the catalyst surface. On the other hand, Fig. 6b makes evident that TOC reduction was largely enhanced using a BDD anode due to the generation of very effective BDD (•OH) oxidant.

To better understand the trends in the above assays, the evolution of the ultimate short-chain aliphatic by-product, i.e., oxalic acid, is depicted in Fig. 6c and d. A much lower content of this acid was accumulated in the Cu/C-catalyzed HEF-like process, since in the conventional EF treatment, very hardly oxidizable Fe(III)-oxalate complexes

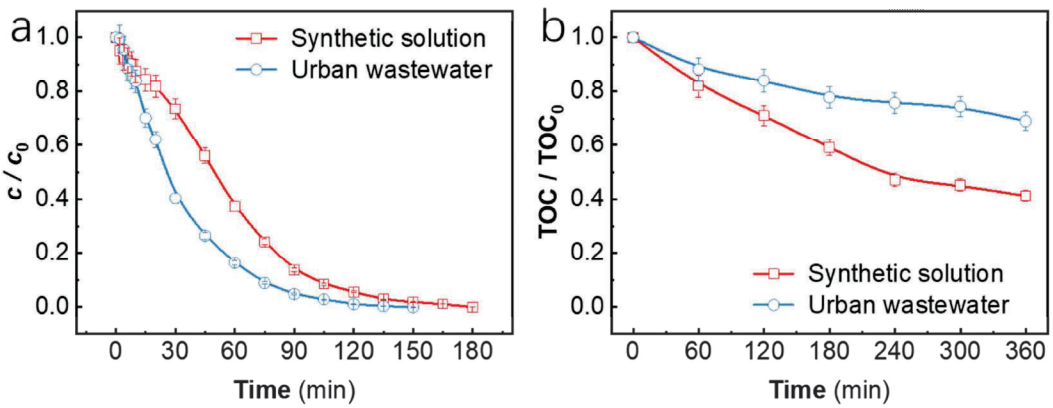

Fig. 5. Change of normalized concentration with electrolysis time during the HEF-like treatment of 14.3 mg L^{-1} (10 mg C L^{-1} TOC_0) of DPH at 25 °C, in a DSA-Cl_2/air-diffusion cell at 16.7 mA cm^{-2} using 0.1 g L^{-1} Cu/C-A2-Ar/H_2 catalyst. (a) Drug disappearance and (b) solution mineralization. The initial pH was 6 when using the synthetic solution and 8 (i.e., natural pH) in the case of the actual wastewater.

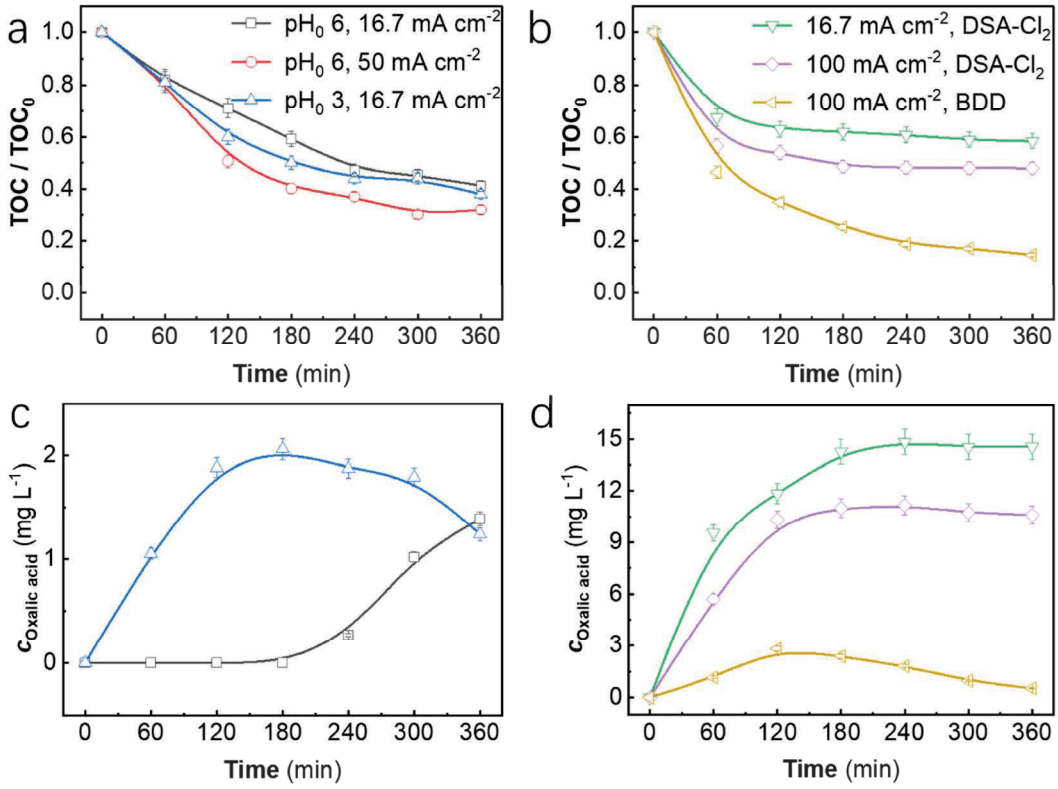

Fig. 6. DPH mineralization during the treatment of 14.3 mg L^{-1} (10 mg C L^{-1} TOC_0) of DPH in 50 mM Na_2SO_4 at 25 °C, in an anode/GDE cell at different current and initial pH values. (a) HEF-like process with 0.1 g L^{-1} Cu/C-A2-Ar/H_2 catalyst and DSA-Cl_2 as the anode. (b) EF process with 0.5 mM Fe^{2+} catalyst and DSA-Cl_2 or BDD as the anode. Time course of oxalic acid concentration during the tests shown in: (c) plot (a), and (d) plot (b), at 16.7 mA cm^{-2}.

are formed (Sirés et al., 2014). This justifies the superior mineralization ability of the former treatment. The much larger TOC removal attained in EF with BDD (see Fig. 6b) is consistent with the smaller accumulation of oxalic acid, as a result of its quicker destruction by •OH formed at BDD.

For completeness sake, EF-like treatments with Cu^+ or Cu^{2+} as homogeneous catalyst were also carried out, at pH_0 3 and 6, under analogous conditions to those of Fig. 4c with DSA-Cl_2 as the anode. The degradation ability of homogeneous EF-like process was clearly inferior to that of HEF-like process (compare Fig. S7a with Fig. 4c). At initial pH 3, the use of Cu^{2+} and Cu^+ led to only 53.0% and 79.1% DPH removal, respectively, which was even worse at pH_0 6. The superiority of Cu/C-catalyzed HEF was even more remarkable in terms of mineralization, since homogeneous EF-like process could only yield 10% TOC abatement at 360 min (compare Fig. S7b with Fig. 6a).

3.5. Reuse tests

The leaching of copper ions with time upon use of the Cu/C-A2-Ar/H_2 catalyst to treat the synthetic solutions at pH_0 3 and 6 in the above HEF-like treatments is shown in Fig. S8. The initial leached concentration, within the first hour, was much greater under acidic conditions. This supports the much greater •OH formation from the soluble Cu^{2+}-catalyzed EF, improving significantly the DPH degradation at pH 3 (see Fig. 4c). In contrast, from the second to the sixth hour, it was slightly increased in 1.522 mg L^{-1} at pH 3 and 1.146 mg L^{-1} at pH 6, i.e., at longer time a very low quantity of copper was additionally dissolved. Fig. S8 also discloses a similar Cu leaching at pH 6 with and without current. These findings suggest that the Cu exposed outside the carbon shell is easy to leach, whereas all metal embedded in the shell is quite stable.

The reusability of the Cu/C-A2-Ar/H_2 catalyst was evaluated by carrying out 5 consecutive cycles of 90 min, as depicted in Fig. S9. While the fresh catalyst degraded a 96% of DPH in 90 min, its performance was severely affected upon reuse, with a reduction down to 34% in the fifth cycle, which means that the reusability must be still further improved. After using ethanol and Milli-Q water to clean the surface and regenerate the catalyst, the degradation efficiency was improved, increasing up to a 56%. The used catalyst was tested by XPS, revealing two strong satellite peaks placed at 943.3 and 963.1 eV (Fig. S10). Hence, according to the Thermo database and Briggs (2005) manual, it can be judged that this catalyst is predominantly composed of Cu(II), which may be the main reason for the reduced efficiency for H_2O_2 activation, with the consequent loss of oxidation power.

3.6. Mineralization pathways

Six aromatic derivatives, and three aliphatic by-products including oxalic acid were formed from DPH (**1**) oxidation in the treated suspension by HEF-like process at pH 6, as identified by GC/MS. Fig. 7 presents the proposed reaction sequence for drug mineralization based on these intermediates. Three parallel initial ways can be envisaged. In *path 1a*, the attack of HClO over **1** originates the chloroderivative (2-chloroethoxy)methylene) dibenzene (**2**), whereas the attack of •OH forms 2-(benzhydryloxy)acetic acid (**3**) and the amine 2-(benzhydryloxy)ethan-1-amine (**4**), Further hydroxylation of these 3 compounds or directly that of **1** via *path 1b* yields diphenylmethanol (**7**). On the other hand, *path 2* involves the •OH attack on the alpha position of **1** to form 2-

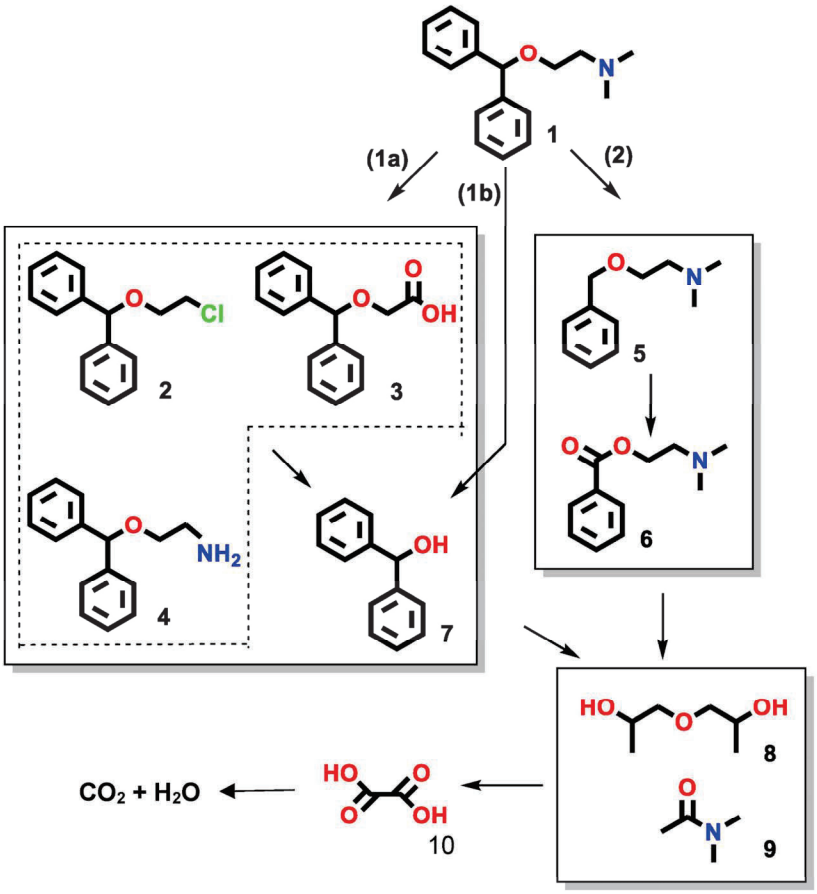

Fig. 7. Reaction pathway for DPH mineralization in the HEF treatment using the Cu/C-A2-Ar/H_2 catalyst.

(dimethylamino)ethyl benzoate (**5**) with loss of a phenyl group, followed by its hydroxylation to 2-(benzyloxy)-N,N-dimethylethan-1-amine (**6**). The cleavage of all aromatics yields aliphatic by-products such as 1,1′-oxybis(propan-2-ol) (**8**) and N,N-dimethylacetamide (**9**), which are finally oxidized to the recalcitrant oxalic acid (**10**) that is directly mineralized to CO_2 and H_2O.

3.7. *Characterization of Cu/C-A2-Ar/H_2 as potential electrocatalyst for ORR*

In all the HEF-like degradation tests described in previous subsections, a commercial GDE based on fossil fuel-derived raw C was employed. However, we consider that exploring the feasibility of Cu/C as electrocatalyst for H_2O_2 production is highly valuable, aiming at developing a highly performing HEF system based on Cu/C as both GDE modifier and Fenton-like catalyst in the near future. Accordingly, the electrochemical ORR performance of the prepared catalyst was evaluated by RRDE in 0.1 M Na_2SO_4 at pH 4 and 6. As shown in Fig. S11, the Cu/C-A2-Ar/H_2 catalyst exhibited a quite good ORR performance under O_2-saturated conditions in both media, especially at circumneutral pH. The limiting current values were −0.24 and −0.76 mA at pH 4 and 6, respectively. After reaching the *plateau*, it was found that at pH 6, the electron transfer number *n* was closer to 2, with a 80% selectivity toward H_2O_2 electrogeneration, whereas at pH 4, *n* was closer to 3 and selectivity was about 60%. This means that Cu/C-A2-Ar/H_2 could also be investigated as a potential modifier for manufacturing GDEs to be applied in wastewater treatment at pH 6.

4. Conclusions

It is shown that the use of low contents (0.1 g L^{-1}) of Cu/C-A2-Ar/H_2 as a heterogeneous catalyst in HEF-like treatment with a DSA/GDE cell enables a rapid and complete removal of DPH from synthetic Na_2SO_4 solutions and urban wastewater at pH 6–8. This is due to the effective formation of •OH from the ≡Cu^{2+}/≡Cu^{+} pair at the catalyst surface. The excess of Cu leaching at pH 3, which became an additional source of •OH soluble Cu^{2+}/Cu^{+} pair, enhanced the DPH degradation, but had low impact on mineralization. The Cu/C-catalyzed HEF-like process yielded a moderate mineralization degree, but much greater than homogeneous EF process with Fe^{2+} catalyst at optimum pH 3, because the formation of refractory complexes is avoided, thereby favoring the TOC abatement. Six aromatic derivatives and three aliphatic by-products were detected, giving rise to three parallel mineralization pathways for DPH. This environmentally-friendly HEF-like treatment with a novel Cu-MOF-derived core-shell catalyst not only solves some deficiency of conventional EF (i.e., production of refractory complexes and iron sludge), but new avenues are envisaged thanks to the potential application of the same catalyst for H_2O_2 production at near-neutral pH. Worth remarking, new strategies such as thermal treatment or co-catalyst integration could induce a greater catalyst stability, thus enhancing the reusability.

CRediT authorship contribution statement

Lele Zhao: Writing – review & editing, Writing – original draft, Methodology, Investigation, Conceptualization. **José A. Padilla:**

Resources, Methodology. **Elena Xuriguera:** Resources. **Pere L. Cabot:** Resources, Funding acquisition. **Enric Brillas:** Writing – review & editing, Writing – original draft, Validation, Formal analysis. **Ignasi Sirés:** Writing – review & editing, Writing – original draft, Validation, Supervision, Resources, Project administration, Methodology, Funding acquisition, Formal analysis, Data curation, Conceptualization.

Declaration of competing interest

The authors declare that they have no known competing financial interests or personal relationships that could have appeared to influence the work reported in this paper.

Data availability

Data will be made available on request.

Acknowledgements

The authors acknowledge the financial support from project PID2022-140378OB-I00 funded by MICIU/AEI/10.13039/501100011033 (Spain) and by ERDF/EU. The Ph.D. scholarship awarded to L.Z. (State Scholarship Fund, CSC, China) is also acknowledged. We also thankful to the Catalan Government for the quality accreditation and funding given to LEMMA/R2EM and DIOPMA groups (projects 2021SGR00596 and 2021SGR00708). DIOPMA is a certified agent TECNIO in the category of technology developers from the Government of Catalonia. XRD, TEM and XPS analyses from the *Centres Científics i Tecnològics de la UB* (CCiT-UB) are also acknowledged.

Appendix A. Supplementary data

Supplementary data to this article can be found online at https://doi.org/10.1016/j.chemosphere.2024.143249.

References

Aziz, S.N., Badawy, A.A., Nessem, D.I., Abd El Malak, N.S., 2020. Promising nanoparticulate system for topical delivery of diphenhydramine hydrochloride: in-vitro and in-vivo evaluation. J. Drug Deliv. Sci. Technol. 55, 101454 https://doi.org/10.1016/j.jddst.2019.101454.

Blosi, M., Albonetti, S., Ortelli, S., Costa, A.L., Ortolani, L., Dondi, M., 2014. Green and easily scalable microwave synthesis of noble metal nanosols (Au, Ag, Cu, Pd) useable as catalysts. New J. Chem. 38, 1401–1409. https://doi.org/10.1039/c3nj00894k.

Bokare, A.D., Choi, W., 2014. Review of iron-free Fenton-like systems for activating H_2O_2 in advanced oxidation processes. J. Hazard Mater. 275, 121–135. https://doi.org/10.1016/j.jhazmat.2014.04.054.

Briggs, D., 2005. X-ray photoelectron spectroscopy (XPS). https://doi.org/10.1002/0470014229.ch22.

Brillas, E., 2020. A review on the photoelectro-Fenton process as efficient electrochemical advanced oxidation for wastewater remediation. Treatment with UV light, sunlight, and coupling with conventional and other photo-assisted advanced technologies. Chemosphere 250, 126198. https://doi.org/10.1016/j.chemosphere.2020.126198.

Brillas, E., Sirés, I., Oturan, M.A., 2009. Electro-Fenton process and related electrochemical technologies based on Fenton's reaction chemistry. Chem. Rev. 109, 6570–6631. https://doi.org/10.1021/cr900136g.

Chou, S., Huang, Y.H., Lee, S.N., Huang, G.H., Huang, C., 1999. Treatment of high strength hexamine-containing wastewater by electro-Fenton method. Water Res. 33, 751–759. https://doi.org/10.1016/S0043-1354(98)00276-0.

Dias, E.M., Petit, C., 2015. Towards the use of metal-organic frameworks for water reuse: a review of the recent advances in the field of organic pollutants removal and degradation and the next steps in the field. J. Mater. Chem. A 3, 22484–22506. https://doi.org/10.1039/c6ta90036d.

dos Santos, A.J., Sirés, I., Alves, A.P.M., Martínez-Huitle, C.A., Brillas, E., 2020. Vermiculite as heterogeneous catalyst in electrochemical Fenton-based processes: application to the oxidation of Ponceau SS dye. Chemosphere 240, 124838. https://doi.org/10.1016/j.chemosphere.2019.124838.

Droguett, C., Salazar, R., Brillas, E., Sirés, I., Carlesi, C., Marco, J.F., Thiam, A., 2020. Treatment of antibiotic cephalexin by heterogeneous electrochemical Fenton-based processes using chalcopyrite as sustainable catalyst. Sci. Total Environ. 740, 140154 https://doi.org/10.1016/j.scitotenv.2020.140154.

Ediati, R., Laharto, P.B.F., Safitri, R., Mahfudhah, H., Oktavia Sulistiono, D., Denisa Syukrie, T., Nadjib, M., 2021. Synthesis of HKUST-1 with addition of Al-MCM-41 as adsorbent for removal of methylene blue from aqueous solution. Mater. Today: Proc. 46, 1799–1806. https://doi.org/10.1016/J.MATPR.2020.06.361.

Feng, C., Shen, Z., Li, Y., Gu, L., Zhang, Y., Lu, G., Huang, X., 2009. PNIPAM-b-(PEA-g-PDMAEA) double-hydrophilic graft copolymer: synthesis and its application for preparation of gold nanoparticles in aqueous media. J. Polym. Sci., Part A: Polym. Chem. 47, 1811–1824. https://doi.org/10.1002/pola.23282.

Fernández, D., Robles, I., Rodríguez-Valadez, F.J., Godínez, L.A., 2018. Novel arrangement for an electro-Fenton reactor that does not require addition of iron, acid and a final neutralization stage. Towards the development of a cost-effective technology for the treatment of wastewater. Chemosphere 199, 251–255. https://doi.org/10.1016/j.chemosphere.2018.02.036.

Ganiyu, S.O., Zhou, M., Martínez-Huitle, C.A., 2018. Heterogeneous electro-Fenton and photoelectro-Fenton processes: a critical review of fundamental principles and application for water/wastewater treatment. Appl. Catal. B Environ. 235, 103–129. https://doi.org/10.1016/j.apcatb.2018.04.044.

He, H., Zhou, Z., 2017. Electro-fenton process for water and wastewater treatment. Crit. Rev. Environ. Sci. Technol. 47, 2100–2131. https://doi.org/10.1080/10643389.2017.1405673.

Kumar, M., Ngasepam, J., Dhangar, K., Mahlknecht, J., Manna, S., 2022. Critical review on negative emerging contaminant removal efficiency of wastewater treatment systems: concept, consistency and consequences. Bioresour. Technol. 352, 127054 https://doi.org/10.1016/j.biortech.2022.127054.

Li, X., Wang, B., Cao, Y., Zhao, S., Wang, H., Feng, X., Zhou, J., Ma, X., 2019. Water contaminant elimination based on metal-organic frameworks and perspective on their industrial applications. ACS Sustain. Chem. Eng. 7, 4548–4563. https://doi.org/10.1021/acssuschemeng.8b05751.

Ltaïef, A.H., Sabatino, S., Proietto, F., Ammar, S., Gadri, A., Galia, A., Scialdone, O., 2018. Electrochemical treatment of aqueous solutions of organic pollutants by electro-Fenton with natural heterogeneous catalysts under pressure using Ti/IrO_2-Ta_2O_5 or BDD anodes. Chemosphere 202, 111–118. https://doi.org/10.1016/j.chemosphere.2018.03.061.

Min Wang, Q., Shen, D., Bülow, M., Ling Lau, M., Deng, S., Fitch, F.R., Lemcoff, N.O., Semanscin, J., 2002. Metallo-organic molecular sieve for gas separation and purification. Microporous Mesoporous Mater. 55, 217–230. https://doi.org/10.1016/S1387-1811(02)00405-5.

Morin-Crini, N., Lichtfouse, E., Fourmentin, M., Ribeiro, A.R.L., Noutsopoulos, C., Mapelli, F., Fenyvesi, E., Vieira, M.G.A., Picos-Corrales, L.A., Moreno-Piraján, J.C., Giraldo, L., Sohajda, T., Huq, M.M., Soltan, J., Torri, G., Magureanu, M., Bradu, C., Crini, G., 2022. Removal of emerging contaminants from wastewater using advanced treatments. A review. Environ. Chem. Lett. 20, 1333–1375. https://doi.org/10.1007/s10311-021-01379-5.

Panizza, M., Cerisola, G., 2009. Direct and mediated anodic oxidation of organic pollutants. Chem. Rev. 109, 6541–6569. https://doi.org/10.1021/cr9001319.

Payam, A.F., Khalil, S., Chakrabarti, S., 2024. Synthesis and characterization of MOF-derived structures: recent advances and future perspectives. Small 20, 2310348. https://doi.org/10.1002/smll.202310348.

Priyadarshini, M., Ahmad, A., Das, S., Ghangrekar, M.M., 2022. Application of innovative electrochemical and microbial electrochemical technologies for the efficacious removal of emerging contaminants from wastewater: a review. J. Environ. Chem. Eng. 10, 108230 https://doi.org/10.1016/j.jece.2022.108230.

Qiao, Z., Wang, Z., Zhang, C., Yuan, S., Zhu, Y., Wang, J., 2012. Catalytic activity of Cu/SBA-15 for peroxidation of pyridine bearing wastewater at atmospheric condition. AIChE J. 59, 215–228. https://doi.org/10.1002/aic.

Ren, G., Lanzalaco, S., Zhou, M., Cabot, P.L., Brillas, E., Sirés, I., 2023. Replacing carbon cloth by nickel mesh as substrate for air-diffusion cathodes: H_2O_2 production and carbenicillin degradation by photoelectro-Fenton. Chem. Eng. J. 454, 140515 https://doi.org/10.1016/j.cej.2022.140515.

Sharma, V.K., Feng, M., 2019. Water depollution using metal-organic frameworks-catalyzed advanced oxidation processes: a review. J. Hazard Mater. 372, 3–16. https://doi.org/10.1016/j.jhazmat.2017.09.043.

Sheng, Y., Sun, Y., Xu, J., Zhang, J., Han, Y.F., 2018. Fenton-like degradation of rhodamine B over highly durable Cu-embedded alumina: kinetics and mechanism. AIChE J. 64, 538–549. https://doi.org/10.1002/aic.15937.

Singh, L., Rekha, P., Chand, S., 2016. Cu-impregnated zeolite Y as highly active and stable heterogeneous Fenton-like catalyst for degradation of Congo red dye. Sep. Purif. Technol. 170, 321–336. https://doi.org/10.1016/j.seppur.2016.06.059.

Sirés, I., Brillas, E., 2021. Upgrading and expanding the electro-Fenton and related processes. Curr. Opin. Electrochem. 27, 100686 https://doi.org/10.1016/j.coelec.2020.100686.

Sirés, I., Brillas, E., Oturan, M.A., Rodrigo, M.A., Panizza, M., 2014. Electrochemical advanced oxidation processes: today and tomorrow. A review. Environ. Sci. Pollut. Res. 21, 8336–8367. https://doi.org/10.1007/s11356-014-2783-1.

Song, G., Zhou, M., Du, X., Su, P., Guo, J., 2021. Mechanistic insight into the heterogeneous electro-Fenton/sulfite process for ultraefficient degradation of pollutants over a wide pH range. ACS ES&T Water 1, 1637–1647. https://doi.org/10.1021/acsestwater.1c00123.

Su, P., Zhou, M., Ren, G., Lu, X., Du, X., Song, G., 2019. A carbon nanotube-confined iron modified cathode with prominent stability and activity for heterogeneous electro-Fenton reactions. J. Mater. Chem. A 7, 24408–24419. https://doi.org/10.1039/c9ta07491k.

Topp, E., Sumarah, M.W., Sabourin, L., 2012. The antihistamine diphenhydramine is extremely persistent in agricultural soil. Sci. Total Environ. 439, 136–140. https://doi.org/10.1016/j.scitotenv.2012.09.033.

Villanueva-Rodríguez, M., Bello-Mendoza, R., Hernández-Ramírez, A., Ruiz-Ruiz, E.J., 2019. Degradation of anti-inflammatory drugs in municipal wastewater by

heterogeneous photocatalysis and electro-Fenton process. Environ. Technol. 40, 2436–2445. https://doi.org/10.1080/09593330.2018.1442880.

Wang, Y., Xue, Y., Zhang, C., 2021. Copper embedded in nitrogen-doped carbon matrix derived from metal-organic frameworks for boosting peroxide production and electro-Fenton catalysis. Electrochim. Acta 368, 137643. https://doi.org/10.1016/j.electacta.2020.137643.

Wolfson, S.J., Porter, A.W., Villani, T.S., Simon, J.E., Young, L.Y., 2018. The antihistamine diphenhydramine is demethylated by anaerobic wastewater microorganisms. Chemosphere 202, 460–466. https://doi.org/10.1016/j.chemosphere.2018.03.093.

Xia, P., Ye, Z., Zhao, L., Xue, Q., Lanzalaco, S., He, Q., Qi, X., Sirés, I., 2023. Tailoring single-atom FeN_4 moieties as a robust heterogeneous catalyst for high-performance electro-Fenton treatment of organic pollutants. Appl. Catal. B Environ. 322, 122116 https://doi.org/10.1016/j.apcatb.2022.122116.

Ye, Z., Oriol, R., Yang, C., Sirés, I., Li, X.Y., 2022. A novel NH_2-MIL-88B(Fe)-modified ceramic membrane for the integration of electro-Fenton and filtration processes: a case study on naproxen degradation. Chem. Eng. J. 433, 133547 https://doi.org/10.1016/j.cej.2021.133547.

Ye, Z., Padilla, J.A., Xuriguera, E., Beltran, J.L., Alcaide, F., Brillas, E., Sirés, I., 2020a. A highly stable metal-organic framework-engineered FeS_2/C nanocatalyst for heterogeneous electro-Fenton treatment: validation in wastewater at mild pH. Environ. Sci. Technol. 54, 4664–4674. https://doi.org/10.1021/acs.est.9b07604.

Ye, Z., Padilla, J.A., Xuriguera, E., Brillas, E., Sirés, I., 2020b. Magnetic MIL(Fe)-type MOF-derived N-doped nano-ZVI@C rods as heterogeneous catalyst for the electro-Fenton degradation of gemfibrozil in a complex aqueous matrix. Appl. Catal. B Environ. 266, 118604 https://doi.org/10.1016/j.apcatb.2020.118604.

Zhang, G., Wang, S., Zhao, S., Fu, L., Chen, G., Yang, F., 2011. Oxidative degradation of azo dye by hydrogen peroxide electrogenerated in situ on anthraquinonemonosulphonate/polypyrrole composite cathode with heterogeneous CuO/γ-Al_2O_3 catalyst. Appl. Catal. B Environ. 106, 370–378. https://doi.org/10.1016/j.apcatb.2011.05.042.

Zhang, Y., Daniel, G., Lanzalaco, S., Isse, A.A., Facchin, A., Wang, A., Brillas, E., Durante, C., Sirés, I., 2022. H_2O_2 production at gas-diffusion cathodes made from agarose-derived carbons with different textural properties for acebutolol degradation in chloride media. J. Hazard Mater. 423, 127005 https://doi.org/10.1016/j.jhazmat.2021.127005.

SUPPLEMENTARY MATERIAL

Enhanced mineralization of pharmaceutical residues at circumneutral pH by heterogeneous electro-Fenton-like process with Cu/C catalyst

Lele Zhao [a], José A. Padilla [b,c], Elena Xuriguera [b], Pere L. Cabot [a], Enric Brillas [a,*], Ignasi Sirés [a,*]

[a] *Laboratori d'Electroquímica dels Materials i del Medi Ambient, Departament de Ciència de Materials i Química Física, Secció de Química Física, Facultat de Química, Universitat de Barcelona, Martí i Franquès 1-11, 08028 Barcelona, Spain*

[b] *DIOPMA, Departament de Ciència de Materials i Química Física, Secció de Ciència de Materials, Facultat de Química, Universitat de Barcelona, Martí i Franquès 1-11, 08028 Barcelona, Spain*

[c] *Grup de Recerca en Tecnologies de Fabricació, Departament d'Enginyeria Mecànica, Escola Tècnica Superior d'Enginyeria Industrial de Barcelona, Av. Diagonal 647, 08028, Barcelona, Spain*

* Corresponding author: brillas@ub.edu (E. Brillas)
i.sires@ub.edu (I. Sirés)

Tables	**Page**
Table S1 - S3	1
Figures	
Fig. S1	2
Fig. S2	2
Fig. S3	3
Fig. S4	3
Fig. S5	4
Fig. S6	4
Fig. S7	5
Fig. S8	6
Fig. S9	6
Fig. S10	7
Fig. S11	7

Table S1

Cu-MOF yield under different synthesis conditions.

Sample	m_p [a] / g	Yield (in %) [b]
Cu-MOF-B	0.2507	9.3
Cu-MOF-A2	0.5526	20.5
Cu-MOF-A12	0.4111	15.3

[a] Mass of the MOF product collected upon centrifugation and drying.

[b] Ratio between the mass of MOF product (m_p) and the total mass of reactants (2.69 g).

Table S2

Cu/C yield under different pyrolysis conditions.

Sample	$m_{p,before}$ [a] / g	$m_{p,after}$ [b] / g	Yield (in %) [c]
Cu/C-B-Ar	0.1001	0.0355	35.5
Cu/C-B-Ar/H_2	0.1007	0.0321	31.9
Cu/C-A2-Ar	0.1805	0.0730	40.4
Cu/C-A2-Ar/H_2	0.1812	0.0679	37.5
Cu/C-A12-Ar	0.2509	0.0961	38.3
Cu/C-A12-Ar/H_2	0.2512	0.0743	29.6

[a] Mass of the MOF product before pyrolysis.

[b] Mass of the MOF product after pyrolysis.

[c] Ratio of $m_{p,after}$ to $m_{p,before}$.

Table S3

Characterization of actual wastewater.

Parameter	Unit	Value
Total carbon (TC)	mg C L^{-1}	48.3
Total organic carbon (TOC) as non-purgeable organic carbon (NPOC)	mg C L^{-1}	9.494 (20.6) [a]
Total nitrogen (TN)	mg N L^{-1}	30.09
Conductance, *G*	mS	1.25
pH		8.04
Cations content	mg L^{-1}	245.3 (Na^+)
		41.8 (K^+)
		114.3 (Ca^{2+})
		31.6 (Mg^{2+})
		0.2 (Fe)
Anions content	mg L^{-1}	146.3 (SO_4^{2-})
		361.1 (Cl^-)
		< 1 (NO_3^-)

[a] After DPH addition, the TOC_0 value of the wastewater is 20.6 mg C L^{-1}.

1

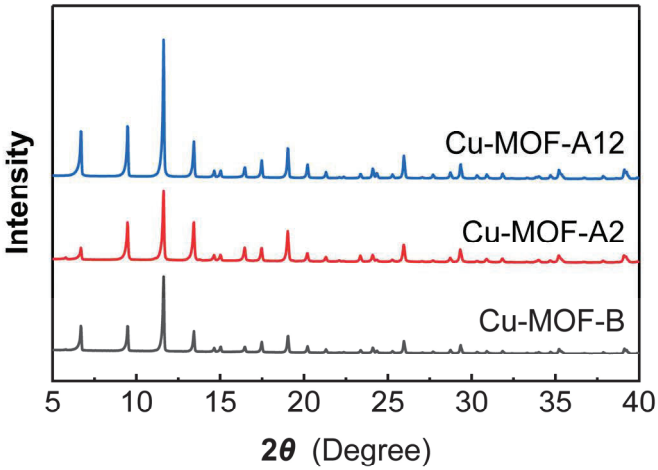

Fig. S1. XRD patterns of synthesized Cu-MOF materials.

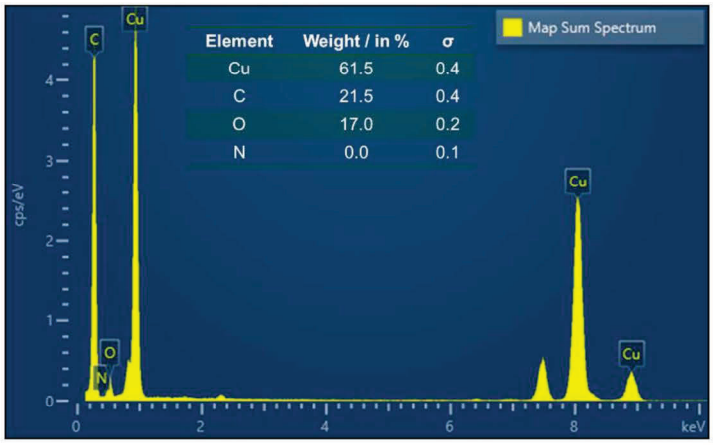

Fig. S2. EDS spectrum of the Cu/C-A2-Ar/H_2 catalyst.

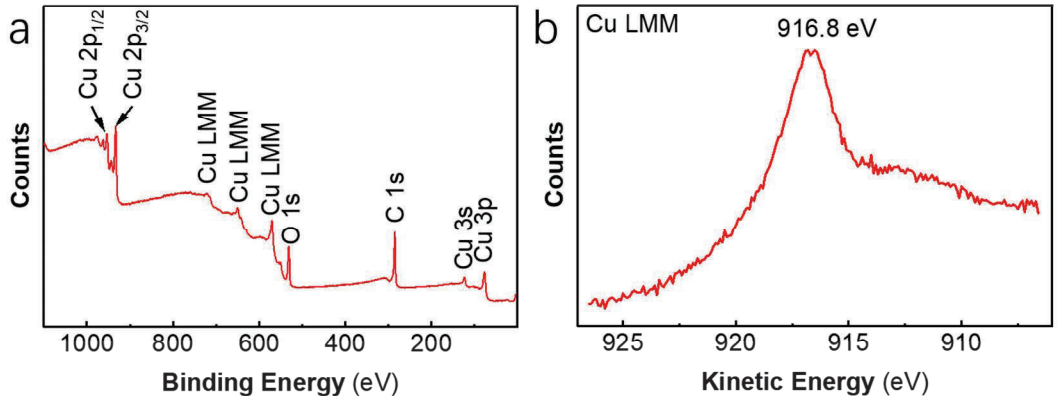

Fig. S3. (a) Full XPS spectrum, and (b) Cu LMM of the as-synthesized Cu/C-A2-Ar/H_2 catalyst.

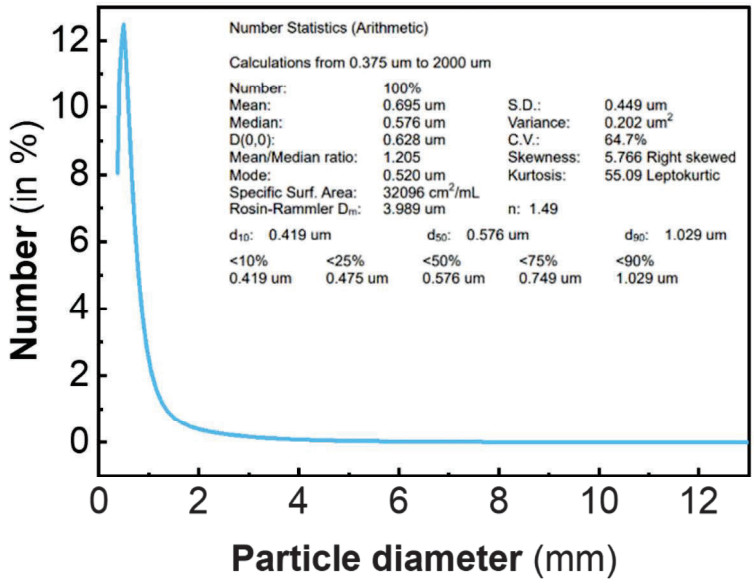

Fig. S4. DLS analysis of the Cu/C-A2-Ar/H_2 catalyst (inset panel: DLS analysis report).

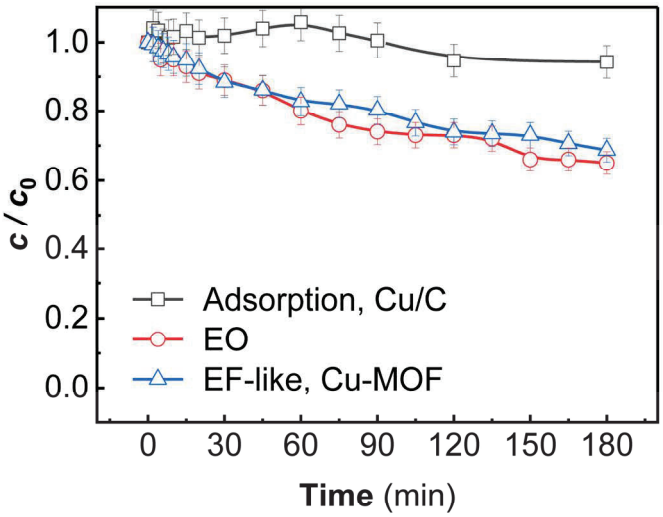

Fig. S5. Normalized DPH concentration decay during different treatments of 150 mL of suspensions with 14.3 mg L^{-1} drug (10 mg C L^{-1} TOC_0) and 50 mM Na_2SO_4 at pH 6. In the adsorption test, 0.1 g L^{-1} Cu/C-A2-Ar/H_2 catalyst was added, and the suspension was stirred continuously. In the electrochemical assays (EO, and EF with Cu-MOF-A2), DSA-Cl_2 and a commercial GDE were employed as the anode and cathode, respectively, at 16.7 mA cm^{-2} and 25 ^oC.

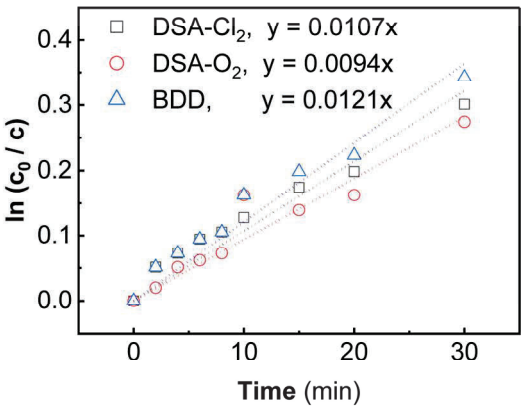

Fig. S6. Pseudo-first-order kinetic analysis of the DPH concentration decays shown in Fig. 4a. The apparent kinetic constants are summarized in the legend.

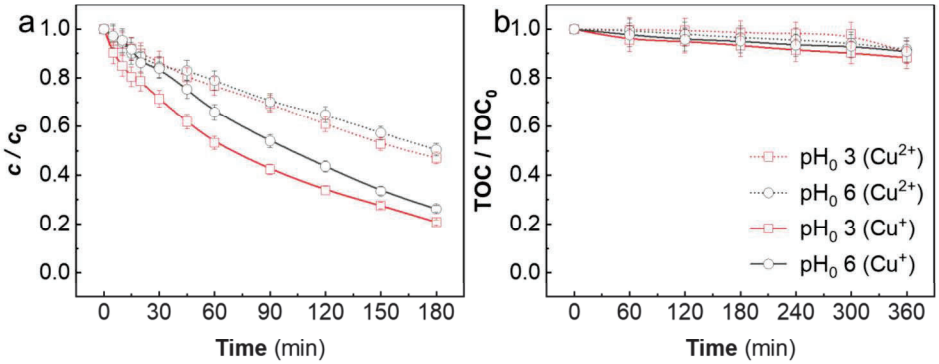

Fig. S7. (a) Normalized DPH concentration, and (b) mineralization vs. electrolysis time during the EF-like treatment (with 0.5 mM Cu^{+} or Cu^{2+} as homogeneous catalyst) of 150 mL of solutions with 14.3 mg L^{-1} drug (10 mg C L^{-1} TOC_0) and 50 mM Na_2SO_4 at 25 °C and at 16.7 mA cm^{-2}, using the DSA-Cl_2/GDE cell.

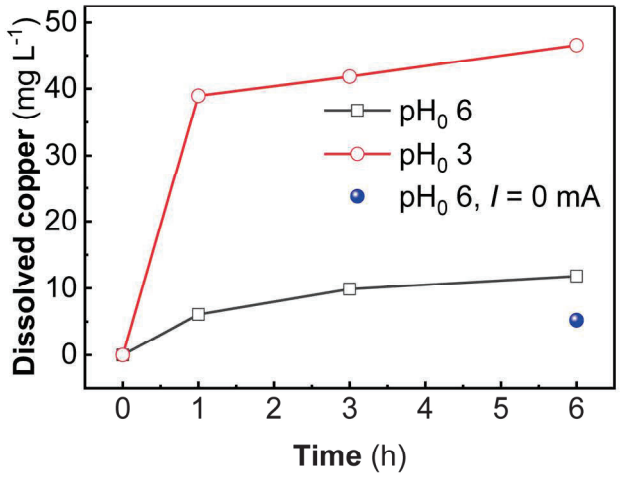

Fig. S8. Leaching tests during the HEF-like treatment of 150 mL of suspensions with 14.3 mg L^{-1} drug (10 mg C L^{-1} TOC_0) and 50 mM Na_2SO_4 at 25 °C and 16.7 mA cm^{-2}, using 0.1 g L^{-1} Cu/C-A2-Ar/H_2 catalyst. DSA-Cl_2 and a commercial GDE were employed as the anode and cathode, respectively (see related DPH degradation tests of Fig. 6). The result obtained at I = 0 mA is shown for comparison.

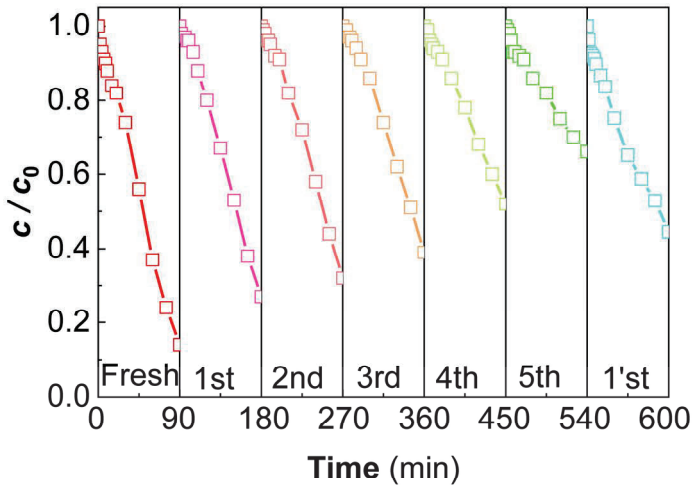

Fig. S9. Reuse of Cu/C-A2-Ar/H_2 catalyst in the HEF-like treatment of 150 mL of suspensions with 14.3 mg L^{-1} drug (10 mg L^{-1} TOC_0) and 50 mM Na_2SO_4 at 25 °C, pH 6 and 16.7 mA cm^{-2} in an undivided cell. DSA-Cl_2 and a commercial GDE were employed as the anode and cathode, respectively. The amount of catalyst recovered each time was accumulated to 0.1 g L^{-1} for the successive stage of testing. At the end of the 5-cycle experiment, a repeated washing by centrifugation in Milli-Q water was carried out as catalyst regeneration procedure.

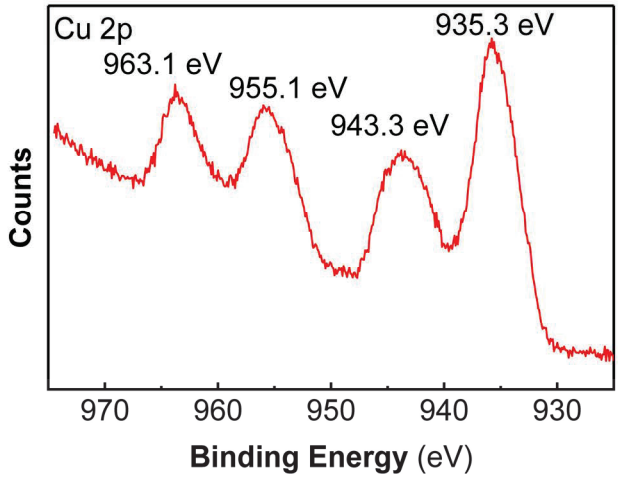

Fig. S10. High-resolution XPS spectrum of Cu 2p for Cu/C-A2-Ar/H_2 catalyst, recovered after 5th run (see Fig. S9).

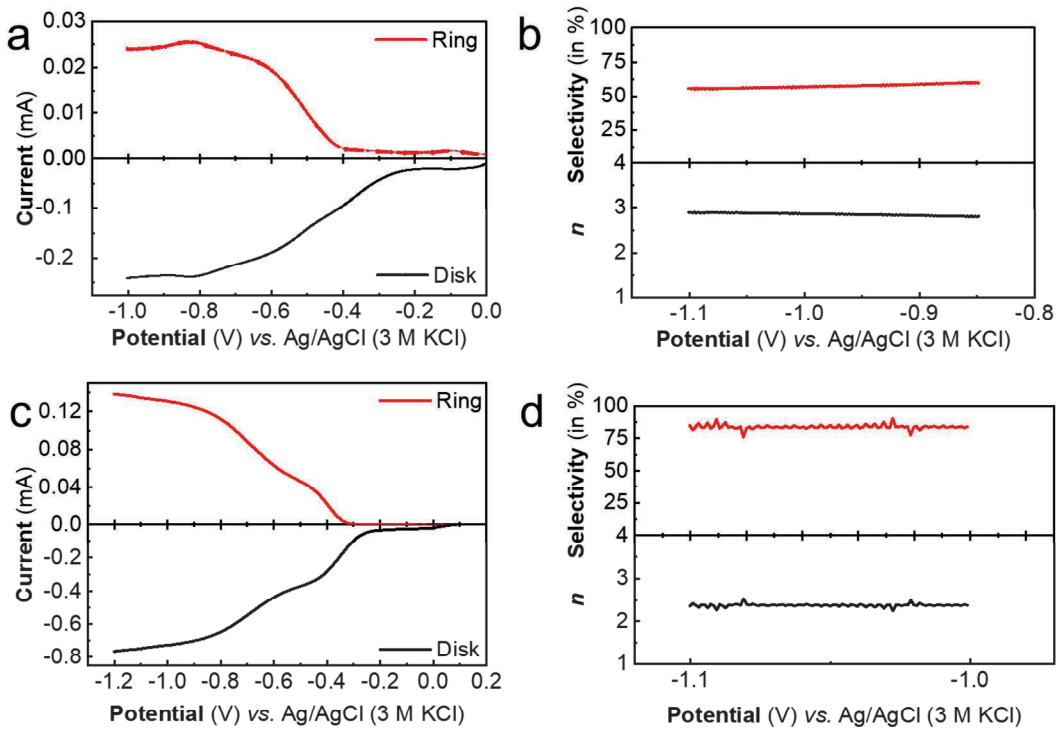

Fig. S11. LSV curves obtained with RRDE modified with Cu/C-A2-Ar/H_2, in O_2-saturated 0.1 M Na_2SO_4 medium (scan rate of 10 mV s^{-1}, rotation rate of 1600 rpm, E_{ring} = 1.0 V, Pt and Ag/AgCl (3 M KCl) as CE and RE, respectively) at (a) pH 4 and (c) pH 6. The calculated electron transfer number (n) and H_2O_2 selectivity (in %) after reaching the limiting current is shown at (b) pH 4 and (d) pH 6.

4.2.2 Bimetallic FeCu-MOF derivatives as heterogeneous catalysts with enhanced stability for electro-Fenton degradation of lisinopril

The previous work opened the door to the use of alternative heterogeneous catalysts for HEF process, where Cu/C allows enhancing the mineralization efficiency but showing a slow degradation of the target pollutant. Recent studies suggest that bimetallic Fe-Cu catalysts could optimize the Fe(II) regeneration, thus leveraging the lower redox potential of copper to thermodynamically support the continuous Fe(III) reduction. FeCu-MOFs and their pyrolyzed derivatives have shown strong promise in Fenton processes. Despite this, the FeCu-based HEF catalysts are still under exploration, with challenges in maintaining effectiveness at neutral pH and ensuring durability across cycles. This study discusses the synthesis of FeCu/NC catalysts, with a carbon capsule for an enhanced stability and electron transfer. Comparative studies with Fe/NC and Cu/NC revealed that Cu(0) significantly enhances the Fe(III) reduction, whereas LC-MS/MS analysis provided insights into the LSN degradation by-products. These findings highlight the potential of FeCu/NC as a stable HEF catalyst for effective, near-neutral pH pollutant removal in wastewater treatment.

A series of characterizations was carried out on the synthesized FeCu/NC, Cu/NC, and Fe/NC catalysts. The XRD analysis confirmed the crystallographic structure of the three catalysts. The FeCu/NC catalyst exhibited diffraction peaks at 44.7°, 65.0°, and 82.3°, corresponding to the (110), (200), and (211) planes of Fe(0), and at 43.3°, 50.4°, and 74.1°, related to the (111), (200), and (220) planes of Cu(0). HRTEM further verified these planes, based on lattice spacing measurements. In contrast, Cu/NC and Fe/NC showed surface oxidation, with the former containing oxides and hydroxides, including CuO, Cu_2O, and $Cu_2(OH)_3Cl$, likely formed during HCl washing; Fe/NC was primarily covered in Fe_3O_4, suggesting a reduced stability in metallic form due to acid pickling. The TEM images showed that the catalysts, prepared through MOF carbonization, displayed a core-shell structure with a carbon layer wrapping the metal core, designed to reduce metal leaching and surface fouling. The size of the FeCu/NC particles was under 50 nm, whereas Fe/NC and Cu/NC had broader particle size distributions in the range of 10-100 nm. BET analysis revealed that Fe/NC had the highest surface area (257.8 $m^2\ g^{-1}$), showing mesoporous properties, whereas

FeCu/NC (98.6 m^2 g^{-1}) and Cu/NC (12.4 m^2 g^{-1}) exhibited nonporous or macroporous characteristics. Elemental mapping indicated that Fe and Cu were embedded within the carbon matrix, with trace N confirming successful doping and slight surface oxidation due to storage. XPS analysis of FeCu/NC, Fe/NC, and Cu/NC catalysts confirmed the presence of C, O, and N, aligning well with TEM observations. Both Fe and Cu were present as expected. For FeCu/NC and Fe/NC, Fe 2p spectra showed peaks linked to Fe(0), FeO, Fe_2O_3, and satellite peaks, with FeCu/NC having a notably higher metallic Fe content (9.6%) as compared to Fe/NC (1.1%). This suggests surface oxidation upon air exposure but minimal impact on the core. Cu(I) was predominantly present on the FeCu/NC surface, while Cu(II) was more evident in Cu/NC, suggesting CuO as the main species in this catalyst. High-resolution N 1s spectra allowed identifying pyridinic and pyrrolic N on all catalysts, with oxidized N present only on Fe/NC and Cu/NC. The presence of multiple oxidation states for Fe and Cu in FeCu/NC, along with pyrrolic N, is favorable for H_2O_2 production on the nanoparticle surface. C_{dl} values were derived from CV curves and compared to N_2 adsorption-desorption data. Fe/NC showed the highest pore volume and smallest pore size, resulting in a high C_{dl}. Worth noting, FeCu/NC exhibited a similar C_{dl} despite its less favorable textural attributes, implying that it is the larger pore volume the factor that more directly correlates with a larger number of electroactive sites. Thus, FeCu/NC was demonstrated to possess a balanced structure and electrochemical properties, being ideal for H_2O_2 activation.

The catalytic efficiency of the three materials was evaluated for HEF treatment of LSN solutions at pH 5.9, with a catalyst concentration of 0.05 g L^{-1}. Minimal LSN removal was observed through pure adsorption, with FeCu/NC achieving the highest (about 10%). Electro-oxidation (i.e., trials without catalyst) led to a removal of 59.5% of LSN in 180 min, primarily due to the action of DSA($^{\bullet}$OH). In HEF treatments, FeCu/NC showed superior catalytic activity, achieving complete LSN degradation within 120 min, outperforming Cu/NC and Fe/NC. Higher current densities (up to 50 mA cm^{-2}) improved the degradation rates, but an of excess H_2O_2 accumulation at higher applied current favored the $^{\bullet}$OH scavenging. Optimal performance was observed at 0.05 g L^{-1} catalyst, with minimal gain beyond this dosage, making it a cost-effective choice. The influence

of initial pH showed the best results at pH 3, where over 70% LSN was removed during pre-electrolytic adsorption, as the neutral form of LSN was more adsorbable and rapidly degraded. Even at pH 5.9, about 80% degradation was achieved in 120 min, demonstrating the effectiveness of FeCu/NC across a broad pH range, from acidic to mildly alkaline conditions.

To assess the mineralization efficiency of FeCu/NC-catalyzed HEF, extended tests were conducted using a DSA/GDE cell at an optimal catalyst dosage of 0.05 g L^{-1}. At pH 3, TOC removal reached 37.1% after 120 min and 45.1% after 360 min, indicating a moderate mineralization due to stable Fe(III)-carboxylate complexes formed in the absence of UVA irradiation. The accumulation of short-chain carboxylic acids, with oxalic acid as the main refractory product, peaked at 60 min, evidencing the existence of limited degradation pathways under these conditions. The reusability of FeCu/NC was promising, with sequential trials showing 100% LSN removal in the second cycle and 86.5% in the fifth, suggesting a relatively strong catalytic durability. The gradual decline in performance was attributed to active site passivation and pore clogging by refractory by-products.

The FeCu/NC-catalyzed HEF process was tested for LSN removal in urban wastewater (UWW) at pH 7.7. Since UWW contains Cl^- and the Ti|RuO_2 anode supports electrochlorination, active chlorine production was assessed under the electrolysis conditions (j = 33.3 mA cm^{-2}), with maximum chlorine accumulation (4.5 mg L^{-1}) reached at 45 min, which later declined due to its interaction with H_2O_2 (produced at the cathode). When LSN was added to the UWW with 4.5 mg L^{-1} active chlorine, 77.3% removal was achieved in 120 min. In HEF trials with 0.05 g L^{-1} FeCu/NC, complete LSN degradation occurred within 60 min, likely due to the role of active chlorine as a secondary oxidant. Catalyst stability tests showed minor iron leaching, with a maximum of 0.19 mg L^{-1}, markedly lower than that of comparable catalysts published by other authors, indicating that Cu doping not only enhances the HEF performance but also improves the catalyst durability by increasing the corrosion resistance of iron.

To further investigate the catalytic role of copper in FeCu/NC, LSV tests of fresh and used (i.e., after one HEF cycle) FeCu/NC and Fe/NC materials were conducted. Fresh catalysts showed no reduction signal; in contrast, a distinct

reduction near 0.77 V appeared in the used samples, indicating the Fe(III) to Fe(II) conversion. Fe/NC displayed a stronger reduction signal, suggesting higher Fe(III) retention, whereas FeCu/NC showed weaker reduced Fe(III) signal, likely due to catalytic role of copper in in-situ Fe(III) reduction. EIS and DRT analysis further revealed that Cu/NC has high ion diffusion, which can serves to explain the greater metal leaching and instability, whereas FeCu/NC had enhanced charge transfer resistance and stability, advantageous for HEF applications.

HPLC-MS analysis informed about the LSN degradation by-products, with primary molecules formed under strong oxidative conditions. A proposed mechanism involves iron and copper species in various oxidation states catalyzing Fenton's and Fenton-like reactions that allow enhancing the $^{\bullet}OH$ production. Fe(II) from Fe(0) drives heterogeneous Fenton's reaction with electrogenerated H_2O_2 as the main $^{\bullet}OH$ source, while Cu(0) and Cu(I) favor the Fe(III) reduction, sustaining the Fe(II) availability. Copper also participates in slower Fenton-like reactions and minor superoxide production, but it primarily supports the Fe(III)/Fe(II) cycling, thereby accelerating the H_2O_2 activation. LSN is sequentially degraded through $^{\bullet}OH$ to short-chain carboxylic acids and ultimately mineralized to CO_2, H_2O, and inorganic ions.

Science of the Total Environment 953 (2024) 176110

Contents lists available at ScienceDirect

Science of the Total Environment

journal homepage: www.elsevier.com/locate/scitotenv

Bimetallic FeCu-MOF derivatives as heterogeneous catalysts with enhanced stability for electro-Fenton degradation of lisinopril

Lele Zhao [a], María F. Murrieta [a], José A. Padilla [b,c], Sonia Lanzalaco [d,*], Pere L. Cabot [a], Ignasi Sirés [a,*]

[a] Laboratori d'Electroquímica dels Materials i del Medi Ambient, Departament de Ciència de Materials i Química Física, Secció de Química Física, Facultat de Química, Universitat de Barcelona, Martí i Franquès 1-11, 08028 Barcelona, Spain
[b] DIOPMA, Departament de Ciència de Materials i Química Física, Secció de Ciència de Materials, Facultat de Química, Universitat de Barcelona, Martí i Franquès 1-11, 08028 Barcelona, Spain
[c] Departament d'Enginyeria Mecànica, Escola Tècnica Superior d'Enginyeria Industrial de Barcelona (ETSEIB), Universitat Politècnica de Catalunya, Av. Diagonal, 647, 08028 Barcelona, Spain
[d] Departament d'Enginyeria Química, EEBE, Universitat Politècnica de Catalunya, C/Eduard Maristany, 10–14, Ed. I2, 08019 Barcelona, Spain

HIGHLIGHTS

- First investigation of lisinopril degradation by electro-Fenton (EF) process
- Low FeCu/N-C dosage (0.05 g L^{-1}) needed for 100 % LSN removal at pH ~6
- After 5 cycles (2 h each), LSN degradation still as high as 86 % and low leaching
- Carbon-wrapped FeCu metallic core from MOF pyrolysis: high activity and stability
- Low-valence Cu promoted Fe(III)-to-Fe(II) conversion in heterogeneous EF.

GRAPHICAL ABSTRACT

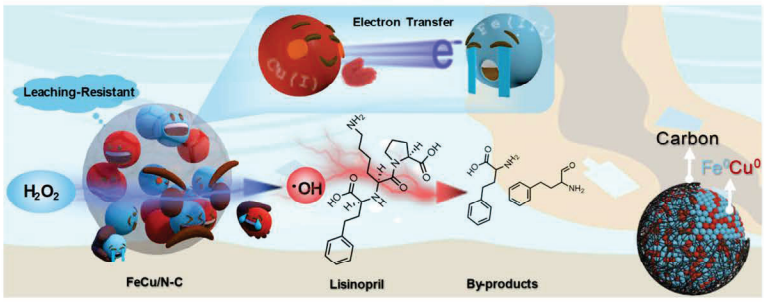

ARTICLE INFO

Editor: Damià Barceló

Keywords:
Electro-Fenton process
Heterogeneous catalysis
Metal leaching
Pharmaceutical pollutant
Wastewater treatment

ABSTRACT

A bimetallic FeCu/NC core-shell catalyst, consisting in nanoparticles where zero-valent Fe and Cu atoms, slightly oxidized on their surface, are encapsulated by carbon has been successfully prepared by modifying the synthesis route of MIL(Fe)-88B. FeCu/NC possessed well-balanced textural and electrochemical properties. According to voltammetric responses, in-situ Fe(III) reduction to Fe(II) by low-valent Cu was feasible, whereas the high double-layer capacitance confirmed the presence of a great number of electroactive sites that was essential for continuous H_2O_2 activation to •OH via Fenton's reaction. Electrochemical impedance and distribution of relaxation times (DRT) analysis informed about the strong leaching resistance of FeCu/NC. To validate the promising features of this catalyst, the advanced oxidation of the antihypertensive lisinopril (LSN) was investigated for the first time. The heterogeneous electro-Fenton (HEF) treatment of 16.1 mg L^{-1} LSN solutions was carried out in a DSA/air-diffusion cell. At pH 3, complete degradation was achieved within 6 min using only 0.05 g L^{-1} FeCu/NC; at near-neutral pH, 100 % removal was also feasible even in actual urban wastewater, requiring 60–75 min. The FeCu/NC catalyst demonstrated high stability, still maintaining 86.5 % of degradation efficiency after 5 cycles

* Corresponding authors.
E-mail addresses: sonia.lanzalaco@upc.edu (S. Lanzalaco), i.sires@ub.edu (I. Sirés).

https://doi.org/10.1016/j.scitotenv.2024.176110
Received 10 August 2024; Received in revised form 4 September 2024; Accepted 5 September 2024
Available online 10 September 2024
0048-9697/© 2024 The Authors. Published by Elsevier B.V. This is an open access article under the CC BY-NC license (http://creativecommons.org/licenses/by-nc/4.0/).

and undergoing low iron leaching. It outperformed the monometallic (Fe/NC and Cu/NC) catalysts, which is explained by the Cu(0)/Cu(I)-catalyzed Fe(II) regeneration mechanism that maintains the Fenton's cycle. LC-MS/MS analysis allowed the identification of two main primary LSN by-products. It can then be concluded that the FeCu/NC-based HEF process merits to be further scaled up for wastewater treatment.

1. Introduction

The integral protection of aquatic ecosystems is becoming increasingly challenging as the discharge of noxious substances is unceasingly growing in terms of both, variety and quantity. Among multiple concerns, the appearance of angiotensin-converting enzyme (ACE) inhibitors is currently a central issue. Lisinopril (LSN) belongs to this class of drugs, being mostly used to relax arteries and veins for controlling blood pressure (Silva-Velasco et al., 2024). Hypertension is the leading cause of premature death globally, with an estimated worldwide impact on 1.28 billion adults aged 30–79 years, according to the World Health Organization (2023). LSN is a very common antihypertensive and, since it is not metabolized at all, it is completely excreted through urine. As a result, 15 ng L^{-1} was detected at the inlet of sewage treatment plants (Stankiewicz et al., 2015). The same authors reported that conventional technologies are unable to remove LSN efficiently. In addition, analysis of fish samples collected from river in Croatia in 2021 and 2022 showed LSN bioaccumulations ranging from 1.0 to 10.2 ng g^{-1} (Ivankovic et al., 2023). LSN was also detected in rivers and estuaries from South Africa, thus becoming the entry route to the Indian Ocean (Netshithothole and Madikizela, 2024).

The advanced oxidation processes (AOPs) are gaining attention for wastewater treatment due to their simplicity, which is combined with high effectiveness (Zhang et al., 2023). The electrochemical AOPs are a subtype that gathers several methods (Martínez-Huitle et al., 2023). Among them, the electro-Fenton (EF) process is especially advantageous in terms of degradation kinetics, also showing easy-to-modulate (re) generation of hydroxyl radical ($^{\bullet}OH$) precursors like H_2O_2 and Fe^{2+} (Sirés and Brillas, 2021). Nonetheless, the iron speciation in conventional EF process is directly affected by pH; above pH 3, soluble iron ions tend to precipitate, thus stopping the H_2O_2 activation, which decelerates the decontamination process (Wang et al., 2024b). To widen the pH range and avoid other shortcomings (e.g., large H_2O_2 consumption, management of final iron sludge), the heterogeneous EF (i.e., HEF) process has become popular (Wang et al., 2024a). In HEF systems, soluble Fe^{2+} catalyst is replaced by immobilized iron. Lately, most research has focused on how to enhance the Fe(III)/Fe(II) redox cycle in the solid phase to improve the catalytic activity and the H_2O_2 utilization rate (Wang et al., 2024a; Xia et al., 2023).

Natural iron ores such and zero-valent iron (ZVI) are commonly used in iron-based heterogeneous catalysis (Xia et al., 2024; Ye et al., 2020a). Nidheesh and Gandhimathi (2014) reported the superiority of the ZVI-catalyzed HEF system over homogeneous EF with iron, and EF-like with copper or manganese to treat textile dyes. However, the formation of dense iron oxides on the surface can easily cause the catalyst passivation, thereby decreasing the degradation performance and limiting the reuse. The loading of ZVI or iron oxides on a solid carrier can minimize this problem as well as particle agglomeration. For example, Dong et al. (2019) used carbon fiber paper to support polyaniline and Fe_3O_4; at current density (*j*) of 5 mA cm^{-2} and pH 3, 20 mg L^{-1} *p*-nitrophenol could be completely degraded in 60 min, with total organic carbon (TOC) decay of 51 %. Bounab et al. (2015) prepared an iron-loaded activated carbon for HEF degradation of *m*-cresol and *tert*-butylhydroquinone, showing excellent adsorption capacity along with high catalytic efficiency. Zhang et al. (2020) used ZVI nanoparticles impregnated on biochar; at pH 7, 50 mg L^{-1} of the pollutant chlorothiazide could be almost completely degraded. However, in these traditional heterogeneous catalysts, the degradation mechanism is mainly based on the Fe^{2+}-mediated Fenton's reaction, since iron atoms are substantially dissolved. Most of these studies have been performed in acidic environment, which easily leads to the collapse of the catalyst and impedes its successful reuse.

Metal-organic frameworks (MOFs) are formed by inorganic nodes (metals or metal clusters) and organic ligands, linked through covalent bonds or other intermolecular forces, and have three-dimensional periodicity comprising interconnected pores (Ye et al., 2020a). Given their easy functionalization arising from a rich diversity of organic ligands and metal centers, MOFs combine key surface and textural properties such as large specific surface area, tunable porosity and abundant active sites. On the other hand, post-synthetic MOF manipulation can also be of interest for enriched catalysis (Deng et al., 2023; Martínez-Huitle et al., 2023; Xu et al., 2023), with carbonization becoming an appealing strategy to improve the structural stability and conductivity. The heat treatment can increase even the catalytic activity because it causes the valence state of metal sites to change, generating more unsaturated metal active sites, which is beneficial for Fenton's reaction (Ye et al., 2020a). Therefore, the use of pyrolyzed MOFs has allowed expanding the application of HEF process. The resulting carbon layer may act as a protective barrier that slows down the metal leaching, simultaneously boosting the Fe(II) recycling by reducing the Fe(III) reduction overpotential (Wang et al., 2023a). Several MOFs have been used as catalysts in AOPs (da Silva et al., 2024). Liu et al. (2019) prepared a variety of heterogeneous catalysts upon high-temperature pyrolysis of the Fe-MIL series to degrade herbicides, with a decaying removal rate in the order: MIL-100(Fe) > NH_2-MIL-88B(Fe) > MIL-88B (Fe).

Worth mentioning, regardless of the nature of the iron-based heterogeneous catalyst, Fe(II) regeneration is known to be the rate-limiting step in chemical Fenton and HEF processes (Cao et al., 2020; Ye et al., 2023). Aiming to solve this problem, scholars have developed bimetallic catalysts in recent years. Copper is considered an interesting candidate to follow this approach (Liu et al., 2024), since the standard reduction potential of Cu^{2+}/Cu^{+} (0.17 V) is lower than that of Fe^{3+}/Fe^{2+} (0.77 V), being the reduction of Fe^{3+} by Cu^{+} thermodynamically feasible (Du et al., 2021). The study of FeCu-MOFs and their pyrolysis-derived analogues has been mostly carried out in the context of chemical Fenton treatment. For example, Wang et al. (2023b) used hydrothermal and microwave-assisted methods to prepare a new bimetallic FeCu-MOF catalyst (BUC-96). Upon addition of 3.9 mM H_2O_2 and 0.2 g L^{-1} BUC-96 catalyst to a solution containing 20 mg L^{-1} chloroquine phosphate, they observed a total pollutant degradation in only 5 min at pH of 5.5. Song et al. (2023) synthesized a Cu@MIL-88B bimetallic catalyst, which could degrade 100 mg L^{-1} of phenol in 30 min at pH 3 after the addition of 8 mM H_2O_2 and 0.1 g L^{-1} of catalyst. Conversely, the application of FeCu-based catalysts in HEF process is very incipient. Zhao et al. (2021) pyrolyzed Fe- and Cu- co-doped ZIF-8 precursors, but they employed the resulting catalyst to modify a carbon paper that was then used as cathode; an efficient degradation of 4-chlorphenol was achieved at pH 5 due to the synergistic effect between dechlorination on monoatomic Cu and $^{\bullet}OH$-mediated oxidation on monoatomic Fe. Very few works have reported on the FeCu-catalyzed HEF. Among them, Du et al. (2021) synthesized Fe/Cu-MOFs by solvothermal method, followed by pyrolysis under Ar atmosphere; sulfamethazine (10 mg L^{-1}) was completed removed in 60 min at 25 mA and pH 4, using a catalyst dose of 0.025 g L^{-1}, but the reuse was poor and only 40 % disappeared at initial pH 6. To reach 100 % drug removal, Wang et al. (2024b) reported the need of 0.1 g L^{-1} $Cu_{0.5}Fe_{2.5}S_4$ at pH 7, whereas Xue et al. (2023) had to employ 0.5 g L^{-1} CuCoFe layered double hydroxide at pH 5.0. In conclusion,

although HEF with FeCu/C is envisioned as a promising process, especially because of the usually lower amount of catalyst needed as compared to chemical Fenton that requires ≥0.1 g L^{-1}, some problems still persist. In particular, the limited degradation performance at near-neutral pH and drastic loss of performance after few cycles.

Considering the great interest of Fe-Cu coupling, carbon-encapsulated bimetallic structures (i.e., FeCu/NC) have been synthesized and investigated as potential HEF catalysts to treat model solutions and urban wastewater at near-neutral pH. Fe/NC and Cu/NC catalysts were also prepared for comparison. The physicochemical and electrochemical properties of the three catalysts were systematically investigated, along with the contribution of Cu(0) to the Fe(III) reduction. Reuse experiments demonstrated the good stability of the bimetallic FeCu/NC catalyst, whereas the main degradation by-products of LSN by an AOP have been elucidated for the first time by LC-MS/MS.

2. Materials and methods

2.1. Chemicals

Lisinopril (pharmaceutical secondary standard, certified reference material) was purchased from Merck. Sodium sulfate, hydroxide pellets, and sulfuric acid (96 %–98 % purity) were of analytical grade from Merck. Ferric nitrate nonahydrate from Probus, as well as copper(II) nitrate trihydrate (99–104 %), 2-aminoterephthalic acid (NH_2-BDC) and. *N,N*-dimethylformamide (DMF, 99.9 %) from Sigma-Aldrich were employed for the synthesis of Cu-, Fe-, FeCu-MOF. Methanol (reag. USP, Ph. Eur. for analysis, ACS, ISO) and ethanol 96 % v/v (reag. USP, Ph. Eur., analytical grade) were from PanReac AppliChem. Formic acid (Optima LC/MS) purchased from Fisher Chemical and acetonitrile (reag. Ph. Eur. for UHPLC Supergradient, ACS) from PanReac Applichem were used to prepare the mobile phase. N,N-Diethyl-*p*-phenylenediamine sulfate salt (DPD) acquired from Fluka Analytical, ethylenediaminetetraacetic acid disodium salt dihydrate (EDTA, 99 %–101 % assay, ACS reagent grade) from Sigma-Aldrich, as well as pure potassium di-hydrogen phosphate (KH_2PO_4, USP, Ph. Eur.) and di-sodium hydrogen phosphate anhydrous (Na_2HPO_4, reag. USP, Ph. Eur., analytical grade) from PanReac AppliChem were used for color development in the determination of active chlorine. 1,10-Phenanthroline monohydrate, (99 + %) from Alfa Aesar, as well as glacial acetic acid (reag. USP, Ph. Eur., analytical grade) and ammonium acetate (reag. USP, Ph. Eur., analytical grade) from PanReac AppliChem, and L-ascorbic acid (anhydrous, ACS reagent, ≥99 %) from Merck were used for color development in the determination of dissolved iron. All these reagents were used as received without further purification. The aqueous solutions were prepared with Milli-Q water (resistivity >18.2 MΩ cm) produced on a Synergy UV device from Merck Life Science.

2.2. Synthesis procedure

The synthesis was based on a previous procedure followed by LEMMA group (Ye et al., 2020a), and it is schematized in Fig. 1. To synthesize the FeCu-MOF, 5 mmol (2.020 g) $Fe(NO_3)_3{\cdot}9H_2O$ and 5 mmol (1.208 g) $Cu(NO_3)_2{\cdot}3H_2O$ was dissolved in 35 mL DMF, respectively. Also, 10 mmol (1.791 g) NH_2-BDC was dissolved in 25 mL DMF. Both solutions were sonicated for 10 min to ensure homogeneity, whereupon they were mixed evenly and transferred to an autoclave, kept at 110 °C for half a day. The resulting dark red powder, corresponding to FeCu-MOF, was collected by centrifugation and repeatedly washed with ethanol. Then, the FeCu-MOF was vacuum-dried at 50 °C overnight. The powder was then pyrolyzed at 800 °C for three hours under N_2 atmosphere (heating rate of 5 °C min^{-1}). The carbonization product was treated by reflux using a 0.2 M HCl solution for 2 h at 50 °C. This was followed by rinsing with deionized water and overnight drying, giving rise to FeCu/NC catalyst. Fe/NC and Cu/NC were obtained similarly, using only one nitrate salt in the first step.

2.3. Catalyst surface characterization

Several techniques were used to analyze the morphological features, structure, composition, size, and other relevant properties of the synthesized materials. The morphology was assessed by high-resolution transmission electron microscopy (HRTEM), using a JEOL JEM-2100 (LaB6) microscope operating at 200 kV in STEM mode with a dark-field detector and coupled to an Oxford Inca energy-dispersive X-ray spectrometer (EDS). HRTEM analysis was made with Digital Micrograph software, whereas mapping acquisition was accomplished with the Inca Microanalysis Suite v. 4.09 software.

Powder X-ray diffraction (XRD) analysis was carried out using a PANalytical X'Pert PRO MPD Alpha-1 powder diffractometer in Bragg-Brentano $\theta/2\theta$ geometry with Cu Kα_1 radiation (λ = 1.5406 Å). The 2θ-scans ranged from 4 to 100°, with a step size of 0.017° and a measuring time of 150 s. Samples were prepared by pressing the powdery materials with a glass plate to yield a flat surface.

The specific surface area was determined using the Brunauer-Emmett-Teller (BET) method, where N_2 was used as the adsorbate gas. The data were obtained using a TriStar 3000 surface area analyzer from Micromeritics within the $0.05 \leq P/P_0 \leq 0.25$ range. Sample outgassing was performed under vacuum at 40 °C for 4 h.

X-ray photoelectron spectroscopy (XPS) analysis was performed with a PHI 5500 Multitechnique System (Physical Electronics) using a monochromatic X-ray source (Al Kα line of 1486.6 eV energy, 350 W), placed perpendicular to the analyzer axis and calibrated using the $3d_{5/2}$ line of Ag with a full width at half maximum (FWHM) of 0.8 eV. The analysis was done on a circular area ($\varnothing$ = 0.8 mm). The selected resolution for the spectra was 187.85 eV of Pass Energy (PE), 0.8 eV/step for the general spectra, and 23.5 eV of PE and 0.1 eV/step for the different elements. The energy electron gun was lower than 10 eV. All

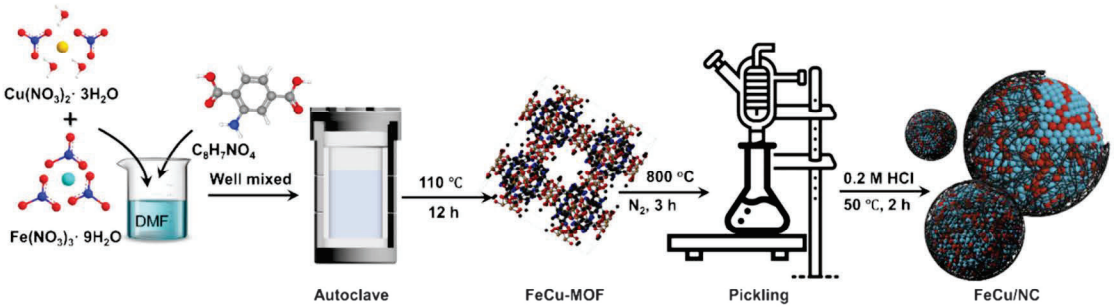

Fig. 1. Scheme of FeCu/NC catalyst synthesis. In the case of Fe/NC and Cu/NC catalysts, only one of the two initial nitrates was employed.

measurements were made under ultra-high vacuum at pressures ranging from 5×10^{-9} to 2×10^{-8} Torr. The spectra were analyzed using ULVAC-PHI MultiPakTM software v. 8.2.

2.4. Electrochemical characterization

The electrochemical characterization of the catalysts was carried out in a conventional three-electrode glass cell containing 0.1 M Na_2SO_4 solution at natural pH, kept at room temperature by recirculating water, and using a Autolab PGSTAT100 potentiostat from Metrohm. The reference and counter electrodes were an Ag|AgCl (3 M KCl) and a Pt spiral, respectively. The working electrode was a Metrohm rotating disk electrode (RDE) comprising a glassy carbon tip ($Ø = 5$ mm, $A = 0.196$ cm^2) covered with a PTFE body. Before ink loading onto the glassy carbon electrode, this was polished with Micropolish II deagglomerated alumina of 0.3 and 0.05 μm on Buehler's PSA-backed white felt cloth. After each polishing step, the glassy carbon tip was sonicated in water. The catalyst ink, which was prepared by mixing 5 mg of catalyst, 60 μL of Nafion, 500 μL of isopropanol, and 500 μL Milli-Q water, was sonicated for one hour before use. Suitable amounts of a given ink were deposited onto the tip to ensure a catalyst loading of 0.5 mg cm^{-2}. After ink loading, the electrode was dried naturally. Linear sweep voltammetry (LSV) analysis was carried out in 100 mL of N_2-saturated electrolyte, at a scan rate of 5 mV s^{-1} and 1600 rpm.

To measure the double-layer capacitance (C_{DL}) of the different catalysts, static cyclic voltammetry (CV) was carried out within a potential range in which no apparent faradaic processes occurred. Hence, all measured current was assumed to be capacitive. That range was typically a 0.1 V potential window centered at the open-circuit potential (OCP) in N_2-saturated 0.1 M Na_2SO_4 solution at natural pH. The same cell and electrodes described above were employed for CV measurements. The working electrode potential was always scanned for several cycles, until the signal became stable, and then the voltammogram was recoded towards less positive potentials, at different scan rates in the range 5–100 mV s^{-1}. The capacitive current values (i.e., $\Delta I = I_a - I_c$, denoting the anodic and cathodic current at OCP) were plotted as a function of the scan rate. From the resulting linear plots, the averaged absolute values of the slopes was the C_{DL}.

Electrochemical impedance spectroscopy (EIS) was carried out using a Solartron SI-1287 potentiostat combined with an SI 1255 frequency response analyzer (Garcia-Cardona et al., 2023). The different ink-loaded RDEs described above served as the working electrode, whereas Pt and a reversible hydrogen electrode (RHE) were used as the counter and reference, respectively. The signals were recorded in an O_2-saturated 0.1 M Na_2SO_4 solution at natural pH and room temperature. The applied potential was 0 V vs. OCP, and the frequency range was from 5 MHz to 0.5 Hz. The distribution of relaxation times (DRT) was analyzed from the EIS data (Li et al., 2019; Wan et al., 2015).

2.5. Electrolytic trials

The degradation experiments were carried out under continuous stirring provided by a PTFE follower in a single-compartment glass cell, open to the atmosphere and thermostated at 25 °C. Each electrolysis was performed at constant current by employing an Amel 2053 potentiostat-galvanostat. The cathode was a 3-cm^2 carbon-PTFE/carbon cloth (Fuel Cell Store) that served as air-diffusion electrode, placed in a tubular gas chamber, and fed with ambient air pumped at 0.4 L min^{-1} to ensure a continuous H_2O_2 production. The 3-cm^2 anode was a commercial Ti plate coated with RuO_2, from NMT Electrodes. The interelectrode gap was 1.0 cm. For each new cathode, an electrolysis was run in 150 mL of a 0.050 M Na_2SO_4 solution at 300 mA for 180 min, allowing the surface cleaning and stabilization. The degradation trials were made with 150 mL of 0.050 M Na_2SO_4 solutions. The HEF treatments were performed in the presence of one of the synthesized catalysts. To reach an adsorption-desorption equilibrium between the catalyst and the target contaminant, a 20-min stirring in the presence of the suspended catalyst was required prior to start the electrolytic trial.

Some experiments were carried out in actual wastewater, which was collected from the secondary decanter of an urban wastewater (UWW) treatment plant located near Barcelona. Right after collection, it was filtered and preserved in a refrigerator at 4 °C to maintain its characteristics. The target pollutant was spiked into this wastewater at a given concentration to evaluate the performance of the degradation process. The specific parameters of the raw wastewater are summarized in Table S1.

2.6. Other instruments and analytical methods

The specific conductivity and pH of solutions were determined from measurements made with a Metrohm 644 conductometer and a Crison GLP 22 pH meter, respectively. Before every analysis, all the samples were microfiltered (0.45 μm, Whatman syringe filters).

Once a sample was collected during the electrolytic trials, the Fenton's reaction was stopped by mixing with the same volume of an aliquot of the mobile phase (see below). TOC from solutions was determined on a Shimadzu TOC-VCNS analyzer, using the non-purgeable organic carbon (NPOC) method, thus obtaining highly reproducible values with ±1 % accuracy. LSN concentration was analyzed by reversed-phase high-performance liquid chromatography (HPLC) using a Waters 600 chromatograph coupled to a Waters 996 photodiode array detector set at 211 nm. A Kinetex 5 μm Biphenyl 100 Å (250 mm × 4.6 mm) LC column, kept at 35 °C, was employed for accurate separation. The mobile phase was a mixture of CH_3CN and 0.1 % formic acid in Milli-Q water, 15:85 (v/v), eluted at 1.0 mL min^{-1}, yielding a peak for LSN at 4.0 min. The carboxylic acids were determined at $\lambda = 210$ nm by ion-exclusion HPLC using the same chromatograph, but equipped with a Bio-Rad Aminex HPX 87H (300 mm × 7.8 mm) column kept at 30 °C. The elution was carried out using a 4 mM H_2SO_4 solution as mobile phase at 0.6 mL min^{-1}.

LC-MS/MS was employed to detect the primary by-products of LSN degradation. A Thermo Fisher Scientific system composed of an Ultimate 3000 HPLC fitted with an Acquity BEH C18 1.7 μm (100 mm × 2.1 mm) column, kept at 40 °C and coupled to a LTQ-Orbitrap Velos and an Accela PDA, was used. The mobile phase contained two components: A (H_2O with 0.2 % acetic acid) and B (acetonitrile with 0.1 % formic acid). The elution gradient was made by increasing the composition of component B, as follows (time in minutes, %B): (0, 5), (1, 5), (10, 95), (10.1, 5), (15, 5). The flow rate was 0.2 mL min^{-1}.

The dissolved Fe^{2+} concentration was obtained by measuring the absorption of the reddish solutions that resulted from the cation complexation with 1,10-phenantroline, at the wavelength that yielded the maximum absorbance ($\lambda = 510$ nm) on a Shimadzu 1800 UV/Vis spectrophotometer. For this, 4 mL of sample were mixed with 1 mL of complex agent (1 g L^{-1}) and 1 mL acetate buffer solution. The total dissolved iron was measured after the Fe^{3+} was reduced to Fe^{2+} upon the addition of ascorbic acid as a solid. The active chlorine concentration was obtained by means of the DPD colorimetric method (4500-Cl. G) (Zhu et al., 2019). The absorbance of the final pink solution was measured at $\lambda = 515$ nm using the same spectrophotometer.

3. Results and discussion

3.1. Characterization of the synthesized catalysts

The crystallographic structure of the FeCu/NC, Cu/NC, and Fe/NC was characterized by XRD (Fig. 2). For the bimetallic catalyst (Fig. 2a), the diffraction peaks appearing at 44.7°, 65.0° and 82.3° can be attributed to (110), (200) and (211) planes of Fe(0) (JCPDS card 87–0721) (Ye et al., 2020a), whereas those at 43.3°, 50.4°, 74.1° correspond to (111), (200), and (220) planes of Cu(0) (JCPDS card 99–0034) (Wang et al., 2016). The (110) crystal plane of Fe(0) and the (111) of Cu(0), which are

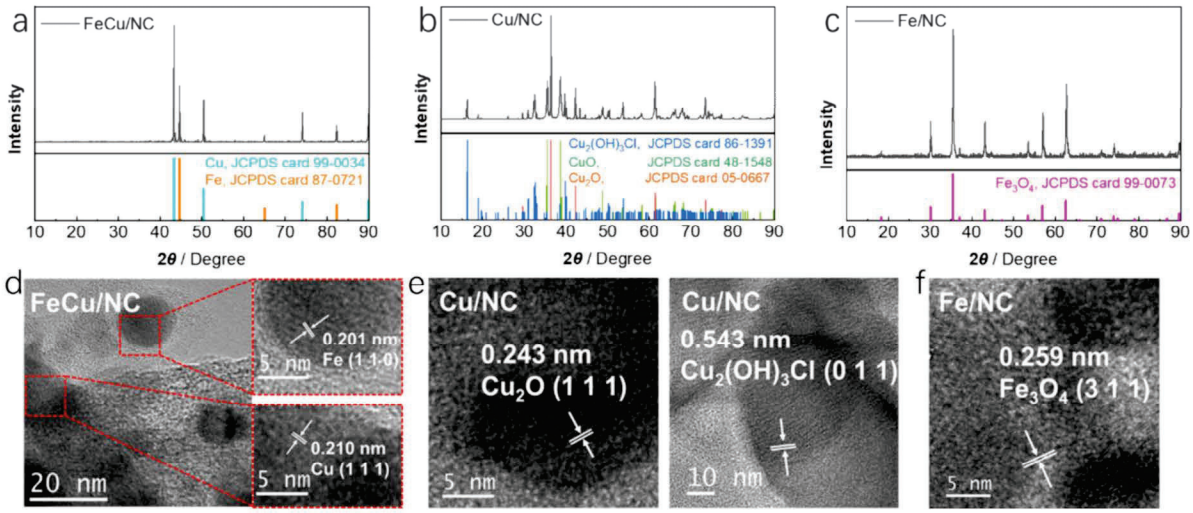

Fig. 2. X-ray diffraction patterns and HRTEM images of (a, d) FeCu/NC, (b, e) Cu/NC, and (c, f) Fe/NC.

the most intense respectively, can also be clearly distinguished by measuring the lattice spacing in the HRTEM images (Fig. 2d) (He et al., 2019). In contrast, the Cu/NC and Fe/NC catalysts showed oxidized surfaces (Fig. 2b and c), especially in the case of Cu/NC that presented multiple oxides (CuO and Cu_2O) and hydroxides ($Cu_2(OH)_3Cl$, probably formed during the washing with HCl), as corroborated by the lattice parameters determined from the HRTEM images (Fig. 2e). From Fig. 2c and f, it is evident that the Fe/NC catalyst surface is mainly composed of Fe_3O_4. In conclusion, Cu/NC and Fe/NC seem to have poor stability in their metallic state, easily undergoing surface oxidation during the acid pickling process.

The three catalysts were obtained by MOF carbonization, and the synthesized catalysts exhibited a core-shell structure, with a protective carbon layer wrapping the metal core (Fig. 3a, Fig. S1a, and S1b). Such an encapsulation is expected to minimize the iron and copper corrosion, thus reducing the metal leaching, as well as to prevent the nanocatalyst surface contamination/fouling typically occurring when inorganic and organic ions and molecules become adsorbed or precipitate. As can be seen in Fig. 3a, the size of the bimetallic FeCu/NC particles is mostly smaller than 50 nm, whereas the particle size distribution of Fe/NC (Fig. S1a) and Cu/NC (Fig. S1b) is less uniform, with sizes ranging around 10–100 nm. The specific surface area and porosity of the three materials were analyzed by means of N_2 adsorption/desorption isotherms (Fig. S2). Fe/NC had a much larger BET surface area, 257.8 m^2 g^{-1}, followed by FeCu/NC and Cu/NC, with 98.6 m^2 g^{-1} and 12.4 m^2 g^{-1}, respectively. The Fe/NC sample displays a type IV isotherm, thus being classified as a mesoporous material. The FeCu/NC and Cu/ NC samples are close to type II and III isotherms, respectively. Both can be classified as nonporous or macroporous materials, although according to the IUPAC, type II isotherms possess better adsorption properties (Thommes et al., 2015).

An area of interest was selected during TEM analysis to obtain the elemental mapping of the FeCu/NC sample. Fig. 3b shows that the location of Fe and Cu elements coincide with that of carbon, meaning that the FeCu particles are randomly embedded in the carbon protective layer. In addition, the presence of trace amounts of N along the particles confirms the successful doping of the carbon matrix. The presence of oxygen suggests that the surface of the sample was slightly oxidized during the storage.

The samples were analyzed using XPS to better understand the chemical composition (metal-based species and type of N functionalities) of the catalyst surface. According to the full XPS spectrum analysis

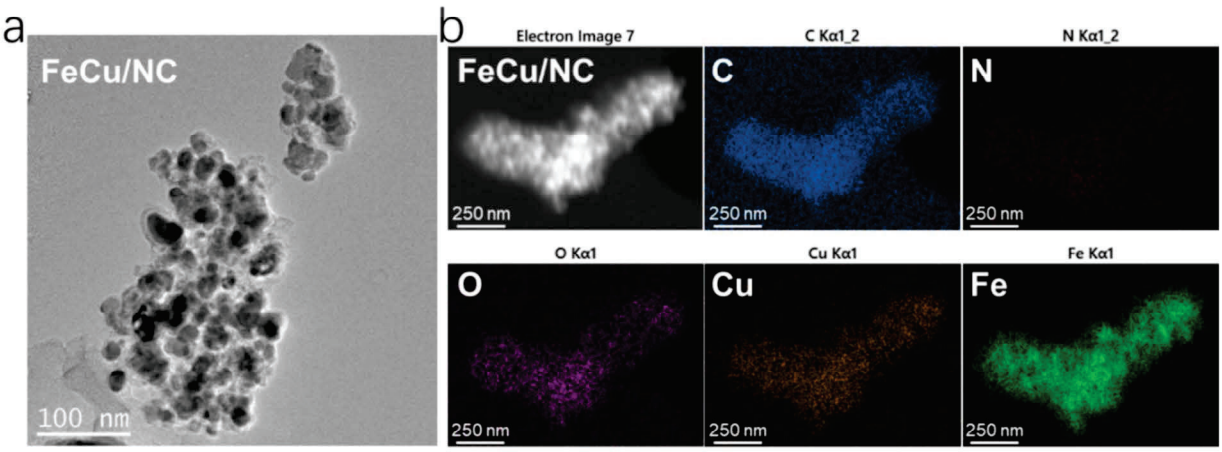

Fig. 3. (a) TEM morphology, and (b) EDX analysis of FeCu/NC catalyst.

of the three samples (Fig. S3), C, O, and a small amount of N were always present, verifying the TEM analysis. Fe and Cu appeared in the samples as expected beforehand. Fig. 4a shows the XPS spectra of Fe 2p for FeCu/NC and Fe/NC, evidencing four clear bands that corresponded to Fe $2p_{1/2}$, Fe $2p_{3/2}$ and two satellites. Overall, these could be deconvoluted into seven and five characteristic peaks for FeCu/NC and Fe/NC, respectively, distributed as follows (Ai et al., 2019; Fang et al., 2020): in the low energy region, the first peak appearing at 706.7 eV in both samples can be related to the presence of metallic iron on the catalyst surface, since the formation of iron carbide would require the presence of a peak at 707.5 eV (Idczak et al., 2016); then, the peaks at 710.9 and 725 eV can be associated with FeO; and two other peaks, at 713.5 and 727 eV, can be related to Fe_2O_3; finally, satellite peaks appeared at 720 and 733 eV. Note, however, that the peak distribution is also compatible with the presence of Fe_3O_4 as main surface oxide, since that is a mixture of Fe(II) and Fe(III) species, and this possibility is reinforced by the results shown in Fig. 2c and f. Another important finding is that, despite the presence of signals related to oxides observed on the surface of both samples, the content of metallic Fe on FeCu/NC was 9.6 %, which was much higher than in the case of Fe/NC (1.1 %). To sum up, the combination of Fig. 4a with Fig. 2a and d suggests that the surfaces of all the prepared electrocatalysts are easily oxidized upon exposure to air contact; however, this oxidation is limited to the surface and does not affect the bulk of the particles.

On the other hand, according to the results depicted in Fig. 4b (kinetic energy in the x axis), the FeCu/NC sample exhibits the characteristic peak of Cu(I) at 916.8 eV, whereas a peak at 917.7 eV attributed to Cu(II) prevails in Cu/NC (Zhang et al., 2016). The presence of lower-valence copper on the surface of the bimetallic catalyst can also be inferred from Fig. S4 (Tang and Wang, 2019). Therefore, coming back to Fig. 2b, it can now be stated that CuO was the prevalent copper species in the Cu/NC surface.

Regarding the high-resolution N 1s XPS spectra of the three catalysts, Fig. 4c shows very strong signals at 398.3–398.5 and 400.8–401.0 eV, corresponding to pyridinic and pyrrolic nitrogen, respectively (Zhu et al., 2018). The quantification of these two types of functionalities in the three samples can be seen in Fig. 4d. Considering that O_2 can be adsorbed on metallic sites, and these have a range of possible oxidation states (Fe(0), Fe(II) and Fe(III); Cu(0), Cu(I), Cu(II)), O_2 can be reduced to H_2O_2 on the nanoparticle surface as the metal sites increase their valence, especially in the presence of pyrrolic N (Martínez-Huitle et al., 2023). In addition, in Fig. 4c it can be observed that the Fe/NC and Cu/NC samples have some oxidized N, unlike the FeCu/NC sample, which is consistent with the greater stability of the latter material against oxidation during the acid pickling, as mentioned above.

The C_{DL} value for each catalyst was obtained from multiple CV curves recorded in the non-faradaic region at different scan rates (Fig. S5) (McCrory et al., 2013), and the results were compared with those determined through N_2 adsorption-desorption tests. From the adsorption-desorption isotherms (Fig. S2), it was found that Fe/NC has the largest pore volume and smallest pore size (Fig. 5a). In turn, this sample presented a very high C_{DL} (Fig. 5b). However, the FeCu/NC sample showed an analogous C_{DL} value despite its apparently worse textural properties. From this, it can be concluded that the pore volume (rather than the pore size) is a parameter that can be correlated with the C_{DL} to a certain extent, thereby informing about a greater number of electroactive sites when they become higher. Based on these results, the Cu/NC sample was proven as the less promising material as catalyst for H_2O_2 activation, whereas the FeCu/NC seemed to possess well-balanced textural and electrochemical properties, which is crucial to ensure good access to an inner surface with a high number of electroactive sites (Chen et al., 2020).

3.2. Evaluation of catalytic performance and catalyst reusability

The catalytic performance of FeCu/NC, Cu/NC, and Fe/NC was thoroughly evaluated by carrying out the HEF treatment of LSN solutions at initial pH 5.9, in which the catalyst powder under study was suspended at a concentration of 0.05 g L^{-1}. Prior to each electrolysis, the suspensions were stirred for 20 min, in order to reach the LSN adsorption equilibrium. Fig. 6a shows that the LSN removal by adsorption was very low for the three materials, being FeCu/NC the most effective with ca. 10 % LSN removal at the end of the stirring period. On the other hand, up to 59.5 % of LSN was degraded after 180 min of electro-oxidation

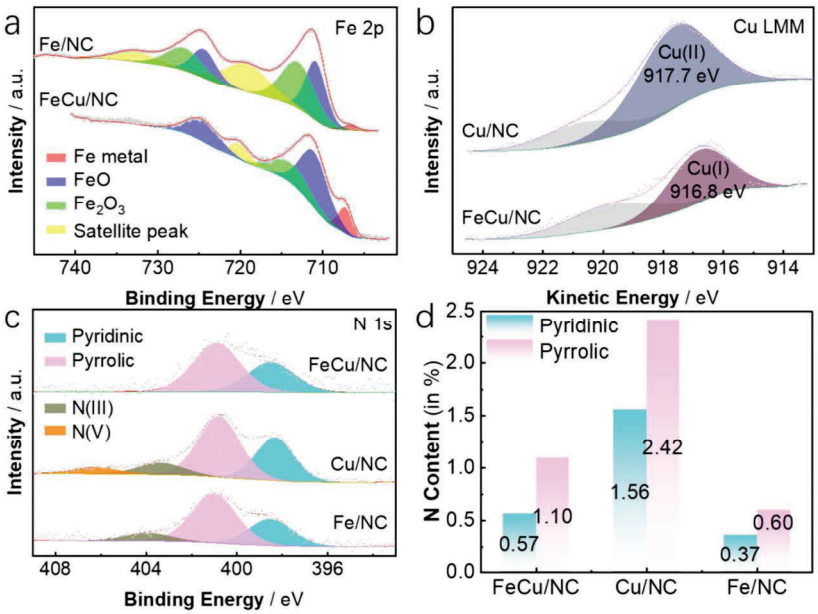

Fig. 4. High-resolution (a) Fe 2p, (b) Cu LMM, and (c) N1s of the FeCu/NC, Cu/NC, and Fe/NC, and (d) the contents of pyridine and pyrrole nitrogen in the three catalysts.

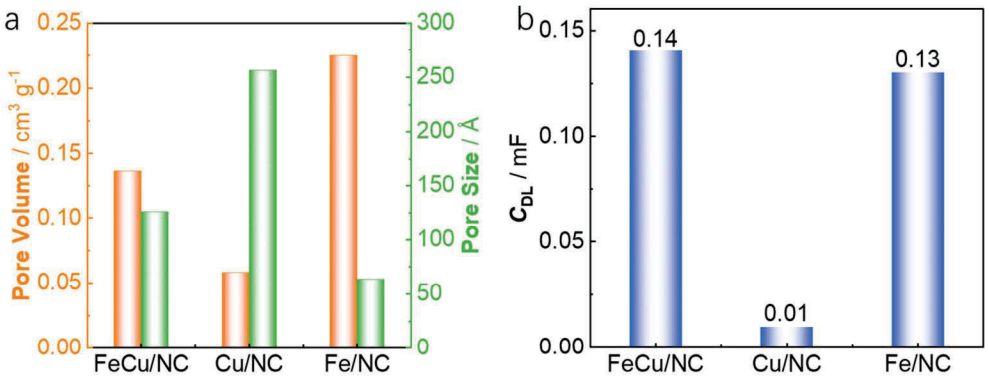

Fig. 5. (a) Pore volume and pore size determined from the N_2 adsorption-desorption isotherms, and (b) the averaged double-layer capacitances obtained from cyclic voltammetry in the non-faradaic region at different rates, for FeCu/NC, Cu/NC, and Fe/NC catalyst.

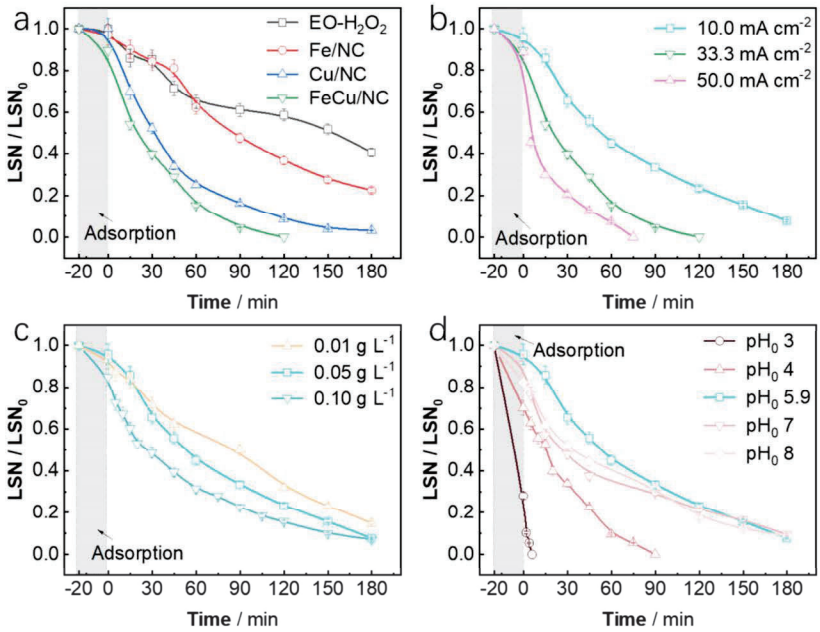

Fig. 6. Normalized lisinopril concentration vs. electrolysis time during EF-like treatment of 150 mL of 16.1 mg L^{-1} drug solutions (10 mg C L^{-1}) with 0.050 M Na_2SO_4 at 25 °C in a RuO_2/air-diffusion cell. (a) at different type of catalyst with a dosage of 0.05 g L^{-1} at initial pH 5.9 and 33.3 mA cm^{-2}. In EO-H_2O_2, no catalyst was added. (b) at different *j*, FeCu/NC as the catalyst with dosage of 0.05 g L^{-1} at initial pH 5.9, (c) at different dosages of FeCu/NC catalyst at $j = 10$ mA cm^{-2} and initial pH 5.9. (d) at different initial pH, FeCu/NC as the catalyst with a dosage of 0.05 g L^{-1} and $j = 10$ mA cm^{-2}.

with H_2O_2 (EO-H_2O_2), i.e., without catalyst. In that process, LSN degradation could be mainly attributed to DSA($^{\bullet}$OH), since H_2O_2 alone was confirmed as a mild oxidant that was ineffective to degrade the drug. The analogous experiments carried out in the presence of a suspended catalyst (i.e., HEF process) at *j* of 33.3 mA cm^{-2} demonstrated the clear superiority over adsorption and EO-H_2O_2 processes. In particular, Fig. 6a shows the excellent catalytic performance of FeCu/NC for the degradation of LSN via H_2O_2 activation. Total LSN disappearance was achieved in 120 min, outperforming the Cu/NC- and Fe/NC-catalyzed HEF treatments that could remove 96.8 % and 77.4 % in 180 min, respectively. Based on the superiority of the FeCu/NC catalyst, all subsequent HEF assays were carried out with that catalyst.

The positive effect of the applied current density can be inferred from Fig. 6b. When *j* was risen from 10 to 33 mA cm^{-2}, a significant enhancement of the LSN removal was observed, moving from 92.3 % degradation in 180 min to complete degradation in 120 min. A further increase in *j* value to 50 mA cm^{-2} allowed attaining the total degradation in only 75 min. This dependence with applied current can be attributed to its main effect on the H_2O_2 accumulation, which in turn affects the $^{\bullet}$OH production via Fenton's reaction (Ye et al., 2022). However, note that such an enhancement is not unlimited. Current densities above 50 mA cm^{-2} did not provide a substantial amelioration, since despite the consequently greater generation of DSA($^{\bullet}$OH) and H_2O_2, the latter effectively acts as radical scavenger when excessive accumulation is attained, thus becoming a parasitic reaction that must be avoided (Sirés and Brillas, 2021).

The impact of the catalyst dosage on the HEF performance is illustrated in Fig. 6c, which shows an increasing LSN removal at 180 min, from 85.2 % to 92.3 % when the catalyst concentration was risen from 0.01 to 0.05 g L^{-1}, at *j* of 10 mA cm^{-2}. A further increase to 0.1 g L^{-1}

showed only a very poor enhancement in LSN degradation at the end of the treatment, reaching 92.9 %, although a certain acceleration was evidenced during the first 60–120 min. This slight effect at the greatest catalyst concentration may be explained by the parasitic reaction between •OH and excess of copper and iron sites (Ye et al., 2020b), resulting in the loss of oxidizing capacity of the system (Sirés and Brillas, 2021). This is very interesting from the application point of view, since a low catalyst dosage is preferred to decrease the operation costs as well as to facilitate the recovery. At this point, being effective at such a low dosage (0.05 g L^{-1}), the HEF process is confirmed as an interesting alternative to chemical Fenton process. In Fig. 6c, it is also worth remarking that the use of 0.1 g L^{-1} FeCu/NC also entailed a larger removal by pre-adsorption, attaining 16 % after the initial 20-min stirring period.

To assess the effect of initial solution pH on LSN degradation, degradation experiments were done in a wide pH_0 range, from 3 to 8, at j of 10 mA cm^{-2}. At pH_0 3, the first relevant finding in Fig. 6d is the very high LSN removal (> 70 %) obtained simply by adsorption during the pre-electrolytic trial. This can be attributed to the existence of four H-containing functional groups, comprising two carboxylic acids and two amines with pK_a values of 2.5, 4.0, 6.7 and 10 at 25 °C (Wang et al., 2002). As compared to all previous experiments performed at pH_0 5.9, the prevailing LSN form at pH_0 3 involves the neutral form (instead of deprotonated) of the less acidic carboxylic group (i.e., the prolyl –COOH), thus reducing the contribution of the negatively charged groups. This was then favorable to adsorb the LSN molecules onto the FeCu/NC surface, whereupon the drug was quickly degraded in 6 min, in good agreement with the expected optimum pH value (~3) for Fenton's reaction (Sirés and Brillas, 2021). At less acidic initial pH values, the LSN degradation efficiency decreased substantially, although at pH_0 4, total removal was still feasible (90 min). When the initial pH was equal or higher to the natural one (5.9), the effect on degradation rate was not so obvious, and about 80 % was degraded in 120 min. At too high pH_0 values (> 8), the H_2O_2 stability if known to decrease due to its decomposition, thus negatively affecting to the •OH production from Fenton's reaction. Therefore, the FeCu/NC catalyst exhibits excellent activity to run the HEF process at acidic, neutral, and even weakly alkaline pH.

To evaluate the mineralization ability of the FeCu/NC-catalyzed HEF process using the optimum dosage (0.05 g L^{-1}), longer tests were conducted in the DSA/air-diffusion cell. As shown in Fig. S6a, the TOC removal at pH_0 3 was 37.1 % and 45.1 % after 120 and 360 min of electrolysis, respectively. The mineralization degree was not so remarkable, as a result of the formation of Fe(III)-carboxylate complexes, which are known to be quite stable in solution when using a DSA anode and no UVA irradiation (Sirés and Brillas, 2021). This is corroborated by the quantification of the short-chain linear carboxylic acids (Fig. S6b, S6c, and S6d). These acids were accumulated in different concentrations depending on the pH_0 value, with oxalic acid predominating as the main refractory product and always exhibiting a concentration peak at 60 min of electrolysis. At pH_0 3, the variety of acids was larger (Fig. S6d), with up to six different compounds in solution due to the larger mineralization attained.

The reusability of FeCu/NC was evaluated by performing sequential experiments employing the used catalyst in subsequent trials. Each experiment lasted for 2 h, and then the powder was recovered using a magnet and used directly in a new degradation test without any cleaning procedure (only air drying). As shown in Fig. 7, the removal efficiency of LSN could still reach 100 % in the second cycle, and it attained 86.5 % in the fifth use. This suggests that the bimetallic catalyst with a core-shell structure has excellent reusability. The light decay in the degradation rate is attributed to the passivation and deactivation of the active sites, as well as to the pore clogging upon adsorption of refractory by-products (Wang et al., 2024a).

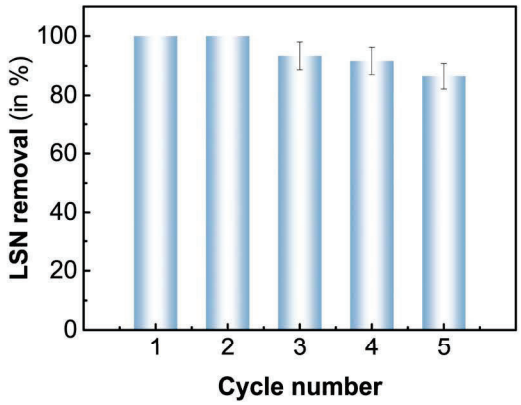

Fig. 7. Percentage of lisinopril removal in five consecutive 2-h tests to evaluate the reuse of FeCu/NC catalyst in the HEF-like treatment of 150 mL of suspensions with 16.1 mg L^{-1} drug (10 mg L^{-1} TOC_0) and 0.050 M Na_2SO_4 at 25 °C, pH 5.9 and 33.3 mA cm^{-2} in an undivided cell. DSA-Cl_2 and a commercial GDE were employed as the anode and cathode, respectively. The amount of catalyst recovered after each cycle was accumulated to 0.05 g L^{-1} for the subsequent cycle. Each new cycle was started without any catalyst post-treatment, apart from air drying.

3.3. Performance of FeCu/NC catalyst in actual wastewater

The performance of the FeCu/NC-catalyzed HEF process was further evaluated by treating LSN spiked into an actual water matrix, i.e., urban wastewater at natural pH 7.7. Since UWW contains Cl^- (Table S1) and the Ti|RuO_2 anode is known to be very active for electrochlorination, first, the active chlorine concentration that can be actually accumulated under the electrolysis conditions of interest (j of 33.3 mA cm^{-2}) was determined. As shown in Fig. S7a, the active chlorine was gradually accumulated in the system until reaching a maximum concentration (4.5 mg L^{-1}) at 45 min of electrolysis. After that, the chlorine species began to decrease at a similar rate, as a result of the interaction between anodic HClO and H_2O_2 that was simultaneously generated at the cathode and then transported to the bulk (Eq. (1)) (Chen et al., 2023; Shah et al., 2015). Once ascertained the production of chlorine, LSN (16.1 mg L^{-1}) was spiked into a solution containing urban wastewater and 4.5 mg L^{-1} of commercial active chlorine. Samples were collected at different times from the solution, which was solely stirred for 120 min. The positive effect of active chlorine as oxidant of LSN can be observed in Fig. S7b, with 54.3 % of the drug being quickly degraded (15 min), and 77.3 % removal achieved at the end of the treatment.

Afterwards, the performance of the HEF process to treat LSN in UWW was investigated in detail, using 0.05 g L^{-1} FeCu/NC in the DSA/air-diffusion cell at j of 33.3 mA cm^{-2} (Fig. 8). The initial removal by adsorption was analogous to that mentioned above in a model solution, but the subsequent degradation by HEF was faster, reaching the complete removal in only 60 min. The enhanced drug concentration decay in the actual water matrix can thus be attributed to the contribution of active chlorine that is continuously electrogenerated.

$$HClO + H_2O_2 \rightarrow Cl^- + {}^1O_2 + H_2O + H^+ \quad (1)$$

The catalyst stability was evaluated during the same HEF treatment carried out in UWW, by measuring the leached iron (Fig. S8). The iron concentration in the UWW was as low as 0.2 mg L^{-1} (Table S1), mainly expected in its Fe^{3+} state, and this value decreased during the pre-adsorption time (i.e., 20-min stirring period). In the same period, an increase of the Fe^{2+} concentration was evidenced, which can be explained by a slight leaching of iron ions from the FeCu/NC catalyst. In the first 30 min of HEF process, the total iron concentration was still decreasing, whereupon it raised again. The Fe^{2+} concentration remained

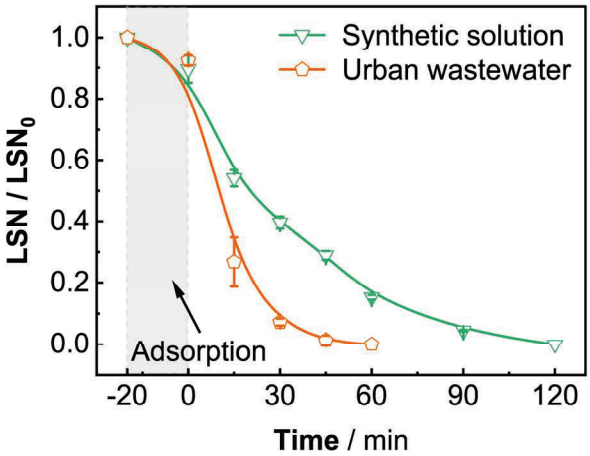

Fig. 8. Normalized LSN concentration with electrolysis time during the HEF treatment of 150 mL of 16.1 mg L^{-1} drug (10 mg C L^{-1}) synthetic solution and urban wastewater at natural pH, 33.3 mA cm^{-2} and 25 °C using 0.05 g L^{-1} of the FeCu/NC catalyst, DSA-Cl_2 and commercial GDE as an anode and cathode, respectively.

stable during the HEF treatment and hence, the growth in total iron can be plausibly associated either to the desorption of the pre-adsorbed iron or to the leaching. Since these profiles are the result of several phenomena that occur simultaneously (adsorption, desorption, leaching, oxidation of Fe^{2+} to Fe^{3+} and reduction of Fe^{3+} to Fe^{2+}, apart from possible complexation of iron with NOM and reaction by-products), it is assumed that all total iron measured at 120 min could have been produced from the catalyst and hence, the maximum leaching is 0.19 mg L^{-1} (i.e., all measured iron coming from the catalyst). This amount was much lower than 1.7 mg L^{-1} reported for $Cu_{0.5}Fe_{2.5}S_4$ at pH 7 (Wang et al., 2024b). This behavior clearly demonstrates that Cu doping not only significantly improved the HEF performance, but also boosted the structural stability of the catalyst. Some authors have explained that Cu doping can increase the corrosion potential of Fe, thereby improving its stability (Oguzie et al., 2010; Wang et al., 2024b).

3.4. Catalytic mechanism and reaction by-products

Aiming to gain better insight into the catalytic role of copper species, FeCu/NC and Fe/NC powders were recovered after a single usage in HEF treatment, followed by vacuum-drying and immediate testing by linear sweep voltammetry. As shown in Fig. 9, the fresh FeCu/NC and Fe/NC catalyst showed no reduction signal. In contrast, a clear reduction near 0.77 V can be observed in the LSV curve of both used FeCu/NC and Fe/NC, which accounts for the Fe(III)-to-Fe(II) conversion (Wang et al., 2022). Among them, the Fe/NC catalyst showed a stronger signal, indicating that a larger amount of Fe(III) (produced during Fenton's reaction in HEF treatment) was present in the catalyst; conversely, the reduction signal of FeCu/NC was much weaker, suggesting the occurrence of the in-situ copper-catalyzed Fe(III) reduction, which thus kept the amount of Fe(III) always comparatively lower.

EIS was employed to analyze the electron transfer / ion transport occurring in the catalysts and, moreover, the DRT curves were calculated. From Fig. S9a, it is evident that the Cu/NC sample had a higher slope in the low frequency part of the Nyquist plot, implying better ion diffusion. This is unfavorable for heterogeneous catalysts, since it means that Cu^{+}/Cu^{2+} may diffuse into the bulk solution more easily. The FeCu/NC catalyst showed the opposite behavior, thus being relatively more stable. It can also be known from Fig. S9b that the Cu/NC catalyst presented the highest peaks in the 10^{-2} - 10^{1} s range, indicating that this material has the greatest surface charge transfer impedance (Iurilli et al., 2022; Semerukhin et al., 2024), being unfavorable for H_2O_2 activation. On the other hand, the FeCu/NC and Fe/NC catalysts showed high peaks in the 10^{-4} - 10^{-2} s range, implying a larger ion transfer impedance (as compared to Cu/NC) between the solid-electrolyte interface; hence, these catalysts are less likely to undergo metal leaching, eventually enhancing their stability.

To elucidate the LSN degradation pathway resulting from the FeCu/NC-catalyzed HEF treatment, the degradation intermediates/by-products were identified by HPLC-MS analysis (Fig. 10, Table S2). Two compounds with mass-to-charge ratios (m/z) of 163 and 180 were identified. These detected species have been described in the literature, although not related to the application of AOPs to LSN treatment (El-Leithy et al., 2017). The formation of these products may be explained by the action of strong oxidizing species.

Considering these conclusions, a mechanism for generating hydroxyl radicals (and other radicals with a minor contribution) is proposed, based on the participation of iron and copper species with different oxidation states. Briefly, zero-valent iron may lose electrons very easily (Eq. (2)); in fact, as discussed above, the FeCu/NC surface is naturally oxidized (Fe_3O_4 or a mixture of Fe(II) and Fe(III) oxides). The resulting Fe(II) triggers the heterogeneous Fenton's reaction with electro-generated H_2O_2, becoming the main route for $^{\bullet}OH$ production (Eq. (3), Fig. 10) (Bounab et al., 2015; Martínez-Huitle et al., 2023). Simultaneously, Cu(0) and Cu(I) present in the C-encapsulated FeCu core favor the continuous Fe(II) regeneration (Eqs. (4) and (5)), thus speeding up the H_2O_2 activation (Du et al., 2021). Of course, the classical Fenton-like reaction (Eq. (6)) can also promote the Fe(III)-to-Fe(II) reduction, which is a parasitic reaction because it consumes H_2O_2 to yield a less oxidizing radical.

In turn, the low-valent copper species can be involved in Fenton-like reactions with H_2O_2 to yield $^{\bullet}OH$ (Eqs. (7) and (8)), although these are slower conversions as compared to the Fe(II)-catalyzed Fenton's reaction

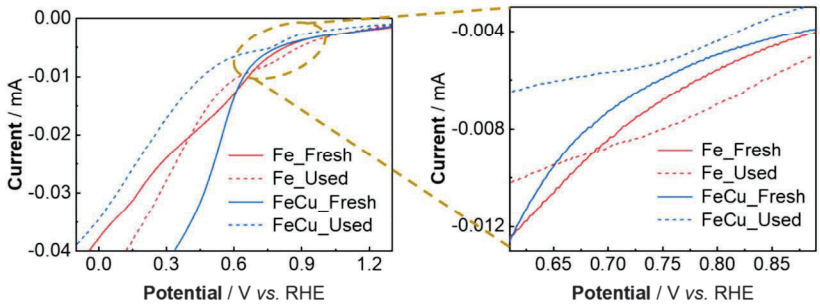

Fig. 9. LSV curves (left) and enlarged view (right) in the region close to the standard reduction potential of Fe^{3+} (0.77 V vs. RHE). The RDE employed as WE was loaded with fresh or used catalyst, and the voltammograms were recorded at a scan rate of 5 mV s^{-1} and rotation rate of 1600 rpm. Solution: N_2-saturated 0.05 M Na_2SO_4. Ag|AgCl (3 M KCl) and Pt were used as RE and CE, respectively.

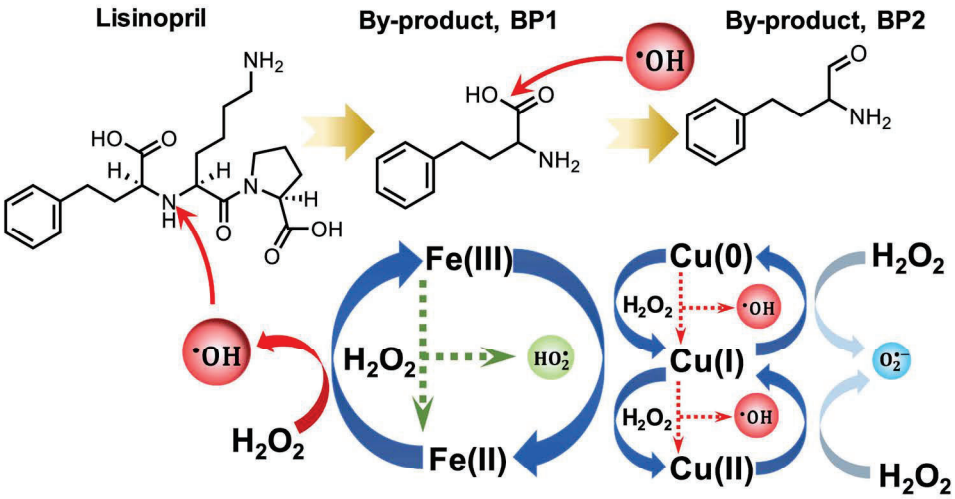

Fig. 10. Reaction mechanism in the FeCu/NC/Hetero-EF process for the LSN removal and two by-products.

(Sirés and Brillas, 2021; Wang et al., 2024b). Additionally, H_2O_2 can be oxidized to superoxide radical by the high-valent copper species (Eqs. (9) and (10)), but again, these are expected to be minor routes because of the high reaction rate of H_2O_2 with iron species. In other words, the main mechanistic role of copper species in Fig. 10 is referred to the Fe (III)/Fe(II) cycle.

Eventually, LSN is progressively degraded by strongly oxidizing $^{\bullet}OH$ to be converted to main primary aromatic by-products (Fig. 10), then to short-chain linear carboxylic acids and, finally, CO_2, H_2O and inorganic ions (Eq. (11)).

$$Fe(0) - 2e^- \rightarrow Fe(II) \quad (2)$$

$$Fe(II) + H_2O_2 \rightarrow Fe(III) + OH^- + {}^{\bullet}OH \quad (3)$$

$$Cu(0) + Fe(III) \rightarrow Cu(I) + Fe(II) \quad (4)$$

$$Cu(I) + Fe(III) \rightarrow Cu(II) + Fe(II) \quad (5)$$

$$Fe(III) + H_2O_2 \rightarrow Fe(II) + HO_2^{\bullet} + H^+ \quad (6)$$

$$Cu(0) + H_2O_2 \rightarrow Cu(I) + OH^- + {}^{\bullet}OH \quad (7)$$

$$Cu(I) + H_2O_2 \rightarrow Cu(II) + OH^- + {}^{\bullet}OH \quad (8)$$

$$Cu(I) + H_2O_2 \rightarrow Cu(0) + O_2^{\bullet -} + 2H^+ \quad (9)$$

$$Cu(II) + H_2O_2 \rightarrow Cu(I) + O_2^{\bullet -} + 2H^+ \quad (10)$$

$$Lisinopril + {}^{\bullet}OH \rightarrow By-products \rightarrow CO_2 + H_2O \quad (11)$$

4. Conclusions

FeCu/NC catalysts with a core-shell structure were synthesized via a three-step process that involved the FeCu-MOF hydrothermal synthesis, followed by pyrolysis and acid pickling. For the first time, the antihypertensive lisinopril was studied as target contaminant in advanced oxidation processes. The FeCu/NC catalyst exhibited excellent properties for activating H_2O_2 into $^{\bullet}OH$ for LSN degradation in HEF treatment, requiring a catalyst concentration as low as 0.05 g L^{-1} to achieve complete LSN degradation in 6 min at acidic pH and 75 min at near-neutral pH. In urban wastewater, owing to the electrogeneration of active chlorine, the degradation was even faster. The presence of pyrrolic-N along with the large capacitance as compared to monometallic catalysts was beneficial for Fenton's reaction. The incorporation of low-valent Cu promoted the continuous Fe(II) regeneration, thus accelerating the H_2O_2 activation. Metal leaching tests, DRT analysis and reuse assays demonstrated the high stability of FeCu/NC catalyst, which is then validated as an excellent candidate for future scale-up of the HEF technology for actual wastewater treatment.

CRediT authorship contribution statement

Lele Zhao: Writing – original draft, Methodology, Investigation, Conceptualization. **María F. Murrieta:** Validation, Methodology. **José A. Padilla:** Resources, Methodology. **Sonia Lanzalaco:** Writing – original draft, Methodology, Formal analysis. **Pere L. Cabot:** Resources, Funding acquisition. **Ignasi Sirés:** Writing – review & editing, Validation, Supervision, Resources, Project administration, Methodology, Funding acquisition, Formal analysis, Data curation, Conceptualization.

Declaration of competing interest

The authors declare that they have no known competing financial interests or personal relationships that could have appeared to influence the work reported in this paper.

Data availability

Data will be made available on request.

Acknowledgments

The authors acknowledge the financial support from project PID2022-140378OB-I00 funded by MICIU/AEI/10.13039/501100011033 and by ERDF/EU. The Ph.D. scholarship awarded to L.Z. (State Scholarship Fund, CSC, China) is also acknowledged. We are also thankful to the Catalan Government for the quality accreditation and funding (projects 2021SGR00596 and 2021SGR00708). DIOPMA is a certified agent TECNIO in the category of technology developers from the Government of Catalonia. BET, XRD, TEM and XPS analyses from the *Centres Científics i Tecnològics de la UB* (CCiT-UB) are also acknowledged.

Appendix A. Supplementary data

Supplementary data to this article can be found online at https://doi.org/10.1016/j.scitotenv.2024.176110.

References

Ai, Q., Yuan, Z., Huang, R., Yang, C., Jiang, G., Xiong, J., Huang, Z., Yuan, S., 2019. One-pot co-precipitation synthesis of Fe_3O_4 nanoparticles embedded in 3D carbonaceous matrix as anode for lithium ion batteries. J. Mater. Sci. 54, 4212–4224. https://doi.org/10.1007/s10853-018-3141-3.

Bounab, L., Iglesias, O., González-Romero, E., Pazos, M., Sanromán, M.Á., 2015. Effective heterogeneous electro-Fenton process of *m*-cresol with iron loaded actived carbon. RSC Adv. 5, 31049–31056. https://doi.org/10.1039/C5RA03050A.

Cao, P., Quan, X., Zhao, K., Chen, S., Yu, H., Niu, J., 2020. Selective electrochemical H_2O_2 generation and activation on a bifunctional catalyst for heterogeneous electro-Fenton catalysis. J. Hazard. Mater. 382, 121102 https://doi.org/10.1016/j.jhazmat.2019.121102.

Chen, H., Liang, X., Liu, Y., Ai, X., Asefa, T., Zou, X., 2020. Active site engineering in porous electrocatalysts. Adv. Mater. 32, 2002435. https://doi.org/10.1002/adma.202002435.

Chen, Z., Xia, P., Wang, D., Niu, X., Ao, L., He, Q., Wang, S., Ye, Z., Sirés, I., 2023. New insights into the mechanism of Fered-Fenton treatment of industrial wastewater with high chloride content: role of multiple reactive species. Sci. Total Environ. 882, 163596 https://doi.org/10.1016/j.scitotenv.2023.163596.

Deng, F., Olvera-Vargas, H., Zhou, M., Qiu, S., Sirés, I., Brillas, E., 2023. Critical review on the mechanisms of Fe^{2+} regeneration in the electro-Fenton process: fundamentals and boosting strategies. Chem. Rev. 123, 4635–4662. https://doi.org/10.1021/acs.chemrev.2c00684.

Dong, P., Liu, W., Wang, S., Wang, H., Wang, Y., Zhao, C., 2019. In situ synthesis of Fe_3O_4 on carbon fiber paper@polyaniline substrate as novel self-supported electrode for heterogeneous electro-Fenton oxidation. Electrochim. Acta 308, 54–63. https://doi.org/10.1016/j.electacta.2019.03.215.

Du, X., Fu, W., Su, P., Su, L., Zhang, Q., Cai, J., Zhou, M., 2021. Trace FeCu@PC derived from MOFs for ultraefficient heterogeneous electro-Fenton process: enhanced electron transfer and bimetallic synergy. ACS EST Eng. 1, 1311–1322. https://doi.org/10.1021/acsestengg.1c00131.

El-Leithy, E., El-Fiky, G., Nabil, M., 2017. Characterization of degradation products resulted from acidic hydrolysis of lisinopril under drastic conditions. J. Adv. Pharm. Res. 1, 201–208. https://doi.org/10.21608/aprh.2017.4041.

Fang, R., Lu, C., Zhong, Y., Xiao, Z., Liang, C., Huang, H., Gan, Y., Zhang, J., Pan, G., Xia, X., Xia, Y., Zhang, W., 2020. Puffed rice carbon with coupled sulfur and metal iron for high-efficiency mercury removal in aqueous solution. Environ. Sci. Technol. 54, 2539–2547. https://doi.org/10.1021/acs.est.9b07385.

Garcia-Cardona, J., Sirés, I., Mazzucato, M., Brandiele, R., Brillas, E., Alcaide, F., Durante, C., Cabot, P.L., 2023. On the viability of chitosan-derived mesoporous carbons as supports for PtCu electrocatalysts in PEMFC. Electrochim. Acta 442, 141911. https://doi.org/10.1016/j.electacta.2023.141911.

He, S., Wang, W., Shen, Z., Li, G., Kang, J., Liu, Z., Wang, G.-C., Zhang, Q., Wang, Y., 2019. Carbon nanotube-supported bimetallic Cu-Fe catalysts for syngas conversion to higher alcohols. Molec. Catal. 479, 110610 https://doi.org/10.1016/j.mcat.2019.110610.

Idczak, K., Idczak, R., Konieczny, R., 2016. An investigation of the corrosion of polycrystalline iron by XPS, TMS and CEMS. Phys. B: Cond. Matter 491, 37–45. https://doi.org/10.1016/j.physb.2016.03.018.

Iurilli, P., Brivio, C., Wood, V., 2022. Detection of lithium-ion cells' degradation through deconvolution of electrochemical impedance spectroscopy with distribution of relaxation time. Energ. Technol. 10, 2200547. https://doi.org/10.1002/ente.202200547.

Ivankovic, K., Jambrosic, K., Mikac, I., Kapetanovic, D., Ahel, M., Terzic, S., 2023. Multiclass determination of drug residues in water and fish for bioaccumulation potential assessment. Talanta 264, 124762. https://doi.org/10.1016/j.talanta.2023.124762.

Li, X., Ahmadi, M., Collins, L., Kalinin, S.V., 2019. Deconvolving distribution of relaxation times, resistances and inductance from electrochemical impedance spectroscopy via statistical model selection: exploiting structural-sparsity regularization and data-driven parameter tuning. Electrochim. Acta 313, 570–583. https://doi.org/10.1016/j.electacta.2019.05.010.

Liu, K., Yu, M., Wang, H., Wang, J., Liu, W., Hoffmann, M.R., 2019. Multiphase porous electrochemical catalysts derived from iron-based metal–organic framework compounds. Environ. Sci. Technol. 53, 6474–6482. https://doi.org/10.1021/acs.est.9b01143.

Liu, M., Li, N., Meng, S., Yang, S., Jing, B., Zhang, J., Jiang, J., Qiu, S., Deng, F., 2024. Bio-inspired Cu_2O cathode for O_2 capturing and oxidation boosting in electro-Fenton for sulfathiazole decay. J. Hazard. Mater. 478, 135484 https://doi.org/10.1016/j.jhazmat.2024.135484.

Martínez-Huitle, C.A., Rodrigo, M.A., Sirés, I., Scialdone, O., 2023. A critical review on latest innovations and future challenges of electrochemical technology for the abatement of organics in water. Appl. Catal. B: Environ. 328, 122430 https://doi.org/10.1016/j.apcatb.2023.122430.

McCrory, C.C.L., Jung, S., Peters, J.C., Jaramillo, T.F., 2013. Benchmarking heterogeneous electrocatalysts for the oxygen evolution reaction. J. Am. Chem. Soc. 135, 16977–16987. https://doi.org/10.1021/ja407115p.

Netshithothole, R., Madikizela, L.M., 2024. Occurrence of selected pharmaceuticals in the East London coastline encompassing major rivers, estuaries, and seawater in the Eastern Cape province of South Africa. ACS Meas. Sci. Au 4, 283–293. https://doi.org/10.1021/acsmeasuresciau.4c00004.

Nidheesh, P.V., Gandhimathi, R., 2014. Comparative removal of rhodamine B from aqueous solution by electro-Fenton and electro-Fenton-like processes. CLEAN – Soil, Air, Water 42, 779–784. https://doi.org/10.1002/clen.201300093.

Oguzie, E.E., Li, J., Liu, Y., Chen, D., Li, Y., Yang, K., Wang, F., 2010. The effect of Cu addition on the electrochemical corrosion and passivation behavior of stainless steels. Electrochim. Acta 55, 5028–5035. https://doi.org/10.1016/j.electacta.2010.04.015.

Semerukhin, D.Yu., Kubarkov, A.V., Sergeyev, V.G., Semenikhin, O.A., Antipov, E.V., 2024. Analysis of the distribution of relaxation times (DRT) responses of Li-ion cells as a function of their preparation conditions. Electrochim. Acta 486, 144092. https://doi.org/10.1016/j.electacta.2024.144092.

Shah, A.D., Liu, Z.Q., Salhi, E., Höfer, T., von Gunten, U., 2015. Peracetic acid oxidation of saline waters in the absence and presence of H_2O_2: secondary oxidant and disinfection byproduct formation. Environ. Sci. Technol. 49, 1698–1705. https://doi.org/10.1021/es503920n.

da Silva, T.F., Cavalheri, P.S., Cardoso, J.C., Nazario, C.E.D., Jorge, J., Martines, M.A.U., Ravaglia, L.M., Alcantara, G.B., Casagrande, G.A., Caires, A.R.L., Cavalcante, R.P., de Oliveira, S.C., Gozzi, F., Sirés, I., Junior, A.M., 2024. Development of a TiO_2 nanotube photoanode decorated with MIL-53(Fe) for the photoelectrochemical degradation of 2,4-dimethylaniline. Catal. Today 431, 114579. https://doi.org/10.1016/j.cattod.2024.114579.

Silva-Velasco, D.L., Cervantes-Pérez, L.G., Sánchez-Mendoza, A., 2024. ACE inhibitors and their interaction with systems and molecules involved in metabolism. Heliyon 10. https://doi.org/10.1016/j.heliyon.2024.e24655.

Sirés, I., Brillas, E., 2021. Upgrading and expanding the electro-Fenton and related processes. Curr. Opinion Electrochem. 27, 100686 https://doi.org/10.1016/j.coelec.2020.100686.

Song, M., Han, J., Wang, Y., Chen, L., Chen, Y., Liao, X., 2023. Effects and mechanisms of Cu species in Fe-MOFs on Fenton-like catalytic activity and stability. ACS Appl. Mater. Interfaces 15, 36201–36213. https://doi.org/10.1021/acsami.3c05928.

Stankiewicz, A., Giebułtowicz, J., Stankiewicz, U., Wroczyński, P., Nałęcz-Jawecki, G., 2015. Determination of selected cardiovascular active compounds in environmental aquatic samples – methods and results, a review of global publications from the last 10 years. Chemosphere 138, 642–656. https://doi.org/10.1016/j.chemosphere.2015.07.056.

Tang, J., Wang, J., 2019. MOF-derived three-dimensional flower-like FeCu@C composite as an efficient Fenton-like catalyst for sulfamethazine degradation. Chem. Eng. J. 375, 122007 https://doi.org/10.1016/j.cej.2019.122007.

Thommes, M., Kaneko, K., Neimark, A.V., Olivier, J.P., Rodriguez-Reinoso, F., Rouquerol, J., Sing, K.S., 2015. Physisorption of gases, with special reference to the evaluation of surface area and pore size distribution (IUPAC technical report). Pure Appl. Chem. 87 (9–10), 1051–1069. https://doi.org/10.1515/pac-2014-1117.

Wan, T.H., Saccoccio, M., Chen, C., Ciucci, F., 2015. Influence of the discretization methods on the distribution of relaxation times deconvolution: implementing radial basis functions with DRT tools. Electrochim. Acta 184, 483–499. https://doi.org/10.1016/j.electacta.2015.09.097.

Wang, S.-L., Chuang, C.-H., Lin, S.-Y., 2002. pH-dependent coordination of metal–lisinopril complex investigated by attenuated total reflection/Fourier transform infrared spectroscopy. Chem. Pharm. Bull. 50, 78–82. https://doi.org/10.1248/cpb.50.78.

Wang, J., Liu, C., Hussain, I., Li, C., Li, J., Sun, X., Shen, J., Han, W., Wang, L., 2016. Iron–copper bimetallic nanoparticles supported on hollow mesoporous silica spheres: the effect of Fe/Cu ratio on heterogeneous Fenton degradation of a dye. RSC Adv. 6, 54623–54635. https://doi.org/10.1039/C6RA08501F.

Wang, D., Li, Y., Hu, S., Hu, J., Hou, H., Liu, B., Zheng, H., Luo, X., Li, H., 2022. A triple-cathode electron-Fenton system for efficient Fe^{2+} regeneration and in-situ H_2O_2 electro-activation. Sep. Purif. Technol. 299, 121704 https://doi.org/10.1016/j.seppur.2022.121704.

Wang, Z., Du, Y., Zhou, P., Xiong, Z., He, C., Liu, Y., Zhang, H., Yao, G., Lai, B., 2023a. Strategies based on electron donors to accelerate Fe(III)/Fe(II) cycle in Fenton or Fenton-like processes. Chem. Eng. J. 454, 140096 https://doi.org/10.1016/j.cej.2022.140096.

Wang, F.-X., Zhang, Z.-W., Wang, F., Li, Y., Zhang, Z.-C., Wang, C.-C., Yu, B., Du, X., Wang, P., Fu, H., Zhao, C., 2023b. Fe-Cu bimetal metal-organic framework for efficient decontamination via Fenton-like process: synthesis, performance and mechanism. J. Colloid Interface Sci. 649, 384–393. https://doi.org/10.1016/j.jcis.2023.06.083.

Wang, J., Li, H., Xia, P., Liu, H., Chen, X., Ye, Z., He, Q., Sirés, I., 2024a. Confined MOF pyrolysis within mesoporous SiO_2 core–shell nanoreactors for superior activity and stability of electro-Fenton catalysts. Chem. Eng. J. 483, 149230 https://doi.org/10.1016/j.cej.2024.149230.

Wang, C., Zhang, W., Wang, J., Xia, P., Duan, X., He, Q., Sirés, I., Ye, Z., 2024b. Accelerating Fe(III)/Fe(II) redox cycling in heterogeneous electro-Fenton process via S/Cu-mediated electron donor-shuttle regime. Appl. Catal. B: Environ. 342, 123457 https://doi.org/10.1016/j.apcatb.2023.123457.

World Health Organization, 2023. Hypertension [WWW Document], n.d. URL. https://www.who.int/news-room/fact-sheets/detail/hypertension (last access on 05.08.24).

Xia, P., Ye, Z., Zhao, L., Xue, Q., Lanzalaco, S., He, Q., Qi, X., Sirés, I., 2023. Tailoring single-atom FeN_4 moieties as a robust heterogeneous catalyst for high-performance electro-Fenton treatment of organic pollutants. Appl. Catal. B: Environ. 322, 122116 https://doi.org/10.1016/j.apcatb.2022.122116.

Xia, P., Zhang, H., Ye, Z., 2024. Recent advances in the application of natural iron and clay minerals in heterogeneous electro-Fenton process. Curr. Opinion Electrochem. 46, 101495 https://doi.org/10.1016/j.coelec.2024.101495.

Xu, Y., Xia, P., Wang, C., Cai, J., Li, H., Ye, Z., Zhang, H., 2023. A mini-review on MOFs activated peroxide processes and the enhancement with the external energy. Chem. Eng. J. 462, 142021 https://doi.org/10.1016/j.cej.2023.142021.

Xue, C., Cao, Z., Tong, X., Yang, P., Li, S., Chen, X., Liu, D., Huang, W., 2023. Investigation of CuCoFe-LDH as an efficient and stable catalyst for the degradation of

acetaminophen in heterogeneous electro-Fenton system: key operating parameters, mechanisms and pathways. J. Environ. Manag. 327, 116787 https://doi.org/10.1016/j.jenvman.2022.116787.

Ye, Z., Padilla, J.A., Xuriguera, E., Brillas, E., Sirés, I., 2020a. Magnetic MIL(Fe)-type MOF-derived N-doped nano-ZVI@C rods as heterogeneous catalyst for the electro-Fenton degradation of gemfibrozil in a complex aqueous matrix. Appl. Catal. B: Environ. 266, 118604 https://doi.org/10.1016/j.apcatb.2020.118604.

Ye, Z., Schukraft, G.E.M., L'Hermitte, A., Xiong, Y., Brillas, E., Petit, C., Sirés, I., 2020b. Mechanism and stability of an Fe-based 2D MOF during the photoelectro-Fenton treatment of organic micropollutants under UVA and visible light irradiation. Water Res. 184, 115986 https://doi.org/10.1016/j.watres.2020.115986.

Ye, Z., Oriol, R., Yang, C., Sirés, I., Li, X.-Y., 2022. A novel NH_2-MIL-88B(Fe)-modified ceramic membrane for the integration of electro-Fenton and filtration processes: a case study on naproxen degradation. Chem. Eng. J. 433, 133547 https://doi.org/10.1016/j.cej.2021.133547.

Ye, Z., Zhang, W., Lanzalaco, S., Zhao, L., Sirés, I., Xia, P., Zhai, J., He, Q., 2023. Ultra-uniform MIL-88B(Fe)/Fe_3S_4 hybrids engineered by partial sulfidation to boost catalysis in electro-Fenton treatment of micropollutants: experimental and mechanistic insights. Chem. Eng. J. 455, 140757 https://doi.org/10.1016/j.cej.2022.140757.

Zhang, R., Hu, L., Bao, S., Li, Ran, Gao, L., Li, Ren, Chen, Q., 2016. Surface polarization enhancement: high catalytic performance of Cu/CuO_x/C nanocomposites derived from Cu-BTC for CO oxidation. J. Mater. Chem. A 4, 8412–8420. https://doi.org/10.1039/C6TA01199C.

Zhang, C., Li, F., Wen, R., Zhang, H., Elumalai, P., Zheng, Q., Chen, H., Yang, Y., Huang, M., Ying, G., 2020. Heterogeneous electro–Fenton using three–dimension NZVI–BC electrodes for degradation of neonicotinoid wastewater. Water Res. 182, 115975 https://doi.org/10.1016/j.watres.2020.115975.

Zhang, Y., Zhang, X., Wang, S., 2023. Recent advances in the removal of emerging contaminants from water by novel molecularly imprinted materials in advanced oxidation processes—a review. Sci. Total Environ. 883, 163702 https://doi.org/10.1016/j.scitotenv.2023.163702.

Zhao, K., Quan, X., Su, Y., Qin, X., Chen, S., Yu, H., 2021. Enhanced chlorinated pollutant degradation by the synergistic effect between dechlorination and hydroxyl radical oxidation on a bimetallic single-atom catalyst. Environ. Sci. Technol. 55, 14194–14203. https://doi.org/10.1021/acs.est.1c04943.

Zhu, Y., Qiu, S., Ma, F., Li, G., Deng, F., Zheng, Y., 2018. Melamine-derived carbon electrode for efficient H_2O_2 electro-generation. Electrochim. Acta 261, 375–383. https://doi.org/10.1016/j.electacta.2017.12.122.

Zhu, Y., Zhu, R., Xi, Y., Zhu, J., Zhu, G., He, H., 2019. Strategies for enhancing the heterogeneous Fenton catalytic reactivity: a review. Appl. Catal. B: Environ. 255, 117739 https://doi.org/10.1016/j.apcatb.2019.05.041.

SUPPLEMENTARY MATERIAL

Bimetallic FeCu-MOF derivatives as heterogeneous catalysts with enhanced stability for electro-Fenton degradation of lisinopril

Lele Zhao [a], María F. Murrieta [a], José A. Padilla [b,c], Sonia Lanzalaco [d,*], Pere L. Cabot [a], Ignasi Sirés [a,*]

[a] *Laboratori d'Electroquímica dels Materials i del Medi Ambient, Departament de Ciència de Materials i Química Física, Secció de Química Física, Facultat de Química, Universitat de Barcelona, Martí i Franquès 1-11, 08028 Barcelona, Spain*

[b] *DIOPMA, Departament de Ciència de Materials i Química Física, Secció de Ciència de Materials, Facultat de Química, Universitat de Barcelona, Martí i Franquès 1-11, 08028 Barcelona, Spain*

[c] *Departament d'Enginyeria Mecànica, Escola Tècnica Superior d'Enginyeria Industrial de Barcelona (ETSEIB), Universitat Politècnica de Catalunya, Av. Diagonal, 647, 08028, Barcelona, Spain*

[d] *Departament d'Enginyeria Química, EEBE, Universitat Politècnica de Catalunya, C/Eduard Maristany, 10–14, Ed. I2, 08019 Barcelona, Spain*

* Corresponding author: s.lanzalaco@upc.edu (S. Lanzalaco)
i.sires@ub.edu (I. Sirés)

Table of Contents

Table S1	Page 2
Table S2	Page 2
Figure S1	Page 3
Figure S2	Page 3
Figure S3	Page 4
Figure S4	Page 4
Figure S5	Page 5
Figure S6	Page 6
Figure S7	Page 6
Figure S8	Page 7
Figure S9	Page 7

Table S1. Characterization of the UWW (collected in June 2024).

Parameter	Value
Total carbon (TC) [a]	75.4 mg L^{-1}
Non-purgeable organic carbon (NPOC) [a]	11.2 mg L^{-1}
Total nitrogen (TN) [a]	17.1 mg L^{-1}
Specific conductivity [b]	1.7 mS cm^{-1}
pH	7.7
Concentration of cations [c]	207.8 mg L^{-1} Na^+ 30.7 mg L^{-1} K^+ 95.1 mg L^{-1} Ca^{2+} 26.6 mg L^{-1} Mg^{2+} 0.2 mg L^{-1} Fe (total) 16.3 mg L^{-1} NH_4^+
Concentration of anions	128.7 mg L^{-1} SO_4^{2-} 401.8 mg L^{-1} Cl^- 7.2 mg L^{-1} NO_3^- 5.9 mg L^{-1} NO_2^-

[a] Measured using a Shimadzu TOC-VCNS analyzer; [b] measured with a Crison Basic 30 conductometer; [c] measured by ICP-OES using a Perkin Elmer Optima 8300 analyzer, except NH_4^+, which was measured by UV/Vis spectrophotometry following the indophenol blue method; [d] measured by ion chromatography using a Shimadzu 10Avp liquid chromatograph.

Table S2. Compounds identified by LC-MS/MS during the degradation of lisinopril (LSN) by heterogeneous electro-Fenton process.

Compound	t_R / min	Observed mass $[M+H]^+$	*m/z* fragments	Structural formula
LSN	4.46	406.2336	389.2073 360.2282 309.1809 291.1703 263.1754 180.1019 142.0861	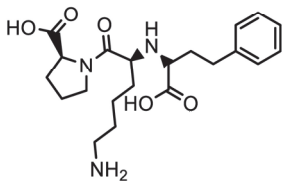
BP1	1.79	162.9693	121.9659	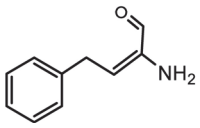
BP2	4.33	180.1023	162.0925 134.0962	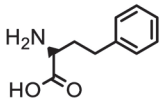

2

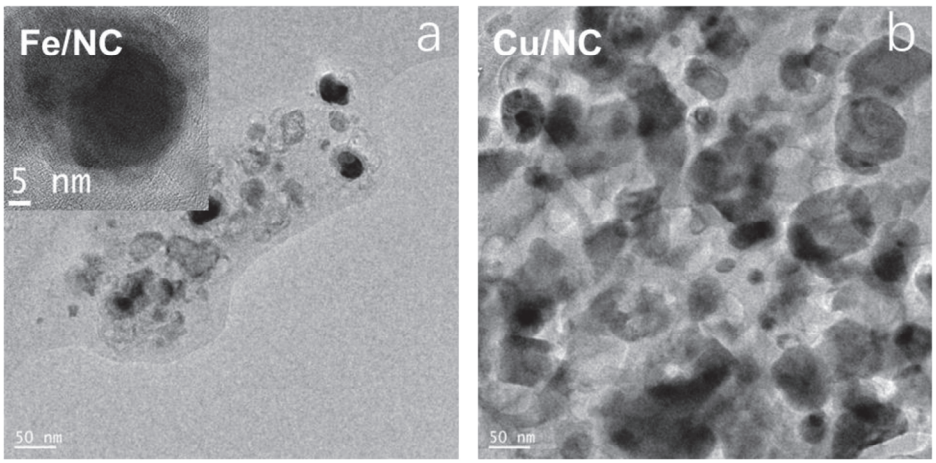

Figure S1. TEM analysis of (a) Fe/NC and (b) Cu/NC catalyst.

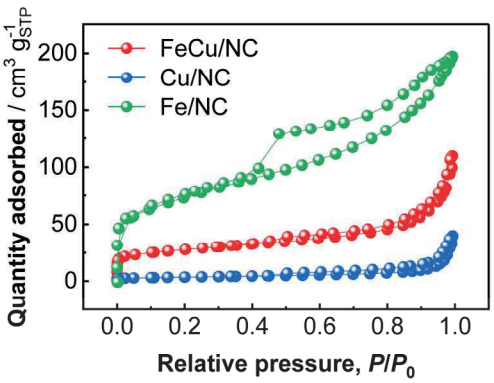

Figure S2. Nitrogen adsorption/desorption isotherms for FeCu/NC, Cu/NC, and Fe/NC catalyst.

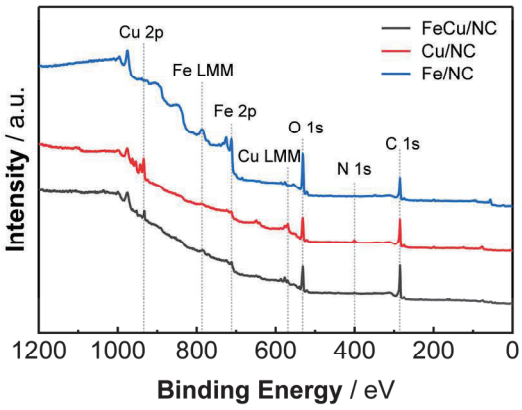

Figure S3. Full XPS spectrum of FeCu/NC, Cu/NC, and Fe/NC catalyst.

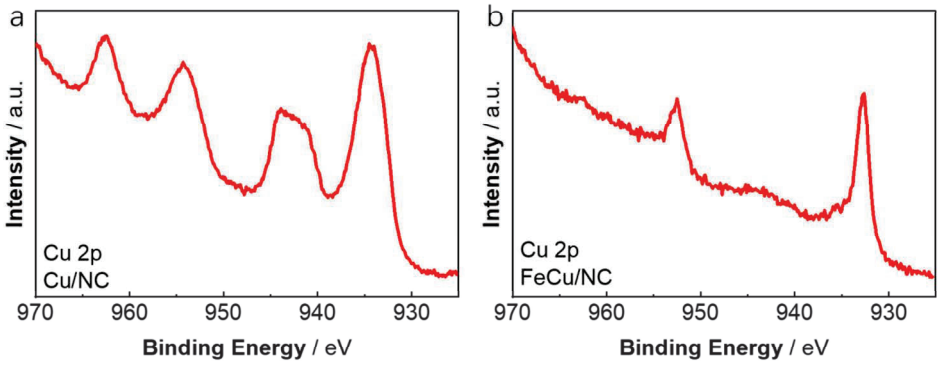

Figure S4. High-resolution Cu 2p XPS spectrum of (a) Cu/NC, and (b) FeCu/NC catalyst.

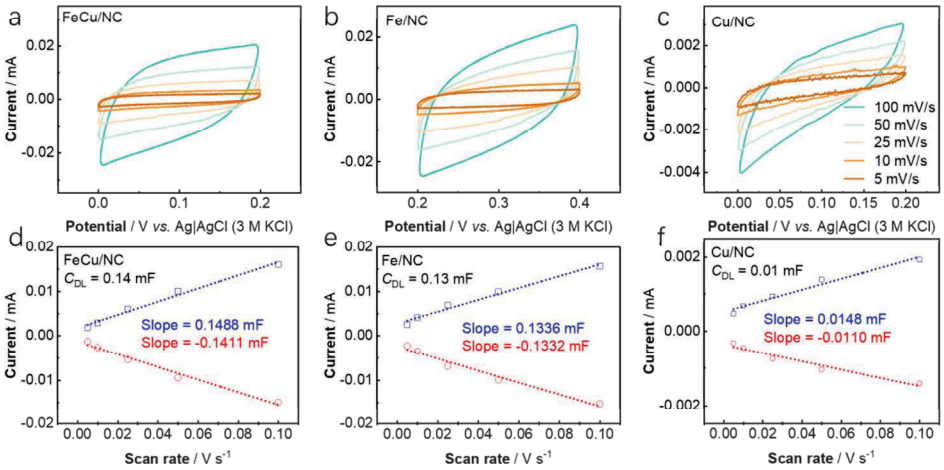

Figure S5. (a-c) Voltammetric measurements of the double-layer capacitance (C_{DL}) of FeCu/NC, Fe/NC, and Cu/NC catalyst, determined in a non-faradaic region at different scan rates, in 0.1 M Na_2SO_4 solution. (d-f) Resulting cathodic and anodic charging currents measured at OCP, plotted as a function of the scan rate. The C_{DL} (written inside each plot) is obtained as the average of the absolute value of the two slopes, which are determined upon linear fitting of the data.

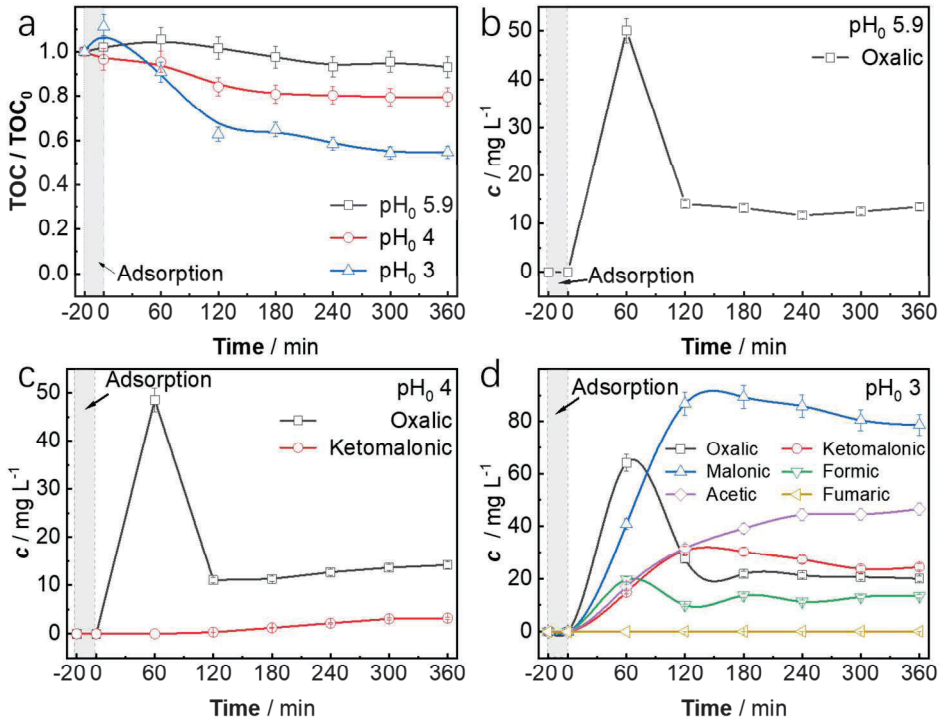

Figure S6. HEF-like degradation of 16.1 mg L^{-1} lisinopril (10 mg C L^{-1}) using 0.05 g L^{-1} FeCu/NC catalyst, at 25 °C and 33.3 mA cm^{-2} (a) Mineralization performance at different initial pH. Time course of linear carboxylic acids at (b) pH_0 5.9, (c) pH_0 4, and (d) pH_0 3.

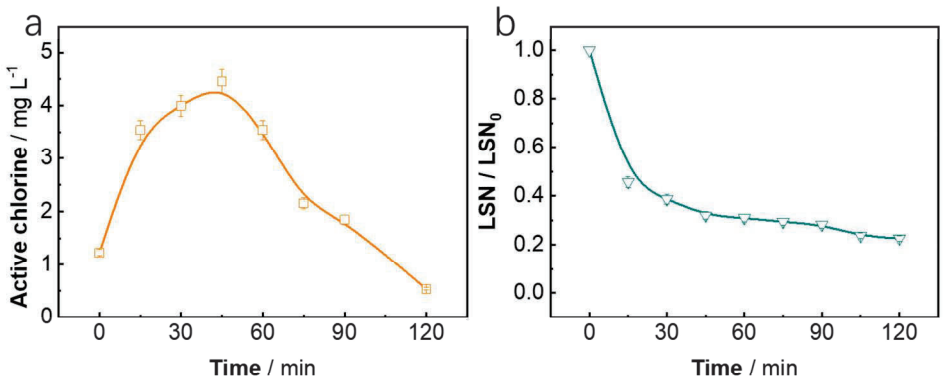

Figure S7. (a) Concentration of active chlorine species over time during the electrolysis of 150 mL of urban wastewater at natural pH, 25 ºC and 33.3 mA cm^{-2}, using a DSA-Cl_2 and a commercial GDE as the anode and cathode, respectively. (b) Evolution of the normalized lisinopril concentration with stirring time when adding 4.5 mg L^{-1} active chlorine to an aqueous solution containing 16.1 mg L^{-1} of the pharmaceutical.

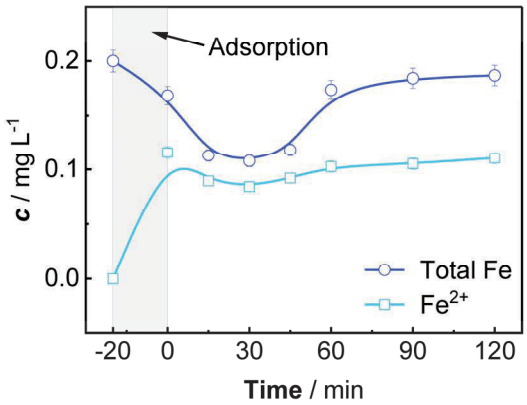

Figure S8. Leached iron concentration with electrolysis time in urban wastewater. The experimental conditions are the same as those described in Figure 8.

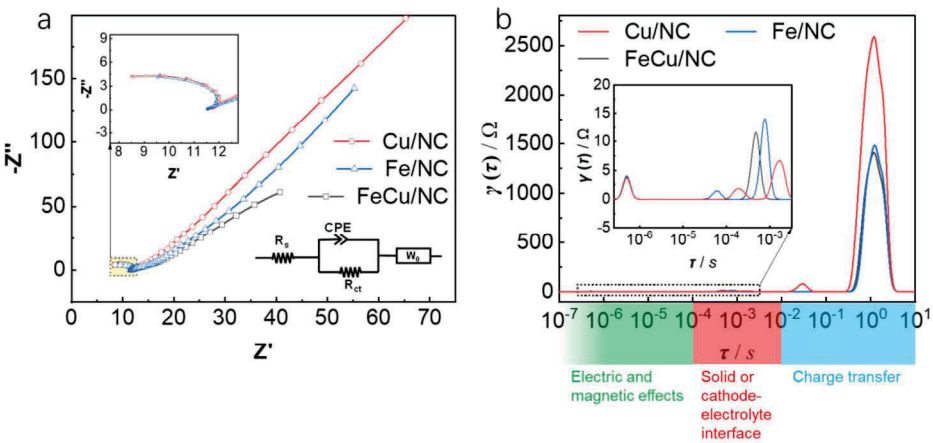

Figure S9. (a) Nyquist plot from the EIS analysis of the three catalysts (see the equivalent circuit in the inset), and (b) distribution of relaxation times (DRT) obtained using the radial basis functions (RBFs) method. The EIS data were recorded in O_2-saturated 0.05 M Na_2SO_4 solution at pH 5.9. Glassy carbon (5 mm diameter), RHE, and Pt were employed as *WE*, *RE*, and *CE*, respectively.

4.3 Ceramic membrane-confined FeCu/NC catalyst for robust flow-through wastewater treatment by electro-Fenton process

Section 4.3 presents one work related to **GO4** and **SG13-15**, including: (i) optimization of catalyst-modified CMs for AMX degradation; and (ii) application of CMs as micropore diffusers for oxygen species generation, enabling simultaneous filtration and catalytic degradation without external aeration.

The work described in this section has not been fully completed; at the moment, preliminary research has been conducted.

Introduction

Membrane filtration is widely established as an effective physical separation method for water and wastewater treatment, particularly with ultrafiltration (UF) and nanofiltration (NF) being extensively applied for the removal of suspended solids and macromolecular pollutants [407]. However, conventional membrane filtration faces notable challenges in wastewater treatment, such as membrane fouling, which not only reduces the water flux but also significantly entails high maintenance and replacement costs [408,409]. Moreover, traditional membranes show a limited efficiency in removing low-molecular-weight organic compounds, since dissolved organic contaminants and micropollutants can easily penetrate membrane pores, affecting the quality of the treated effluent. These limitations restrict the broader application of membrane technology in wastewater treatment [410,411]. As a result, coupling membrane filtration with other robust treatment methods to address fouling issues and minimize the presence of pollutant residues in the permeate is becoming a hot research topic.

As described and justified throughout this Thesis, EF process offers an effective solution, converting O_2 to H_2O_2 through the $2e^-$ ORR pathway, and further generating $^{\bullet}OH$ upon catalytic activation, thus efficiently degrading recalcitrant organic pollutants in wastewater [412]. Conventional homogeneous Fenton systems typically operate under acidic conditions (pH ~3) to maintain the activity of iron ions, limiting their flexibility in practical applications [398]. However, the introduction of heterogeneous catalysts effectively activates H_2O_2, and it also significantly broadens the applicable pH range, increasing the viability of the EF process for wastewater treatment [398]. For instance, metal-based

heterogeneous catalysts such as those investigated in Section 4.2 demonstrate excellent H_2O_2 activation under neutral conditions, offering a highly efficient and durable solution for actual wastewater treatment systems [8]. Nonetheless, although heterogeneous catalysts perform well in the HEF process, they are often dispersed in water as suspended particles, which can lead to particle aggregation and a consequent reduction in $^{\bullet}OH$ production efficiency. Additionally, while these catalysts can be reused, recovery processes can be complex and lead to high loss rates and costs, with the risk of small particles remaining in the water and causing secondary pollution [394].

Lately, ceramic membranes (CMs) have been proven more suitable for demanding wastewater treatment environments, as compared to polymer membranes, owing to their superior mechanical strength, chemical stability, and thermal resilience [413]. CMs offer a longer operational lifespan, demonstrate sufficiently high flux and strong anti-fouling performance during extended use. Furthermore, combining CMs with other functional components imparts multifunctional properties, enabling a more efficient pollutant removal [414].

The limitations of traditional membrane filtration and HEF processes are simultaneously addressed by leveraging the advantages of CM materials to develop an electrified membrane (i.e., electrocatalytic membrane cathode). According to reports, electrified membrane systems can be categorized into dead-end filtration flow and cross-flow filtration, depending in the direction of the water flow in relation to the membrane [415]. The HEF process coupled with CM exhibited a significantly greater removal rate for florfenicol at 10.2 ± 0.1 mg m^{-2} h^{-1} compared to both single filtration (2.5 ± 0.1 mg m^{-2} h^{-1}) and batch HEF processes (4.3 ± 0.05 mg m^{-2} h^{-1}) [416]. In addition, dead-end mode led to more than 2- and 3-fold increases in AMX removal efficiency (97.9 %) compared with the cross-flow (48.5 %) and batch modes (38.0 %), and the power consumption in dead-end mode was reduced by 59.2 % and 69.3 % relative to the cross-flow and batch modes, respectively [417].

Herein, an FeCu/NC-MOF-derived catalyst, presumably in the form of a SAC, was coated on the surface of a commercial CM to create an electrocatalytic membrane. Acting as a cathode, this membrane generates H_2O_2 in-situ through the $2e^-$ ORR pathway and, under the synergistic effect of Fe and Cu, it further

activates H_2O_2 to produce $^{\bullet}OH$. The experimental setup utilizes a dead-end recirculation mode in an electrochemical flow reactor, where the solution undergoes initial filtration through the catalyzed CM and subsequently interacts with the $^{\bullet}OH$ electrogenerated on the membrane surface, achieving an advanced purification. Investigations into the effects of initial pH, flow rate, and applied current on the pollutant degradation efficiency, along with long-term testing, confirm the anti-fouling performance and stability of the membrane, which becomes a nice proof of concept to provide a more efficient and scalable solution for wastewater treatment.

Materials and methods

The ceramic membrane disks with a diameter of 46 mm, a thickness of 3 mm, and a pore size of 220 nm were purchased from Morui Xincailiao Shop. The target pollutant AMX (95.0 – 102.0% anhydrous basis) was acquired from Sigma-Aldrich. The synthesis of SAC was carried out using CTAB (≥99.0% (for ion pair chromatography)) from Merck, ferric nitrate nonahydrate ($Fe(NO_3)_3•9H_2O$, 100%) from PROBUS, S.A., 2-methylimidazole (99%), copper(II) nitrate trihydrate ($Cu(NO_3)_2•3H_2O$, 99–104%) and zinc nitrate hexahydrate ($Zn(NO_3)_2•6H_2O$, reagent grade, 98%) purchased from Sigma-Aldrich, and methanol (CH_3OH, ≥ 99.9%) from Scharlau. The ink was prepared using Nafion (Sigma-Aldrich, 5 wt.% in a mixture of lower aliphatic alcohols and water, 45% water content) and 2-propanol dry (PanReac AppliChem, max. 0.01% water). The mobile phase for HPLC analysis is composed of formic acid (Optima LC/MS) purchased from Fisher Chemical and acetonitrile (reag. Ph. Eur. for UHPLC Supergradient, ACS) from PanReac Applichem. Anhydrous Na_2SO_4 employed as supporting electrolyte was supplied by Merck.

All aqueous solutions were prepared with Milli-Q water from a Merck Life Science Synergy UV device (resistivity > 18.2 MΩ cm).

The procedure for preparing the FeCu/NC-SAC and catalyst-loaded CM cathodes are detailed in Section 3.3.1.

Electrocatalytic filtration experiments

The degradation performance of the FeCu/NC-SAC/CM for pharmaceutical removal during electrocatalytic filtration was evaluated in an electrochemical

flow cell operating in dead-end mode. For details, see Section 3.4. The quantification method of AMX is described in Section 3.5.1.

Note that during the treatment, samples were collected simultaneously from the reactor outlet and the reservoir for analysis. As the degradation rates at both locations were very similar at each given time, only the results from the reservoir samples are presented.

Results and Discussion

The performance of the XC72R/CM, and FeCu/NC-SAC/CM regarding the pharmaceutical elimination during the electrocatalytic filtration was investigated with AMX as the target pollutant, respectively.

Fig. 48 shows the impact of different current density, and catalyst loading on the removal efficiency of AMX using XC72R/CM. The results as shown Fig. 48a at a current density of 10 mA cm^{-2}. In the first stage, without applied current (highlighted in yellow), all configurations exhibited minimal physical removal (i.e., filtration and/or adsorption) of AMX, suggesting a limited filtration capacity of the pristine CM. At 10 mA cm^{-2}, EO alone (without CM, using Ni mesh as a cathode) yielded approximately 80% degradation efficiency after 120 min. The introduction of the unmodified commercial CM in the latter system resulted in a slightly lower performance (about 70% degradation efficiency at 120 min), likely due to the CM interfering in the EO process, which was not counterbalanced by an effective filtration by the membrane; however, note that the AMX removal during the first 60 min was enhanced, which could be attributed to electrosorption phenomena. Loading uncatalyzed XC72R carbon onto the CM surface, to act as a cathode, significantly enhanced the removal performance, which means that XC72R facilitates the in-situ electrogeneration of H_2O_2, as well as the electrosorption process. With a loading of 1 mg cm^{-2}, complete disappearance of AMX was achieved within 40 min. However, increasing the loading to 2 mg cm^{-2} led to a removal rate of approximately 80% in the same time period, possibly due to excessive catalyst causing blockage of the CM pores. In the dead-end filtration mode, the solution is thus forced to flow through only a portion of the pores, rendering parts of the cathode inactive to adsorption and H_2O_2 production. When the catalyst loading was increased to 4 mg cm^{-2}, 100% degradation was still

achieved within 40 min, as the catalyst still caused pore blockage but could provide a larger number of active sites that is beneficial for H_2O_2 production, as well as for adsorption. Therefore, a catalyst loading of 1 mg cm^{-2} was considered the most suitable value for subsequent tests.

Fig. 48b presents the experimental results at a current density of 2 mA cm^{-2}. The overall degradation efficiency decreased, as expected; however, the electrocatalytic filtration using the CM loaded with catalyst still outperformed the EO process. Interestingly, when the CM had a higher catalyst loading (2 mg cm^{-2}), greater removal efficiency was achieved as compared to CM loading of 1 mg cm^{-2}. This may be because, at lower current densities, the electron supply rate is reduced, limiting the reaction rates. In such cases, increasing the catalyst loading provides more active sites, promoting the ORR and counteracting the insufficient electron supply, thereby enhancing the overall removal efficiency. Taking into account that the energy consumption decrease was at the expense of a greater catalyst usage, this slight improvement was not deemed significant, thereby maintaining 1 mg cm^{-2} as the optimal loading.

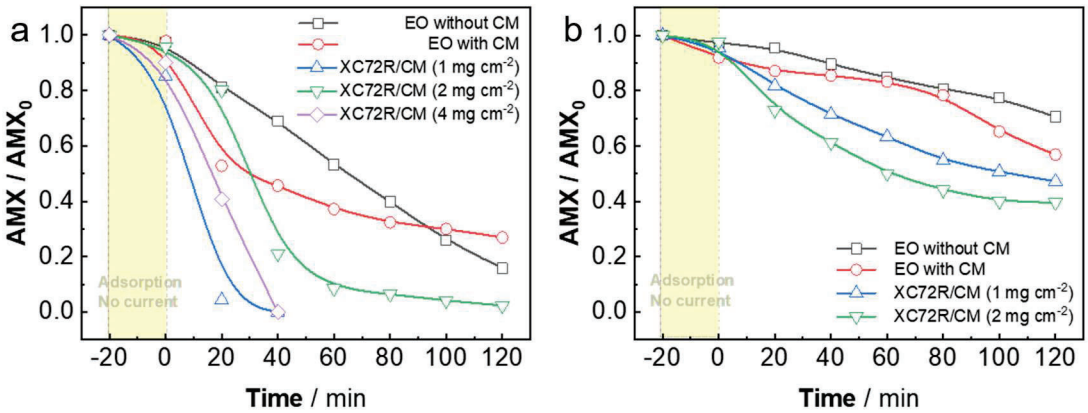

Figure 48. Time course of AMX ($C_{16}H_{19}N_3O_5S$) concentration during the treatment of 200 mL of solutions containing 10 mg C L^{-1} drug in 0.050 M Na_2SO_4 at room temperature. The electrochemical reactor was equipped with the CM (except in the pure EO trial without CM), either unmodified or coated with XC72R carbon as electrocatalyst at different loadings, and was operated in dead-end filtration mode with recirculation. Conditions: EO with DSA-O_2 as the anode, flow rate of 13.5 mL min^{-1}, natural pH 5.9. (a) 10 mA cm^{-2}; (b) 2 mA cm^{-2}. Samples were collected from the reservoir.

Fig. 49 illustrates the visual appearance of XC72R catalyst layers with varying loadings on the CM. At a loading of 2 mg cm^{-2}, the catalyst layer appears

uniform and free of cracks. As the loading increases to 4 mg cm^{-2}, minor clustering and peeling of the catalyst are observed. At 8 mg cm^{-2}, significant cracking of the surface becomes evident, and the catalyst layer is prone to detachment. Based on these observations, catalyst loadings of 1 mg cm^{-2} and 2 mg cm^{-2} were considered more suitable.

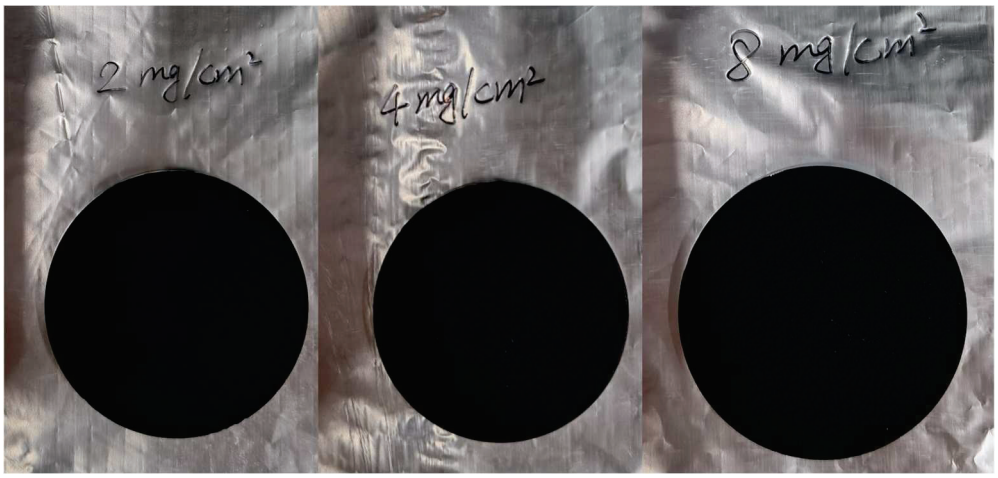

Figure 49. CMs with different loadings of XC72R catalyst.

Fig. 50a illustrates the performance of different electrocatalytic CMs regarding the removal of AMX. The results indicate that the FeCu/NC-SAC/CM outperforms the XC72R/CM, demonstrating that FeCu/NC-SAC functions efficiently as a bifunctional catalyst. Its carbon-based structure facilitates the selective in-situ generation of H_2O_2 via the $2e^-$ ORR, while the presence of Fe and Cu single sites rapidly activates H_2O_2 into $^{\bullet}OH$, enhancing the AMX degradation. Although reducing the loading to 0.5 mg cm^{-2} yielded a similar final degradation, it might result in uneven coating, thereby increasing the process complexity. Notably, the CM with a mixed loading of FeCu/NC-SAC and XC72R exhibited the poorest performance, possibly due to interference between the active sites of the two catalysts or the introduction of different electron transfer pathways, causing uneven electron distribution among active sites and eventually reducing the overall reaction efficiency.

To verify the synergistic effect between Fe and Cu, single-metal catalysts and a metal-free material were synthesized using the same synthesis procedure, as shown in Fig. 50b.

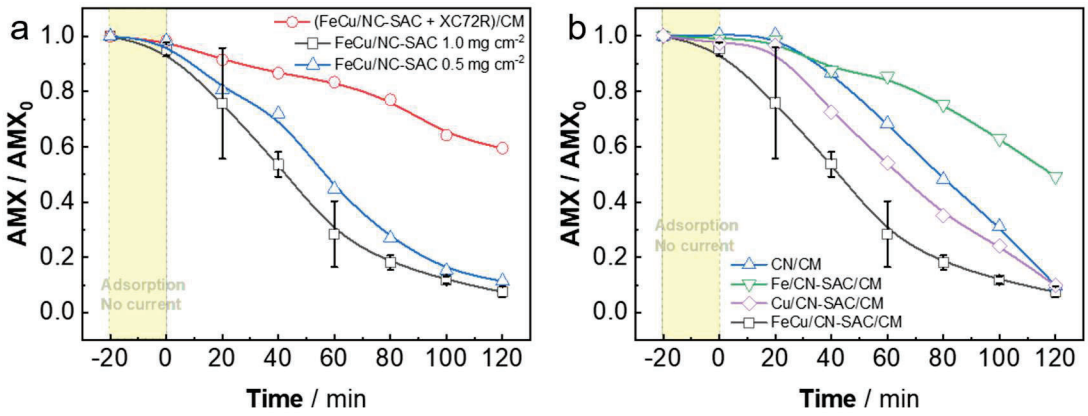

Figure 50. Analogous to Fig. 48, but using the FeCu/NC-SAC electrocatalyst. Conditions: HEF treatment (except CN/CM in plot (b), which is EO process) using DSA-O_2 as the anode, flow rate of 13.5 mL min^{-1}, natural pH 5.9, *j* of 2 mA cm^{-2}. Samples were collected from the reservoir. In (a), the mixed loading (red curve) was done with 1 mg cm^{-2} of each electrocatalyst. In (b), the loading was 1 mg cm^{-2} of each electrocatalyst.

FeCu/NC-SAC/CM exhibited the fastest initial AMX degradation. Although the degradation efficiencies of all catalysts were similar at 120 min, FeCu/NC-SAC/CM maintained a consistently higher degradation rate throughout the reaction process, indicating a stronger catalytic activity in the initial stages and a more rapid degradation of AMX. This performance advantage is in agreement with the synergistic interaction between iron and copper explained in previous section, providing more active sites and promoting the activation of H_2O_2.

Conclusions

In this preliminary study, a bifunctional FeCu/NC-SAC catalyst-modified electrocatalytic CM was successfully developed. The inherent carbon content of the catalyst facilitates the in-situ electrogeneration of H_2O_2 via the $2e^-$ ORR pathway. The active metals, Fe and Cu, efficiently activate H_2O_2 to produce $^{\bullet}OH$, thereby effectively degrading AMX. This study, however, has not addressed the effect of other relevant factors such as flow rate, initial pH of treated solution (with potential impact on the adsorption of organic molecules on the catalyst and membrane surfaces), as well as a broader range of current densities. A detailed physicochemical characterization is also needed to assess the properties of FeCu/NC-SAC and FeCu/NC-SAC/CM regarding their morphology, structure, and composition. We are especially interested in demonstrating the presence of single atoms and, with the acquisition of a new TEM by the UB, which is able to

perform high-angle annular dark-field scanning transmission (HAADF-STEM) analysis, it is expected to achieved their identification. Further research is necessary to explore these aspects to fully understand the performance of the electrified membranes under varied operation conditions.

Chapter 5

Conclusions and Perspectives

CHAPTER 5. Conclusions and Perspectives

5.1 Conclusions

This Thesis is primarily dedicated to the development and optimization of new ORR electrocatalysts for H_2O_2 electrogeneration, as well as the design of Cu-MOF-based heterogeneous catalysts for H_2O_2 activation and the proposal a potential system for future scale-up of the technology. The catalysts were applied in the HEF process under near-neutral conditions to achieve the efficient degradation of organic micro-contaminants, with special attention on pharmaceuticals. From the results described in the five sections of Chapter 4, a series of conclusions can defined, in good agreement with the general objectives (GO) and specific goals (SG) listed in Chapter 2.

Regarding Chapter 4.1 (GO1 and SG1-4):

- The electrocatalysts were synthesized by different methods, and their crystal structures, surface chemical compositions, pore structures, and morphological features were analyzed by EA, XRD, XPS, Raman, N_2 physisorption, FT-IR, SEM, TEM, and XAS, to gain an in-depth understanding of the microstructures and physicochemical properties for electrocatalysts.
- The electron transfer number and H_2O_2 selectivity of the electrocatalysts —Sn-doped carbons, N-doped carbons, and PMHS-modified carbons— were determined under near-neutral pH conditions using the RRDE technique. These measurements provided insight into the efficiency of catalysts in promoting the ORR and their ability to selectively generate H_2O_2 in a controlled electrochemical environment.
- The incorporation of Sn into carbon supports significantly enhanced the ORR activity as compared to that of Sn-free carbons. The strong affinity of Sn for oxygen molecules facilitates their activation on the electrode surface, thereby enhancing the ORR efficiency. This characteristic allowed the Sn/C electrocatalysts to exhibit excellent electrolysis performance.
- Nitrogen doping enhanced the efficiency and selectivity of carbon-

based catalysts for the $2e^-$ ORR, producing higher H_2O_2 yields. Pyrrolic nitrogen, in particular, plays a critical role in promoting the O_2 adsorption and stabilizing the OOH* intermediate, essential for $2e^-$ ORR. The presence of a balanced nitrogen functionality, especially pyrrolic and graphitic nitrogen, improved the electron distribution, ensuring a controlled ORR process that favored the H_2O_2 production. Such optimal nitrogen distribution conferred a high selectivity to the N-doped carbons.

- The pore distribution played a critical role in enhancing the performance of $2e^-$ ORR electrocatalysts by optimizing mass transport of reactants and products. Carbon materials with a well-balanced combination of micropores and mesopores offered a suitable surface area, providing a higher density of active sites that facilitate oxygen diffusion and adsorption. Mesopores allowed the rapid evacuation of H_2O_2, preventing its accumulation and subsequent reduction to water, eventually favoring the $2e^-$ ORR selectivity. Micropores supplied highly dispersed active sites, while mesopores create efficient mass transport channels, contributing to excellent H_2O_2 production.
- Hydrophobicity significantly had clear impact on the $2e^-$ ORR performance by enhancing oxygen availability at the catalyst surface. A hydrophobic surface facilitates the diffusion of oxygen by repelling water, ensuring that active sites are readily accessible. This contributes to maintaining the $2e^-$ pathway by minimizing water interference (i.e., flooding).
- The binder nature and loading had a great effect on the performance and mechanical stability of GDEs. The use of a hydrophobic binder enhanced the oxygen diffusion by maintaining an oxygen-rich environment at the reaction interface, thereby improving the efficiency of H_2O_2 generation. Additionally, an appropriate binder distribution prevented catalyst particle aggregation, ensuring optimal exposure of active sites.
- Optimizing the catalyst loading on GDEs was essential for maximizing the H_2O_2 electrogeneration efficiency. At a suitable catalyst loading, an

optimal number of active sites was obtained, thus boosting the H_2O_2 production rates. However, excessive loading could restrict the oxygen mass transport, negatively affecting the generation efficiency. Therefore, balancing the quantity of active sites with oxygen transport efficiency is crucial for achieving the optimal H_2O_2 yield.

- Higher current densities generally promoted an increased H_2O_2 production rate due to enhanced electron transfer and oxygen reduction activity at the electrode surface. However, excessive current was detrimental due to side reactions, including further reduction of H_2O_2 to water, which lowers the overall CE. Optimal current density values must therefore balance the H_2O_2 production and the energy losses, ensuring sustainable operation.
- Although lower pH values traditionally favor a higher H_2O_2 stability and radical formation in the EF process, the GDEs fabricated in this Thesis exhibited substantial H_2O_2 production at near-neutral pH, demonstrating their adaptability to environmentally relevant conditions. This versatility allows these GDEs to function without electrolyte acidification, making them suitable for applications within a broader pH range.
- The new GDEs have shown effective pollutant degradation in EF systems. Under optimal conditions, these electrodes achieved substantial contaminant removal, highlighting their potential in environmental applications. At circumneutral pH (~5.9), the degradation process for specific pollutants was completed within approximately 120 min, demonstrating the system viability without the need for highly acidic conditions.

Regarding Chapter 4.2 (GO2 and SG5-9):

- Hydrothermal synthesis conditions and pyrolysis atmosphere significantly impact the properties of Cu-MOFs and Cu/NC catalysts. The synthesis yield at room temperature was below 10%, while hydrothermal treatment at 120 ºC for 2 h improved it to over 20%. Extending the hydrothermal duration to 12 h further increased the yield, although 2 h was chosen as a good compromise. During pyrolysis, an

Ar atmosphere led to partial oxidation, causing the formation of Cu_2O, whereas an Ar/H_2 atmosphere preserved metallic Cu, maximizing the yield and maintaining the desired catalytic properties.

- Under near-neutral pH conditions, a current density of 50 mA cm^{-2}, a catalyst dosage of 0.1 g L^{-1}, and the use of a DSA-Cl_2 anode allowed maximizing the degradation and mineralization efficiency for the treatment of DPH solutions. High current densities accelerated the H_2O_2 production, enhancing degradation rates, whereas the selected catalyst dosage balanced the active radical availability without promoting their quenching. Although the BDD anode demonstrated the highest $^{\bullet}OH$ production, the DSA-Cl_2 anode was chosen due to its cost-effectiveness.
- Under those optimal conditions, the HEF process achieved high degradation and mineralization efficiency in actual wastewater at near-neutral pH. This setup effectively removed organics in a complex matrix, demonstrating the applicability of the Cu/C catalyst.
- DPH was investigated as a target pollutant in the EF processes for the first time, with key intermediates identified, including hydroxylated and ring-opened compounds. The proposed degradation pathway was initiated with hydroxylation, followed by ring cleavage and oxidation to simpler acids, ultimately leading to mineralization as CO_2 and H_2O, illustrating effective breakdown of complex pharmaceutical compounds under near-neutral conditions.
- Cu-based MOF-derived catalysts exhibited a high ORR activity, with H_2O_2 selectivity reaching up to 85% under near-neutral conditions, which can be considered as a promising result for sustainable H_2O_2 electrogeneration.

Regarding Chapter 4.2 (GO3 and SG10-12):

- Bimetallic FeCu-MOF catalysts and their FeCu/NC derivatives were synthesized to enhance the Fe(II) regeneration and accelerate pharmaceutical degradation in wastewater under near-natural pH in the HEF process. The synergy between Fe and Cu sites facilitated the effective Fe(II)/Fe(III) cycling, enabling continuous $^{\bullet}OH$ generation. These catalysts demonstrated stability and high activity, achieving

efficient degradation rates, highlighting their potential for sustainable wastewater treatment in practice.

- The structure of the MOFs effectively retained Fe and Cu within the catalyst matrix, reducing the metal leaching to the solution. This stability under operation conditions ensured a sustained catalytic activity and extended the catalyst lifespan, making it suitable for long-term treatment applications.
- The electrochemical analysis highlighted the advantages of bimetallic FeCu/NC catalysts, demonstrating enhanced redox properties compared to monometallic counterparts. CV and EIS allowed demonstrating the improved electron transfer kinetics and facilitated Fe(II)/Fe(III) cycling, which are essential for continuous $^{\bullet}OH$ production in the HEF process. The synergy between Fe and Cu sites resulted in lower charge transfer resistance and higher catalytic efficiency, underscoring the effectiveness of bimetallic catalysts in wastewater treatment applications.

Regarding Chapter 4.3 (GO4 and SG13-15):

- Optimal parameters for the catalyst-modified CMs were identified for efficient AMX degradation, with a current density of 10 mA cm^{-2} and catalyst loading of 1 mg cm^{-2} yielding complete removal within 40 min. FeCu-SAC catalyst exhibited enhanced performance due to the synergistic effects of Fe and Cu, which promoted efficient H_2O_2 generation and activation. Excessive catalyst loading reduced the efficiency due to potential pore blockage.
- The CM can physically fragment O_2, acting as micropore diffuser that facilitates the generation of reactive oxygen species. This phenomenon eliminates the need for external aeration, highlighting the dual functionality of CMs in supporting both filtration and catalytic (electro)degradation.

5.2 Perspectives

This Thesis project explored aspects of different relevant cornerstones for the development and scale-up of EF technology: several types of electrocatalysts,

a GDE modification method, two heterogeneous catalysts, and a novel electrocatalytic filtration system that integrates CMs. The great performance of EF, HEF, and HEF-like processes to treat organic micro-contaminants in model solutions and actual wastewater across a wide pH range has been proven. These findings provide a robust foundation for developing effective water treatment technologies with practical applications. However, several challenges remain unresolved, warranting further investigation to enhance the competitiveness of EF process for realistic applications

To scale-up the EF processes effectively, three main challenges should be prioritized: (a) Improve the catalyst yield, minimizing material loss and eventually reducing the production costs; (b) enhance the activity of heterogeneous catalysts to boost the H_2O_2 activation rate, thereby shortening the degradation time with special impact on the initial activation stage; and (c) facilitate practical deployment by advancing reactor design and process integration to meet the demands of industrial wastewater treatment.

In this study, both Cu/NC and FeCu/NC were derived from MOF materials, while Sn-doped and N-doped carbon catalysts also required high-temperature pyrolysis to obtain desirable carbon-based catalysts. However, the pyrolysis process typically results in significant material loss, limiting the overall yield. For example, yields for Sn-doped carbon, N-doped carbon, Cu/NC, and FeCu/NC were approximately 19.5%, 43.8%, 7.7%, and 15.0%, respectively. These yield limitations not only increase the preparation cost but also affect the economic feasibility of applying these catalysts on a large scale. Future research should focus on improving the yield of MOF-derived and doped carbon materials through multiple approaches, such as optimizing MOF precursors, developing low-temperature pyrolysis methods, using dopants to enhance thermal stability, or investigating alternative synthesis procedures (e.g., mechanochemical synthesis). Improving the yield would contribute to lower production costs, paving the way for industrial-scale water treatment applications.

While Cu/NC and FeCu/NC heterogeneous catalysts show stability, their H_2O_2 activation rate remains lower than that of homogeneous catalysts. Heterogeneous catalysts require some time to reach optimal activation in solution, causing initial reaction delays, whereas homogeneous catalysts can achieve activation more rapidly. Future work could improve the H_2O_2 activation rate by

refining the surface structure of FeCu bimetallic catalysts, optimizing the distribution of catalytic sites, or increasing the exposure of active sites. Obviously, control at the atomic scale, as exemplified by research on SACs, as well as on clusters and other atomic distributions would enhance the atomic efficiency, although the long-term stability of such catalysts is not ensured and is nowadays a matter of great complexity. Progress in these areas would significantly enhance the efficiency of the EF process for treating actual wastewater.

Finally, to move EF technology to next level (i.e., practical use), it is essential to translate laboratory-scale results into scalable processes suited for industrial applications. Developing modular reactor designs would allow flexible integration into wastewater treatment facilities. Additionally, enhancing mass transport efficiency within reactors is critical, especially in high-flow or complex wastewater environments, where effective mass transport is essential to maximize catalyst performance. Introducing CMs or gas diffusion electrodes could further optimize gas-liquid interfacial reactions in the EF system, accelerating the path to real-world application. The hybridization of these technologies, as proposed in the last section of this Thesis, seems a right way in this regard, and is an ongoing research topic in LEMMA research group. Finally, conducting long-term testing in pilot-scale facilities will provide the necessary data and technical support for widespread EF process implementation. Life cycle assessment (LCA) and techno-economic evaluation would be incorporated at that stage of development, since it is mostly meaningless at the scale at which this Thesis has been focused.

Resum

La crisi mundial de l'aigua ha impulsat la recerca de recursos hídrics no convencionals per tal de satisfer una demanda que va en augment. Les aigües residuals, degut a la seva abundància i facilitat d'accés, son considerades cada cop més com un recurs amb gran valor afegit. Malgrat això, la presència de productes farmacèutics a certes aigües residuals planteja un desafiament significatiu per a la seva reutilització eficient i segura L'eliminació d'aquests contaminants, derivats principalment de l'ús intensiu de fàrmacs a escala global, és complexa. La seva descàrrega agreuja la degradació dels ecosistemes i suposa greus riscos per a la salut humana. Afrontar aquests desafiaments exigeix el desenvolupament de tecnologies quaternàries de tractament d'aigües residuals més eficients i respectuoses amb el medi ambient, amb un enfocament particular en la degradació completa de residus farmacèutics.

En els darrers anys, els processos electroquímics d'oxidació avançada han rebut una atenció considerable per al tractament d'aigües residuals. Entre aquests, el procés electro-Fenton (EF) ha demostrat un rendiment notable en la degradació de contaminants orgànics. Tot i això, els sistemes EF tradicionals enfronten limitacions pràctiques, com els alts costos operatius associats a l'ajust del pH i la desactivació del catalitzador. Aquesta Tesi aborda aquests desafiaments mitjançant dues innovacions clau: (1) El desenvolupament d'electrocatalitzadors altament actius i selectius per a la reacció de reducció bielectrònica d'oxigen ($2e^-$ ORR), necessària per a l'electrogeneració in situ de H_2O_2; i (2) la síntesi de catalitzadors heterogenis avançats amb estructura nucli-escorça i mecanismes sinèrgics que incrementen significativament l'eficiència d'activació de l'H_2O_2, minimitzant la lixiviació. A més, la integració del procés EF heterogeni (HEF) amb la filtració mitjançant membranes ceràmiques (CM) ha permès el desenvolupament duna membrana electrificada bifuncional per a la degradació de contaminants en un reactor de flux continu.

Per a l'electrogeneració in situ de H_2O_2, es van explorar dos nous electrocatalitzadors amb una eficiència millorada per a l'ORR. Diversos materials de carboni dopats amb Sn, sintetitzats mitjançant un mètode tèrmic directe, van mostrar una selectivitat excel·lent, del 98,0% i un nombre d'electrons transferits

de 2,04. Els elèctrodes de difusió de gas (GDEs) fabricats amb aquests materials van aconseguir una concentració acumulada d'H_2O_2 de 20,4 mM aplicant un baix corrent en condicions òptimes. La seva estructura micromesoporosa adequada va permetre la ràpida generació i alliberament d'H_2O_2, evitant la seva oxidació posterior. A pH natural, el procés HEF va aconseguir gairebé un 100% de degradació del fàrmac antihistamínic difenhidramina (DPH) en 120 minuts. D'altra banda, una sèrie de carbonis dopats amb nitrogen, preparats mitjançant la pirròlisi de negre de carboni barrejat amb melamina, van presentar un contingut de nitrogen pirròlic del 3,5% i una selectivitat del 95,3%. Els GDE resultants van mostrar taxes de producció d'H_2O_2 superiors en comparació amb els GDE comercials, assolint 18 mg h^{-1} cm^{-2}, i van demostrar un rendiment excepcional a pH 5,9. A més, els GDEs basats en carbó modificats amb petites quantitats de polimetilhidrosiloxà (PMHS) van superar els GDEs convencionals basats en PTFE en la generació d'H_2O_2 (1874,8 mg L^{-1} enlloc de 1087,4 mg L^{-1}). Els càlculs de teoria del funcional de densitat (DFT) realitzats per col·laboradors van revelar que els grups $-CH_3$ confereixen propietats superhidrofòbiques a la capa catalítica.

Per tal d'activar l'H_2O_2, es van desenvolupar catalitzadors Cu/NC i FeCu/NC derivats de xarxes metal·lorgàniques (MOFs). Al tractament HEF amb el primer material, es va aconseguir la degradació completa de DPH a pH 6–8, superant l'EF homogeni amb catalitzador Fe^{2+} en condicions àcides en termes de mineralització. Els catalitzadors FeCu/NC, sintetitzats usant MIL(Fe)-88B com a precursor, van mostrar un rendiment notable amb només 0,05 g L^{-1} de catalitzador, aconseguint un 100% d'eliminació del fàrmac antihipertensiu lisinopril (LSN) en 6 minuts a pH 3 i en 75 minuts a pH natural. La sinergia Fe-Cu va accelerar la regeneració de Fe(II), mentre que l'estructura nucli-escorça va minimitzar la lixiviació de metalls. El catalitzador va mantenir una eficiència de degradació del 86,5% després de cinc cicles, demostrant una notable estabilitat i capacitat de reutilització.

Finalment, es va investigar la integració dels processos HEF amb la filtració mitjançant CM. La membrana electrocatalítica fabricada en aquest estudi va permetre tant la generació in situ d'H_2O_2 com la seva activació immediata en un reactor de flux continu operat en mode de recirculació.

En conclusió, aquesta Tesi proposa un conjunt d'estratègies electroquímiques innovadores que aborden amb èxit el desafiament de

l'eliminació de contaminants farmacèutics d'aigües residuals a escala de laboratori. Aquest treball ha donat com a resultat cinc publicacions científiques.

Paraules clau: Catàlisi heterogènia; Filtració per membrana; Procés electro-Fenton; Reacció de reducció d'oxigen; Tractament avançat d'aigües residuals.

References

[1] P. Ball, Water as an Active Constituent in Cell Biology. *Chem. Rev.* 108 (2008) 74–108. https://doi.org/10.1021/cr068037a.

[2] J.E. Hall, Guyton and hall textbook of medical physiology. 12. ed, Saunders, Elsevier, Philadelphia, Pa, 2011.

[3] M. Behnassi, A.A. Al-Shaikh, A. Gurib-Fakim, M. Barjees Baig, M. Bahir, eds., The Water, Climate, and Food Nexus: Linkages, Challenges and Emerging Solutions. Springer International Publishing, Cham, 2024. https://doi.org/10.1007/978-3-031-50962-9_1.

[4] V. Davamani, J.E. John, C. Poornachandhra, B. Gopalakrishnan, S. Arulmani, E. Parameswari, A. Santhosh, A. Srinivasulu, A. Lal, R. Naidu, A critical review of climate change impacts on groundwater resources: A focus on the current status, future possibilities, and role of simulation models. *Atmosphere* 15 (2024) 122. https://doi.org/10.3390/atmos15010122.

[5] O. Iji, O. Iji, Perspective chapter: Boiling point, melting point, freezing point – water is the essence of life, and what we need to do to avert calamity. IntechOpen, 2024. https://doi.org/10.5772/intechopen.1006069.

[6] How much water do we really have? A look at the global freshwater distribution. World Economic Forum (2023). https://www.weforum.org/agenda/2023/07/global-distribution-fresh-water-withdrawals/ (accessed August 23, 2024).

[7] United Nations Sustainable Development Goals. (2024). https://sdgs.un.org/ (accessed December 4, 2024).

[8] The water crisis is worsening. Researchers must tackle it together. *Nature.* 613 (2023) 611–612. https://doi.org/10.1038/d41586-023-00182-2.

[9] UN world water development report 2024. UN-Water (2024). https://www.unwater.org/publications/un-world-water-development-report-2024 (accessed September 23, 2024).

[10] State of global water resources 2022. World Meteorological Organization (2023). https://wmo.int/publication-series/state-of-global-water-resources-2022 (accessed September 23, 2024).

[11] Y.C. Goh, Z. Zainol, M.Z. Mat Amin, Assessment of future water availability under the changing climate: case study of Klang River Basin. Malaysia, *Int. J. River Basin Ma.* 14 (2016) 65–73. https://doi.org/10.1080/15715124.2015.1068178.

[12] M.M. Mekonnen, A.Y. Hoekstra, Four billion people facing severe water scarcity. *Sci. Adv.* 2 (2016) e1500323. https://doi.org/10.1126/sciadv.1500323.

[13] R. Mukhopadhyay, B. Sarkar, H.S. Jat, P.C. Sharma, N.S. Bolan, Soil salinity under climate change: Challenges for sustainable agriculture and food security. *J. Environ. Manage.* 280 (2021) 111736. https://doi.org/10.1016/j.jenvman.2020.111736.

[14] S. Kuzma, L. Saccoccia, M. Chertock, 25 countries, housing one-quarter of the population, face extremely high water stress. (2023). https://www.wri.org/insights/highest-water-stressed-countries (accessed August 27, 2024).

[15] Global water scarcity: Causes & solutions for water crisis. Bank of America Institute (2023). https://institute.bankofamerica.com/sustainability/global-water-scarcity.html (accessed August 27, 2024).

[16] UN world water development report 2023. UN-Water (2023). https://www.unwater.org/publications/un-world-water-development-report-2023 (accessed September 23, 2024).

[17] Z. Khan, I. Thompson, C.R. Vernon, N.T. Graham, T.B. Wild, M. Chen, Global monthly sectoral water use for 2010–2100 at 0.5° resolution across alternative futures. *Sci. Data.* 10 (2023) 201. https://doi.org/10.1038/s41597-023-02086-2.

[18] B. Pratap, S. Kumar, S. Nand, I. Azad, R.N. Bharagava, L.F. Romanholo Ferreira, V. Dutta, Wastewater generation and treatment by various eco-friendly technologies: Possible health hazards and further reuse for environmental safety. *Chemosphere* 313 (2023) 137547.

https://doi.org/10.1016/j.chemosphere.2022.137547.

[19] E.R. Jones, M.T.H. Van Vliet, M. Qadir, M.F.P. Bierkens, Country-level and gridded estimates of wastewater production, collection, treatment and reuse. *Earth Syst. Sci. Data.* 13 (2021) 237–254. https://doi.org/10.5194/essd-13-237-2021.

[20] G.L. Karia, R.A. Christian, N.D. Jariwala, Wastewater treatment: Concepts and design approach, third edition. PHI Learning Pvt. Ltd., 978-81-19364-17-6, (2023). https://books.google.es/books?id=plzjEAAAQBAJ

[21] P.M. Chapman, Determining when contamination is pollution — Weight of evidence determinations for sediments and effluents. *Environ. Int.* 33 (2007) 492–501. https://doi.org/10.1016/j.envint.2006.09.001.

[22] J. Fito, S.W.H. Van Hulle, Wastewater reclamation and reuse potentials in agriculture: towards environmental sustainability. *Environ. Dev. Sustain.* 23 (2021) 2949–2972. https://doi.org/10.1007/s10668-020-00732-y.

[23] B. Senthil Rathi, P. Senthil Kumar, J. Natanya Ida Susana, J. Francia Virgin, R. Dharani, S. Sanjay, G. Rangasamy, Recent research progress on the removal of heavy metals from wastewater using modified zeolites: A critical review. *Desalin. Water Treat.* 319 (2024) 100573. https://doi.org/10.1016/j.dwt.2024.100573.

[24] A. Chakraborty, A. Pal, B.B. Saha, A critical review of the removal of radionuclides from wastewater employing activated carbon as an adsorbent. *Materials* 15 (2022) 8818. https://doi.org/10.3390/ma15248818.

[25] M. Montaña, A. Camacho, R. Devesa, I. Vallés, R. Céspedes, I. Serrano, S. Blàzquez, V. Barjola, The presence of radionuclides in wastewater treatment plants in Spain and their effect on human health. *J. Clean. Prod.* 60 (2013) 77–82. https://doi.org/10.1016/j.jclepro.2011.07.007.

[26] Y. Zhang, X. Wang, Z. Hu, Q. Xiao, Y. Wu, Capturing and recovering phosphorus in water via composite material: Research progress, future directions, and challenges. *Sep. Purif. Technol.* 353 (2025) 128453.

https://doi.org/10.1016/j.seppur.2024.128453.

[27] A. Choudhury, P.K. Ojha, S. Ray, Hazards of antiviral contamination in water: Dissemination, fate, risk and their impact on fish. *J. Hazard. Mater.* 476 (2024) 135087.
https://doi.org/10.1016/j.jhazmat.2024.135087.

[28] J. Ali, Y. Yang, G. Pan, Oxygen micro-nanobubbles for mitigating eutrophication induced sediment pollution in freshwater bodies. *J. Environ. Manage.* 331 (2023) 117281.
https://doi.org/10.1016/j.jenvman.2023.117281.

[29] L.G.A. Barboza, S.C. Lourenço, A. Aleluia, G.P. Senes, X.L. Otero, L. Guilhermino, Are microplastics a new cardiac threat? A pilot study with wild fish from the North East Atlantic Ocean. *Environ. Res.* 261 (2024) 119694.
https://doi.org/10.1016/j.envres.2024.119694.

[30] K.P. Goswami, G. Pugazhenthi, Credibility of polymeric and ceramic membrane filtration in the removal of bacteria and virus from water: A review. *J. Environ. Manage.* 268 (2020) 110583.
https://doi.org/10.1016/j.jenvman.2020.110583.

[31] I. Girón-Guzmán, S. Sánchez-Alberola, E. Cuevas-Ferrando, I. Falcó, A. Díaz-Reolid, P. Puchades-Colera, S. Ballesteros, A. Pérez-Cataluña, J.M. Coll, E. Núñez, M.J. Fabra, A. López-Rubio, G. Sánchez, Longitudinal study on the multifactorial public health risks associated with sewage reclamation. *Npj Clean Water.* 7 (2024) 72.
https://doi.org/10.1038/s41545-024-00365-y.

[32] F. Aguilera, J. Méndez, E. Pásaro, B. Laffon, Review on the effects of exposure to spilled oils on human health. *J. Appl. Toxicol.* 30 (2010) 291–301.
https://doi.org/10.1002/jat.1521.

[33] H. Singh, N. Bhardwaj, S.K. Arya, M. Khatri, Environmental impacts of oil spills and their remediation by magnetic nanomaterials. *Environ. Nanotechnol. Monit. Manag.* 14 (2020) 100305.
https://doi.org/10.1016/j.enmm.2020.100305.

[34] K. Sayed, L. Baloo, S.R.B.M. Kutty, F. Makba, Potential biodegradation of Tapis Light Crude Petroleum Oil, using palm oil mill effluent final

discharge as biostimulant for isolated halotolerant *Bacillus* strains. *Mar. Pollut. Bull.* 172 (2021) 112863. https://doi.org/10.1016/j.marpolbul.2021.112863.

[35] ITOPF handbook. (2024). https://www.itopf.org/knowledge-resources/documents-guides/itopf-handbook/ (accessed September 23, 2024).

[36] S. Mitra, R.K. Saran, S. Srivastava, C. Rensing, Pesticides in the environment: Degradation routes, pesticide transformation products and ecotoxicological considerations. *Sci. Total Environ.* 935 (2024) 173026. https://doi.org/10.1016/j.scitotenv.2024.173026.

[37] M. Gajewska, K. Fitobór, W. Artichowicz, R. Ulańczyk, M. Kida, K. Kołecka, Occurrence of specific pollutants in a mixture of sewage and rainwater from an urbanized area. *Sci. Rep.* 14 (2024) 18119. https://doi.org/10.1038/s41598-024-69099-8.

[38] F.G. Calvo-Flores, J. Isac-García, J.A. Dobado, Emerging pollutants: Origin, structure, and properties. John Wiley & Sons, 2018.

[39] B.I. Escher, H.M. Stapleton, E.L. Schymanski, Tracking complex mixtures of chemicals in our changing environment. *Science* 367 (2020) 388–392. https://doi.org/10.1126/science.aay6636.

[40] R. Carson, Silent Spring. Penguin Books London, 978-0395075067, 1962.

[41] S. Sauvé, M. Desrosiers, A review of what is an emerging contaminant. *Chem. Cent. J.* 8 (2014) 15. https://doi.org/10.1186/1752-153X-8-15.

[42] N. Liu, X. Jin, C. Feng, Z. Wang, F. Wu, A.C. Johnson, H. Xiao, H. Hollert, J.P. Giesy, Ecological risk assessment of fifty pharmaceuticals and personal care products (PPCPs) in Chinese surface waters: A proposed multiple-level system. *Environ. Int.* 136 (2020) 105454. https://doi.org/10.1016/j.envint.2019.105454.

[43] J.L. Wilkinson, A.B.A. Boxall, D.W. Kolpin, K.M.Y. Leung, R.W.S. Lai, C. Galbán-Malagón, A.D. Adell, J. Mondon, M. Metian, R.A. Marchant, A. Bouzas-Monroy, A. Cuni-Sanchez, A. Coors, P. Carriquiriborde, M. Rojo, C. Gordon, M. Cara, M. Moermond, T. Luarte, V. Petrosyan, Y. Perikhanyan, C.S. Mahon, C.J. McGurk, T. Hofmann, T. Kormoker, V. Iniguez, J. Guzman-Otazo, J.L. Tavares, F. Gildasio De Figueiredo, M.T.P.

Razzolini, V. Dougnon, G. Gbaguidi, O. Traoré, J.M. Blais, L.E. Kimpe, M. Wong, D. Wong, R. Ntchantcho, J. Pizarro, G.-G. Ying, C.-E. Chen, M. Páez, J. Martínez-Lara, J.-P. Otamonga, J. Poté, S.A. Ifo, P. Wilson, S. Echeverría-Sáenz, N. Udikovic-Kolic, M. Milakovic, D. Fatta-Kassinos, L. Ioannou-Ttofa, V. Belušová, J. Vymazal, M. Cárdenas-Bustamante, B.A. Kassa, J. Garric, A. Chaumot, P. Gibba, I. Kunchulia, S. Seidensticker, G. Lyberatos, H.P. Halldórsson, M. Melling, T. Shashidhar, M. Lamba, A. Nastiti, A. Supriatin, N. Pourang, A. Abedini, O. Abdullah, S.S. Gharbia, F. Pilla, B. Chefetz, T. Topaz, K.M. Yao, B. Aubakirova, R. Beisenova, L. Olaka, J.K. Mulu, P. Chatanga, V. Ntuli, N.T. Blama, S. Sherif, A.Z. Aris, L.J. Looi, M. Niang, S.T. Traore, R. Oldenkamp, O. Ogunbanwo, M. Ashfaq, M. Iqbal, Z. Abdeen, A. O'Dea, J.M. Morales-Saldaña, M. Custodio, H. De La Cruz, I. Navarrete, F. Carvalho, A.B. Gogra, B.M. Koroma, V. Cerkvenik-Flajs, M. Gombač, M. Thwala, K. Choi, H. Kang, J.L.C. Ladu, A. Rico, P. Amerasinghe, A. Sobek, G. Horlitz, A.K. Zenker, A.C. King, J.-J. Jiang, R. Kariuki, M. Tumbo, U. Tezel, T.T. Onay, J.B. Lejju, Y. Vystavna, Y. Vergeles, H. Heinzen, A. Pérez-Parada, D.B. Sims, M. Figy, D. Good, C. Teta, Pharmaceutical pollution of the world's rivers. *Proc. Natl. Acad. Sci. U.S.A.* 119 (2022) e2113947119. https://doi.org/10.1073/pnas.2113947119.

[44] D.G.J. Larsson, C.-F. Flach, Antibiotic resistance in the environment. *Nat. Rev. Microbiol.* 20 (2022) 257–269. https://doi.org/10.1038/s41579-021-00649-x.

[45] M.R. Montinari, S. Minelli, R. De Caterina, The first 3500 years of aspirin history from its roots – A concise summary. *Vasc. Pharmacol.* 113 (2019) 1–8. https://doi.org/10.1016/j.vph.2018.10.008.

[46] K. Samal, S. Mahapatra, M. Hibzur Ali, Pharmaceutical wastewater as Emerging Contaminants (EC): Treatment technologies, impact on environment and human health. *Energy Nexus* 6 (2022) 100076. https://doi.org/10.1016/j.nexus.2022.100076.

[47] R. Natarajan, K. Saikia, S.K. Ponnusamy, A.K. Rathankumar, D.S. Rajendran, S. Venkataraman, D.B. Tannani, V. Arvind, T. Somanna, K. Banerjee, N. Mohideen, V.K. Vaidyanathan, Understanding the factors

affecting adsorption of pharmaceuticals on different adsorbents – A critical literature update. *Chemosphere* 287 (2022) 131958. https://doi.org/10.1016/j.chemosphere.2021.131958.

[48] O. Fraiha, N. Hadoudi, N. Zaki, A. Salhi, H. Amhamdi, E.H. Akichouh, F. Mourabit, M. Ahari, Comprehensive review on the adsorption of pharmaceutical products from wastewater by clay materials. *Desalin. Water Treat.* 317 (2024) 100114. https://doi.org/10.1016/j.dwt.2024.100114.

[49] The global use of medicines 2024: Outlook to 2028. (2024). https://www.iqvia.com/insights/the-iqvia-institute/reports-and-publications/reports/the-global-use-of-medicines-2024-outlook-to-2028 (accessed September 23, 2024).

[50] L. Wang, Y. Xu, T. Qin, M. Wu, Z. Chen, Y. Zhang, W. Liu, X. Xie, Global trends in the research and development of medical/pharmaceutical wastewater treatment over the half-century. *Chemosphere* 331 (2023) 138775. https://doi.org/10.1016/j.chemosphere.2023.138775.

[51] C. Gadipelly, A. Pérez-González, G.D. Yadav, I. Ortiz, R. Ibáñez, V.K. Rathod, K.V. Marathe, Pharmaceutical industry wastewater: Review of the technologies for water treatment and reuse. *Ind. Eng. Chem. Res.* 53 (2014) 11571–11592. https://doi.org/10.1021/ie501210j.

[52] Permit guidance document: Pharmaceutical manufacturing point source category. (2006).

[53] R. Gupta, B. Sati, A. Gupta, Treatment and recycling of wastewater from pharmaceutical industry. in: R.L. Singh, R.P. Singh (Eds.), Advances in Biological Treatment of Industrial Waste Water and Their Recycling for a Sustainable Future, Springer, Singapore, 2019: pp. 267–302. https://doi.org/10.1007/978-981-13-1468-1_9.

[54] A. Moarefian, H.A. Golestani, H. Bahmanpour, Removal of amoxicillin from wastewater by self-made Polyethersulfone membrane using nanofiltration. *J. Environ. Health. Sci. Eng.* 12 (2014) 1–10. https://doi.org/10.1186/s40201-014-0127-1.

[55] L. Yang, W. Hu, Z. Chang, T. Liu, D. Fang, P. Shao, H. Shi, X. Luo,

Electrochemical recovery and high value-added reutilization of heavy metal ions from wastewater: Recent advances and future trends. *Environ. Int.* 152 (2021) 106512.
https://doi.org/10.1016/j.envint.2021.106512.

[56] K. Samal, S. Mahapatra, M. Hibzur Ali, Pharmaceutical wastewater as Emerging Contaminants (EC): Treatment technologies, impact on environment and human health. *Energy Nexus* 6 (2022) 100076. .
https://doi.org/10.1016/j.nexus.2022.100076.

[57] A.K. Thakur, R. Kumar, A. Kumar, R. Shankar, N.A. Khan, K.N. Gupta, M. Ram, R.K. Arya, Pharmaceutical waste-water treatment via advanced oxidation based integrated processes: An engineering and economic perspective. *J. Water Process Eng.* 54 (2023) 103977.
https://doi.org/10.1016/j.jwpe.2023.103977.

[58] M.V.P. Singh, K.R. Shankar, Next-generation hybrid technologies for the treatment of pharmaceutical industry effluents. *J. Environ. Manage.* 353 (2024) 120197.
https://doi.org/10.1016/j.jenvman.2024.120197.

[59] C. Hignite, D.L. Azarnoff, Drugs and drug metabolites as environmental contaminants: Chlorophenoxyisobutyrate and salicylic acid in sewage water effluent. *Life Sci.* 20 (1977) 337–341.
https://doi.org/10.1016/0024-3205(77)90329-0.

[60] O. Cardoso, J.-M. Porcher, W. Sanchez, Factory-discharged pharmaceuticals could be a relevant source of aquatic environment contamination: Review of evidence and need for knowledge. *Chemosphere* 115 (2014) 20–30.
https://doi.org/10.1016/j.chemosphere.2014.02.004.

[61] E. Abahussain, M. Waheedi, S. Koshy, Practice, awareness and opinion of pharmacists toward disposal of unwanted medications in Kuwait. *Saudi Pharm. J.* 20 (2012) 195–201.
https://doi.org/10.1016/j.jsps.2012.04.001.

[62] P. Łukaszewicz, A. Białk-Bielińska, J. Dołżonek, J. Kumirska, M. Caban, P. Stepnowski, A new approach for the extraction of tetracyclines from soil matrices: application of the microwave-extraction technique. *Anal. Bioanal. Chem.* 410 (2018) 1697–1707.

https://doi.org/10.1007/s00216-017-0815-7.

[63] M. Patel, R. Kumar, K. Kishor, T. Mlsna, C.U. Pittman, D. Mohan, Pharmaceuticals of emerging concern in aquatic systems: Chemistry, occurrence, effects, and removal methods. *Chem. Rev.* 119 (2019) 3510–3673.
https://doi.org/10.1021/acs.chemrev.8b00299.

[64] N.H. Tran, K.Y.-H. Gin, H.H. Ngo, Fecal pollution source tracking toolbox for identification, evaluation and characterization of fecal contamination in receiving urban surface waters and groundwater. *Sci. Total Environ.* 538 (2015) 38–57.
https://doi.org/10.1016/j.scitotenv.2015.07.155.

[65] Q. Bu, X. Shi, G. Yu, J. Huang, B. Wang, J. Wang, Pay attention to non-wastewater emission pathways of pharmaceuticals into environments. *Chemosphere* 165 (2016) 515–518.
https://doi.org/10.1016/j.chemosphere.2016.09.078.

[66] M. Caban, P. Stepnowski, How to decrease pharmaceuticals in the environment? A review. *Environ. Chem. Lett.* 19 (2021) 3115–3138.
https://doi.org/10.1007/s10311-021-01194-y.

[67] C.G. Daughton, Pharmaceuticals and the Environment (PiE): Evolution and impact of the published literature revealed by bibliometric analysis. *Sci. Total Environ.* 562 (2016) 391–426.
https://doi.org/10.1016/j.scitotenv.2016.03.109.

[68] F. Rahimi, A. Nasiri, M. Hashemi, S. Rajabi, S. Abolghasemi, Advances in three-dimensional electrochemical degradation: A comprehensive review on pharmaceutical pollutants removal from aqueous solution. *Chemosphere* 362 (2024) 142620.
https://doi.org/10.1016/j.chemosphere.2024.142620.

[69] M. Ortúzar, M. Esterhuizen, D.R. Olicón-Hernández, J. González-López, E. Aranda, Pharmaceutical pollution in aquatic environments: A concise review of environmental impacts and bioremediation systems. *Front. Microbiol.* 13 (2022) 869332.
https://doi.org/10.3389/fmicb.2022.869332.

[70] J. Ma, X. Wang, H. Sun, W. Tang, Q. Wang, A review on three-dimensional electrochemical technology for the antibiotic wastewater treatment.

Environ. Sci. Pollut. Res. 30 (2023) 73150–73173.
https://doi.org/10.1007/s11356-023-27565-2.

[71] N. Taoufik, W. Boumya, F.Z. Janani, A. Elhalil, F.Z. Mahjoubi, N. Barka, Removal of emerging pharmaceutical pollutants: A systematic mapping study review. *J. Environ. Chem. Eng.* 8 (2020) 104251.
https://doi.org/10.1016/j.jece.2020.104251.

[72] A. Nasiri, N. Golestani, S. Rajabi, M. Hashemi, Facile and green synthesis of recyclable, environmentally friendly, chemically stable, and cost-effective magnetic nanohybrid adsorbent for tetracycline adsorption. *Heliyon* 10 (2024) e24179.
https://doi.org/10.1016/j.heliyon.2024.e24179.

[73] K.O. K'oreje, L. Vergeynst, D. Ombaka, P. De Wispelaere, M. Okoth, H. Van Langenhove, K. Demeestere, Occurrence patterns of pharmaceutical residues in wastewater, surface water and groundwater of Nairobi and Kisumu city, Kenya. *Chemosphere* 149 (2016) 238–244.
https://doi.org/10.1016/j.chemosphere.2016.01.095.

[74] A.C. Faleye, A.A. Adegoke, K. Ramluckan, J. Fick, F. Bux, T.A. Stenström, Concentration and reduction of antibiotic residues in selected wastewater treatment plants and receiving waterbodies in Durban, South Africa. *Sci. Total Environ.* 678 (2019) 10–20.
https://doi.org/10.1016/j.scitotenv.2019.04.410.

[75] S.K. Behera, H.W. Kim, J.-E. Oh, H.-S. Park, Occurrence and removal of antibiotics, hormones and several other pharmaceuticals in wastewater treatment plants of the largest industrial city of Korea. *Sci. Total Environ.* 409 (2011) 4351–4360.
https://doi.org/10.1016/j.scitotenv.2011.07.015.

[76] T. Jiang, W. Wu, M. Ma, Y. Hu, R. Li, Occurrence and distribution of emerging contaminants in wastewater treatment plants: A globally review over the past two decades. *Sci. Total Environ.* 951 (2024) 175664.
https://doi.org/10.1016/j.scitotenv.2024.175664.

[77] H. Sá, M. Michelin, T. Tavares, B. Silva, Current challenges for biological treatment of pharmaceutical-based contaminants with oxidoreductase enzymes: Immobilization processes, real aqueous matrices and hybrid techniques. *Biomolecules* 12 (2022) 1489.

https://doi.org/10.3390/biom12101489.

[78] A.H.A. Khan, R. Barros, Pharmaceuticals in water: Risks to aquatic life and remediation strategies. *Hydrobiology* 2 (2023) 395–409. https://doi.org/10.3390/hydrobiology2020026.

[79] Guidance on wastewater and solid waste management for manufacturing of antibiotics. (2024). https://www.who.int/publications/i/item/9789240097254 (accessed September 23, 2024).

[80] 40 CFR part 439 - Pharmaceutical manufacturing point source category. (n.d.). https://www.ecfr.gov/current/title-40/part-439 (accessed December 4, 2024).

[81] Directive 2000/60/EC of the European Parliament and of the Council of 23 October 2000 establishing a framework for community action in the field of water policy, 2000. http://data.europa.eu/eli/dir/2000/60/oj/eng (accessed September 19, 2024).

[82] Directive 2013/39/EU of the European Parliament and of the Council of 12 August 2013 amending directives 2000/60/EC and 2008/105/EC as regards priority substances in the field of water policy text with EEA relevance, 2013.

[83] European Commission, European Union strategic approach to pharmaceuticals in the environment (COM(2019) 128 final), 2019. https://eur-lex.europa.eu/legal-content/EN/TXT/?uri=CELEX%3A52019DC0128&qid=1605854880622 (accessed September 19, 2024).

[84] E. Malmqvist, D. Fumagalli, C. Munthe, D.G.J. Larsson, Pharmaceutical pollution from human use and the polluter pays principle. *Public Health Ethics*. 16 (2023) 152–164. https://doi.org/10.1093/phe/phad012.

[85] European Commission, Commission welcomes provisional agreement for more thorough and more cost-effective urban wastewater management. *Press Release*, 2024. https://ec.europa.eu/commission/presscorner/api/files/document/print/en/ip_24_504/IP_24_504_EN.pdf (accessed December 4, 2024).

[86] Government of Spain, Royal Decree No. 1085/2024: Approval of the Water Reuse Regulation. Boletín Oficial del Estado (BOE), October 22, 2024. https://www.boe.es/eli/es/rd/2024/10/22/1085/con

[87] European Parliament and Council, Directive No. 2024/3019 (Revised): Concerning Urban Wastewater Treatment. Official Journal of the European Union (OJ), November 27, 2024. http://data.europa.eu/eli/dir/2024/3019/oj

[88] Presidência da República, Lei nº 12.305, de 2 de agosto de 2010. 2010. http://www.planalto.gov.br/ccivil_03/_Ato2007-2010/2010/Lei/L12305.htm.

[89] Australian guidelines for water recycling: Managing health and environmental risks (phase 1) - resources • SuSanA, 2006. https://www.susana.org/en/knowledge-hub/resources-and-publications/library/details/1533# (accessed September 23, 2024).

[90] Water pollution control law. Ministry of the Environment, Government of Japan, 1970. https://www.env.go.jp/en/laws/water/wlaw/index.html (accessed September 19, 2024).

[91] U.N. Environment, Sanitation and wastewater atlas of Africa | UNEP - UN Environment Programme, 2020. https://www.unep.org/resources/publication/sanitation-and-wastewater-atlas-africa (accessed September 23, 2024).

[92] D.T. Wong, K.W. Perry, F.P. Bymaster, The Discovery of Fluoxetine Hydrochloride (Prozac). *Nat. Rev. Drug. Discov*. 4 (2005) 764–774. https://doi.org/10.1038/nrd1821.

[93] S. Chiavegatto, C.A. Oliveira, M.M. Bernardi, Prenatal exposure of rats to diphenhydramine: Effects on physical development, open field, and gonadal hormone levels in adults. *Neurotoxicol. Teratol.* 19 (1997) 511–516. https://doi.org/10.1016/S0892-0362(97)00045-7.

[94] J.E. Blundell, J.C.G. Halford, Serotonin and appetite regulation: implications for the pharmacological treatment of obesity. *CNS Drugs* 9 (1998) 473–495. https://doi.org/10.2165/00023210-199809060-00005.

[95] E.B. Estrada-Arriaga, J.E. Cortés-Muñoz, A. González-Herrera, C.G. Calderón-Mólgora, M.L. Rivera-Huerta, E. Ramírez-Camperos, L. Montellano-Palacios, S.L. Gelover-Santiago, S. Pérez-Castrejón, L. Cardoso-Vigueros, A. Martín-Domínguez, L. García-Sánchez, Assessment of full-scale biological nutrient removal systems upgraded with physico-chemical processes for the removal of emerging pollutants present in wastewaters from Mexico. *Sci. Total Environ.* 571 (2016) 1172–1182. https://doi.org/10.1016/j.scitotenv.2016.07.118

[96] A.L. Ehrhart, E.F. Granek, PPCPs in coastal wastewater treatment plant effluent and uptake by Pacific oysters (*Crassostrea gigas*): Findings from a laboratory experiment. *Sci. Total Environ.* 900 (2023) 165728. https://doi.org/10.1016/j.scitotenv.2023.165728

[97] J.P. Berninger, B. Du, K.A. Connors, S.A. Eytcheson, M.A. Kolkmeier, K.N. Prosser, T.W. Valenti, C.K. Chambliss, B.W. Brooks, Effects of the antihistamine diphenhydramine on selected aquatic organisms. *Enviro. Toxic. Chem.* 30 (2011) 2065–2072. https://doi.org/10.1002/etc.590.

[98] P.M. Clyde, C.-S. Lee, R.E. Price, A.K. Venkatesan, B.J. Brownawell, Occurrence and removal of PPCPs from on-site wastewater using nitrogen removing biofilters. *Water Res.* 206 (2021) 117743. https://doi.org/10.1016/j.watres.2021.117743.

[99] M. Bayati, T.L. Ho, D.C. Vu, F. Wang, E. Rogers, C. Cuvellier, S. Huebotter, E.C. Inniss, R. Udawatta, S. Jose, C.-H. Lin, Assessing the efficiency of constructed wetlands in removing PPCPs from treated wastewater and mitigating the ecotoxicological impacts. *Int. J. Hyg. Envir. Heal.* 231 (2021) 113664. https://doi.org/10.1016/j.ijheh.2020.113664.

[100] N. Mokhtari, A.R. Solaimany Nazar, M. Farhadian, P. Eskandari, B. Jeon, Silver deposition on titanium oxide thin glass films for efficient visible light-induced photocatalytic removal of diphenhydramine and venlafaxine. *Int. J. Environ. Sci. Technol.* 19 (2022) 12465–12476. https://doi.org/10.1007/s13762-022-04486-0.

[101] N. López-Vinent, A. Cruz-Alcalde, L.E. Romero, M.E. Chávez, P. Marco, J. Giménez, S. Esplugas, Synergies, radiation and kinetics in photo-Fenton

process with UVA-LEDs. *J. Hazard. Mater.* 380 (2019) 120882. https://doi.org/10.1016/j.jhazmat.2019.120882.

[102] N. López, S. Plaza, A. Afkhami, P. Marco, J. Giménez, S. Esplugas, Treatment of Diphenhydramine with different AOPs including photo-Fenton at circumneutral pH. *Chem. Eng. J.* 318 (2017) 112–120. https://doi.org/10.1016/j.cej.2016.05.127.

[103] D.L. Silva-Velasco, L.G. Cervantes-Pérez, A. Sánchez-Mendoza, ACE inhibitors and their interaction with systems and molecules involved in metabolism. *Heliyon* 10 (2024). https://doi.org/10.1016/j.heliyon.2024.e24655.

[104] P. Ruggenenti, N. Mise, R. Pisoni, F. Arnoldi, A. Pezzotta, A. Perna, D. Cattaneo, G. Remuzzi, Diverse Effects of Increasing Lisinopril Doses on Lipid Abnormalities in Chronic Nephropathies. *Circulation* 107 (2003) 586–592. https://doi.org/10.1161/01.CIR.0000047526.08376.80.

[105] B.G. Katzung, S.B. Masters, A.J. Trevor, eds., Basic & clinical pharmacology. 12th ed, McGraw-Hill Medical, New York, 2012.

[106] A. Stankiewicz, J. Giebułtowicz, U. Stankiewicz, P. Wroczyński, G. Nałęcz-Jawecki, Determination of selected cardiovascular active compounds in environmental aquatic samples – Methods and results, a review of global publications from the last 10 years. *Chemosphere* 138 (2015) 642–656. https://doi.org/10.1016/j.chemosphere.2015.07.056.

[107] K. Ivankovic, K. Jambrosic, I. Mikac, D. Kapetanovic, M. Ahel, S. Terzic, Multiclass determination of drug residues in water and fish for bioaccumulation potential assessment. *Talanta.* 264 (2023) 124762. https://doi.org/10.1016/j.talanta.2023.124762.

[108] R. Netshithothole, L.M. Madikizela, Occurrence of selected pharmaceuticals in the east london coastline encompassing major rivers, estuaries, and seawater in the eastern cape province of south africa. *ACS Meas. Sci. Au.* 4 (2024) 283–293. https://doi.org/10.1021/acsmeasuresciau.4c00004.

[109] R. Selvaraj, T. Al Fahdi, B. Al-Wahaibi, S.M.Z. Al-Kindy, K. Al-Nofli, H. Al-Lawati, Nanotechnology: A clean and sustainable technology for the

degradation of pharmaceuticals present in water and wastewater. *Rev. Environ. Health* 31 (2016) 75–78.
https://doi.org/10.1515/reveh-2015-0039.

[110] A. Yazidi, M. Atrous, F. Edi Soetaredjo, L. Sellaoui, S. Ismadji, A. Erto, A. Bonilla-Petriciolet, G. Luiz Dotto, A. Ben Lamine, Adsorption of amoxicillin and tetracycline on activated carbon prepared from durian shell in single and binary systems: Experimental study and modeling analysis. *Chem. Eng. J.* 379 (2020) 122320.
https://doi.org/10.1016/j.cej.2019.122320.

[111] J.O. Ighalo, C.A. Igwegbe, C.O. Aniagor, S.N. Oba, A review of methods for the removal of penicillins from water. *J. Water Process Eng.* 39 (2021) 101886.
https://doi.org/10.1016/j.jwpe.2020.101886.

[112] S. Rodriguez-Mozaz, I. Vaz-Moreira, S. Varela Della Giustina, M. Llorca, D. Barceló, S. Schubert, T.U. Berendonk, I. Michael-Kordatou, D. Fatta-Kassinos, J.L. Martinez, C. Elpers, I. Henriques, T. Jaeger, T. Schwartz, E. Paulshus, K. O'Sullivan, K.M.M. Pärnänen, M. Virta, T.T. Do, F. Walsh, C.M. Manaia, Antibiotic residues in final effluents of European wastewater treatment plants and their impact on the aquatic environment. *Environ. Int.* 140 (2020) 105733.
https://doi.org/10.1016/j.envint.2020.105733.

[113] M. Amarasiri, D. Sano, S. Suzuki, Understanding human health risks caused by antibiotic resistant bacteria (ARB) and antibiotic resistance genes (ARG) in water environments: Current knowledge and questions to be answered. *Crit. Rev. Env. Sci. Tec.* 50 (2020) 2016–2059.
https://doi.org/10.1080/10643389.2019.1692611.

[114] L. Sharma, G. Siedlewicz, K. Pazdro, The toxic effects of antibiotics on freshwater and marine photosynthetic microorganisms: state of the art. *Plants* 10 (2021) 591.
https://doi.org/10.3390/plants10030591.

[115] Y. Jia, Y. Ou, S.K. Khanal, L. Sun, W. Shu, H. Lu, Biochar-based strategies for antibiotics removal: Mechanisms, factors, and application. *ACS EST Eng.* 4 (2024) 1256–1274.
https://doi.org/10.1021/acsestengg.3c00605.

[116] E.K. Putra, R. Pranowo, J. Sunarso, N. Indraswati, S. Ismadji, Performance of activated carbon and bentonite for adsorption of amoxicillin from wastewater: Mechanisms, isotherms and kinetics. *Water Res.* 43 (2009) 2419–2430.
https://doi.org/10.1016/j.watres.2009.02.039.

[117] M. Belhachemi, S. Djelaila, Removal of amoxicillin antibiotic from aqueous solutions by date pits activated carbons. *Environ. Process* 4 (2017) 549–561.
https://doi.org/10.1007/s40710-017-0245-8.

[118] F. Ay, F. Kargi, Advanced oxidation of amoxicillin by Fenton's reagent treatment. *J. Hazard. Mater.* 179 (2010) 622–627.
https://doi.org/10.1016/j.jhazmat.2010.03.048.

[119] S. Yang, X. Liu, S. He, C. Jia, H. Zhong, Amoxicillin degradation in persulfate activation system induced by concrete-based hydrotalcites: Efficiency, mechanism, and degradation pathway. *J. Mol. Liq.* 394 (2024) 123688.
https://doi.org/10.1016/j.molliq.2023.123688.

[120] A.Ž. Gotvajn, U. Rozman, T. Antončič, T. Urbanc, M. Vrabeľ, J. Derco, Fe^{2+} and UV catalytically enhanced ozonation of selected environmentally persistent antibiotics. *Processes* 9 (2021) 521.
https://doi.org/10.3390/pr9030521.

[121] E.S. Elmolla, M. Chaudhuri, Photocatalytic degradation of amoxicillin, ampicillin and cloxacillin antibiotics in aqueous solution using UV/TiO_2 and UV/H_2O_2/TiO_2 photocatalysis. *Desalination* 252 (2010) 46–52.
https://doi.org/10.1016/j.desal.2009.11.003.

[122] D.A. Palacio, Y. Becerra, B.F. Urbano, B.L. Rivas, Antibiotics removal using a chitosan-based polyelectrolyte in conjunction with ultrafiltration membranes. *Chemosphere* 258 (2020) 127416.
https://doi.org/10.1016/j.chemosphere.2020.127416.

[123] A. Moarefian, H.A. Golestani, H. Bahmanpour, Removal of amoxicillin from wastewater by self-made Polyethersulfone membrane using nanofiltration. *J. Environ. Health Sci. Eng.* 12 (2014) 127.
https://doi.org/10.1186/s40201-014-0127-1.

[124] M. Hijosa-Valsero, G. Fink, M.P. Schlüsener, R. Sidrach-Cardona, J.

Martín-Villacorta, T. Ternes, E. Bécares, Removal of antibiotics from urban wastewater by constructed wetland optimization. *Chemosphere* 83 (2011) 713–719.
https://doi.org/10.1016/j.chemosphere.2011.02.004.

[125] C. Zhang, M. Zhou, G. Ren, X. Yu, L. Ma, J. Yang, F. Yu, Heterogeneous electro-Fenton using modified iron–carbon as catalyst for 2,4-dichlorophenol degradation: Influence factors, mechanism and degradation pathway. *Water Res.* 70 (2015) 414–424.
https://doi.org/10.1016/j.watres.2014.12.022.

[126] L. Liu, G. Deng, X. Shi, Adsorption characteristics and mechanism of p-nitrophenol by pine sawdust biochar samples produced at different pyrolysis temperatures. *Sci. Rep.* 10 (2020) 5149.
https://doi.org/10.1038/s41598-020-62059-y.

[127] A.M. Farag, A. Fawzy, M.Y. El-Naggar, K.M. Ghanem, Biodegradation and enhancement of 2,4-dichlorophenol by marine halophilic Bacillus subtilis AAK. *Egypt. J. Aquat. Res.* 47 (2021) 117–123.
https://doi.org/10.1016/j.ejar.2021.04.005.

[128] X. Zhang, F. Wei, S. Wang, Adsorption and catalytic degradation by $CoFe_2O_4$ coated on metal–organic framework for the removal of 4-nitrophenol and 2,4-dichlorophenol. *Sep. Purif. Technol.* 354 (2025) 129458.
https://doi.org/10.1016/j.seppur.2024.129458.

[129] F. Gao, W. Lu, H. Liu, J. Li, L. Chen, Dispersive liquid–liquid microextraction of five chlorophenols in water samples followed by determination using capillary electrophoresis. *Electrophoresis* 39 (2018) 2431–2438.
https://doi.org/10.1002/elps.201800205.

[130] M. Chu, K. Hu, J. Wang, Y. Liu, S. Ali, C. Qin, L. Jing, Synthesis of g-C_3N_4-based photocatalysts with recyclable feature for efficient 2,4-dichlorophenol degradation and mechanisms. *Appl. Catal. B: Environ.* 243 (2019) 57–65.
https://doi.org/10.1016/j.apcatb.2018.10.008.

[131] C. Descorme, Catalytic wastewater treatment: Oxidation and reduction processes. Recent studies on chlorophenols. *Catal. Today.* 297 (2017) 324–

334.
https://doi.org/10.1016/j.cattod.2017.03.039.

[132] Y. Li, Y. Zhang, W. Yang, Y. Lin, The reaction pathway and mechanism of 2,4-dichlorophenol removal by modified fly ash-loaded nZVI/Ni particles. *Environ. Sci. Pollut. Res.* 30 (2023) 77408–77419.
https://doi.org/10.1007/s11356-023-27770-z.

[133] M.M. Moja, A.B. Mapossa, E.M.N. Chirwa, S. Tichapondwa, Photocatalytic degradation of 2,4-dichlorophenol using nanomaterials silver halide catalysts. *Environ. Sci. Pollut. Res.* 31 (2024) 11857–11872.
https://doi.org/10.1007/s11356-024-31921-1.

[134] W. Huang, A. Liu, B. Tang, Y. Fu, J. Zhang, Efficient degradation of 2,4-dichlorophenol in water by sequential electrocatalytic reduction and oxidation with a Pd-MWCNTs/Ni-foam electrode. *Environ. Sci. Pollut. Res.* 30 (2023) 70760–70770.
https://doi.org/10.1007/s11356-023-27464-6.

[135] X. Pan, J. Wei, M. Zou, J. Chen, R. Qu, Z. Wang, Products distribution and contribution of (de)chlorination, hydroxylation and coupling reactions to 2,4-dichlorophenol removal in seven oxidation systems. *Water Res.* 194 (2021) 116916.
https://doi.org/10.1016/j.watres.2021.116916.

[136] P. Sahay, D. Mohite, S. Arya, K. Dalmia, Z. Khan, A. Kumar, Removal of the emergent pollutants (hormones and antibiotics) from wastewater using different kinds of biosorbent—a review. *Emergent Mater.* 6 (2023) 373–404.
https://doi.org/10.1007/s42247-023-00460-9.

[137] Y. Shu, M. Hu, M. Zhou, H. Yin, P. Liu, H. Zhang, H. Zhao, Emerging electrocatalysts for electrochemical advanced oxidation processes (EAOPs): recent progress and perspectives. *Mater. Chem. Front.* 7 (2023) 2528–2553.
https://doi.org/10.1039/D2QM01294D.

[138] Z.-H. Xie, C.-S. He, D.-N. Pei, Y. Dong, S.-R. Yang, Z. Xiong, P. Zhou, Z.-C. Pan, G. Yao, B. Lai, Review of characteristics, generation pathways and detection methods of singlet oxygen generated in advanced oxidation processes (AOPs). *Chem. Eng. J.* 468 (2023) 143778.

https://doi.org/10.1016/j.cej.2023.143778.

[139] M.P. Rayaroth, C.T. Aravindakumar, N.S. Shah, G. Boczkaj, Advanced oxidation processes (AOPs) based wastewater treatment - unexpected nitration side reactions - a serious environmental issue: A review. *Chem. Eng. J.* 430 (2022) 133002.
https://doi.org/10.1016/j.cej.2021.133002.

[140] E. Brillas, I. Sirés, M.A. Oturan, Electro-Fenton process and related electrochemical technologies based on Fenton's reaction chemistry. *Chem. Rev.* 109 (2009) 6570–6631.
https://doi.org/10.1021/cr900136g.

[141] J.L. Wang, L.J. Xu, Advanced oxidation processes for wastewater treatment: Formation of hydroxyl radical and application. *Crit. Rev. Env. Sci. Tec.* 42 (2012) 251–325.
https://doi.org/10.1080/10643389.2010.507698.

[142] R. Yuan, Z. Jiang, Z. Wang, S. Gao, Z. Liu, M. Li, G. Boczkaj, Hierarchical MnO_2 nanoflowers blooming on 3D nickel foam: A novel micro-macro catalyst for peroxymonosulfate activation. *J. Colloid Interf. Sci.* 571 (2020) 142–154.
https://doi.org/10.1016/j.jcis.2020.03.041.

[143] P.N. Karungamye, Methods used for removal of pharmaceuticals from wastewater: A review. *J. Environ. Eng. Sci.* 4 (2020) 412-428.
https://doi.org/10.48422/IMIST.PRSM/ajees-v6i4.23828.

[144] P. Ge, H. Yu, J. Chen, J. Qu, Y. Luo, Photolysis mechanism of sulfonamide moiety in five-membered sulfonamides: A DFT study. *Chemosphere* 197 (2018) 569–575.
https://doi.org/10.1016/j.chemosphere.2018.01.041.

[145] J.J. López-Peñalver, M. Sánchez-Polo, C.V. Gómez-Pacheco, J. Rivera-Utrilla, Photodegradation of tetracyclines in aqueous solution by using UV and UV/H_2O_2 oxidation processes. *J. Chem. Technol. Biot.* 85 (2010) 1325–1333.
https://doi.org/10.1002/jctb.2435.

[146] A. Tufail, W.E. Price, F.I. Hai, A critical review on advanced oxidation processes for the removal of trace organic contaminants: A voyage from individual to integrated processes. *Chemosphere* 260 (2020) 127460.

https://doi.org/10.1016/j.chemosphere.2020.127460.

[147] A.Y. Lin, M. Reinhard, Photodegradation of common environmental pharmaceuticals and estrogens in river water. *Enviro. Toxic. Chem.* 24 (2005) 1303–1309.
https://doi.org/10.1897/04-236R.1.

[148] Y. Guo, Z. Guo, J. Wang, Z. Ye, L. Zhang, J. Niu, Photodegradation of three antidepressants in natural waters: Important roles of dissolved organic matter and nitrate. *Sci. Total Environ.* 802 (2022) 149825.
https://doi.org/10.1016/j.scitotenv.2021.149825.

[149] K. Changanaqui, E. Brillas, H. Alarcón, I. Sirés, $ZnO/TiO_2/Ag_2Se$ nanostructures as photoelectrocatalysts for the degradation of oxytetracycline in water. *Electrochim. Acta* 331 (2020) 135194.
https://doi.org/10.1016/j.electacta.2019.135194.

[150] J. Iqbal, N.S. Shah, Z.U.H. Khan, M. Rizwan, B. Murtaza, F. Jamil, A. Shah, A. Ullah, Y. Nazzal, F. Howari, Visible light driven doped CeO_2 for the treatment of pharmaceuticals in wastewater: A review. *J. Water Process Eng.* 49 (2022) 103130.
https://doi.org/10.1016/j.jwpe.2022.103130.

[151] M. Rohan Khizer, Z. Saddique, M. Imran, A. Javaid, S. Latif, D. Mantzavinos, M. Momotko, G. Boczkaj, Polymer and graphitic carbon nitride based nanohybrids for the photocatalytic degradation of pharmaceuticals in wastewater treatment – A review. *Sep. Purif. Technol.* 350 (2024) 127768.
https://doi.org/10.1016/j.seppur.2024.127768.

[152] N.S. Shah, J. Iqbal, M. Sayed, A.A. Ghfar, J.A. Khan, Z.U.H. Khan, B. Murtaza, G. Boczkaj, F. Jamil, Enhanced solar light photocatalytic performance of Fe-ZnO in the presence of H_2O_2, $S_2O_8^{2-}$, and HSO^{5-} for degradation of chlorpyrifos from agricultural wastes: Toxicities investigation. *Chemosphere* 287 (2022) 132331.
https://doi.org/10.1016/j.chemosphere.2021.132331.

[153] N.S. Shah, J.A. Khan, M. Sayed, Z.U.H. Khan, A.D. Rizwan, N. Muhammad, G. Boczkaj, B. Murtaza, M. Imran, H.M. Khan, G. Zaman, Solar light driven degradation of norfloxacin using as-synthesized Bi^{3+} and Fe^{2+} Co-doped ZnO with the addition of HSO^{5-}: Toxicities and degradation

pathways investigation. *Chem. Eng. J.* 351 (2018) 841–855. https://doi.org/10.1016/j.cej.2018.06.111.

[154] J.A. Khan, C. Han, N.S. Shah, H.M. Khan, M.N. Nadagouda, V. Likodimos, P. Falaras, K. O'Shea, D.D. Dionysiou, Ultraviolet–visible light–sensitive high surface area phosphorous-fluorine–Co-doped TiO_2 nanoparticles for the degradation of atrazine in water. *Environ. Eng. Sci.* 31 (2014) 435–446. https://doi.org/10.1089/ees.2013.0486.

[155] J.A. Khan, M. Sayed, N.S. Shah, S. Khan, A.A. Khan, M. Sultan, A.M. Tighezza, J. Iqbal, G. Boczkaj, Synthesis of N-doped TiO_2 nanoparticles with enhanced photocatalytic activity for 2,4-dichlorophenol degradation and H_2 production. *J. Environ. Chem. Eng.* 11 (2023) 111308. https://doi.org/10.1016/j.jece.2023.111308.

[156] N. Bibi, M. Sayed, N.S. Shah, F. Rehman, A. Naeem, T. Mahmood, S. Hussain, J. Iqbal, I. Gul, S. Gul, M. Bushra, Development of zerovalent iron and titania (Fe^0/TiO_2) composite for oxidative degradation of dichlorophene in aqueous solution: synergistic role of peroxymonosulfate (HSO^{5-}). *Environ. Sci. Pollut. Res.* 29 (2022) 63041–63056. https://doi.org/10.1007/s11356-022-20174-5.

[157] M. Ge, Z. Hu, J. Wei, Q. He, Z. He, Recent advances in persulfate-assisted TiO_2-based photocatalysis for wastewater treatment: Performances, mechanism and perspectives. *J. Alloys Compd.* 888 (2021) 161625. https://doi.org/10.1016/j.jallcom.2021.161625.

[158] C. Jing, W. Yibo, Z. Yaxue, Z. Wenjuan, Z. Rui, W. Zhe, W. Shaopo, Oxidation of ibuprofen in water by UV/O_3 process: Removal, byproducts, and degradation pathways. *J. Water Process Eng.* 53 (2023) 103721. https://doi.org/10.1016/j.jwpe.2023.103721.

[159] D.B. Miklos, C. Remy, M. Jekel, K.G. Linden, J.E. Drewes, U. Hübner, Evaluation of advanced oxidation processes for water and wastewater treatment – A critical review. *Water Res.* 139 (2018) 118–131. https://doi.org/10.1016/j.watres.2018.03.042.

[160] F. Mansouri, K. Chouchene, N. Roche, M. Ksibi, Removal of pharmaceuticals from water by adsorption and advanced oxidation processes: State of the art and trends. *Appl. Sci.* 11 (2021) 6659. https://doi.org/10.3390/app11146659.

[161] J.-A. Park, M. Pineda, M.-L. Peyot, V. Yargeau, Degradation of oxytetracycline and doxycycline by ozonation: Degradation pathways and toxicity assessment. *Sci. Total Environ.* 856 (2023) 159076. https://doi.org/10.1016/j.scitotenv.2022.159076.

[162] J. Martini, C.A. Orge, J.L. Faria, M.F.R. Pereira, O.S.G.P. Soares, Sulfamethoxazole degradation by combination of advanced oxidation processes. *J. Environ. Chem. Eng.* 6 (2018) 4054–4060. https://doi.org/10.1016/j.jece.2018.05.047.

[163] T.H. Ho, C.H. Wu, T.Y. Han, W.J. Syu, Mineralization of sulfonamides from wastewater using ozone-based systems. *Water Sci. Technol.* 84 (2021) 1379–1388. https://doi.org/10.2166/wst.2021.325.

[164] C.V. Rekhate, J.K. Srivastava, Recent advances in ozone-based advanced oxidation processes for treatment of wastewater- A review. *Chem. Eng. J. Adv.* 3 (2020) 100031. https://doi.org/10.1016/j.ceja.2020.100031.

[165] P. Liu, Z. Wu, A.V. Abramova, G. Cravotto, Sonochemical processes for the degradation of antibiotics in aqueous solutions: A review. *Ultrason. Sonochem.* 74 (2021) 105566. https://doi.org/10.1016/j.ultsonch.2021.105566.

[166] Q.-P. Isariebel, J.-L. Carine, J.-H. Ulises-Javier, W. Anne-Marie, D. Henri, Sonolysis of levodopa and paracetamol in aqueous solutions. *Ultrason. Sonochem.* 16 (2009) 610–616. https://doi.org/10.1016/j.ultsonch.2008.11.008.

[167] E.A. Serna-Galvis, J. Silva-Agredo, A.L. Giraldo-Aguirre, R.A. Torres-Palma, Sonochemical degradation of the pharmaceutical fluoxetine: Effect of parameters, organic and inorganic additives and combination with a biological system. *Sci. Total Environ.* 524–525 (2015) 354–360. https://doi.org/10.1016/j.scitotenv.2015.04.053.

[168] C. Lu, K. Deng, C. Hu, L. Lyu, Dual-reaction-center catalytic process continues Fenton's story. *Front. Environ. Sci. Eng.* 14 (2020) 82. https://doi.org/10.1007/s11783-020-1261-x.

[169] J.P. Ribeiro, M.I. Nunes, Recent trends and developments in Fenton processes for industrial wastewater treatment – A critical review. *Environ.*

Res. 197 (2021) 110957.
https://doi.org/10.1016/j.envres.2021.110957.

[170] A. Babuponnusami, K. Muthukumar, A review on Fenton and improvements to the Fenton process for wastewater treatment. *J. Environ. Chem. Eng.* 2 (2014) 557–572.
https://doi.org/10.1016/j.jece.2013.10.011.

[171] F. Ghanbari, M. Moradi, Application of peroxymonosulfate and its activation methods for degradation of environmental organic pollutants: Review. *Chem. Eng. J.* 310 (2017) 41–62.
https://doi.org/10.1016/j.cej.2016.10.064.

[172] Y. Liu, X. He, Y. Fu, D.D. Dionysiou, Kinetics and mechanism investigation on the destruction of oxytetracycline by UV-254 nm activation of persulfate. *J. Hazard. Mater.* 305 (2016) 229–239.
https://doi.org/10.1016/j.jhazmat.2015.11.043.

[173] X. Wang, A. Wang, J. Ma, Visible-light-driven photocatalytic removal of antibiotics by newly designed C_3N_4@$MnFe_2O_4$-graphene nanocomposites *J. Hazard. Mater.* 336 (2017) 81–92.
https://doi.org/10.1016/j.jhazmat.2017.04.012.

[174] M. Kohantorabi, G. Moussavi, S. Giannakis, A review of the innovations in metal- and carbon-based catalysts explored for heterogeneous peroxymonosulfate (PMS) activation, with focus on radical vs. non-radical degradation pathways of organic contaminants. *Chem. Eng. J.* 411 (2021) 127957.
https://doi.org/10.1016/j.cej.2020.127957.

[175] Y. Ji, Y. Shi, W. Dong, X. Wen, M. Jiang, J. Lu, Thermo-activated persulfate oxidation system for tetracycline antibiotics degradation in aqueous solution. *Chem. Eng. J.* 298 (2016) 225–233.
https://doi.org/10.1016/j.cej.2016.04.028.

[176] J. Wang, S. Wang, Activation of persulfate (PS) and peroxymonosulfate (PMS) and application for the degradation of emerging contaminants. *Chem. Eng. J.* 334 (2018) 1502–1517.
https://doi.org/10.1016/j.cej.2017.11.059.

[177] J. Yan, M. Lei, L. Zhu, M.N. Anjum, J. Zou, H. Tang, Degradation of sulfamonomethoxine with Fe_3O_4 magnetic nanoparticles as heterogeneous

activator of persulfate. *J. Hazard. Mater.* 186 (2011) 1398–1404. https://doi.org/10.1016/j.jhazmat.2010.12.017.

[178] M. Kohantorabi, G. Moussavi, S. Giannakis, A review of the innovations in metal- and carbon-based catalysts explored for heterogeneous peroxymonosulfate (PMS) activation, with focus on radical vs. non-radical degradation pathways of organic contaminants. *Chem. Eng. J.* 411 (2021) 127957. https://doi.org/10.1016/j.cej.2020.127957.

[179] J. Liang, X. Xu, W. Qamar Zaman, X. Hu, L. Zhao, H. Qiu, X. Cao, Different mechanisms between biochar and activated carbon for the persulfate catalytic degradation of sulfamethoxazole: Roles of radicals in solution or solid phase. *Chem. Eng. J.* 375 (2019) 121908. https://doi.org/10.1016/j.cej.2019.121908.

[180] Y. Zhang, Y.-G. Zhao, Y. Hu, M. Gao, L. Guo, J. Ji, Insight in degradation of tetracycline in mariculture wastewater by ultraviolet/persulfate advanced oxidation process. *Environ. Res.* 212 (2022) 113324. https://doi.org/10.1016/j.envres.2022.113324.

[181] S. Nasseri, A.H. Mahvi, M. Seyedsalehi, K. Yaghmaeian, R. Nabizadeh, M. Alimohammadi, G.H. Safari, Degradation kinetics of tetracycline in aqueous solutions using peroxydisulfate activated by ultrasound irradiation: Effect of radical scavenger and water matrix. *J. Mol. Liq.* 241 (2017) 704–714. https://doi.org/10.1016/j.molliq.2017.05.137.

[182] Z. Guo, Y. Zhang, H. Jia, J. Guo, X. Meng, J. Wang, Electrochemical methods for landfill leachate treatment: A review on electrocoagulation and electrooxidation. *Sci. Total Environ.* 806 (2022) 150529. https://doi.org/10.1016/j.scitotenv.2021.150529.

[183] A. Fernandes, M.J. Pacheco, L. Ciríaco, A. Lopes, Review on the electrochemical processes for the treatment of sanitary landfill leachates: Present and future. *Appl. Catal. B: Environ.* 176–177 (2015) 183–200. https://doi.org/10.1016/j.apcatb.2015.03.052.

[184] S.O. Ganiyu, C.A. Martínez-Huitle, Nature, mechanisms and reactivity of electrogenerated reactive species at thin-film boron-doped diamond (BDD) electrodes during electrochemical wastewater treatment.

ChemElectroChem 6 (2019) 2379–2392.
https://doi.org/10.1002/celc.201900159.

[185] C.A. Martínez-Huitle, M. Panizza, Electrochemical oxidation of organic pollutants for wastewater treatment. *Curr. Opin. Electroche.* 11 (2018) 62–71.
https://doi.org/10.1016/j.coelec.2018.07.010.

[186] C.A. Martínez-Huitle, M.A. Rodrigo, I. Sirés, O. Scialdone, Single and coupled electrochemical processes and reactors for the abatement of organic water pollutants: A critical review. *Chem. Rev.* 115 (2015) 13362–13407.
https://doi.org/10.1021/acs.chemrev.5b00361.

[187] J. Vidal, C. Huiliñir, R. Santander, J. Silva-Agredo, R.A. Torres-Palma, R. Salazar, Degradation of ampicillin antibiotic by electrochemical processes: evaluation of antimicrobial activity of treated water. *Environ. Sci. Pollut. Res.* 26 (2019) 4404–4414.
https://doi.org/10.1007/s11356-018-2234-5.

[188] Y. Xia, Q. Dai, Electrochemical degradation of antibiotic levofloxacin by PbO_2 electrode: Kinetics, energy demands and reaction pathways. *Chemosphere* 205 (2018) 215–222.
https://doi.org/10.1016/j.chemosphere.2018.04.103.

[189] J. Mora-Gomez, E. Ortega, S. Mestre, V. Pérez-Herranz, M. García-Gabaldón, Electrochemical degradation of norfloxacin using BDD and new Sb-doped SnO_2 ceramic anodes in an electrochemical reactor in the presence and absence of a cation-exchange membrane. *Sep. Purif. Technol.* 208 (2019) 68–75.
https://doi.org/10.1016/j.seppur.2018.05.017.

[190] A. Fabiańska, A. Białk-Bielińska, P. Stepnowski, S. Stolte, E.M. Siedlecka, Electrochemical degradation of sulfonamides at BDD electrode: Kinetics, reaction pathway and eco-toxicity evaluation. *J. Hazard. Mater.* 280 (2014) 579–587.
https://doi.org/10.1016/j.jhazmat.2014.08.050.

[191] I. Sirés, E. Brillas, M.A. Oturan, M.A. Rodrigo, M. Panizza, Electrochemical advanced oxidation processes: Today and tomorrow. A review. *Environ. Sci. Pollut. Res.* 21 (2014) 8336–8367.

https://doi.org/10.1007/s11356-014-2783-1.

[192] E. Brillas, I. Sirés, M.A. Oturan, Electro-Fenton process and related electrochemical technologies based on Fenton's reaction chemistry, *Chem. Rev.* 109 (2009) 6570–6631. https://doi.org/10.1021/cr900136g.

[193] F. Deng, H. Olvera-Vargas, M. Zhou, S. Qiu, I. Sirés, E. Brillas, Critical review on the mechanisms of Fe^{2+} regeneration in the electro-Fenton process: Fundamentals and boosting strategies. *Chem. Rev.* 123 (2023) 4635–4662. https://doi.org/10.1021/acs.chemrev.2c00684.

[194] L. Clarizia, D. Russo, I. Di Somma, R. Marotta, R. Andreozzi, Homogeneous photo-Fenton processes at near neutral pH: A review. *Appl. Catal. B: Environ.* 209 (2017) 358–371. https://doi.org/10.1016/j.apcatb.2017.03.011.

[195] M.D. Engelmann, R.T. Bobier, T. Hiatt, I.F. Cheng, Variability of the Fenton reaction characteristics of the EDTA, DTPA, and citrate complexes of iron. *Biometals.* 16 (2003) 519–527. https://doi.org/10.1023/A:1023480617038.

[196] Z. Ye, E. Brillas, F. Centellas, P.L. Cabot, I. Sirés, Expanding the application of photoelectro-Fenton treatment to urban wastewater using the Fe(III)-EDDS complex. *Water Res.* 169 (2020) 115219. https://doi.org/10.1016/j.watres.2019.115219.

[197] Z. Ye, E. Brillas, F. Centellas, P.L. Cabot, I. Sirés, Electro-Fenton process at mild pH using Fe(III)-EDDS as soluble catalyst and carbon felt as cathode. *Appl. Catal. B: Environ.* 257 (2019) 117907. https://doi.org/10.1016/j.apcatb.2019.117907.

[198] B.M. Souza, M.W.C. Dezotti, R.A.R. Boaventura, V.J.P. Vilar, Intensification of a solar photo-Fenton reaction at near neutral pH with ferrioxalate complexes: A case study on diclofenac removal from aqueous solutions. *Chem. Eng. J.* 256 (2014) 448–457. https://doi.org/10.1016/j.cej.2014.06.111.

[199] I. Sirés, E. Brillas, Upgrading and expanding the electro-Fenton and related processes. *Curr. Opin. Electroche.* 27 (2021) 100686. https://doi.org/10.1016/j.coelec.2020.100686.

[200] V. Poza-Nogueiras, E. Rosales, M. Pazos, M.Á. Sanromán, Current advances and trends in electro-Fenton process using heterogeneous catalysts – A review. *Chemosphere* 201 (2018) 399–416. https://doi.org/10.1016/j.chemosphere.2018.03.002.

[201] B. Bouzayani, M.Á. Sanromán, Polymer-supported heterogeneous Fenton catalysts for the environmental remediation of wastewater. *Molecules* 29 (2024) 2188. https://doi.org/10.3390/molecules29102188.

[202] Z. Wang, M. Liu, F. Xiao, G. Postole, H. Zhao, G. Zhao, Recent advances and trends of heterogeneous electro-Fenton process for wastewater treatment-review. *Chinese Chem. Lett.* 33 (2022) 653–662. https://doi.org/10.1016/j.cclet.2021.07.044.

[203] Z. Wan, J. Wang, Degradation of sulfamethazine using Fe_3O_4-Mn_3O_4/reduced graphene oxide hybrid as Fenton-like catalyst. *J. Hazard. Mater.* 324 (2017) 653–664. https://doi.org/10.1016/j.jhazmat.2016.11.039.

[204] A.L.-T. Pham, F.M. Doyle, D.L. Sedlak, Inhibitory effect of dissolved silica on H_2O_2 decomposition by iron(III) and manganese(IV) oxides: implications for H_2O_2 -based in situ chemical oxidation. *Environ. Sci. Technol.* 46 (2012) 1055–1062. https://doi.org/10.1021/es203612d.

[205] J. Ma, W. Ma, W. Song, C. Chen, Y. Tang, J. Zhao, Y. Huang, Y. Xu, L. Zang, Fenton degradation of organic pollutants in the presence of low-molecular-weight organic acids: Cooperative effect of quinone and visible light. *Environ. Sci. Technol.* 40 (2006) 618–624. https://doi.org/10.1021/es051657t.

[206] Z. Ye, W. Zhang, S. Lanzalaco, L. Zhao, I. Sirés, P. Xia, J. Zhai, Q. He, Ultra-uniform MIL-88B(Fe)/Fe_3S_4 hybrids engineered by partial sulfidation to boost catalysis in electro-Fenton treatment of micropollutants: Experimental and mechanistic insights. *Chem. Eng. J.* 455 (2023) 140757. https://doi.org/10.1016/j.cej.2022.140757.

[207] R. Yang, Y. Zhou, Y. Xing, D. Li, D. Jiang, M. Chen, W. Shi, S. Yuan, Synergistic coupling of CoFe-LDH arrays with NiFe-LDH nanosheet for highly efficient overall water splitting in alkaline media. *Appl. Catal. B:*

Environ. 253 (2019) 131–139.
https://doi.org/10.1016/j.apcatb.2019.04.054.

[208] C. Gregor, M. Hermanek, D. Jancik, J. Pechousek, J. Filip, J. Hrbac, R. Zboril, The effect of surface area and crystal structure on the catalytic efficiency of iron(III) oxide nanoparticles in hydrogen peroxide decomposition. *Eur. J. Inorg. Chem.* 2010 (2010) 2343–2351.
https://doi.org/10.1002/ejic.200901066.

[209] L. Labiadh, M.A. Oturan, M. Panizza, N.B. Hamadi, S. Ammar, Complete removal of AHPS synthetic dye from water using new electro-Fenton oxidation catalyzed by natural pyrite as heterogeneous catalyst. *J. Hazard. Mater.* 297 (2015) 34–41.
https://doi.org/10.1016/j.jhazmat.2015.04.062.

[210] N. Barhoumi, H. Olvera-Vargas, N. Oturan, D. Huguenot, A. Gadri, S. Ammar, E. Brillas, M.A. Oturan, Kinetics of oxidative degradation/mineralization pathways of the antibiotic tetracycline by the novel heterogeneous electro-Fenton process with solid catalyst chalcopyrite. *Appl. Catal. B: Environ.* 209 (2017) 637–647.
https://doi.org/10.1016/j.apcatb.2017.03.034.

[211] A. Khataee, S. Sajjadi, A. Hasanzadeh, B. Vahid, S.W. Joo, One-step preparation of nanostructured martite catalyst and graphite electrode by glow discharge plasma for heterogeneous electro-Fenton like process. *J. Environ. Manage.* 199 (2017) 31–45.
https://doi.org/10.1016/j.jenvman.2017.04.095.

[212] Y. Tian, M. Zhou, Y. Pan, J. Cai, G. Ren, Pre-magnetized Fe^0 as heterogeneous electro-Fenton catalyst for the degradation of p-nitrophenol at neutral pH. *Chemosphere* 240 (2020) 124962.
https://doi.org/10.1016/j.chemosphere.2019.124962.

[213] Y. Tian, W. Fu, Q. Wang, Y. Tang, M. Zhou, High electron transfer rate and efficiency on Fe^0 modified by sulfidation and pre-magnetization for carbamazepine degradation by heterogeneous electro-Fenton in wide pH ranges. *Chem. Eng. J.* 427 (2022) 131694.
https://doi.org/10.1016/j.cej.2021.131694.

[214] S. Campos, R. Salazar, N. Arancibia-Miranda, M.A. Rubio, M. Aranda, A. García, P. Sepúlveda, L.C. Espinoza, Nafcillin degradation by

heterogeneous electro-Fenton process using Fe, Cu and Fe/Cu nanoparticles. *Chemosphere* 247 (2020) 125813. https://doi.org/10.1016/j.chemosphere.2020.125813.

[215] L. Chu, Z. Sun, G. Fang, L. Cang, X. Wang, D. Zhou, J. Gao, Highly effective removal of BPA with boron-doped graphene shell wrapped FeS_2 nanoparticles in electro-Fenton process: Performance and mechanism. *Sep. Purif. Technol.* 267 (2021) 118680. https://doi.org/10.1016/j.seppur.2021.118680.

[216] T. Hu, F. Deng, H. Feng, J. Zhang, B. Shao, C. Feng, W. Tang, L. Tang, Fe/Co bimetallic nanoparticles embedded in MOF-derived nitrogen-doped porous carbon rods as efficient heterogeneous electro-Fenton catalysts for degradation of organic pollutants. *Appl. Mater. Today.* 24 (2021) 101161. https://doi.org/10.1016/j.apmt.2021.101161.

[217] X. Du, W. Fu, P. Su, J. Cai, M. Zhou, Internal-micro-electrolysis-enhanced heterogeneous electro-Fenton process catalyzed by Fe/Fe_3C@PC core–shell hybrid for sulfamethazine degradation. *Chem. Eng. J.* 398 (2020) 125681. https://doi.org/10.1016/j.cej.2020.125681.

[218] X. Du, W. Fu, P. Su, Q. Zhang, M. Zhou, S-doped MIL-53 as efficient heterogeneous electro-Fenton catalyst for degradation of sulfamethazine at circumneutral pH. *J. Hazard. Mater.* 424 (2022) 127674. https://doi.org/10.1016/j.jhazmat.2021.127674.

[219] Z. Ye, J.A. Padilla, E. Xuriguera, E. Brillas, I. Sirés, Magnetic MIL(Fe)-type MOF-derived N-doped nano-ZVI@C rods as heterogeneous catalyst for the electro-Fenton degradation of gemfibrozil in a complex aqueous matrix. *Appl. Catal. B: Environ.* 266 (2020) 118604. https://doi.org/10.1016/j.apcatb.2020.118604.

[220] J. Guo, G. Song, Y. Zheng, J. Gu, S. Li, M. Zhou, Single iron atoms embedded in MOF-derived nitrogen-doped carbon as an efficient heterogeneous electro-Fenton catalyst for degradation of carbamazepine over a wide pH. *Sep. Purif. Technol.* 302 (2022) 122141. https://doi.org/10.1016/j.seppur.2022.122141.

[221] A.D. Bokare, W. Choi, Review of iron-free Fenton-like systems for activating H_2O_2 in advanced oxidation processes. *J. Hazard. Mater.* 275

(2014) 121–135.
https://doi.org/10.1016/j.jhazmat.2014.04.054.

[222] Y. Yang, Y. Liu, X. Fang, W. Miao, X. Chen, J. Sun, B.-J. Ni, S. Mao, Heterogeneous electro-Fenton catalysis with HKUST-1-derived Cu@C decorated in 3D graphene network. *Chemosphere* 243 (2020) 125423.
https://doi.org/10.1016/j.chemosphere.2019.125423.

[223] Y. Liu, J. Wang, Multivalent metal catalysts in Fenton/Fenton-like oxidation system: A critical review. *Chem. Eng. J.* 466 (2023) 143147.
https://doi.org/10.1016/j.cej.2023.143147.

[224] T. Hu, L. Tang, H. Feng, J. Zhang, X. Li, Y. Zuo, Z. Lu, W. Tang, Metal-organic frameworks (MOFs) and their derivatives as emerging catalysts for electro-Fenton process in water purification. *Coordin. Chem. Rev.* 451 (2022) 214277.
https://doi.org/10.1016/j.ccr.2021.214277.

[225] J. Guo, G. Song, X. Zhang, M. Zhou, Transition metal catalysts in the heterogeneous electro-Fenton process for organic wastewater treatment: a review. *Environ. Sci.: Water Res. Technol.* 9 (2023) 2429–2445.
https://doi.org/10.1039/D3EW00302G.

[226] T. Hu, F. Deng, H. Feng, J. Zhang, B. Shao, C. Feng, W. Tang, L. Tang, Fe/Co bimetallic nanoparticles embedded in MOF-derived nitrogen-doped porous carbon rods as efficient heterogeneous electro-Fenton catalysts for degradation of organic pollutants. *Appl. Mater. Today.* 24 (2021) 101161.
https://doi.org/10.1016/j.apmt.2021.101161.

[227] X. Du, W. Fu, P. Su, Q. Zhang, M. Zhou, FeMo@porous carbon derived from MIL-53(Fe)@MoO_3 as excellent heterogeneous electro-Fenton catalyst: Co-catalysis of Mo. *J. Environ. Sci.* 127 (2023) 652–666.
https://doi.org/10.1016/j.jes.2022.06.031.

[228] J. Hu, S. Wang, J. Yu, W. Nie, J. Sun, S. Wang, Duet Fe_3C and FeN_x sites for H_2O_2 generation and activation toward enhanced electro-Fenton performance in wastewater treatment. *Environ. Sci. Technol.* 55 (2021) 1260–1269.
https://doi.org/10.1021/acs.est.0c06825.

[229] M. Mazzucato, A. Facchin, M. Parnigotto, C. Durante, New and revised aspects of the electrochemical synthesis of hydrogen peroxide: From model

electrocatalytic systems to scalable materials. *ACS Catal.* 14 (2024) 6369–6403.
https://doi.org/10.1021/acscatal.4c01011.

[230] H.S. Wroblowa, Yen-Chi-Pan, G. Razumney, Electroreduction of oxygen. *J. Electroanal. Chem. Interfacial Electrochem.* 69 (1976) 195–201.
https://doi.org/10.1016/S0022-0728(76)80250-1.

[231] K. Wang, J. Huang, H. Chen, Y. Wang, S. Song, Recent advances in electrochemical 2e oxygen reduction reaction for on-site hydrogen peroxide production and beyond. *Chem. Commun.* 56 (2020) 12109–12121.
https://doi.org/10.1039/D0CC05156J.

[232] Y. Pang, H. Xie, Y. Sun, M.-M. Titirici, G.-L. Chai, Electrochemical oxygen reduction for H_2O_2 production: catalysts, pH effects and mechanisms. *J. Mater. Chem.* A 8 (2020) 24996–25016.
https://doi.org/10.1039/D0TA09122G.

[233] N. Wang, S. Ma, P. Zuo, J. Duan, B. Hou, Recent progress of electrochemical production of hydrogen peroxide by two-electron oxygen reduction reaction. *Adv. Sci.* 8 (2021) 2100076.
https://doi.org/10.1002/advs.202100076.

[234] X. Guo, S. Lin, J. Gu, S. Zhang, Z. Chen, S. Huang, Simultaneously achieving high activity and selectivity toward two-electron O_2 electroreduction: The power of single-atom catalysts. *ACS Catal.* 9 (2019) 11042–11054.
https://doi.org/10.1021/acscatal.9b02778.

[235] Y. Tian, D. Deng, L. Xu, M. Li, H. Chen, Z. Wu, S. Zhang, Strategies for sustainable production of hydrogen peroxide via oxygen reduction reaction: from catalyst design to device setup. *Nano-Micro Lett.* 15 (2023) 122.
https://doi.org/10.1007/s40820-023-01067-9.

[236] A.M. Gómez-Marín, A. Boronat, J.M. Feliu, Electrocatalytic oxidation and reduction of H_2O_2 on Au single crystals. *Russ. J. Electrochem.* 53 (2017) 1029–1041.
https://doi.org/10.1134/S1023193517090063.

[237] R. Svensson, H. Grönbeck, Site communication in direct formation of H_2O_2 over single-atom Pd@Au nanoparticles. *J. Am. Chem. Soc.* 145 (2023) 11579–11588.

https://doi.org/10.1021/jacs.3c00656.

[238] J.S. Jirkovský, M. Halasa, D.J. Schiffrin, Kinetics of electrocatalytic reduction of oxygen and hydrogen peroxide on dispersed gold nanoparticles. *Phys. Chem. Chem. Phys.* 12 (2010) 8042. https://doi.org/10.1039/C002416C.

[239] J.S. Jirkovský, I. Panas, E. Ahlberg, M. Halasa, S. Romani, D.J. Schiffrin, Single atom hot-spots at Au–Pd nanoalloys for electrocatalytic H_2O_2 production. *J. Am. Chem. Soc.* 133 (2011) 19432–19441. https://doi.org/10.1021/ja206477z.

[240] S. Siahrostami, A. Verdaguer-Casadevall, M. Karamad, D. Deiana, P. Malacrida, B. Wickman, M. Escudero-Escribano, E.A. Paoli, R. Frydendal, T.W. Hansen, I. Chorkendorff, I.E.L. Stephens, J. Rossmeisl, Enabling direct H_2O_2 production through rational electrocatalyst design. *Nature Mater.* 12 (2013) 1137–1143. https://doi.org/10.1038/nmat3795.

[241] A. Verdaguer-Casadevall, D. Deiana, M. Karamad, S. Siahrostami, P. Malacrida, T.W. Hansen, J. Rossmeisl, I. Chorkendorff, I.E.L. Stephens, Trends in the electrochemical synthesis of H_2O_2 : Enhancing activity and selectivity by electrocatalytic site engineering. *Nano Lett.* 14 (2014) 1603–1608. https://doi.org/10.1021/nl500037x.

[242] F. Sun, C. Deng, S. Tian, Q. Tang, Oxygen electrocatalysis by $[Au_{25}(SR)_{18}]$: charge, doping, and ligand removal effect. *ACS Catal.* 11 (2021) 7957–7969. https://doi.org/10.1021/acscatal.1c01030.

[243] C.H. Choi, H.C. Kwon, S. Yook, H. Shin, H. Kim, M. Choi, Hydrogen peroxide synthesis via enhanced two-electron oxygen reduction pathway on carbon-coated Pt surface. *J. Phys. Chem. C.* 118 (2014) 30063–30070. https://doi.org/10.1021/jp5113894.

[244] S. Siahrostami, A. Verdaguer-Casadevall, M. Karamad, D. Deiana, P. Malacrida, B. Wickman, M. Escudero-Escribano, E.A. Paoli, R. Frydendal, T.W. Hansen, I. Chorkendorff, I.E.L. Stephens, J. Rossmeisl, Enabling direct H_2O_2 production through rational electrocatalyst design. *Nat. Mater.* 12 (2013) 1137–1143.

https://doi.org/10.1038/nmat3795.

[245] L. Osmieri, A.H.A. Monteverde Videla, P. Ocón, S. Specchia, Kinetics of oxygen electroreduction on Me–N–C (Me = Fe, Co, Cu) catalysts in acidic medium: Insights on the effect of the transition metal. *J. Phys. Chem. C.* 121 (2017) 17796–17817.
https://doi.org/10.1021/acs.jpcc.7b02455.

[246] E. Jung, H. Shin, B.-H. Lee, V. Efremov, S. Lee, H.S. Lee, J. Kim, W. Hooch Antink, S. Park, K.-S. Lee, S.-P. Cho, J.S. Yoo, Y.-E. Sung, T. Hyeon, Atomic-level tuning of Co–N–C catalyst for high-performance electrochemical H_2O_2 production. *Nat. Mater.* 19 (2020) 436–442.
https://doi.org/10.1038/s41563-019-0571-5.

[247] Q. Zhang, X. Tan, N.M. Bedford, Z. Han, L. Thomsen, S. Smith, R. Amal, X. Lu, Direct insights into the role of epoxy groups on cobalt sites for acidic H_2O_2 production. *Nat. Commun.* 11 (2020) 4181.
https://doi.org/10.1038/s41467-020-17782-5.

[248] P.T. Smith, Y. Kim, B.P. Benke, K. Kim, C.J. Chang, Supramolecular tuning enables selective oxygen reduction catalyzed by cobalt porphyrins for direct electrosynthesis of hydrogen peroxide. *Angew. Chem. Int. Ed.* 59 (2020) 4902–4907.
https://doi.org/10.1002/anie.201916131.

[249] Y. Wang, R. Shi, L. Shang, G.I.N. Waterhouse, J. Zhao, Q. Zhang, L. Gu, T. Zhang, High-efficiency oxygen reduction to hydrogen peroxide catalyzed by nickel single-atom catalysts with tetradentate N_2O_2 coordination in a three-phase flow cell. *Angew. Chem. Int. Ed.* 132 (2020) 13157–13162.
https://doi.org/10.1002/ange.202004841.

[250] X. Zhang, Y. Xia, C. Xia, H. Wang, Insights into practical-scale electrochemical H_2O_2 synthesis. *Trends Chem.* 2 (2020) 942–953.
https://doi.org/10.1016/j.trechm.2020.07.007.

[251] T. Ricciardulli, S. Gorthy, J.S. Adams, C. Thompson, A.M. Karim, M. Neurock, D.W. Flaherty, Effect of Pd coordination and isolation on the catalytic reduction of O_2 to H_2O_2 over PdAu bimetallic nanoparticles. *J. Am. Chem. Soc.* 143 (2021) 5445–5464.
https://doi.org/10.1021/jacs.1c00539.

[252] R.T. Hannagan, G. Giannakakis, M. Flytzani-Stephanopoulos, E.C.H. Sykes, Single-atom alloy catalysis. *Chem. Rev.* 120 (2020) 12044–12088. https://doi.org/10.1021/acs.chemrev.0c00078.

[253] Y. Ji, Y. Liu, B.-W. Zhang, Z. Xu, X. Qi, X. Xu, L. Ren, Y. Du, J. Zhong, S.X. Dou, Morphology engineering of atomic layer defect-rich $CoSe_2$ nanosheets for highly selective electrosynthesis of hydrogen peroxide. *J. Mater. Chem.* A 9 (2021) 21340–21346. https://doi.org/10.1039/D1TA05731F.

[254] K. Dong, J. Liang, Y. Wang, Y. Ren, Z. Xu, H. Zhou, L. Li, Q. Liu, Y. Luo, T. Li, A.M. Asiri, Q. Li, D. Ma, X. Sun, Plasma-induced defective TiO_2-x with oxygen vacancies: A high-active and robust bifunctional catalyst toward H_2O_2 electrosynthesis. *Chem Catalysis.* 1 (2021) 1437–1448. https://doi.org/10.1016/j.checat.2021.10.011.

[255] L. Yan, X. Cheng, Y. Wang, Z. Wang, L. Zheng, Y. Yan, Y. Lu, S. Sun, W. Qiu, G. Chen, Exsolved Co_3O_4 with tunable oxygen vacancies for electrocatalytic H_2O_2 production. *Mater. Today Energy* 24 (2022) 100931. https://doi.org/10.1016/j.mtener.2021.100931.

[256] P. Xia, C. Wang, Q. He, Z. Ye, I. Sirés, MOF-derived single-atom catalysts: The next frontier in advanced oxidation for water treatment. *Chem. Eng. J.* 452 (2023) 139446. https://doi.org/10.1016/j.cej.2022.139446.

[257] K. Li, Y. Sun, Z. Zhao, T. Zhu, Encapsulation of Co nanoparticles with single-atomic Co sites into nitrogen-doped carbon for electrosynthesis of hydrogen peroxide. *Phys. Chem. Chem. Phys.* 26 (2024) 3044–3050. https://doi.org/10.1039/D3CP05492F.

[258] G. Wei, X. Liu, Z. Zhao, C. Men, Y. Ding, S. Gao, Constructing ultrahigh-loading unsymmetrically coordinated Zn-N_3O single-atom sites with efficient oxygen reduction for H_2O_2 production. *Chem. Eng. J.* 455 (2023) 140721. https://doi.org/10.1016/j.cej.2022.140721.

[259] B. Shao, Y. Zhu, Y. Du, D. Yang, S. Gai, F. He, P. Yang, Mn-doped single atom nanozyme composited Au for enhancing enzymatic and photothermal therapy. *J. Colloid Interface Sci.* 628 (2022) 419–434. https://doi.org/10.1016/j.jcis.2022.08.053.

[260] S. Shin, J. Kim, S. Park, H.-E. Kim, Y.-E. Sung, H. Lee, Changes in the oxidation state of Pt single-atom catalysts upon removal of chloride ligands and their effect for electrochemical reactions. *Chem. Commun.* 55 (2019) 6389–6392.
https://doi.org/10.1039/C9CC01593K.

[261] J.H. Kim, D. Shin, J. Lee, D.S. Baek, T.J. Shin, Y.-T. Kim, H.Y. Jeong, J.H. Kwak, H. Kim, S.H. Joo, A general strategy to atomically dispersed precious metal catalysts for unravelling their catalytic trends for oxygen reduction reaction. *ACS Nano.* 14 (2020) 1990–2001.
https://doi.org/10.1021/acsnano.9b08494.

[262] S.K. Sahoo, Y. Ye, S. Lee, J. Park, H. Lee, J. Lee, J.W. Han, Rational design of TiC-supported single-atom electrocatalysts for hydrogen evolution and selective oxygen reduction reactions. *ACS Energy Lett.* 4 (2019) 126–132.
https://doi.org/10.1021/acsenergylett.8b01942.

[263] M. Ledendecker, E. Pizzutilo, G. Malta, G.V. Fortunato, K.J.J. Mayrhofer, G.J. Hutchings, S.J. Freakley, Isolated Pd sites as selective catalysts for electrochemical and direct hydrogen peroxide synthesis. *ACS Catal.* 10 (2020) 5928–5938.
https://doi.org/10.1021/acscatal.0c01305.

[264] R. Shen, W. Chen, Q. Peng, S. Lu, L. Zheng, X. Cao, Y. Wang, W. Zhu, J. Zhang, Z. Zhuang, C. Chen, D. Wang, Y. Li, High-concentration single atomic Pt sites on hollow CuSx for selective O_2 reduction to H_2O_2 in acid solution. *Chem.* 5 (2019) 2099–2110.
https://doi.org/10.1016/j.chempr.2019.04.024.

[265] S.J. Tauster, Strong metal-support interactions. *Acc. Chem. Res.* 20 (1987) 389–394.
https://doi.org/10.1021/ar00143a001.

[266] X. Yu, J. Deng, Y. Liu, L. Jing, Z. Hou, W. Pei, H. Dai, Single-atom catalysts: Preparation and applications in environmental catalysis. *Catalyst* 12 (2022) 1239.
https://doi.org/10.3390/catal12101239.

[267] J. Xue, Y. Zhao, L. Yu, S. Guo, Preparation of nitrogen-doped carbon pyrolyzed from ZIF-8 and its performance in electrocatalytic oxygen reduction to hydrogen peroxide. *J. Electroanal. Chem.* 960 (2024) 118202.

https://doi.org/10.1016/j.jelechem.2024.118202.

[268] B.S. Rawah, M. Albloushi, W. Li, Highly efficient electrochemical synthesis of hydrogen peroxide (H_2O_2) enabled by amino acid glycine-derived metal-free nitrogen-doped ordered mesoporous carbon. *ACS Sustainable Chem. Eng.* 10 (2022) 5453–5462.
https://doi.org/10.1021/acssuschemeng.1c08285.

[269] T.-N. Pham-Truong, T. Petenzi, C. Ranjan, H. Randriamahazaka, J. Ghilane, Microwave assisted synthesis of carbon dots in ionic liquid as metal free catalyst for highly selective production of hydrogen peroxide. *Carbon* 130 (2018) 544–552.
https://doi.org/10.1016/j.carbon.2018.01.070.

[270] Y. Zhang, Y. Pang, D. Xia, G. Chai, Regulable pyrrolic-N-doped carbon materials as an efficient electrocatalyst for selective O_2 reduction to H_2O_2. *New J. Chem.* 46 (2022) 14510–14516.
https://doi.org/10.1039/D2NJ02393H.

[271] P. Su, M. Zhou, X. Lu, W. Yang, G. Ren, J. Cai, Electrochemical catalytic mechanism of N-doped graphene for enhanced H_2O_2 yield and in-situ degradation of organic pollutant. *Appl. Catal. B: Environ.* 245 (2019) 583–595.
https://doi.org/10.1016/j.apcatb.2018.12.075.

[272] Y. Pang, K. Wang, H. Xie, Y. Sun, M.-M. Titirici, G.-L. Chai, Mesoporous carbon hollow spheres as efficient electrocatalysts for oxygen reduction to hydrogen peroxide in neutral electrolytes. *ACS Catal.* 10 (2020) 7434–7442.
https://doi.org/10.1021/acscatal.0c00584.

[273] L. Liang, M. Zhou, X. Lu, P. Su, J. Sun, High-efficiency electrogeneration of hydrogen peroxide from oxygen reduction by carbon xerogels derived from glucose. *Electrochim. Acta* 320 (2019) 134569.
https://doi.org/10.1016/j.electacta.2019.134569.

[274] K. Zhao, Y. Su, X. Quan, Y. Liu, S. Chen, H. Yu, Enhanced H_2O_2 production by selective electrochemical reduction of O_2 on fluorine-doped hierarchically porous carbon. *J. Catal.* 357 (2018) 118–126.
https://doi.org/10.1016/j.jcat.2017.11.008.

[275] W. Wang, X. Lu, P. Su, Y. Li, J. Cai, Q. Zhang, M. Zhou, O. Arotiba,

Enhancement of hydrogen peroxide production by electrochemical reduction of oxygen on carbon nanotubes modified with fluorine. *Chemosphere* 259 (2020) 127423.
https://doi.org/10.1016/j.chemosphere.2020.127423.

[276] Y. Xia, X. Zhao, C. Xia, Z.-Y. Wu, P. Zhu, J.Y. Kim, X. Bai, G. Gao, Y. Hu, J. Zhong, Y. Liu, H. Wang, Highly active and selective oxygen reduction to H_2O_2 on boron-doped carbon for high production rates. *Nat. Commun.* 12 (2021) 4225.
https://doi.org/10.1038/s41467-021-24329-9.

[277] Y. Chang, J. Li, J. Ma, Y. Liu, R. Xing, Y. Wang, G. Zhang, Oxygenated boron-doped carbon via polymer dehalogenation as an electrocatalyst for high-efficiency O_2 reduction to H_2O_2. *Sci. China Mater.* 65 (2022) 1276–1284.
https://doi.org/10.1007/s40843-021-1891-2.

[278] G. Chen, J. Liu, Q. Li, P. Guan, X. Yu, L. Xing, J. Zhang, R. Che, A direct H_2O_2 production based on hollow porous carbon sphere-sulfur nanocrystal composites by confinement effect as oxygen reduction electrocatalysts. *Nano Res.* 12 (2019) 2614–2622.
https://doi.org/10.1007/s12274-019-2496-3.

[279] J. Gao, X. Chu, H. Lu, H. Wang, X. Li, Z. Yin, X. Tan, Efficient carbon-based electrocatalyst derived from biomass for hydrogen peroxide generation. *Mater. Today Commun.* 26 (2021) 102051.
https://doi.org/10.1016/j.mtcomm.2021.102051.

[280] A.D. Pozzo, L.D. Palma, C. Merli, E. Petrucci, An experimental comparison of a graphite electrode and a gas diffusion electrode for the cathodic production of hydrogen peroxide. *J. Appl. Electrochem.* 35 (2005) 413–419.
https://doi.org/10.1007/s10800-005-0800-2.

[281] P. Petsi, K. Plakas, Z. Frontistis, I. Sirés, A critical assessment of the effect of carbon-based cathode properties on the in situ electrogeneration of H_2O_2. *Electrochim. Acta* 470 (2023) 143337.
https://doi.org/10.1016/j.electacta.2023.143337.

[282] G. Zhang, F. Yang, M. Gao, X. Fang, L. Liu, Electro-Fenton degradation of azo dye using polypyrrole/anthraquinonedisulphonate composite film

modified graphite cathode in acidic aqueous solutions. *Electrochim. Acta* 53 (2008) 5155–5161.
https://doi.org/10.1016/j.electacta.2008.01.008.

[283] H. Rabl, D. Wielend, S. Tekoglu, H. Seelajaroen, H. Neugebauer, N. Heitzmann, D.H. Apaydin, M.C. Scharber, N.S. Sariciftci, Are polyaniline and polypyrrole electrocatalysts for oxygen (O_2) reduction to hydrogen peroxide (H_2O_2)? *ACS Appl. Energy Mater* 3 (2020) 10611–10618.
https://doi.org/10.1021/acsaem.0c01663.

[284] A.R. Khataee, M. Safarpour, M. Zarei, S. Aber, Electrochemical generation of H_2O_2 using immobilized carbon nanotubes on graphite electrode fed with air: Investigation of operational parameters. *J. Electroanal. Chem.* 659 (2011) 63–68.
https://doi.org/10.1016/j.jelechem.2011.05.002.

[285] W. Lai, G. Xie, R. Dai, C. Kuang, Y. Xu, Z. Pan, L. Zheng, L. Yu, S. Ye, Z. Chen, H. Li, Kinetics and mechanisms of oxytetracycline degradation in an electro-Fenton system with a modified graphite felt cathode. *J. Environ. Manage.* 257 (2020) 109968.
https://doi.org/10.1016/j.jenvman.2019.109968.

[286] B. Jiang, Y. Wang, D. Wang, M. Yao, C. Fan, J. Dai, Modifying graphite felt cathode by HNO_3 or KOH to improve the degradation efficiency of electro-Fenton for landfill leachate. *Water Sci. Technol.* 80 (2019) 2412–2421.
https://doi.org/10.2166/wst.2020.072.

[287] T.X.H. Le, C. Charmette, M. Bechelany, M. Cretin, Facile preparation of porous carbon cathode to eliminate paracetamol in aqueous medium using electro-Fenton system. *Electrochim. Acta* 188 (2016) 378–384.
https://doi.org/10.1016/j.electacta.2015.12.005.

[288] M.R. Haider, W.-L. Jiang, J.-L. Han, H.M.A. Sharif, Y.-C. Ding, H.-Y. Cheng, A.-J. Wang, In-situ electrode fabrication from polyaniline derived N-doped carbon nanofibers for metal-free electro-Fenton degradation of organic contaminants. *Appl. Catal. B: Environ.* 256 (2019) 117774.
https://doi.org/10.1016/j.apcatb.2019.117774.

[289] F. Yu, M. Zhou, X. Yu, Cost-effective electro-Fenton using modified graphite felt that dramatically enhanced on H_2O_2 electro-generation

without external aeration. *Electrochim. Acta* 163 (2015) 182–189. https://doi.org/10.1016/j.electacta.2015.02.166.

[290] E. Mousset, Z.T. Ko, M. Syafiq, Z. Wang, O. Lefebvre, Electrocatalytic activity enhancement of a graphene ink-coated carbon cloth cathode for oxidative treatment. *Electrochim. Acta* 222 (2016) 1628–1641. https://doi.org/10.1016/j.electacta.2016.11.151.

[291] J.M. Friedrich, C. Ponce-de-León, G.W. Reade, F.C. Walsh, Reticulated vitreous carbon as an electrode material. *J. Electroanal. Chem.* 561 (2004) 203–217. https://doi.org/10.1016/j.jelechem.2003.07.019.

[292] F.C. Walsh, L.F. Arenas, C. Ponce De León, G.W. Reade, I. Whyte, B.G. Mellor, The continued development of reticulated vitreous carbon as a versatile electrode material: Structure, properties and applications, *Electrochim. Acta* 215 (2016) 566–591. https://doi.org/10.1016/j.electacta.2016.08.103.

[293] E. Petrucci, A. Da Pozzo, L. Di Palma, On the ability to electrogenerate hydrogen peroxide and to regenerate ferrous ions of three selected carbon-based cathodes for electro-Fenton processes. *Chem. Eng. J.* 283 (2016) 750–758. https://doi.org/10.1016/j.cej.2015.08.030.

[294] Y. Jin, Y. Shi, R. Chen, X. Chen, X. Zheng, Y. Liu, Electrochemical disinfection using a modified reticulated vitreous carbon cathode for drinking water treatment. *Chemosphere* 215 (2019) 380–387. https://doi.org/10.1016/j.chemosphere.2018.10.057.

[295] L. Tao, Y. Yang, F. Yu, Highly efficient electro-generation of H_2O_2 by a nitrogen porous carbon modified carbonaceous cathode during the oxygen reduction reaction. *New J. Chem.* 44 (2020) 15942–15950. https://doi.org/10.1039/D0NJ02360D.

[296] E. Brillas, E. Mur, R. Sauleda, L. Sànchez, J. Peral, X. Domènech, J. Casado, Aniline mineralization by AOP's: anodic oxidation, photocatalysis, electro-Fenton and photoelectro-Fenton processes. *Appl. Catal. B: Environ.* 16 (1998) 31–42. https://doi.org/10.1016/S0926-3373(97)00059-3.

[297] E. Isarain-Chávez, C. Arias, P.L. Cabot, F. Centellas, R.M. Rodríguez, J.A.

Garrido, E. Brillas, Mineralization of the drug β-blocker atenolol by electro-Fenton and photoelectro-Fenton using an air-diffusion cathode for H_2O_2 electrogeneration combined with a carbon-felt cathode for Fe^{2+} regeneration. *Appl. Catal. B: Environ.* 96 (2010) 361–369. https://doi.org/10.1016/j.apcatb.2010.02.033.

[298] Q. Zhao, J. An, S. Wang, Y. Qiao, C. Liao, C. Wang, X. Wang, N. Li, Superhydrophobic air-breathing cathode for efficient hydrogen peroxide generation through two-electron pathway oxygen reduction reaction. *ACS Appl. Mater. Interfaces* 11 (2019) 35410–35419. https://doi.org/10.1021/acsami.9b09942.

[299] Q. Zhang, M. Zhou, G. Ren, Y. Li, Y. Li, X. Du, Highly efficient electrosynthesis of hydrogen peroxide on a superhydrophobic three-phase interface by natural air diffusion. *Nat. Commun.* 11 (2020) 1731. https://doi.org/10.1038/s41467-020-15597-y.

[300] Q. Zhao, N. Li, C. Liao, L. Tian, J. An, X. Wang, The UV/H_2O_2 process based on H_2O_2 in-situ generation for water disinfection. *J. Hazard. Mater.* 2 (2021) 100020. https://doi.org/10.1016/j.hazl.2021.100020.

[301] Q. Zhang, M. Zhou, G. Ren, Y. Li, Y. Li, X. Du, Highly efficient electrosynthesis of hydrogen peroxide on a superhydrophobic three-phase interface by natural air diffusion. *Nat. Commun.* 11 (2020) 1731. https://doi.org/10.1038/s41467-020-15597-y.

[302] H. Dong, B. Dong, L. Sun, Z. Chi, M. Wang, H. Yu, Electro-UV/H_2O_2 system with RGO-modified air diffusion cathode for simulative antibiotic-manufacture effluent treatment. *Chem. Eng. J.* 390 (2020) 124650. https://doi.org/10.1016/j.cej.2020.124650.

[303] W. Zhou, X. Meng, L. Rajic, Y. Xue, S. Chen, Y. Ding, K. Kou, Y. Wang, J. Gao, Y. Qin, A.N. Alshawabkeh, "Floating" cathode for efficient H_2O_2 electrogeneration applied to degradation of ibuprofen as a model pollutant. *Electrochem. Commun.* 96 (2018) 37–41. https://doi.org/10.1016/j.elecom.2018.09.007.

[304] Q. Zhang, M. Zhou, Z. Lang, X. Du, J. Cai, L. Han, Dual strategies to enhance mineralization efficiency in innovative electrochemical advanced oxidation processes using natural air diffusion electrode: Improving both

H_2O_2 production and utilization efficiency. *Chem. Eng. J.* 413 (2021) 127564.
https://doi.org/10.1016/j.cej.2020.127564.

[305] S.A. Mauger, J.R. Pfeilsticker, M. Wang, S. Medina, A.C. Yang-Neyerlin, K.C. Neyerlin, C. Stetson, S. Pylypenko, M. Ulsh, Fabrication of high-performance gas-diffusion-electrode based membrane-electrode assemblies. *J. Power Sources* 450 (2020) 227581.
https://doi.org/10.1016/j.jpowsour.2019.227581.

[306] M. Muñoz-Morales, A. Ramírez, A. Cañizares, J. Llanos, C. Ania, Evaluating key properties of carbon materials as cathodes for the electrogeneration of hydrogen peroxide. *Carbon* 210 (2023) 118082.
https://doi.org/10.1016/j.carbon.2023.118082.

[307] Q. Zhao, J. An, S. Wang, Y. Qiao, C. Liao, C. Wang, X. Wang, N. Li, Superhydrophobic air-breathing cathode for efficient hydrogen peroxide generation through two-electron pathway oxygen reduction reaction. *ACS Appl. Mater. Interfaces* 11 (2019) 35410–35419.
https://doi.org/10.1021/acsami.9b09942.

[308] H. Rabiee, L. Ge, X. Zhang, S. Hu, M. Li, Z. Yuan, Gas diffusion electrodes (GDEs) for electrochemical reduction of carbon dioxide, carbon monoxide, and dinitrogen to value-added products: a review. *Energy Environ. Sci.* 14 (2021) 1959–2008.
https://doi.org/10.1039/D0EE03756G.

[309] W. Zhou, L. Xie, Y. Wang, Y. Ding, X. Meng, F. Sun, J. Gao, G. Zhao, Oxygen-rich hierarchical activated coke-based gas diffusion electrode enables highly efficient H_2O_2 synthesis via O_2 electroreduction. *Sep. Purif. Technol.* 307 (2023) 122740.
https://doi.org/10.1016/j.seppur.2022.122740.

[310] L. Han, W. Zhou, C. Xiang, High-rate electrochemical reduction of carbon monoxide to ethylene using Cu-nanoparticle-based gas diffusion electrodes. *ACS Energy Lett.* 3 (2018) 855–860.
https://doi.org/10.1021/acsenergylett.8b00164.

[311] L.-C. Weng, A.T. Bell, A.Z. Weber, Modeling gas-diffusion electrodes for CO_2 reduction. *Phys. Chem. Chem. Phys.* 20 (2018) 16973–16984.
https://doi.org/10.1039/C8CP01319E.

[312] I. Ali, K. Van Eyck, S. De Laet, R. Dewil, Recent advances in carbonaceous catalyst design for the in situ production of H_2O_2 via two-electron oxygen reduction. *Chemosphere* 308 (2022) 136127. https://doi.org/10.1016/j.chemosphere.2022.136127.

[313] J. Xie, J. Jing, J. Gu, J. Guo, Y. Li, M. Zhou, Hydrogen peroxide generation from gas diffusion electrode for electrochemical degradation of organic pollutants in water: A review. *J. Environ. Chem. Eng.* 10 (2022) 107882. https://doi.org/10.1016/j.jece.2022.107882.

[314] J. Zhao, X. Li, Z. Liu, The effect of ink dilution and evaporation on the microstructures of catalyst layers in polymer electrolyte membrane fuel cells. *Int. J. Energy. Res.* 43 (2019) er.4671. https://doi.org/10.1002/er.4671.

[315] G. Daniel, Y. Zhang, S. Lanzalaco, F. Brombin, T. Kosmala, G. Granozzi, A. Wang, E. Brillas, I. Sirés, C. Durante, Chitosan-derived nitrogen-doped carbon electrocatalyst for a sustainable upgrade of oxygen reduction to hydrogen peroxide in UV-assisted electro-Fenton water treatment. *ACS Sustainable Chem. Eng.* 8 (2020) 14425–14440. https://doi.org/10.1021/acssuschemeng.0c04294.

[316] Z. Ye, D.R.V. Guelfi, G. Álvarez, F. Alcaide, E. Brillas, I. Sirés, Enhanced electrocatalytic production of H_2O_2 at Co-based air-diffusion cathodes for the photoelectro-Fenton treatment of bronopol. *Appl. Catal. B: Environ.* 247 (2019) 191–199. https://doi.org/10.1016/j.apcatb.2019.01.029.

[317] G. Álvarez, F. Alcaide, P.L. Cabot, M.J. Lázaro, E. Pastor, J. Solla-Gullón, Electrochemical performance of low temperature PEMFC with surface tailored carbon nanofibers as catalyst support. *Int. J. Hydrogen Energy*. 37 (2012) 393–404. https://doi.org/10.1016/j.ijhydene.2011.09.055.

[318] Y.C. Tan, K.B. Lee, H. Song, J. Oh, Modulating local CO_2 concentration as a general strategy for enhancing C−C coupling in CO_2 electroreduction. *Joule* 4 (2020) 1104–1120. https://doi.org/10.1016/j.joule.2020.03.013.

[319] D. Kopljar, A. Inan, P. Vindayer, N. Wagner, E. Klemm, Electrochemical reduction of CO_2 to formate at high current density using gas diffusion

electrodes. *J. Appl. Electrochem.* 44 (2014) 1107–1116.
https://doi.org/10.1007/s10800-014-0731-x.

[320] Q. Wang, H. Dong, H. Yu, Fabrication of a novel tin gas diffusion electrode for electrochemical reduction of carbon dioxide to formic acid. *RSC Adv.* 4 (2014) 59970–59976.
https://doi.org/10.1039/C4RA10775F.

[321] B.A. Rosen, A. Salehi-Khojin, M.R. Thorson, W. Zhu, D.T. Whipple, P.J.A. Kenis, R.I. Masel, Ionic liquid–mediated selective conversion of CO_2 to CO at low overpotentials. *Science* 334 (2011) 643–644.
https://doi.org/10.1126/science.1209786.

[322] W. Luc, X. Fu, J. Shi, J.-J. Lv, M. Jouny, B.H. Ko, Y. Xu, Q. Tu, X. Hu, J. Wu, Q. Yue, Y. Liu, F. Jiao, Y. Kang, Two-dimensional copper nanosheets for electrochemical reduction of carbon monoxide to acetate. *Nat. Catal.* 2 (2019) 423–430.
https://doi.org/10.1038/s41929-019-0269-8.

[323] F. Gao, S. Hu, X. Zhang, Y. Zheng, H. Wang, Z. Niu, P. Yang, R. Bao, T. Ma, Z. Dang, Y. Guan, X. Zheng, X. Zheng, J. Zhu, M. Gao, S. Yu, High-curvature transition-metal chalcogenide nanostructures with a pronounced proximity effect enable fast and selective CO_2 electroreduction. *Angew. Chem. Int. Edit.* 132 (2020) 8784–8790.
https://doi.org/10.1002/ange.201912348.

[324] Y. Zhang, L. Li, S. Guo, X. Zhang, F. Li, A.M. Bond, J. Zhang, Two-dimensional electrocatalysts for efficient reduction of carbon dioxide. *ChemSusChem* 13 (2020) 59–77.
https://doi.org/10.1002/cssc.201901794.

[325] G. Wang, D. Huang, M. Cheng, S. Chen, G. Zhang, L. Lei, Y. Chen, L. Du, R. Li, Y. Liu, Metal-organic frameworks template-directed growth of layered double hydroxides: A fantastic conversion of functional materials. *Coord. Chem. Rev.* 460 (2022) 214467.
https://doi.org/10.1016/j.ccr.2022.214467.

[326] O.M. Yaghi, M. O'Keeffe, N.W. Ockwig, H.K. Chae, M. Eddaoudi, J. Kim, Reticular synthesis and the design of new materials. *Nature* 423 (2003) 705–714.
https://doi.org/10.1038/nature01650.

[327] D. Zacher, O. Shekhah, C. Wöll, R.A. Fischer, Thin films of metal–organic frameworks. *Chem. Soc. Rev.* 38 (2009) 1418. https://doi.org/10.1039/B805038B.

[328] P.Z. Moghadam, A. Li, S.B. Wiggin, A. Tao, A.G.P. Maloney, P.A. Wood, S.C. Ward, D. Fairen-Jimenez, Development of a cambridge structural database subset: A collection of metal–organic frameworks for past, present, and future. *Chem. Mater.* 29 (2017) 2618–2625. https://doi.org/10.1021/acs.chemmater.7b00441.

[329] K. Chen, C. Wu, Transformation of metal-organic frameworks into stable organic frameworks with inherited skeletons and catalytic properties. *Angew. Chem. Int. Ed.* 58 (2019) 8119–8123. https://doi.org/10.1002/anie.201903367.

[330] K. Chen, J. Ling, C. Wu, In situ generation and stabilization of accessible Cu/Cu_2O heterojunctions inside organic frameworks for highly efficient catalysis. *Angew. Chem. Int. Ed.* 59 (2020) 1925–1931. https://doi.org/10.1002/anie.201913811.

[331] X. Cao, C. Tan, M. Sindoro, H. Zhang, Hybrid micro-/nano-structures derived from metal–organic frameworks: preparation and applications in energy storage and conversion. *Chem. Soc. Rev.* 46 (2017) 2660–2677. https://doi.org/10.1039/C6CS00426A.

[332] K. Gao, J. Li, M. Chen, Y. Jin, Y. Ma, G. Ou, Z. Wei, ZIF-67 derived magnetic nanoporous carbon coated by poly(m-phenylenediamine) for hexavalent chromium removal. *Sep. Purif. Technol.* 277 (2021) 119436. https://doi.org/10.1016/j.seppur.2021.119436.

[333] Z. Ye, J.A. Padilla, E. Xuriguera, J.L. Beltran, F. Alcaide, E. Brillas, I. Sirés, A highly stable metal–organic framework-engineered FeS_2/C nanocatalyst for heterogeneous electro-Fenton treatment: Validation in wastewater at mild pH. *Environ. Sci. Technol.* 54 (2020) 4664–4674. https://doi.org/10.1021/acs.est.9b07604.

[334] J. Wang, H. Li, P. Xia, H. Liu, X. Chen, Z. Ye, Q. He, I. Sirés, Confined MOF pyrolysis within mesoporous SiO_2 core–shell nanoreactors for superior activity and stability of electro-Fenton catalysts. *Chem. Eng. J.* 483 (2024) 149230. https://doi.org/10.1016/j.cej.2024.149230.

[335] A. Bigham, N. Islami, A. Khosravi, A. Zarepour, S. Iravani, A. Zarrabi, MOFs and MOF-Based composites as next-generation materials for wound healing and dressings. *Small* 20 (2024) 2311903. https://doi.org/10.1002/smll.202311903.

[336] Y. Qi, F. Luo, Y. Che, J. Zheng, Hydrothermal synthesis of metal−organic frameworks based on aromatic polycarboxylate and flexible bis(imidazole) ligands. *Cryst. Growth Des.* 8 (2008) 606–611. https://doi.org/10.1021/cg700758c.

[337] H. Li, M. Eddaoudi, M. O'Keeffe, O.M. Yaghi, Design and synthesis of an exceptionally stable and highly porous metal-organic framework. *Nature* 402 (1999) 276–279. https://doi.org/10.1038/46248.

[338] S.S.-Y. Chui, S.M.-F. Lo, J.P.H. Charmant, A.G. Orpen, I.D. Williams, A chemically functionalizable nanoporous naterial $[Cu_3\ (TMA)_2(H_2O)_3]_n$. *Science* 283 (1999) 1148–1150. https://doi.org/10.1126/science.283.5405.1148.

[339] H.F. Barton, A.K. Davis, D.T. Lee, G.N. Parsons, Solvothermal synthesis of MIL-96 and UiO-66-NH_2 on atomic layer deposited metal oxide coatings on fiber mats. *J. Vis. Exp.* (2018) 57734. https://doi.org/10.3791/57734.

[340] N. Campagnol, T. Van Assche, T. Boudewijns, J. Denayer, K. Binnemans, D. De Vos, J. Fransaer, High pressure, high temperature electrochemical synthesis of metal–organic frameworks: films of MIL-100 (Fe) and HKUST-1 in different morphologies. *J. Mater. Chem. A* 1 (2013) 5827. https://doi.org/10.1039/C3TA10419B.

[341] C. Dey, T. Kundu, B.P. Biswal, A. Mallick, R. Banerjee, Crystalline metal-organic frameworks (MOFs): synthesis, structure and function. *Acta. Crystallogr. B.* 70 (2014) 3–10. https://doi.org/10.1107/S2052520613029557.

[342] H. Zhang, Z. Ma, G. Liu, L. Shi, J. Tang, H. Pang, K. Wu, T. Takei, J. Zhang, Y. Yamauchi, J. Ye, Highly active nonprecious metal hydrogen evolution electrocatalyst: ultrafine molybdenum carbide nanoparticles embedded into a 3D nitrogen-implanted carbon matrix. *NPG Asia Mater.* 8 (2016) e293–e293.

https://doi.org/10.1038/am.2016.102.

[343] P. Xia, Z. Ye, L. Zhao, Q. Xue, S. Lanzalaco, Q. He, X. Qi, I. Sirés, Tailoring single-atom FeN_4 moieties as a robust heterogeneous catalyst for high-performance electro-Fenton treatment of organic pollutants. *Appl. Catal. B: Environ.* 322 (2023) 122116. https://doi.org/10.1016/j.apcatb.2022.122116.

[344] F. Zheng, Y. Yang, Q. Chen, High lithium anodic performance of highly nitrogen-doped porous carbon prepared from a metal-organic framework. *Nat. Commun.* 5 (2014) 5261. https://doi.org/10.1038/ncomms6261.

[345] M. Ren, J. Lei, J. Zhang, B.I. Yakobson, J.M. Tour, Tuning metal elements in open frameworks for efficient oxygen evolution and oxygen reduction reaction catalysts. *ACS Appl. Mater. Interface* 13 (2021) 42715–42723. https://doi.org/10.1021/acsami.1c10441.

[346] X. Sun, Y. Li, H. Su, X. Zhang, Y. Xu, W. Zhou, M. Liu, W. Cheng, Q. Liu, Dissecting π-conjugated covalent-coupling over conductive MOFs toward efficient two-electron oxygen reduction. *Appl. Catal. B: Environ.* 317 (2022) 121706. https://doi.org/10.1016/j.apcatb.2022.121706.

[347] M. Liu, Y. Li, Z. Qi, H. Su, W. Cheng, W. Zhou, H. Zhang, X. Sun, X. Zhang, Y. Xu, Y. Jiang, Q. Liu, S. Wei, Self-nanocavity-confined halogen anions boosting the high selectivity of the two-electron oxygen reduction pathway over Ni-based MOFs. *J. Phys. Chem. Lett.* 12 (2021) 8706–8712. https://doi.org/10.1021/acs.jpclett.1c01981.

[348] R.D. Ross, H. Sheng, Y. Ding, A.N. Janes, D. Feng, J.R. Schmidt, C.U. Segre, S. Jin, Operando elucidation of electrocatalytic and redox mechanisms on a 2D metal organic framework catalyst for efficient electrosynthesis of hydrogen peroxide in neutral media. *J. Am. Chem. Soc.* 144 (2022) 15845–15854. https://doi.org/10.1021/jacs.2c06810.

[349] K. Dong, J. Liang, Y. Wang, L. Zhang, Z. Xu, S. Sun, Y. Luo, T. Li, Q. Liu, N. Li, B. Tang, A.A. Alshehri, Q. Li, D. Ma, X. Sun, Conductive two-dimensional magnesium metal–organic frameworks for high-efficiency O_2 electroreduction to H_2O_2. *ACS Catal.* 12 (2022) 6092–6099.

https://doi.org/10.1021/acscatal.2c00819.

[350] B. Liu, K. Vellingiri, S.-H. Jo, P. Kumar, Y.S. Ok, K.-H. Kim, Recent advances in controlled modification of the size and morphology of metal-organic frameworks. *Nano Res.* 11 (2018) 4441–4467. https://doi.org/10.1007/s12274-018-2039-3.

[351] G. Wang, Z. Bao, S. Zhang, Y. Li, X. Peng, L. Ding, Y. Li, X. Li, J. Wang, Self-growing MZIF8/GDE bonding by N–Zn–O boosts electrochemical oxygen reduction to H_2O_2. *ACS Sustainable Chem. Eng.* 11 (2023) 1610–1617. https://doi.org/10.1021/acssuschemeng.2c07479.

[352] Y. Liu, X. Quan, X. Fan, H. Wang, S. Chen, High-yield electrosynthesis of hydrogen peroxide from oxygen reduction by hierarchically porous carbon. *Angew. Chem. Int. Ed.* 54 (2015) 6837–6841. https://doi.org/10.1002/anie.201502396.

[353] K. Zhao, Y. Su, X. Quan, Y. Liu, S. Chen, H. Yu, Enhanced H_2O_2 production by selective electrochemical reduction of O_2 on fluorine-doped hierarchically porous carbon. *J. Catal.* 357 (2018) 118–126. https://doi.org/10.1016/j.jcat.2017.11.008.

[354] Y. Jia, Z. Xue, J. Yang, Q. Liu, J. Xian, Y. Zhong, Y. Sun, X. Zhang, Q. Liu, D. Yao, G. Li, Tailoring the electronic structure of an atomically dispersed zinc electrocatalyst: Coordination environment regulation for high selectivity oxygen reduction. *Angew. Chem. Int. Ed.* 61 (2022) e202110838. https://doi.org/10.1002/anie.202110838.

[355] N. Wang, X. Zhao, R. Zhang, S. Yu, Z.H. Levell, C. Wang, S. Ma, P. Zou, L. Han, J. Qin, L. Ma, Y. Liu, H.L. Xin, Highly selective oxygen reduction to hydrogen peroxide on a carbon-supported single-atom Pd electrocatalyst. *ACS Catal.* 12 (2022) 4156–4164. https://doi.org/10.1021/acscatal.1c05633.

[356] C. Zhang, R. Lu, C. Liu, J. Lu, Y. Zou, L. Yuan, J. Wang, G. Wang, Y. Zhao, C. Yu, Trimetallic Sulfide Hollow Superstructures with Engineered d-Band Center for Oxygen Reduction to Hydrogen Peroxide in Alkaline Solution. *Adv. Sci.* 9, 12 (2022) 2104768. https://doi.org/10.1002/advs.202104768.

[357] M. Wang, N. Zhang, Y. Feng, Z. Hu, Q. Shao, X. Huang, Partially

pyrolyzed binary metal–organic framework nanosheets for efficient electrochemical hydrogen peroxide synthesis. *Angew. Chem. Int. Ed.* 59 (2020) 14373–14377.
https://doi.org/10.1002/anie.202006422.

[358] Y. He, Z. Wang, H. Wang, Z. Wang, G. Zeng, P. Xu, D. Huang, M. Chen, B. Song, H. Qin, Y. Zhao, Metal-organic framework-derived nanomaterials in environment related fields: Fundamentals, properties and applications. *Coord. Chem. Rev.* 429 (2021) 213618.
https://doi.org/10.1016/j.ccr.2020.213618.

[359] S. Cheng, C. Shen, H. Zheng, F. Liu, A. Li, OCNTs encapsulating Fe-Co PBA as efficient chainmail-like electrocatalyst for enhanced heterogeneous electro-Fenton reaction. *Appl. Catal. B: Environ.* 269 (2020) 118785.
https://doi.org/10.1016/j.apcatb.2020.118785.

[360] Z. Ye, G.E.M. Schukraft, A. L'Hermitte, Y. Xiong, E. Brillas, C. Petit, I. Sirés, Mechanism and stability of an Fe-based 2D MOF during the photoelectro-Fenton treatment of organic micropollutants under UVA and visible light irradiation. *Water Res.* 184 (2020) 115986.
https://doi.org/10.1016/j.watres.2020.115986.

[361] M. Hao, M. Qiu, H. Yang, B. Hu, X. Wang, Recent advances on preparation and environmental applications of MOF-derived carbons in catalysis. *Sci. Total Environ.* 760 (2021) 143333.
https://doi.org/10.1016/j.scitotenv.2020.143333.

[362] J. Tang, J. Wang, Fenton-like degradation of sulfamethoxazole using Fe-based magnetic nanoparticles embedded into mesoporous carbon hybrid as an efficient catalyst. *Chem. Eng. J.* 351 (2018) 1085–1094.
https://doi.org/10.1016/j.cej.2018.06.169.

[363] Y. Wang, Y. Xue, C. Zhang, Copper embedded in nitrogen-doped carbon matrix derived from metal-organic frameworks for boosting peroxide production and electro-Fenton catalysis. *Electrochim. Acta* 368 (2021) 137643.
https://doi.org/10.1016/j.electacta.2020.137643.

[364] K. Liu, M. Yu, H. Wang, J. Wang, W. Liu, M.R. Hoffmann, Multiphase porous electrochemical catalysts derived from iron-based metal–organic framework compounds. *Environ. Sci. Technol.* 53 (2019) 6474–6482.

https://doi.org/10.1021/acs.est.9b01143.

[365] A. Fdez-Sanromán, M. Pazos, M.A. Sanromán, E. Rosales, Heterogeneous electro-Fenton system using Fe-MOF as catalyst and electrocatalyst for degradation of pharmaceuticals. *Chemosphere* 340 (2023) 139942. https://doi.org/10.1016/j.chemosphere.2023.139942.

[366] X. Du, W. Fu, P. Su, L. Su, Q. Zhang, J. Cai, M. Zhou, Trace FeCu@PC derived from MOFs for ultraefficient heterogeneous electro-Fenton process: Enhanced electron transfer and bimetallic synergy. *ACS EST Eng.* 1 (2021) 1311–1322. https://doi.org/10.1021/acsestengg.1c00131.

[367] T. Hu, F. Deng, H. Feng, J. Zhang, B. Shao, C. Feng, W. Tang, L. Tang, Fe/Co bimetallic nanoparticles embedded in MOF-derived nitrogen-doped porous carbon rods as efficient heterogeneous electro-Fenton catalysts for degradation of organic pollutants. *Appl. Mater. Today.* 24 (2021) 101161. https://doi.org/10.1016/j.apmt.2021.101161.

[368] X. Zhou, D. Xu, Y. Chen, Y. Hu, Enhanced degradation of triclosan in heterogeneous E-Fenton process with MOF-derived hierarchical Mn/Fe@PC modified cathode. *Chem. Eng. J.* 384 (2020) 123324. https://doi.org/10.1016/j.cej.2019.123324.

[369] J. Tang, J. Wang, MOF-derived three-dimensional flower-like FeCu@C composite as an efficient Fenton-like catalyst for sulfamethazine degradation. *Chem. Eng. J.* 375 (2019) 122007. https://doi.org/10.1016/j.cej.2019.122007.

[370] Z. Liang, C. Qu, D. Xia, R. Zou, Q. Xu, Atomically dispersed metal sites in MOF-based materials for electrocatalytic and photocatalytic energy conversion. *Angew. Chem. Int. Ed.* 57 (2018) 9604–9633. https://doi.org/10.1002/anie.201800269.

[371] P. Cao, X. Quan, K. Zhao, S. Chen, H. Yu, Y. Su, High-efficiency electrocatalysis of molecular oxygen toward hydroxyl radicals enabled by an atomically dispersed iron catalyst. *Environ. Sci. Technol.* 54 (2020) 12662–12672. https://doi.org/10.1021/acs.est.0c03614.

[372] A. Gopinath, L. Pisharody, A. Popat, P.V. Nidheesh, Supported catalysts for heterogeneous electro-Fenton processes: Recent trends and future

directions. *Curr. Opin. Sold. St. M.* 26 (2022) 100981. https://doi.org/10.1016/j.cossms.2022.100981.

[373] Y. Liu, C. Kong, L. Liu, X. Jiang, C. Liu, F. Liu, J. Sun, Y. Wang, Progress in copper-based supported heterogeneous electro-Fenton catalysts. *Chem. Eng. J.* 486 (2024) 150217. https://doi.org/10.1016/j.cej.2024.150217.

[374] L. Xu, K. Yan, Y. Mao, D. Wu, Enhancing the dioxygen activation for arsenic removal by Cu^0 nano-shell-decorated nZVI: Synergistic effects and mechanisms. *Chem. Eng. J.* 384 (2020) 123295. https://doi.org/10.1016/j.cej.2019.123295.

[375] J. Ma, N. Jia, C. Shen, W. Liu, Y. Wen, Stable cuprous active sites in Cu^+-graphitic carbon nitride: Structure analysis and performance in Fenton-like reactions. *J. Hazard. Mater.* 378 (2019) 120782. https://doi.org/10.1016/j.jhazmat.2019.120782.

[376] R. Salazar, E. Brillas, I. Sirés, Finding the best Fe^{2+}/Cu^{2+} combination for the solar photoelectro-Fenton treatment of simulated wastewater containing the industrial textile dye Disperse Blue 3. *Appl. Catal. B: Environ.* 115–116 (2012) 107–116. https://doi.org/10.1016/j.apcatb.2011.12.026.

[377] C. Wang, W. Zhang, J. Wang, P. Xia, X. Duan, Q. He, I. Sirés, Z. Ye, Accelerating Fe(III)/Fe(II) redox cycling in heterogeneous electro-Fenton process via S/Cu-mediated electron donor-shuttle regime. *Appl. Catal. B: Environ.* 342 (2024) 123457. https://doi.org/10.1016/j.apcatb.2023.123457.

[378] X. Sun, B. Li, X. Zhang, Y. Xu, J. Zhang, Y. Jiang, Y. Li, Q. Liu, Active-site-transformation-promoted electrochemical H_2O_2 production on carbon-wrapped copper oxides. *CCS Chem.* (2024) 1–12. https://doi.org/10.31635/ccschem.024.202404377.

[379] Y. Liu, X. Wang, X. Lu, D. Wang, W. Li, Y. Fu, W. Qi, Bimetallic center metal–organic framework catalysts for the two-electron oxygen reduction reaction. *ACS Appl. Nano Mater.* 7 (2024) 10137–10143. https://doi.org/10.1021/acsanm.4c00544.

[380] B. Díez, R. Rosal, A critical review of membrane modification techniques for fouling and biofouling control in pressure-driven membrane processes.

Nanotechnol. Environ. Eng. 5 (2020) 15.
https://doi.org/10.1007/s41204-020-00077-x.

[381] A. Bottino, G. Capannelli, A. Comite, C. Costa, R. Firpo, A. Jezowska, M. Pagliero, Treatment of olive mill wastewater through integrated pressure-driven membrane processes. *Membranes* 10 (2020) 334.
https://doi.org/10.3390/membranes10110334.

[382] S. Bolisetty, M. Peydayesh, R. Mezzenga, Sustainable technologies for water purification from heavy metals: review and analysis. *Chem. Soc. Rev.* 48 (2019) 463–487.
https://doi.org/10.1039/C8CS00493E.

[383] M.M. Pendergast, E.M.V. Hoek, A review of water treatment membrane nanotechnologies. *Energy Environ. Sci.* 4 (2011) 1946.
https://doi.org/10.1039/C0EE00541J.

[384] Z. He, Z. Lyu, Q. Gu, L. Zhang, J. Wang, Ceramic-based membranes for water and wastewater treatment. *Colloid. Surface.* A 578 (2019) 123513.
https://doi.org/10.1016/j.colsurfa.2019.05.074.

[385] M. Reig, X. Vecino, J.L. Cortina, Use of membrane technologies in dairy industry: An overview. *Foods* 10 (2021) 2768.
https://doi.org/10.3390/foods10112768.

[386] W. Guo, H.-H. Ngo, J. Li, A mini-review on membrane fouling. *Bioresource Technol.* 122 (2012) 27–34.
https://doi.org/10.1016/j.biortech.2012.04.089.

[387] C. Echevarría, C. Valderrama, J.L. Cortina, I. Martín, M. Arnaldos, X. Bernat, A. De La Cal, M.R. Boleda, A. Vega, A. Teuler, E. Castellví, Hybrid sorption and pressure-driven membrane technologies for organic micropollutants removal in advanced water reclamation: A techno-economic assessment. *J. Clean. Prod.* 273 (2020) 123108.
https://doi.org/10.1016/j.jclepro.2020.123108.

[388] X. Zhang, T. Zhang, J. Ng, D.D. Sun, High-performance multifunctional TiO_2 nanowire ultrafiltration membrane with a hierarchical layer structure for water treatment. *Adv. Funct. Mater.* 19 (2009) 3731–3736.
https://doi.org/10.1002/adfm.200901435.

[389] C. Morgante, X. Ma, X. Chen, D. Wang, V. Boffa, V. Stathopoulos, J. Lopez, J.L. Cortina, A. Cipollina, A. Tamburini, G. Micale, Metal-organic-

framework-based nanofiltration membranes for selective multi-cationic recovery from seawater and brines. *J. Membrane Sci.* 685 (2023) 121941. https://doi.org/10.1016/j.memsci.2023.121941.

[390] M. Sun, X. Wang, L.R. Winter, Y. Zhao, W. Ma, T. Hedtke, J.-H. Kim, M. Elimelech, Electrified membranes for water treatment applications. *ACS EST Eng.* 1 (2021) 725–752. https://doi.org/10.1021/acsestengg.1c00015.

[391] W. Jiang, M.R. Haider, Y. Duan, J. Han, Y. Ding, B. Mi, A. Wang, Metal-free electrified membranes for contaminants oxidation: Synergy effect between membrane rejection and nanoconfinement. *Water Res.* 248 (2024) 120862. https://doi.org/10.1016/j.watres.2023.120862.

[392] X. Li, L. Liu, F. Yang, CFC/PVDF/GO-Fe^{3+} membrane electrode and flow-through system improved E-Fenton performance with a low dosage of aqueous iron. *Sep. Purif. Technol.* 193 (2018) 220–231. https://doi.org/10.1016/j.seppur.2017.11.018.

[393] Z. Lin, L. Liu, C. Zhang, P. Su, X. Zhang, X. Li, Y. Jiao, Emerging conductive ceramic membranes for water purification and membrane fouling mitigation. *Chem. Eng. J.* 493 (2024) 152474. https://doi.org/10.1016/j.cej.2024.152474.

[394] Z. Ye, R. Oriol, C. Yang, I. Sirés, X.-Y. Li, A novel NH_2-MIL-88B(Fe)-modified ceramic membrane for the integration of electro-Fenton and filtration processes: A case study on naproxen degradation. *Chem. Eng. J.* 433 (2022) 133547. https://doi.org/10.1016/j.cej.2021.133547.

[395] L. Zhao, M. Mazzucato, S. Lanzalaco, M. Parnigotto, A. Khan, A. Zitolo, P.L. Cabot, C. Durante, I. Sirés, Boosting the O_2-to-H_2O_2 selectivity using Sn-doped carbon electrocatalysts: Towards highly efficient cathodes for actual water decontamination. *ChemSusChem* 18 (2025) e202401758. https://doi.org/10.1002/cssc.202401758.

[396] L. Zhao, M. Mazzucato, S. Lanzalaco, M. Parnigotto, P.L. Cabot, C. Durante, I. Sirés, Complete antihistamine degradation in wastewater matrix using a metal-free N-doped carbon with superior electrocatalytic performance for in-situ H_2O_2 production. *Sep. Purif. Technol.* 361 (2024)

131590.

[397] P. Xia, L. Zhao, X. Chen, Z. Ye, Z. Zheng, Q. He, I. Sirés, Polymethylhydrosiloxane-modified gas-diffusion cathode for more efficient and durable H_2O_2 electrosynthesis in the context of water treatment. *Appl. Catal. B: Environ.* 343 (2024) 123467. https://doi.org/10.1016/j.apcatb.2023.123467.

[398] L. Zhao, J.A. Padilla, E. Xuriguera, P.L. Cabot, E. Brillas, I. Sirés, Enhanced mineralization of pharmaceutical residues at circumneutral pH by heterogeneous electro-Fenton-like process with Cu/C catalyst. *Chemosphere* 364 (2024) 143249. https://doi.org/10.1016/j.chemosphere.2024.143249.

[399] L. Zhao, M.F. Murrieta, J.A. Padilla, S. Lanzalaco, P.L. Cabot, I. Sirés, Bimetallic FeCu-MOF derivatives as heterogeneous catalysts with enhanced stability for electro-Fenton degradation of lisinopril. *Sci. Total Environ.* 953 (2024) 176110. https://doi.org/10.1016/j.scitotenv.2024.176110.

[400] M. Thommes, K. Kaneko, A.V. Neimark, J.P. Olivier, F. Rodriguez-Reinoso, J. Rouquerol, K.S.W. Sing, Physisorption of gases, with special reference to the evaluation of surface area and pore size distribution (IUPAC Technical Report). *Pure Appl. Chem.* 87 (2015) 1051–1069. https://doi.org/10.1515/pac-2014-1117.

[401] T. Muddemann, D. Haupt, M. Sievers, U. Kunz, Electrochemical reactors for wastewater treatment. *ChemBioEng Rev.* 6 (2019) 142–156. https://doi.org/10.1002/cben.201900021.

[402] Medición del potencial en el contraelectrodo con VIONIC impulsado por INTELLO. (n.d.). https://www.metrohm.com/es_es/applications/application-notes/autolab-applikationen-anautolab/an-ec-027.html (accessed December 6, 2024).

[403] J. Hoyos-Arbeláez, M. Vázquez, J. Contreras-Calderón, Electrochemical methods as a tool for determining the antioxidant capacity of food and beverages: A review. *Food Chem.* 221 (2017) 1371–1381. https://doi.org/10.1016/j.foodchem.2016.11.017.

[404] P.T. Kissinger, W.R. Heineman, Cyclic voltammetry. *J. Chem. Educ.* 60 (1983) 702.

https://doi.org/10.1021/ed060p702.

[405] G. Denuault, M. Sosna, K.-J. Williams, Classical experiments, in: Handbook of Electrochemistry. Elsevier, 2007: pp. 431–469. https://doi.org/10.1016/B978-044451958-0.50024-0.

[406] J. Zhang, H. Zhang, M. Cheng, Q. Lu, Tailoring the electrochemical production of H_2O_2 : Strategies for the rational design of high-performance electrocatalysts. *Small* 16 (2020) 1902845. https://doi.org/10.1002/smll.201902845.

[407] X. Wang, M. Sun, Y. Zhao, C. Wang, W. Ma, M.S. Wong, M. Elimelech, In situ electrochemical generation of reactive chlorine species for efficient ultrafiltration membrane self-cleaning. *Environ. Sci. Technol.* 54 (2020) 6997–7007. https://doi.org/10.1021/acs.est.0c01590.

[408] Y. Zhao, Y. Zhao, X. Yu, D. Kong, X. Fan, R. Wang, S. Luo, D. Lu, J. Nan, J. Ma, Peracetic acid integrated catalytic ceramic membrane filtration for enhanced membrane fouling control: Performance evaluation and mechanism analysis. *Water Res.* 220 (2022) 118710. https://doi.org/10.1016/j.watres.2022.118710.

[409] O. Vieira, R.S. Ribeiro, M. Pedrosa, A.R. Lado Ribeiro, A.M.T. Silva, Nitrogen-doped reduced graphene oxide – PVDF nanocomposite membrane for persulfate activation and degradation of water organic micropollutants. *Chem. Eng. J.* 402 (2020) 126117. https://doi.org/10.1016/j.cej.2020.126117.

[410] Z. Zhang, G. Huang, Y. Li, X. Chen, Y. Yao, S. Ren, M. Li, Y. Wu, C. An, Electrically conductive inorganic membranes: A review on principles, characteristics and applications. *Chem. Eng. J.* 427 (2022) 131987. https://doi.org/10.1016/j.cej.2021.131987.

[411] N. Liu, J. Yang, X. Hu, H. Zhao, H. Chang, Y. Liang, L. Pang, Y. Meng, H. Liang, Fouling and chemically enhanced backwashing performance of low-pressure membranes during the treatment of shale gas produced water. *Sci. Total Environ.* 840 (2022) 156664. https://doi.org/10.1016/j.scitotenv.2022.156664.

[412] C.A. Martínez-Huitle, M.A. Rodrigo, I. Sirés, O. Scialdone, A critical review on latest innovations and future challenges of electrochemical

technology for the abatement of organics in water. *Appl. Catal. B: Environ.* 328 (2023) 122430.
https://doi.org/10.1016/j.apcatb.2023.122430.

[413] Z. He, Z. Lyu, Q. Gu, L. Zhang, J. Wang, Ceramic-based membranes for water and wastewater treatment. *Colloid. Surface A.* 578 (2019) 123513.
https://doi.org/10.1016/j.colsurfa.2019.05.074.

[414] C. Mansas, J. Mendret, S. Brosillon, A. Ayral, Coupling catalytic ozonation and membrane separation: A review. *Sep. Purif. Technol.* 236 (2020) 116221.
https://doi.org/10.1016/j.seppur.2019.116221.

[415] A. Ruiz-García, N. Melián-Martel, I. Nuez, Short review on predicting fouling in RO desalination. *Membranes* 4 (2017) 62.
https://doi.org/10.3390/membranes7040062.

[416] W. Jiang, X. Xia, J. Han, Y. Ding, M.R. Haider, A. Wang, Graphene modified electro-Fenton catalytic membrane for in situ degradation of antibiotic florfenicol. *Environ. Sci. Technol.* 17 (2018) 9972-9982.
https://doi.org/10.1021/acs.est.8b01894.

[417] R. Ren, Y. Jia, C. Li, Y. Liu, Z. Wang, F. Li, F. Qi, A. Ikhlaq, J. Kumirska, E.M. Siedlecka, O. Ismailova, Convective diffusion of oxidants by electro-Fenton membrane drives residual drug removal and membrane self-cleaning. *J. Membr. Sci.* 712 (2024): 123246.
https://doi.org/10.1016/j.memsci.2024.123246.

Publications and Meetings

Publications in scientific indexed journals

[1] Xia, P., Ye, Z., **Zhao, L.**, Xue, Q., Lanzalaco, S., He, Q., Qi, X., Sirés, I. (2023). Tailoring single-atom FeN_4 moieties as a robust heterogeneous catalyst for high-performance electro-Fenton treatment of organic pollutants. *Applied Catalysis B: Environmental*, 322, 122116. IF = 20.3 (Q1).
Doi: https://doi.org/10.1016/j.apcatb.2022.122116

[2] Ye, Z., Zhang, W., Lanzalaco, S., **Zhao, L.**, Sirés, I., Xia, P., Zhai, J., He, Q. (2023). Ultra-uniform MIL-88B (Fe)/Fe_3S_4 hybrids engineered by partial sulfidation to boost catalysis in electro-Fenton treatment of micropollutants: Experimental and mechanistic insights. *Chemical Engineering Journal*, 455, 140757. IF = 13.4 (Q1).
Doi: https://doi.org/10.1016/j.cej.2022.140757

[3] **Zhao, L.**, Murrieta, M. F., Padilla, J. A., Lanzalaco, S., Cabot, P. L., Sirés, I. (2024). Bimetallic FeCu-MOF derivatives as heterogeneous catalysts with enhanced stability for electro-Fenton degradation of lisinopril. *Science of the Total Environment*, 953, 176110. IF = 8.2 (Q1).
Doi: https://doi.org/10.1016/j.scitotenv.2024.176110

[4] **Zhao, L.**, Padilla, J. A., Xuriguera, E., Cabot, P. L., Brillas, E., Sirés, I. (2024). Enhanced mineralization of pharmaceutical residues at circumneutral pH by heterogeneous electro-Fenton-like process with Cu/C catalyst. *Chemosphere*, 364, 143249. IF = 8.1 (Q1).
Doi: https://doi.org/10.1016/j.chemosphere.2024.143249

[5] **Zhao, L.**, Mazzucato, M., Lanzalaco, S., Parnigotto, M., Cabot, P. L., Durante, C., Sirés, I. (2024). Complete antihistamine degradation in wastewater matrix using a metal-free N-doped carbon with superior electrocatalytic performance for in-situ H_2O_2 production. *Separation and Purification Technology*, 361, 131590. IF = 8.2 (Q1).
Doi: https://doi.org/10.1016/j.seppur.2025.131590

[6] Xia, P., **Zhao, L.**, Chen, X., Ye, Z., Zheng, Z., He, Q., & Sirés, I. (2024). Polymethylhydrosiloxane-modified gas-diffusion cathode for more efficient and durable H_2O_2 electrosynthesis in the context of water treatment. *Applied Catalysis B: Environmental*, 343, 123467. IF = 20.3 (Q1).
Doi: https://doi.org/10.1016/j.apcatb.2023.123467

[7] **Zhao, L.**, Mazzucato, M., Lanzalaco, S., Parnigotto, M., Khan, A., Zitolo, A., Cabot, P. L., Durante, C., Sirés, I. (2025). Boosting the O_2-to-H_2O_2 selectivity using Sn-doped carbon electrocatalysts: Towards highly efficient cathodes for actual water decontamination. *ChemSusChem*, 18, e202401758. IF = 7.5 (Q1).
Doi: https://doi.org/10.1002/cssc.202401758

[8] Shaldehi, T. J., **Zhao, L.**, Andreu, T., Rowshanzamir, S., Sirés, I. (2025). Integration of a non-precious pyrolyzed Cu-doped ZIF as an oxygen depolarized cathode in an advanced chlor-alkali electrolyzer. *Electrochimica Acta*, Minor revision. IF = 5.5 (Q1).

[9] **Zhao, L.**, Ye, Z., Lanzalaco, S., Sirés, I. Ceramic membrane-confined FeCu/N-C catalyst for robust flow-through electro-Fenton wastewater treatment. *In preparation*.

Oral presentations in meetings

[1] **L. Zhao**, M. F. Murrieta, J. A. Padilla, S. Lanzalaco, P. L. Cabot, I. Sirés. "Bimetallic FeCu-MOF derivatives as heterogeneous catalysts in electro-Fenton process". *XLIV Reunión del Grupo Especializado de Electroquímica de la Real Sociedad Española de Química y el V Simposio E3 del Mediterráneo*, 3-5 July 2024, Bilbao (Spain).

[2] **L. Zhao**, M. Mazzucato, S. Lanzalaco, A. A. Isse, P. L. Cabot, C. Durante, I. Sirés. "Outstanding N-doped electrocatalysts from melamine pyrolysis for cathodic H_2O_2 production in advanced water treatment". *8th National Conference on Water Treatment and Reuse of China*, 12-14 April 2024, Chengdu (China).

[3] **L. Zhao**, C. Durante, S. Lanzalaco, A. A. Isse, M. Mazzucato, P. L. Cabot, I. Sirés. "Selective electrocatalytic oxygen reduction to H_2O_2 using N-doped

tin-based catalysts at neutral pH". *74th Annual Meeting of the International Society of Electrochemistry*, 3-8 September 2023, Lyon (France).

[4] **L. Zhao**, M. Mazzucato, S. Lanzalaco, A. A. Isse, P. L. Cabot, C. Durante, I. Sirés. "Metal-free gas-diffusion electrode made from melamine-derived N-doped carbon for highly efficient H_2O_2 electrogeneration in water treatment". *XLIII Reunión del Grupo Especializado de Electroquímica de la Real Sociedad Española de Química / VI E3TECH Workshop: Towards Electrochemical Sustainability*, 3-5 July 2023, Ciudad Real (Spain).

[5] **L. Zhao**, R. Brandiele, M. Mazzucato, C. Durante, S. Lanzalaco, P. L. Cabot, E. Brillas, I. Sirés. "Carbon-supported FeCu bimetallic nanoparticles as on-site catalyst for heterogeneous electro-Fenton process". *73rd Annual Meeting of the International Society of Electrochemistry*, 12-16 September 2022, Online.

[6] **L. Zhao**, J. A. Padilla, E. Xuriguera, P.L. Cabot, E. Brillas, I. Sirés. "Use of Cu-MOFs derivatives in electro-Fenton process for water treatment at circumneutral pH: Beyond Fe-based catalysts". *XLII Reunión del Grupo Especializado de Electroquímica de la Real Sociedad Española de Química*, 6-8 July 2022, Santander (Spain).

Poster presentations in meetings

[1] **L. Zhao**, I. Sirés. "Electrocatalytic materials for advanced electro-Fenton treatment of wastewater at natural pH: Preparation of heterogeneous catalysts and enhancement of H_2O_2 production". *4th European School on Environmental Applications of Advanced Oxidation Processes*, 4-6 November 2024, Thessaloniki (Greece).

[2] **L. Zhao**, Z. Ye, S. Lanzalaco, I. Sirés. "Ceramic membrane-confined FeCu/N-C catalyst for robust flow-through electro-Fenton wastewater treatment". *XLIV Reunión del Grupo Especializado de Electroquímica de la Real Sociedad Española de Química y el V Simposio E3 del Mediterráneo*, 3-5 July 2024, Bilbao (Spain).

[3] **L. Zhao**, M. F. Murrieta, C. Salazar, N. Escaja, F. Alcaide, P. L. Cabot, I. Sirés. "Hydroxyl radical-mediated electrolytic depolymerization of lignin".

74th Annual Meeting of the International Society of Electrochemistry, 3-8 September 2023, Lyon (France).

[4] **L. Zhao**, S. Lanzalaco, J. A. Padilla, E. Xuriguera, P. L. Cabot, I. Sirés. "ORR performance of bimetallic FeCu-MOF derivatives at different pH". *XLIII Reunión del Grupo Especializado de Electroquímica de la Real Sociedad Española de Química / VI E3TECH Workshop: Towards Electrochemical Sustainability*, 3-5 July 2023, Ciudad Real (Spain).

[5] Garza, B.R., **Zhao, L.**, Brillas, E., Cabot, P.L., Sirés, I. "Circular approach to the removal of pharmaceutical residues from wastewater using two pyrolyzed MOFs". *4th E3 Mediterranean Symposium: Electrochemistry for Environment and Energy*, 15-17 September 2022, Orvieto (Italy).

[6] B. R. Garza, **L. Zhao**, E. Brillas, P.L. Cabot, I. Sirés. "Regeneración electroquímica de grafeno saturado con fármacos empleando un catalizador heterogéneo magnético". *XLII Reunión del Grupo Especializado de Electroquímica de la Real Sociedad Española de Química*, 6-8 July 2022, Santander (Spain).

[7] J. Garcia-Cardona, **L. Zhao**, I. Sirés, E. Brillas, F. Alcaide, P.L. Cabot. "Catalizadores de PtCu soportados a partir de redes metal-orgánicas". *XLII Reunión del Grupo Especializado de Electroquímica de la Real Sociedad Española de Química*, 6-8 July 2022, Santander (Spain).

[8] **L. Zhao**, J. Garcia-Cardona, P.L. Cabot, E. Brillas, I. Sirés. "Carbon-protected Cu particles as heterogeneous catalyst for electro-Fenton-like degradation of a drug residue in model aqueous solutions". *XXV Meeting of the Sociedad Iberoamericana de Electroquimica*, 3-6 April 2022, Mexico (Online).

[9] **L. Zhao**, J. Garcia-Cardona, P.L. Cabot, E. Brillas, I. Sirés. "Assessing the viability of Cu-MOF and its derivatives for advanced electrochemical water treatment." *Current Trends in Electrochemistry*, which comprises the *41st Meeting of the Electrochemistry Group of the Spanish Royal Society of Chemistry and the 1st French-Spanish Atelier/Workshop on Electrochemistry*, 6-9 July 2021, Paris (France).